Electric field characterization of atmospheric pressure Helium plasma jets through numerical simulations and comparisons with experiments

Pedro Arsénio Nunes Aleixo Viegas

université PARIS-SACLAY

NNT : 2018SACLX061

Thèse de doctorat

Electric field characterization of atmospheric pressure Helium plasma jets through numerical simulations and comparisons with experiments

Thèse de doctorat de l'Université Paris-Saclay
préparée à l'École Polytechnique

École doctorale n°572 Ondes et Matière (EDOM)
Spécialité de doctorat: Physique des Plasmas

Thèse présentée et soutenue à Palaiseau, le 17 Décembre 2018, par

Pedro Arsénio Nunes Aleixo Viegas

Composition du Jury :

M. Jean-Michel Pouvesle Dir. de Recherche CNRS, Université d'Orléans, GREMI, France	Président
Mme. Natalia Babaeva Dir. de Recherche, Joint Institute for High Temperatures, Russian Academy of Sciences	Rapporteur
M. Jean-Hugues Paillol Professeur, Université de Pau et des Pays de l'Adour, SIAME, France	Rapporteur
Mme. Paola Diomede Chercheur, Dutch Institute for Fundamental Energy Research	Examinateur
M. Olivier Guaitella Ing. de Recherche, École Polytechnique, LPP, France	Examinateur
M. Zdenek Bonaventura Chercheur, Masaryk University, Brno, Czech Republic	Examinateur
Mme. Anne Bourdon Dir. de Recherche CNRS, École Polytechnique, LPP, France	Directrice de thèse

Acknowledgments

Firstly, I would like to thank my supervisor, Anne Bourdon, who I've had the pleasure to work with during the last three years at Laboratoire de Physique des Plasmas (LPP). I thank her for the opportunity to work together on this subject and for guaranteeing that I've had all the conditions to proceed with the PhD work. More importantly, I thank her for her patience, guidance and support at every stage of the development of this thesis and for her fundamental contribution to my formation as a modeler and as a researcher.

I thank Jean-Hugues Paillol and Natalia Babaeva for accepting to be reporters of this thesis, as well as all the other members of the jury that have assisted the PhD thesis defense: Jean-Michel Pouvesle, Olivier Guaitella, Paola Diomede and Zdenek Bonaventura. Their questions and remarks at the defense have allowed to have fruitful and interesting discussions.

During the development of this thesis at LPP, I've had the opportunity to work closely with François Péchereau and Zdenek Bonaventura, whose suggestions have helped me understand and develop the numerical model and who have taken the time to have important discussions with me on modeling of atmospheric pressure discharges. I have also had the chance to spend two weeks at the Masaryk Univeristy in Brno, Czech Republic, working in collaboration with Petr Bílek, Adam Obrusník and Zdenek Bonaventura on the coupling of plasma and flow models and on the sensitivity analysis and scheme reduction of plasma chemistry. I thank them for welcoming me, for the good times spent together, for their optimism and good mood and for the important work developed together.

A factor of major importance for the development of this thesis has been the productive collaboration with the experimentalists of LPP and of the Eindhoven University of Technology: Ana Sobota, Elmar Slikboer, Marlous Hofmans and Olivier Guaitella. I thank them for this opportunity. The convergence between experiments and simulations would not have been possible without the regular communication, the mutual effort to understand different points of view and the enthusiasm of Elmar and Olivier. I also appreaciate the opportunities I've had to communicate and learn from the experimentalists at GREMI, Université d'Orléans: Eric Robert, Jean-Michel Pouvesle, Thibault Darny and Xavier Damany.

During the last three years I have had the pleasure to work within a very pleasant environment at LPP. I wish to thank everyone at LPP for making my life easier, the stay enjoyable, work more profitable and my experience richer. I thank all the colleagues in the low-temperature plasma team for the availability to help and discuss, as well as for creating an atmosphere of friendship and comradeship within the team. I am grateful also to the administration and informatics teams of LPP for helping with numerous issues, from conference registrations to computer malfunctions, and to the 'devdej' organizers and participants for motivating me to be more curious about different numerical tools. A special mention goes to Catherine Jégu and Édouard Bouchet, that have helped me countless times, and to Nicolas Marsac, whose help has been immeasurable. I also thank LPP and École Polytechnique for the access to the calculation clusters Hopper and Zoidberg, that have had a crucial role in the development

of this thesis. Finally, I wish to thank those at LPP that are close friends and thus carry great responsibility for my happiness during the last three years: Victor Montagud, Mélissa Menu, Ana Morillo, Pierre Morel, Shaokang Xu, Ozgur Gurcan, Abhyuday Chatterjee, Elmar Slikboer, Polina Ogloblina, Marlous Hofmans, Roberto Martorelli and Jihane Kamil.

I am also grateful to all those involved in my formation before my PhD: from my high-school physics teacher Eduardo Gomes, to all the colleagues and professors at IST in Lisbon and during my stay as Erasmus student in Paris, to the colleagues I've worked with at IPFN-IST and at EM2C-ECP and to my MSc thesis supervisors, professors Vasco Guerra and Luís Alves. I wish to show my gratitude as well to my friend Carla Alves for the help with the 'pôt de thèse'. Finally, I wish to thank the countless friends and relatives outside of LPP supporting and encouraging me during the last three years and throughout life, with a special mention to my girlfriend Susana. I will be forever grateful to my family for the love and support received throughout the years, in particular to my parents Isabel Nunes and Carlos Viegas.

This work has been supported by a French governmental grant attributed by the École Doctorale Ondes et Matière and the École Polytechnique. It has also been done partially within the LABEX Plas@par project, and received financial state aid managed by the Agence Nationale de la Recherche (ANR), as part of the programme "Investissements d'avenir" under the reference ANR-11-IDEX-0004-02.

Résumé

Dans cette thèse de doctorat, un modèle fluide bidimensionnel est utilisé pour caractériser les jets de plasma d'Hélium pulsés. En particulier, les distributions spatiales et temporelles de champ électrique sont analysées pour complémenter des mesures récentes de champ électrique.

Le modèle fluide bidimensionnel axisymmétrique permet de simuler les jets de plasma d'Hélium dans des atmosphères de N_2 et O_2 et leur interaction avec des cibles. Pour décrire le plasma entre la sortie du tube et la cible, l'inhomogenéité spatiale du mélange gazeux est prise en compte en couplant une solution stationnaire d'un calcul d'écoulement avec le modèle instationnaire de décharge. Puis, pour décrire l'interaction entre des décharges positives et des cibles de permittivité élevée, l'équation d'énergie des électrons est discutée et implémentée dans le modèle, avec l'approximation d'énergie moyenne des électrons locale, pour remplacer l'approximation de champ électrique local.

Le rôle du tube sur la propagation et la structure des décharges d'Hélium est étudié. Les résultats des simulations montrent que le confinement mécanique du tube se traduit par une augmentation du champ électrique dans le front de la décharge, des densités d'espèces chargées et de la vitesse de propagation. Avec un tube, les décharges négatives sont plus homogènes et les positives plus filamentaires, à cause des interactions différentes entre les décharges positives et négatives avec le tube diélectrique.

La propagation d'un jet de plasma dans un mélange gazeux inhomogène entre la sortie du tube diélectrique et une cible a été étudiée. Dans nos conditions standard, nous avons démontré que les mécanismes de propagation les plus importants sont l'ionisation par impact électronique de He et de N_2/O_2 et l'ionisation Penning, même si ce dernier processus n'est pas crucial pour la détermination de la structure de la décharge. Les résultats de simulation montrent que l'impact le plus important du couplage plasma-écoulement sur la décharge est dû à la prise en compte d'un mélange variable dans les termes sources de chimie, à la fois pour les densités du mélange et pour les coefficients de réaction.

La dynamique des décharges dans les jets d'Hélium impactant une cible métallique à la masse est analysée pour les polarités de tension appliquée positive et négative. Les résultats des simulations montrent qu'un premier front d'ionisation se propage de l'électrode haute tension vers la cible métallique à la masse, et puis, dans le canal conducteur formé entre les deux électrodes, un front de rebond se propage de la cible vers l'électrode haute tension, avec les mêmes caractéristiques que celles reportées dans les travaux expérimentaux. Nous avons également montré que le front de rebond se propage comme une onde de neutralisation avec une polarité inverse par rapport à celle du premier front d'ionisation. L'effet combiné des deux fronts augmente la formation des espèces chimiquement actives près de la cible après l'impact.

L'interaction entre des jets de plasma d'Hélium positifs et différentes cibles est simulée pour étudier l'influence des propriétés électriques de la cible sur la dynamique de la décharge. Nous avons montré que les cibles diélectriques de forte permittivité sont favorables au rebond et que les cibles de faible permittivité sont favorables à l'étalement radial sur la surface de la cible. De plus, les conditions de simulation pour modéliser une cible métallique à potentiel flottant sont proposées et l'interaction de la décharge avec des cibles métalliques à potentiel flottant est éxaminée et comparée aux cas de cibles diélectrique flottante et métallique à la masse.

En polarité positive et avec différentes cibles, la dynamique des charges et des champs électriques est analysée à la fin du pulse de tension. Quand la tension appliquée chute, une redistribution de potentiel électrique dans le canal s'impose, ce qui est parfois appelé dans la litérature 'back discharge'. Quand le potentiel appliqué est égal à zéro et le plasma n'est pas complètement neutralisé, un champ électrique en sens inverse subsiste dans le plasma. Nous avons montré que dans les cas étudiés cette redistribution de potentiel à la fin du pulse consiste dans une redistribution des charges de volume et surface qui neutralise le plasma complètement sans ionisation ou propagation d'une onde ou d'un front.

L'interaction plasma-cible entre un jet de plasma d'Hélium pulsé positif et une cible diélectrique BSO a été examinée en détail et les résultats ont été comparés directement avec les expériences. Le focus est mis sur les évolutions des densités des charges en volume ρ et des charges en surface σ et leur contributions au champ électrique total et la comparaison directe du champ électrique dû à σ moyenné dans la cible ($E_{zav\sigma}$) avec le champ électrique mesuré par polarimétrie Mueller. Cette étude numérique a permis de compléter l'information obtenue expérimentalement pour mieux comprendre les interactions plasma-cible qui sont cruciales pour beaucoup d'applications des jets de plasma à pression atmosphérique.

Abstract

In this PhD thesis numerical simulations based on a two-dimensional fluid model are used to characterize pulsed Helium plasma jets. In particular, the spatial and temporal distributions of electric field are analyzed to complement the information obtained from recent electric field measurements.

The two-dimensional axisymmetric fluid model for Helium plasma jets allows to describe He jets flowing in N_2 and O_2 atmospheres and interacting with targets. To describe the plasma in the tube-target gap, the spatial inhomogeneity of the gas mixtures is taken into account by coupling the static solution of flow calculations to the transient discharge model. Then, in order to describe the interaction between positive discharges and targets of high permittivity, the electron energy equation is discussed and implemented in the model, along with the local mean electron energy approximation, that replaces the local electric field approximation.

The role of the tube in He discharge propagation and structure is studied. It is shown that the mechanical confinement induced to a He discharge by the introduction of a tube leads to an increase of electric field on the discharge front, charged species densities and velocity of propagation. With tube, the negative discharges are more homogeneous and the positive ones more filamentary. It is demonstrated that the source of those differences is mostly the different type of interaction between positive and negative discharges with the dielectric tube.

Plasma jet configurations where the discharge propagates between a tube and a target in a spatially inhomogeneous gas mixture are considered and the mechanisms defining the path of propagation of the discharge front are investigated. In our standard conditions, it is demonstrated that the most important propagation mechanisms are electron-impact direct ionization of both He and N_2/O_2 and Penning ionization, even though this last process is not crucial for the determination of the discharge structure. It is also proved that the most important aspect in the plasma-flow coupling in regions with He and small admixtures of N_2 or O_2 is the consideration of the variable mixture in the chemistry source terms, both as densities and as rate coefficients.

The discharge dynamics in He jets impacting a grounded metallic target is analyzed with both positive and negative polarities of applied voltage. It is shown that a first ionization front propagates from the powered electrode towards the grounded metallic target and then, in the conductive channel formed between both metallic electrodes, a rebound front propagates from the target to the powered electrode, with the same characteristics as those reported from experimental results. It is demonstrated that the rebound front propagates as a neutralization wave with reverse polarity with respect to the first ionization front. The combined effect of the two fronts increases the densities of chemically active species close to the target after the impact.

The interaction between positive He jets and different targets is simulated to investigate the influence of the electrical character of the target on the discharge dynamics. It is shown that the presence and intensity of the rebound are directly related to the electric potential on the target surface after the impact and thus to the drop of potential in the plasma channel and between the plasma and the target. Hence, high target permittivity is favorable to the rebound and low target permittivity is favorable to discharge spreading radially on the target surface. Moreover, the simulation conditions to model a metallic target at floating potential are proposed and the character of the discharge interaction with metallic targets at floating potential is examined.

With positive polarity and different targets, the dynamics of charges and electric fields is analyzed at the end of a pulse of applied voltage. When the applied voltage falls, a redistribution of electric potential in the channel is imposed, which is sometimes called in the literature 'back discharge'. While the applied voltage is zero and the plasma is not completely neutralized, an electric field of reverse direction subsists in the plasma and in the plasma-target interface. It is shown that in the cases under study this redistribution of potential at the end of the pulse consists in a redistribution of surface and volume charges that neutralizes the plasma completely without ionization or propagation as a wave or front.

The plasma-target interaction occurring between a positive pulsed Helium plasma jet and a BSO dielectric target is investigated in detail and results are directly compared with experiments. Focus is put on the evolution of volume charge density ρ and surface charge density σ and of their electric field contributions and direct comparison of electric field due to σ averaged inside the target ($E_{zav\sigma}$) with the electric field measured by Mueller polarimetry. This numerical investigation allows to complement the information obtained experimentally to better understand plasma-target interactions that are crucial for many applications of atmospheric pressure plasma jets.

List of Publications

In the scope of this PhD thesis, two articles have been published in international journals with peer-review:

- P. Viegas, F. Pechereau, and A. Bourdon (2018), Numerical study on the time evolutions of the electric field in helium plasma jets with positive and negative polarities, *Plasma Sources Sci. Technol.*, **27** (025007)

- P. Viegas, E. Slikboer, A. Obrusník, Z. Bonaventura, A. Sobota, E. Garcia-Caurel, O. Guaitella, and A. Bourdon (2018), Investigation of a plasma–target interaction through electric field characterization examining surface and volume charge contributions: modeling and experiment, *Plasma Sources Sci. Technol.*, **27** (094003)

Contents

Acknowledgments . . . iii
Résumé . . . v
Abstract . . . vii
List of Publications . . . ix
Table of Contents . . . xi
List of Tables . . . xv
List of Figures . . . xvii
Nomenclature . . . xxv

I Introduction and state of the art **1**
I.1 Low-temperature atmospheric pressure plasma jets . . . 2
I.1.1 Low-temperature atmospheric pressure plasmas . . . 2
I.1.2 Helium plasma jets and applications . . . 2
I.2 Physics and chemistry of plasma jets . . . 4
I.2.1 Mechanisms of streamer propagation . . . 4
I.2.2 Discharge dynamics inside dielectric tubes . . . 6
I.2.3 Influence of admixtures to the buffer gas inside the tube on discharge dynamics . . . 7
I.2.4 Discharge dynamics in the plasma plume . . . 9
I.2.5 Influence of the polarity of applied voltage . . . 11
I.3 Interactions between plasma jets and dielectric and metallic targets . . . 12
I.3.1 Discharge interaction with metallic targets and the rebound front . . . 15
I.3.2 Discharge interaction with dielectric targets . . . 17
I.4 Electric Field characterization of plasma jets . . . 18
I.4.1 Optical measurements of electric field . . . 18
I.4.2 Electric field measurements through electro-optic probes and laser diagnostic techniques . . . 19
I.4.3 Electric field measurements through Mueller polarimetry . . . 20
I.5 Memory effects and flow channeling in repetitive plasma jets . . . 21
I.5.1 Initial conditions for discharge repeatability . . . 22
I.5.2 Plasma jet effect on flow . . . 22
I.6 Motivations and plan of this thesis . . . 25

II Numerical model for Helium plasma jets at atmospheric pressure 27
II.1 Introduction . . . 28
II.2 Physical model for Helium discharges at atmospheric pressure . . . 28
II.2.1 Plasma characteristics . . . 28
II.2.2 Discharge model . . . 29
II.3 Two-dimensional axisymmetric fluid model for Helium discharges . . . 31
II.3.1 Introduction . . . 31
II.3.2 Conservation equations . . . 32
II.3.3 Poisson's equation and determination of charge contributions to the electric field distribution . . . 37
II.3.4 Reaction scheme, initial conditions, rate coefficients, photo-ionization and transport parameters . . . 39
II.4 Modeling of plasma jets with flowing He-N_2 and He-O_2 gas mixtures . . . 42
II.4.1 Introduction . . . 42
II.4.2 Investigation and implementation of chemistry models . . . 43
II.4.3 Coupling of flow calculations with the plasma model . . . 51
II.4.4 Code parallelization and profiling . . . 54
II.4.5 Study of the electron energy equation and the mean electron energy approximation . . . 56
II.5 Simulation conditions . . . 62

III General characterization of Helium plasma jets through numerical simulations 63
III.1 Introduction . . . 64
III.2 Role of the dielectric tube on discharge propagation in positive and negative polarities . . . 64
III.2.1 Introduction . . . 64
III.2.2 Studied conditions . . . 65
III.2.3 General characterization of Helium discharge propagation without tube 67
III.2.4 Influence of the mechanical confinement of the tube on discharge propagation in positive and negative polarities . . . 71
III.2.5 Role of the tube permittivity on discharge propagation . . . 78
III.2.6 Influence of the secondary electron emission on the mechanical confinement of the tube for positive polarity . . . 80
III.2.7 Conclusions . . . 83
III.3 Influence of the electrode geometry on discharge propagation . . . 83
III.4 Influence of the shape of the applied voltage on discharge propagation in short tubes . . . 86
III.5 Dynamics of propagation of He discharges with N_2 and O_2 admixtures inside dielectric tubes . . . 88
III.6 Discharge propagation in the plasma plume . . . 93
III.6.1 Introduction . . . 93
III.6.2 Studied conditions . . . 93
III.6.3 Influence of flow and tube-target distance on discharge dynamics . . . 95

III.6.4 Effect of the polarity of the applied voltage on the discharge dynamics in the plasma plume . . . 97
III.6.5 Discharge propagation mechanisms in the plasma plume . . . 100
III.6.6 Role of each property of the gas mixing in the plasma plume on discharge dynamics . . . 105
III.6.7 Conclusions . . . 109
III.7 Conclusions . . . 110

IV Study of a plasma jet interacting with a grounded metallic target: comparison with experiments 111
IV.1 Introduction . . . 112
IV.2 Studied conditions to comply with experiments . . . 113
IV.3 Dynamics of discharge propagation inside a dielectric tube closed by a grounded metallic target . . . 115
IV.4 Influence of the discharge dynamics on the electric field outside the dielectric tube: comparison with experiments . . . 122
IV.5 Rebound front as ionization wave of partial neutralization of the plasma channel 125
IV.6 Derivation of discharge properties from the electric field outside the dielectric tube: how simulations can complement experiments . . . 128
IV.7 Dynamics of first ionization and rebound fronts in plasma jet configurations and influence on the production of reactive species . . . 133
IV.8 Conclusions . . . 138

V Discharge interaction with targets of different electrical character 139
V.1 Introduction . . . 140
V.2 Modeling of the discharge interaction with different targets . . . 141
V.2.1 Experimental diagnostics . . . 141
V.2.2 Simulation conditions . . . 142
V.2.3 Model used for a metallic target at floating potential . . . 144
V.3 Influence of the permittivity of the dielectric target on the discharge dynamics 145
V.3.1 Model used for a dielectric target . . . 145
V.3.2 Influence of the permittivity of the dielectric target on the discharge dynamics . . . 149
V.4 Influence of the electrical character of the target on the discharge dynamics . . 152
V.4.1 Propagation dynamics for different targets . . . 152
V.4.2 Post-impact dynamics for different targets . . . 154
V.4.3 End of pulse dynamics for different targets . . . 157
V.5 Conclusions . . . 161

VI Electric field characterization of He plasma jets interacting with a floating dielectric target: comparison with experiments 163
VI.1 Introduction . . . 164
VI.2 Previous studies of electric field in plasma-target interaction . . . 165
VI.3 Electric field distribution in plasma-dielectric target interaction . . . 169
VI.3.1 Studied conditions to comply with experiments . . . 169

VI.3.2 Electric field distribution in plasma-dielectric target interaction and comparison with experiments . . . 171
VI.3.3 Analysis of the electric field inside the target . . . 177
VI.4 Conclusions . . . 181

VII Conclusions and prospects for future research **183**
VII.1 Contributions of this thesis . . . 183
VII.2 Prospects for future research . . . 186

A Key results from *Bourdon et al.* [2016] **191**

B Influence of electrode geometry on the Laplacian distribution of electric field **193**

C Solution of a chemistry problem with coupled rate coefficient calculation against an exact stationary solution **195**

D He-O_2 reaction scheme for atmospheric pressure plasmas from *Liu et al.* [2010] **199**

E Key results from *Viegas et al.* [2018a] **207**

F Positive discharge interaction with dielectric targets with He-N_2 and He-O_2 mixtures **209**

G Effect of the magnitude of the applied voltage on the electric field distribution in positive plasma-dielectric target interaction **211**
G.1 Dynamics of discharge propagation . . . 211
G.2 Electric field inside the target . . . 214
G.3 Conclusions . . . 216

Bibliography **217**

List of Tables

II.1 Table of He-N_2 reactions. 49

III.1 Impact time and average velocity of propagation with the several gas-mixtures. 92

IV.1 Comparison of ρ/σ_{av} obtained from the simulation results with ρ/σ_{fit} obtained from fitting $E_r(r)$ outside the tube, for $V_P = +6$ kV and $V_P =$ -6 kV. 132

G.1 Relationship between maximum $E_z(r = 0)$ in the plume, inside the target, inside the target exclusively due to σ and the maximum $\sigma(r = 0)$ for each case of applied voltage. 216

List of Tables

List of Figures

I.1 Jet propagation in long tubes and application in the plasma plume. 3
I.2 Schematics of positive streamer propagation. 5
I.3 Role of photo-ionization source term in positive streamer propagation. 5
I.4 Ring shape of the electron density and ionization source term of discharge propagation in *Boeuf et al.* [2013]. 10
I.5 Image plots of normalized N_2(C-B) radiation intensity for positive and negative voltage polarity from *Naidis* [2011a]. 12
I.6 Plume interaction with different targets from *Darny et al.* [2016]. 13
I.7 End-of-pulse discharge from *Yue et al.* [2018]. 15
I.8 Retrun stroke from *Klarenaar et al.* [2018]. 16
I.9 Radial profiles of electric field components inside a dielectric target from *Slikboer et al.* [2018b]. 21
I.10 Helium channeling dynamics as a function of the number of voltage pulses for negative polarity from *Darny et al.* [2017a]. 24

II.1 Representation of the numerical grid with control volumes. 33
II.2 Evolution of μ_e, D_e and associated time-steps with the electric field magnitude. 42
II.3 Electron-impact ionization coefficients in He-N_2 mixtures. 44
II.4 Input reduced electric field in the zero-D model and results for He-O_2. 46
II.5 Zero-D model results for He-O_2. 47
II.6 Zero-D model results for He-N_2. 47
II.7 Example of BOLSIG+ output and generated function. 50
II.8 Example of reaction declaration in "kinet.inp". 50
II.9 Example of source terms generated by the parser. 51
II.10 Model set-up before and after coupling with the flow calculations. 53
II.11 Code profiling: Time per iteration. 55
II.12 Code profiling: Speed-up. 55
II.13 Numerical problem when a grounded ring is wrapped around the tube. . . . 56
II.14 Evolution of time-steps with the mean electron energy. 59
II.15 Comparison of results with LFA and LMEA. 60
II.16 Comparison of results with LMEA with and without grounded ring wrapped around the tube. 61

II.17 Axial profiles of surface charge density at several times, with LMEA and grounded ring wrapped around the tube. 62

III.1 Side view schematics of the discharge set-ups used in section III.2. 66
III.2 Cross sectional views of the magnitude of the electric field, for a 2 cm long domain without tube with a grounded target for $V_P = +4$ kV. 67
III.3 Cross sectional views of the magnitude of the electric field, for a 2 cm long domain without tube with a grounded target for $V_P = -4$ kV. 68
III.4 Cross sectional views of the electron density, for a 2 cm long domain without tube with a grounded target for $V_P = +4$ kV. 69
III.5 Cross sectional views of ρ, E_z, E_r and S_e, for a 2 cm long domain without tube with a grounded target for $V_P = +4$ kV. 69
III.6 Axial velocity of propagation and magnitude of $|E_z|_{MAX}$ between the powered electrode and the target, for a 2 cm long domain without tube with a grounded target for both polarities. 70
III.7 Axial profiles of V at $r = 0$, at several times, for a 2 cm long domain without tube with a grounded target for both polarities. 71
III.8 Cross sectional views of the magnitude of the electric field, for a 2 cm long tube with $r_{in} = 2$ mm and $\epsilon_r = 1$, closed by a grounded target for $V_P = +4$ kV. 72
III.9 Cross sectional views of the magnitude of the electric field, for a 2 cm long tube with $r_{in} = 2$ mm and $\epsilon_r = 1$, closed by a grounded target for $V_P = -4$ kV. 73
III.10 Cross sectional views of ρ, E_z, E_r and n_e, for a 2 cm long tube with $r_{in} = 2$ mm and $\epsilon_r = 1$, closed by a grounded target for $V_P = +4$ kV. 74
III.11 Cross sectional views of ρ, E_z, E_r and n_e, for a 2 cm long tube with $r_{in} = 2$ mm and $\epsilon_r = 1$, closed by a grounded target for $V_P = -4$ kV. 75
III.12 Axial profiles of σ on the tube walls at $r_{in} = 2$ mm, at several times, for a 2 cm long tube closed by a grounded target, for both polarities. 76
III.13 Radial profiles of n_e and n_i, for a 2 cm long domain, with and without tube and with a grounded target, for both polarities. 77
III.14 $|E_z|_{MAX}$ along the propagation between the powered electrode and the target, for a 2 cm long domain, with and without tube and with a grounded target, for both polarities. 78
III.15 Cross sectional views of the magnitude of the electric field, for a 2 cm long tube with $r_{in} = 2$ mm and $\epsilon_r = 4$, closed by a grounded target for $V_P = +4$ kV. 79
III.16 Cross sectional views of the magnitude of the electric field, for a 2 cm long tube with $r_{in} = 2$ mm and $\epsilon_r = 4$, closed by a grounded target for $V_P = -4$ kV. 80
III.17 Cross sectional views of ρ, E_z, E_r and n_e, for a 2 cm long tube with $r_{in} = 2$ mm, $\epsilon_r = 1$ and a Neumann BC for the electron flux, closed by a grounded target for $V_P = +4$ kV. 81
III.18 Radial profiles of n_e, n_i and n_ρ and axial profiles of σ, for a 2 cm long tube with $r_{in} = 2$ mm, $\epsilon_r = 1$ and a Neumann BC for the electron flux, closed by a grounded target for $V_P = +4$ kV. 82
III.19 Side view schematics of the discharge set-ups used in section III.3. 84
III.20 Cross sectional views of n_e at a time of arrival on the target, with $V_P = +4$ kV and with the different electrode configurations. 85

III.21 Axial profiles of σ at the instant of impact on the target, with V_P = +4 kV and with the different electrode configurations. 86
III.22 Temporal profiles of the discharge velocity of propagation and of the pulses of applied voltage with the different shapes used in section III.4. 87
III.23 Cross-sectional views of species densities at t = 150 ns for 99% He - 1 % N_2 mixture. 89
III.24 Cross-sectional views of species densities at t = 150 ns for 99% He - 1 % O_2 mixture. 90
III.25 Cross-sectional views of species densities at t = 150 ns for 99% He - 1 % O_2 mixture. 90
III.26 Cross-sectional views of electron densities at t = 150 ns for six different gas-mixtures. 92
III.27 Side-view schematics of the discharge set-ups used in section III.6, with 2 slm of He flowing into a N_2 atmosphere. 94
III.28 Cross sectional views of the electron-impact ionization source term, for a 1 cm long tube with 2.5 cm tube-target distance, 2 slm flow of He into N_2 atmosphere and V_P = -6 kV. 96
III.29 Cross sectional views of the electron-impact ionization source term, for different tube lengths and tube-target distances, with 2 slm of He flowing into N_2 atmosphere and V_P = -6 kV. 97
III.30 Cross sectional views of S_e, S_p, E_t and n_e, for V_P = +6 kV and V_P = -6 kV during propagation in the plasma plume. 98
III.31 Cross sectional views of S_e, S_p, E_t and n_e, for V_P = +6 kV and V_P = -6 kV at arrival on the target. 99
III.32 Cross sectional views of E_t and n_e, for a 1.5 cm long tube with 1.0 cm tube-target distance, 2 slm flow of He into N_2 atmosphere and V_P = +4 kV. . 101
III.33 Cross sectional views of the ionization source terms through electron-impact and photoionization, for a 1.5 cm long tube with 1.0 cm tube-target distance, 2 slm flow of He into N_2 atmosphere and V_P = +4 kV. 102
III.34 Cross sectional views of the electron-impact direct and stepwise He ionization source terms, for a 2.5 cm long tube with 1.0 cm tube-target distance, 2 slm flow of He into N_2 and O_2 atmospheres and V_P = +6 kV. 103
III.35 Cross sectional views of the electron-impact N_2 and O_2 ionization source terms, for a 2.5 cm long tube with 1.0 cm tube-target distance, 2 slm flow of He into N_2 and O_2 atmospheres and V_P = +6 kV. 103
III.36 Cross sectional views of the Penning and associative ionization source terms, for a 2.5 cm long tube with 1.0 cm tube-target distance, 2 slm flow of He into N_2 and O_2 atmospheres and V_P = +6 kV. 104
III.37 Cross sectional views of the recombination and attachment loss terms, for a 2.5 cm long tube with 1.0 cm tube-target distance, 2 slm flow of He into N_2 and O_2 atmospheres and V_P = +6 kV. 105
III.38 Cross sectional views of the total ionization source term, for several mixing conditions, 0.5 slm flow of He into N_2 atmosphere and V_P = +6 kV. 107

III.39 Cross sectional views of the total ionization source term, for several conditions of plasma-flow coupling, with 0.5 slm flow of He into N_2 atmosphere and V_P = +6 kV. 108

IV.1 Experimental set-up and results of $E_z(t)$ and $E_r(t)$ from *Darny et al.* [2017b]. 112
IV.2 Side view schematics of the discharge set-ups used in chapter IV. 115
IV.3 Cross sectional views of the magnitude of the electric field, for a 3 cm long tube closed by a grounded target for V_P = +6 kV. 116
IV.4 Cross sectional views of the magnitude of the electric field, for a 3 cm long tube closed by a grounded target for V_P = -6 kV. 117
IV.5 Cross sectional views of the electron-impact ionization source term, for a 3 cm long tube closed by a grounded target for V_P = +6 kV. 118
IV.6 Cross sectional views of the electron-impact ionization source term, for a 3 cm long tube closed by a grounded target for V_P = -6 kV. 119
IV.7 Temporal profiles with ns resolution of the axial position of the maximum axial component of electric field $|E_z|$ on the symmetry axis ($r = 0$). 119
IV.8 Temporal profiles of the axial component of electric field E_z on the symmetry axis ($r = 0$), for V_P = +6 kV and V_P = -6 kV. 120
IV.9 Axial profiles of the surface charge density σ deposited on the tube inner wall. 121
IV.10 Temporal profiles of the axial component of electric field E_z on the symmetry axis at $r = 0$ and outside the tube at $r = 0.6$ cm. 122
IV.11 Temporal profiles of the axial component E_z and radial component E_r of electric field outside the tube at $r = 0.6$ cm. 123
IV.12 Temporal profiles of E_r and E_z outside the tube at $r = 0.6$ cm, and its three contributions: Laplacian, from ρ and from σ. 124
IV.13 Comparison of the time evolution of the radial component of electric field E_r at $r = 0.6$ cm, for 3 cm and 5 cm long tubes closed by a grounded target. . . . 125
IV.14 Side view schematics of the rebound discharge dynamics described in chapter IV. 126
IV.15 Axial profiles of the electric potential V on the symmetry axis ($r = 0$) before and after the rebound and its three contributions: Laplacian, from ρ and from σ. 127
IV.16 Radial profiles of the electric field components at $z = 1$ cm and several times, for a 3 cm long dielectric tube closed by a grounded target. 128
IV.17 Radial profiles of the radial component of electric field E_r and of its three contributions: Laplacian, from ρ and from σ. 130
IV.18 Axial profiles of the surface and volume nt charge densities, along with their averages through the tube length. 131
IV.19 Radial profiles of the radial component of electric field E_r at $z = 1$ cm with the radial mesh spatial resolution, and fit to equations IV.2 and IV.3. 132
IV.20 Cross sectional views of the magnitude of the electric field at t = 40, 130, 178 and 185 ns, for a 2.5 cm long tube and a 0.5 cm tube-target distance, for V_P = +6 kV. 133

IV.21 Cross sectional views of the magnitude of the electric field at t = 30, 141, 202 and 220 ns, for a 2.5 cm long tube and a 0.5 cm tube-target distance, for V_P = -6 kV. 134
IV.22 Temporal profiles of the axial component of electric field E_z on the symmetry axis ($r = 0$) and at z = 0.25, 1.0 and 1.75 cm, for the same conditions as in Figures IV.20 and IV.21. 135
IV.23 Temporal profiles of the density of electrons on the axis of symmetry ($r = 0$) at z = 0.25 cm and z = 1.0 cm, for a 2.5 cm long tube with 0.5 cm target-tube distance for He-N_2 and He-O_2 mixtures. 136
IV.24 Temporal profiles of the density of metastable He(2^3S,2^1S) on the axis of symmetry ($r = 0$) at z = 0.25 cm and z = 1.0 cm, for a 2.5 cm long tube with 0.5 cm target-tube distance for He-N_2 and He-O_2 mixtures. 137

V.1 Jet design used in the experiments, with floating target. 141
V.2 Imaging of light emission showing the discharge propagation between the end of the capillary tube and the target. 142
V.3 Side view schematics of the discharge set-up used in the simulations in chapter V. 143
V.4 Cross sectional views of the electron density, for several conditions of discharge interaction with a dielectric target, with V_P = +4 kV. 146
V.5 Cross sectional views of n_e, S_e and E_t, for several conditions of discharge interaction with a dielectric target, with V_P = +4 kV. 147
V.6 Cross sectional views of the magnitude of electric field E_t, at several times, for the cases with floating dielectric targets of $\epsilon_r = 4$ and $\epsilon_r = 40$ and with V_P = +6 kV. 149
V.7 Temporal profiles of $|E_z|_{MAX}$, E_{rMAX}, $\sigma(r = 0)$ and Q, for two floating dielectric targets with $\epsilon_r = 4$ and $\epsilon_r = 40$, with V_P = +6 kV. 150
V.8 Temporal profiles of E_z and axial profiles of V, for two floating dielectric targets with $\epsilon_r = 4$ and $\epsilon_r = 40$, with V_P = +6 kV. 151
V.9 Cross sectional views of the magnitude of the electric field, for a 1 cm length plume and several targets, with V_P = +4 kV. 153
V.10 Velocity of propagation and $|E_z|_{MAX}$ at $r = 0$ between the powered electrode and the target, for floating dielectric, floating metallic and grounded metallic targets and V_P = +4 kV. 154
V.11 Temporal profiles of E_z at $r = 0$ and z = 0.25 cm and of E_r at r = 0.6 cm and z = 0.25 and 1.0 cm, for floating dielectric, floating metallic and grounded metallic targets and V_P = +4 kV. 155
V.12 Axial profiles of V at $r = 0$, at several times, for floating dielectric, floating metallic and grounded metallic targets and V_P = +4 kV. 156
V.13 Axial profiles of V at $r = 0$, at several times, for floating dielectric, floating metallic and grounded metallic targets and V_P = +4 kV. 158
V.14 Temporal profiles of E_z at $r = 0$ and at z = 0.25 and 2.5 cm, after the rebound propagation, for floating dielectric, floating metallic and grounded metallic targets and V_P = +4 kV. 159

V.15 Temporal profiles of E_r at $r = 0.6$ cm and at $z = 0.25$ and 2.5 cm, after the rebound propagation, along with its charge contributions, for floating dielectric target and $V_P = +4$ kV. 159
V.16 Cross sectional views of the electron-impact ionization source term at the end of the pulse of applied voltage, for the case with a floating dielectric target and with $V_P = +4$ kV. 160

VI.1 The obtained electric field patterns (axial E_z and radial E_x and E_y) inside the electro-optic target (top-view), due to σ deposited by the ionization wave, for $V_P = +4$ kV. The pulse ends at $t_d = 1$ μs. Afterwards, a different color scale is used. Figure from *Viegas et al.* [2018b]. 166
VI.2 Temporal evolutions of radial position of the discharge front on the target and of the axial component of electric field measured inside the target at $r = 0.$ 167
VI.3 Temporal profiles of the axial component of electric field E_z at $r = 0.0$ mm in the plasma plume at $z = 0.4$ mm and inside the dielectric target, averaged through its thickness. 168
VI.4 Side view schematics of the discharge set-up used in the simulations in section VI.3. 170
VI.5 Cross sectional views of n_e, E_t and S_e when the discharge front reaches the target. 172
VI.6 Cross sectional views of the volume charge density and of the magnitude of the axial and radial components of electric field during plasma-dielectric interaction. 173
VI.7 Radial profiles of the surface charge density deposited on the dielectric target surface. 174
VI.8 Cross sectional views of the ρ and σ contributions to E_z and E_r during plasma-dielectric interaction. 175
VI.9 Temporal profiles of the σ contribution to the electric field components, averaged inside the target: Simulation and experimental results. 177
VI.10 Radial profile of E_z at $z = 0$ and $t = 1000$ ns, along with its σ contribution at the same position and averaged inside the target. 178
VI.11 Radial profile of E_r at $z = 0$ and $t = 1000$ ns, along with its σ contributions at the same position and averaged inside the target. 179
VI.12 Axial profiles of E_z and E_r at $r = 1.5$ mm and $t = 1000$ ns, along with their ρ and σ contributions. 179
VI.13 Temporal profiles of $E_{z\sigma}$, $E_{zav\sigma}$, σ and Q and the ratios between them. . . . 181

VII.1 Temporal profiles of electron temperature and electron density. 190

A.1 Discharge front propagation velocity as function of distance from the ring electrode for different conditions from *Bourdon et al.* [2016]. 191
A.2 Discharge front propagation velocity and ignition times for different preionization values from *Bourdon et al.* [2016]. 192
A.3 Ionization front velocity and ignition times for different He-N_2 mixtures from *Bourdon et al.* [2016]. 192

B.1 Axial profiles of Laplacian V and E_z at $r = 0$ with applied voltage +4 kV, with the different electrode configurations presented in section III.3. 193
B.2 Axial profiles of Laplacian V and E_z at $r = 1.5$ mm with applied voltage +4 kV, with the different electrode configurations presented in section III.3. . . . 194
B.3 Radial profiles of Laplacian V and E_r at $z = 1.45$ cm with applied voltage +4 kV, with the different electrode configurations presented in section III.3. . 194

C.1 Analytical rate coefficients and solution given in the proposal. 196
C.2 Relative errors of the rate coefficients calculated considering a Boltzmann EEDF. 196
C.3 Relative errors of the solution considering exact rate coefficients and time of convergence. 197
C.4 Relative errors of the solution considering exact rate coefficients and time of convergence. 198
C.5 Relative errors of the solution considering calculated rate coefficients. 198

D.1 Table of He-O_2 reactions from *Liu et al.* [2010]. 206

E.1 Cross sectional views of the magnitude of the electric field at $t = 40$, 129, 171 and 180 ns, for a 2.5 cm long tube with 0.5 cm target-tube distance (i.e. $x_{target} = 0.0$ cm and $x_{tube} = 0.5$ cm) for a 99% He - 1% N_2 mixture and $V_P =$ +6 kV. 207
E.2 Temporal profiles of the axial component of electric field E_x on the symmetry axis ($r = 0.0$ cm) and at $x = 0.25$, 1.0 and 1.75 cm, for the same conditions as in Figure E.1, for $V_P = +6$ kV and $V_P =$ -6 kV. 208
E.3 Temporal profiles of the density of metastable He(2^3S,2^1S) on the axis of symmetry ($r = 0.0$ cm) at $x = 0.25$ cm and $x = 1.0$ cm, for a 2.5 cm long tube with 0.5 cm target-tube distance (i.e. $x_{target} = 0.0$ cm and $x_{tube} = 0.5$ cm) for He-N_2 and He-O_2 mixtures. 208

F.1 Spatial distributions of n_e with He-N_2 and He-O_2 mixtures and dielectric target. 209

G.1 Cross sectional views of E_t of the discharge in the plasma plume and spreading on the target surface, for several applied voltages. 212
G.2 Radial profiles of E_z inside the tube and in the plasma plume, at the time of maximum $|E_z|$, with different positive applied voltages. 214
G.3 Radial profiles of σ deposited on the surface of the dielectric target, for several applied voltages. 214
G.4 Temporal evolutions of E_z averaged through the thickness of the dielectric target, with different applied voltages. 215

Nomenclature

Abbreviation	Definition
r	Radial position
z	Axial position
t	Time of the physics under study
n_r	Number of mesh cells in the radial direction
n_z	Number of mesh cells in the axial direction
r_{in}	Inner radius of the tube
r_{out}	Outer radius of the tube
ϵ	Dielectric permittivity
ϵ_0	Vacuum permittivity
ϵ_r	Relative dielectric permittivity
E	Electric field
N	Gas number density
E/N	Reduced electric field
E_t	Magnitude of the electric field
E_z	Axial component of electric field
E_r	Radial component of electric field
σ	Net surface charge density
Q	Total net charge deposited in a surface
ρ	Net volume charge density
$E_{z\sigma}$	Surface charge contribution to E_z
$E_{z\rho}$	Volume charge contribution to E_z
$E_{r\sigma}$	Surface charge contribution to E_r
$E_{r\rho}$	Volume charge contribution to E_r
T_g	Gas Temperature
V_P	Plateau value of the pulse of applied voltage
t_P	Duration of the plateau of applied voltage
t_{rise}	Rise-time and decrease-time of the pulse of applied voltage
V_{MAX}	Peak value of the pulse of applied voltage
V_{APP}	Instantaneous value of the applied voltage
f	Frequency of applied voltage
n_{init}	Initial number density
n_e	Number density of electrons
n_i	Sum of the number densities of ions
n_ρ	Number density of the net charge
L	Tube length
d	Tube-target distance
γ	Coefficient of secondary electron emission by ion impact
Γ	Flux of electric field through a circular surface

Abbreviation	Definition
S_i	Total ionization source term
S_e	Electron-impact ionization source term
S_p	Photo-ionization source term
A_{ph}	Photo-ionization source
ξ	Photo-ionization coefficient
X_k	Proportion of species k in the gas-mixture
ϵ_m	Mean electron energy
T_e	Electron Temperature
k_B	Boltzmann constant
λ_D	Debye radius
n_k	Number density of species k
j_k	Flux of species k
J_k	Flux density of species k
S_k	Total source/loss term of species k
S_l	Source/loss term of reaction l
K_l	Rate coefficient of reaction l
v_k	Electric drift velocity of species k
μ_k	Mobility of species k
D_k	Diffusion coefficient of species k
q_k	Electric charge of species k
q_e	Electric charge of electrons

Chapter I

Introduction and state of the art

Contents

I.1 Low-temperature atmospheric pressure plasma jets 2

I.1.1 Low-temperature atmospheric pressure plasmas 2

I.1.2 Helium plasma jets and applications 2

I.2 Physics and chemistry of plasma jets 4

I.2.1 Mechanisms of streamer propagation 4

I.2.2 Discharge dynamics inside dielectric tubes 6

I.2.3 Influence of admixtures to the buffer gas inside the tube on discharge dynamics 7

I.2.4 Discharge dynamics in the plasma plume 9

I.2.5 Influence of the polarity of applied voltage 11

I.3 Interactions between plasma jets and dielectric and metallic targets 12

I.3.1 Discharge interaction with metallic targets and the rebound front . 15

I.3.2 Discharge interaction with dielectric targets 17

I.4 Electric Field characterization of plasma jets 18

I.4.1 Optical measurements of electric field 18

I.4.2 Electric field measurements through electro-optic probes and laser diagnostic techniques 19

I.4.3 Electric field measurements through Mueller polarimetry 20

I.5 Memory effects and flow channeling in repetitive plasma jets . . 21

I.5.1 Initial conditions for discharge repeatability 22

I.5.2 Plasma jet effect on flow 22

I.6 Motivations and plan of this thesis 25

I.1 Low-temperature atmospheric pressure plasma jets

I.1.1 Low-temperature atmospheric pressure plasmas

Low-temperature plasmas are weakly ionized gases where ions, electrons and neutral species coexist, although the electron density n_e is much lower than the neutral density N ($n_e/(n_e + N) < 0.1$). These species are not in thermal equilibrium with each other and usually heavy species (ions and neutrals) stay near room temperature (300 K, $T_g < 10^4$ K) while electrons are accelerated to kinetic energies in the 1-30 eV range ($10^4 - 10^5$ K). Ions and neutral species exist not only in their ground-states but also in excited rotational, vibrational and electronic levels which usually are not in thermal equilibrium among themselves and which carry internal energy. This non-equilibrium leads to a high level of reactivity inside the plasma, since species carry kinetic and internal energy which can be exchanged by means of collisions, and this will be determinant for the development of the plasma. Therefore, low-temperature plasmas are described as very chemically reactive, energetically economic (no or moderate heating) and non-destructive. These characteristics raise interest in cold plasmas not only from a fundamental point of view but also due to their potential applications. A recent publication [*von Keudell and von den Gathen*, 2017] introduces the main concepts in low-temperature plasma physics. Laboratory plasmas are characterized by the gas they are created from, the way they are created and sustained, the geometry in which they exist and the gas density used to produce them. In the last thirty years, there has been an increasing interest about low-temperature plasmas at high pressures (0.1 - 10 bar, 100's Torr, $10^4 - 10^6$ Pa) and particularly about plasmas at room temperature and atmospheric pressure ($N = 2.45 \times 10^{19}$ cm^{-3}), since in some cases they are not confined to vacuum chambers, thus avoiding expensive pumping systems. In this thesis we consider low-temperature plasmas at atmospheric pressure.

A recent review on atmospheric pressure non-equilibrium plasmas [*Bruggeman et al.*, 2017] provides an overview of the key underlying processes that are important for the generation and stabilization of these plasmas and summarizes the physical and chemical properties of theses discharges. At high pressures, during the application of an electric field to a gas, as the frequency of electron-neutral collisions is high, electrons have less time to acquire enough kinetic energy from the applied field to provoke ionizing collisions. This means that, even though the number of collisions is higher at higher pressures, the applied electric field to create a plasma is usually higher than at low/intermediate pressures, around 10's kV/cm [*Raizer*, 1991]. In reality, this electric field is not applied equally to the whole volume of gas and ionization is strongly localized leading to very heterogeneous plasmas. This type of discharge has a strong concentration of active species, local heating may be non-negligible and the discharge may not be reproducible.

I.1.2 Helium plasma jets and applications

The possibility of propagating reproducible low-temperature plasmas at atmospheric pressure into open space is very interesting. Such systems are called plasma jets. They can propagate away from the electrodes into open space and touch any target, including the human body, directly. This propagation occurs inside thin dielectric tubes, allowing the plasma to be ap-

plied somewhere farther without spatial confinement. The region of discharge propagation at the exit of the tube is called the plasma plume. For instance, the discharge setup called plasma gun has been shown to allow for the propagation of discharges in dielectric capillaries flushed with neon or helium flow rates over tens of centimeters, before inducing plasma plume formation in ambient air [*Robert et al.*, 2009, 2012, 2013, 2015]. One example of jets with propagation in long tubes and very practical application is shown in Figure I.1.

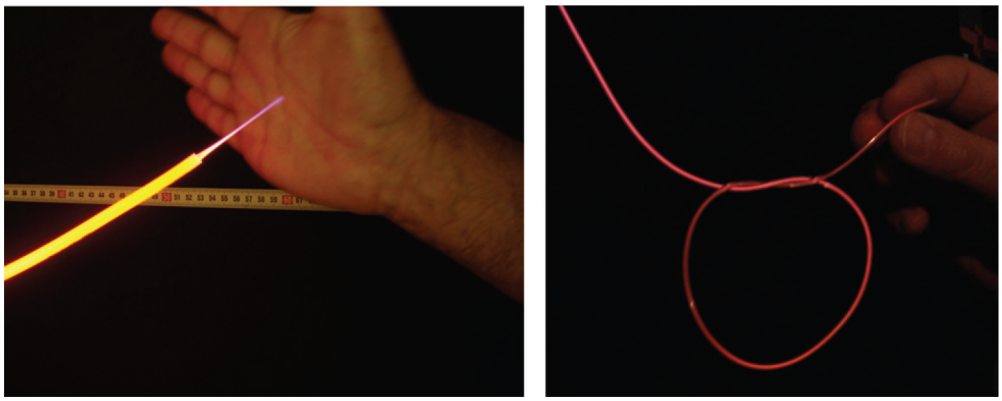

Figure I.1: Propagation of a neon jet through long thin tubes and practical application on a target human body. Figures from *Robert et al.* [2009].

Due to emerging applications, jets have attracted a lot of attention in the past 20 years. Several groups have studied plasma jets experimentally and numerically and several reviews on jets have been published in the last years [*Schutze et al.*, 1998; *Laimer and Stori*, 2007; *Laroussi and Akan*, 2007; *Lu et al.*, 2012, 2014; *Winter et al.*, 2015a; *Lu and Ostrikov*, 2018]. There, different configurations, applications and properties of jets have been reported.
Different gases have been studied for jet propagation but usually the jets work with noble gases, eventually mixed with a small percentage of reactive gases. It is difficult to generate atmospheric pressure air plasma jets due to the low energy excitation reactions in air molecular gases that make electron-impact ionization harder. The helium jet is the most studied case and has shown long propagation lengths. This happens due to the high direct electron-impact ionization coefficient for He at the typical reduced electric fields that create jets, below 200 Td, which makes generation and production of jets in He much easier than in air. A He plasma jet is therefore a very efficient way to generate and control non-equilibrium plasmas at atmospheric pressure at low power densities, thus limiting the development of thermal instabilities. In *Teschke et al.* [2005]; *Lu and Laroussi* [2006] it has been shown for the first time that the plasma jet luminosity is not continuous as seen by the naked eye, but it consists of plasma bullets traveling like ionization waves at high speeds of the order of 10-100 $km.s^{-1}$. Furthermore, it has been observed that in the plume the plasma bullet has a ring shape and propagates in the channel formed by helium in air *Lu et al.* [2012]. The discharge propagates guided by the tube and then by the flow towards the air, as demonstrated in *Naidis* [2010]; *Boeuf et al.* [2013] where two-dimensional simulations of positive discharge propagation in He jets injected into ambient air have been performed under the assumption that helium and air do not mix.
Hence, jets have the ability to deliver in remote locations a wide range of reactive species (NO, OH, NO_2, H_2O_2, O, O_3), charged species, high electric fields and UV photons. They

are very promising devices for applications in the areas of material science and biomedicine. These are highlighted in several papers and reviews [*Fridman et al.*, 2008; *Kong et al.*, 2009; *Fridman and Friedman*, 2013; *Collet et al.*, 2014; *Graves*, 2015; *Topala and Nagatsu*, 2015; *Barwe et al.*, 2015; *Laroussi*, 2015; *Weltmann and von Woedtke*, 2017; *Reuter et al.*, 2018] and include decontamination, microbial sterilization, cancer treatment, coagulation, wound healing, dental treatment, surface functionalization and treatment for agriculture. The plasma jet developed at INP (kinpenMed) is a certified medical device and is currently used in hospital on patients [*Metelmann et al.*, 2013]. Among the applications, we would like to highlight the role of the electric field in the discharge when applied on living tissues. In some applications where the jet is used to destroy (or cause the apoptosis of) diseased cells, electric field produce the electroporation of the cells, which allows for reactive species or even therapeutic drugs to be successfully introduced into the cells [*Kim et al.*, 2010; *Mirpour et al.*, 2014; *Zhang et al.*, 2014].

I.2 Physics and chemistry of plasma jets

I.2.1 Mechanisms of streamer propagation

In *Sands et al.* [2008]; *Naidis* [2010, 2011b]; *Breden et al.* [2011, 2012]; *Boeuf et al.* [2013] it has been shown that plasma jets are ionization waves that propagate with the same mechanisms as streamer discharges. Here we present a short review of those mechanisms.
The concept of streamer discharges has been put forward by Meek, Raether and Loeb [*Meek*, 1940; *Loeb and Meek*, 1940a, b] to explain very fast phenomena not explained by Townsend's theory. Streamers are filamentary plasmas driven by their own space-charge electric field. Free electrons in a gas (natural preionization around 10^4 cm^{-3}) are accelerated by an external electric field that leads them to perform ionizing collisions and then to separate in space from the positive ions. If this phenomenon is intense enough, a space-charge layer is created that produces an electric field high enough to drive a spatial propagation. Then the streamer has ignited and its dynamics of propagation is mainly controlled by the high-field region called streamer head or discharge front. On the left side of Fig. I.2 the head of the streamer is depicted as a crescent shape. In the discharge front, the net charge is high and positive or negative for positive or negative streamers, respectively. The polarity of the streamer is defined by the direction of the electric field that primarily ignites it. If it is ignited by an electric field that pulls electrons towards an anode powered electrode, the streamer is positive. On the other hand, if the applied electric field pushes the electrons away from a cathode powered electrode, the streamer is negative.
In the case of positive streamers, on the one hand, as electrons ahead of the front (upstream the front) are accelerated by the strong space-charge electric field, they produce ionizing collisions between the front and the cathode. On the other hand, electrons ahead of the front drift downstream towards the source and away from the produced ions and neutralize the former positive space-charge region. Thus, the charge pattern is repeated at a position closer to the cathode, leaving behind a quasi-neutral channel with high electron/ion density. If the electrons are amplified enough to compensate the positive head of the streamer, then the streamer can propagate in a stable manner as an ionization wave *Raizer* [1991]. Hence,

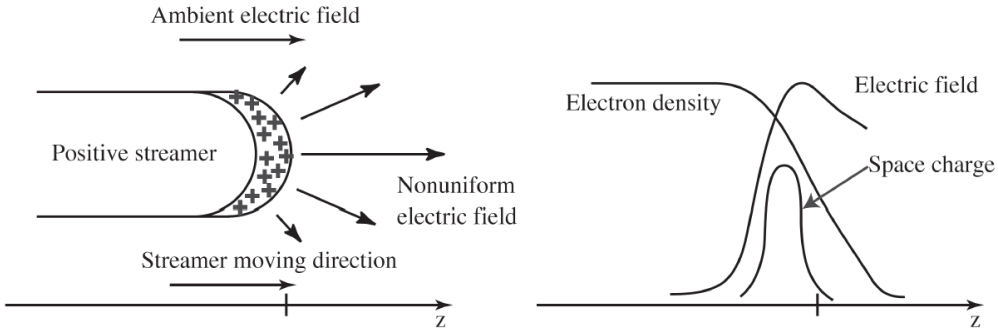

Figure I.2: Schematics of positive streamer propagation. From *Bazelyan and Raizer* [1998].

the positive streamer propagates in the direction of the ambient field and in the opposite direction of the electron drift. The electrons upstream the discharge front, called seed electrons, are necessary for the positive streamer propagation. These electrons may come from the natural electron background, essentially due to natural radioactivity and cosmic rays, from a pre-ionization of the gas due to previous discharges, from a memory effect from previous discharges that leave behind excited species or negative ions that allow easier electron production or from photo-ionization, i.e. from ionizing collisions between energetic photons generated at the discharge front and the gas upstream. Photo-ionization has been found to play a crucial role in the production of seed electrons in positive streamers [*Liu et al.*, 2007], as shown in Fig. I.3. In the result in that figure, even though the rate of electron production through photo-ionization is lower than through electron-impact in the discharge front, it is higher upstream.

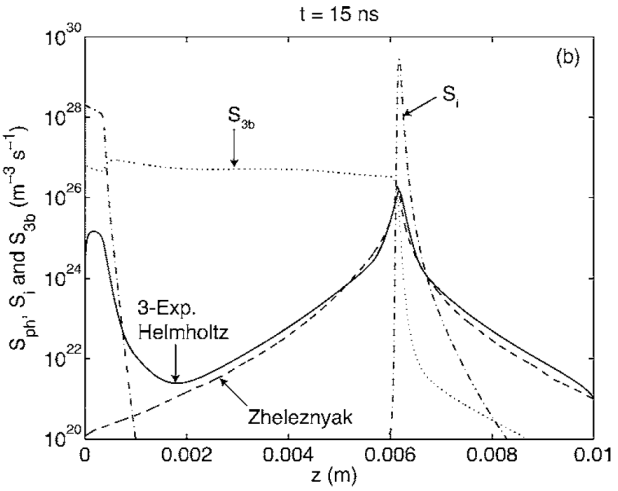

Figure I.3: Role of photo-ionization in an air positive streamer propagation. Source terms: S_i for electron-impact ionization, S_{3b} for three-body electron-attachment and S_{ph} for photo-ionization, calculated through different models. From *Liu et al.* [2007].

For negative streamers, the principle of propagation is the same but the net charge in the head is negative and it propagates in the opposite direction of the electric field, i.e. in the direction of electron drift. Ionization takes place in the streamer head where the field is highest and electron density is high. Then electrons drift upstream and thus the negative space charge propagates. Seed electrons are in principle less important in the case of negative

streamers but can still play important roles in their structures and guide their propagation. For both streamer polarities, the forward-moving streamer head leaves behind a quasi-neutral plasma, where the electric field is very low, that connects the potential in the powered electrode to that in the discharge front [*Shashurin et al.*, 2012]. The potential drop along the quasi-neutral channel increases linearly with length, thanks to the electrical resistance of the plasma channel [*Boeuf et al.*, 2013]. This means that the electric field on the discharge front that defines the discharge propagation and is dependent on the potential of the discharge front depends on the conductivity of the plasma channel. Therefore, in jet propagation that can last μs, long life-time species and active plasma chemistry in the channel can affect the discharge propagation.

I.2.2 Discharge dynamics inside dielectric tubes

In this thesis the discharge propagation takes place inside dielectric tubes and then in the jet plume, before interacting with targets. In fact, dielectric thin tubes are widely used to channel discharge propagation for application at atmospheric pressure, in particular using Helium as buffer gas. Inside the tube the gas-mixture is homogeneous and the discharge interacts radially with a dielectric surface while propagating along the direction of tube length. Detailed propagation mechanisms in such tubes require dedicated analysis.
In *Jánský et al.* [2010, 2011] simulations and experiments have been performed to study the influence of the cylindrical constraint of a tube on the structure and dynamics of a positive air discharge, using relative permittivities ϵ_r of the tube between 1 and 10 and tube inner radius (r_{in}) between 37.5 μm and 600 μm. It has been shown that in the presence of a tube the discharge fills the tube and propagates with a rather planar front, faster than without tube and with higher electron density and electric field maximum. Furthermore, it has been reported that an increase of ϵ_r and of r_{in} both lead to a decrease in the discharge velocity of propagation. Both factors lead to a more tubular structure and a decrease of the electron density and the electric field on the axis of propagation. Simulations of Ne-Xe ionization wave propagation inside capillaries of radius 600 μm in *Xiong and Kushner* [2012] confirm that increasing ϵ_r between 1 and 16 decreases the velocity of propagation in tubes for both polarities of applied voltage. However, in *Robert et al.* [2012]; *Sarron* [2013] (chapter III.6), experiments of He discharge propagation find that the tube material has a negligible influence on the velocity of propagation. Then, in *Jánský and Bourdon* [2011b] simulations of the dynamics of surface charging by an air positive discharge inside a tube have been presented. These have shown that the surface charge density is inversely proportional to r_{in} as it varies between 100 μm and 250 μm and proportional to the tube permittivity between 1 and 5 and to the magnitude of the applied voltage. Moreover, in *Pechereau* [2013] (chapter 9) the propagation of both air and He-N_2 positive discharges in a dielectric tube have been investigated numerically, with different applied voltages. It has been found that, for the same conditions, a rather homogeneous radial structure is obtained in air with tubes of inner radius around 200 μm with constant applied voltage 40 kV, while in He-N_2 the radius should be around 2 mm with 6 kV of constant applied voltage.
Concerning He jets with discharge propagation both inside and outside the dielectric tube, the influence of the tube diameter on the plasma properties with both polarities of applied voltage

has been investigated experimentally in *Jogi et al.* [2014]; *Talviste et al.* [2016]; *Talviste* [2016]; *Wu et al.* [2016] and numerically with positive polarity in *Breden et al.* [2012]; *Boeuf et al.* [2013]; *Cheng et al.* [2015]. Those studies have shown that the electric field on the axis of propagation, the velocity of propagation and the electron density in the plasma channel increase with decreasing tube radius. Moreover, the maximum of electron density is closer to the axis with lower tube radius. Furthermore, in *Jogi et al.* [2014]; *Cheng et al.* [2015] the sustaining applied voltage of the discharge increases with decreasing radius due to higher electron wall losses. Then, in *Liu et al.* [2014] 2D simulations of a He jet with positive polarity have shown that a positive sheath forms near the dielectric tube inner surface and shields the channel from the tube surface. The formation of the sheath is attributed to the repulsion of electrons in the region between the quasi-neutral plasma and the tube. Moreover, the off-axis peak ionization is explained by the high electric field in the sheath region.

I.2.3 Influence of admixtures to the buffer gas inside the tube on discharge dynamics

Several experimental works have used admixtures in the tube, generally of air-related species, to study the generation of reactive species and the optimization of plasma jet application. For instance, in *van Gessel et al.* [2013] the admixture of N_2, O_2 or air, up to 4% of the gas density, to a radio-frequency Argon jet has been shown to have an effect on the electron density and electron temperature measured in the plasma plume. Furthermore, in *Gaens et al.* [2015], a zero-dimensional model has predicted that the production of several species in an Argon jet can be manipulated by up to one order of magnitude, by varying the admixture of N_2, O_2 or N_2+O_2 up to 1% of gas density. The review in *Winter et al.* [2015a] gives several examples of gas-mixtures in different jet configurations. Moreover, in numerical modeling of He parallel plate DBDs [*Lazarou et al.*, 2015], it has been reported that the level of nitrogen impurities in the range 0.1-500 ppm affects the dominant ion species in post-discharge due to Penning ionization and charge transfer reactions. The variation of dry air admixture up to 1500 ppm in a He parallel plate DBD has also been shown to affect discharge ignition and the discharge structure [*Lazarou et al.*, 2016]. It has been reported that with low (0-55 ppm) and high (over 1000 ppm) air concentration, the discharge is not ignited during the AC cycle. As air concentration increases in the mixture up to 225 ppm, ionization of N_2 and O_2 increases, mostly due to Penning ionization and the ignition voltage decreases. By increasing the air concentration further, in the range from 225 to 1000 ppm, the electron losses significantly increase and thus the ignition voltage increases.

Concerning Helium jets, it has been reported in *Darny et al.* [2014] the modification of the measured propagation velocity of a μs Helium plasma gun discharge with N_2 gas admixture up to 1.5% in the helium buffer. From 0.1% to 0.8% of N_2, the ionization front is up to 1.5 times faster, more extended and with stronger luminous intensity, compared to the case with high purity helium. Inclusively, the velocity has a maximum, for approximately 0.3% of N_2. In the same work, the imaging of the ionization front shows a more centered structure inside the tube with 0.5% N_2 than in pure Helium.

In *Bourdon et al.* [2016] a numerical and experimental study of the influence of N_2 admixture on the dynamics of a He-N_2 discharge with positive applied voltage in a 10 cm long dielectric

tube with a high voltage ring electrode wrapped around has been carried through. A μs high voltage power supply has been used with 2 μs rise-time and 2 μs fall-time. In the experiments, the pulse shape is identical from pulse-to-pulse for different positive voltage amplitudes up to 20 kV, with 1 kHz frequency. The work in *Bourdon et al.* [2016] constitutes a starting point for this thesis and some of its key results are presented. For the sake of brevity, the figures have been put in appendix A.

The discharge structure and the spatio-temporal distribution of the species in a He plasma with 1000 ppm of N_2 (0.1%) while propagating in a tube have been described. The comparison between experiments and simulations on the ionization front propagation velocity in the tube has put forward the importance of taking into account a detailed kinetic scheme for the He-N_2 mixture in the simulations to obtain a good agreement with the experiments. The two- and three-body Penning ionization reactions occurring in the plasma column behind the ionization front have been shown to be essential to keep ionization in the plasma channel and for the ionization front velocity in the tube (left side of Fig. A.1). These results have clearly confirmed the role of kinetics in discharge propagation. In fact, through charge production and loss, the discharge kinetics can affect the conductivity of the plasma column. The importance of the conductivity of the plasma column for discharge dynamics has been put forward in *Shashurin et al.* [2009, 2012]; *Xiong and Kushner* [2012]; *Boeuf et al.* [2013]. Without these Penning reactions, the plasma channel is less conductive and the discharge propagation is slower. Furthermore, in that work it has also been shown that without charge exchange reactions between He and N_2 ions, more ions and electrons remain in the plasma channel, due to the lower recombination coefficient of He_2^+ than N_2^+ and $N_2^+(B)$. With lower recombination rates, the plasma channel is more conductive and the velocity of the discharge is higher (left side of Fig. A.1).

A significant influence of the amplitude of the applied voltage (10 to 16 kV) on the ionization front propagation velocity has also been observed (right side of Fig. A.1). Besides the increase of velocity with the maximum amplitude of applied voltage, it has been verified that the velocity increases during propagation only with a pulse whose amplitude increases in time. In the same figure it has been shown that the value of the photo-ionization coefficient considered in simulations $\xi = A_{ph}/X$ (X is the concentration of N_2 or O_2), varied between 1 and 10, has only a small influence on the results.

The preionization value considered in the model has also been shown to have an effect on both the ignition time and the velocity of discharge propagation in the tube (Fig. A.2). The comparison of experimental and simulated ignition times and ionization front propagation velocities has shown a better agreement for low preionization levels of $n_{init} = 10^4$ cm^{-3} of electrons and one positive ion, which is close to the natural preionization.

Then, as the amount of N_2 varies, the decrease of the ignition time with increasing admixtures of N_2 up to 5000 ppm has been reported for both experiments and simulations (right side of Fig. A.3). It has been shown by the simulations that the ionization front velocity, which is a very macroscopic quantity, depends on the complex coupling between the kinetics of the discharge, the photo-ionization, the preionization and the 2D structure of the discharge in the tube. In the conditions studied in *Bourdon et al.* [2016], with experimental and numerical conditions adjusted for proper comparisons, the amount of N_2 has been shown to have only a small influence on the ionization front velocity in experiments (left side of Fig. A.3) and

simulations. Finally, simulations have shown that the magnitude of the axial electric field on the discharge axis depends weakly on the amount of N_2, conversely to the magnitude of the off-axis peak electric field. This quantity decreases rapidly as the amount of N_2 increases up to 1000 ppm and then increases slowly for higher amounts of N_2, which confirms an effect of the gas-mixture on the discharge radial structure.

I.2.4 Discharge dynamics in the plasma plume

Once the discharge front exits the dielectric capillary, it enters in a region that is not mechanically confined radially and where the gas-mixture is spatially inhomogeneous. The inhomogeneity in this region implies more complex mechanisms of discharge propagation.

Propagation mechanisms and ring-shape in the plasma plume of He jets

Firstly, in *Mericam-Bourdet et al.* [2009] the ring-shape of the ionization front of a He plasma jet propagating in air has been found in photographs and thus the jet has been described as a surface ionization wave propagating at the interface between two media. Moreover, optical emission spectroscopy results in that paper suggest that Penning ionization of N_2 by He metastables may play an important role in the definition of the ring-shape and thus on the discharge propagation mechanisms. Then, in *Sakiyama et al.* [2010], using a fluid model with inhomogeneous gas mixing, the ring-shaped emission pattern observed experimentally has been explained by the off-centered Penning ionization peak that generates an off-centered peak of electron density, even though Penning ionization plays only a minor role in sustaining the discharge. However, in *Naidis* [2010]; *Boeuf et al.* [2013] two-dimensional simulations of positive discharge propagation in He jets injected into ambient air have been performed under the assumption that helium and air do not mix. In those conditions, streamer structures of two types can be formed: one with maxima of electric field and electron number density on the axis and another with maxima of these parameters near the boundary between He and air. The structure depends on the jet radius and its relationship with the profile of initial electron density, which is also suggested in *Liu et al.* [2014], where the ring shape is attributed primarily to the enhancement of electric field in the interface between the dielectric tube and air. Hence, in the simulations in *Naidis* [2010]; *Boeuf et al.* [2013] no gas mixing and Penning ionization are required to obtain a ring-shaped jet propagation. In *Naidis* [2011b]; *Breden et al.* [2011] it has been confirmed with simulations that in a positive He jet mixing with air Penning ionization reactions are not essential for the discharge ring structure in the plume. The ring shape is maintained because the electric field in the streamer head is sufficient to provide significant ionization of He but not of air. Therefore, for discharge propagation in the plume it is crucial to have a core He region. The ring shape of electron density and ionization source term obtained in *Boeuf et al.* [2013] are presented in Fig. I.4.
Then, *Naidis* [2011b] has shown with simulations that the radial position where the concentration of electron and metastable nitrogen molecules reach a maximum coincides with the position where the air molar fraction is about 1% and thus the mixing layer is crucial for an accurate description. The mixing layer is defined by geometry and the flow value of buffer gas. The same work has suggested that the formation of the ring structure is governed mainly by the dependence of the direct electron-impact ionization rate in He-air mixtures on

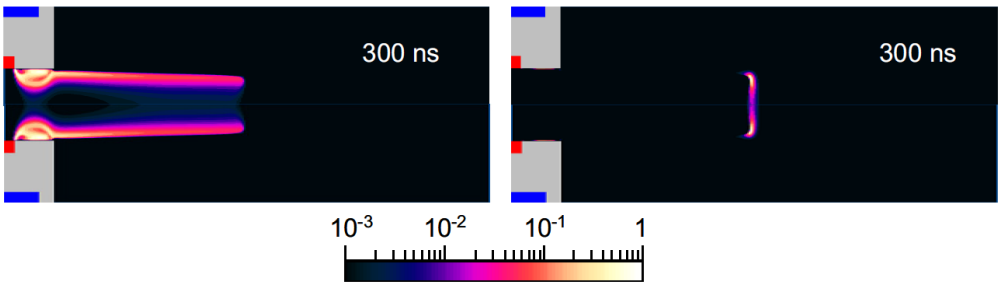

Figure I.4: Ring shape of the electron density (on the left) and electron-impact ionization source term (on the right) of discharge propagation in *Boeuf et al.* [2013] in units relative to 3×10^{13} cm^{-3} and 0.4×10^{21} cm^{-3}.s^{-1}.

the air molar fraction. In *Breden et al.* [2011] it has been added that photo-ionization, while being important in determining the positive discharge propagation speed, is not an essential process for discharge propagation in He jets. Since, many works have suggested a preferential path of He-air gas-mixture for the ionization wave propagation in the plume of He jets [*Naidis*, 2011b; *Breden et al.*, 2012; *Schmidt-Bleker et al.*, 2015; *Wang et al.*, 2016a; *Ning et al.*, 2018]. In *Breden et al.* [2012] the peak electron density of the propagating discharge occurs at a location where the air molar fraction is 1-2%, but it has also been concluded that the position of this mixing layer itself does not play a significant role in the kinetics of discharge propagation as long as a significant helium core region exists. In *Schmidt-Bleker et al.* [2015] the ionization wave and electron density move towards the axis upon exiting the tube, approximately following a 0.1% molar fraction of surrounding gas, either N_2, O_2 or air. Also in *Wang et al.* [2016a]; *Ning et al.* [2018] the ionization wave propagation follows the 1% air molar fraction.
Finally, in *Naidis* [2012] it has been shown that the increase of flow velocity and applied voltage lead to the increase of the discharge radius in the plasma plume and of the distance of propagation required for the ring shape to become spherical. Moreover, in *Naidis* [2015] simulation results have shown, in agreement with experiments [*Xian et al.*, 2014b], that the addition of air (3% of total gas density) to the He buffer gas leads the structure of the radiation flux to transition from ring-shaped to centered. A more centered structure with admixture of air gases is present also in simulations and experiments in *Wu et al.* [2011]; *Breden et al.* [2012]; *Ning et al.* [2018]. Thus, the formation of ring-shaped profiles has been attributed in *Naidis* [2015] to the radial non-uniformity of ionization rate of gas species by electron impact.

Influence of different surrounding gases

The study of different environment gases at the tube exit is interesting both for potential optimization of applications and to understand the physical phenomena taking place when the buffer gas mixes with air environment gas and has been carried out by several groups. In this thesis as well different surrounding gases N_2 and O_2 are used as first approximation to air surrounding gas.
It has been reported in experiments with He and Ar jets with different surrounding gases in *Xian et al.* [2014a] that with increasing oxygen in the surrounding gas seed electrons

decrease and therefore the jet length decreases too. Moreover, *Schmidt-Bleker et al.* [2015] have investigated experimentally and numerically the role of electronegativity by using N_2/O_2 mixtures as shielding gas of a He jet powered by a sinusoidal voltage. From results of modeling they have found that when a pure N_2 shielding gas is used, electrons spread radially outward at the edge of the nozzle. This spreading does not occur if the shielding gas contains O_2 and electronegativity. Furthermore, in the experimental measurements of He metastable (He*) in *Winter et al.* [2015b] a severe effect has been observed due to the choice of the surrounding gas. Compared to ambient air conditions, a pure O_2 shielding gas leads to a He* density decrease of only 30% whereas with pure N_2 surrounding gas the He* density falls below the detection limit. Then, recently, in *Razavizadeh et al.* [2018] measurements of He jet dynamics have shown that the velocity of guided ionization waves is higher in oxygen containing gases. In that paper, the proposed mechanisms to explain the higher speed of ionization waves in dry air and oxygen rather than nitrogen are electron detachment and photoionization.

I.2.5 Influence of the polarity of applied voltage

We have noticed in section I.2.1 that positive and negative streamers propagate with different mechanisms. Then, it is interesting to study how the different polarities of applied voltage can influence discharge dynamics and structure in He jets, both inside dielectric tubes and in the plasma plume.

Many experimental and numerical works have evaluated the differences between the structure and dynamics of propagation of streamer-like discharges with different polarities of applied voltage outside tubes [*Babaeva and Naidis*, 1997; *Georghiou et al.*, 2005; *Luque et al.*, 2008; *Jiang et al.*, 2009; *Naidis*, 2009; *Xiong et al.*, 2010; *Urabe et al.*, 2010; *Naidis*, 2011a; *Wang et al.*, 2016b]. In *Babaeva and Naidis* [1997], calculations of streamer propagation in air have shown that the electric field in the streamer head, the electron density in the plasma channel and the velocity of propagation are higher for positive polarity than for negative polarity. Furthermore, it has been reported that the electric field in the plasma channel is higher for negative polarity. Moreover, in the simulations in *Luque et al.* [2008] it has been argued that negative streamers in air can be slower than positive ones because electron drift broadens the streamer head and decreases the electric field enhancement. Higher velocity of propagation with positive polarity also takes place in the plasma plume of jets in *Jiang et al.* [2009]; *Xiong et al.* [2010]; *Naidis* [2011a]; *Wang et al.* [2016b]. Then, in *Naidis* [2011a], simulations of the plasma plume of He jets have shown that the discharge structures are dependent on polarity. With positive polarity the discharge head has a spherical form, while with negative polarity the shape of the head is like that of a sword, as shown in Fig. I.5, in agreement with the experiments in *Jiang et al.* [2009]; *Xiong et al.* [2010]. This feature has been explained in that work from the difference between electric field values in the channels of positive and negative streamers. With positive polarity the electric field in the channel is low and radiation is insignificant, being produced mostly in the head region. With negative polarity the values of electric field in the channel are much higher and radiation is generated effectively in the whole channel. It has been noticed there, as in *Urabe et al.* [2010], that plasma jets driven by negative voltage pulses are similar to glow plasmas.

However, only a few works have assessed the difference induced by polarity on the discharge

Figure I.5: Image plots of normalized N_2(C-B) radiation intensity for positive (on the left) and negative (on the right) voltage polarity from *Naidis* [2011a].

structure and propagation inside tubes. In *Robert et al.* [2012], the propagation of a negative Ne discharge in a capillary is faster than the positive one. In the simulations of Ne-Xe ionization wave propagation in capillaries in *Xiong and Kushner* [2012], the average speed is two times higher for negative polarity than for positive one. Yet, the electron density and electric field at the ionization front are reported to be one order of magnitude lower for negative polarity than for positive polarity, which results in a more resistive plasma channel, with higher potential drop and higher electric field behind the ionization front, as well as a more diffusive structure. Conversely, in *Darny* [2016] it has been shown that in experiments with μs pulses, the velocity of propagation of He discharges inside the tube is higher in positive polarity. Then, in *Darny et al.* [2017b] it has been reported that the experimentally observed structure of a He discharge propagating in a tube is highly dependent on the polarity: quite homogeneous for negative polarity voltage pulse and more filamentary for positive polarity. In the experiments in *Yonemori and Ono* [2015], it has also been reported that the shape of the He discharge in the tube is more filamentary for positive polarity, and it has been indicated that the polarity of the discharge affects the densities of some reactive species produced in plasma jets. The more filamentary structure for positive polarity agrees with the simulation results in *Xiong and Kushner* [2012] where the maximum of electric field during propagation with positive polarity is close to the tube, while the front of propagation with negative polarity is more radially homogeneous inside the tube. Finally, in the experiments in *Chen et al.* [2018] the polarity of applied voltage has been shown to have an effect on the production of H_2O_2 of a He jet interacting with a water target.

I.3 Interactions between plasma jets and dielectric and metallic targets

After propagating inside the capillaries and in the plasma plume, plasma jets are applied on surfaces of different kinds. In industrial processing, the substrate is often a dielectric piece (such as organic materials and polymers). For plasma medicine application, the target is typically a liquid or a fluid covered tissue. Conductive surfaces such as metal plates may also be used in surface modification applications. On the one hand, the plasma has an effect on the target. The target material can heat, radical species and UV radiation are produced and transported to the target surface, charges are deposited on the target surface and electric fields are generated inside the target. On the other hand, discharge dynamics can vary dramatically when interacting with different surfaces. Different structures of plasma plume interacting with different targets are exemplified in Fig. I.6. Therefore, a proper understanding of discharge dynamics during plasma impingement is essential for the optimization of jet

applications and thus the interest in jet-target interactions has been increasing.

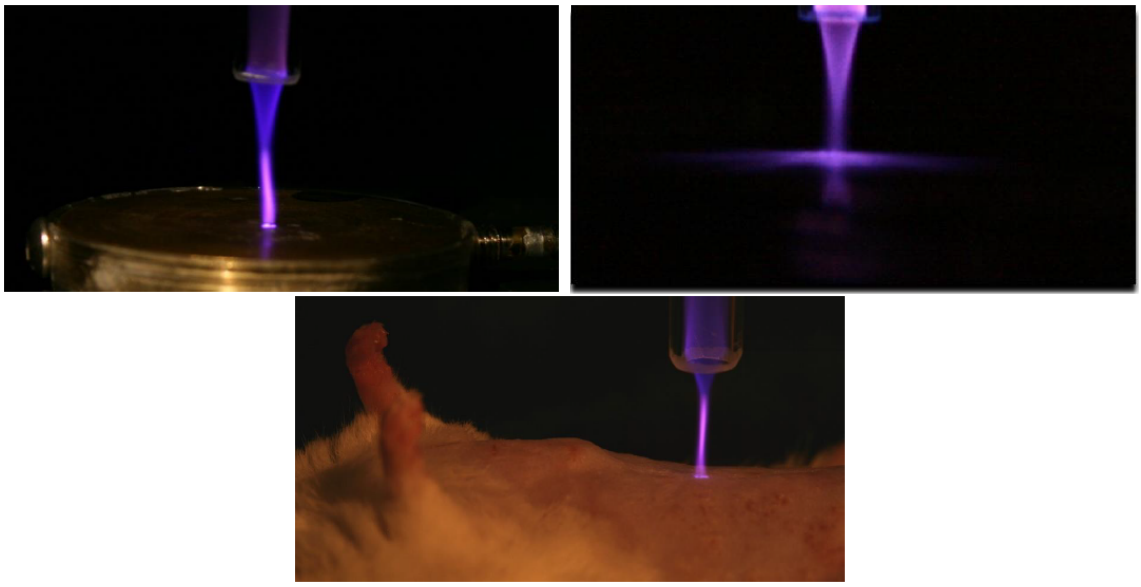

Figure I.6: Plume interaction with different targets. On top, on the left, with metallic grounded target. On top, on the right, with dielectric target. On bottom, with a living mouse. Figures from *Darny et al.* [2016].

Several groups have studied discharge propagation in jets impacting onto surfaces. *Sakiyama et al.* [2008] have numerically investigated a Helium plasma needle interacting with different surfaces and their results suggest that the plasma structure strongly depends on the electrical properties of the treated surface, with a more centered interaction with conductive surfaces. In experiments as well, *Mussard et al.* [2015] have shown that the jet impact diameter on a liquid target surface increases with a decrease in the conductivity of the target. Then, in *Bornholdt et al.* [2010] a comparison has been made of an Ar jet impinging either on a copper or a glass surface, finding through video imaging that the plasma is more homogeneous over the glass than the copper surface, in which case many filaments are randomly distributed. Moreover, in *Urabe et al.* [2010], it has been observed a higher He metastable density with a metallic target in front of a jet, compared to free jet operation. In *Ito et al.* [2010] different target configurations have been used in He jet experiments to show that charge deposited on the surface increases with the capacitance of the target (proportional directly to the target permittivity and inversely to the target thickness). In *Hofmann et al.* [2014] it has been shown experimentally that in an Ar jet the power dissipation and gas temperature significantly increase when the plasma is in direct contact with a conductive substrate. The increase of power is attributed to a change of the equivalent electrical circuit, that leads to a more favorable matching between the power input and the plasma source. It has also been reported by experiments that the He flow channeling (phenomenon depicted in Fig. I.10) is very different over metallic or insulating targets [*Boselli et al.*, 2014] and over grounded or floating potential metallic targets [*Robert et al.*, 2015]. Then, in *Norberg et al.* [2015a] it has been studied numerically in 2D the impact of He jets on dielectric and metallic grounded surfaces with a -15 kV voltage pulse. The approach of the ionization waves has been described, followed by the spreading on the target surface in the case of dielectric targets of different permittivities, along with the resulting electric field distribution inside

the target. Furthermore,the differences between the different targets have been reported, along with their impact on species production in the plasma plume. With low values of ϵ_r the target has lower capacitance and a shorter RC time constant for charging the surface, which quickly leads to the depletion of the axial component of electric field and the rise of the radial component that sustains the propagation of the discharge on the surface. With high values of ϵ_r and with metallic targets, the charging of the surface is slower or inexistent, there is no radial component of electric field and no discharge propagation on the surface. Instead, higher voltage drop remains in the gap, which promotes the rebound front propagation (called restrike of the ionization wave in *Norberg et al.* [2015a]) and the formation of a conductive channel until the target surface. *Wang et al.* [2016a] have also studied the interaction of He jets with dielectric surfaces of different permittivity, but with positive polarity of applied voltage. In agreement with *Norberg et al.* [2015a], they have shown that the lower impedance of the dielectric with higher ϵ_r enhances the electric field in the plasma column, leading to an increase of the electron density in the plasma column. In *Hofmans* [2017] the electric field has been measured through Stark shift in the front of propagation of a He jet with different targets at floating potential and it has been confirmed that a higher dielectric permittivity of the target leads to a higher electric field in the front of propagation. Then, in *Klarenaar et al.* [2018] the electron densities and temperatures have been experimentally obtained through Thomson scattering with spatial and temporal resolution in a He jet freely expanding or interacting with floating targets of different electrical properties. The same macroscopic behaviors reported in *Norberg et al.* [2015a] have been observed and their effect on the electron properties have been reported. In *Ji et al.* [2018], experiments and simulations of He jets have been used to compare the discharge dynamics with floating and grounded dielectric and metallic targets, obtaining higher velocities of propagation, maximum electric fields, higher species production and higher *E. coli* cell inactivation with the grounded targets. These characteristics are also higher with the floating metallic target than with the floating glass target, but the difference between the discharge propagation in the two cases occurs mostly close to the target. Moreover, in *Liu et al.* [2017] He plasma jet interaction with an ITO glass target has been investigated changing pulse voltage polarity. The change of pulse voltage polarity causes different propagation behavior spreading radially on the target. Additionally, it has been found that with different dielectric materials, the plasma jet interaction with the target under positive polarity presents different structures with possibility of random filaments, while under negative polarity, the structure is always similar without any filaments. Finally, in *Yue et al.* [2018] an experimental investigation through imaging of the plasma dynamics using a pulsed voltage and three different kinds of grounded substrates (dielectric glass, distilled water and metal plate) has found the same tendencies as in *Norberg et al.* [2015a].

It has also been reported in *Yue et al.* [2018] a very faint discharge at the fall of the voltage pulse, observed in the whole plasma channel, with all three targets, shown in Fig. I.7. The faint glow is attributed to the neutralization of the space charge in the plasma channel. In the experiments in *Lu et al.* [2017] a secondary discharge has also been observed at the end of the pulse in a free jet and it has been found to have opposite polarity with respect to the first discharge. A back discharge at the end of the voltage pulse has also been reported in the experiments in *Klarenaar et al.* [2018]. The same kind of secondary discharge has

been reported in jet experiments with dielectric targets using AC voltages at the reversion of applied voltage polarity [*Sobota et al.*, 2013; *Mussard*, 2015; *Guaitella and Sobota*, 2015; *Slikboer et al.*, 2016; *Bohm et al.*, 2016]. In *Norberg et al.* [2015a] the dynamics of charges at the fall of the voltage pulse has been described, not as a new discharge but as a balance between remaining positive and negative charges in the plasma and on the target surface. In fact, in *Kim et al.* [2018] the electric field reversal at the falling edge of a positive voltage pulse and consequent secondary ionization have been investigated with a full kinetic treatment in argon discharges between planar electrodes on nanosecond time scales. It is claimed that the secondary ionization is induced by charge transport in the bulk plasma region.

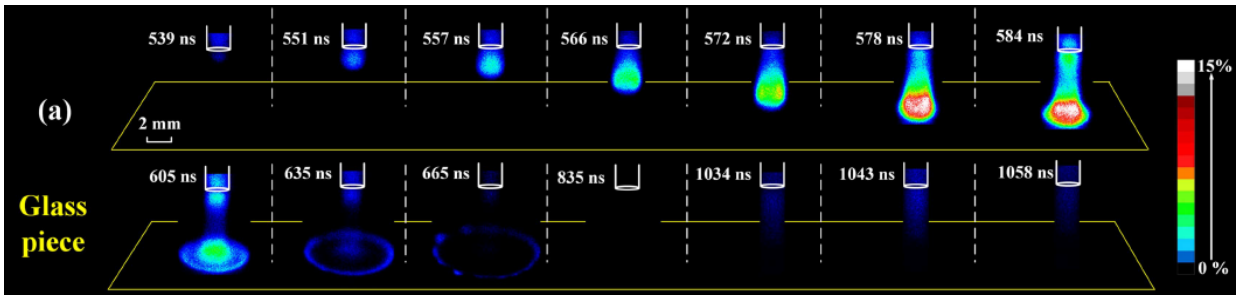

Figure I.7: High-speed photographs of the discharge dynamics with exposure time 3 ns, a glass plate target and a pulse of 6 kV and 1 μs width. End-of-pulse discharge between 1000 and 1050 ns. The color bar quantifies the intensity of each pixel as a percentage of the highest intensity observed across the experiments. Figure from *Yue et al.* [2018].

I.3.1 Discharge interaction with metallic targets and the rebound front

In *Darny* [2016]; *Darny et al.* [2017b], a detailed experimental study has been carried out to measure the helium metastable density and electric field components, both spatially and temporally resolved, for a plasma jet interacting with a grounded metallic target. The time-resolved electric field components have been measured with an electro-optic probe in the vicinity of the dielectric tube [*Robert et al.*, 2015]. For both positive and negative polarities, with a plasma jet impinging a grounded metallic target, it has been shown in *Darny et al.* [2017b] that the axial component of the electric field outside the tube presents a first peak corresponding to the first ionization wave propagating from the high voltage electrode towards the metallic target. After the impact of the first ionization wave on the grounded metallic target, a second peak has been observed, corresponding to a second ionization front propagating more rapidly from the target to the high voltage electrode. This second ionization front has a different character than the 'back' discharge since it takes place during the pulse of applied voltage and not at its reversal. Then, smaller peaks of the axial component of the electric field have been observed in *Darny et al.* [2017b], attributed to several reflections of ionization waves. The secondary ionization front propagating from metallic and water targets has also been observed in other recent experimental works [*Gerling et al.*, 2012; *Hu et al.*, 2013; *Mussard*, 2015; *Yang et al.*, 2018; *Yue et al.*, 2018; *Klarenaar et al.*, 2018]. In *Gerling et al.* [2012], a needle-to-plane discharge with sinusoidal applied voltage in flowing He at atmospheric pressure has been studied with temporally resolved photography, and several

back and forth directed plasma bullets have been observed as long as the ionized channel persists. In both *Yue et al.* [2018] and *Klarenaar et al.* [2018] where the He jet dynamics is investigated experimentally using a pulsed DC voltage and different kinds of targets, this secondary ionization front is observed with water and metallic targets, either at floating or grounded electric potentials and not with glass targets. This difference is attributed to the electrical properties of the targets.

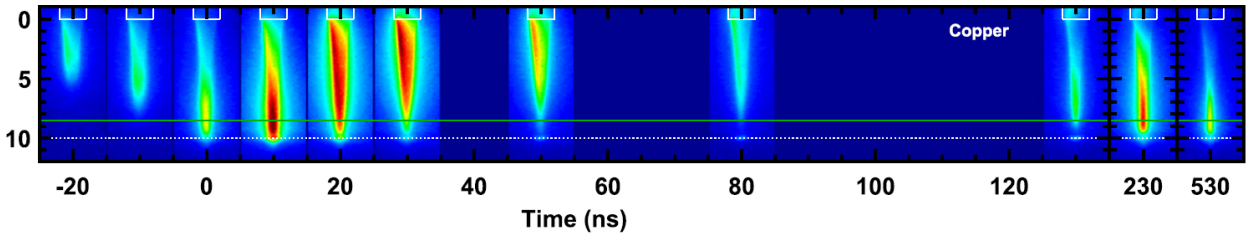

Figure I.8: Emission of the ionization wave versus time. On the vertical axis, 0 is the position of the tube nozzle and 10 (mm) is the position of the copper target at floating potential. 0 ns is defined as the moment when the ionization wave makes initial contact with the target. The exposure time is 10 ns. The first return stroke is visible between 20 and 50 ns and later several reflections are visible. Figure from *Klarenaar et al.* [2018].

In *Darny et al.* [2017b], the rebounds of ionization waves observed are attributed to the impedance mismatching between the conductive ionized channel, the high voltage electrode and the grounded metallic plane. Indeed, after the impact of the first ionization wave on the grounded metallic target, an ionized channel is formed between the two metallic electrodes. This channel acts as a transient transmission line between the electrodes. The high voltage applied on the inner electrode is transiently and partially transferred to the metallic target through the conductive ionized channel, with a voltage drop due to the channel impedance. The impedance mismatching between the ionized channel impedance and the very low metallic target impedance leads to a reflection phenomenon, with a secondary ionization front starting from the metallic target towards the inner electrode. Then, successive but damped reflections propagate in the ionized channel between both metallic electrodes, as long as the ionized channel persists. In the study of streamers propagating in air between a high voltage point electrode and a grounded plate, as in the study carried out in *Sigmond* [1984], it is mentioned that just after the primary streamer impact, a return wave can be generated as a propagating potential disturbance between the two electrodes, and can be followed (as long as the ionized channel between the electrodes persists) by a succession of reflected ionization waves. The return wave had already been described in *Loeb* [1965] as a potential wave of ionization at very high speed. The origin of the return wave is explained in *Sigmond* [1984] by the potential difference between the streamer head and the grounded plate just before contact, that would generate enough ionization to launch an opposite polarity ionization wave. In *Raizer* [1991], the return wave is described as a wave of decay of potential and of neutralization of the charge in the plasma channel. In simulation studies of streamer discharges in air at atmospheric pressure between a high voltage point and a grounded metallic cathode plane, after the arrival of the first streamer at the cathode, a very fast redistribution of the electric field in the gap is observed, as shown in *Komuro et al.* [2013]; *Eichwald et al.* [2008]. However, in studies on streamer discharges in air at atmospheric pres-

sure between a high voltage point and a grounded metallic cathode plane, more attention is paid to the so-called "secondary streamer" [*Marode*, 1975; *Eichwald et al.*, 2008; *Komuro et al.*, 2012, 2013, 2015]. This phenomenon is not an ionization wave but corresponds to an electric field plateau formed close to the point electrode during the first streamer propagation. This plateau extends slowly towards the grounded plane after the streamer head arrival at the cathode, in agreement with experiments, as shown in [*Marode*, 1975; *Eichwald et al.*, 2008; *Komuro et al.*, 2012]. It is important to note that, in air, attachment processes play a key role on the discharge dynamics after the arrival of the first streamer at the cathode. As the electric field in the secondary streamer is high enough for the production of radicals in air, several studies have been done on the relative efficiency of radical production in the primary and secondary streamers [*Eichwald et al.*, 2008; *Komuro et al.*, 2012, 2013, 2015].

I.3.2 Discharge interaction with dielectric targets

Several studies have also taken place on filamentary discharges interacting with dielectric materials. In *Allen and Mikropoulos* [1999]; *Sobota et al.* [2009]; *Goldberg et al.* [2015] the interaction of streamer discharges with dielectric surfaces parallel to discharge propagation has been investigated experimentally and it has been shown that discharges propagate over the surface rather than through the gas. Then, in *Babaeva et al.* [2006], in a point-to-plane geometry, the interaction of a positive streamer discharge in air with dielectric particles has been investigated. In particular, it has been shown that while small dielectric particles ($< 10s$ μm) are enveloped by the streamer, larger particles can intercept and re-initiate streamers. In *Guaitella and Sobota* [2015] the impingement of a He jet on a glass surface has been studied experimentally using a kHz AC-driven power source and through a parametric study of flow rates, incident angles, tube-target distances and target thickness and capacitance. The glass surface has been shown to impact the discharge dynamics through the local enhancement of electric field and the supply of pre-deposited charges, investigated with respect to the propagation of the discharge on the surface. In *Celestin et al.* [2009a], filamentary air discharges impacting on a dielectric surface have been studied both experimentally and numerically and the role of volume and surface charges on the discharge structure has been discussed. Then, in *Pechereau et al.* [2012]; *Pechereau and Bourdon* [2014]; *Pechereau* [2013], a discharge in air in point-to-plane configuration has been numerically investigated and the influence of the capacitance of the dielectric layer on the velocity of the discharge propagation on the surface has been studied. Moreover, the radial spreading of the discharge over the dielectric surface has been described in detail for both polarities of applied voltage, as well as the formation and evolution of the sheath between the plasma and the target and the electric field and surface charge distributions. It has been shown there, as also in the simulations in *Wang et al.* [2016a] with a He jet, that lower permittivity, and thus lower capacitance, leads to a faster radial spreading and higher electric field tangential to the surface. The amount of surface charge deposited on the dielectric surface is reported to increase with the capacitance, along with the electric field perpendicular to the surface. Then, in the numerical study in *Norberg et al.* [2015a] with dielectric targets of different permittivity the electric field distribution inside the target resulting from jet impact has been reported. Other studies have described numerically the propagation of a He discharge and its interaction with a dielectric target,

such as *Breden and Raja* [2014]; *Yan et al.* [2014]; *Wang et al.* [2016a]; *Ning et al.* [2018]. Concerning plasma-surface interaction, these works have mostly investigated the influence of several physical parameters on the global discharge dynamics, the sheath evolution and the fluxes of reactive species to the surface. Other experimental studies have focused on the examination of electric field and temperature [*Slikboer et al.*, 2018a] inside dielectric targets exposed to discharge impact. These will be explained in detail in the next section I.4.

I.4 Electric Field characterization of plasma jets

Currently many efforts are done to carry out detailed measurements in plasma jets. In particular, several optical diagnostics have been used to measure different reactive species of interest for biomedical applications [*Ono*, 2016]. Then, a fundamental property in both discharge dynamics and in jet applications is the electric field that determines the electron energy distribution function and consequently the plasma kinetics, as well as the electric drift. In plasma simulations, the electric field can be calculated at each point of a computational domain at each time-step. However, in experiments, due to the filamentary and transient character of streamer-like discharges, electric field measurements are hard to carry out. In the past there have been efforts to relate analytically the electric field in streamer-like discharges with other quantities of the discharge that are more easily accessible [*Kulikovsky*, 1997, 1998a, b; *Bazelyan and Raizer*, 1998]. Recently, many experimental groups are working on different techniques to directly measure electric field.

I.4.1 Optical measurements of electric field

For discharges in air, the electric field can be derived in a non-intrusive way from the emissions of the second positive system (SPS) of N_2: $C^3\Pi_u \rightarrow B^3\Pi_g$ and of the first negative system (FNS) of N_2: $B^2\Sigma_u^+ \rightarrow X^2\Sigma_g^+$. If the populations of the emitting states are assumed to be in steady state, the intensity ratio of the two emissions can be related to the ratio of excitation rates, which is a sensitive function of the electric field and thus allows to determine the electric field in air discharges. This procedure has been used in many experimental works [*Gallimberti et al.*, 1974; *Pancheshnyi et al.*, 2000; *Kozlov et al.*, 2001; *Starikovskaia et al.*, 2010; *Hoder et al.*, 2016] and many theoretical and numerical works have focused on corrections to accurately evaluate the measured results using this technique [*Naidis*, 2009; *Celestin and Pasko*, 2010; *Bonaventura et al.*, 2011; *Obrusník et al.*, 2018; *Bílek et al.*, 2018]. Then, for He jets, *Sretenovic et al.* [2011] has first used the classical emission spectroscopy technique based on the application of the polarization-dependent Stark splitting and shifting of He I 492.19 nm line and its forbidden counterpart for electric field measurements, following the same methods as in *Kuraica and Konjevic* [1997]; *Obradovic et al.* [2008]. The axial component of electric field has been reported along the axis of propagation of the AC-driven discharge front propagating in air and as radial profiles in the plasma plume, with maximum values in the order of 20 $kV.cm^{-1}$ and good agreement with model predictions. The Stark splitting and shifting is only detected with relatively high electric fields. In conditions in which the Stark method cannot be used, another spectroscopic method based on He line intensity ratio (He I 667.8 nm and He I 728.1 nm) is possible [*Ivkovic et al.*, 2014]. This method

relies on the local field approximation and therefore requires relatively high (atmospheric) pressure. Then, in *Sretenovic et al.* [2014a] the Stark polarization technique has been used again to measure the electric field in the He discharge head and a relation between the electric field and the discharge velocity has been documented. Moreover, *Sretenovic et al.* [2014b] have proposed to confirm this relation by using a simple model, called the 'isolated head' model based on Meek's criterion of an avalanche to streamer transition in a uniform field [*Meek*, 1940]. Following the steps proposed in *Kulikovsky* [1998a, b] for air streamers where the head is assumed to be equivalent to a uniformly charged ball, the relations between velocity and electric field for pure He and He-air mixtures have been derived and compared with experimental outcomes, with qualitative agreement on the order of magnitude for fields lower than 20 kV.cm^{-1}. In *Wu et al.* [2016] the electric field of a pulsed He discharge inside different tubes has also been measured through Stark polarization and the same model based on Meek's criterion has been used to estimate velocity and compare it with experimental results. They have concluded that the velocity is not only dependent on the electric field but also proportional to the discharge front diameter. Moreover, in *Sretenovic et al.* [2017] the Stark shift method has been used to measure the electric field in the AC-driven discharge front on the axis both inside the dielectric tube and in the plasma plume and then a method to estimate the electron density from the electric field measurements has been applied, following the steps in *Boeuf et al.* [2013]. This method assumes there is only electron drift and electron-impact ionization in the region of maximum electric field and thus equates the inverse of the Maxwell relaxation time to the ionization frequency, obtaining $n_e = (\epsilon_0/e)\alpha * E*$, where $E*$ is the maximum electric field and $\alpha*$ is the Townsend ionization coefficient calculated at $E*$. For measured electric field values in the range 5-20 kV.cm^{-1}, this procedure provides electron densities between 10^9 and 2×10^{12} cm^{-3}. Then, in *Hofmans* [2017] the same electric field measurement technique has been used for a pulsed He jet with different targets at floating potential and it has been confirmed that a higher dielectric permittivity of the target leads to a higher electric field in the front of propagation. The same has been done in *Kovacevic et al.* [2018] with AC voltage and a water target with different conditions of flow and tube-target distance. It is interesting to notice that a slope increase of electric field has been detected at the last mm of propagation before impact on the target. Other works [*Olszewski et al.*, 2014; *Sobota et al.*, 2016; *Lu et al.*, 2017] have used the Stark polarization technique to measure the electric field at the discharge front in helium, along its axis of propagation, with different parameters, and have found values with the same order of magnitude 10-25 kV.cm^{-1}. All the measurements have been carried out with positive applied voltage. This technique offers the advantage of being non-intrusive and providing electric field values in the plasma, but the value of electric field measured corresponds only to the maximum of light recovered and thus has limited spatial resolution.

I.4.2 Electric field measurements through electro-optic probes and laser diagnostic techniques

Other techniques have been used to measure the electric field in plasma jets. In *Begum et al.* [2013] an intrusive dielectric probe has been used to measure the maximum of electric field along the axis of the He jet propagation in air and has found values between 5 and 20

kV.cm^{-1}. In *Robert et al.* [2015]; *Bourdon et al.* [2016]; *Darny et al.* [2017b], time-resolved electric field components in the vicinity of the dielectric tube have been measured with a dielectric electro-optic probe. This technique allows to obtain the full temporal evolution of both radial and axial components of electric field at a given position outside the plasma. Other groups use laser diagnostic techniques. In *Goldberg et al.* [2015] the electric field vector components have been measured with temporal and spatial resolution in a ns-pulsed surface ionization wave discharge in H_2 sustained between two copper electrodes on an alumina ceramic dielectric surface, using a picosecond CARS-based four-wave mixing technique with detection lower limit 0.4 kV.cm^{-1}. This technique allows to obtain the electric field at high pressure in sheaths and filamentary discharges where N_2 or H_2 are present. The same technique has been used to determine the electric field strength with a rectangular μs pulse operated filamentary DBD in N_2-H_2 mixtures in *Bohm et al.* [2016] and in N_2 plasma jets in *van der Schans et al.* [2017]. Then, in atmospheric air, it has been used in a nanosecond pulse discharge sustained between a razor edge high-voltage electrode and a plane grounded electrode covered by a thin quartz plate in *Simeni et al.* [2017], between two parallel cylinder electrodes covered by dielectric tubes, and between a razor edge high-voltage electrode and distilled water surface in *Simeni et al.* [2018]. For now, to our knowledge, these techniques have not been used in plasmas in mixtures containing He at atmospheric pressure.

I.4.3 Electric field measurements through Mueller polarimetry

Furthermore, as mentioned earlier, other experimental studies have focused on the examination of electric fields inside dielectric targets exposed to discharge impact. These can be investigated with Mueller polarimetry using electro-optic crystals, since their refractive index changes linearly with the induced electric field. The measured change in refractive index can be used to visualize the electric field to which the crystals are exposed to. The electric field can be obtained with temporal resolution and along the length of the crystal, but not along its thickness. Thus, it is considered as the field averaged through the crystal thickness. As the electric field values are solely due to charge deposition on the surface, an estimation of the surface charge densities can be made when a homogeneous field approximation is applicable or a homogeneously charged disk is considered [*Slikboer et al.*, 2017]. The visualization of electric field or surface charge density using electro-optic targets has been applied by *Kawasaki et al.* [1991]; *Zhu et al.* [1995] to study the propagation of streamers on dielectrics. It has also been used with He plasma jets by *Sobota et al.* [2013]; *Wild et al.* [2014]; *Slikboer et al.* [2016] and DBDs by *Stollenwerk et al.* [2007]; *Bogaczyk et al.* [2012]; *Tschiersch et al.* [2014]. It offers an unique way to estimate the fields and surface charge densities these targets are exposed to. The conventional investigation of the electro-optic crystals allows for the detection of the electric field perpendicular to the surface. Recent developments show the possibility to simultaneously measure and decouple all electric field components (axial and radial) inside the electro-optic crystal [*Slikboer et al.*, 2018b]. The simultaneous detection of the axial and radial components of the electric field, as in the example in Fig. I.9, is an important tool to also investigate the dynamics of the discharge propagation on the surface. In Fig. I.9 the axial component of electric field is centered at the location of discharge impact and the radial component is distributed around the edges of the region of charge deposition.

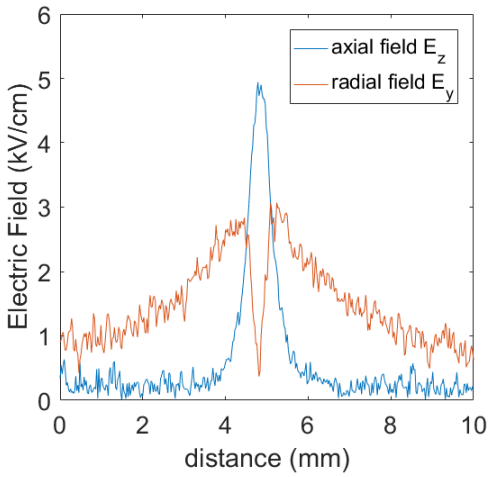

Figure I.9: Radial profiles of axial and radial electric field components inside a dielectric target, exclusively due to surface charges deposited on its surface, after the impact of an AC-driven He discharge. Figure from *Slikboer et al.* [2018b].

The recent developments in electric field measurements in He plasma jets in experiments are exciting news concerning the detailed characterization of He jets and their applications on targets. Each method has its particularities. Then, in *Bourdon et al.* [2016], it has been shown the interest to use plasma jet experiments and simulations in a complementary way to derive from measured values of electric field, its value in locations where it is not measured.

I.5 Memory effects and flow channeling in repetitive plasma jets

The experimental results reported on He plasma jets, either AC-driven or pulsed (usually in the kHz range), usually refer to reproducible discharge dynamics. This characteristic of jets is highly attractive as it promises a high degree of control in many applications. However, experimentalists also report that the first few discharges ignited and propagated are not reproducible, i.e. the first discharges behave differently than the rest. This implies that the initial conditions differ from pulse to pulse until repeatability is reached. The physical quantities building up from pulse to pulse and thus consisting on the initial conditions for discharge ignition and propagation are called memory effects. These can be the accumulation of species densities in volume: electrons that become seed electrons in the next discharge, positive ions, negative ions that can be detached in the next discharge, excited species and radicals that can either ionize or attach easily in the next discharge; the remaining of charges deposited on surfaces that can either attract or repulse the next discharge; gas heating that changes plasma chemistry; modification of flow and thus of the spatial distribution of the main species densities. Moreover, memory effects depend on the discharge conditions, and particularly, on the gas-mixture. In fact, one additional reason for discharges to be guided through the He channel in the plasma plume, apart from the higher ionization coefficient, can be the different initial conditions.

I.5.1 Initial conditions for discharge repeatability

In *Wu and Lu* [2014] the length and velocity of a μs positive pulsed He jet plume have been reported to decrease between the 1^{st}, 2^{nd} and 3^{rd} pulses and be repeatable from the 3^{rd} pulse, while the discharge ignition only becomes repeatable at the 100^{th} pulse. They suggest that the decrease of length and velocity between the first three pulses is due to positive charges deposited on the tube wall that decrease the electric field in volume and thus the plume length is shorter for higher pulse frequency. Then, by measuring current, they have estimated that the stochastic character of the ignition is only canceled when the residual electron density reaches 10^9 cm^{-3}. A recent review about the repeatability of guided ionization waves [*Lu and Ostrikov*, 2018] also concludes that, in order to propagate in a repeatable mode, the discharge, in whatever gas, must propagate in a channel with a high seed electron density (HSED), which is of the order of 10^9 cm^{-3}. Conversely, in *Mussard* [2015] the length of propagation of an AC-driven discharge in positive phase in a tube has been shown to increase from pulse to pulse and this effect has been attributed to the accumulation of positive surface charges in the tube inner wall. Also in *Guaitella and Sobota* [2015], where an AC-driven He jet impacts a glass target, it has been suggested that positive charges remain on the dielectric target surface. In that work an ionization wave reaches the surface only during the positive voltage slope of the voltage cycle. Then, the footprint of the positive charge deposited induces a low light emission during the negative voltage slope when the plasma appears to vanish. In *Schmidt-Bleker et al.* [2015] another memory effect has been proposed based on the presence of O_2 in the surrounding environment. As negative ions are formed on the edge of the He channel in the plasma plume, they help to focus the propagation of the ionization wave on the axis, similarly to negatively charging the walls of a capillary. Memory effects are therefore an important subject on He plasma jets that is still largely unknown. It influences discharge repeatability, discharge kinetics and dynamics and plasma-surface interactions. Moreover, for plasma models as the one used in this thesis, the initial simulation conditions are of paramount importance for the accurate description of discharge dynamics and these are hard to obtain from the modeling results because usually only single discharges are self-consistently simulated due to constraints in computational time.

I.5.2 Plasma jet effect on flow

Besides the determination of initial densities of species in volume and on surfaces, it is interesting to notice that plasma effects on the flow appear in long timescales, and thus can be considered as memory effects, as each new distribution of gases has an influence on the next pulse. The action of the plasma on the gas flow is an exciting new topic in the study of He plasma jets. In one of the first studies to report on the gas flow modifications [*Oh et al.*, 2011], they have visualized the He flow with Schlieren imaging and reported that the plasma enhanced the transition from laminar to turbulent regime. Two hypothesis have been proposed: thermal effects associated with the gas heating and electrohydrodynamic (EHD) force due to momentum transfers of charged particles to neutrals by effect of the electric field during discharge and/or in post-discharge. These effects are known from other low-temperature plasmas [*Fruchtman*, 2017]. Since then, many experimental studies have reported on gas flow modifications by effect of plasma jets. In the study of *Zhang et al.* [2015], with an Ar

plasma jet, the gas temperature has been measured through Rayleigh scattering and it has been observed that the increase of the temperature near the capillary outlet is responsible for an increase of the gas flow velocity and the onset of vortex structures at the jet effluent. Nevertheless, for a higher plasma power, the authors have observed a stabilization of the flow and an increase of the jet length, for which the role of EHD force has not been excluded. In the experimental work with pulsed He jets in *Robert et al.* [2014, 2015], it has been shown that the He flow is differently affected with a metallic target set downstream at grounded or at floating potential, and with the use of positive or negative applied voltage polarity. Then, in *Darny et al.* [2017a], with a He jet directed downwards with a low flow rate, it has been shown that the plasma activation greatly enhances the He flow downstream expansion, allowing to reach a target a few cm below the capillary. This leads to the generation of a stable cylindrical He channel with a spreading of the flow over the whole grounded target surface, as long as the plasma is turned on, as presented in Fig. I.10. Such stable flow conditions are not achieved in *Darny et al.* [2017a] using positive polarity pulses, where the He channel remains in this case perturbed during plasma activation. It has been suggested that this dependence on the voltage polarity is due to the drift direction of long life-time negative ions through EHD. Moreover, Fig. I.10 provides evidence that the plasma effect on the flow has a memory component, as it is dependent on the pulse frequency and builds up with number of pulses, requiring at least 150 pulses to stabilize. Then, in *Park et al.* [2018], with a horizontal pulsed plasma jet, the He gas flow trajectories have been observed to become relatively horizontal in the presence of plasma, which is attributed to EHD, since heating is considered negligible. Finally, in *van Doremaele et al.* [2018], with pulsed positive and negative He jets impinging downstream on a glass substrate, gas temperature measurements through optical emission spectroscopy have found an increase of less than 15 K and air concentration measurements in the jet effluent through Rayleigh scattering have found a broadening of the He channel through plasma effect, with stronger effect with positive rather than negative polarity. In that work, the He channeling (i.e. the broadening of the He channel) is attributed to EHD forces in long timescales related to surface charges remaining on the glass surface.

Numerical modeling is a possible strategy to better understand these plasma-flow interactions. *Shao et al.* [2013], for an Ar plasma jet, considering multipulse conditions, have found that adding an EHD force term ($\vec{F} = q_e(n_+ - n_-)\vec{E}$) in Navier-Stokes equation in a fluid dynamics model in 3D, using several approximations concerning the electric field, allowed to obtain a forward momentum in the flow, in agreement with experimental observations. In *Papadopoulos et al.* [2014] as well, with both Schlieren visualization and a fluid dynamics model of a He jet, having included an estimated EHD force term (5000 $\mathrm{N.m^{-3}}$) in the model, have found evidence of weak effect of gas heating and of a strong effect of EHD capable to force the flow to overcome buoyancy and to accelerate it in the helium jet direction, in agreement with the patterns observed in experiments. We should notice that in these models the electric field and the charged species densities are not self-consistently calculated with plasma equations. Then, in *Hasan and Bradley* [2016], with a 2D discharge model for ns single pulsed He jets including Poisson's equation, time-averaged EHD and gas heating are furnished to a fluid dynamics model that calculates the evolution of flow for 20 μs. In these conditions, they have found that the magnitude of the EHD forces in a He jet is approximately an order of magnitude lower than typically in DBD air actuator configurations. Moreover, the dominant

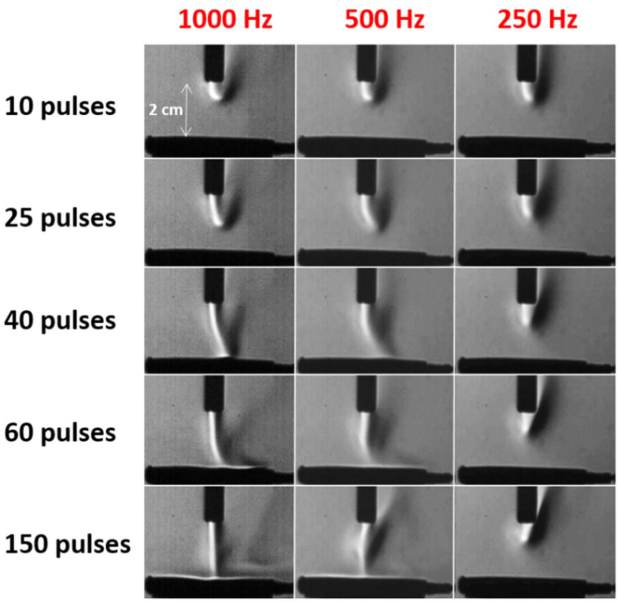

Figure I.10: Helium channeling dynamics as a function of the number of voltage pulses after the plasma has been turned on, for three different pulse repetition rates. The applied voltage is a -14 kV pulse of 4 μs width. Figure from *Darny et al.* [2017a].

heating mechanism has been shown to be the inelastic losses of electrons, increasing the gas temperature by 100 K with pure He as buffer gas and up to 180 K with O_2 and N_2. Thus, they have shown that in their conditions the gas heating is the dominant mechanism responsible for the perturbation of the background gas flow pattern whose velocity increases and density decreases. In *Lietz et al.* [2017] the plasma dynamics has been solved together with modified Navier-Stokes equations and it has been found that localized gas heating takes place in a He jet at the powered electrode during a single voltage pulse of 100 ns and produces an acoustic wave, consistent with experimental results [*Boselli et al.*, 2014; *Qaisrani et al.*, 2016], that propagates at the gas flow velocity in the μs timescale. EHD forces are claimed to not have an effect on flow in these timescales.
The predominance of either the EHD force with electric wind or the thermal effects with gas heating regarding the gas flow modifications through action of plasma jets remains an open question. Given the diversity of plasma jet configurations and power supplies, the influence of each effect is probably highly dependent on the particular jet conditions and on the timescales evaluated.

I.6 Motivations and plan of this thesis

Considering the current state of the research on He plasma jets, increasingly detailed characterization of jets is required in specific conditions close to applications. In particular, experimental techniques to measure electric field in plasma jets have made significant progresses in the last years. Electric field is a key physical parameter in these discharges that may have an impact on applications directly, but also through its influence on the production of reactive species. Then, this thesis aims at providing a contribution to deepen the understanding on some fundamental questions, using a two-dimensional fluid model:

- How do discharge dynamics and structure inside the tubes differ for positive and negative polarities of applied voltage?

- What are the properties of the gas mixing between He and air gases in the plasma plume that define the discharge path of propagation?

- What is the rebound front reported in section I.3.1 for jets impacting metallic surfaces?

- How does the rebound front impact the production of species close to the target?

- How can electric field measurements outside the tube as those in *Darny et al.* [2017b] be related to discharge properties?

- What is the 'back discharge' reported in section I.3 and how does it depend on the electrical character of the target?

- How do the electric field values measured in the discharge front and measured inside a dielectric target relate to those experienced by the target and to discharge dynamics?

Thus, this thesis is organized as follows:

- Chapter II presents the two-dimensional fluid model used to describe discharge dynamics in this thesis, both in its initial state and with developments carried out during this thesis. Focus is given to the implementation of chemistry models that allow to describe He jets interacting with air molecular gases; the coupling between flow calculations and the discharge model to describe the spatial distribution of species in jets with He flowing into air; the inclusion of electron energy transport in the model to improve the ability to describe plasma-surface interactions.

- Chapter III provides a general characterization of discharge dynamics of propagation in He jets before considering its interaction with targets, using the 2D discharge model. Different configurations are investigated for the following parameters: tube radius and permittivity, polarity of applied voltage, electrode geometry, temporal profile of applied voltage, gas-mixture, flow rate and tube-target distance. Particular attention is paid to fundamental questions about the role of the tube on discharge propagation and structure and how it differs for positive and negative polarities of applied voltage, as well as about the propagation mechanisms that confine the discharge front radially when gas mixing is taken into account in the plasma plume.

- Chapter IV presents the discharge dynamics when interacting with a grounded metallic target. In particular the rebound front reported in section I.3.1 is described as an ionization wave of partial neutralization of the plasma channel and qualitative comparison is carried out with the electric field measurements on the outside of the tube in *Darny et al.* [2017b]. The effect of the rebound front on the production of reactive species close to the target is also examined. Moreover, it is evaluated how simulations can complement experiments, deriving discharge properties and relating them to the electric field outside the tube and how the rebound front impacts the production of species close to a metallic target.

- Chapter V shows how the different electrical character of the targets influences the discharge dynamics. This examination is carried out for dielectric targets of different permittivity, as well as for metallic targets grounded and at floating potential. Not only the propagation and post-impact dynamics are described, but also the discharge evolution after the end of the pulse of applied voltage and the associated 'back discharge' reported in section I.3. Additionally, a proposal on how to describe metallic targets at floating potential is put forward.

- Chapter VI carries out a detailed comparison with the electric field inside a dielectric target experimentally measured by Elmar Slikboer, Ana Sobota and Olivier Guaitella at LPP. The simulation results allow to relate the electric field values measured in the front of propagation in the plasma plume and inside the dielectric target. Moreover, they allow to relate the measured electric field, averaged over the thickness of the target and due exclusively to surface charges, to the electric field on the target surface, the surface charge density distribution and the electric field associated also to charges in volume.

- Chapter VII presents a summary of the conclusions taken from the studies in this thesis and some propositions to carry on research on He plasma jets through numerical simulations.

Chapter II

Numerical model for Helium plasma jets at atmospheric pressure

Contents

II.1 Introduction 28

II.2 Physical model for Helium discharges at atmospheric pressure . 28

II.2.1 Plasma characteristics 28

II.2.2 Discharge model 29

II.3 Two-dimensional axisymmetric fluid model for Helium discharges 31

II.3.1 Introduction 31

II.3.2 Conservation equations 32

II.3.3 Poisson's equation and determination of charge contributions to the electric field distribution 37

II.3.4 Reaction scheme, initial conditions, rate coefficients, photo-ionization and transport parameters 39

II.4 Modeling of plasma jets with flowing He-N_2 and He-O_2 gas mixtures 42

II.4.1 Introduction 42

II.4.2 Investigation and implementation of chemistry models 43

II.4.3 Coupling of flow calculations with the plasma model 51

II.4.4 Code parallelization and profiling 54

II.4.5 Study of the electron energy equation and the mean electron energy approximation 56

II.5 Simulation conditions 62

II.1 Introduction

The main tool used in this thesis to investigate the physics of single-pulse Helium plasma jets at atmospheric pressure is a numerical model that allows to simulate the temporal and spatial evolution of the physics in the plasma. It consists in a two-dimensional axisymmetric fluid model for gas discharges, derived from Boltzmann's kinetic theory. This numerical model has been used during this thesis on two multi-core clusters:

- "Hopper", that belongs to several laboratories of École Polytechnique. Its main queue is composed of 32 nodes DELL C6200 bi-pro with two 8-core processors (16 cores per node), 64 GB of memory and 2.6 GHz frequency per node. The maximum number of cores that can be used at once is 128 and the usual number of cores used for calculations in this thesis is 32.

- "Zoidberg", that belongs to Laboratoire de Physique des Plasmas. It is composed of four multi-core machines with Supermicro motherboard with 4 AMD Opteron (6274 or 6370P) 16-core processors (64 cores per machine), 256 GB of memory and 2.0-2.5 GHz frequency per node. The usual number of cores used for calculations in this thesis is 32 or 64.

In section II.2 the physical foundations to describe the discharges studied in this thesis are exposed. These include the temporal and spatial scales that characterize the dynamics of these plasmas, as well as the equations that describe streamer discharges. Then, in section II.3 the formulation of the numerical model is presented. The model exposed in that section is the one existing at the beginning of the work leading to this thesis, inherited from the PhD thesis of François Péchereau [*Pechereau*, 2013].
However, modeling the plasma jet conditions addressed in this thesis has required the development of the numerical model. In section II.4 the challenges to model Helium plasma jets with flowing gas mixtures and surface interactions are exposed and the improvements carried on the model and implemented during the work leading to this thesis are presented. These include the investigation of chemistry reaction schemes, the coupling between flow calculations and the discharge model, and the implementation of the electron energy equation and the local mean energy approximation. Furthermore, the profiling of the parallelized code in the multi-core cluster "Hopper" of École Polytechnique is presented. Finally, in section II.5 the different simulation conditions used throughout the thesis are briefly exposed.

II.2 Physical model for Helium discharges at atmospheric pressure

II.2.1 Plasma characteristics

In this thesis we study discharges at atmospheric pressure and we consider that in Helium discharges there is no gas heating $T_g = 300$ K. Therefore, the gas density is invariable $N = 2.45 \times 10^{19}$ cm^{-3} and the plasma is highly collisional. We assess the propagation of Helium discharges as single ionization waves typically in lengths of some cm during some hundreds

ns, with velocities in the order of 10 cm.μs^{-1} (i.e. 10^7 cm.s^{-1} or 10^5 m.s^{-1} or 100 km.s^{-1}). As such, the discharge under study is transient, i.e. non-stationary, and filamentary, i.e. inhomogeneous in volume. After discharge propagation, the plasma post-discharge is studied in the μs timescale. The discharge can propagate in volume without surface constraints or inside a tube with a radial constraint typically of 1 or 2 mm radius or towards a surface positioned perpendicularly to discharge propagation. Two examples of geometries used in this thesis are shown later in this chapter in Figure II.10. The layers of strong net volume charge at the discharge front or in plasma-surface interactions have dimensions typically of the order of a few Debye lengths, some dozens μm. The resolution required to describe the dynamics of the ionization wave is usually of the order of ps in time and of 10 μm in space. Overall, the system to describe has multiple scales in time and space.
The magnitude of the electric fields in the discharge front typically has values of $10s$ kV.cm^{-1} (if $E = 10$ kV.cm^{-1}, $E/N = 40$ Td), reaching up to 100 kV.cm^{-1} (400 Td) in some plasma-surface interactions. In the plasma channel, the electric field is lower, typically around 1 kV.cm^{-1} (4 Td), and in post-discharge it can decrease to zero. The mean electron energy ϵ_m and the electron temperature T_e ($T_e = \epsilon_m \times 2/3$) are usually of the order of units or $10s$ eV (1 eV = 11 605 K) and can reach up to 50 eV in some surface interactions. Typical electron densities n_e are of the order of $10^{11} - 10^{13}$ cm^{-3}, and can reach up to 10^{14} cm^{-3}. The plasma is generally quasi-neutral but deviations to quasi-neutrality are considered.
In a plasma, we consider the charges are screened inside a sphere of Debye radius:

$$\lambda_D = \sqrt{\frac{\epsilon_0 k_B T_e}{n_e q_e^2}} = \sqrt{\frac{T_e\,(\mathrm{K})}{n_e\,(\mathrm{m}^{-3})}} \times 95.24\,(\mathrm{m}^{-1/2}.\mathrm{K}^{-1/2}) \tag{II.1}$$

The Debye radius defines the scale above which we can consider the charged particles act collectively in a plasma and a macroscopic fluid formulation is accurate to describe the dynamics of charged particles. In the studies carried out in this thesis, typical values can be, with $n_e = 10^{18}$ m^{-3} and $T_e = 10\,000$ K or $n_e = 10^{19}$ m^{-3} and $T_e = 100\,000$ K, $\lambda_D = 9.5$ μm.

II.2.2 Discharge model

A recent publication [*Alves et al.*, 2018] introduces different plasma models and arguments to use them and presents, among other features, the foundations of fluid models, as the one used and developed in this thesis. In fact, the distribution function f_k of particles of species k in a weakly ionized plasma satisfies the Boltzmann equation from the elementary kinetic theory of gases:

$$\frac{\partial f_k}{\partial t} + \vec{v_k}.\nabla_r f_k + \frac{\vec{F_k}}{m_k}.\nabla_v f_k = \left(\frac{\partial f_k}{\partial t}\right)_c \tag{II.2}$$

where ∇_r and ∇_v represent the gradient operators in configuration space and in velocity space, respectively; $\vec{v_k}$ and $\vec{F_k}$ are the velocity and force exerted on the particles; m_k is the mass of particle k and $\left(\frac{\partial f_k}{\partial t}\right)_c$ accounts for the temporal change in f_k due to collisions. Then, the fluid or hydrodynamic equations emerge by calculating the moments of the Boltzmann equation. The moments of the Boltzmann equation are conservation laws for any quantity $\chi(\vec{r}, \vec{v_k}, t)$ associated with a species k. In order to derive a macroscopic conservation law for this quantity, equation II.2 is multiplied by χ and integrated in velocity space. By making

$\chi = 1$, the first moment gives the equation for the conservation of the number density of species k, i.e. the continuity equation. With $\chi = m_k\vec{v_k}$ (second moment), the equation for the momentum conservation or Euler equation is obtained. Finally, the equation for energy conservation can be obtained with $\chi = m_k|\vec{v_k}|^2/2$.
In the version of the model used in most of this thesis, only the continuity and momentum conservation equations are considered. In section II.4.5 the equation for energy conservation will be discussed. Thus, the formulation we use is the most widely studied to describe transient discharge dynamics at atmospheric pressure, and has proven its efficiency [*Kulikovsky*, 1997]. It is based firstly on the continuity equations for all the species k in the plasma:

$$\frac{\partial n_k}{\partial t} + \nabla.\vec{j_k} = S_k \tag{II.3}$$

where n_k is the number density, $\vec{j_k}$ is the flux and S_k is the source/loss term of species k. Sources and losses of species k are defined by chemical reactions and photo-ionization. For the charged species (electrons, positive ions and negative ions), we have considered the flux to follow the classical drift-diffusion approximation. This is obtained from the momentum conservation equation under the assumption of high plasma collisionality, valid at pressures as high as atmospheric pressure, and negligible flow, valid in the timescales under study in this thesis. It is written as:

$$\vec{j_k} = n_k\vec{v_k} - D_k\nabla n_k \tag{II.4}$$

$$\vec{v_k} = (q_k/|q_e|)\mu_k\vec{E} \tag{II.5}$$

where $\vec{v_k}$ is the electric drift velocity, μ_k is the mobility, D_k is the diffusion coefficient and q_k is the electric charge of species k (either $+q_e$ or -q_e), $\vec{E}$ is the electric field and q_e is the electron charge. Neutral species are not transported through electric drift but can have a flux due to diffusion. However, the diffusion of neutrals is only relevant in timescales longer than 10 μs ($\Delta t \sim \frac{\Delta x^2}{D} \sim \frac{(10^{-3}\,\mathrm{cm})^2}{10^{-1}\,\mathrm{cm^2.\,s^{-1}}} = 10$ μs). As in this thesis the timescales of relevance are shorter than 10 μs, we do not consider the transport of neutral species through diffusion, and thus the temporal evolution of their densities is defined exclusively by the source and loss terms. The total source and loss terms for every species k are obtained by summing (for sources) and subtracting (for losses) the term corresponding to each reaction. These terms can take different forms, but for chemical reactions they are the product of the rate coefficient by the densities of the reacting species. For example, the source term for a reaction l with rate coefficient K_l between species $k1$ and $k2$ can be written as $S_l = K_l \times n_{k1} \times n_{k2}$. The electron transport coefficients μ_e and D_e and the electron-impact rate coefficients are dependent on the gas-mixture and can be obtained by solving the electron Boltzmann equation (EBE) to obtain the electron energy distribution function (EEDF), which requires using an EBE solver complementary to the fluid model. Moreover, they can be assumed to be dependent on the local reduced electric field E/N or on the local mean electron energy ϵ_m, as will be explained in section II.4.5. The initial version of the model used in this thesis assumes the local field approximation, where the coefficients are dependent on E/N.
Finally, the system of equations to study the discharge dynamics is closed with Poisson's

equation that takes into account different dielectric permittivities (gas or dielectric material):

$$\epsilon_0 \nabla.(\epsilon_r \nabla V) = -\rho - \sigma\delta_s \tag{II.6}$$

$$\vec{E} = -\vec{\nabla} V; \rho = \sum q_k n_k \tag{II.7}$$

where V is the electric potential, ϵ_0 the vacuum permittivity, ϵ_r the relative permittivity, ρ the net volume charge density, σ the net surface charge density and δ_s the Kronecker delta (equal to 1 on the dielectric/gas interfaces: tube and target). Poisson's equation, coupled to the continuity equations, guarantees that the calculation of charges and electric fields is self-consistent. In this model, magnetic field effects on the discharge propagation are neglected as discussed in *Celestin* [2008] for air streamers.
The temporal evolution of the discharge dynamics proceeds in the model as follows:

- Initial densities of species are set in the domain, guaranteeing quasi-neutrality.
- An applied voltage is provided to the electrodes in the domain, defining a Laplacian electric potential and electric field distribution.
- Continuity equations, under the effect of the electric field, lead the species in the plasma to evolve through transport and chemistry.
- The movement and production of charges generates ρ and σ in the domain.
- The new electric field in the domain is determined not only by the applied voltage but also by ρ and σ, it acts on the transport and chemistry of species in the plasma, and the cycle starts over.

II.3 Two-dimensional axisymmetric fluid model for Helium discharges

II.3.1 Introduction

The numerical model used and developed in this thesis is inherited from the numerical models developed in the group, exposed in several PhD thesis [*Celestin*, 2008; *Tholin*, 2012; *Pechereau*, 2013] for air streamers. Then, these have been adapted for Helium discharges [*Jánský and Bourdon*, 2011a; *Jánský et al.*, 2012; *Jánský and Bourdon*, 2014]. Finally, the numerical model presented here is directly inherited from the model for Helium discharges presented in *Pechereau* [2013] (chapters 4.3 and 9) and used and validated against experimental results in *Bourdon et al.* [2016].
Before presenting the model, a brief introduction of the challenges to simulate transient and filamentary discharge dynamics at atmospheric pressure is required. First, we should notice that the phenomena studied in this thesis require a two-dimensional description of the discharge dynamics. As the studied phenomena are axisymmetric, the discharge domain is described in cylindrical coordinates: axial z and radial r. Since the electric field associated to discharge propagation and charge transport is coupled with the net volume charge layer at the discharge front and between the plasma and surfaces, strong gradients of electric field

are present. Thus, the spatio-temporal evolutions of electric field and species in the plasma require high numerical accuracy to be correctly described. Moreover, these discharges are spatially and temporally multi-scale phenomena, as noticed in section II.2.1. This implies that the model needs to describe space and time scales separated by several orders of magnitude (μm to cm and ps to μs) and therefore the mesh size and iteration time-step are permanent concerns. In this thesis, the mesh is constant during a simulation and its size in the whole region where the plasma dynamics takes place, both in the radial and axial directions, is generally of 10 μm. Results of discharge dynamics have been compared with 5 μm and 10 μm mesh size and the difference is of the order of 1%.

II.3.2 Conservation equations

This section presents the methods and parameters used to solve the conservation equations II.3 for every species in the plasma. These equations describe the temporal evolution of the local number density of each species by means of transport through electric drift and through diffusion and by local gains and losses through reactions.

Finite volume methods

The model in this thesis is written in Fortran 90 in a finite volume setting. Finite volume methods are based on the integral formulation of the partial differential equations to be solved. By construction, these methods guarantee the conservation of the transported physical quantity [*Ferziger and Peric*, 2002]. For discharge modeling, this property is crucial for the conservation of charge during the simulation. In finite volume (or control volume) methods, the domain is subdivided into a finite number of small control volumes by a grid or mesh. In this work we use only structured grids. In this type of grid one can work either with the nodes centered in control volumes (see Figure II.1) or with the faces centered between nodes [*Ferziger and Peric*, 2002]. In the present work we have used node-centered grids.

Temporal splitting approach

We calculate the local temporal variation of species densities in each control volume (cell) described by eq. II.3 by splitting it into three temporal variations:

$$\frac{\partial n}{\partial t} = S \tag{II.8}$$

$$\frac{\partial n}{\partial t} = -\nabla.\vec{j}_{diff} = D\nabla^2 n \tag{II.9}$$

$$\frac{\partial n}{\partial t} = -\nabla.\vec{j}_{drift} = -\nabla.(n\vec{v}) \tag{II.10}$$

Then, the solution at time $t + \Delta t$ (represented by the operator $U^{t+\Delta t}$) can be obtained using a first order operator splitting method, i.e. applying sequentially the temporal evolutions in Δt by chemistry (operator $R^{\Delta t}$), diffusion ($D^{\Delta t}$) and drift ($C^{\Delta t}$) to the solution at time t (operator U^t):

$$U^{t+\Delta t} = C^{\Delta t} D^{\Delta t} R^{\Delta t} U^t \tag{II.11}$$

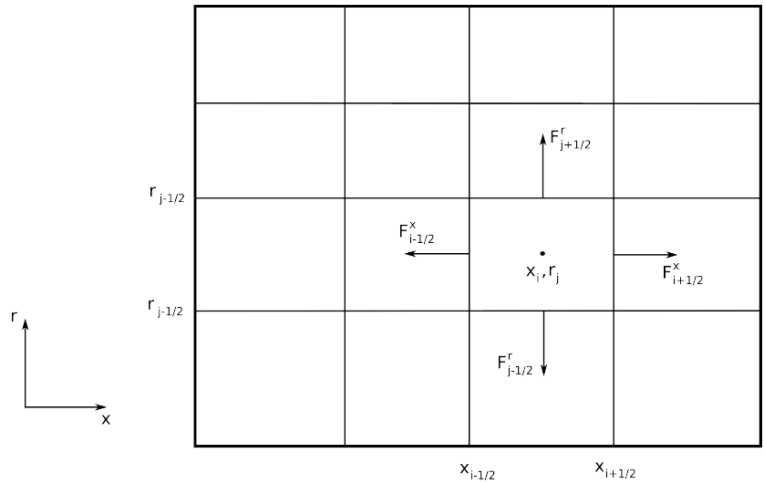

Figure II.1: Representation of the numerical grid. Control volumes are referenced by their centers and are defined by their edges between $x_{i-1/2}$ and $x_{i+1/2}$, and between $r_{j-1/2}$ and $r_{j+1/2}$. The arrows represent the outward unit normal vectors of the boundaries of the cell (i, j), through which quantities are transported between cells. Figure from *Celestin* [2008]. There, the axial coordinate is called x, while in this thesis it is called z.

Solution of transport equations in a finite volume setting

Transport equations II.9 and II.10 are solved in a finite volume setting firstly by integration over the volume $\Omega_{i,j}$ of the cell (i, j):

$$\frac{\partial n_{i,j}}{\partial t} + \frac{1}{\Omega_{i,j}} \int_{\Omega_{i,j}} \nabla . \vec{j} d\Omega = 0 \tag{II.12}$$

where $n_{i,j}$ is the average density over $\Omega_{i,j}$. Using the Gauss-Ostrogradsky theorem we have:

$$\frac{\partial n_{i,j}}{\partial t} + \frac{1}{\Omega_{i,j}} \int_{\partial\Omega_{i,j}} \vec{j} . \vec{n} d\Sigma = 0 \tag{II.13}$$

where $d\Sigma$ measures the infinitesimal surface of the cell boundaries and $\vec{n}$ is the outward unit normal vector. In cylindrical coordinates, the volume and surfaces of each cell are defined as:

$$\Sigma_{i+1/2,j} = \pi(r^2_{i,j+1/2} - r^2_{i,j-1/2}) \tag{II.14}$$

$$\Sigma_{i,j+1/2} = 2\pi r_{i,j+1/2}(z_{i+1/2,j} - z_{i-1/2,j}) \tag{II.15}$$

$$\Omega_{i,j} = \pi(r^2_{i,j+1/2} - r^2_{i,j-1/2})(z_{i+1/2,j} - z_{i-1/2,j}) \tag{II.16}$$

Decomposing the surface integral on the four surfaces of the cell, we obtain:

$$\frac{\partial n_{i,j}}{\partial t} + \frac{1}{\Omega_{i,j}}(F^z_{i+1/2,j} + F^z_{i-1/2,j} + F^r_{i,j+1/2} + F^r_{i,j-1/2}) = 0 \tag{II.17}$$

where $F^{z,r}_{i,j\pm1/2}$ are the fluxes due to drift or diffusion, defined with respect to the outward normal vector, respectively along z through the surface at $z_{i+1/2}$ and $z_{i-1/2}$ and along r through the surface at $r_{j+1/2}$ and $r_{j-1/2}$. Then, through a simple first-order Euler time

integration, from the density $n_{i,j}^k$ we obtain the density $n_{i,j}^{k+1}$ after a time-step Δt:

$$n_{i,j}^{k+1} = n_{i,j}^k - \frac{\Delta t}{\Omega_{i,j}}(F_{i+1/2,j}^z + F_{i-1/2,j}^z + F_{i,j+1/2}^r + F_{i,j-1/2}^r) \tag{II.18}$$

Next, we will see how the diffusion and drift fluxes are determined at each cell interface. These fluxes depend on the (unknown) values of the densities at the interfaces and not on the (known) averaged values of the density $n_{i,j}$ inside the control volume. Thus, the question to answer is how to express the different fluxes as approximate functions of $n_{i,j}$. Different methods can be used to solve this question. In *Pechereau* [2013] (chapter 3) different numerical schemes have been compared and it has been demonstrated that using the UNO3 scheme coupled with the MACHO operator for the calculation of the drift flux and a classical second order scheme for the calculation of the diffusion flux provides good robustness and accuracy to the discharge calculation. In this thesis, those are the schemes used as well.

Calculation of the drift fluxes

The third order UNO3 scheme is described extensively in *Li* [2008] and in *Pechereau* [2013] (chapter 3). The scheme is not only exposed in one dimension, it is also explained how to extend the 1D scheme to a 2D scheme. The purpose of the scheme is to estimate the density value on each cell boundary from the known densities of the neighboring cells. Then, to account for electric drift, the fluxes in eq. II.18 can be replaced by:

$$F_{i+1/2,j}^z = n_{i+1/2,j} v_{i+1/2,j}^z \Sigma_{i+1/2,j}; F_{i,j+1/2}^r = n_{i,j+1/2} v_{i,j+1/2}^r \Sigma_{i,j+1/2} \tag{II.19}$$

where v is the drift velocity (eq. II.5) defined at each cell boundary.

Calculation of the diffusion fluxes

We have used a classical second-order central-difference scheme. Then, to account for diffusion, the fluxes in eq. II.18 can be replaced by:

$$F_{i+1/2,j}^z = -D_{i+1/2,j}^z \frac{n_{i+1,j} - n_{i,j}}{z_{i+1} - z_i} \Sigma_{i+1/2,j}; F_{i,j+1/2}^r = -D_{i,j+1/2}^r \frac{n_{i,j+1} - n_{i,j}}{r_{j+1} - r_j} \Sigma_{i,j+1/2} \tag{II.20}$$

where D is the diffusion coefficient defined at each cell boundary.

Boundary conditions

In this work, the plasma interacts with several dielectric and metallic surfaces, both in the radial and axial directions. However, the transport equations described above have to be solved differently at plasma-surface interfaces. Diffusion fluxes only take place between plasma cells. Moreover, only transport of charged species is considered in the model and thus neutral species do not interact with the surfaces. Then, concerning electric drift of charged particles, different boundary conditions can be considered. As in these boundaries the densities of plasma species only exist on one side, the densities at the center of the cells are used to estimate the boundary fluxes, instead of the densities on the cell interfaces. In our model, ions behave the same way interacting with metallic or dielectric surfaces. They can

not be emitted by the surfaces and they can be recombined in metallic surfaces or deposited in dielectric surfaces. The flux density (flux per surface) $\vec{J_k}$ of ion k is therefore determined with respect to the outward normal of the surface $\vec{n}$ (inward to the plasma) as:

$$\vec{J_k} = n_k min(0, \vec{v}_k.\vec{n}).\vec{n} \tag{II.21}$$

where n_k and $\vec{v}_k$ are respectively the density (at the center of the last plasma cell) and drift velocity of the ion (either positive or negative). However, as ion mobility is around 100 times lower than electron mobility, the definition of their flux boundary conditions is not as important as that for electrons. Electrons can also be recombined in metallic surfaces and deposited in dielectric surfaces. However, as they are transported inside the metals and can be emitted by effect of the electric field, we consider a Neumann boundary condition for the electron flux between the plasma and the surface, i.e. no flux gradient in that interface, and we express it in the following way:

$$\vec{J_e} = n_e \vec{v}_e \tag{II.22}$$

where $\vec{J_e}$, n_e and $\vec{v}_e$ are respectively the flux density, the density (at the center of the last plasma cell) and the drift velocity of electrons. Electrons are not emitted the same way from dielectric surfaces. We consider they are emitted from the dielectric surface proportionally to the impact of ions (species k), following a secondary emission coefficient $\gamma = 0.1$. This relatively high value for this coefficient is a way to roughly take into account other secondary emission processes such as photoemission and secondary emission of electrons by impact of metastable species. In the experimental study of *Tschiersch et al.* [2017], the effective secondary electron emission coefficients for different dielectric materials are reported to be between 0.02 and 0.4. Our value is within this range. The electron flux on the dielectric boundary can thus be expressed as:

$$\vec{J_e} = n_e min(0, \vec{v}_e.\vec{n}).\vec{n} - \gamma \vec{J_k} \tag{II.23}$$

Finally, on the open boundaries, we consider all charged species k can leave the domain but not enter:

$$\vec{J_k} = n_k min(0, \vec{v}_k.\vec{n}).\vec{n} \tag{II.24}$$

Charge deposition on dielectric surfaces

On dielectric surfaces, as the electric conductivity of charges is very low, we consider charges remain deposited locally. Therefore, a net surface charge density σ_i is accumulated in time at each plasma-dielectric cell interface i of surface Σ_i by the electric drift flux (inwards, opposite to $\vec{n}$, and outwards, in the sense of $\vec{n}$) of all charged species k:

$$\sigma_i = \sigma_{0i} - \int_t \sum_k \frac{q_k}{|q_e|} n_k \vec{v}_k.\vec{n} dt; Q = \sum_i \sigma_i \Sigma_i \tag{II.25}$$

where σ_{0i} is the initial local surface charge density, generally set to zero. The total charge on a dielectric surface Q is the surface integration of all the σ_i on that surface. The calculation of the net volume charge density ρ in each plasma cell from the local number densities of charged species has already been described in eq. II.7.

Time integration of source terms

The temporal variation of species densities due to the chemistry between species is a local phenomenon, i.e. there is no transport of particles between cells. Thus, the temporal evolution of species densities exclusively due to chemistry has to conserve the mass and total net charge inside each control volume (cell). Then, the ordinary differential equation II.8 is solved by temporally integrating the contributions of each reaction to the density of each species. While for the drift and diffusion fluxes and for the photo-ionization source term a simple first-order Euler time integration is used (eq. II.18), for chemistry a higher order method is used. As in *Pechereau* [2013] (chapters 4.3 and 9) the implicit 5^{th} order RADAU5 solver [*Hairer and Wanner*, 1996] has been used for the chemistry temporal integration. RADAU5 provides a numerical solution of a stiff system of first order ordinary differential equations, using an implicit Runge-Kutta method of order 5. The relative and absolute error tolerances of the solver have been set as 10^{-10}. The accuracy of the solver is evaluated in appendix C.

Time integration and time-step

The time-step Δt over which the temporal integration is realized to obtain the solution at $t + \Delta t$ (eq. II.11) is variable. For stability and accuracy of the solution, the time-step has to be limited by several considerations. These are the Courant-Friedrichs-Lewy (CFL) conditions, necessary conditions for convergence while solving certain partial differential equations numerically. They arise in the numerical analysis of explicit time integration schemes, when these are used for the numerical solution. As a consequence, the time step must be less than that determined by the CFL conditions in all the domain, otherwise the simulation produces incorrect results. The conditions are described in *Courant et al.* [1928], and can be summarized as $\Delta t \leq C\frac{\Delta x}{v}$, where C is dimensionless (called Courant number), v is the magnitude of velocity of the process, Δt is the time-step and Δx is the length interval, therefore the mesh size. In our simulations, as described in *Pechereau* [2013], we evaluate the time-steps associated to electric drift Δt_c, diffusion Δt_d, chemistry Δt_I and dielectric relaxation Δt_{Diel}:

$$\Delta t_c = min\left[\frac{\Delta z_i}{v^k_{z_{i,j}}}, \frac{\Delta r_j}{v^k_{r_{i,j}}}\right]; \Delta t_d = min\left[\frac{(\Delta z_i)^2}{D^k_{z_{i,j}}}, \frac{(\Delta r_j)^2}{D^k_{r_{i,j}}}\right] \tag{II.26}$$

$$\Delta t_I = min\left[\frac{n^k_{i,j}}{S^k_{i,j}}\right]; \Delta t_{Diel} = min\left[\frac{\epsilon_0}{q^k \mu^k_{z,r_{i,j}} n^k_{i,j}}\right] \tag{II.27}$$

where k is the species index.
Considering the plasma from a dielectric point of view, as the local electric field changes, the polarization of the material takes some time to relax towards an equilibrium. The dielectric relaxation time-step corresponds to the time required for the charged species to align themselves according to the direction of the local electric field. In section II.3.3 it will be described how the dielectric relaxation can be accounted for semi-implicitly in the resolution of Poisson's equation, and then the CFL condition is not required for this process. Likewise, as the chemistry dynamics is solved implicitly, there is no need to consider its associated

time-step. Thus, the time-step of the calculation is determined as:

$$\Delta t = min(A_c \Delta t_c, A_d \Delta t_d) \tag{II.28}$$

In this thesis we use $A_c = 0.5$ and $A_d = 0.125$, which have been verified to assure stability. Therefore, the time-step is dependent on the mesh size, electric field and transport parameters. In section II.3.4 the dependence of the time-step with the electric field and transport parameters will be exposed.

II.3.3 Poisson's equation and determination of charge contributions to the electric field distribution

In our discharge simulations, the electric field is a key parameter, as it defines the transport parameters, the electric drift and the electron-impact source terms. Thus, it is directly related to the evolutions of charged species densities. It is derived from the spatial derivative of electric potential and therefore it is of paramount importance to accurately calculate the electric potential distribution through Poisson's equation.

Discretization of Poisson's equation

In this thesis we solve Poisson's equation in cylindrical coordinates as in *Pechereau* [2013] (chapter 1.3.1 and appendix C), considering different permittivities, net charge density ρ in volume and net surface charge density σ on plasma-dielectric interfaces. Taking $V_{i,j}$ as the electric potential at (z_i, r_j) and using finite volume methods and the local Gauss equation at each cell interface (interface at $i+1/2$: $\epsilon_{i+1} E_{i+1/2 \to i+1} - \epsilon_i E_{i \to i+1/2} = \sigma$), the second order discretization of Poisson's equation II.6 gives the classical five-diagonal system:

$$V^E_{i,j} V_{i+1,j} + V^W_{i,j} V_{i-1,j} + V^N_{i,j} V_{i,j+1} + V^S_{i,j} V_{i,j-1} + V^C_{i,j} V_{i,j} = \pi \rho'_{i,j} \Delta z_i \Delta r_j^2 \tag{II.29}$$

$$\Delta z_i = z_{i+1/2} - z_{i-1/2}; \Delta r_j^2 = r_{j+1/2}^2 - r_{j-1/2}^2 \tag{II.30}$$

$$V^E_{i,j} = -\pi \Delta r_j^2 \frac{\epsilon_{i+1,j} \epsilon_{i,j}}{\epsilon_{i+1,j}(z_{i+1/2} - z_i) + \epsilon_{i,j}(z_{i+1} - z_{i+1/2})} \tag{II.31}$$

$$V^W_{i,j} = V^E_{i-1,j} \tag{II.32}$$

$$V^N_{i,j} = -2\pi r_{j+1/2} \Delta z_i \frac{\epsilon_{i,j+1} \epsilon_{i,j}}{\epsilon_{i,j+1}(r_{j+1/2} - r_j) + \epsilon_{i,j}(r_{j+1} - r_{j+1/2})} \tag{II.33}$$

$$V^S_{i,j} = V^N_{i,j-1} \tag{II.34}$$

$$V^C_{i,j} = -(V^E_{i,j} + V^W_{i,j} + V^N_{i,j} + V^S_{i,j}) \tag{II.35}$$

$$\rho'_{i*+1,j} = \rho_{i*+1,j} + \frac{\epsilon_{i+1,j} \sigma_j (z_{i+1/2} - z_i) \pi \Delta r_j^2}{\epsilon_{i,j}(z_{i+1} - z_{i+1/2}) + \epsilon_{i+1,j}(z_{i+1/2} - z_i)} \tag{II.36}$$

$$\rho'_{i*,j} = \rho_{i*,j} + \frac{\epsilon_{i,j} \sigma_j (z_{i+1} - z_{i+1/2}) \pi \Delta r_j^2}{\epsilon_{i,j}(z_{i+1} - z_{i+1/2}) + \epsilon_{i+1,j}(z_{i+1/2} - z_i)} \tag{II.37}$$

where $(z_{i*+1/2}, r_j)$ is the position of σ_j. Then, the electric field is calculated outward each cell interface:

$$E_{i+1/2,j} = \frac{\sigma(z_{i+1/2} - z_i) + \epsilon_i(V_i - V_{i+1})}{\epsilon_{i,j}(z_{i+1} - z_{i+1/2}) + \epsilon_{i+1,j}(z_{i+1/2} - z_i)} \tag{II.38}$$

Semi-implicit scheme for Poisson's equation

In *Pechereau* [2013] (chapter 2.4), to circumvent the time-step limitation by the dielectric relaxation, a semi-implicit scheme that changes the discretization of Poisson's equation has been implemented. The same scheme is used in this thesis. The idea of the semi-implicit scheme is to use throughout the calculations the electric field at $t+\Delta t$. We do so by including in Poisson's equation a prediction of the net volume charge density ρ at a future time, that we simplify as being originated only by electric drift:

$$\epsilon_0 \nabla.(\epsilon_r \nabla V(t + \Delta t)) = -[\rho^t + \Delta t \frac{\partial \rho}{\partial t}] \tag{II.39}$$

$$\frac{\partial \rho}{\partial t} = \nabla.[\sum_i |q_e| \mu_i^t n_i^t \vec{E}^{t+\Delta t}] \tag{II.40}$$

By combining these equations and doing some rewriting, we obtain:

$$\nabla.(\epsilon' \nabla V(t + \Delta t)) = -\rho^t \tag{II.41}$$

$$\epsilon' = \epsilon_0 \epsilon_r + \Delta t \sum_i |q_e| \mu_i^t n_i^t \tag{II.42}$$

This means that by implicitly solving the electric field that way, we are actually changing the permittivity/conductivity of the gas to account for the changes in ρ due to electric drift.

Boundary conditions

In this thesis several electrode configurations are used. Poisson's equation is not solved inside electrodes at fixed potential. Therefore, Poisson's equation has boundaries both at the boundaries of the domain and at every electrode boundary. Then, two different types of boundary conditions can be used, as in *Pechereau* [2013] (chapter 1.3.1).

- The homogeneous Neumann boundary condition ($\nabla V.\vec{n} = 0$) at the open boundaries.
- The Dirichlet boundary condition, for boundaries at fixed potential V_{APP}. Moreover, at every electrode interface, the ghost fluid method is used [*Celestin*, 2008; *Celestin et al.*, 2009b], that allows to consider the actual position of any electrode surface in the calculation of the electric potential and electric field.

Numerical method to solve Poisson's equation

As in *Bourdon et al.* [2016], to solve Poisson's equation II.29 in this thesis we use the iterative solver SMG in the *HYPRE* [2007] library. In *Pechereau* [2013] this solver has been tested and compared with others and its parallelization performances have been evaluated. There, the number of iterations, the solution error and the computation time have been studied as

function of the solver tolerance and the number of MPI processes. In this thesis we have used a tolerance Tol = 10^{-12}.

Determination of charge contributions to the electric field distribution

We see in eq. II.29 that the solution to Poisson's equation takes into account different physical contributions to the potential distribution: a Laplacian distribution of potential, defined by the boundary conditions; a net volume charge density ρ contribution included in $\rho'_{i,j}$; a net surface charge density σ contribution included in $\rho'_{i,j}$. Thus, it is possible to calculate the electric potential distribution associated to each contribution. The calculation of separate contributions to the potential and electric field distributions is an approach that has been used in other works, such as *Kulikovsky* [1997]; *Celestin et al.* [2009a]; *Pechereau and Bourdon* [2014]. In this thesis, that is done, in order to obtain more detail into the dynamics between each type of charge and the electric field components. Although the self-consistent electric field in the discharge model is always the total field, at the instants of output of the numerical results we perform extra calculations of Poisson's equation:

- Setting all the $\rho'_{i,j} = 0$, to obtain the Laplacian distributions of V and $\vec{E}$ exclusively. These are shown in appendix B for different electrode configurations.
- Setting all the $\rho'_{i,j} = \rho_{i,j}$ and the voltage applied to the electrodes to zero, to obtain the contribution of ρ in volume to V and $\vec{E}$.
- Setting all the $\rho_{i,j} = 0$ and the voltage applied to the electrodes to zero, to obtain the contribution of σ at the surfaces to V and $\vec{E}$.

II.3.4 Reaction scheme, initial conditions, rate coefficients, photoionization and transport parameters

Reaction scheme, initial conditions and rate coefficients

At the start of this thesis, the model could describe He discharges with small admixtures of N_2, using the same reaction scheme as in *Bourdon et al.* [2016], with 10 species (e, He^+, He_2^+, N_2^+, $N_2^+(B)$, N_4^+, $He(2^3S)$, $N_2(C)$, He, N_2) and 31 reactions. That kinetic scheme is for the most part derived in *Pouvesle et al.* [1982], based on the detailed experimental study of an atmospheric pressure post-discharge in helium with 6 to 700 ppm of N_2.
As initial conditions, besides the definition of geometry, gas and applied voltage, we set densities of particular species in the plasma. We consider that we simulate a single discharge in repetitive conditions. As we consider pulsed discharges, charged and excited species are created during the pulse and then tend to disappear in the time between pulses. Then, the initial densities to take into account are dependent on the reaction scheme, gas-mixture and pulse repetition and will be discussed later in section II.4.2, together with the implementation of chemistry models. Moreover, we usually suppose the net surface charge density σ deposited on dielectric walls is zero at the beginning of each pulse.
It is assumed that the electron-impact excitation and ionization rate coefficients are functions of the local reduced electric field E/N. E is the magnitude of the electric field. As the

chemistry equations are solved at the center of each cell and the model calculates the electric field at the cell boundaries, an electric field magnitude E_t at each cell is defined:

$$E^t_{i,j} = \sqrt{\left(\frac{E^z_{i+1/2,j} + E^z_{i-1/2,j}}{2}\right)^2 + \left(\frac{E^r_{i,j+1/2} + E^r_{i,j-1/2}}{2}\right)^2} \tag{II.43}$$

Then, the rate coefficients, as well as the electron temperature T_e, are retrieved from the electron Boltzmann equation solver BOLSIG+ [*Hagelaar and Pitchford*, 2005] (version 07/2015), using the IST-Lisbon electron cross section database [*IST*, 2014] in the LXCat platform [*Pancheshnyi et al.*, 2012]. These are obtained for each He-N_2 gas-mixture in the form of tables, function of E/N. Thus, the rate coefficients in each cell are obtained through linear interpolation of the BOLSIG+ tables, using a binary search algorithm, for each $E^t_{i,j}/N$.

Photo-ionization

For the photo-ionization model, we use the same approach as in *Naidis* [2010]; *Jánský et al.* [2012]. It is assumed that ionizing VUV radiation emitted by excited helium species is absorbed by molecules of impurities (N_2 and O_2) that have low ionization thresholds. The ionizing radiation is emitted mainly by excited molecules He_2(A). It is also considered that the number of ionizing photons emitted per unit time from a given cell is proportional to the excitation rate S_{He*} of He atoms by electron impact. The absorption coefficient of the ionizing radiation k_p is assumed to depend on the level of impurity admixture in each cell, as $k_p = NX_{N_2/O_2}\sigma_p$, where for the photo-ionization cross section a typical value of $\sigma_p = 3 \times 10^{-17} cm^2$ [*Hasted*, 1964] is assumed. Then, the photo-ionization source term S_p at position $\vec{r}$ of the domain of volume V', i.e. the rate of generation of electron and ions, that takes part in eq. II.8, has the structure:

$$S_p(r) = A_{ph} \int_{V'} S_{He*}(\vec{r'}) \frac{exp(-k_p R)}{4\pi R^2} dV' \tag{II.44}$$

where $R = |\vec{r} - \vec{r'}|$. The photo-ionization source term is proportional to the amount of impurity admixture and we use $A_{ph} = \xi X_{N_2/O_2}$. In *Naidis* [2010] A_{ph} has been varied in the range 0.1-1, and in *Bourdon et al.* [2016] the proportionality coefficient ξ has been varied in the range 1-10. There, the best agreements with experiments have been obtained with $\xi = 10$, which is the value used in this thesis. For the calculation of the photo-ionization source term, the SP3 approximation of the radiative transfer equation [*Bourdon et al.*, 2007] with Larsen's boundary condition [*Liu et al.*, 2007] is used considering for the He-N_2 and He-O_2 mixtures only one absorption length. Indeed, two Poisson's-like equations have to be solved with Larsen's boundary conditions that require to iterate three times their solution (total of 6 resolutions of Poisson's-like equations). Further details about the calculation can be found in *Bourdon et al.* [2007]; *Celestin* [2008] (chapter III). It is important to note that in the simulations presented in this thesis, as in *Pechereau* [2013], S_p is updated only every 6 time steps. We have checked that this has a negligible influence on the results.

Transport parameters

Just like the electron-impact rate coefficients, electron transport parameters (D_e, μ_e) are obtained for each gas-mixture from BOLSIG+ [*Hagelaar and Pitchford*, 2005], as function of E/N. As we evaluate the transport parameters at each cell interface and not at the cell center, the magnitude of the electric field considered is not $E^t_{i,j}$ (eq. II.43), but, for instance at $(z_{i+1/2}, r_j)$:

$$E^t_{i+1/2,j} = \sqrt{\left(E^z_{i+1/2,j}\right)^2 + \left(\frac{E^r_{i,j+1/2} + E^r_{i,j-1/2} + E^r_{i+1,j+1/2} + E^r_{i+1,j-1/2}}{4}\right)^2} \tag{II.45}$$

At boundaries, only the electric field components in the plasma are considered, i.e. those in plasma-plasma interfaces and in plasma-surface interfaces. Then, to calculate the drift velocity of species k, $v^k_{i+1/2,j} = \mu^k_{i+1/2,j} \times E^z_{i+1/2,j}$.
Concerning ion transport parameters, at the beginning of this thesis μ_i was derived from *Ellis et al.* [1976] and considered constant. Even though ion mobility is much lower than that for electrons, its value is crucial to determine the temporal evolution of surface charge densities in plasma-dielectric interactions. Then, to have a more accurate description, we have retrieved positive and negative ion mobilities in He from LXCat databases [*Pancheshnyi et al.*, 2012; *Ellis et al.*, 1976] for 300 K as function of E/N for $E/N \leq 100$ Td and extended until 4000 Td using the formula from *Kawakami et al.* [1995] with $n = 8$ (n chosen to obtain a smoother evolution):

$$\mu_i \times N \propto (E/N)^{-(n-4)/(2n-4)} \tag{II.46}$$

Diffusion coefficients for ions D_i are evaluated using the Einstein relation with a gas temperature of $T_i = T_g = 300$ K: $D_i = \mu_i k_B T_i/|q_i|$. μ_i have values in the order of magnitude of 10 $\mathrm{cm^2.V^{-1}.s^{-1}}$ and D_i of a few $\mathrm{cm^2.s^{-1}}$. The electron transport parameters are several (2 to 4) orders of magnitude higher. Thus, the electron parameters determine the time-step calculation in eq. II.26. In Figure II.2 it is shown how the time-steps evolve with the electron transport parameters and how these evolve with the local value of electric field for $N = 2.45 \times 10^{19}$ $\mathrm{cm^{-3}}$. The parameters have been taken from BOLSIG+ for a mixture 99.9% He - 0.1% N_2, and the mesh size is taken as 10 μm, the most used value in this thesis. The electric field taken here for the calculation of the drift velocity is considered the same as the one for evaluation of μ_e and D_e.
It is visible in Figure II.2 that the resulting time-steps have the same order of magnitude, and the resulting calculation time-step is in the range $10^{-12} - 10^{-10}$ s. Using the coefficients $A_c = 0.5$ and $A_d = 0.125$, the lowest time-step is the one associated to electron diffusion.

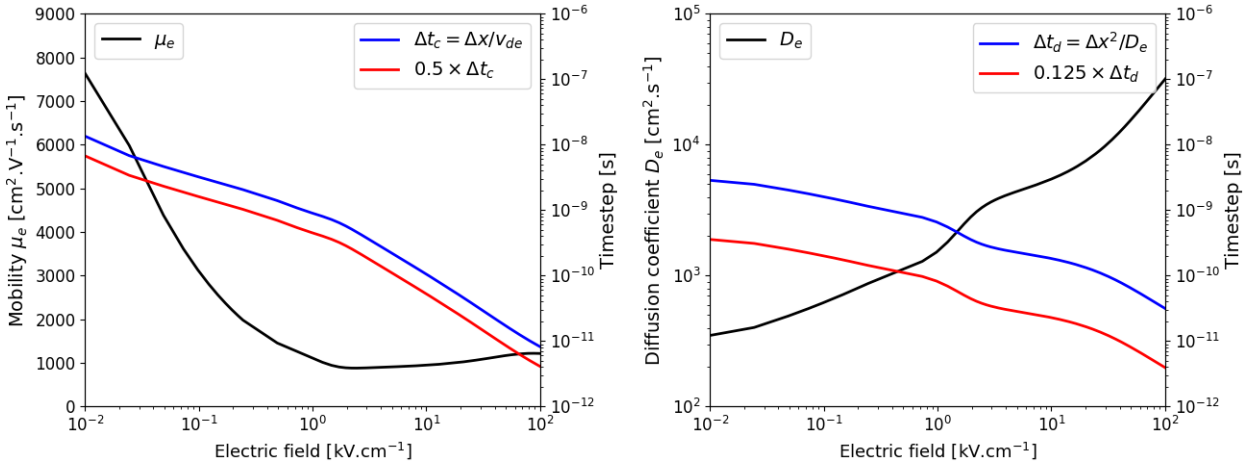

Figure II.2: Evolution of μ_e, Δt_c and $A_c \Delta t_c$ (on the left) and of D_e, Δt_d and $A_d \Delta t_d$ (on the right) with the electric field magnitude. The gas-mixture is 99.9% He - 0.1% N_2. The mesh size is taken as 10 μm.

II.4 Modeling of plasma jets with flowing He-N_2 and He-O_2 gas mixtures

II.4.1 Introduction

The model presented in section II.3 allows to describe the discharge dynamics inside a dielectric tube with a spatially homogeneous He-N_2 gas-mixture. In order to study He discharges with O_2 admixtures instead of N_2 admixtures, new reaction schemes have to be studied, tested and implemented in the model. Moreover, as in plasma jet experiments the buffer gas (for instance pure He) is flowing through the tube and the tube is placed in an environment of a different gas (air or other), then the gas-mixture at the end of the tube is not spatially homogeneous. To describe the discharge dynamics in the plasma plume and its interaction with targets, the spatial distribution of gases in this region where the buffer gas and the environment gas mix has to be considered in the model. In this section, the developments introduced in the model during the work leading to this thesis are described. These intend to model plasma jets with flowing gas mixtures and surface interactions.
Furthermore, during the work leading to this thesis, a contribution has been submitted to the discussion (called *Round Robin*) in the international low-temperature plasma community. The aim of the *Round Robin* is to improve the practice of modeling complex plasma chemistries. As a first step, Miles Turner from Dublin University has written a proposal ("A proposal for a test of plasma chemistry solvers against an exact stationary solution") as a challenge for members of the community to perform and compare code verification. This is, to demonstrate in which measure the codes they are using or developing are correctly implemented and correctly compute what they are supposed to. In the case of the *Round Robin*, this applies to electron Boltzmann equation solvers that calculate electron rate coefficients and to chemistry (time integration) solvers. Our contribution to *Round Robin* is presented in appendix C. In that appendix the precision of the numerical tools we use is evaluated.

II.4.2 Investigation and implementation of chemistry models

In this thesis we study the discharge dynamics in gas-mixtures of He and the main gases in air: N_2 and O_2. N_2 and O_2 can be present either as part of the buffer gas as impurities or admixtures, or as part of the environment in the plasma plume. In this thesis the discharge dynamics always takes place in gas-mixtures with N_2 or O_2 relative densities between 10 ppm and 5%. A He-N_2 reaction scheme had already been implemented in the model described in section II.3. Then, before simulating a He-air mixture, we have decided to implement in the model a reaction scheme for He-O_2. In this section we describe the implementation of the He-O_2 chemistry model and of improvements to the He-N_2 model. This is presented following a sequence of studies required for that implementation: electron kinetics, investigation and test of reaction schemes and implementation in the discharge model.

Electron kinetics in He-N_2-O_2 mixtures

The electron-impact rate coefficients are obtained from the numerical resolution of the electron Boltzmann equation (EBE). We have used the off-line version of the stationary and homogeneous two-term EBE solver BOLSIG+ (version 07/2015 for Windows) [*Hagelaar and Pitchford*, 2005]. We have used the Default configurations, i.e. with 200 energy intervals, 10^{-10} precision and 10^{-5} convergence criterion. As electron-impact cross sections, we have taken the all the e-He, e-N_2 and e-O_2 cross sections from LXCat *Pancheshnyi et al.* [2012]; *IST* [2018]. These have a range of 1000 eV. In *Viegas* [2015] the e-He, e-N_2 and e-O_2 collisional data have been validated for pure gases through comparison of the obtained swarm results with experimental data as function of E/N. Then, in that MSc thesis, the influence of He-N_2, He-O_2 and He-N_2-O_2 mixtures on the electron energy distribution function (EEDF) and on the electron-impact ionization coefficients has been examined. The atomic gas He presents a much more energetic EEDF than the molecular gases. The excited and ionized states of He have very-high energy thresholds (24.6 eV for ionization), in contrast with the low-energy electronic and vibrational excited states of N_2 and O_2, leading to a depletion of the EEDF tail when these gases are admixed. However, for admixtures up to 1%, the EEDF is still very similar to that of He, i.e. very energetic, and the ionization processes of N_2 and O_2 with lower threshold (15.5 eV for N_2 and 12.1 eV for O_2) acquire some importance. The coefficient for N_2 and O_2 ionization increases and then the global ionization coefficient $k_{ion} = \frac{[He]k_{He^+} + [N_2]k_{N_2^+}}{N}$ slightly increases with small admixtures of N_2 or O_2. This effect is represented on the left-hand side of Figure II.3 for the case of He-N_2 plasmas. For He-O_2 the result concerning ionization is similar.
The right-hand side of Fig. II.3 shows that the contribution of the molecular gas to the global ionization coefficient increases significantly with small admixtures and has different maxima according to E/N. We should notice that the contribution of He evolves in the opposite sense, decreasing with small admixtures of N_2 or O_2. The result is a global k_{ion} that is higher with admixtures of N_2 or O_2 up to 1% than for pure He, which can explain, for instance, the lower time of ignition in *Bourdon et al.* [2016] with N_2 admixtures. This is only the case for relatively low electric field values. For typical values of E/N in the ionization front, of dozens of Td, k_{ion} is approximately the same with admixtures up to 1%. With N_2 or O_2 relative densities higher than 1%, k_{ion} decreases as the amount of admixture increases, for the whole

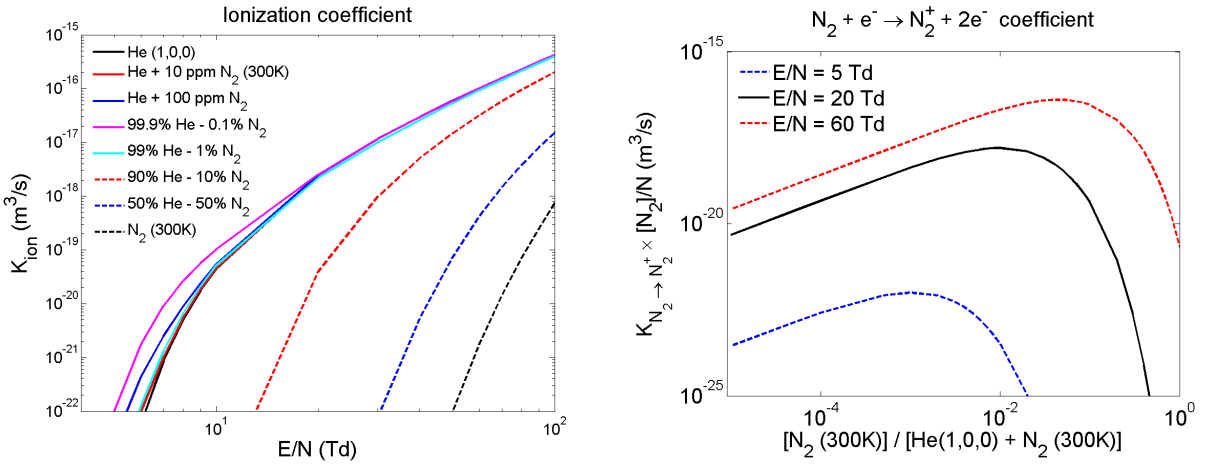

Figure II.3: On the left, the global electron-impact ionization coefficient as function of E/N for several He-N_2 mixtures. On the right, the contribution of the electron-impact ionization coefficient of N_2 as function of its relative density in the He-N_2 mixture, for three values of E/N. The gas temperature is taken as 300 K. Figures from *Viegas* [2015].

electric field range. As already discussed in *Naidis* [2011b], this will guide the discharge in the plasma plume in regions with a sufficiently low density of air gases.

Investigation of He-O_2 and He-N_2 reaction schemes

In order to develop the chemistry in the discharge model, reaction schemes have to be chosen or developed. Several reaction schemes exist in the literature but it cannot be said that a reference scheme exists for He-N_2, He-O_2 or He-air at atmospheric pressure. Investigating He-O_2 reaction schemes, we have considered the following schemes in literature:

- *Murakami et al.* [2013a] used for an atmospheric pressure RF-driven He jet with 5000 ppm of O_2 and 500 ppm of humid air, with a total of 59 species and 1048 reactions, among which 23 He-O_2 species and around 300 He-O_2 reactions.
- *Stafford and Kushner* [2004] used for a low-pressure (10s of Torr) RF-driven He discharge with 3% O_2, with 17 species and 170 reactions.
- *Turner* [2015] used for an atmospheric pressure RF-driven He jet with variable O_2 admixture up to 3.5%, with 25 species and 373 reactions.
- *Turner* [2016], a reduction from the previous model with 12 species and 50 reactions, lacking He_2^+ and negative ions.
- *Kang et al.* [2010] for an atmospheric pressure dielectric barrier He discharge with O_2 densities only up to 10 ppm.
- *Waskoenig et al.* [2010] for an atmospheric pressure RF-driven He jet with 5000 ppm of O_2, with 16 species and 116 reactions.
- *Niemi et al.* [2011], an extension from the previous model with 20 species and 184 reactions.

- *Liu et al.* [2010] used in a global model for atmospheric pressure RF He plasmas with O_2 admixtures from 1 ppm until 10%, with 5 negative species, 5 positive ions, 11 neutral species and 267 reactions.

After several considerations and some tests, we have chosen to implement the reaction scheme in *Liu et al.* [2010]. The choice has been driven mostly by the completeness of the scheme, with a wide range of O_2 density and the fact that it has been used and validated for atmospheric pressure and neutral gas temperature $T_g = 300$ K. The scheme in that paper has been obtained from other studies of plasmas with related chemistries. The rate coefficients have been taken from the literature and the electron-neutral two-body rate coefficients have been calculated based on cross section data. As the reaction scheme is quite long, it is shown in appendix D to ease the reading of the manuscript. Then, in *Liu et al.* [2010] three regimes of oxygen relative density have been considered (1 to 10 ppm, 10 to 5000 ppm and 0.5 to 10% O_2) and sensitivity analysis (considering a steady-state solution) has been performed to select the main species and reactions in each regime. In this thesis, plasma dynamics takes place in regions where O_2 density is spatially inhomogeneous and thus the whole reaction scheme for the whole O_2 density range is considered. Most electron-impact cross sections have been taken from the LXCat database [*Pancheshnyi et al.*, 2012; *IST*, 2018]. Those not available there have been taken as in *Liu et al.* [2010].
Before implementing the chosen reaction scheme in the 2D discharge model, the reaction scheme has been tested using an in-house zero-dimensional model for transient discharges. This model has been written in Fortran 90 and is designed to follow the time evolution of the species densities (eq. II.8) in a non-thermal plasma with an arbitrarily complex chemistry in a fixed gas-mixture. The input plasma chemistry file is in a text format that is user-friendly. The electron-impact rate coefficients are obtained from the output files of BOLSIG+ [*Hagelaar and Pitchford*, 2005] and interpolated for each particular E/N. E/N at each time is inserted. We should notice that in this model, unlike in the 2D discharge model, the electric field is not self-consistently calculated and thus the electric field profile introduced is chosen as an estimation of the temporal evolution of the local field in the discharge front from the 2D simulations, that can reproduce results close to those obtained in 2D. The E/N profile is written as:

$$E/N = E_{min} + (E_{MAX} - E_{min}) \times \left(\frac{1}{1 + e^{-\lambda(t - t_{shift})}} + \frac{1}{1 + e^{+\lambda(t - t_{shift} - t_{width} - t_{rise})}} - 1 \right) \quad \text{(II.47)}$$

The parameters are adjustable. For instance, to describe the profile of E/N represented on the left side of Figure II.4 the following parameters have been used: $E_{min} = 10^{-4}$ Td, $E_{MAX} = 77.5$ Td, $t_{rise} = 6$ ns, $\lambda = 8/t_{rise}$, $t_{width} = 0.2$ ns, $t_{shift} = 7$ ns. Using this model, the interval of time when the field is applied is a simulation of the discharge front at a given point and the time posterior to the field application, which we call post-discharge, simulates what happens in the channel after the passage of the ionization front. The temporal integration is solved with the implicit 5^{th} order solver RADAU5 [*Hairer and Wanner*, 1996] with relative and absolute tolerances 10^{-12}.
The initial conditions are those of natural preionization, and we take 10^4 cm^{-3} of electrons and He^+. Then, in zero-dimensions, we can easily and quickly simulate the effect of pulse repetition. For that, we apply the same shape of E/N repetitively with the same frequency

and time between pulses of the applied voltage. At typical repetition frequencies around 1 kHz and gas flow velocities in jets around 1 mm.ms^{-1} the shift of the gas between the pulses is of the order of 1 mm, much shorter than the length of discharge propagation. Hence each new ionization front propagates in a gas excited by previous pulses and each piece of gas is thus affected by dozens of ionization fronts. By this procedure we can estimate the initial densities of species at the beginning of each pulse in repeatability conditions, i.e. when the results during pulse $n+1$ are the same as those during pulse n. Typically, about 20 pulses are needed to reach repeatability with this model.
We have used this procedure with several He-O_2 gas-mixtures and applied voltage frequencies to have an idea of the typical evolutions of species densities during the ionization front and in post-discharge using the new reaction scheme. As an example, on the right side of Figure II.4 are presented results of densities of electron and positive ion densities during the 20^{th} pulse (discharge + post-discharge) in a 99.5% He - 0.5% O_2 mixture and considering $f = 1$ kHz and time between pulses 1 ms. These are complemented in Figure II.5 by the densities of the negative ions and of some excited species.

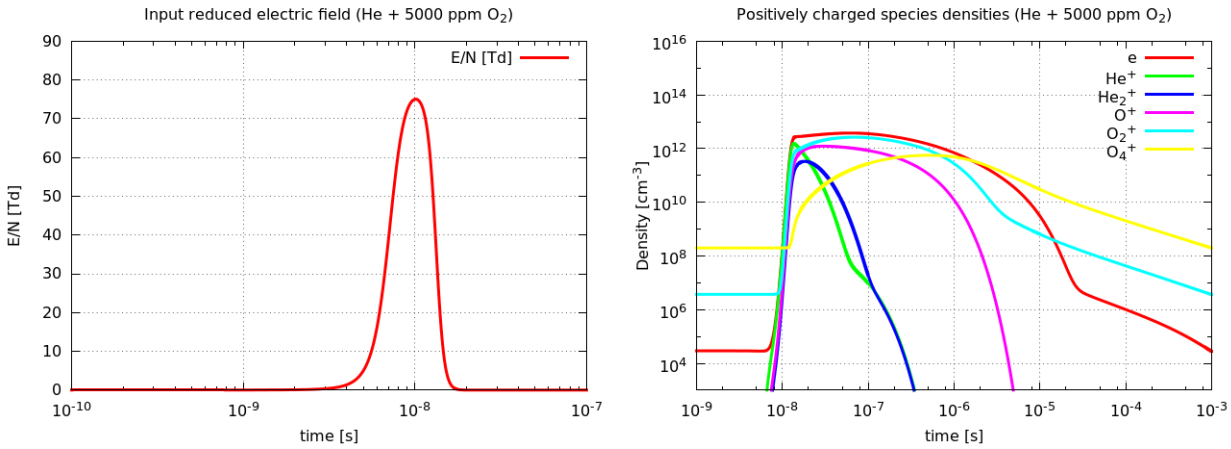

Figure II.4: On the left, the input reduced electric field in the zero-D model. On the right, temporal evolution of electron and positive ion densities during the 20^{th} pulse for a 99.5% He - 0.5% O_2 mixture and $f = 1$ kHz.

Figures II.4 and II.5 allow to have an idea about the important species in the plasma and their temporal derivatives, particularly during discharge propagation and in early post-discharge (μs timescales), which are the intervals we describe in this thesis. Moreover, the results also show an important influence of pulse repetition on the initial densities in the plasma in repetitive conditions. However, there are some limitations if we want to use this procedure to estimate initial densities. In fact, this model does not include losses of neutral species in long timescales through flow, wall reactions and interaction with air impurities in jet configurations. As a result, with this model, in ms timescales, neutral oxygen species accumulate (O_3 density overcomes 10^{16} cm^{-3}) and attachment (mostly reactions 76 and 77) is overestimated. Therefore, we take this procedure to estimate temporal evolutions in the discharge and early post-discharge. Concerning initial densities, we believe this procedure allows to have an idea of the order of magnitude of the total charge densities, but not those of neutral species and negative ions. The procedure to correctly simulate long timescales, pulse repetition and memory effects on species densities is described in section VII.2. In the particular

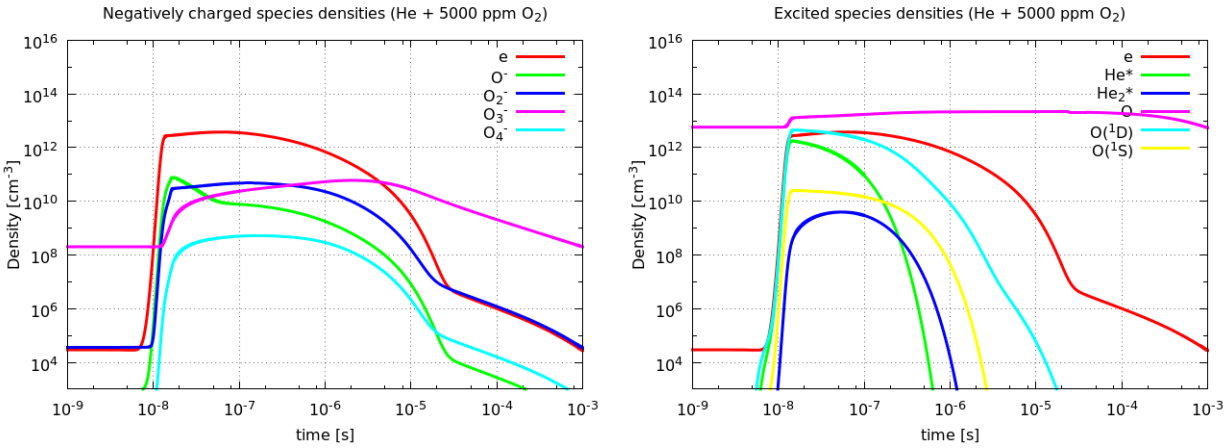

Figure II.5: Temporal evolution of species densities in the zero-D model, during the 20^{th} pulse for a 99.5% He - 0.5% O_2 mixture and $f = 1$ kHz. On the left, negative species. On the right, electrons and some excited species.

case under study, we notice in Figures II.4 and II.5 that the initial densities of charged species in repetitive conditions stand between 10^8 and 10^9 cm^{-3}. Then, in the discharge model, we usually take 10^9 cm^{-3} electrons and O_2^+ as initial conditions, the value suggested in *Wu and Lu* [2014]; *Lu and Ostrikov* [2018] to allow the discharge to propagate in a repeatable mode in experiments. It has been verified that the choice of any specific positive ion (O_2^+ or O_4^+) as initial species is not relevant for discharge dynamics, as it does not change the production of charged and excited species by effect of the front of electric field.

Then, we should notice that the reaction scheme for He-N_2 used in *Bourdon et al.* [2016] and the one for He-O_2 described here do not have the same He reactions. Thus, even though the difference is small, to make sure that in the limit of low molecular gas admixture the discharge dynamics is the same with the He-N_2 and with the He-O_2 schemes, the He-N_2 scheme has been updated to have the same He reactions and is presented in table II.1.

The same zero-D model used with He-O_2 has been used to test the He-N_2 scheme. The temporal profiles of charged species obtained in a case with $f = 1$ kHz and 0.5% N_2 are presented in Figure II.6. In He-N_2 the repeatability is reached at the third pulse.

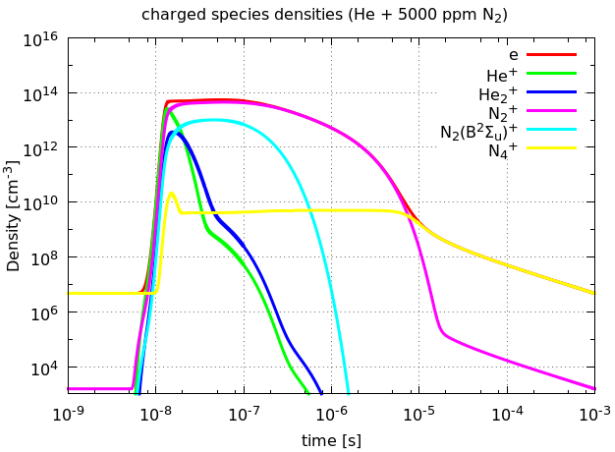

Figure II.6: Temporal evolution of charged species densities in the zero-D model, during the 5^{th} pulse for a 99.5% He - 0.5% N_2 mixture and $f = 1$ kHz.

Nbr	Reaction	Rate coefficient	Reference
R1	$He + e \rightarrow He^+ + 2e$	$f(E/N)$	
R2	$He^* + e \rightarrow He^+ + 2e$	$f(E/N)$	
R3	$N_2 + e \rightarrow N_2^+ + 2e$	$f(E/N)$	
R4	$He_2^* + e \rightarrow He_2^+ + 2e$	$9.8 \times 10^{-10}.T_e^{0.71}.e^{-3.4/T_e}$	*Wang et al.* [2006]
R5	$He + e \rightarrow He^* + e$	$f(E/N)$	
R6	$He^* + e \rightarrow He + e$	$f(E/N)$	
R7	$He_2^* + e \rightarrow He + He + e$	3.8×10^{-9}	*Deloche et al.* [1976]
R8	$He^+ + e \rightarrow He^*$	$6.8 \times 10^{-13} \times T_e^{-0.5}$	*Stafford and Kushner* [2004]
R9	$He_2^+ + e \rightarrow He^* + He$	$7.1 \times 10^{-15} \times (T_e/T_g)^{-1.5}$	*Golubovskii et al.* [2003]
R10	$He^+ + 2e \rightarrow He^* + e$	$7.8 \times 10^{-38} \times (T_e/T_g)^{-4.4}$	*Wang et al.* [2006]
R11	$He_2^+ + 2e \rightarrow He^* + He + e$	2.8×10^{-20}	*Deloche et al.* [1976]
R12	$He_2^+ + 2e \rightarrow He_2^* + e$	1.2×10^{-21}	*Deloche et al.* [1976]
R13	$He^+ + e + He \rightarrow He^* + He$	$7.4 \times 10^{-35} \times (T_e/T_g)^{-2.0}$	*Wang et al.* [2006]
R14	$He_2^+ + e + He \rightarrow He^* + 2He$	3.5×10^{-27}	*Deloche et al.* [1976]
R15	$He_2^+ + e + He \rightarrow He_2^* + He$	1.5×10^{-27}	*Deloche et al.* [1976]
R16	$He^+ + 2He \rightarrow He_2^+ + He$	$1.4 \times 10^{-31}.(T_g/300)^{-0.6}$	*Wang et al.* [2006]
R17	$He^* + He^* \rightarrow He_2^+ + e$	$2.0 \times 10^{-9}.(T_g/300)^{0.5}$	*Wang et al.* [2006]
R18	$He^* + He^* \rightarrow He^+ + He + e$	$8.7 \times 10^{-10}.(T_g/300)^{0.5}$	*Wang et al.* [2006]
R19	$He^* + He_2^* \rightarrow He^+ + 2He + e$	$5.0 \times 10^{-10}.(T_g/300)^{0.5}$	*Deloche et al.* [1976]
R20	$He^* + He_2^* \rightarrow He_2^+ + He + e$	$2.0 \times 10^{-9}.(T_g/300)^{0.5}$	*Deloche et al.* [1976]
R21	$He_2^* + He_2^* \rightarrow He^+ + 3He + e$	$3.0 \times 10^{-10}.(T_g/300)^{0.5}$	*Deloche et al.* [1976]
R22	$He_2^* + He_2^* \rightarrow He_2^+ + 2He + e$	$1.2 \times 10^{-9}.(T_g/300)^{0.5}$	*Deloche et al.* [1976]
R23	$He_2^* + He \rightarrow 3He$	1.5×10^{-15}	*Golubovskii et al.* [2003]
R24	$He_2^* + N_2 \rightarrow 2He + N_2$	1.5×10^{-15}	*Golubovskii et al.* [2003]
R25	$He^* + 2He \rightarrow He_2^* + He$	2.0×10^{-34}	*Golubovskii et al.* [2003]
R26	$He^* + N_2 \rightarrow He + N_2^+ + e$	$0.5 \times 7.6 \times 10^{-11}$	*Pouvesle et al.* [1982]
R27	$He^* + N_2 + He \rightarrow 2He + N_2^+ + e$	$0.5 \times 3.3 \times 10^{-30}$	*Pouvesle et al.* [1982]
R28	$N_2^+ + e \rightarrow N + N$	$0.5 \times 2.0 \times 10^{-7}$	*Pouvesle et al.* [1982]
R29	$He_2^+ + N_2 \rightarrow N_2^+ + 2He$	$0.25 \times 1.1 \times 10^{-9}$	*Pouvesle et al.* [1982]
R30	$He_2^+ + N_2 + He \rightarrow N_2^+ + 3He$	$0.25 \times 1.36 \times 10^{-29}$	*Pouvesle et al.* [1982]
R31	$He^+ + N_2 \rightarrow He + N_2^+$	1.2×10^{-9}	*Pouvesle et al.* [1982]
R32	$He^+ + N_2 + He \rightarrow 2He + N_2^+$	2.2×10^{-29}	*Pouvesle et al.* [1982]
R33	$N_2 + e \rightarrow N_2(C^3\Pi_u) + e$	$f(E/N)$	
R34	$N_2(C^3\Pi_u) + N_2 \rightarrow 2N_2$	8.0×10^{-11}	*Naidis* [2011b]
R35	$N_2(C^3\Pi_u) + He \rightarrow N_2 + He$	1.0×10^{-12}	*Naidis* [2011b]
R36	$N_2(C^3\Pi_u) \rightarrow N_2(B^3\Pi_g) + h\nu$	2.4×10^7	*Naidis* [2011b]
R37	$N_2 + e \rightarrow N_2^+(B^2\Sigma_u^+) + 2e$	$f(E/N)$	
R38	$He^* + N_2 \rightarrow He + N_2^+(B^2\Sigma_u^+) + e$	$0.5 \times 7.6 \times 10^{-11}$	*Pouvesle et al.* [1982]
R39	$He^* + N_2 + He \rightarrow 2He + N_2^+(B) + e$	$0.5 \times 3.3 \times 10^{-30}$	*Pouvesle et al.* [1982]
R40	$N_2^+(B^2\Sigma_u^+) + e \rightarrow N + N$	$0.5 \times 2.0 \times 10^{-7}$	*Pouvesle et al.* [1982]
R41	$He_2^+ + N_2 \rightarrow N_2^+(B^2\Sigma_u^+) + 2He$	$0.75 \times 1.1 \times 10^{-9}$	*Pouvesle et al.* [1982]
R42	$He_2^+ + N_2 + He \rightarrow N_2^+(B) + 3He$	$0.75 \times 1.36 \times 10^{-29}$	*Pouvesle et al.* [1982]
R43	$N_2^+(B) \rightarrow N_2^+ + h\nu$	1.5×10^7	*Pouvesle et al.* [1982]
R44	$N_2^+ + 2N_2 \rightarrow N_4^+ + N_2$	5×10^{-29}	*Kossyi et al.* [1992]

Nbr	Reaction	Rate coefficient	Reference
R45	$N_4^+ + e \rightarrow N_2(C^3\Pi_u) + N_2$	$2 \times 10^{-6} \times (T_g/T_e(K))^{0.5}$	*Kossyi et al.* [1992]
R46	$N_4^+ + N_2 \rightarrow N_2^+ + 2N_2$	2.4×10^{-15}	*Kossyi et al.* [1992]
R47	$N + N + He \rightarrow N_2 + He$	1.15×10^{-29}	*Pouvesle et al.* [1982]
R48	$He_2^* + N_2 \rightarrow N_2^+ + 2He + e$	3.0×10^{-11}	*Golubovskii et al.* [2003]

Table II.1: Table of He-N_2 reactions. He* represents He(2^3S) and He(2^1S); He_2* represents $He_2(a^3\Sigma_u^+)$; Rate coefficients have units $cm^3.s^{-1}$ for two-body reactions, $cm^6.s^{-1}$ for three-body reactions and s^{-1} for radiative transitions; T_e has units eV; T_g has units K. $f(E/N)$ indicates that the rate coefficient is obtained using the electron-impact cross sections.

Figure II.6 shows the densities of the important ions in the 99.5% He - 0.5% N_2 plasma. We can notice that in He-N_2 the maximum electron density is higher than in He-O_2 by one order of magnitude with the same E/N profile. Moreover, unlike in He-O_2, in He-N_2 only electrons and positive ions N_2^+ and N_4^+ remain in long post-discharge. The figure also points out that a high ionization remains in the plasma at the end of a pulse and beginning of a new one. The differences in repeatability and left-over electron densities between He-O_2 and He-N_2 mixtures observed in Figures II.4 to II.6 are fundamentally due to the presence of attachment in He-O_2 and its absence in He-N_2. As this is a simplified model, as for He-O_2, we take for He-N_2 mixtures initial densities 10^9 cm^{-3} electrons and N_2^+. As for He-O_2, it has been verified that the choice of ion as initial species is not relevant for discharge dynamics.

Implementation of chemistry models

The chemistry models we want to implement in the 2D fluid model contain different types of rate coefficients. Furthermore, these models require the previous solution of the electron Boltzmann equation (EBE) and calculation of the electron energy distribution function (EEDF) to obtain the electron swarm parameters and the electron-impact rate coefficients. The resolution of the EBE depends on each local reduced electric field E/N, the local gas-mixture and the compiled collision cross sections. This results in a large quantity of parameters to input in a 2D discharge code to study plasma chemistry. In order to allow to easily change these parameters and to avoid errors, a user-friendly system has been developed, with input files that are easy to read and write. The executable that provides the information in an input file into a piece of compilable code in the plasma model is called a parser. The parsers used in this work have been developed together with Zdenek Bonaventura, from Masaryk University, Brno, Czech Republic. They consist in one parser for the use of electron swarm parameters and electron-impact rate coefficients and one parser for the plasma chemistry source terms.

After retrieving the electron-impact collision cross sections, the electron swarm parameters and the electron-impact rate coefficients have been calculated by the EBE solver BOLSIG+ [*Hagelaar and Pitchford*, 2005] for each gas-mixture we want to study and several values of E/N. These have been 10^{-4}, 10^{-3} and 10^{-2} Td; from 0.1 to 1.0 Td with steps of 0.1 Td; from 1 until 100 Td with steps of 1 Td; from 100 until 1000 Td with steps of 10 Td; from 1000 until 1900 Td with steps of 100 Td; a total of 211 points. The results are saved in a single output data file, in a readable format "Separate tables vs E/N". An example of results in such an output data file is presented on the left side of Figure II.7. Then, a Python code

parses the BOLSIG+ output file and writes a module in Fortran 90, included in the discharge code. The parsing is performed before the compilation of the code. The header of each table is identified and the columns of each table are stocked in a subroutine "bolsig_init" as vectors with a corresponding name. For instance, "y_bolsig_mobility_N". A function is created to interpolate the data in each of the stored vectors, as function of E/N. An example of such a function is found on the right side of Figure II.7. The type of interpolation can be specified. In this thesis we use linear interpolation with a binary search algorithm. Gathering these functions, module "mod_bolsig" is written by the parser. The functions created by the parser are called in the discharge code. In particular, the rate coefficients $k(E/N)$ are used to calculate the source and loss terms in the density continuity equations II.8.

```
C20   He    Ionization    24.59 eV
E/N (Td)        Rate coefficient (m3/s)
4.000   0.000
5.000   0.8894E-26
6.000   0.1547E-23
7.000   0.4168E-22
8.000   0.3979E-21
9.000   0.2056E-20
10.00   0.7183E-20
```

```
function bolsig_C20(x) result(rate) ! x: E/N [Td]
  real(DP),intent(IN) :: x
  real(DP) :: rate !
  rate = interpolated(y_bolsig_C20, x_data, x , Ndata)
!  print *, rate
end function bolsig_C20
```

Figure II.7: On the left: example of BOLSIG+ output in format "Separate tables vs E/N". On the right: Example of function generated by the parser in "mod_bolsig".

Then, to generate the chemistry source terms an easy-to-read-and-write input file "kinet.inp" is written. Every parameter necessary for plasma chemistry is declared, such as N, T_g, gas-mixture, number of species and their charge. The species included in the model are listed and named. The initial density of each species is declared. The list of species created through photo-ionization is added: e, O_2^+ and N_2^+. The list of species with fixed densities is added: He, N_2 and O_2. A minimum of species densities can be added. In this thesis we use natural ionization 10^4 cm^{-3} of electrons and N_2^+ or O_2^+ as minimum density for this species. The whole set of reactions is written in a direct way, along with their rate coefficients. The rate coefficients can have various forms and dependencies. An example of set of reactions is presented in Figure II.8.

```
e + O3 => O + O2^-                !bolsig_C58_O3(EN)*1e6
O2^+ + O2^- + He => O2 + O2 + He !2.0d-25*(Tg/300.d0)**(-2.5d0)
e + O2^+ => O + O                 !1.2d-8*Te**(-0.7d0)
```

Figure II.8: Example of reaction declaration in "kinet.inp".

Then, another Python code parses the chemistry input file and writes a module in Fortran 90, included in the discharge code. The parsing is performed before the compilation of the code. The species and reactions listed are numbered. The declarations, charges and initial densities are identified and written in a subroutine "initiate_reaction_scheme". The numbered reaction rates are written in a subroutine "compute_rates", as well as the arguments for the rates. Then, by identifying each species in the written reactions, the source and loss terms associated to each reaction are listed. An example is presented on the left side of Figure II.9. These terms are summed up to give the total contribution of chemistry to the time derivative of each species density, as in the example on the right side of Figure II.9. As a result, the module "mod_reaction_scheme" is written. The source terms are later called by

the numerical solver RADAU5 to compute the temporal evolution of species densities in each cell of the simulation domain.

```
drate(15) = y(1)*y(3)*y(12)*Rate(15)        dydx(5) = + drate(37) + drate(38) + drate(39) -
drate(16) = y(2)*y(12)*y(12)*Rate(16)      drate(41) + drate(42) - drate(43)
```

Figure II.9: Example of source terms generated by the parser in "mod_reaction_scheme". On the left, source terms associated to each reaction. On the right, the sum of the source terms associated to a species.

Finally, it has been shown how parsers can be used in a 2D fluid discharge model. The use of parsers definitely makes it faster to perform changes in gas mixture, cross section set, species list, reaction list and rate coefficients. Furthermore, it decreases the risk of errors.

II.4.3 Coupling of flow calculations with the plasma model

At the beginning of this thesis, the model describes a domain with a single gas-mixture, invariable in space and time. To describe the physics taking place in the jet plume, i.e. in the region where the buffer gas mixes with the environment gas, we need to consider inhomogeneous gas-mixtures. To obtain the spatial distribution of gases in this region, we use flow calculations and couple them with the discharge model. Different approaches can be used to couple fluid and plasma dynamics. The most complete approach consists on solving plasma and fluid equations simultaneously on the same mesh and time-step. As an example, in *Lietz et al.* [2017] the plasma dynamics has been solved together with modified Navier-Stokes equations and it has been found that localized gas heating takes place in a He jet at the powered electrode during the voltage pulse of 100 ns and produces an acoustic wave that propagates at the gas flow velocity. Kinetic equations provide a source term to the fluid equations and the fluid equations update the gas density and temperature that are used to calculate photo-ionization parameters and rate coefficients. However, usually the temporal and spatial scales to solve plasma and fluid equations are significantly different (ps and μm for plasma and ms and mm for fluid). In that case, it is more efficient to calculate these equations separately, using different meshes and time-steps. Then, the plasma calculation can be used as initial condition for the fluid simulation or vice-versa. For instance, in *Tholin and Bourdon* [2013] the dynamics of a nanosecond spark discharge is calculated during the voltage pulse and provides gas heating. Then, the hydrodynamic expansion is followed by calculating only Euler equations in post-discharge.
In this thesis, the gas flow velocity is typically of the order of 3 μm/μs. Therefore, the model takes a static gas hypothesis, relevant in the μs timescale studied in this work, during which the gas flow can be considered to be frozen with no diffusion of neutral species. Moreover, we neglect effects of plasma on flow, as those described in section I.5. Hence, we precalculate the spatial distribution of gases without plasma and provide it to the discharge model, whose resolution is dependent on the densities of each gas. This approach of coupling a static-solution gas flow with a transient plasma model has been used in other works, such as *Sakiyama et al.* [2010]; *Breden et al.* [2012]; *Naidis* [2012]. In most He plasma jet experiments, the buffer gas He flows into environment air. As we solve the discharge model for either He-N_2 or He-O_2 mixtures, the fluid calculations take either N_2 or O_2 as environment gas. Thus, the model considers a flow of He with some N_2 or O_2 admixture flowing downstream into

a N_2 or O_2 environment. As N_2 and O_2 are the main gases in air and we are investigating plasma dynamics in regions with He relative density higher than 95%, we consider N_2 or O_2 are good first approximations for air environment. In particular, both experiments and simulations [*Winter et al.*, 2015b; *Schmidt-Bleker et al.*, 2015] have shown that the use of O_2 or air as surrounding gas for a He jet present similarities with respect to discharge dynamics in the plasma plume. In *Naidis* [2011b]; *Schmidt-Bleker et al.* [2015] the important role of the electronegativity of the surrounding gas, either O_2 or air, has been highlighted.
The flow calculations have been carried out by Adam Obrusník, from Masaryk University. They are described and validated in *Vorác et al.* [2014]; *Synek et al.* [2015] for Ar jets and torches and then adapted for He jets in *Arjunan et al.* [2016] and used also in *Sobota et al.* [2016]. The flow model has been developed using the COMSOL software [*COMSOL*, 2017] with the Computational Fluid Dynamic module. It solves the stationary Navier-Stokes equations for laminar and turbulent flows of an inhomogeneous He-N_2 or He-O_2 gas-mixture self-consistently with the diffusion equation for the same mixing. As we consider the gas to stay at $T_g = 300$ K, there is no need to solve the heat transfer equation. The model can provide reliable results for both laminar and fully turbulent flow. In the cases studied in this thesis, experiments show that the flow is laminar (Reynolds number is below 200) and thus the model is solved for laminar flow conditions. A buoyant force term ($\vec{f} = (\rho_{mix} - \rho_{N_2})\vec{g}$, where ρ_{mix} is the mass density of the local gas-mixture, ρ_{N_2} is the mass density of N_2 or O_2 and $\vec{g}$ is the gravitational acceleration) has been added to the momentum Navier-Stokes equation. To describe the mixing of the two components involved (He and N_2 or O_2), diffusion is considered using a Fick-like expression for the flux with diffusion coefficient calculated from binary diffusion coefficients using the rule of mixtures and the Chapman-Enskog theory, with coefficients taken from *Cussler* [2009]. Several calculations have been performed with this model, considering different parameters: input flow between 0.5 slm and 2.0 slm; tube inner radius 1.25 mm and 2.0 mm; inlet He gas with N_2 or O_2 admixtures of 10 ppm, 100 ppm and 1000 ppm; tube-target distance between 0.5 cm and 2.5 cm. The mesh is rectangular and its size is 40 μm radially and 80 μm axially. The calculation provides the spatial distribution of the relative densities of He and N_2 or O_2. It is solved in a domain with 2 cm radius and 2 cm tube length and thus the total number of cells is variable between 150 and 300 thousand, depending on the tube-target distance.
Figure II.10 shows the effect that the plasma-flow coupling has on the model set-up in the plume region between the tube and the target. As an example, we take a case with a tube of $\epsilon_r = 4$ of 2.5 cm length and $r_{in} = 2$ mm. The tube-target distance is 0.5 cm and the inlet is 2 slm of a 99.9% He - 0.1% O_2 mixture flowing into an O_2 atmosphere. In section III.6 the influence of the plasma-flow coupling on discharge results will be evaluated.
To couple the flow calculations with the discharge model, the following changes have been introduced in the discharge model:

- As the plasma domain was limited radially by the tube inner radius, in order to describe the plasma plume we had to open the domain radially between the tube and the target.
- The possibility to have two different dielectrics simultaneously (a radial dielectric barrier, the tube, and an axial one, the target) has been included.
- The results of spatial distribution of species densities from the flow calculation are read

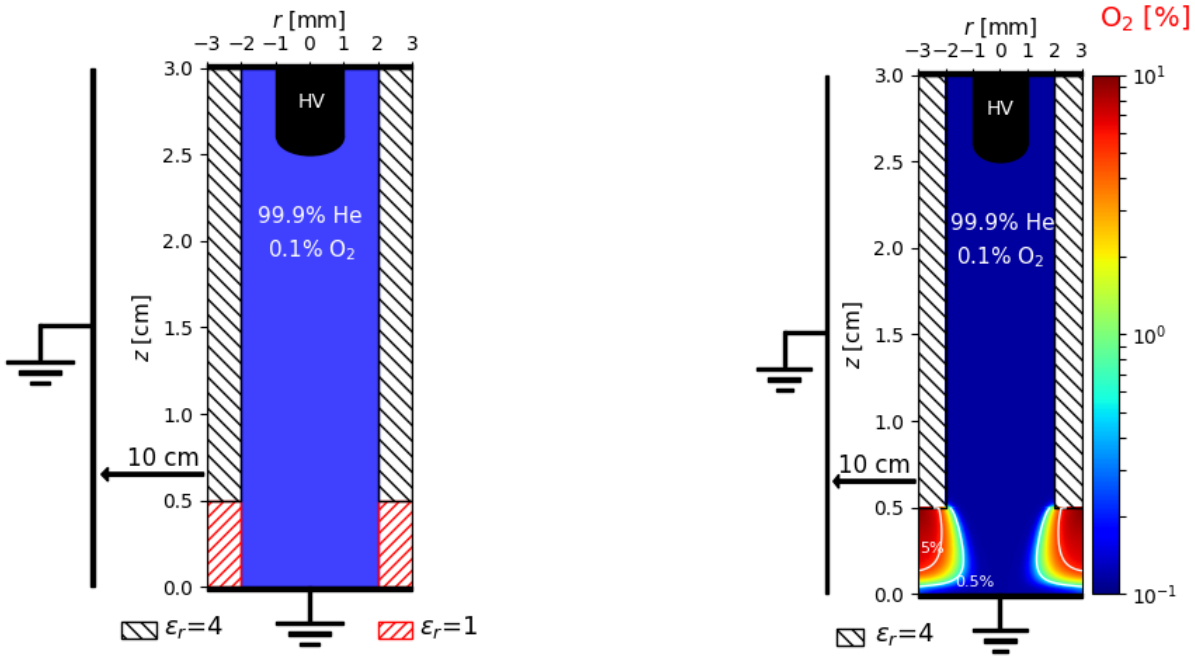

Figure II.10: Model set-up before (on the left) and after (on the right) coupling with the flow calculations. The discharge propagates between a point powered metallic electrode and a grounded metallic plate in a dielectric tube of relative permittivity $\epsilon_r = 4$ and then in air. On the left, the gas-mixture is fixed and a tube of $\epsilon_r = 1$ simulates air between the tube and the target. On the right, He and O_2 mix between the tube and the target. The colour plot and the white curves show an example of the O_2 spatial distribution in a He-O_2 mixture (percentage over a total of 2.45×10^{19} cm^{-3} gas density).

by the discharge model and mapped to its mesh, which is thinner in the plasma region. The mapping has been carried out through linear interpolation. When the plasma cell is located between a flow cell and a boundary, the densities are taken as equal to the last flow cell. This procedure applies only to the region inside the dielectric tube and between the tube and the target. For $z < z_{target}$ ($z_{target} = 0$ in Fig. II.10) and for $z > z_{tube}$ and $r > r_{in}$ ($z_{tube} = 0.5$ cm and $r_{in} = 2$ mm in Fig. II.10) the domain is considered as a dielectric with variable permittivity ($\epsilon_r = 1$ where there is no target nor tube). This procedure is performed only once, at code initialization.

- The densities of He, N_2 and O_2 in the continuity equations are now considered as spatially inhomogeneous and determined by the flow calculation. The spatial distribution of these densities has a direct effect on the calculation of the chemistry source terms.

- In the photo-ionization source term (eq. II.44), where absorption through both A_{ph} and k_p is dependent on the admixture density, these coefficients are now spatially dependent.

- The electron transport parameters (μ_e and D_e) and electron-impact rate coefficients, that were dependent on the local E/N, are now dependent on both the local E/N and the local gas-mixture $k(mix, E/N)$ (Fig. II.3 shows the dependence of the ionization coefficient on the gas-mixture).

- In order to obtain the local coefficients, first, instead of parsing only one BOLSIG+

output file at code initialization, 13 are parsed, all with equal tabulation of E/N, corresponding to the following relative densities of N_2 or O_2: 10 ppm, 100 ppm, 0.1%, 0.25%, 0.5%, 0.75%, 1%, 2.5%, 5%, 7.5%, 10%, 50%, 100%. It has been confirmed that a higher refinement of gas-mixtures for these tables only leads to negligible changes in the results of discharge dynamics. Then, at each call of the coefficients with a local E/N and mix, a binary search algorithm finds the upper and lower tabulated E/N and mix (E_d, E_u, m_d and m_u) and then the local coefficients are found through linear interpolation:

$$k(m_d, E/N) = k(m_d, E_d) + \frac{k(m_d, E_u) - k(m_d, E_d)}{E_u - E_d} \times (E/N - E_d) \quad \text{(II.48)}$$

$$k(m_u, E/N) = k(m_u, E_d) + \frac{k(m_u, E_u) - k(m_u, E_d)}{E_u - E_d} \times (E/N - E_d) \quad \text{(II.49)}$$

$$k(mix, E/N) = k(m_d, E/N) + \frac{k(m_u, E/N) - k(m_d, E/N)}{m_u - m_d} \times (mix - m_d) \quad \text{(II.50)}$$

II.4.4 Code parallelization and profiling

In this thesis we use a code parallelized with MPI (Message Passing Interface), that is, with parallel distributed memory. The implementation of MPI parallelization is described in *Pechereau* [2013] (chapter 4). At code initialization, when the mesh is created, the domain is decomposed according to the number of MPI processes requested. The plasma equations are solved inside each sub-domain and, to assure accuracy of the calculations, some quantities have to be communicated between the MPI processors.

The performance of the parallelized code is evaluated in Figures II.11 and II.12, in terms of calculation time and speed-up. We use the code as described until here, as it is the most used version in this thesis, with the coupling between flow calculations and plasma model, in typical conditions. We take two cases. One in a He-N_2 mixture, where continuity equations are solved for 13 species and one in a He-O_2 mixture, with 21 species. He with 10 ppm admixture flows at 1 slm in a tube with 2.5 cm length, $r_{in} = 1.25$ mm and $r_{out} = 2$ mm. The tube-target distance is 0.5 cm, the target is a grounded plane and the applied voltage is +4 kV after a 50 ns rise-time. The mesh size in the plasma region is 10 μm both axially and radially The total number of cells is $n_z \times n_r = 3500 \times 370 = 1.295$ million. The calculation has ran until $t = 200$ ns, when the discharge front propagates in the middle of the tube. Then, we perform runs of 5 ns, always between 200 and 205 ns, with different numbers of MPI processes on the multi-core cluster "Hopper", where each node contains 16 cores. That corresponds to 618 iterations in the case with He-N_2 and 614 with He-O_2, which means that the time-step is on average of 8 ps. In Figures II.11 and II.12 the two most computationally expensive processes are discriminated: chemistry, i.e. the resolution of the ordinary differential equations with RADAU5, and interpolations, either of transport parameters or of rate coefficients, over electric field or mixture. The so-called "Rest" includes all the other processes: transport calculation, Poisson's equation and photo-ionization that only takes place every 6 time-steps.

In Figure II.11, the time to compute one complete time-step is presented. The total computational time always decreases with the number of MPI processes. With He-N_2 it is variable

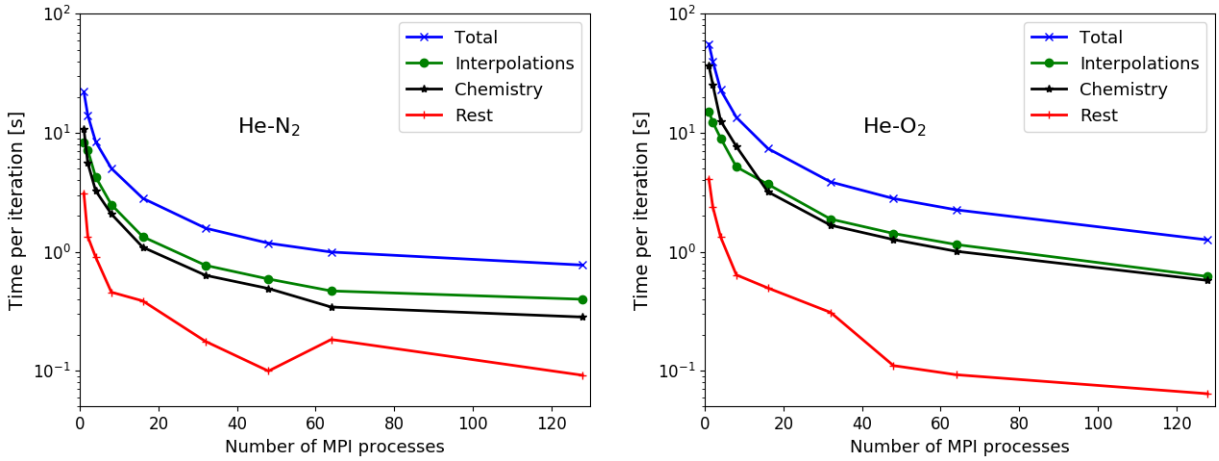

Figure II.11: Computational time to compute a complete time-step depending on the number of MPI processes for cases with $n_z \times n_r = 3500 \times 370 = 1.295$ million. On the left: with a He-N_2 mixture with 13 species. On the right: with a He-O_2 mixture with 21 species.

between 22.1 s with one single process and 0.8 s with 128 processes. These values are highly dependent on the number of species, as with He-O_2 (21 species instead of 13) they are approximately the double: 55.8 s with one single process and 1.3 s with 128 processes. This is expected, as with more species more ODE's have to be solved and with more electron-impact rate coefficients more interpolations have to be carried through. This result reinforces the need for reduced reaction schemes, that allow to describe the discharge dynamics in several gas-mixtures with a low number of species. We should notice that in the performance study presented in *Pechereau* [2013] (chapter 4) Poisson's equation was the most expensive equation to solve, chemistry coming second. That is the case because the number of species for which chemistry equations were solved was 3 in *Pechereau* [2013], and thus the relative importance of Poisson's equation in calculation time was higher.

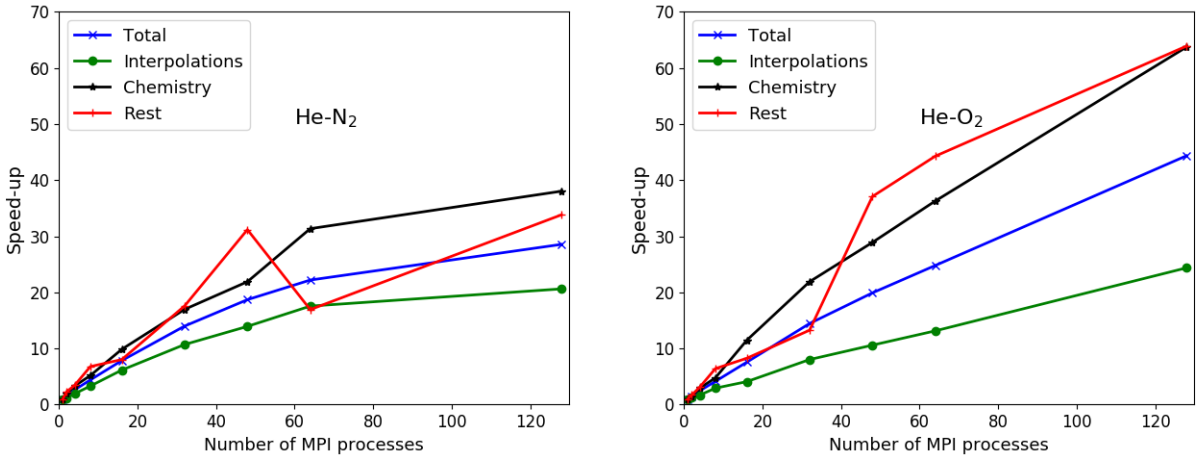

Figure II.12: Speed-up to compute a complete time-step depending on the number of MPI processes for cases with $n_z \times n_r = 3500 \times 370 = 1.295$ million. On the left: with a He-N_2 mixture with 13 species. On the right: with a He-O_2 mixture with 21 species.

In Figure II.12, the speed-up is presented, calculated as $time(1proc.)/time(nbr.proc.)$. We should notice that as chemistry and interpolations take place locally, inside each cell, their

scalability with the number of sub-domains is quite reasonable. As a result, in both simulations, with 64 processes a total speed-up above 20 is obtained and with 32 processes the speed-up is around 14. These values are close to those presented in *Pechereau* [2013]. We remind that 64 and 32 are the number of processes used in the calculations in this thesis.

II.4.5 Study of the electron energy equation and the mean electron energy approximation

Formulation of the problem

With the fluid model described so far, based on the local field approximation (LFA), convergence issues appear in the simulations of the interaction between positive discharges and surfaces with limited electron emission. That is the case with dielectrics of permittivity higher than 4 or if a grounded electrode is placed behind a dielectric. An example of such convergence issues is presented in Figure II.13. In the case presented, a voltage of +6 kV is applied to a ring inside the tube of $r_{in} = 0.125$ mm, close to which the discharge ignites. A grounded ring of dimensions 0.2 mm $\times$ 0.2 mm is wrapped around the tube of $\epsilon_r = 4$ at 7 mm distance from the powered electrode. The discharge propagates from the powered electrode towards the grounded ring and then towards the end of the tube.

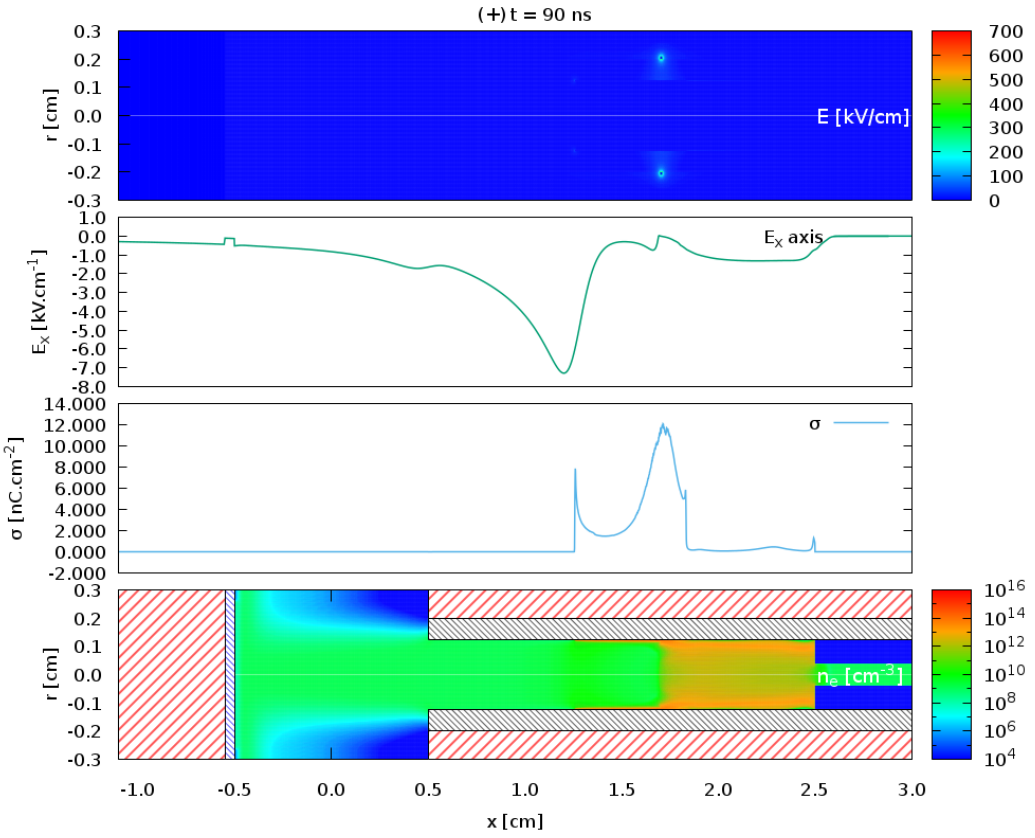

Figure II.13: Representation of a numerical problem when a grounded ring is wrapped around the tube. At $t = 90$ ns, from top to bottom: $E_t(z, r)$, $E_z(z, r = 0)$, σ on the tube wall, $n_e(z, r)$. In the figure the axial coordinate is called x instead of z.

Figure II.13 shows that the electric field magnitude between the plasma and the grounded

ring is very high. In fact, when the positive discharge approaches the dielectric surface, a positive sheath is formed due to the limitation on electron emission from the surface to the plasma. That sheath reinforces the electric field between the plasma and the surface. With high permittivity or with a ground behind the dielectric, that reinforcement is higher and the sheath thinner. The ionization rate increases with the electric field, which produces electrons, which leads again to an increase of the ionization rate. In the present case, the electric field and the ionization rate become so high that the sheath collapses and the discharge becomes stuck to the dielectric surface. We see in the figure that the discharge can keep propagating axially but with very high (above 10^{15} cm^{-3}) electron density only very close to the surface. These values of n_e are higher than expected and do not fill the volume inside the tube. Moreover, we notice that the surface charge density deposited σ is very high and presents a weird axial profile. These numerical results are not physical and are a limitation of the fluid model presented so far.
Using the LFA, a local relation between the kinetic coefficients and E/N is considered. Since the electric field in the region of the ionization front changes rapidly in space and time, nonlocal effects may have to be considered. In this thesis it is important to describe the interaction with dielectric targets of high permittivity and with tubes with a grounded ring wrapped around. Hence, a solution has to be found for the type of inconsistency shown in Fig. II.13. The solution has been searched for in collaboration with Zdenek Bonaventura from Masaryk University.

Implementation of the electron energy equation

One possible solution to the problems raised by the steep electric field gradients in discharge fronts is to introduce corrections to the ionization rate proportional to the gradients of electron density or electric field [*Naidis*, 1997; *Soloviev and Krivtsov*, 2009]. In *Odrobina and Cernak* [1995] the ionization source term is corrected by an estimation of reduction of high-energy electrons by backward diffusion. We have implemented this approach in the discharge model and the results were satisfying. However, a more consistent approach to account for non-locality is to evaluate the mean electron energy through the inclusion of the electron energy balance equation in the model and then use the local mean energy approximation (LMEA) instead of the LFA. We have decided to discard the correction to the ionization source term and to implement the electron energy equation in our model.
The energy equation is implemented in several fluid models for discharges at atmospheric pressure [*Norberg et al.*, 2015b; *Lazarou et al.*, 2015; *Levko and Raja*, 2017] and is recommended with respect to the use of the LFA in several works [*Eichwald et al.*, 2006; *Sakiyama and Graves*, 2007; *Grubert et al.*, 2009]. As described in *Zhu* [2018] (chapter 3), between the discharge and a wall, where there is high electric field and high n_e gradient, the electron diffusion flux can be higher than the drift flux ($D_e|\nabla n_e| > \mu_e n_e E$). The electrons transported through drift move in the sense of the $\vec{E}$ acceleration and are thus heated, while the electrons transported through diffusion, in the opposite sense of acceleration, are cooled. This is not the case only if the local equilibrium of electrons is reached instantaneously, i.e. if the timescales of variations of electric field and n_e are long compared to that of energy relaxation. The LFA, with the approximation of mean electron energy ϵ_m only dependent on the local E/N, does not take these physical aspects into account, and thus overestimates or

underestimates electron-impact rate coefficients. In the case of interaction between positive streamers and surfaces, the LFA tendentiously overestimates these coefficients.
As described in section II.2.2, to derive the macroscopic conservation law for the mean electron energy, equation II.2 is multiplied by $\chi = m_e|\vec{v_e}|^2/2$. Adopting the same approximations as in *Alves et al.* [2018]; *Hagelaar and Pitchford* [2005], the electron energy conservation equation is written:

$$\frac{\partial}{\partial t}(n_e\epsilon_m) + \nabla.\vec{j_\epsilon} = -|q_e|\vec{E}.\vec{j_e} - \Theta_e \tag{II.51}$$

$$\vec{j_\epsilon} = -n_e\epsilon_m\mu_\epsilon\vec{E} - D_\epsilon\nabla(n_e\epsilon_m) \tag{II.52}$$

The terms on the left side of equation II.51 represent the time-variation of the electron energy density and the transport of this quantity through drift and diffusion. On the right side of the same equation there are the source/loss terms due to acceleration/cooling by the electric field and the loss term Θ_e due to the power lost in collisions. Thus, eq. II.51 takes the same form of the continuity equations II.3 with drift-diffusion approximation for the electron energy density that we redefine as $n_\epsilon = n_e\epsilon_m$. We see in eq. II.51 that if $\vec{E}.\vec{j_e} > 0$ (transport of electrons opposite to acceleration) a loss of energy is induced and if $\vec{E}.\vec{j_e} < 0$ (transport of electrons in the sense of acceleration, which is always the case through drift) a gain of energy is induced. Both the electron and electron energy transport parameters and Θ_e can be obtained by the integration of the EEDF.
The implementation of eq. II.51 in the code is fairly easy. We add the electron energy as if it was a new species with density n_ϵ. Thus, the model now solves continuity equations for 14 species in He-N_2 and for 22 species in He-O_2. Θ_e is obtained directly from the BOLSIG+ tables, gathering "Inelastic power loss", "Elastic power loss" and "Growth power". Concerning the source/loss term through heating/cooling, we calculate it locally as:

$$(\vec{E}.\vec{j_e})_{i,j} = \left(\frac{E^z_{i-1/2,j} + E^z_{i+1/2,j}}{2}\right)\left(\frac{j^e_{i-1/2,j} + j^e_{i+1/2,j}}{2}\right) + \tag{II.53}$$

$$+ \left(\frac{E^r_{i,j-1/2} + E^r_{i,j+1/2}}{2}\right)\left(\frac{j^e_{i,j-1/2} + j^e_{i,j+1/2}}{2}\right) \tag{II.54}$$

As initial conditions, we consider electrons have low energies in the whole domain: $n_\epsilon = n_e \times$ 0.04 eV. The boundary conditions for the flux of n_ϵ are the same as for n_e. At the boundaries where electrons are transported from the plasma to the surface $j^\epsilon_{i+1/2,j} = j^e_{i+1/2,j} \times \epsilon^m_{i,j}$. At those where electrons are injected from the surface into the plasma, we consider they are injected with low energy $j^\epsilon_{i+1/2,j} = j^e_{i+1/2,j} \times 0.04$ eV.
Then, we apply the LMEA. All the parameters obtained from BOLSIG+ tables are now function of the local mean electron energy instead of the local reduced electric field. Thus, we have $\Theta_e(\epsilon_m, mix), \mu_e(\epsilon_m, mix), \mu_\epsilon(\epsilon_m, mix), D_e(\epsilon_m, mix), D_\epsilon(\epsilon_m, mix), k(\epsilon_m, mix)$, where k are all the electron-impact rate coefficients. To implement this change, the BOLSIG+ calculations have been ran for the same gas-mixtures, but saved as "Separate tables vs mean energy". Moreover, we have changed the range of E/N for the BOLSIG+ calculations. They have been ran for 10^{-4}, 10^{-3} and 10^{-2} Td and then for an exponential progression with 200 points between 0.1 Td and 1900 Td, with a total of 203 points. Discharge simulations in typical conditions have been performed with the LMEA and the two sets of tables and the

results are exactly the same. In Fig. II.14, on the left, the range of ϵ_m corresponding to the range of electric field in Fig. II.2 (from BOLSIG+, without accounting for the electron energy transport) is shown to not exceed 100 eV. We should notice that although E/N is no longer the input parameter for all the electron coefficients, the self-consistent calculation of electric field is still crucial, as it defines the drift velocity of charged species, the heating/cooling term in eq. II.51 and serves as input for the tabulation of ion mobilities. Finally, to implement these changes, the numerical schemes for species transport have been modified. In this version of the code with the electron energy equation and the LMEA, instead of the third-order UNO3 scheme for drift and the second-order scheme for diffusion, we use the classical explicit Scharfetter-Gummel (SG) scheme for drift and diffusion together [*Scharfetter and Gummel*, 1969]. We have compared discharge simulations in typical conditions with the LFA with UNO3 and with SG schemes and the difference in results is below 1%.

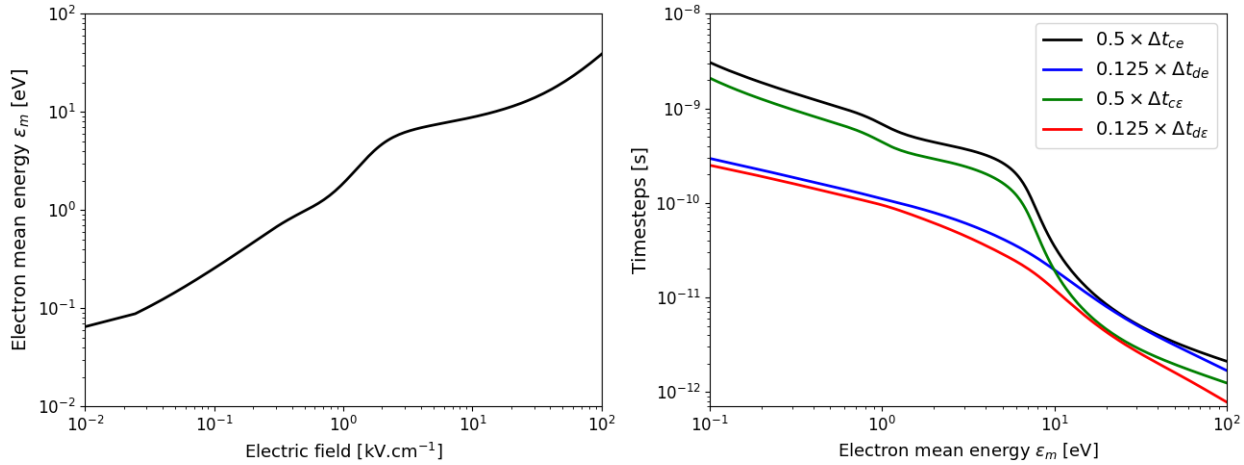

Figure II.14: On the left, evolution of ϵ_m with E. On the right, $A_c\Delta t_c$ and $A_d\Delta t_d$ associated to electrons and to electron energy as function of ϵ_m. The gas-mixture is 99.9% He - 0.1% N_2. The mesh size is taken as 10 μm.

The implementation of the electron energy equation and the LMEA removes limitations to the code's capabilities. Its drawback concerns calculation time. On the one hand, one more species is added for the calculation of continuity equations. On the other hand, and most importantly, the time-steps through the conditions in eq. II.26 decrease due to the higher values of D_ϵ and μ_ϵ with respect to D_e and μ_e. On the right side of Fig. II.14 the newly calculated time-steps associated to drift and diffusion of electrons ($\Delta t_{ce} = \Delta x/(E\mu_e), \Delta t_{de} = (\Delta x)^2/D_e$) and electron energy ($\Delta t_{c\epsilon} = \Delta x/(E\mu_\epsilon), \Delta t_{d\epsilon} = (\Delta x)^2/D_\epsilon$) as function of ϵ_m are presented. It is shown that the time-steps associated to the transport of electron energy (green and red curves) are always lower than those associated to the same component of transport of electrons (black and blue curves). As a result, including the electron energy, the simulation time-step is about one half of that with the LFA and thus the calculation time is approximately double. For instance, if the maximum ϵ_m is 20 eV, the calculation time-step is around 10 ps without energy transport and 5 ps including the energy equation.

Discharge results with LFA and LMEA

In order to evaluate the effect of the change of model, in Figure II.15 are represented discharge results in conditions in which both models work. The spatial distribution of the electric field magnitude E_t and the electron density n_e are presented. The model called "LFA" is the one described until section II.4.4, using the local field approximation, without electron energy equation and with the UNO3 scheme for drift and second-order diffusion scheme. The model called "LMEA" is the one described in this section, using the local mean energy approximation and the SG scheme for the calculation of drift-diffusion fluxes and describing electron energy transport. The geometry is the same in both cases with a tube of $\epsilon_r = 4$, r_{in} = 1.25 mm, r_{out} = 2 mm and length 1.8 mm filled with a 99% He - 1% N_2 gas, a grounded plane at $z = 0$ and a ring electrode inside the tube at $z = 1.3$ mm. The results are presented in both cases at $t = 120$ ns.

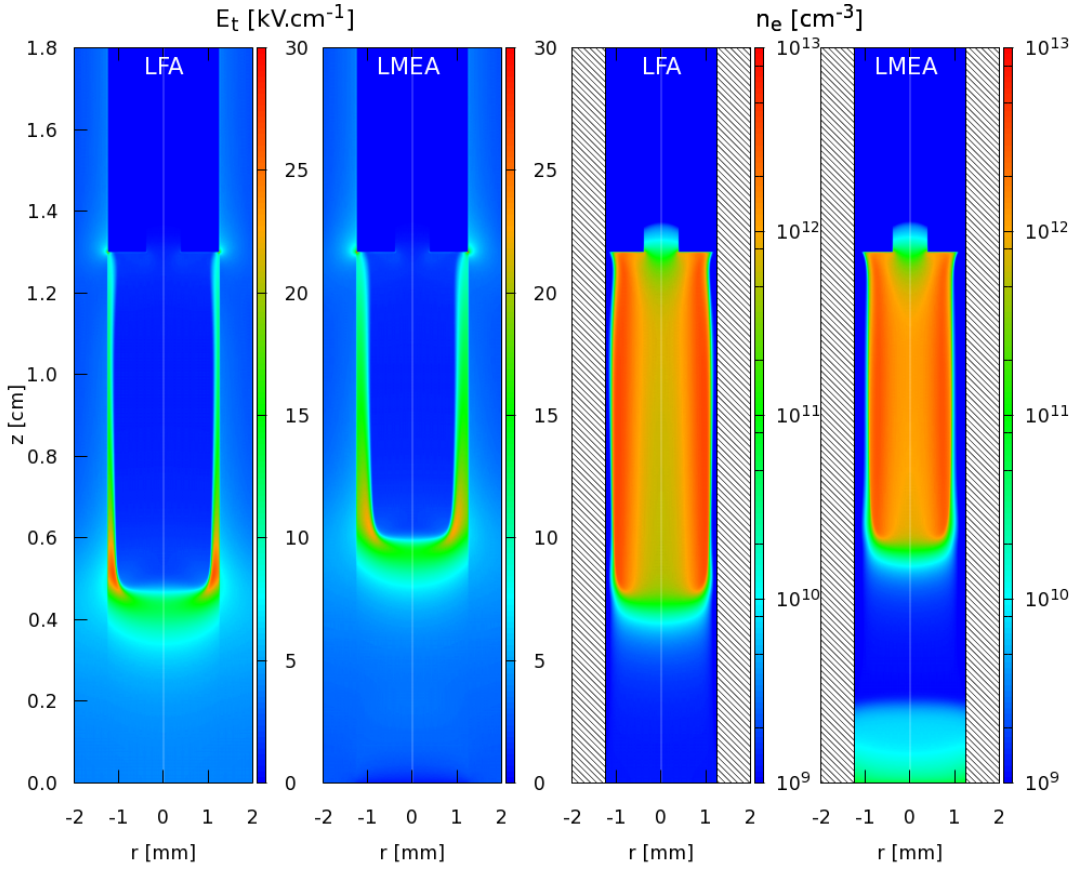

Figure II.15: Comparison of results with LFA and LMEA. On the left, the electric field magnitude E_t. On the right, the electron density n_e. Results at $t = 120$ ns.

Figure II.15 shows that the general discharge dynamics is the same in both cases, with discharge ignition near $t = 45$ ns and approximately the same axial electric field during propagation. However, some differences should be noted. When losses of energy are accounted for by solving the electron energy equation, the discharge structure is more centered, the positive sheath between the discharge and the tube is wider and the propagation is slower. As a result, the impact on the target takes place at 153 ns instead of 140 ns with the LFA, a difference of 9.3%. Moreover, in the current conditions, a small electron production is visible near the target with the LMEA and not the LFA.

Then, to study the influence of the grounded ring wrapped around the tube on the discharge dynamics, we compare in Fig. II.16 discharge results using the LMEA model with and without grounded ring. In the case without grounded ring, the geometry is the same as in Fig. II.15. In the case with grounded ring the only difference is its addition between $z = 0.5$ and 0.8 cm, with radius between $r = 2$ and 2.5 mm. Both results of the spatial distributions of E_t, n_e and ϵ_m are represented at $t = 120$ ns.

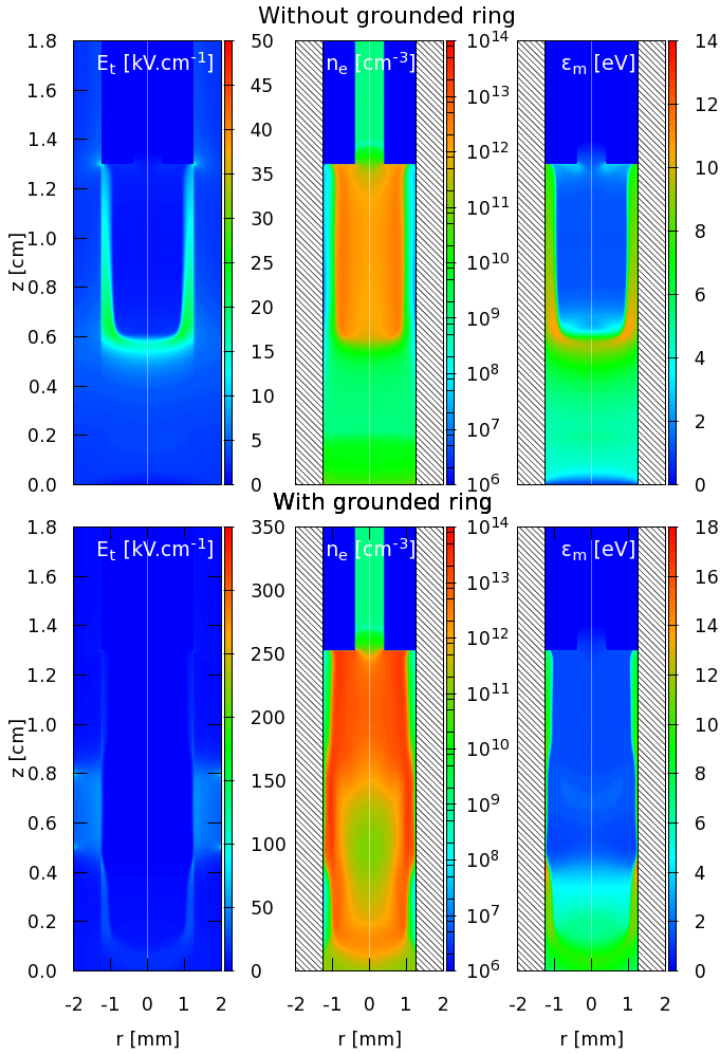

Figure II.16: Comparison of results with LMEA with (on bottom) and without (on top) grounded ring wrapped around the tube. At $t = 120$ ns, from left to right: E_t, n_e and ϵ_m.

With the grounded ring, the Laplacian electric field is higher between the rings (see appendix B). Hence, the discharge ignition takes place slightly earlier, close to $t = 40$ ns instead of $t = 45$ ns without ring, and the propagation until $z = 0.8$ cm (where the grounded ring begins) takes 25 ns instead of 55 ns without the ring. Then, in the case with ring, the discharge takes 22 ns to reach $z = 0.5$ cm (end of grounded ring) and 34 ns from there until $z = 0$, where impact takes place at $t = 121$ ns. On the other hand, without the grounded ring, the discharge takes 27 ns between $z = 0.8$ and 0.5 cm and then 46 ns until the impact. We can conclude that the discharge propagates faster with the grounded ring not only between the two ring electrodes but also afterwards. Besides velocity of propagation, Fig. II.16 shows that the discharge has a much more tubular structure close to the grounded ring due to the

enhancement of radial electric field but then tends to recenter after crossing the grounded ring. Moreover, we see that the electric field magnitude between the plasma and the grounded ring rises to hundreds of kV.cm^{-1} but ϵ_m is lower than 18 eV at $t = 120$ ns. Even when the discharge front passes close to the grounded ring, ϵ_m does not surpass 25 eV. Due to the more tubular structure, the surface charge deposition on the tube walls with and without grounded ring is very different. In fact, without grounded ring the surface charge density σ does not overcome 0.1 nC.cm^{-2}. With grounded ring, it reaches values as high as 16 nC.cm^{-2}, as shown in Fig. II.17. We should notice that the σ axial profiles shown in Fig. II.17 are smooth and completely different from that in Fig. II.13.

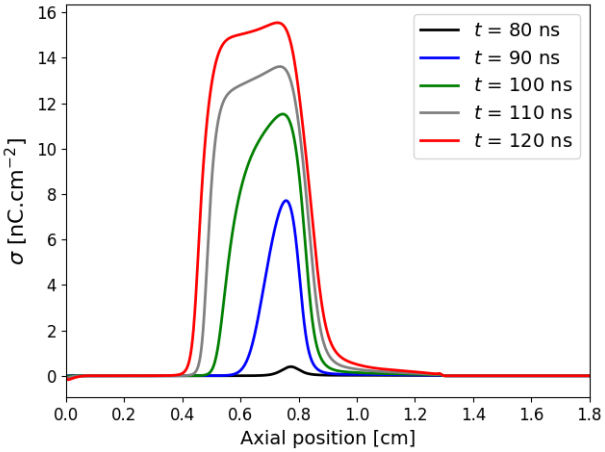

Figure II.17: Axial profiles of surface charge density at $t = 80$, 90, 100, 110 and 120 ns, with LMEA and grounded ring wrapped around the tube.

II.5 Simulation conditions

In this thesis, most calculations have been carried out with the fluid model described until section II.4.4, unless noted otherwise. That means they take the chemistry models described in section II.4.2 for He-N_2 and He-O_2 mixtures and the plasma-flow coupling described in section II.4.3 but keep the local field approximation. The exceptions are the calculations in section V.3.2 and in chapter VI, where the model described in section II.4.5 is used with the LMEA. There, the interaction between positive discharges and dielectric targets of high permittivity (40 and 56) takes place, as well as the use of a wrapped ring around the dielectric tube. Hence, the description of energy balance and the use of the local mean energy approximation are required. Along the thesis, different geometries, gas-mixtures, shapes of applied voltage and boundary conditions are used, that are described in each section or chapter.

Chapter III

General characterization of Helium plasma jets through numerical simulations

Contents

III.1 Introduction 64

III.2 Role of the dielectric tube on discharge propagation in positive and negative polarities 64

III.2.1 Introduction 64

III.2.2 Studied conditions 65

III.2.3 General characterization of Helium discharge propagation without tube 67

III.2.4 Influence of the mechanical confinement of the tube on discharge propagation in positive and negative polarities 71

III.2.5 Role of the tube permittivity on discharge propagation 78

III.2.6 Influence of the secondary electron emission on the mechanical confinement of the tube for positive polarity 80

III.2.7 Conclusions 83

III.3 Influence of the electrode geometry on discharge propagation . 83

III.4 Influence of the shape of the applied voltage on discharge propagation in short tubes 86

III.5 Dynamics of propagation of He discharges with N_2 and O_2 admixtures inside dielectric tubes 88

III.6 Discharge propagation in the plasma plume 93

III.6.1 Introduction 93

III.6.2 Studied conditions 93

III.6.3 Influence of flow and tube-target distance on discharge dynamics . 95

III.6.4 Effect of the polarity of the applied voltage on the discharge dynamics in the plasma plume 97

III.6.5 Discharge propagation mechanisms in the plasma plume 100

III.6.6 Role of each property of the gas mixing in the plasma plume on discharge dynamics 105
III.6.7 Conclusions 109
III.7 Conclusions 110

III.1 Introduction

In this chapter, the dynamics of ignition and propagation of He plasma jets is characterized. Focus is given to the discharge dynamics inside tubes and in the plasma plume, before the discharge interacts with a solid target. The work presented in this chapter is intended at the same time to address interesting questions of the physics of plasma jets and to provide fundamental understanding about the discharge propagation that is helpful to follow the next chapters, where the highlight will be put on electric field characterization and the interaction with different targets.
First, in section III.2, the role of the tube on discharge propagation is assessed. In order to understand this role, the Helium discharge is firstly characterized without tube and then compared to cases when tubes of different permittivities are added. It is investigated why do discharges with positive and negative polarities have different structures inside the tubes.
Then, in sections III.3 and III.4 the influence on discharge propagation, respectively, of different electrode geometries and shapes of applied voltage is examined. As in different experiments and simulations different geometries and pulses of applied voltage are used, it is important to show the influence of these conditions on discharge ignition and propagation.
In section III.5 the effect of N_2 and O_2 admixtures on the dynamics of ignition and propagation of He discharges inside dielectric tubes is studied, both due to the interest expressed in the literature for the addition of molecular gases to Helium for optimization of plasma jet applications and because the gas mixtures studied in this thesis are variable.
Finally, in section III.6 we address plasma jet configurations, with gas mixing between the tube and the target, and we study the discharge propagation in the plasma plume. We investigate the influence of several parameters, including the polarity of applied voltage and the environment gas, and we examine in detail what are the properties of gas mixing in the plasma plume that set the discharge path of propagation.

III.2 Role of the dielectric tube on discharge propagation in positive and negative polarities

III.2.1 Introduction

In this section, we study how the presence of dielectric tubes affects the dynamics of a He discharge and how this dynamics in tubes differs according to the polarity of applied voltage. The state of the art on these two subjects has been exposed in sections I.2.2 and I.2.5.
Here, we highlight only that it has been shown in simulations and experiments [*Jánský et al.*, 2010, 2011] that positive air discharges in tubes at atmospheric pressure tend to fill the tube

and propagate faster than without tube and with higher electron density and electric field values. Furthermore, it has been reported that an increase of ϵ_r and of the tube radius both lead to a more tubular discharge structure and to a decrease of the electron density and electric field on the axis of propagation and of the discharge velocity of propagation. Then, in *Darny et al.* [2017b]; *Darny* [2016] it has been reported that the experimentally observed structure of a He discharge propagating in a tube is highly dependent on the polarity: quite homogeneous for negative polarity voltage pulse and more filamentary for positive polarity. In this section the influence of the dielectric tube on the discharge dynamics is shown by providing a detailed explanation on the formation of charges in volume and on the surface of the tube and how these charges affect the electric field and electric potential distribution, and thus the discharge propagation for both positive and negative polarities of applied voltage. Moreover, this section intends to address the characteristics of the tubes that will be used in the rest of the thesis and how these affect the discharge dynamics. In section III.2.2 the studied conditions are explained. Then, in sections III.2.3 and III.2.4 the influence of the mechanical cylindrical constraint of the tube on the discharge dynamics is assessed. The presence of a tube with $\epsilon_r = 1$ is used and compared to a situation without tube. Besides the influence of the presence of the tube, focus is given to the differences in dynamics and structure between discharge propagation inside tubes with positive and negative polarities of applied voltage. In section III.2.5 the influence of the tube permittivity is evaluated through a short comparison between tubes with $\epsilon_r = 1$ and $\epsilon_r = 4$ as the ones in experiments. Furthermore, the influence of the electron flux between the plasma and the tube walls in the case of the positive discharge is studied in section III.2.6. Finally, in section III.2.7 the results are summarized.

III.2.2 Studied conditions

In this thesis the discharge propagation is studied inside two different dielectric tubes, corresponding to different experimental conditions. Both are tubes with relative permittivity $\epsilon_r \sim 4$. The one used in the experiments of Xavier Damany, Jean-Michel Pouvesle and Eric Robert in GREMI, Université d'Orléans, made of quartz, has inner radius $r_{in} = 2$ mm and outer radius $r_{out} = 3$ mm. The other, used in the experiments of Elmar Slikboer, Ana Sobota and Olivier Guaitella in Laboratoire de Physique des Plasmas, École Polytechnique and in EPG, Eindhoven University of Technology, made of pyrex, has $r_{in} = 1.25$ mm and $r_{out} = 2$ mm. The length of discharge propagation inside the tube is variable. In this section, the influence of these tubes on discharge propagation is studied. For that, the two different geometric set-ups shown in Figure III.1 are used: without tube (on the left) and with tube with $r_{in} = 2$ mm and $r_{out} = 3$ mm (on the right). The tube with $r_{in} = 1.25$ mm is not used in this section, but the effect of radius reduction is commented in section III.2.7. The set-up without tube corresponds to the case of discharge propagation in a chamber with controlled gas-mixture. In all the cases studied in this section the length of the domain is of 2 cm in the axial direction. A powered point electrode is set in the axis of the domain. It is composed of a cylinder with 4 mm length and 1 mm radius and a spherical tip of 1 mm radius. The axial position of the tip of the point is fixed at $z = 1.5$ cm. A grounded metallic target is set at $z = 0$ and therefore the inter-electrode distance is always 1.5 cm in this section. As shown

in Figure III.1, all the discharge set-ups are placed inside a grounded cylinder with a radius of 10 cm. The discharge is powered by a voltage that rises linearly between 0 and V_P, and then is constant with a plateau value V_P. The rise-time is 50 ns and the voltage can be either positive or negative, with plateau values of $V_P = +4$ kV or $V_P = -4$ kV. The gas mixture in this section is always considered as 99% He - 1% N_2, and the kinetic scheme described in section II.4.2 for He-N_2 plasmas at atmospheric pressure is used. As in most of this thesis, a uniform initial preionization density $n_{init} = 10^9$ cm^{-3} of electrons and N_2^+ ions is considered, to account for the effect of repetitive voltage pulses (see section II.4.2). A cartesian mesh is used with an axial size of 10 μm. Radially, the mesh size is 10 μm between $r = 0$ and $r = 15$ mm, in the case of the set-up without tube, or between $r = 0$ and $r = 3$ mm in the cases with tube. The radial mesh size is then expanded using two geometric progressions until reaching the boundary of the computational domain: 20 cells for 1 mm thickness (until $r = 16$ mm without tube or $r = 4$ mm with tube) and then 50 cells until $r = 10$ cm. This refinement requires a mesh of $n_z \times n_r = 2000 \times 1570 = 3.14$ million points without tube and of $n_z \times n_r = 2000 \times 370 = 0.74$ million points with tube. The average computational time required for a simulation run without tube to obtain the results presented in this section is of three days with 32 MPI processes on the multi-core machines that compose the cluster "Zoidberg". For the simulation cases with tube, the average computational time is reduced to 18 hours on the same machines. All along the section, the discharge results have been obtained every 5 ns since the beginning of the pulsed voltage application, and are therefore analyzed with a 5 ns temporal resolution.

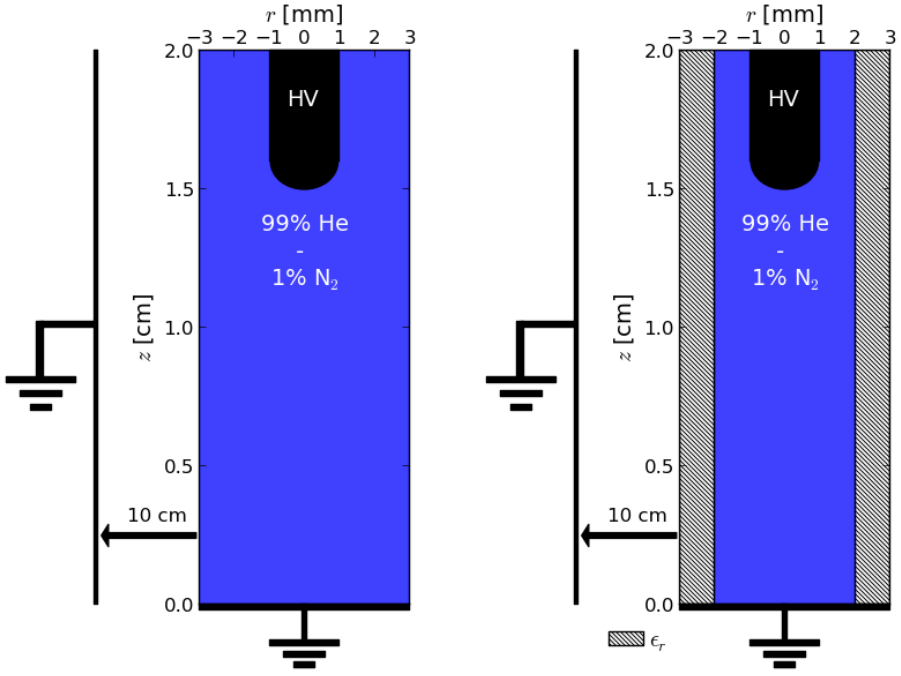

Figure III.1: Side view schematics of the discharge set-ups used in this section. On the left, the set-up used without tube. On the right, the set-up with tube of relative permittivity ϵ_r and $r_{in} = 2$ mm and $r_{out} = 3$ mm.

III.2.3 General characterization of Helium discharge propagation without tube

In this section, we study the discharge ignition and propagation in a He-N_2 chamber in a point-plane configuration without tube. In Figures III.2 and III.3 are represented the spatial distributions of the magnitude of electric field E_t at different times for $V_P = +4$ kV and $V_P = -4$ kV, respectively. For each case, E_t is represented at an instant close to discharge ignition, during discharge propagation at $t = 100$ ns, shortly before the discharge front hits the target and once it hits the target.

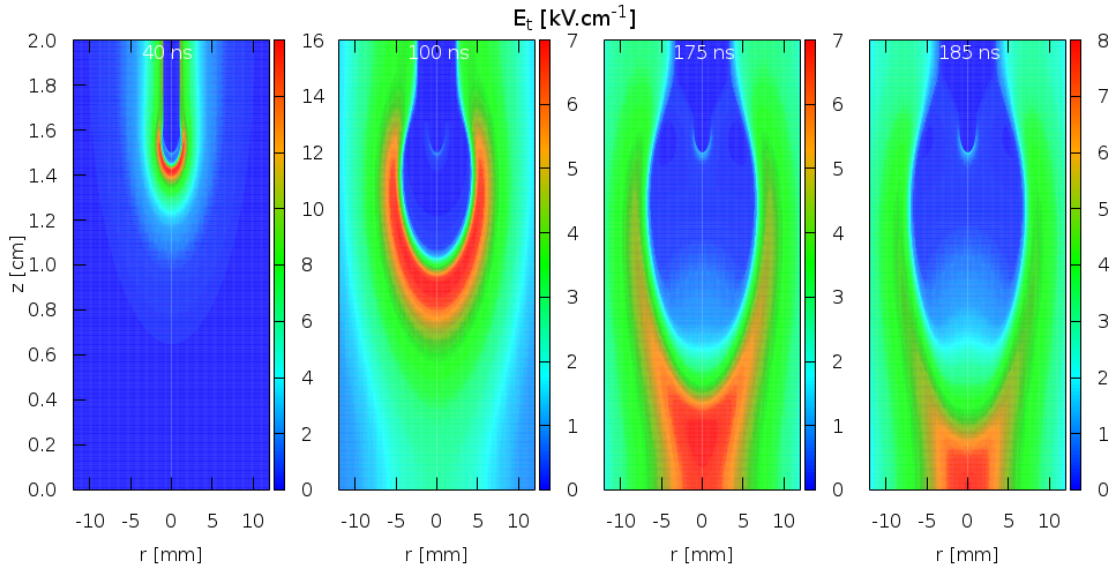

Figure III.2: Cross sectional views of the magnitude of the electric field at $t = 40$, 100, 175 and 185 ns, for a 2 cm long domain without tube with a grounded target for $V_P = +4$ kV.

In both figures we notice that the discharge ignition takes place close to the tip of the point powered electrode, where the Laplacian electric field is highest (see appendix B). The discharge front or ionization front is identified by the strong and localized electric field generated by the charge separation. In our two-dimensional axisymmetric setting, this electric field has both an axial E_z and a radial E_r component. The quantity E_t observed in Figures III.2 and III.3 is the norm of the two components. It is noticeable that the discharge ignition happens slightly earlier and requires lower electric field values in negative polarity (~ 12 kV.cm^{-1}) than in positive polarity (~ 16 kV.cm^{-1}), due to the relative easiness to form an ionization wave through negative streamer mechanisms. Then, we notice in Figures III.2 and III.3 that between the discharge ignition and $t = 100$ ns the discharge front expands both radially and axially, with maximum E_t located on the axis of symmetry. Moreover, in Figures III.2 and III.3, it is put forward that at $t = 175$ ns for $V_P = +4$ kV and at $t = 140$ ns for $V_P = -4$ kV the discharge front is located at a few mm from the grounded target with an electric field on the axis close to 7 kV.cm^{-1}. The differences observed here between the two polarities, with earlier ignition, faster propagation and bigger radius (~ 10 mm for $V_P = -4$ kV and ~ 8 mm for $V_P = +4$ kV) for negative polarity have been reported also in the case of an air discharge propagating between a point electrode and a dielectric plane in *Pechereau and Bourdon* [2014]; *Pechereau* [2013].

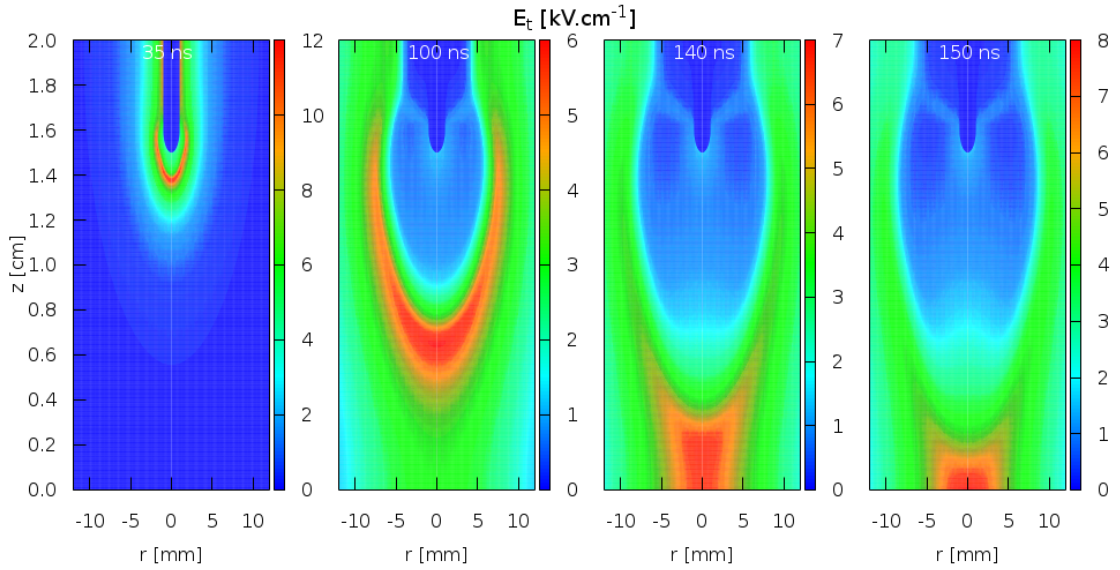

Figure III.3: Cross sectional views of the magnitude of the electric field at $t = 35$, 100, 140 and 150 ns, for a 2 cm long domain without tube with a grounded target for $V_P = -4$ kV.

In Figure III.4 is represented the spatial distribution of the electron density n_e for the same case and at the same instants as in Figure III.2. The results of n_e for $V_P = -4$ kV are qualitatively the same as for positive polarity and are not shown here. The electron density reaches values between 10^{12} and 10^{13} cm^{-3} close to the tip of the point electrode, where E_t is highest. Then, as the discharge propagates with a lower electric field on the discharge front, the electron density generated in the plasma channel behind the ionization front is closer to 10^{11} cm^{-3}. We can therefore characterize this discharge as being very diffusive. To provide more detail into the discharge dynamics, in Figure III.5 are represented the spatial distributions, for $V_P = +4$ kV and at an instant shortly before the impact of the discharge front on the target ($t = 175$ ns), of the net charge density ρ, the axial and radial components of electric field E_z and E_r and the source term of ionization through electron-impact reactions S_e (all the electron-impact ionization reactions listed in table II.1). Once more, the results of the same quantities for negative polarity of applied voltage are not shown here, since they are very close (with opposite signs of ρ, E_z and E_r) to those obtained for $V_P = +4$ kV.
Firstly, Figure III.5 shows that on the edge of the region of quasi-neutrality lies a region of positive net charge density ρ, created by the charge separation between electrons and positive ions. Then, electric field is generated between ρ and the electrodes at fixed potential. Concerning the axial direction, we notice that E_z is highest in magnitude close to the axis and in the region between ρ and the grounded plane at $z = 0$. E_z at this position is directed downwards, reaches values ~ 7 kV.cm^{-1} and has crucial importance in the propagation between the electrodes. Moreover, in the radial direction, it is visible that E_r is directed outwards and is positioned on the radial edge of the plasma, with maximum value ~ 4.5 kV.cm^{-1} located in the region where the plasma is larger in radius. Finally, S_e (determined by n_e and the electron-impact ionization coefficients, dependent on the local reduced electric field) is distributed in the same region as the electric field magnitude. We observe in Figure III.5 that E_z created between ρ and the target, with magnitude ~ 7 kV.cm^{-1}, originates an ionization source term with values between 10^{19} and 10^{20} cm^{-3}.s^{-1} in the discharge front. This S_e,

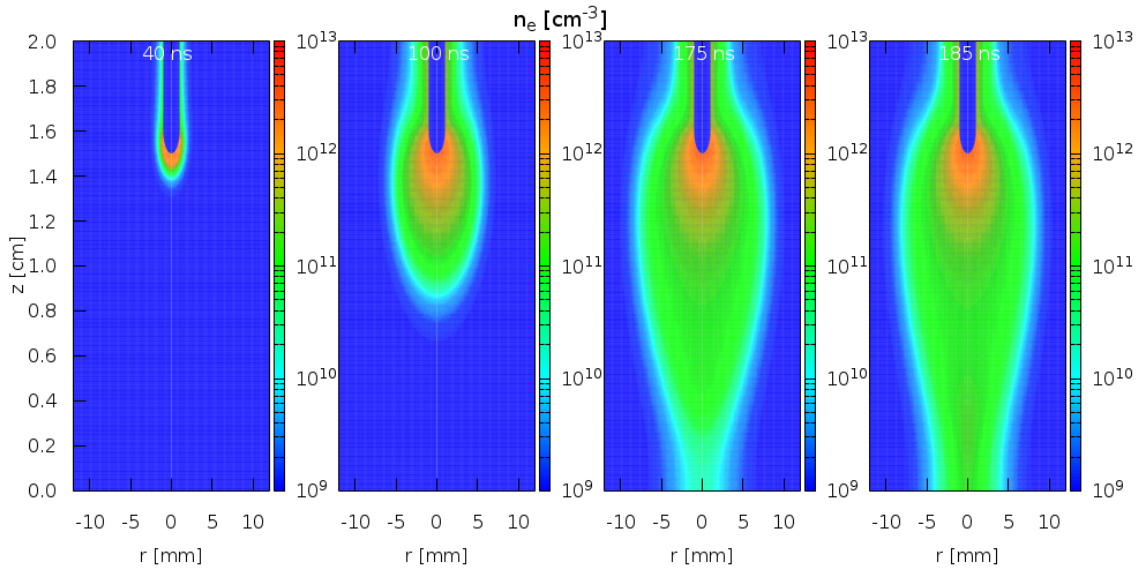

Figure III.4: Cross sectional views of the electron density at $t = 40$, 100, 175 and 185 ns, for a domain without tube and with a grounded target, for $V_P = +4$ kV.

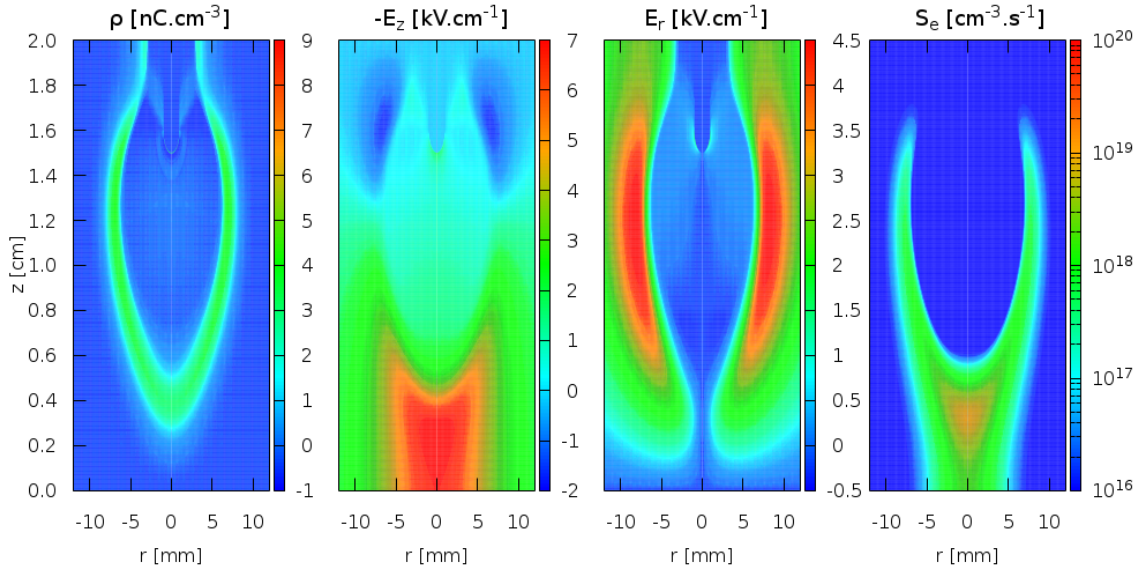

Figure III.5: Cross sectional views of ρ, E_z, E_r and S_e at $t = 175$ ns, for a 2 cm long domain without tube with a grounded target for $V_P = +4$ kV.

along with the photo-ionization source term (shown and compared with S_e in section III.6 for different conditions), guarantee the creation of new electrons and ions in the discharge front and the extension of the plasma axially until reaching the target.

Figure III.6 shows the velocity of propagation (on the left side) of the discharge front between the two electrodes, for both polarities of applied voltage. In this figure, the powered electrode is represented on the left and the grounded target on the right. The velocity is obtained firstly by identifying every 5 ns the position of the maximum of the axial component of electric field, that is located at the discharge front. Radially, $|E_z|_{MAX}$ is always located on the axis of symmetry at $r = 0$, and therefore the evolution of its position is completely axial. Then, the difference between two successive positions is divided by the temporal difference

to obtain the value of velocity. On the right side of the same figure is presented the value of the maximum of the axial component of electric field $|E_z|_{MAX}$.

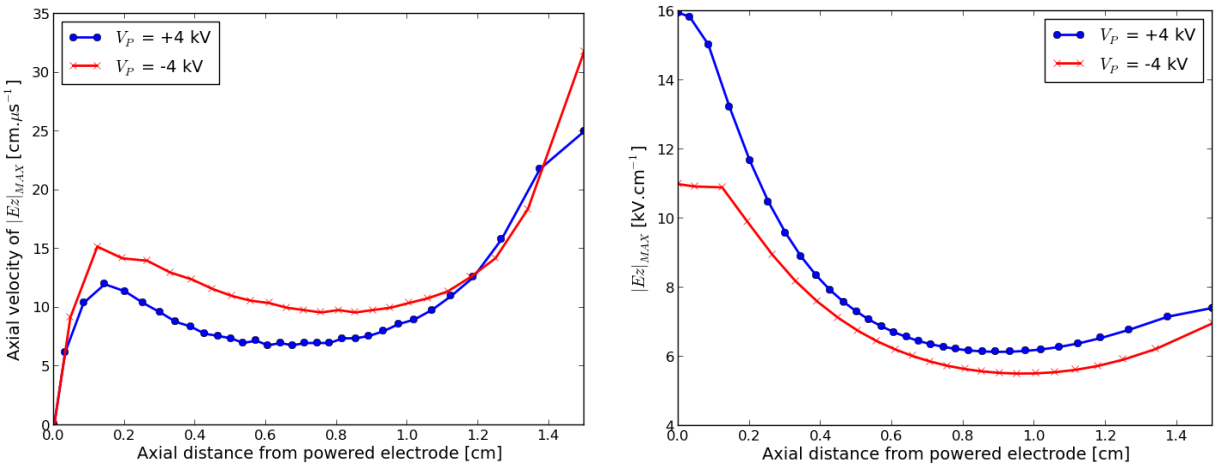

Figure III.6: Axial velocity of propagation and magnitude of $|E_z|_{MAX}$ between the powered electrode and the target, with 5 ns temporal resolution, for a 2 cm long domain without tube with a grounded target for both polarities. On the left, $vel(z)$. On the right, $|E_z|_{MAX}(z)$.

It is visible in Figure III.6 that the velocity of propagation first increases during discharge ignition. This first trajectory corresponds to the ionization and charge separation close to the tip of the point electrode. Then, the discharge dynamics is determined by the electric field generated by the net charge density created around the tip. We notice that for both polarities $|E_z|_{MAX}$ first decreases as the discharge front gets further away from the powered electrode, before increasing when it gets as close as 5 mm to the target. The velocity of propagation follows the same trend as $|E_z|_{MAX}$, first decreasing and then increasing. Furthermore, Figure III.6 shows that in the current conditions the axial velocity is higher in negative polarity than in positive polarity during most of the propagation, although the maximum of electric field is always higher in positive polarity, which is explained by the different mechanisms of streamer propagation [*Babaeva and Naidis*, 1997].
The discharge propagates between the electrodes because the electric potential in its head is connected by a conductive plasma channel to the powered electrode. In Figure III.7 it is shown the distribution of electric potential in the plasma between the two electrodes for V_P = +4 kV (on the left) and for $V_P = -4$ kV (on the right), at several instants in time. In this figure, the powered electrode is represented on the right, between $z = 1.5$ cm and $z = 2$ cm, and the grounded target on the left at $z = 0$. The distribution of potential is represented on the axis of symmetry at $r = 0$. The distribution is shown at a moment close to discharge ignition, and then at three instants during propagation until the discharge front is close to the grounded plane target. Moreover, the Laplacian distribution of potential for $t > 50$ ns, i.e., the distribution generated exclusively by the electrode configuration when the applied voltage is equal to V_P, is also represented.
In Figure III.7, at the time of discharge ignition, the slope of the electric potential distribution close to the tip of the point electrode is what determines the maximum electric field at the tip ($E_z = -dV/dz$), represented in Figure III.6. Then, as the discharge propagates downwards, i.e., towards lower axial positions, we notice that there is a first slope of electric

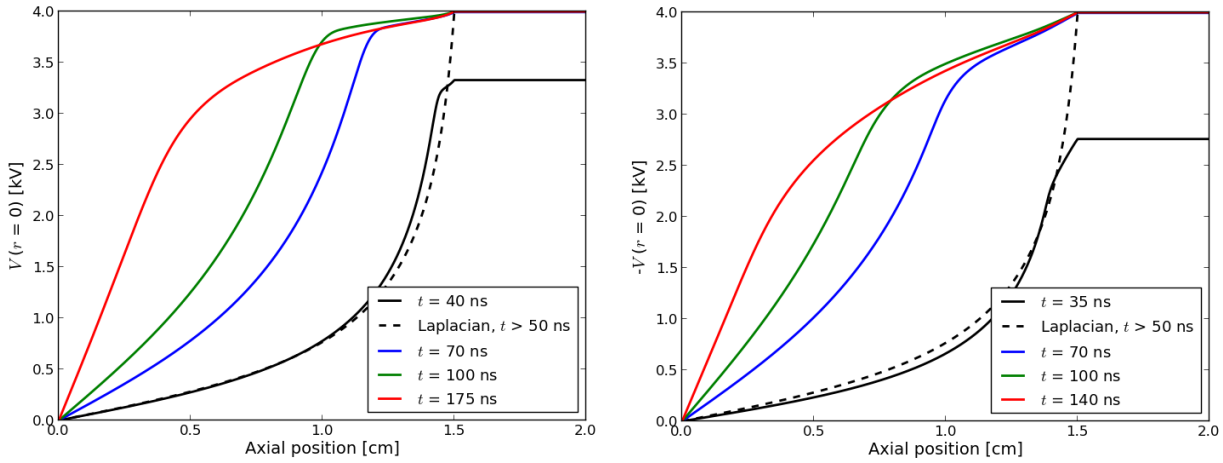

Figure III.7: Axial profiles of V at $r = 0$, at several times, along with the Laplacian component of V during the plateau of applied voltage, for a 2 cm long domain without tube with a grounded target. On the left, for $V_P = +4$ kV, at $t = 40$, 70, 100 and 175 ns. On the right, for $V_P = -4$ kV, at $t = 35$, 70, 100 and 140 ns.

potential between the powered electrode at $z = 1.5$ cm and the discharge front. This region is the plasma channel connecting the powered electrode and the discharge front and the slope in this region is the low electric field left behind the propagation. The higher E_z behind the front of propagation for negative polarity is consistent with results reported in other works on ionization front propagation [*Babaeva and Naidis*, 1997; *Luque et al.*, 2008; *Naidis*, 2011a]. The distributions of electric potential described above provide explanation for the variations of $|E_z|_{MAX}$ during the propagation, studied in Fig. III.6. Firstly, we can notice that in a first stage of the propagation, as the potential in the discharge front gets further away from the powered electrode, the potential difference between the front and the ground decreases, therefore decreasing $|E_z|_{MAX}$. Moreover, in a later stage of the propagation, when the discharge front is close to the target, the closer the front approaches the ground, the higher the slope of potential and therefore $|E_z|_{MAX}$ and the velocity of propagation. Finally, we can notice that, for the same axial position of the front, as the connectivity of potential is higher for $V_P = +4$ kV than $V_P = -4$ kV, the potential slope is higher for $V_P = +4$ kV, and so is $|E_z|_{MAX}$ at the discharge front. The difference in $|E_z|_{MAX}$ between the two polarities is explained in part by the difference of potential in the plasma channel and therefore the ρ distribution left by the discharge propagation. On the other hand, the lower $|\rho|$ with $V_P = -4$ kV is explained by the lower fields required for its propagation.

III.2.4 Influence of the mechanical confinement of the tube on discharge propagation in positive and negative polarities

In this section we study the discharge ignition and propagation in He-N_2 confined radially by a tube. The same electrode geometry and applied voltages with $V_P = +4$ kV and $V_P = -4$ kV are used as in the previous section without tube. The inner radius of the tube is of 2 mm, therefore lower than the radius of the discharges studied without tube. Furthermore, the dielectric permittivity of the tube is the same as in air with $\epsilon_r = 1$, so that the difference

in initial conditions with respect to the cases without tube is only mechanical. In Figures III.8 and III.9 are represented the spatial distributions of the magnitude of electric field E_t at different times for $V_P = +4$ kV and $V_P = -4$ kV, respectively. For each case, E_t is represented at an instant close to discharge ignition, during discharge propagation at $t = 100$ ns, shortly before the discharge front hits the target and once it hits the target.

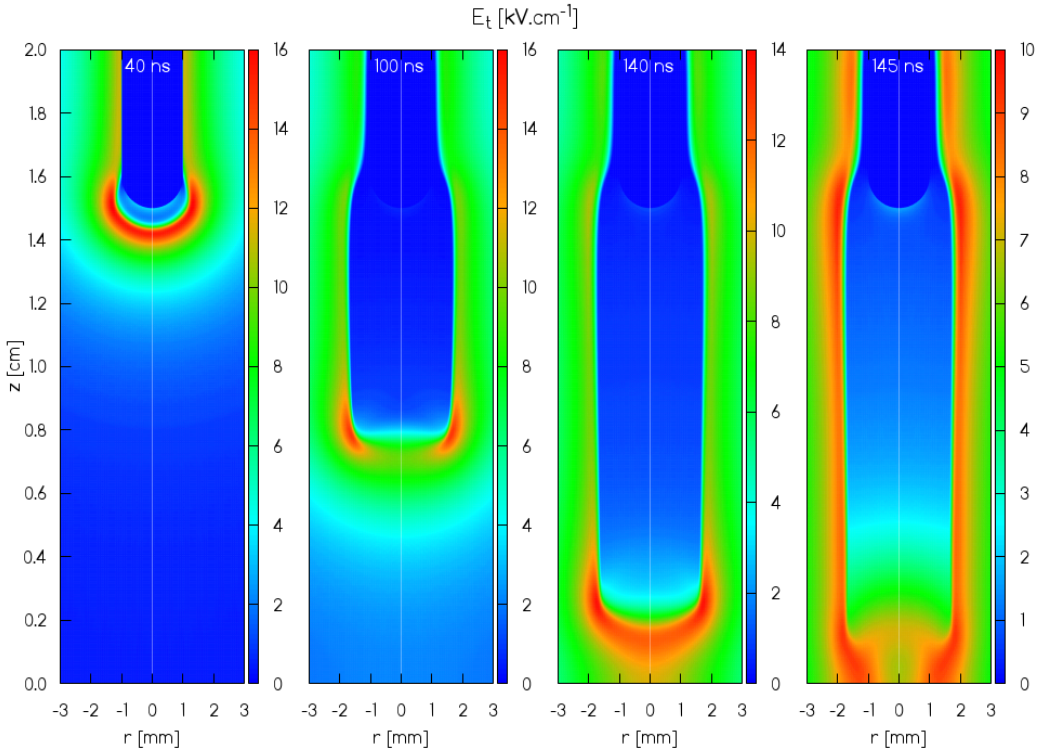

Figure III.8: Cross sectional views of the magnitude of the electric field at $t = 40$, 100, 140 and 145 ns, for a 2 cm long tube with $r_{in} = 2$ mm, $r_{out} = 3$ mm and $\epsilon_r = 1$, closed by a grounded target for $V_P = +4$ kV.

We notice in Figures III.8 and III.9 that the discharge propagation is significantly different than in the cases without tube. After the discharge ignition, the discharge front expands both radially and axially. As it encounters the tube surface at $r = 2$ mm, the discharge front then propagates only axially, with maximum E_t located close to the tube surface, for both polarities. The maximum of E_t is significantly higher for positive than negative polarity at $t = 100$ ns and when the front hits the target, and both are significantly higher than for the corresponding cases without tube. Unlike the cases without tube, it is put forward in Figures III.8 and III.9 that the structure of the discharge propagating in the tube is dependent on the polarity, with clear maximum of E_t for $V_P = +4$ kV at the discharge front close to the tube, while for $V_P = -4$ kV E_t at the front is less dependent on the radial position. Moreover, when analyzing the quasi-neutral channel left behind the discharge propagation, where the electric field is very low, we notice that for $V_P = -4$ kV it fills the whole tube radius and also the region next to the point electrode, while for $V_P = +4$ kV it is straighter close to the cylinder of the point electrode, where there was no discharge propagation, and its radius is lower than the tube inner radius. The difference in the structure of discharges propagating in tubes according to polarity, more homogeneous for negative discharge and more filamentary

for positive discharge, has been reported in other studies in He and in Ne-Xe [*Xiong and Kushner*, 2012; *Darny et al.*, 2017b; *Yonemori and Ono*, 2015]. Finally, Figures III.8 and III.9 show that the arrival of the discharge front on the target takes place slightly earlier with the tube than without the tube, the difference being greater for positive polarity (40 ns) than for negative polarity (15 ns).

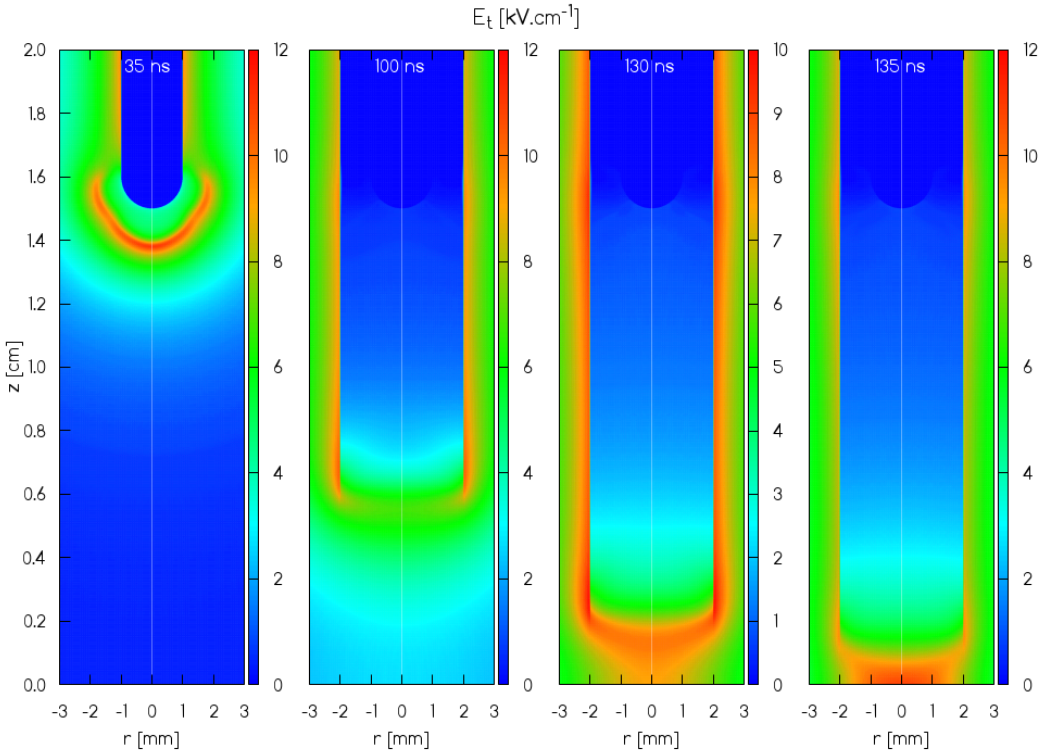

Figure III.9: Cross sectional views of the magnitude of the electric field at $t = 35$, 100, 130 and 135 ns, for a 2 cm long tube with $r_{in} = 2$ mm, $r_{out} = 3$ mm and $\epsilon_r = 1$, closed by a grounded target for $V_P = -4$ kV.

In order to have more insight on the differences of discharge dynamics inside tubes between the polarities of applied voltage, Figures III.10 and III.11 present the spatial distributions for positive and negative polarities, respectively, at an instant shortly before the impact of the discharge front on the target ($t = 140$ ns for $V_P = +4$ kV and $t = 130$ ns for $V_P = -4$ kV), of the net charge density ρ, the axial and radial components of electric field E_z and E_r and the electron density n_e.

Firstly, in Figure III.10 it is shown that on the edge of the region of quasi-neutrality lies a region of positive net charge density ρ. This region is delimited radially by the tube inner radius and axially by the front of propagation. Therefore, we can say there is a positive radial sheath between the plasma bulk and the tube wall, also observed in simulations in *Liu et al.* [2014]. It is remarkable that the net charge density has values of some dozens nC.cm^{-3} in this region, reaching as high as 100 nC.cm^{-3} at the discharge front. These values are much higher than the ones obtained without tube for positive polarity in Figure III.5, where ρ stays lower than 10 nC.cm^{-3}. We can conclude that the radial confinement imposed by the tube induces the generation of a more concentrated net charge density. Then, if we compare the distribution of ρ in the tube in positive polarity (Figure III.10) with the one in negative

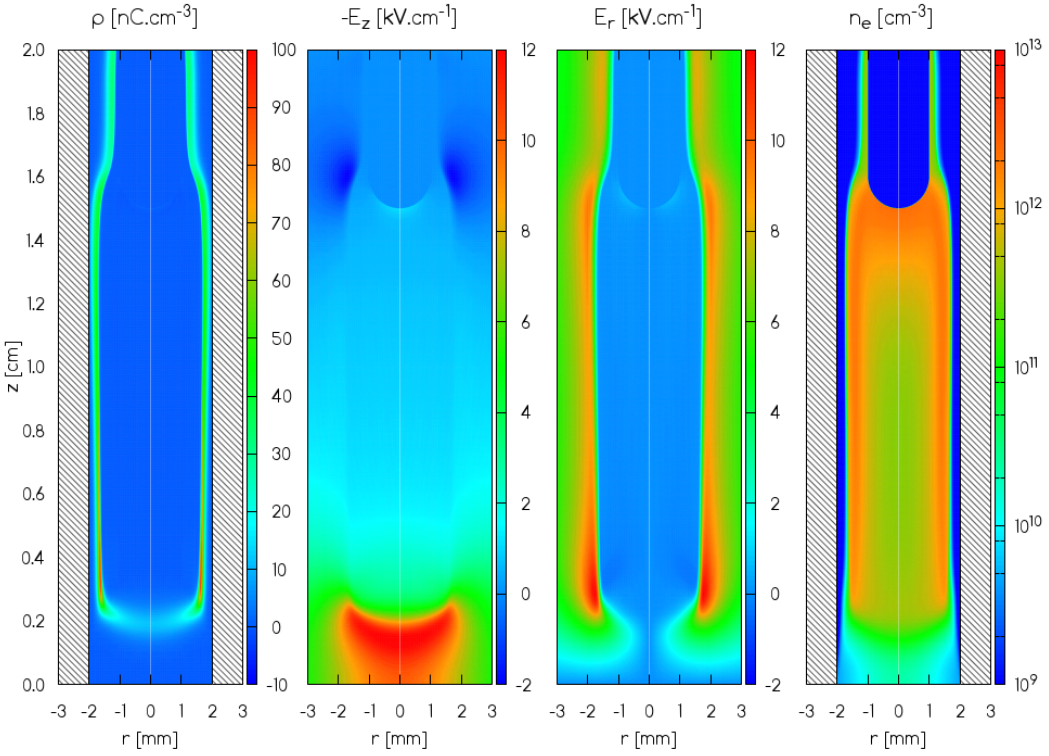

Figure III.10: Cross sectional views of ρ, E_z, E_r and n_e at $t = 140$ ns, for a 2 cm long tube with $r_{in} = 2$ mm, $r_{out} = 3$ mm and $\epsilon_r = 1$, closed by a grounded target for $V_P = +4$ kV.

polarity (Figure III.11), we observe crucial differences. In the latter case, the negative net charge density at $t = 130$ ns stays lower in magnitude than 20 nC.cm^{-3} and is concentrated at the discharge front. On the other hand, while the plasma channel behind the propagation is generally quasi-neutral, we notice there is also a very thin region of positive net charge density close to the tube inner wall, where ρ reaches values as high as 40 nC.cm^{-3}.
In order to better understand the different radial sheaths of net charge density according to polarity, it is helpful to assess the temporal evolution of the surface charge density σ deposited on the tube inner walls for both polarities, as represented in Figure III.12. There, we observe that surface charge deposition through positive ion flux in positive polarity is very slow and σ remains at very low values during the propagation, below 0.040 nC.cm^{-2}. In this case, σ does not play an important role in the discharge dynamics. Conversely, for the case in negative polarity, surface charge deposition through electric drift flux of electrons is faster, due to the different mechanisms of propagation, and also to the higher mobilities of electrons with respect to positive ions ($\mu_e \sim 100 \times \mu_i$, see section II.3.4). At $t = 50$ ns, for $V_P = -4$ kV, σ has already arisen in magnitude close to the tip of the point electrode, where the discharge first contacts the tube wall, up to 1.15 nC.cm^{-2}. Then, as the discharge front propagates towards the target, $|\sigma|$ rises very close to the discharge front up to $\sim 0.8 - 1.0$ nC.cm^{-2}. At the same time, behind the front of propagation, in the region where a high $|\sigma|$ is deposited, the negative σ generates an electric field in the plasma in the radial direction, that attracts positive charges to the tube inner wall. This E_r induces a charge separation in the plasma channel, that forms the thin region of positive ρ close to the tube wall that is visible in Figure III.11. The positive ρ shields the negative σ and therefore there is no E_r in

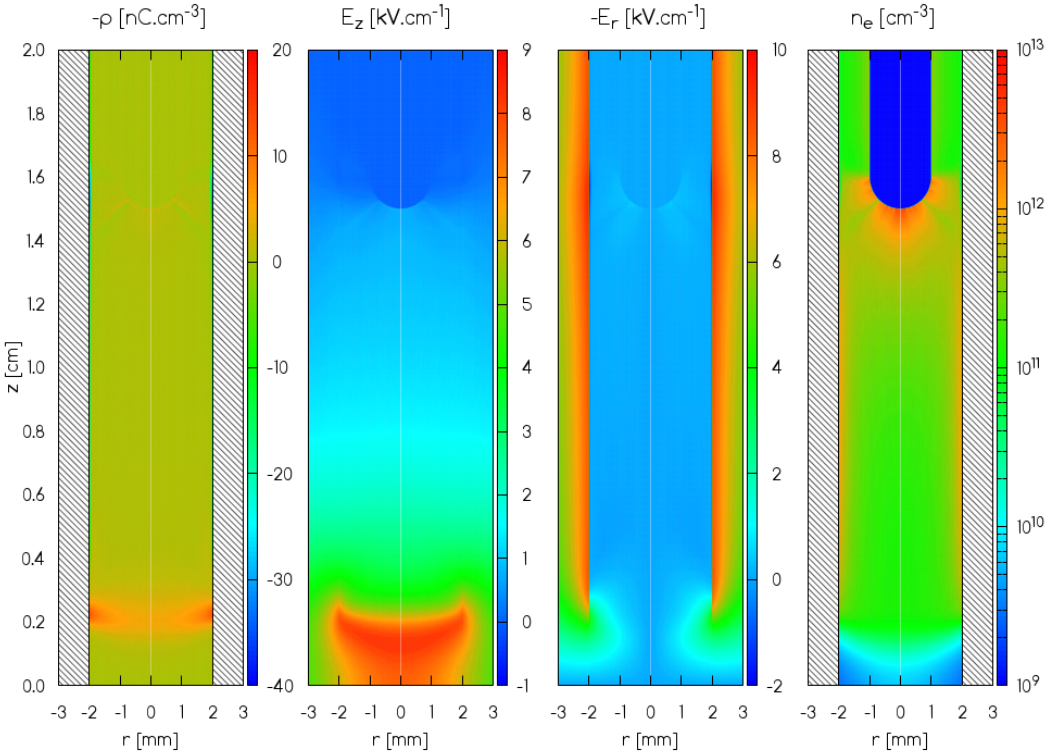

Figure III.11: Cross sectional views of ρ, E_z, E_r and n_e at $t = 130$ ns, for a 2 cm long tube with $r_{in} = 2$ mm, $r_{out} = 3$ mm and $\epsilon_r = 1$, closed by a grounded target for $V_P = -4$ kV.

the quasi-neutral channel until the radial sheath.

Figures III.10 and III.11 also show the axial and radial components of electric field at the studied instants in the plasma and inside the dielectric tube. In the case of positive polarity, as σ has a negligible effect on discharge dynamics, the electric field components are generated between ρ and the electrodes at fixed potential. Concerning the axial direction, E_z is close to zero in the channel behind the front of propagation, in the region between the powered electrode and the discharge front. As in the case without tube, E_z is concentrated at the discharge front, between the region where ρ is strongest and the grounded plane. As ρ is higher in the case with tube than without, so is $|E_z|$, with maximum around 12 kV.cm^{-1}, rather than 7 kV.cm^{-1}. Then, in the radial direction, for $V_P = +4$ kV, it is visible that E_r is close to zero in the plasma and is directed outwards in the tube. E_r is positioned on the radial edge of the plasma, defined by the region of radial positive sheath with maximum value ~ 12 kV.cm^{-1} located in the region of higher ρ, close to the discharge front. In the case of negative polarity, Figure III.11 shows that E_z is directed upwards at the discharge front, with a maximum close to 9 kV.cm^{-1}, higher than in the case without tube (~ 6 kV.cm^{-1}). This value is lower than in positive polarity but the region of high E_z in the discharge front presents a broader radial profile for $V_P = -4$ kV than for $V_P = +4$ kV. Moreover, in the radial direction, we observe that for $V_P = -4$ kV E_r is close to zero in the plasma but is as high as 10 kV.cm^{-1} in the dielectric tube. As there is no negative ρ in the plasma channel behind the front of propagation, we conclude that the negative charging of the tube that provides E_r is guaranteed by the negative deposited surface charges.

Finally, in Figures III.10 and III.11 are presented the spatial distributions of electron density

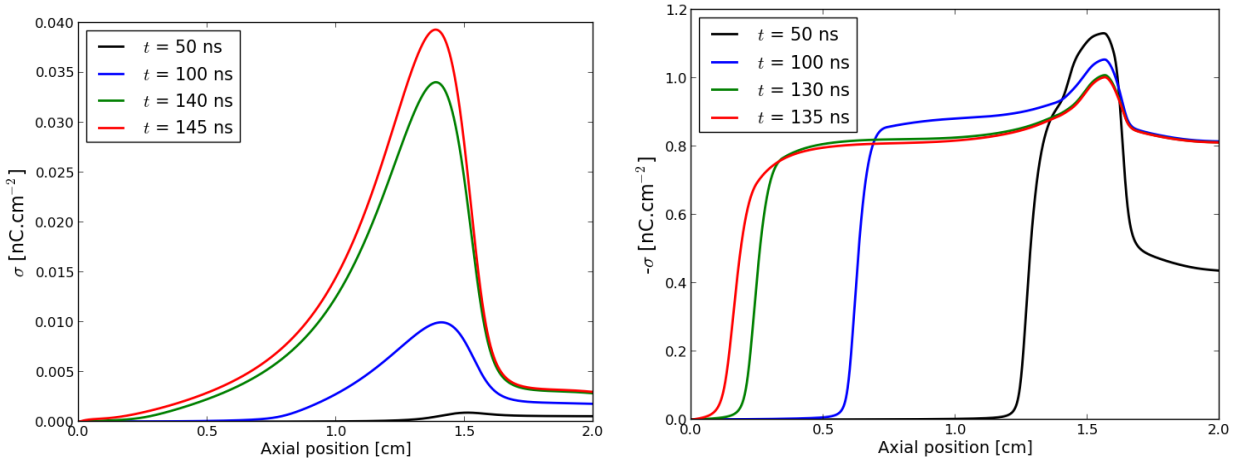

Figure III.12: Axial profiles of σ on the tube walls at $r_{in} = 2$ mm, at several times, for a 2 cm long tube with $r_{in} = 2$ mm and $\epsilon_r = 1$, closed by a grounded target, for both polarities. On the left, for $V_P = +4$ kV. On the right, for $V_P = -4$ kV.

n_e. We can notice that n_e is generally higher in the cases with tube than in the case without tube presented in Figure III.4. Figure III.13 gives more insight into the radial distribution of n_e. In this figure are represented the radial profiles of n_e, at a fixed axial position at 5 mm from the target ($z = 0.5$ cm), for $V_P = +4$ kV (on the left) and for $V_P = -4$ kV (on the right), and for the cases with and without tube. For each case, an instant is chosen when the discharge front has already crossed the axial position studied $z = 0.5$ cm and has not yet hit the target at $z = 0$. The figure represents not only $n_e(r)$, but also the radial profiles of the total ion density (only positive ions in He-N_2) $n_i(r)$. The number density of the net charge can be inferred from the n_e and n_i: $n_\rho = n_i - n_e$.

The first feature that is visible in Figure III.13 is that in the cases without tube, the radial profiles of the charged species densities extend much more broadly radially than in the cases with the tube inner wall at $r_{in} = 2$ mm. Then, considering the cases without tube, we notice that the densities of charged species for both polarities never overcome 2×10^{11} cm^{-3}, and that the deviation to quasi-neutrality (positive for $V_P = +4$ kV and negative for $V_P = -4$ kV) is always less than $|n_\rho| = 2 \times 10^{10}$ cm^{-3}. Comparing them with the cases with tube, we see that, at $r = 0$, the tube induces an increase in the densities of charged species of around a factor 3 for $V_P = +4$ kV and around a factor 2 for $V_P = -4$ kV. Unlike the cases without tube, when the tube is present the densities of charged species are not maximal at $r = 0$. Indeed, for $V_P = +4$ kV, the densities of charged species increase radially until around $r = 1.5$ mm, where they reach $\sim 1.5 \times 10^{12}$ cm^{-3}, and then decrease in the radial sheath until the tube at $r = 2$ mm. While n_ρ is very low in the plasma bulk, it severely increases in those last 500 μm of radial sheath up to 5×10^{11} cm^{-3}, more than one order of magnitude higher than in the case without tube. For $V_P = -4$ kV, the densities of charged species also increase radially but have their maximum closer to the tube at $r = 2$ mm.

Figure III.14 shows the maximum value of the axial component of electric field $|E_z|_{MAX}$ during the discharge propagation between the electrodes for positive (on the left) and negative (on the right) polarities. In the figure are presented the axial profiles for the cases without tube, as in Figure III.6, as well as with tube. In the latter case, to show that the maximum

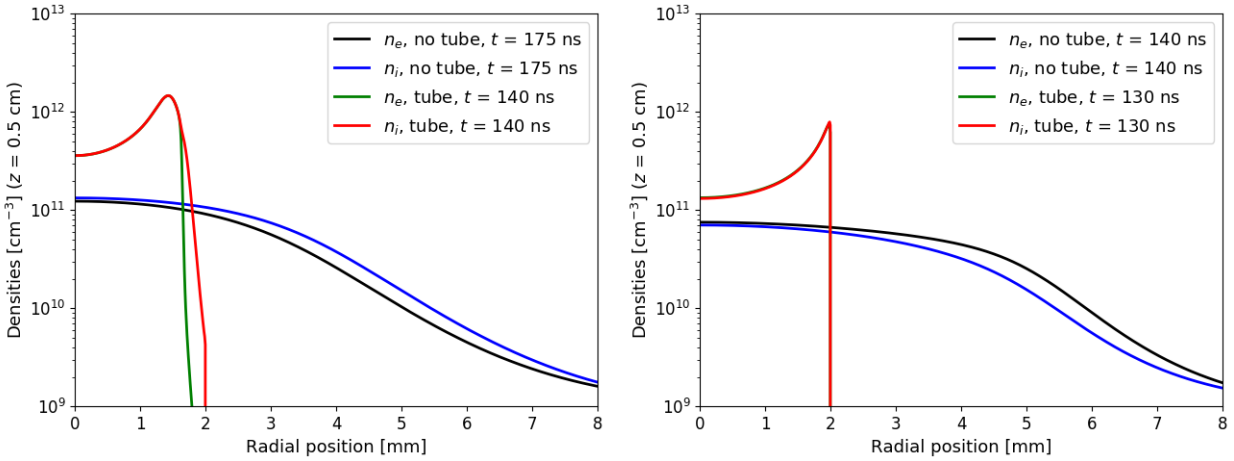

Figure III.13: Radial profiles of n_e and n_i, at $z = 0.5$ cm, with and without tube ($r_{in} = 2$ mm and $\epsilon_r = 1$) and with a grounded target, for both polarities. On the left, for $V_P = +4$ kV. On the right, for $V_P = -4$ kV.

value of E_z is not always placed on the axis of symmetry at $r = 0$, are presented both the maximum value during propagation specifically at $r = 0$, and the maximum value at any radial position. In this figure, the powered electrode is represented on the left and the grounded target on the right. For both cases of polarity of applied voltage, we notice that $|E_z|_{MAX}$ is at first, close to the powered electrode, very similar between the cases with and without tube. Then, as the volume charge density ρ is higher due to the spatial confinement of the tube, $|E_z|$ is higher in the front of propagation in the cases with tube, and so is $|E_z|_{MAX}$. The higher electric fields, electron density and velocity of propagation with the radial constraint of the tube had already been reported for an air positive discharge in *Jánský et al.* [2010, 2011]. Moreover, we can notice in Figure III.14 the difference between $|E_z|_{MAX}$ at $r = 0$ and $|E_z|_{MAX}$ at any radial position, that can be located closer to the tube wall. For both cases of polarity, $|E_z|_{MAX}$ is located at $r = 0$ at the beginning of propagation, before the discharge interaction with the tube, and then the two $|E_z|_{MAX}$ differ during most of the propagation in the tube, before rejoining when the discharge front is at only 2 mm from the grounded plane. It is remarkable that for $V_P = -4$ kV the difference between the two $|E_z|_{MAX}$ is subtle, while for $V_P = +4$ kV the difference between the two $|E_z|_{MAX}$ reaches 2 kV.cm^{-1}. These differences are the reflection of the radial profles of each discharge front evaluated earlier in Figures III.10 and III.11. As a consequence of the $|E_z|_{MAX}$ profiles, the velocity of propagation is generally higher due to the mechanical confinement of the tube, as had already been noticed by the difference on the time of impact at the target. Furthermore, the difference between the velocities with and without tube is significantly higher for positive polarity (up to 5 cm.μs^{-1}) than for negative polarity (less than 3 cm.μs^{-1}).

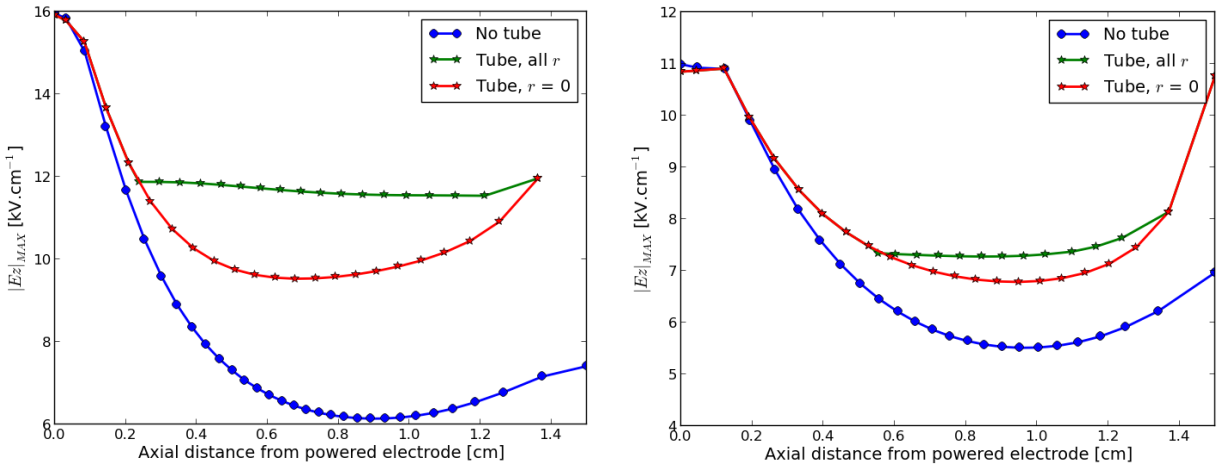

Figure III.14: $|E_z|_{MAX}$ along the propagation between the powered electrode and the grounded target, with 5 ns temporal resolution, with and without tube (r_{in} = 2 mm and $\epsilon_r = 1$). In the cases with tube, $|E_z|_{MAX}$ is found and shown both at $r = 0$ and in the whole domain. On the left, for $V_P = +4$ kV. On the right, for $V_P = -4$ kV.

III.2.5 Role of the tube permittivity on discharge propagation

The tubes used in plasma jet experiments have different values of dielectric permittivity. In this thesis, calculations are performed with tubes of relative permittivity $\epsilon_r = 4$ and compared with experiments using quartz or pyrex tubes, of approximately the same value. Then, in this section, we compare the results of discharge dynamics in a tube of $\epsilon_r = 1$ studied earlier, with those in a quartz tube of $\epsilon_r = 4$, for both $V_P = +4$ kV and $V_P = -4$ kV. All the simulation conditions are kept the same, except the relative permittivity of the tube between r_{in} = 2 mm and r_{out} = 3 mm. Since there is no mechanical difference between the two configurations, the comparison allows to isolate the electrical role of the tube on the discharge dynamics, for both positive and negative polarities of applied voltage. Firstly, in Figures III.15 and III.16 are represented the spatial distributions of E_t at several instants in time, since the discharge ignition until after the impact on the grounded target. These figures can be compared, respectively, with Figures III.8 and III.9.

The first thing we can notice in Figures III.15 and III.16 is that the discharge ignition around the tip of the point electrode is not equally axial and radial, despite the spherical geometry of the tip. The higher ϵ_r of the tube induces an increase of the magnitude of the electric field in the radial direction in the plasma, in agreement with Gauss's law at the interface between the tube and the plasma, at r_{in} = 2 mm: $(\epsilon_0 \epsilon_r E_{r\rightarrow r^+}) - (\epsilon_0 E_{r^-\rightarrow r}) = \sigma$. Thus, by comparing the results of E_t for $\epsilon_r = 1$ and for $\epsilon_r = 4$, we observe that the discharge interacts with the tube earlier for higher permittivity of the dielectric tube. Then, by comparing the two cases with positive polarity, it is visible that the structure of the discharge propagating in the tube is similar with maximum of E_t at the discharge front and close to the tube inner wall. However, the maximum of E_t is higher at the front close to the wall (at t = 100 ns, around 19 kV.cm^{-1} instead of 15 kV.cm^{-1}), due to the increase of $|E_r|$ in the plasma explained earlier, that reaches up to 18 kV.cm^{-1} against 12 kV.cm^{-1} for $\epsilon_r = 1$. Conversely, E_t and E_r in the tube region are lower with $\epsilon_r = 4$ than with $\epsilon_r = 1$, in agreement with Gauss's law. With higher E_t in the plasma region during the propagation of the discharge front with $\epsilon_r = 4$,

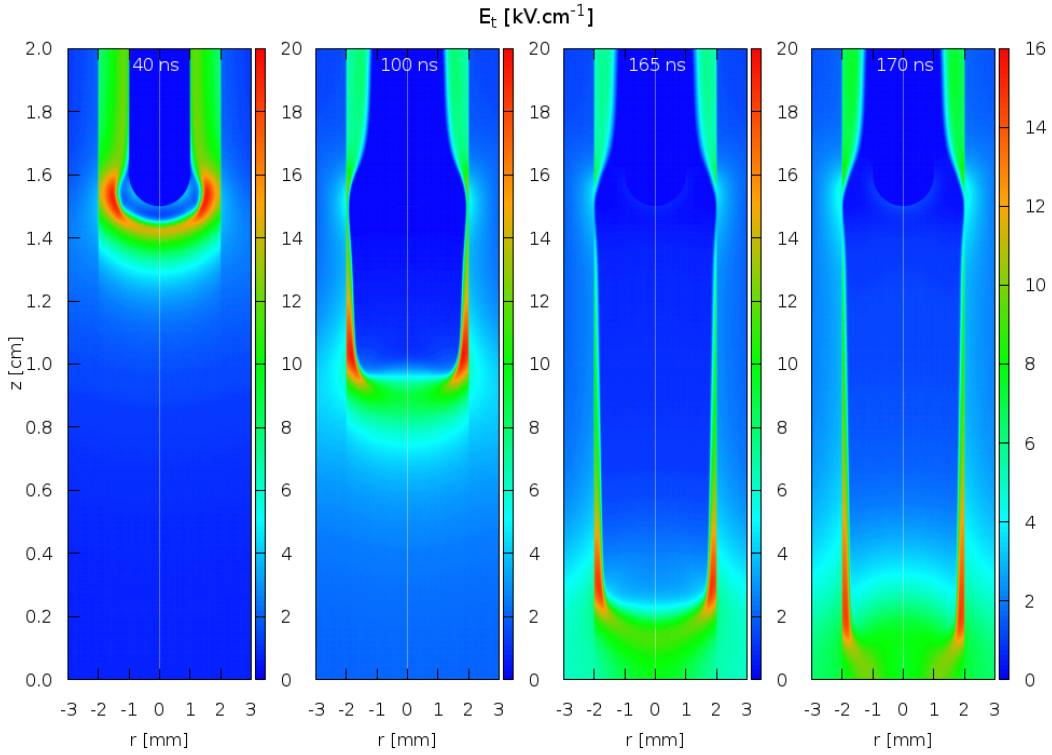

Figure III.15: Cross sectional views of the magnitude of the electric field at $t = 40$, 100, 165 and 170 ns, for a tube with $\epsilon_r = 4$, closed by a grounded target for $V_P = +4$ kV.

higher values of n_e and ρ are created behind the front close to the tube wall. ρ reaches up to 180 nC.cm^{-3} during the propagation, against 100 nC.cm^{-3} with $\epsilon_r = 1$. On the other hand, the comparison of Figures III.15 and III.8 shows that the region of the radial sheath is thinner for $\epsilon_r = 4$. The connection between the electric potential in the discharge front and in the powered electrode is not assured solely by the maximum value of ρ behind the discharge front. In the current case, despite the higher maximum value of ρ for $\epsilon_r = 4$, E_z at the discharge front for $\epsilon_r = 1$ and $\epsilon_r = 4$ present only small differences and the propagation is indeed faster for $\epsilon_r = 1$ (impact on the target at $z = 0$ between $t = 140$ ns and $t = 145$ ns) than for $\epsilon_r = 4$ (impact between $t = 165$ ns and $t = 170$ ns).

The comparison of the two cases with negative polarity (Figures III.16 for $\epsilon_r = 4$ and III.9 for $\epsilon_r = 1$) leads to a slightly different analysis. In fact, we observe higher maximum values of E_t for $\epsilon_r = 1$ (around 11 kV.cm^{-1} during most of the propagation) than for $\epsilon_r = 4$ (around 7 kV.cm^{-1} during most of the propagation). That is the case because for $\epsilon_r = 1$, the maximum of E_t corresponds to the locations of maximum of $|E_r|$, which are in the tube, at a radial position immediately superior to r_{in}, while for $\epsilon_r = 4$ the magnitude $|E_r|$ is significantly lower in this region. However, in the plasma region, E_r and E_t are higher for $\epsilon_r = 4$, as in the case with positive polarity. The difference in creation of n_e and ρ is not significant, and also in the case of negative polarity the propagation is slower with $\epsilon_r = 4$, with impact between $t = 165$ ns and $t = 170$ ns, same time as in positive polarity (with $\epsilon_r = 1$ and $V_P = -4$ kV, impact between $t = 130$ ns and $t = 135$ ns).

Concerning surface charge deposition, with positive polarity, the increase of $|E_r|$ in the plasma towards the tube provoked by the increase of ϵ_r leads σ to rise up to 1.4 nC.cm^{-2} at $t = 165$

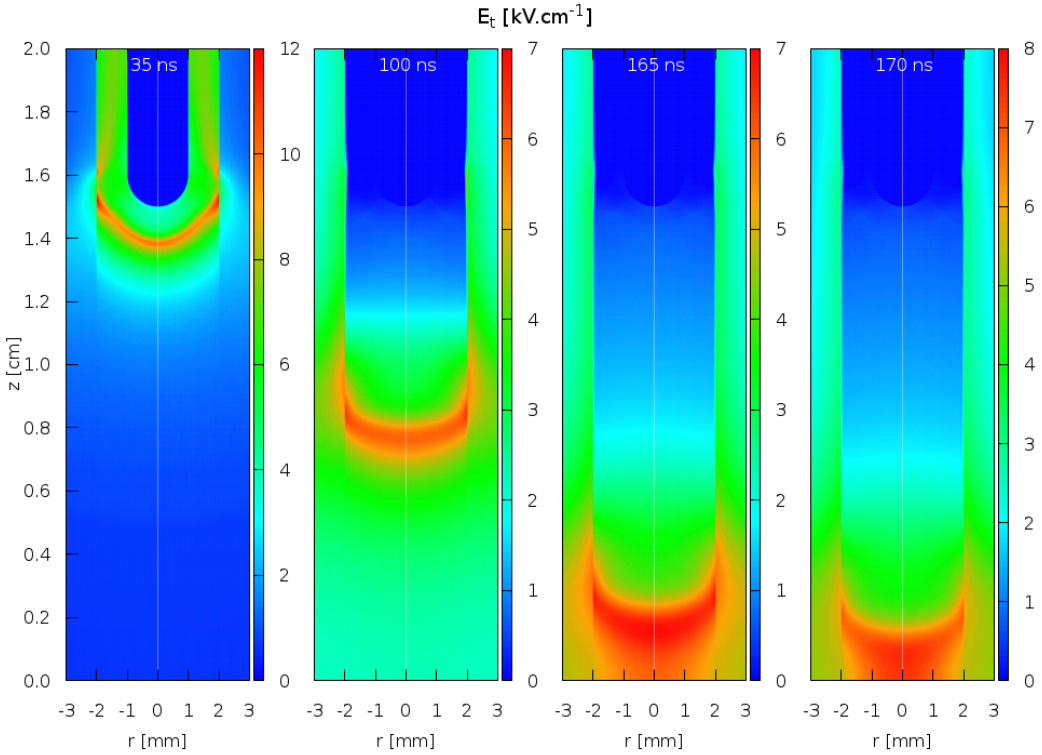

Figure III.16: Cross sectional views of the magnitude of the electric field at $t = 35$, 100, 165 and 170 ns, for a tube with $\epsilon_r = 4$, closed by a grounded target for $V_P = -4$ kV.

ns, with a peak at the position where the discharge front first impacts the dielectric tube, while with $\epsilon_r = 1$ σ remains lower than 0.04 nC.cm^{-2} at $t = 140$ ns. The significant increase of surface charge deposition with ϵ_r in positive polarity has been reported for an air discharge in *Jánský and Bourdon* [2011b]. Likewise, for negative polarity, with $\epsilon_r = 4$, σ remaining all along the tube wall shortly before the discharge impacts the target is around -1.2 nC.cm^{-2}, higher in absolute value than -0.8 nC.cm^{-2} with $\epsilon_r = 1$. Then, for both polarities, even though the higher σ contributes to transfer potential to the discharge front, with the stronger $|E_r|$ and a more tubular discharge structure with $\epsilon_r = 4$, the ρ contribution to the electric field is less centered than with $\epsilon_r = 1$. Thus, $|E_z|$ at the discharge front tends to be lower with $\epsilon_r = 4$ than with $\epsilon_r = 1$.

III.2.6 Influence of the secondary electron emission on the mechanical confinement of the tube for positive polarity

The different mechanisms of streamer propagation lead to a different effect of the mechanical confinement of the discharge by the tube. On the one hand, in negative polarity, as electrons drift in the sense of propagation outwards, the presence of the tube constitutes a barrier to the radial movement. On the other hand, in positive polarity, electrons are pulled towards the positive front of propagation. In the latter case, the discharge is confined radially because the electron flux directed inwards towards the discharge is limited by the presence of the tube. In this thesis, the electron flux from the dielectric tube wall towards the plasma is calculated as 10% of the flux of positive ions from the plasma towards the wall, which explains the

formation of a positive radial sheath. In order to show that the electron flux between the dielectric tube wall and the plasma plays an important role on the mechanical confinement of the positive discharge by the tube, we now study the hypothesis of a continuous flux of electrons. That is, we consider that the tube is a dielectric at floating potential but its surface can emit as many electrons as the discharge requires only through effect of the electric field, following a Neumann condition for the electron drift flux between the plasma and the tube at $r_{in} = 2$ mm. This condition does not correspond to any physical situation but allows to isolate the influence of the electron flux while keeping the propagation of a discharge with positive polarity of applied voltage ($V_P = +4$ kV). In Figure III.17 it is shown the structure of this discharge at an instant shortly before the impact of the discharge front on the target, at $t = 145$ ns. The figure presents the spatial distributions of ρ, E_z, E_r and n_e, and is therefore comparable with Figures III.10 and III.11 for the standard cases studied previously with $V_P = +4$ kV and $V_P = -4$ kV, respectively.

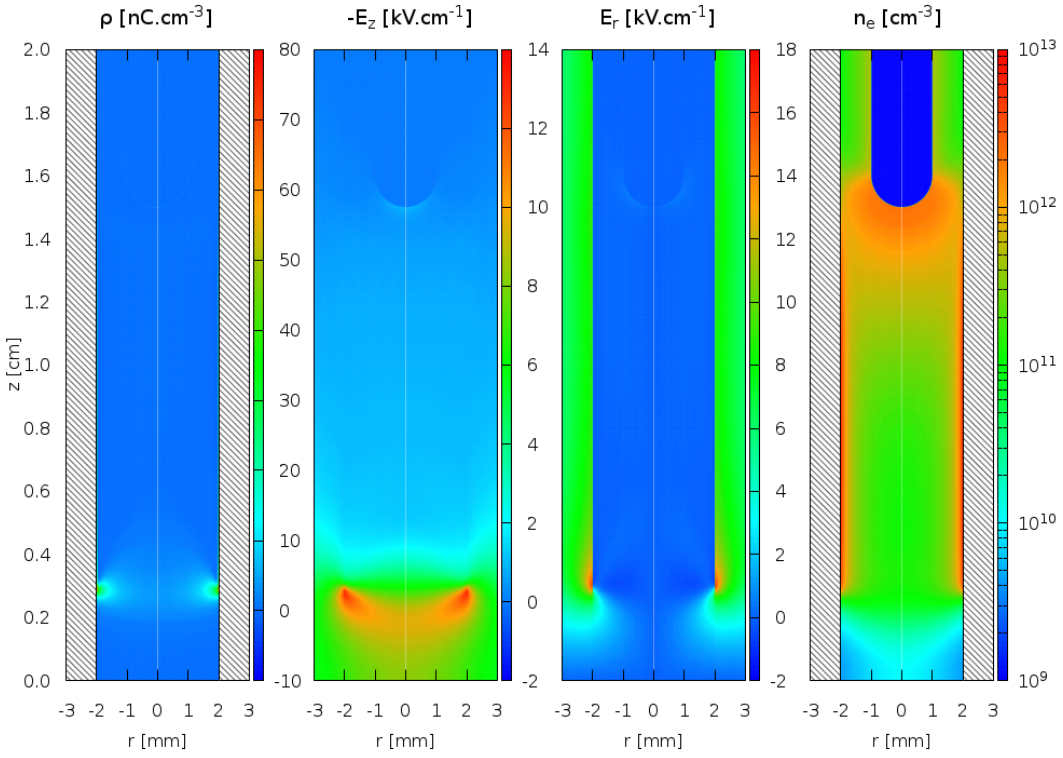

Figure III.17: Cross sectional views of ρ, E_z, E_r and n_e at $t = 145$ ns, for a tube with $\epsilon_r = 1$ and a Neumann BC for the electron flux, closed by a grounded target, for $V_P = +4$ kV.

Figure III.17 shows that the distribution of ρ is more similar to that of Fig. III.11 for $V_P = -4$ kV than with that of Fig. III.10 for $V_P = +4$ kV. The positive ρ is visible only at the discharge front, and not forming a radial sheath along the plasma channel. Then, E_z, directed downwards at the discharge front, presents a broader radial profile than in Fig. III.10 and has a clear maximum very close to the tube wall, with a value as high as 14 kV.cm^{-1}. As a consequence, $|E_z|_{MAX}$ at $r = 0$ during the propagation in the case under study presents values between those without tube and with tube in the standard conditions, but $|E_z|_{MAX}$ close to the tube wall is significantly higher than in any other case during most of the propagation. From the moment the discharge impacts the dielectric tube, as high values

of both volume and surface charge densities are formed at the discharge front close to the tube wall, a strong $|E_z|$ is present at that position during most of the propagation. Despite this much higher $|E_z|_{MAX}$ in the case of tube without sheath, the velocity of propagation in this case is generally lower than in the case of tube with sheath and higher than in the case without tube, as is $|E_z|_{MAX}$ at $r = 0$. In Figure III.18 we assess, on the left, the radial profiles of n_e, n_i and n_ρ at $t = 145$ ns and $z = 0.5$ cm, comparable with Figure III.13, and on the right, the axial profiles of σ on the tube wall at several times, comparable with Figure III.12. The positive σ is calculated by integrating the fluxes of species directed outwards and subtracting those directed inwards, thus conserving charge. In the current case, that means at first integrating all the positive ion fluxes towards the wall and subtracting the fluxes of electrons from the wall towards the plasma.

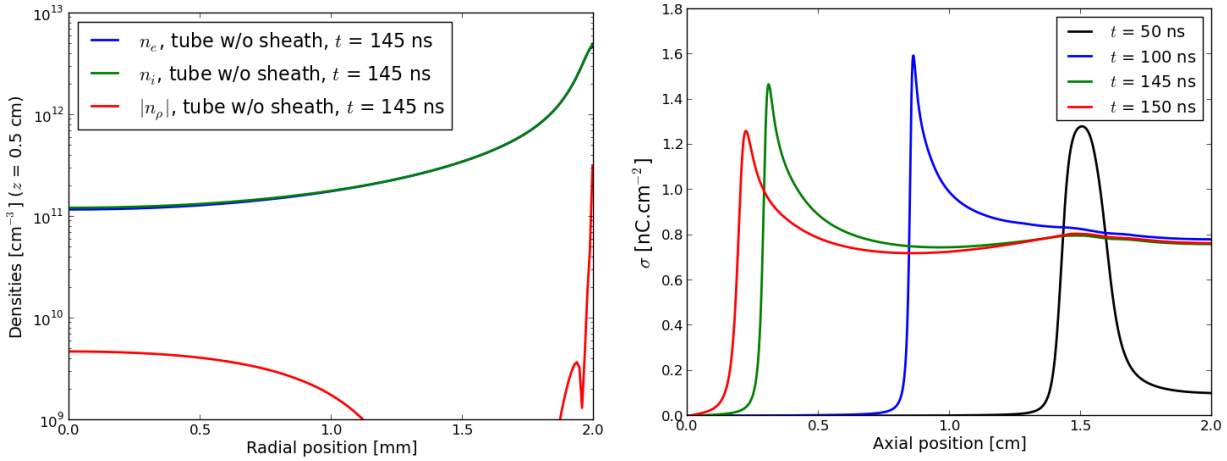

Figure III.18: Radial profiles of n_e, n_i and n_ρ and axial profiles of σ, for a 2 cm long tube with $r_{in} = 2$ mm, $r_{out} = 3$ mm, $\epsilon_r = 1$ and a Neumann BC for the electron flux, closed by a grounded target for $V_P = +4$ kV. On the left, $n_e(r)$, $n_i(r)$ and $n_\rho(r)$. On the right, $\sigma(z)$.

Figure III.18 shows that the radial profiles of charged species densities in the case with $V_P = +4$ kV and Neumann electron flux at $r = 2$ mm are similar to those in the case with $V_P = -4$ kV. The positive region of lack of quasi-neutrality formed close to the tube wall is only of a few dozens μm, as for $V_P = -4$ kV, and not hundreds μm as for $V_P = +4$ kV. Then, concerning σ on the dielectric tube inner wall, we notice in Fig. III.18 that its deposition is fast, as for the negative polarity case, and attains values of the same order of magnitude (~ 0.8 nC.cm^{-2}) behind the discharge front. That result shows that the crucial difference of rate and values of σ deposition between polarities studied in Fig. III.12 is fundamentally due to the condition of electron flux that stops the positive discharge from propagating closer to the tube. Furthermore, we notice in Fig. III.18 that σ is significantly higher on the discharge front, up to 1.6 nC.cm^{-2}, than behind the front of propagation where it decreases to ~ 0.8 nC.cm^{-2}. As the discharge propagates, it charges the tube positively. The positive charge on the wall generates a radial electric field directed inwards that leads to a fast deposition of electrons that partly compensates the positive σ and cancels the radial electric field.
This study has allowed to conclude that part of the difference between the dynamics of discharge propagation with and without tube with positive polarity is due to the radial sheath of positive net charge density between the quasi-neutral plasma and the tube wall,

that helps to transfer the potential from the powered electrode to the discharge front and helps discharge propagation. Likewise, the difference of structure of the discharges propagating in tubes between the polarities of applied voltage is partly due to the different conditions of electron flux that are inherent to the different mechanisms of propagation and to the presence of a solid wall at $r = r_{in}$.

III.2.7 Conclusions

The results exposed in this section have intended to provide a basis to understand the results of next chapters where different tubes are used, but also to improve our understanding on the role of the tube on discharge dynamics and on the differences in discharge structure with opposite polarities of applied voltage. We list the conclusions arising from this study:

- Point-plane discharges in a 1.5 cm gap without tube with $V_P = +4$ kV and $V_P = -4$ kV present very similar structures.
- The radial constraint of the tube induces an important increase of ρ in positive polarity and introduces an important σ on the tube wall in negative polarity.
- With the introduction of the tube, the plasma presents an homogeneous structure for $V_P = -4$ kV and a more filamentary structure for $V_P = +4$ kV.
- These differences are mostly induced by the fundamentally different type of interaction between the positive and negative streamers with dielectric surfaces. A non-physical condition of continuity of the electron flux between the plasma and the tube has been tested to confirm that it is the direction of electron drift that justifies the positive radial sheath in positive polarity and the different structures.

III.3 Influence of the electrode geometry on discharge propagation

Studied conditions

The different electrode configurations exposed in this section are represented in Figure III.19. In all the cases studied here the tube geometry is the same as in section III.2, with a tube with 2 mm inner radius and $\epsilon_r = 1$ in all the domain. The pulse of applied voltage is also the same, with 50 ns rise-time and $V_P = +4$ kV. In all the cases, a grounded metallic plane is placed at $z = 0$ and a grounded cylinder is present at $r = 10$ cm. The 4 cases of different geometries of the powered electrode are listed below, and are represented in Fig. III.19:

- Case 1: Powered point with 1 mm radius and spheric tip at $z = 1.5$ cm, as in the previous section.
- Case 2: Same point as in case 1, with an additional cylindrical powered plane, serving as point holder, placed at $z = 2.0$ cm, with 3 mm radius.

- Case 3: Powered ring inside the tube at $z = 1.5$ cm, with 0.4 mm inner radius and 2 mm outer radius, i.e. filling the tube.
- Case 4: Same powered ring inside the tube as in case 3, with an additional grounded ring around the tube, with 3 mm inner radius and 3.5 mm outer radius, between $z = 0.7$ cm and $z = 1.0$ cm. Contrarily to the other geometries, the discharge in case 4 has been simulated with the model described in section II.4.5, i.e., with the addition of the electron energy equation and the use of the local mean energy approximation. The differences induced by using the different models have been assessed in section II.4.5.

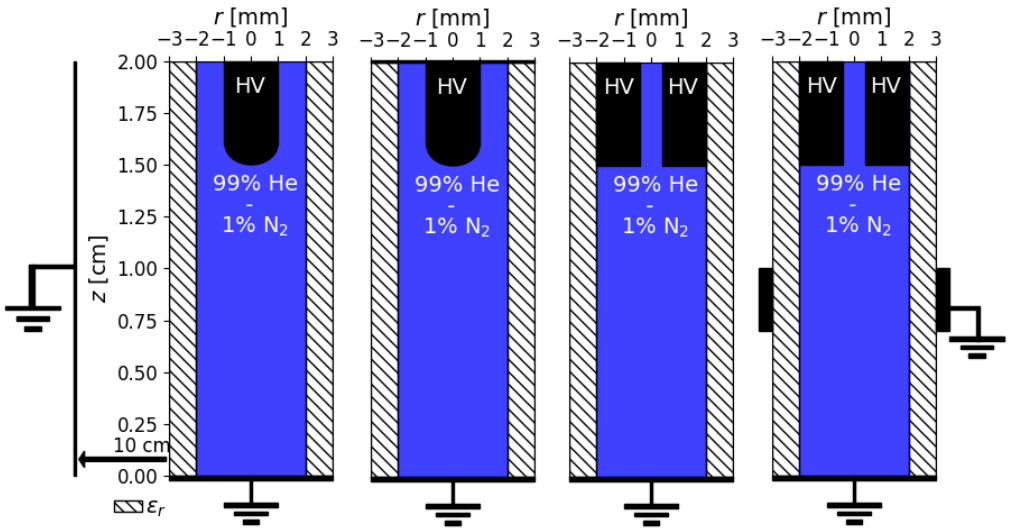

Figure III.19: Side view schematics of the discharge set-ups used in this section. From left to right: cases 1 to 4 listed above.

In this section we study the influence of these different electrode configurations on discharge dynamics. The different Laplacian distributions of electric potential and electric field induced by each electrode geometry can be found in appendix B.

Influence of the electrode geometry on discharge propagation

With the first two geometries, with point electrode, the Laplacian distribution of electric field at the tip of the powered electrode is very similar and then so is the ignition. The discharge ignites around the tip of the point, where the electric field is reinforced, in both cases slightly before $t = 40$ ns. However, with the powered plane behind the point (case 2), E_t radially next to the point is lower, due to the lower radial component of electric field in this region. With the powered ring inside the tube (case 3), the distribution of electric field is significantly different than with the point electrode, even though the time of ignition is only slightly higher. The maximum of electric field is located on the edge of the ring, at $r = 2$ mm, and therefore the ignition is not centered. Finally, with powered ring inside the plasma and grounded ring wrapped around it (case 4), which is the case in many experiments, the ignition is similar to case 3, but it happens slightly earlier and with higher electric fields due to the proximity to the ground.
Then, to study the effect of the electrode configuration on the discharge dynamics, it is

shown in Figure III.20 the distribution of electron density when the discharge is about to hit the grounded plane, along with the corresponding time. Moreover, in Figure III.21 are represented the axial profiles of the surface charge density σ on the tube walls for all 4 geometries at the same instants.

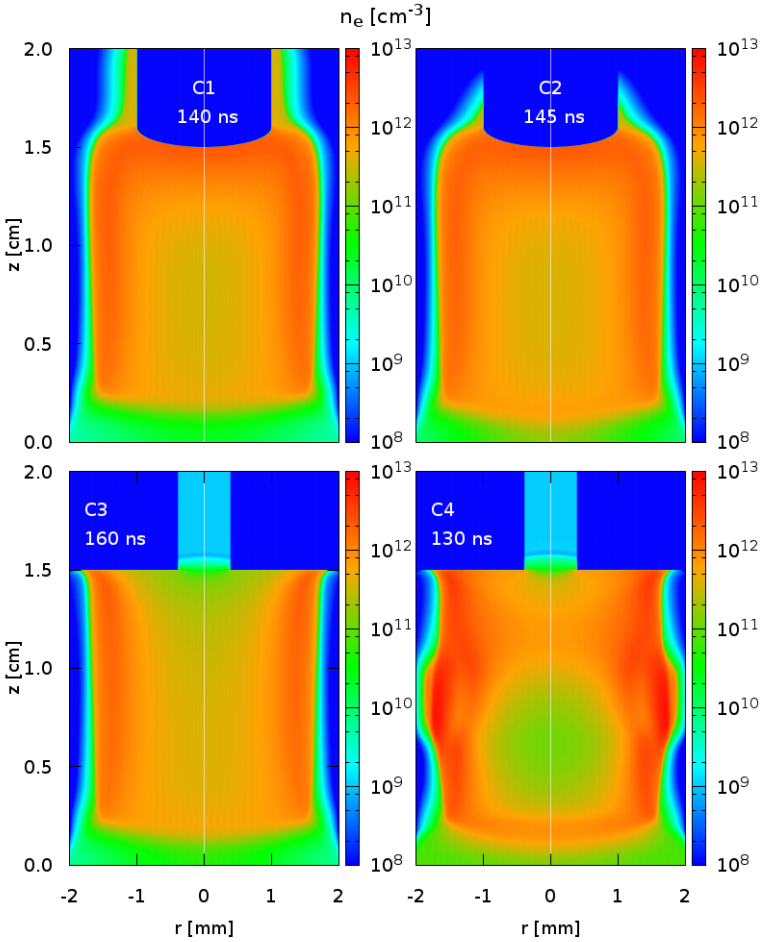

Figure III.20: Cross sectional views of the electron density n_e at a time of discharge arrival on the grounded plane, with $V_P = +4$ kV and with the different electrode configurations. On top, cases 1 and 2. On bottom, cases 3 and 4.

In fact, by comparing cases 1 and 2, we notice that the propagation is only negligibly slower by introducing the powered plane (case 2), as both have an average velocity ~ 8 cm.μs^{-1}. Moreover, the discharge structure between the point and the target is not changed. Since the powered plane reduces the radial component of electric field close to the point, σ in case 2 is slightly lower than in case 1. Then, if we consider the propagation with powered inner ring (case 3), despite the different ignition with respect to cases 1 and 2, the tubular structure of n_e ends up being similar during most of the propagation. Finally, by adding the grounded ring around the tube (case 4), the discharge front is firstly directed towards the grounded ring, where it significantly charges the tube, and then the propagation continues towards the grounded target. Overall, the introduction of the grounded ring leads to a faster discharge propagation, higher surface charge deposition close to the grounded ring and higher charge production, but the tubular structure of discharge propagation between the grounded ring and the target does not significantly change with respect to cases 1, 2 and 3.

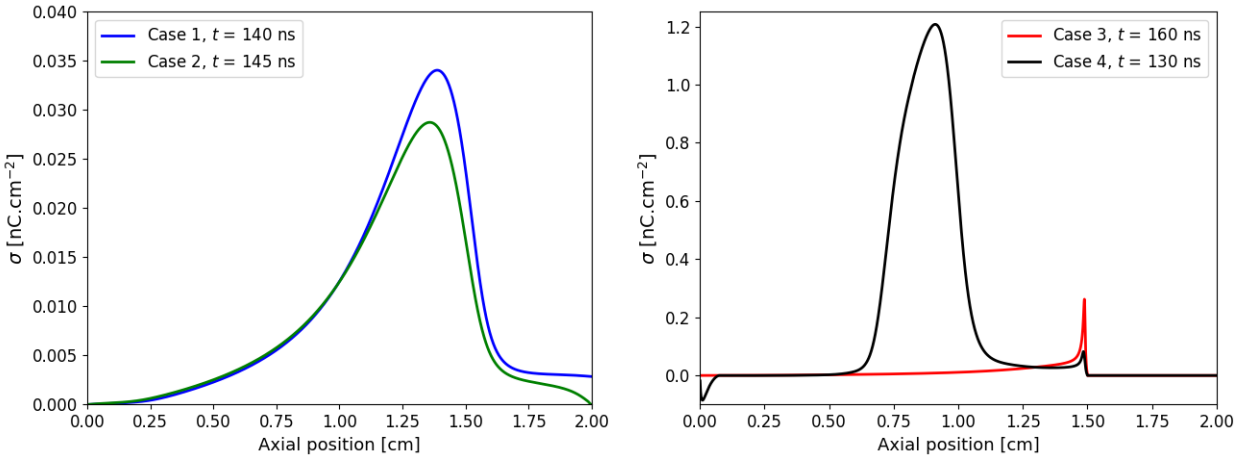

Figure III.21: Axial profiles of σ at the instant of impact on the target, with $V_P = +4$ kV and the different electrode configurations.

Conclusions

The study of different electrode configurations performed in this section has allowed us to conclude that the introduction of a powered point holder reduces the radial component of electric field close to the point electrode but its impact on discharge propagation is negligible. Furthermore, the use of a ring powered electrode inside the tube leads the discharge ignition to take place near the edge of the ring and not on the axis, as it happens with the point electrode. Then, by adding a grounded ring wrapped around the tube, placed between the powered electrode and the target, discharge ignition and propagation are faster all the way until the target and an important charging of the tube surface is induced. However, the tubular structure of the discharge remains in all these cases.

III.4 Influence of the shape of the applied voltage on discharge propagation in short tubes

Studied conditions

The conditions studied in this section are the same as in section III.2, with a 2 cm domain, a powered point electrode without point holder and a tube of $r_{in} = 2$ mm and $r_{out} = 3$ mm. This geometry is represented on the right side of Figure III.1. However, here we use for the relative permittivity of the tube $\epsilon_r = 4$, as in the experiments, and not $\epsilon_r = 1$ as in the previous section. The applied voltage is always positive and the 4 temporal shapes studied in this section are represented in Figure III.22 (right-side axis), in the timescale of interest in this section, and listed below:

- Shape 1: Constant applied voltage with value +4 kV.
- Shape 2: 50 ns rise-time and then constant applied voltage with value $V_P = +4$ kV, which is the shape used in the previous sections and in most of this thesis.
- Shape 3: The pulse used in GREMI, with 2.2 μs rise-time and maximum +4 kV.

- Shape 4: Same as the previous shape but with a maximum of +10 kV.

Influence of the shape of the applied voltage on discharge propagation

To study the influence of the shape of the pulse of applied voltage on discharge dynamics, we show in Fig. III.22 the temporal profiles of the discharge velocities of propagation inside the tube, obtained by following the maximum of $|E_z|$, for every case listed above. The figure allows to observe for every situation the instant of discharge ignition and the evolution of velocity with the applied voltage. By comparing pulses 1 and 2, we see that the ignition takes place earlier when the applied voltage (V_{APP}) has a constant value of 4 kV since the beginning, around $t = 5$ ns, than when $t_{rise} = 50$ ns. In this second case, the ignition happens around $t = 35$ ns when V_{APP} is close to 2.5 kV. However, once the discharges are ignited and both $V_{APP} = +4$ kV, the velocity of propagation in the tube is approximately the same, around 10 cm.μs^{-1}, until approximately 0.5 cm from the target, where the proximity of the discharge front to the ground leads to an increase of the velocity. Thus, the discharge in case 1 reaches the target earlier ($t = 130$ ns) than the discharge in case 2 ($t = 165$ ns) due to the difference of around 30 ns in ignition time and the small difference of velocity before V_{APP} in case 2 reaches +4 kV. This result shows that the velocity of propagation is proportional to the value of V_{APP} at each moment in time and, for short rise-times, is not significantly affected by the value of V_{APP} at the instant of discharge ignition. As the electric potential in the electrode is connected to the edges of the plasma through the quasi-neutral channel, the increase of V_{APP} induces higher potential in the front and then higher velocity. The discharge structure is also the same with shapes 1 and 2.

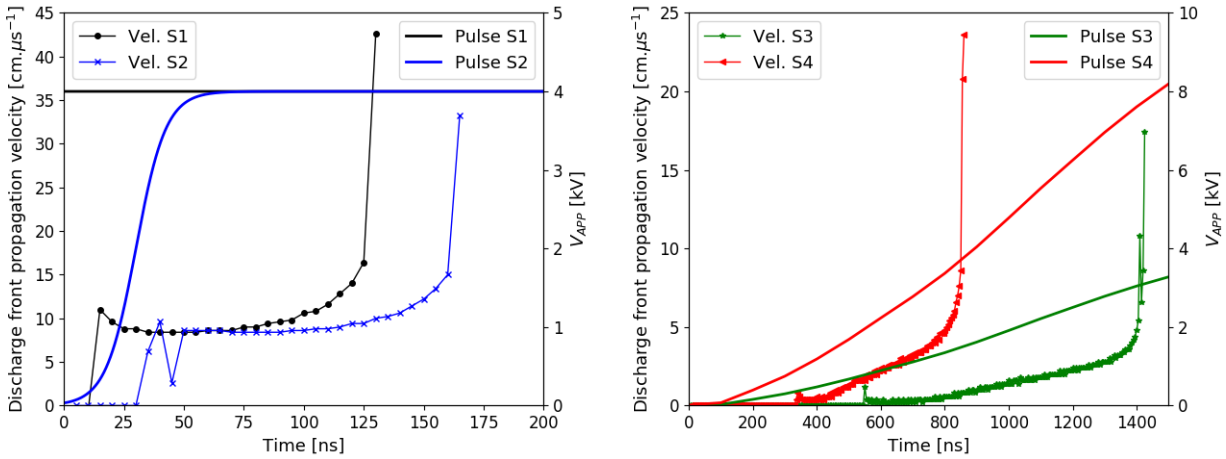

Figure III.22: Temporal profiles of the discharge velocity of propagation and of the pulses of applied voltage with the different shapes used in this section. On the left-side axis, the velocities. On the right-side axis, the applied voltages. On the left-side figure, concerning shapes 1 and 2. On the right-side figure, concerning shapes 3 and 4.

Then, the results of discharge velocity with shapes 3 and 4 of applied voltage confirm this conclusion. In each case, the discharge starts propagating with a very thin radius when the applied voltage is around 1.5 kV, and then the discharge front radius and the velocity of propagation increase proportionally to the applied voltage until the discharge is close to the grounded target. As a result, with shape 3 the discharge hits the target with a radius of

the discharge front around 1.2 mm, after 1420 ns when $V_{APP} \sim 3.1$ kV, while with shape 4 the impact takes place after 855 ns when $V_{APP} \sim 3.7$ kV, with a discharge radius at the front around 1.7 mm. We should notice that in the current cases the tube is short and the grounded target is close and thus the discharge front reaches the target while the applied voltage is still increasing. However, in *Bourdon et al.* [2016] with long tubes the simulations have also found that using the shape of pulse used in GREMI leads to an increase of velocity during the propagation in the tube.

Conclusions

By examining the discharge propagation with the different pulses of applied voltage we have concluded that with a plateau of constant applied voltage, preceded by a short rise-time, changing this rise-time induces a change in discharge ignition, but not on discharge velocity of propagation and structure. However, with long rise-times, the temporal profile of V_{APP} significantly affects the discharge propagation and structure in short tubes, as the discharge grows faster and larger with the increase of V_{APP}.

III.5 Dynamics of propagation of He discharges with N_2 and O_2 admixtures inside dielectric tubes

The results presented in the previous sections have been obtained with a fixed gas-mixture 99% He - 1% N_2. However, in this thesis different He-N_2 and He-O_2 gas-mixtures are used. In order to understand the differences in discharge dynamics induced by the change of gas-mixture, here we simulate discharge propagation in a simplified geometry inside a dielectric tube of short length using 6 different gas-mixtures: He with 10 ppm N_2, He with 1.000 ppm N_2 (99.9% He - 0.1 % N_2) and He with 10.000 ppm N_2 (99% He - 1 % N_2); and the same mixtures with O_2 admixture instead of N_2. As the He buffer gas used in experiments is never completely pure, here we consider 10 ppm as a minimum of impurity and thus both He with 10 ppm N_2 and He with 10 ppm O_2 can be seen as almost-pure He. The model set-up is as in Figure III.19 (case 2) with a powered point electrode with a plane point-holder, but the domain has 3 cm length and thus the inter-electrode gap is 2.5 cm. The tube has $r_{in} = 2$ mm, $r_{out} = 3$ mm and $\epsilon_r = 4$. The applied voltage has a 50 ns rise-time and then is constant with +6 kV. The initial densities are set in every case as 10^9 cm^{-3} electrons and N_2^+ or O_2^+.

Dynamics of species in 99% He - 1% N_2 and in 99% He - 1% O_2

The distribution of the main species is shown for a He plasma with 1% N_2 in Figure III.23 and with 1% O_2 in Figures III.24 and III.25. These mixtures have been chosen because they are representative of the range studied in this thesis. Firstly, we notice that both He-N_2 and He-O_2 discharges presented here have a tubular structure in the tube, and the 99% He - 1% O_2 discharge has propagated further (2.1 cm rather than 1.9 cm) than the 99% He - 1% N_2 until $t = 150$ ns.

Figure III.23 presents the spatial distribution of only the ion densities in the 99% He - 1% N_2 plasma, using the reaction scheme in table II.1. As electrons are the only negative species

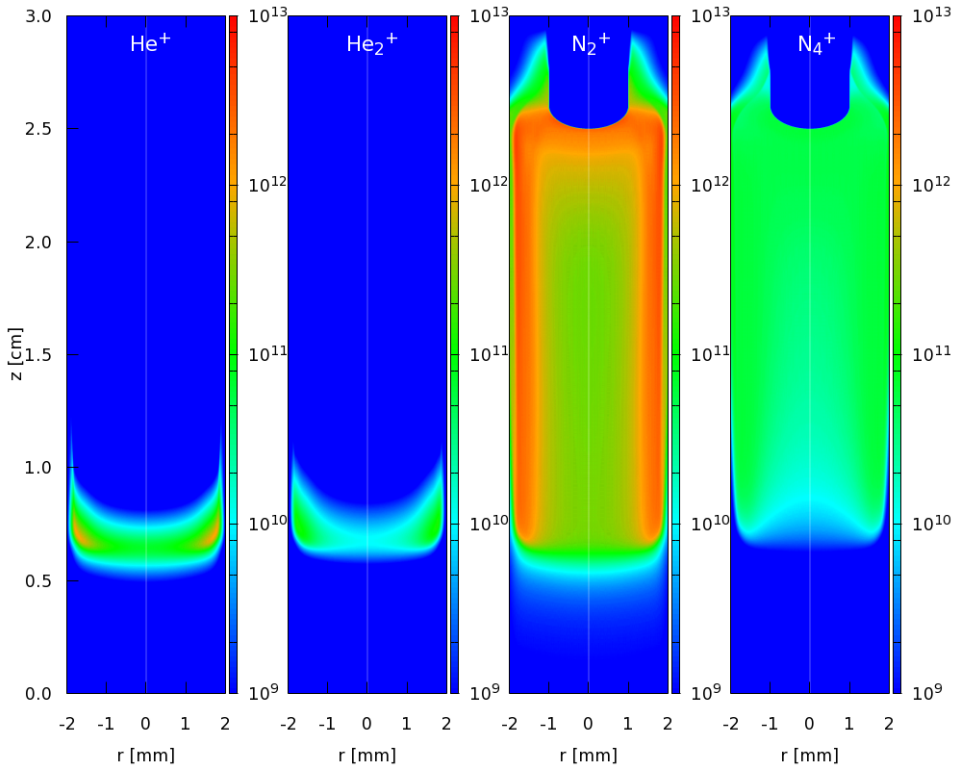

Figure III.23: Cross-sectional views of species densities at $t = 150$ ns for 99% He - 1 % N_2 mixture: He^+, He_2^+, N_2^+ and N_4^+.

in this plasma, their density is not shown but can be considered as the sum of the positive species densities. As mentioned in *Bourdon et al.* [2016], the distribution of each species can be quite different. He^+ is formed in the ionization front by electron-impact ionization. Then, they are rapidly converted through charge transfer in He_2^+, N_2^+ and N_2^+(B). Metastable He* is not shown in Figure III.23 but its distribution is similar to the one presented in Figure III.25 for a He-O_2 mixture, being quenched in the plasma column to ionize N_2. We can also take note that N_2^+ is present in front of the ionization wave, due to photoionization. Thanks to Penning ionization and charge transfer reactions, N_2^+ is the major ion in the plasma column. Moreover, Figure III.23 shows that in the studied timescales N_4^+ is only a minor ion in the plasma column. As shown in *Bourdon et al.* [2016] (Figure A.1), it has also been verified in the current conditions that Penning ionization reactions, taking place behind the ionization front, are essential to keep ionization in the plasma channel and for the ionization front velocity in the tube. Without these reactions, the plasma channel is less conductive and the discharge propagation is slower. Furthermore, in that work it has also been shown that without charge exchange reactions between He and N_2 ions, more ions and electrons remain in the plasma channel, due to the lower recombination coefficient of He_2^+ (R9, $\sim 8.9 \times 10^{-9}$ $cm^3.s^{-1}$) than N_2^+ and N_2^+(B) (R28, R40, 1.0×10^{-7} $cm^3.s^{-1}$). Likewise, N_4^+ has a higher recombination coefficient (R45, $\sim 2.0 \times 10^{-6}$ $cm^3.s^{-1}$) than N_2^+ and therefore the charge exchange reactions between N_2^+ and N_4^+ affect the ionization level in the channel. With lower recombination rates, the plasma channel is more conductive and the velocity of the discharge is higher (Figure A.1).

Then, Figures III.24 and III.25 present the spatial distribution of species densities in the 99%

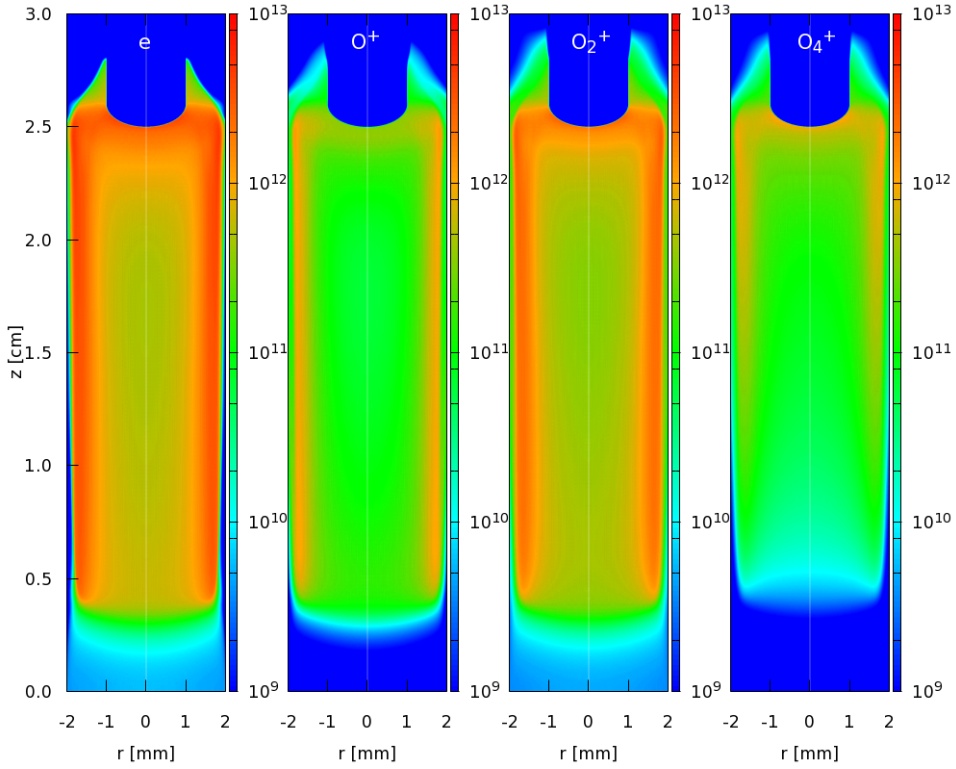

Figure III.24: Cross-sectional views of species densities at $t = 150$ ns for 99% He - 1 % O_2 mixture: electrons, O^+, O_2^+ and O_4^+.

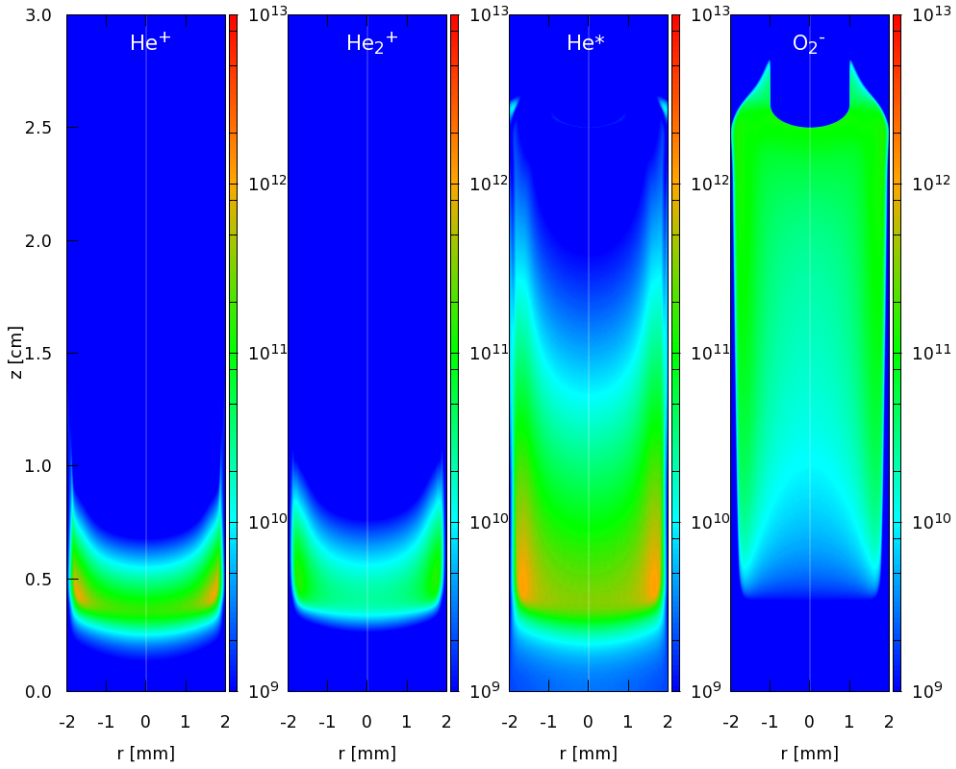

Figure III.25: Cross-sectional views of species densities at $t = 150$ ns for 99% He - 1 % O_2 mixture: He^+, He_2^+, He* and O_2^-.

He - 1% O_2 plasma, using the reaction scheme in Fig. D.1. In Figure III.24 are presented the main charged species in this plasma, electrons and the oxygen positive ions. Then, in Figure III.25 are shown the most relevant He species (He^+, He_2^+, He*), along with the most important negative ion in these timescales O_2^-. As in the He-N_2 plasma, the He^+ and He* species are created in the discharge front by electron-impact. Then, He_2^+ and He_2* are generated quickly behind the front through charge exchange and energy exchange reactions, respectively. He* density is always more relevant than He_2* density. In the plasma channel, O^+ and O_2^+ are produced by charge exchange and Penning ionization reactions, through both helium and oxygen excited states (O, O(^{1}D), $O_2(a)$, $O_2(b)$ and $O_2(v)$, not shown here, have relevant densities), which makes O_2^+ the dominant ion in the channel. Then, O_4^+ is produced by charge exchange reactions. Therefore, the recombination in the plasma channel is shared between e-O^+, (R55, R69-70), e-O_2^+ (R56-58, R71) and e-O_4^+ (R59) reactions. Finally, in the conditions under study, with only 1% O_2, in the timescales studied here, and considering the conditions of first pulse (only electrons and O_2^+ considered as initial species), negative ion densities are irrelevant when compared to electrons and positive ion densities. Negative ion densities in this case are always lower than 10^{12} cm^{-3}, O^- having the highest density in the discharge front, and O_2^- in the channel behind the front. Thus, electron loss through attachment, electron production through detachment and ion-ion recombination play a small role in the discharge dynamics in the current conditions.

Propagation with different gas-mixtures

Most of the mentioned reactions, like charge transfer and Penning ionization, are dependent on the relative densities of He and the admixture gas (N_2 or O_2). Therefore, differences in the gas-mixture can be expected to change the dynamics of discharge propagation in the tubes. In order to study the influence of the gas-mixture on the macroscopic dynamics of discharge propagation in small tubes, in Figure III.26 are compared the spatial distributions of electron density at $t = 150$ ns, for different gas-mixtures. On top are visible the results with several He-N_2 mixtures: 10 ppm, 1000 ppm (0.1%) and 10 000 ppm (1%). On the bottom, the results for the same mixtures of He-O_2 are shown.
First, we should notice in Figure III.26 that the temporal evolutions of velocity in the cases with 10 ppm N_2 and 10 ppm O_2 are very close. As 10 ppm is a very small quantity, corresponding to impurities in the gas supplies, we consider either of these cases as being equivalent to pure He flowing through the tube in experiments. Moreover, the pure He reactions in table II.1 and Fig. D.1 are the same. As such, we expect the general dynamics to be the same in the two cases, which is verified. Then, we can notice that in every mixture the maximum electron density is around 5×10^{12} cm^{-3} and thus not very variable in this range of mixtures. In both He-N_2 and He-O_2 cases, the discharge structure is more homogeneous with higher N_2 or O_2 admixture and more filamentary closer to pure He. At the same time, the discharge radius appears to be proportional to the admixture, even though the variations are small. The evolutions of surface charge density σ reflect this proportionality, with a maximum of σ during propagation of 0.8 nC.cm^{-2} in the cases with 10 ppm admixture, and of 1.6 nC.cm^{-2} in the cases with 1% N_2 or O_2. Furthermore, the discharge ignition always takes place around the same time $t = 35$ ns. In *Bourdon et al.* [2016] the ignition time was variable according to the mixture but the pulse of applied voltage had a much higher rise-time and the initial

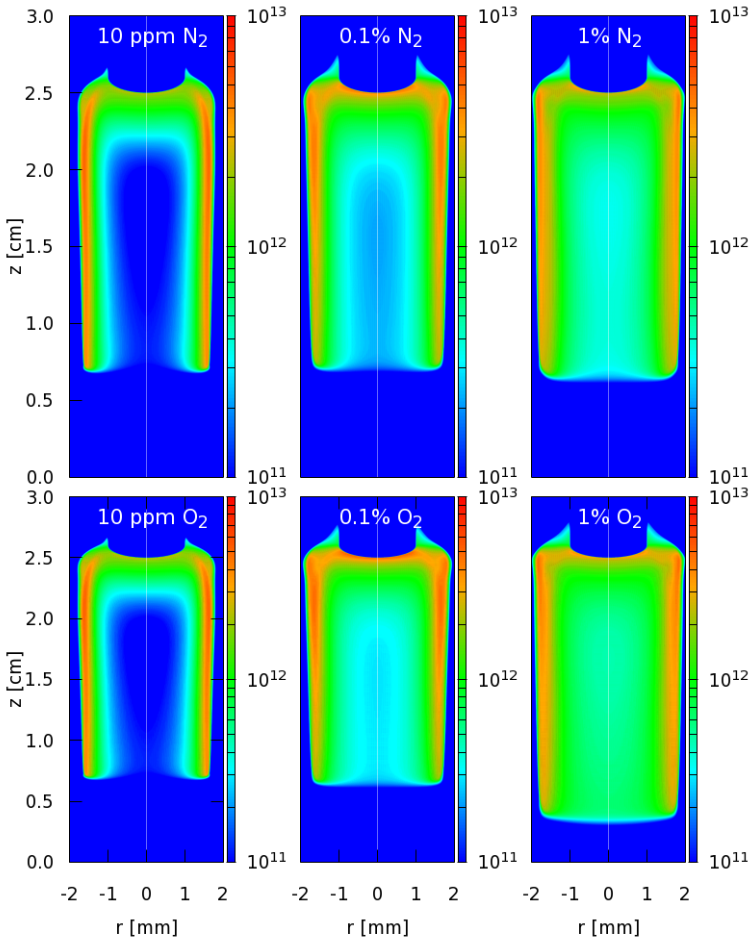

Figure III.26: Cross-sectional views of electron densities at $t = 150$ ns for all six gas-mixtures.

pre-ionization considered was of only 10^4 cm^{-3}. Then, in table III.1 are presented the times of impact on the grounded plane at $z = 0$ and the average velocities of propagation (between $z = 2.5$ cm and $z = 0$ from ignition time until impact time), for each gas-mixture.

Mixture	Time of impact [ns]	Average velocity [cm.μs^{-1}]
He + 10 ppm N_2	178	17.5
99.9% He - 0.1% N_2	176	17.7
99% He - 1% N_2	169	18.7
He + 10 ppm O_2	178	17.5
99.9% He - 0.1% O_2	172	18.2
99% He - 1% O_2	157	20.5

Table III.1: Impact time and average velocity of propagation with the several gas-mixtures.

As is noticeable in table III.1, the velocities of propagation are dependent on to the N_2 or O_2 admixture. In *Bourdon et al.* [2016] it has been noted that as the velocity of propagation is a very macroscopic quantity, the influence of the gas-mixture on it is rather the result of the complex coupling between kinetics, photoionization and discharge structure. Indeed the different discharge structures and velocities are the product of higher ionization coefficient for low electric field magnitudes (see Fig. II.3), higher Penning ionization through quenching of

He* in the plasma channel and higher photon absorption with higher N_2 or O_2 densities. Still, the influence of small N_2 and O_2 admixtures to He on the discharge dynamics of propagation in small tubes is very subtle.

Conclusions

In this section the different dynamics of species in 99% He - 1% N_2 and 99% He - 1% O_2 have been presented. Considering single pulse conditions, timescales of hundreds ns and admixtures of O_2 up to 1%, the electronegativity of O_2 is not felt in the He-O_2 discharge. Moreover, different He discharges with N_2 or O_2 admixtures from 10 ppm up to 1% have been studied in terms of electron density, discharge radial structure and axial velocity of propagation. It has been clearly shown that these are not sensitive quantities with respect to gas-mixture in the conditions under study. Thus, in order to deepen the understanding of discharge physics and to characterize plasma jets in detail, less macroscopic quantities have to be studied.

III.6 Discharge propagation in the plasma plume

III.6.1 Introduction

In this section, we consider plasma jet configurations, with a gap between the tube and the target. We study the effect of the gas-mixture in the gap on discharge propagation and the mechanisms of propagation of the discharge in the plasma plume. The influence of the polarity of applied voltage on the discharge dynamics in the plume is also examined. The state of the art on these subjects has been exposed in sections I.2.4 and I.2.5.
In this section, we seek to deepen the understanding of the radial confinement of the discharge front in the plasma plume and how the gas mixing affects the mechanisms of propagation of the discharge. First, in section III.6.3 the radial confinement of a negative discharge propagating in the plume is shown and the influence of the tube-target distance on the discharge structure is investigated. Then, in section III.6.4 it is shown that the path of propagation of the discharge front in the plasma plume, and thus its structure, is not only dependent on flow and geometry conditions, but also on the applied voltage, inclusively on its polarity. Moreover, in section III.6.5 the role of the gas mixing in the plasma plume on the mechanisms of discharge propagation is investigated in detail for cases of positive polarity of applied voltage. The role of preionization and photoionization to provide seed electrons for discharge propagation is quantified, both in the tube and in the plume, and the mechanisms of electron production and loss when the discharge propagates in the plume are identified in both He-N_2 and He-O_2 mixtures; Finally, the properties of the gas mixing are separated in the model to evaluate the role of each one in section III.6.6.

III.6.2 Studied conditions

In chapters IV, V and VI of this thesis the discharge dynamics is studied in conditions with a certain tube-target distance and gas mixing in the tube-target gap. In these cases, it is considered that He or He with N_2 or O_2 admixture flows through the tube and mixes with

a N_2 or O_2 environment at the end of the tube. This mixture then remains static. The coupling between the transient plasma model and the static gas mixture has been described in section II.4.3. In this section, we investigate how the plasma plume affects the discharge dynamics while its front propagates towards a grounded metallic target. The investigation is carried through by comparing results of discharge dynamics with different conditions of flow, tube length (L), tube-target distance (d), polarity of applied voltage and gas-mixture. Some of the set-ups used in this section are shown in Figure III.27, with the gas-mixture shown by means of color plots and contours.

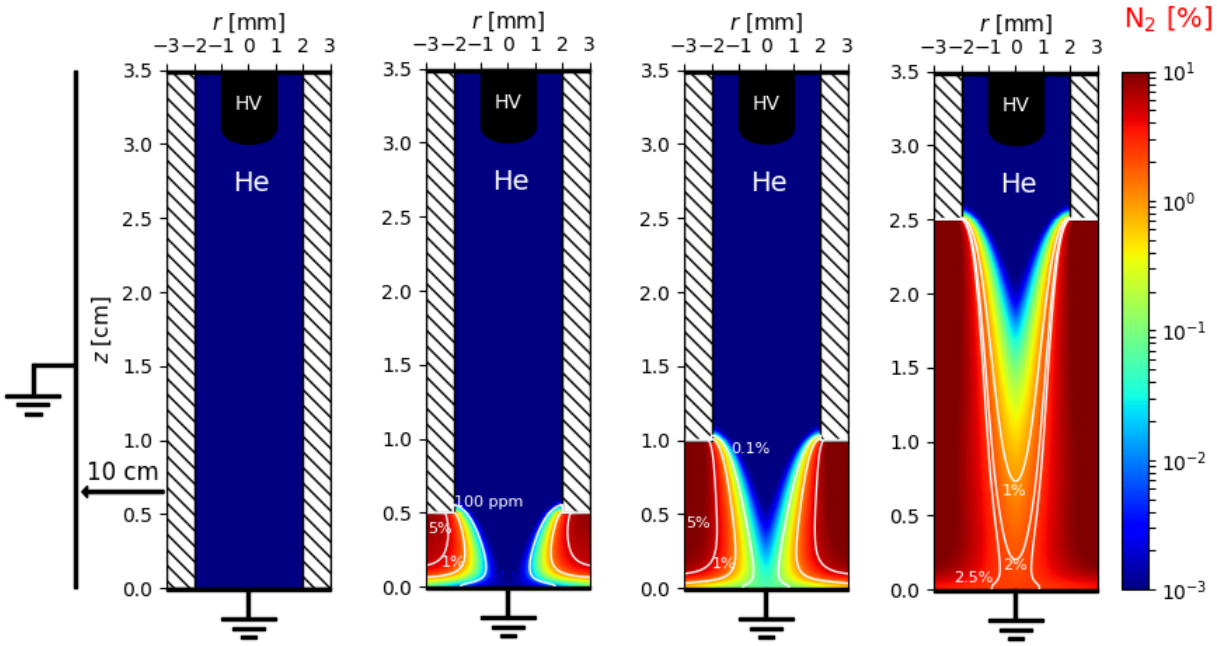

Figure III.27: Side-view schematics of the discharge set-ups used in this section, with 2 slm of He flowing into a N_2 atmosphere. From left to right: $L = 3.5$ cm, $d = 0.0$ cm; $L = 3.0$ cm, $d = 0.5$ cm; $L = 2.5$ cm, $d = 1.0$ cm; $L = 1.0$ cm, $d = 2.5$ cm;

In all the cases described in this section, quartz tubes with relative permittivity $\epsilon_r = 4$ are considered. In all the configurations, a grounded metallic plane target is placed at $z = 0$. A powered point electrode is set in the axis of the domain. It is composed of a cylinder and a spherical tip of 1 mm radius. Behind the point electrode, a point holder plane is placed, with radius r_{out}. As shown in Figure III.27, all the discharge set-ups are placed inside a grounded cylinder with a radius of 10 cm. The discharge is powered by a voltage that rises linearly between 0 and V_P, and then is constant with a plateau value V_P. The rise-time is 50 ns and the voltage can be either positive or negative. The gas-mixture in this section is always composed of either He and N_2 or He and O_2, and the kinetic schemes described in section II.4.2 for He-N_2 and He-O_2 plasmas at atmospheric pressure are used. Inside the tube, it is considered that helium with a minimum of impurities (10 ppm N_2 or 10 ppm O_2) is used as buffer gas, unlike previous sections, to focus on the mixing in the plume. As in most of this thesis, unless stated otherwise, a uniform initial preionization density $n_{init} = 10^9$ cm^{-3} of electrons and N_2^+ or O_2^+ ions is considered, to account for the effect of repetitive voltage pulses (see section II.4.2).
A cartesian mesh is used with an axial size of 10 μm. Radially, the mesh size is 10 μm between

$r = 0$ and r_{out}. The radial mesh size is then expanded using two geometric progressions until reaching the boundary of the computational domain: 20 cells for 1 mm thickness and then 50 cells until $r = 10$ cm. This refinement requires in most of the cases studied here a mesh of $n_z \times n_r = 3500 \times 370 = 1.295$ million points. The average computational time required for a simulation run to obtain the results presented in this section is of two days with 32 MPI processes on the multicore machines that compose the cluster "Zoidberg".

III.6.3 Influence of flow and tube-target distance on discharge dynamics

Radial confinement of discharge propagation in the plasma plume

In order to understand how the gas mixing in the plasma plume affects the discharge dynamics, we start by the observation of the radial confinement of the discharge as it propagates from the end of the tube towards the target. In Figure III.28 the spatial distribution of the electron-impact ionization source term S_e (reactions in table II.1 in section II.4.2) is shown at several times in the jet configuration on the right side of Figure III.27 with 2.5 cm of tube-target distance. He with 10 ppm of N_2 flows with 2 slm into a N_2 atmosphere and the voltage pulse with V_P = -6 kV is applied. As in *Babaeva and Kushner* [2014], where the air mole fraction in a He jet plume is shown as the background for discharge parameters, here the gas-mixtures of 1%, 2% and 2.5% of N_2 are represented as contours in Figure III.28. S_e is presented at an instant when the discharge front is reaching the end of the tube (t = 60 ns), and then during the propagation in the plasma plume (t = 120, 190, 250 ns). The distribution of S_e gives an indication of the position of both strong n_e and strong electric field.

Figure III.28 shows that the maximum of S_e when the discharge front crosses the end of the tube forms a front as broad as the tube radius, as studied for the electric field in section III.2. Then, as the discharge propagates in the plume, the maximum of S_e is more localized at a given radial position (t = 120 ns) and then progressively approaches the center at $r = 0$ (between t = 120, 190 and 250 ns), reaching it around t = 250 ns, after approximately 1.5 cm of propagation in the plasma plume and at a position where the N_2 concentration at $r = 0$ is below 1%. In the case under study, the radial confinement is completed (i.e. the front reaches $r = 0$) in a region where the target has a negligible influence on the flow distribution, and therefore in conditions close to free flow. We should notice that in this case the maximum of S_e during the propagation until t = 250 ns appears to follow the lines of gas-mixture 1-2.5% N_2. Likewise, behind the discharge front, as n_e, ρ and electric field are present, a channel of S_e is visible, that is also radially confined by the gas-mixture.

Influence of the tube-target distance on discharge dynamics

Then, we study how the radial confinement and the effect of the gas mixing on discharge propagation are dependent on the specific geometry under study. In Figure III.29 is represented the electron-impact ionization source term in the four configurations of Figure III.27. In every case, it is considered that 2 slm of He with 10 ppm of N_2 flow through a tube of 2 mm inner radius and V_P = -6 kV. The difference between each case lies on the tube length

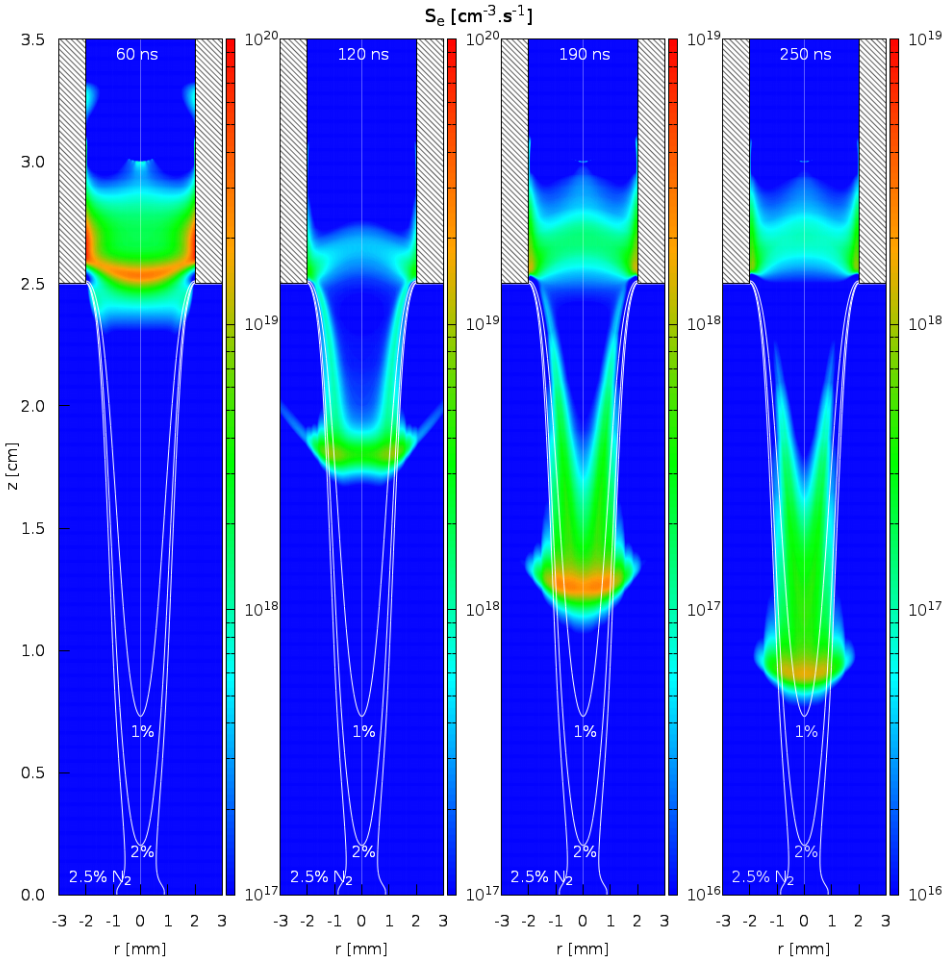

Figure III.28: Cross sectional views of the electron-impact ionization source term at t = 60, 120, 190 and 250 ns, for a 1 cm long tube with 2.5 cm tube-target distance, 2 slm flow of He into N_2 atmosphere and V_P = -6 kV.

(L) and tube-target distance (d) and then on how He and N_2 distribute in the tube-target gap. Contours in the figures point out some particular values of gas-mixture. For each case, S_e is shown at an instant close to discharge impact on the metallic target.
It is visible in Figure III.29 that the shape of the S_e distribution as it approaches the target is variable. With $d = 0$ the discharge front reaches the target with a radial distribution filling the tube. Then, with $d = 5$ mm, the maximum of S_e presents an annular shape at the end of the tube, following the gas-mixture close to 1% N_2. With $d = 10$ mm, the discharge front is radially confined along the propagation in the plasma plume, approximately following the trajectory defined by the gas-mixtures with 0.1 and 1% N_2. Finally, with $d = 25$ mm, the propagation after the radial confinement observed in Figure III.28 remains centered, although it is progressively slower and more diffusive ($E_{zMAX}(r = 0)$ decreases from 8 kV.cm^{-1} at the end of the tube to 4 kV.cm^{-1} close to the target). In both cases with $d = 10$ mm and $d = 25$ mm it is visible that the S_e distribution close to the target tends to spread radially, following the He gas flow. Furthermore, we should notice that in all the cases an S_e distribution with values between 10^{17} and 10^{18} cm^{-3} is present at the end of the tube. This is due to an increase of the electric field provoked by the change of permittivity of the tube and the discontinuity of surface charges on the tube inner wall. Finally, we can conclude that the

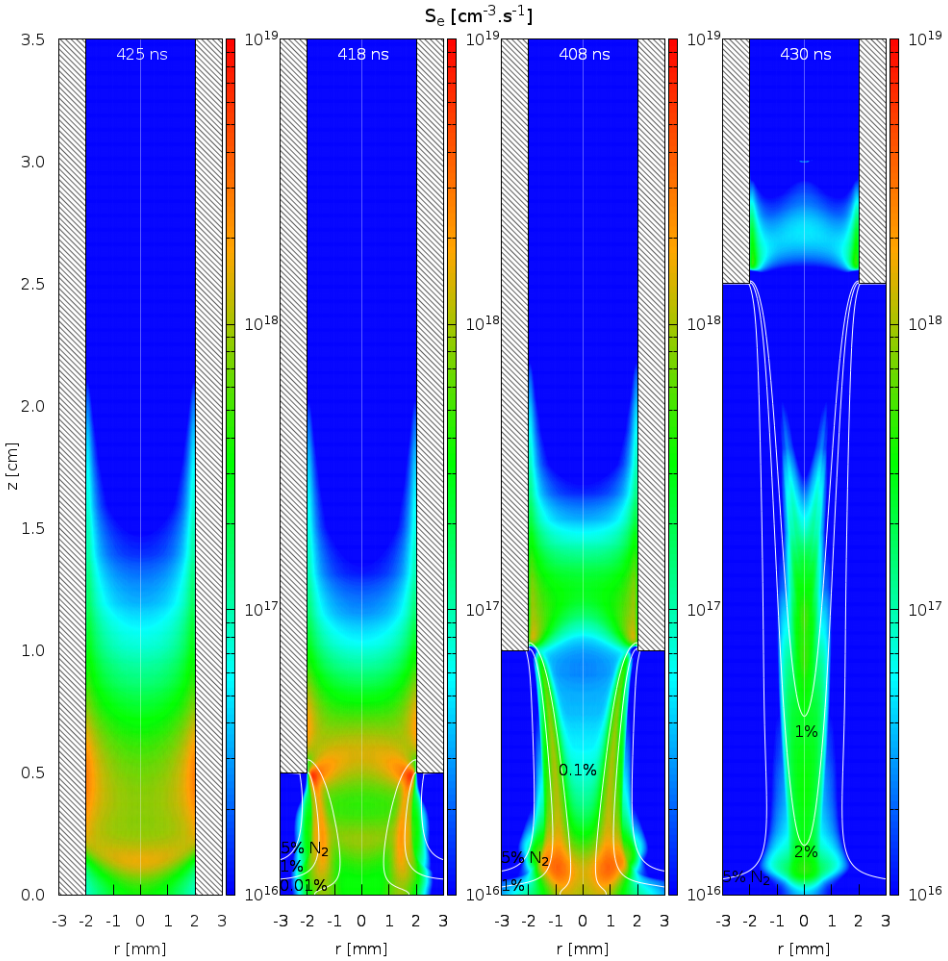

Figure III.29: Cross sectional views of the electron-impact ionization source term, for different tube lengths and tube-target distances, at times shortly before impact on target, with 2 slm of He flowing into N_2 atmosphere and V_P = -6 kV.

time of propagation is not very sensitive to the tube-target distance and corresponding gas mixing in the cases under study. However, the mixing with small concentrations of N_2 at the end of the tube in the cases with $d = 5$ mm and $d = 10$ mm tends to slightly increase the velocity of propagation. With $d = 25$ mm, the velocity of propagation is slightly higher in the region with $[N_2](r = 0) \lesssim 1\%$, but slightly lower afterwards.

III.6.4 Effect of the polarity of the applied voltage on the discharge dynamics in the plasma plume

Here it is analyzed the effect on the discharge dynamics in the plume of the applied voltage, in particular the role of its polarity, keeping the same magnitude. The effect of the magnitude of the applied voltage in positive polarity will be studied later in appendix G. In Figures III.30 and III.31 the two cases of discharge dynamics, with V_P = -6 kV and V_P = +6 kV, are compared. The same geometry and flow conditions are used as in the third case in Figure III.27 with $d = 1.0$ cm. For each case, in Figure III.30 are represented the spatial distributions of S_e and S_p (on top) and of E_t and n_e (on bottom) during the propagation in the plasma plume, before the discharge front reaches the target. In each figure, the distribution of some

particular gas-mixtures is shown with contours. In Figure III.31 the same quantities are represented at an instant shortly before the discharge front hits the target.

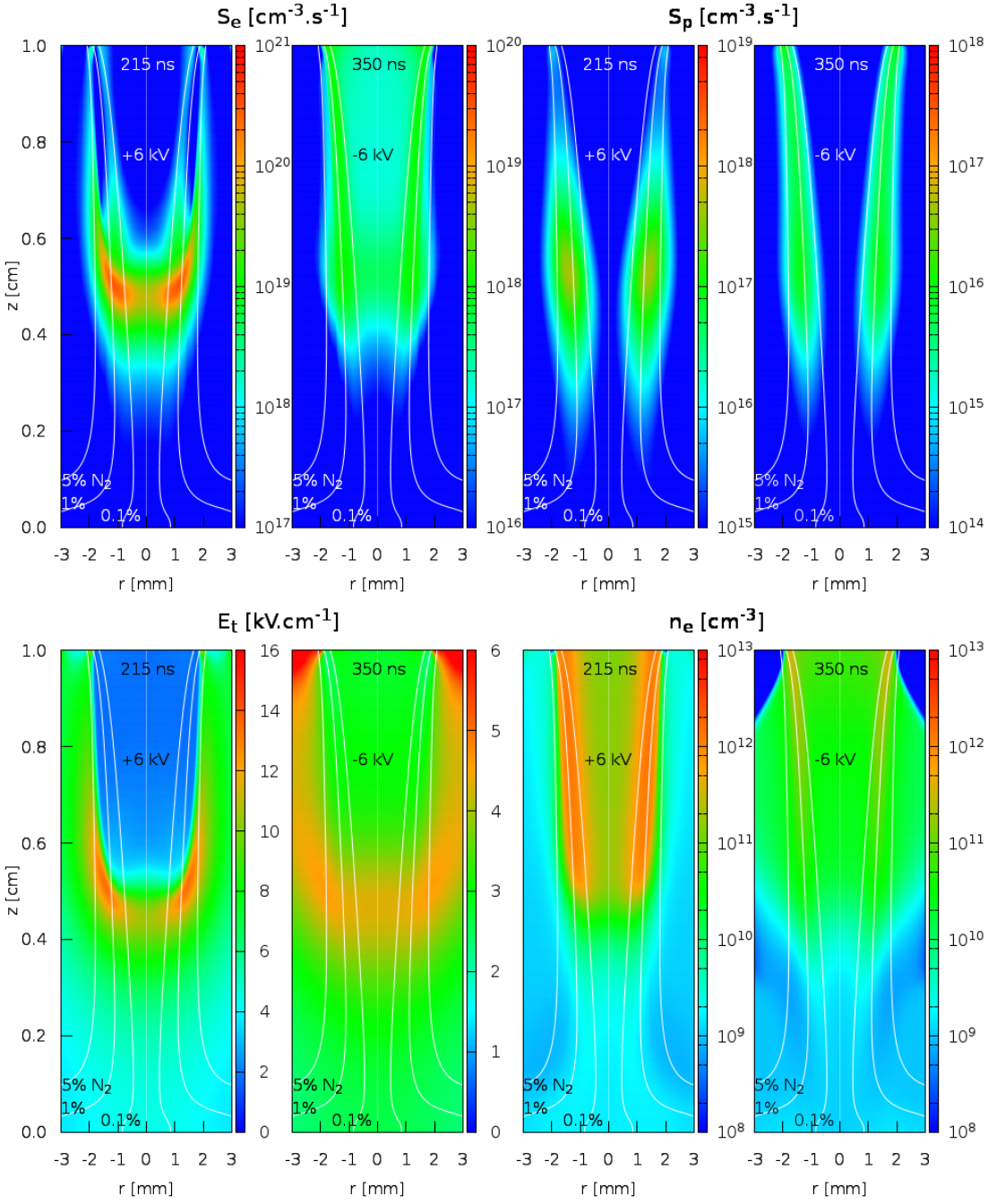

Figure III.30: Cross sectional views of the electron-impact and photoionization source terms (on top), and of the magnitude of the electric field and the electron density (on bottom), with 2 slm He flowing into a N_2 environment, during the discharge propagation in the plasma plume, for V_P = +6 kV and V_P = -6 kV.

Firstly, we should take into account that the difference in polarity of applied voltage leads to differences in discharge dynamics already during the propagation inside the tube. These have been studied in section III.2.4. In fact, in the cases under study here, the discharges reach the end of the tube at t = 180 ns with V_P = +6 kV and at t = 270 ns with V_P = -6 kV. Then, in Figures III.30 and III.31 we notice at first that S_e, S_p, E_t and n_e tend to

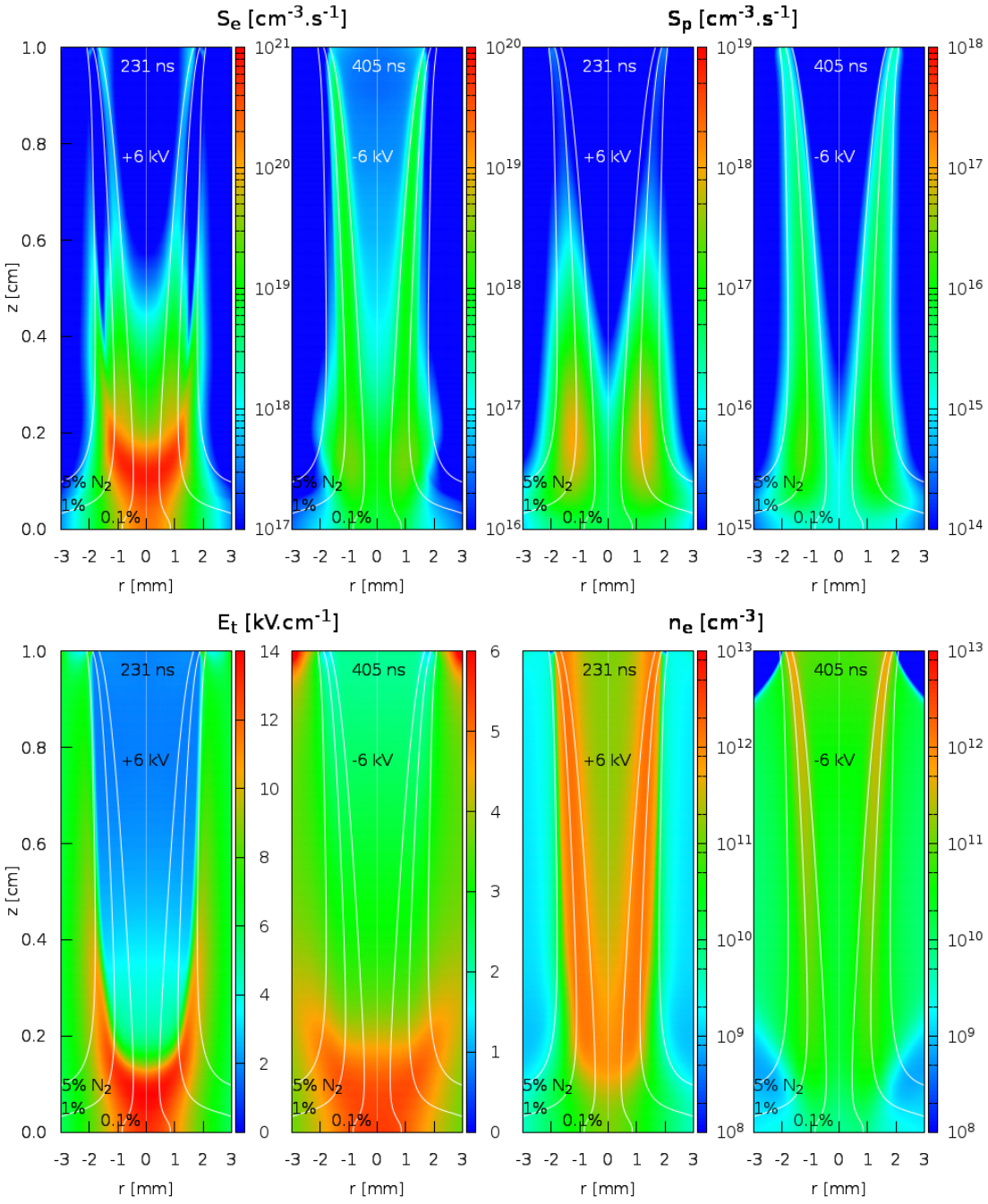

Figure III.31: Cross sectional views of S_e, S_p, E_t and n_e, with 2 slm He flowing into a N_2 environment, shortly before the discharge hits the target, for V_P = +6 kV and V_P = -6 kV.

present significantly higher maximum values in the plasma plume with V_P = +6 kV than with V_P = -6 kV. In both cases the radial confinement as the discharge approaches the target can be noticed. Furthermore, it is interesting to notice that the distributions of S_e and S_p during propagation in the plume are different in each case and are clearly influenced by the gas-mixture.

In fact, with V_P = +6 kV, the radial confinement leads to an approximately centered impact on the target, even though the radial profile of E_t at the end of the tube is not centered. The discharge front and the plasma channel are clearly distinguishable. However, with positive polarity, the plasma channel is broader and occupies the region with N_2 density up to 5%.

With negative polarity, n_e is more localized in the region between 0.1% N_2 and 1% N_2, and S_e is almost as high in the plasma channel as in the discharge head, as a consequence of the distribution of electric field that, as has been shown in section III.2, tends to be higher in the front with positive polarity and higher in the channel with negative polarity. As a result, we tendentiously find the same discharge structures reported in *Naidis* [2011a]: spherical head with positive polarity and sword-shaped channel with negative polarity. These distributions tendentiously follow the path set by the production of seed electrons ahead of the discharge front in positive polarity and the production of electrons at the front in negative polarity. For instance, with V_P = -6 kV, the distribution of n_e at t = 405 ns approximately follows the path set by S_e and S_p ahead of the front already at t = 350 ns. These results show that for the same geometric configuration, the interaction of the discharge propagation with the gas mixing and the structure that the plasma takes in the plume are dependent on the value and polarity of applied voltage.

III.6.5 Discharge propagation mechanisms in the plasma plume

We seek to investigate in detail what are the properties of the gas mixing in the plasma plume that affect the discharge dynamics. This investigation is carried through firstly by identifying the propagation mechanisms in the plume, with He flowing into N_2 and O_2 atmospheres, and later in section III.6.6 by isolating each physical aspect of the gas mixing. For the sake of brevity, this study is only carried out for positive polarity of applied voltage.

Role of preionization and photoionization on discharge propagation

Firstly, we evaluate the role of preionization and photoionization on the production of seed electrons ahead of the discharge front with positive polarity, that allow the discharge to propagate and set the path of propagation of the discharge. This study is performed by comparing the ionization source terms by electron-impact (S_e) and by photoionization (S_p) ahead of the discharge front in a case with the usual preionization 10^9 cm^{-3}, and in another case with lower preionization 10^6 cm^{-3} of electrons and N_2^+. The geometry is slightly different than in the previous results, with a shorter tube of L = 1.5 cm (tip of the point electrode at z = 2.0 cm), but same radius r_{in} = 2 mm. He is flowing at a rate of 2 slm into a N_2 atmosphere, with d = 1 cm tube-target distance, and V_P = +4 kV. However, first, in Figure III.32, it is shown how the choice of preionization affects the discharge dynamics in the tube. E_t and n_e are represented for the two cases of n_{init}, at an instant during propagation in the tube.
We see in Figure III.32 that the discharge structure changes significantly with the preionization value already inside the tube. We should first notice that there is only 10 ppm N_2 inside the tube, and then photoionization is negligible and preionization is the only source of seed electrons, therefore having a paramount importance. In fact, with n_{init} = 10^9 cm^{-3} the discharge ignites around t = 30 ns, when E_z at the tip of the point electrode is close to 15 kV.cm^{-1}, while with n_{init} = 10^6 cm^{-3} the ignition takes place around t = 40 ns, with E_z close to 23 kV.cm^{-1}. Then, the propagation with lower n_{init} requires higher peak electric field at the discharge front, and consequently higher electron production is obtained, as is visible in Figure III.32. It is also shown that the discharge structure, despite being tubular in both cases, is more diffusive with higher n_{init}, when there are more seed electrons, and

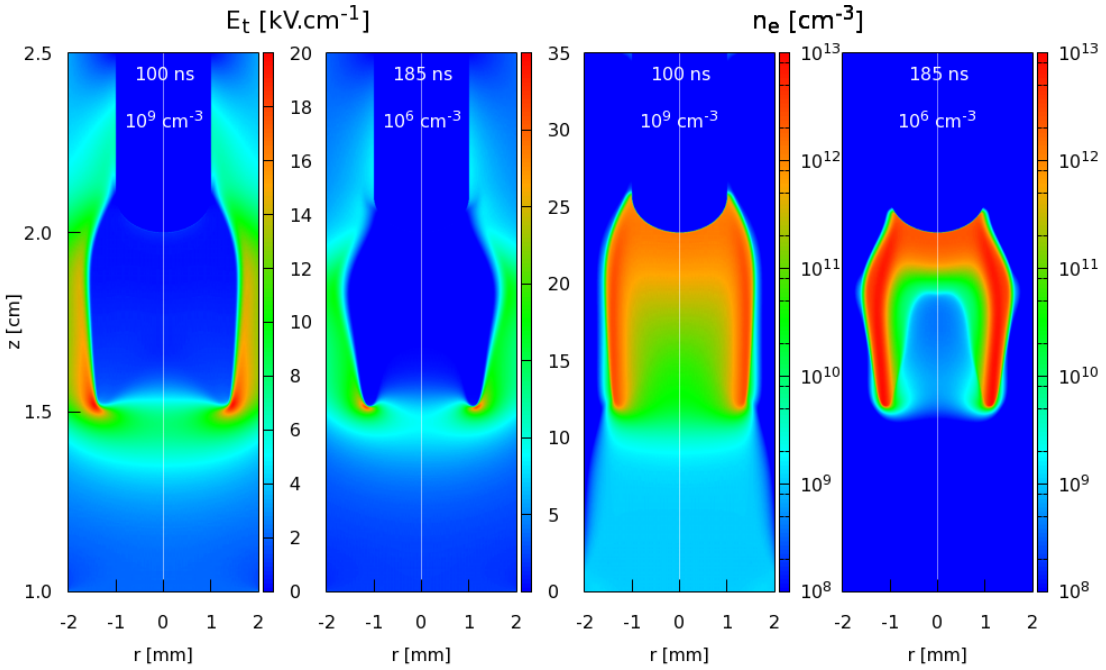

Figure III.32: Cross sectional views of E_t and n_e, during propagation in the tube, with L = 1.5 cm and d = 1.0 cm, 2 slm flow of He into N_2 atmosphere and V_P = +4 kV.

is more filamentary with $n_{init} = 10^6$ cm^{-3}, with higher and more localized peak of E_t. The lower velocity and more filamentary structure registered here for the case with $n_{init} = 10^6$ cm^{-3} during propagation in the tube are also verified in the plasma plume but become less obvious as the N_2 density and photoionization increase. In fact, both with $n_{init} = 10^9$ cm^{-3} and $n_{init} = 10^6$ cm^{-3}, the propagation between the end of the tube and the target takes approximately 105 ns. Then, to evaluate the role of preionization and photoionization on the production of seed electrons in the plasma plume, we represent in Figure III.33 S_e and S_p for the two cases of n_{init} during propagation in the plume. The colorscales are adapted for direct comparison between S_e and S_p.

Figure III.33 shows that even though S_e is higher on the discharge front with $n_{init} = 10^6$ cm^{-3} and higher peak E_t, it is significantly lower than with $n_{init} = 10^9$ cm^{-3} 1 mm ahead of the front. In fact, in the regions with low electric field, S_e is mostly proportional to n_e. Thus, in the case with $n_{init} = 10^9$ cm^{-3} it is visible that S_e has higher values and extends further ahead of the discharge front than S_p, which shows that S_e is a more important source of seed electrons and has a major role structuring the shape of the discharge in the plasma plume. This is only possible due to the very low threshold of ionization of He and of He with small concentrations of N_2 (see section II.4.2). However, with $n_{init} = 10^6$ cm^{-3}, the values of S_e and S_p ahead of the discharge front are comparable. Even though the absolute values of S_p are close in both cases, with $n_{init} = 10^6$ cm^{-3} S_p becomes relatively as important as S_e for the production of seed electrons. Furthermore, as the production of seed electrons due to S_e tends to be more centered than due to S_p (i.e. S_e higher for lower N_2 concentrations than S_p), the propagation of the discharge front is more centered with $n_{init} = 10^9$ cm^{-3} and more tubular with $n_{init} = 10^6$ cm^{-3}. Therefore, we can conclude that the identification of the propagation mechanisms that produce seed electrons and set the path of propagation is highly dependent on preionization.

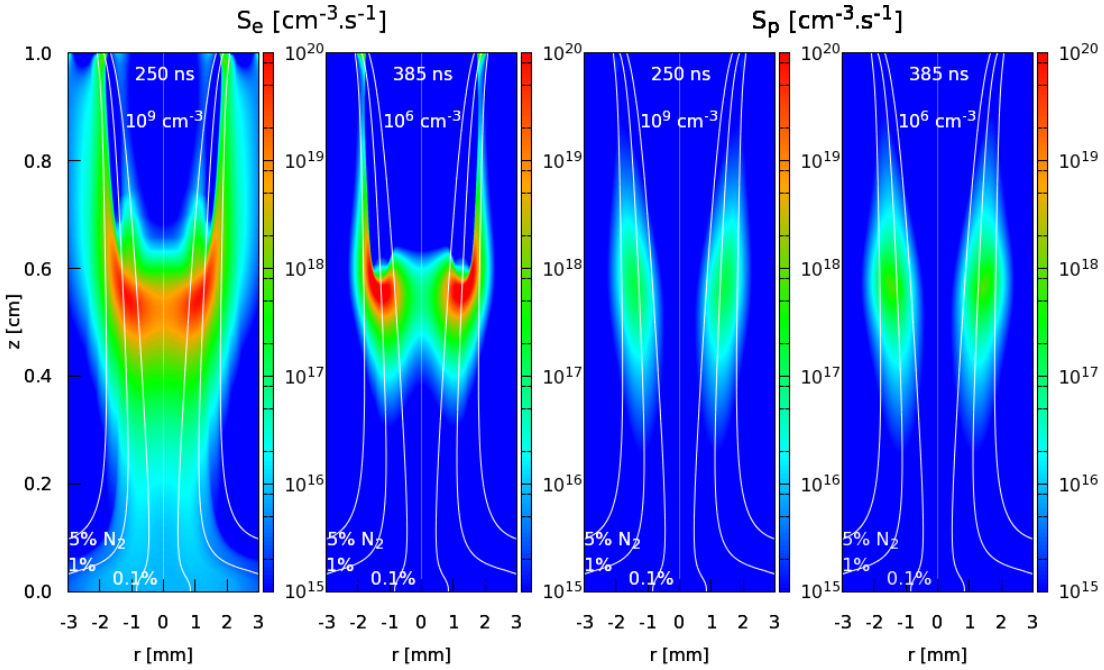

Figure III.33: Cross sectional views of the ionization source terms through electron-impact (on the left) and photoionization (on the right), during propagation in the plume, with L = 1.5 cm and d = 1.0 cm, 2 slm flow of He into N_2 atmosphere and V_P = +4 kV.

Propagation mechanisms in the plasma plume in He-N_2 and He-O_2 mixtures

Then, to identify in detail the propagation mechanisms in the plasma plume in positive polarity, we compare different source terms of both electron production and loss. The goal of this study is to identify the influent processes not only in the discharge front and in the plasma channel, but mostly ahead of the discharge front to set its path of propagation. Moreover, we want to understand how these processes vary with the gas mixing and with the choice of N_2 or O_2 as environment. In the cases studied here the geometry is the same as in the third case in Figure III.27. Two cases are studied, with 2 slm of He flowing into either N_2 or O_2. In Figures III.34-III.37 the distributions of some values of gas-mixture are represented by contours, and show that the distributions of He in N_2 and O_2 atmospheres are only slightly different, with He spreading a little more in N_2 than in O_2. The preionization is as usual n_{init} = 10^9 cm^{-3}. We have seen that in this case the role of the photoionization source term is not crucial. The source terms to be compared are shown in both cases at t = 210 ns, during propagation in the tube-target gap, and are the following:

- Figure III.34: Ionization through electron impact with ground-state He (direct) and with excited-state He (stepwise).
- Figure III.35: Ionization through electron impact with ground-state N_2/O_2 (direct) and with other O species (stepwise and others).
- Figure III.36: Penning ionization through quenching of excited He by N/O species and associative ionization by collisions between He excited species.
- Figure III.37: Recombination between electrons and N/O positive ions and attachment

between electrons and O neutral species.

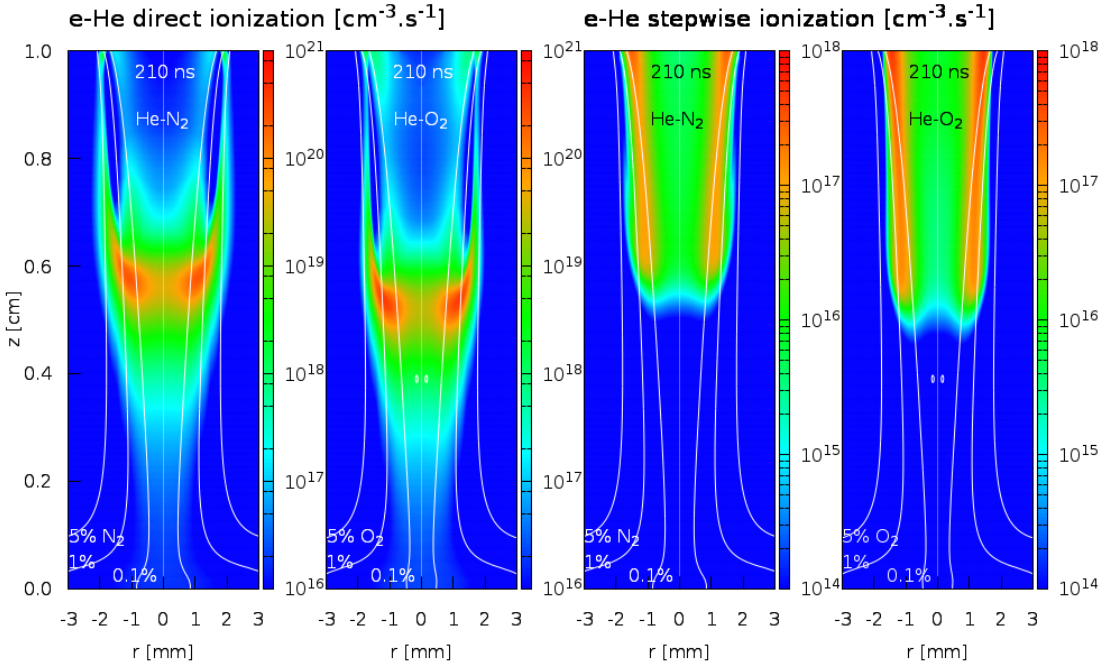

Figure III.34: Cross sectional views of the electron-impact He ionization (direct on the left, stepwise on the right) source terms, during propagation in the plume, with $L = 2.5$ cm and $d = 1.0$ cm, 2 slm flow of He into N_2 and O_2 atmospheres and $V_P = +6$ kV.

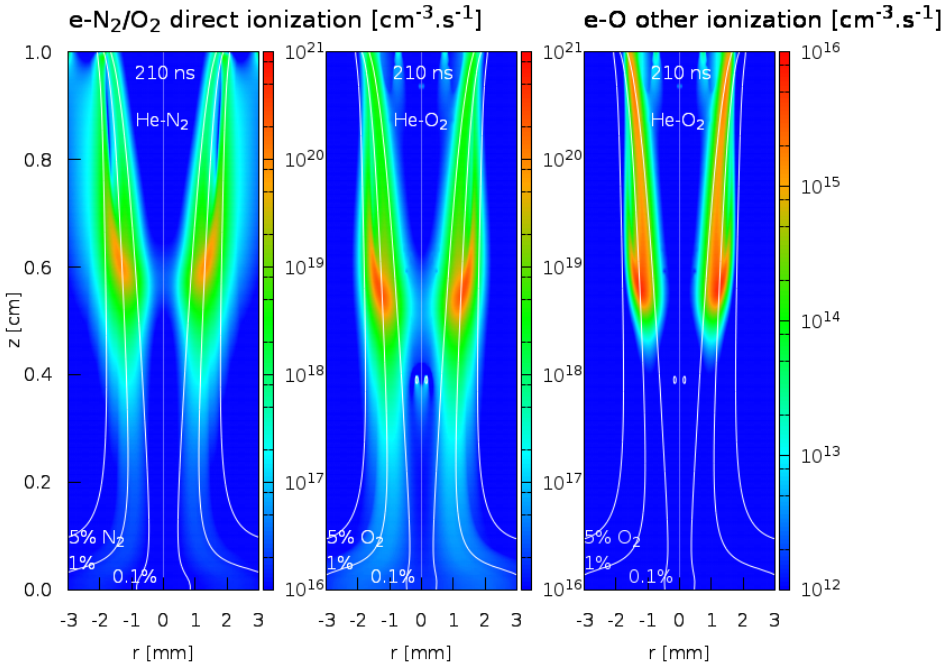

Figure III.35: Cross sectional views of the electron-impact N_2/O_2 ionization (direct on the left, stepwise/others on the right) source terms, during propagation in the plume, with $L = 2.5$ cm and $d = 1.0$ cm, 2 slm flow of He into N_2 and O_2 atmospheres and $V_P = +6$ kV.

Firstly, we should point out that, as only 10 ppm of N_2 or O_2 are present in the buffer gas, the discharge dynamics inside the tube is approximately the same in the two cases presented in

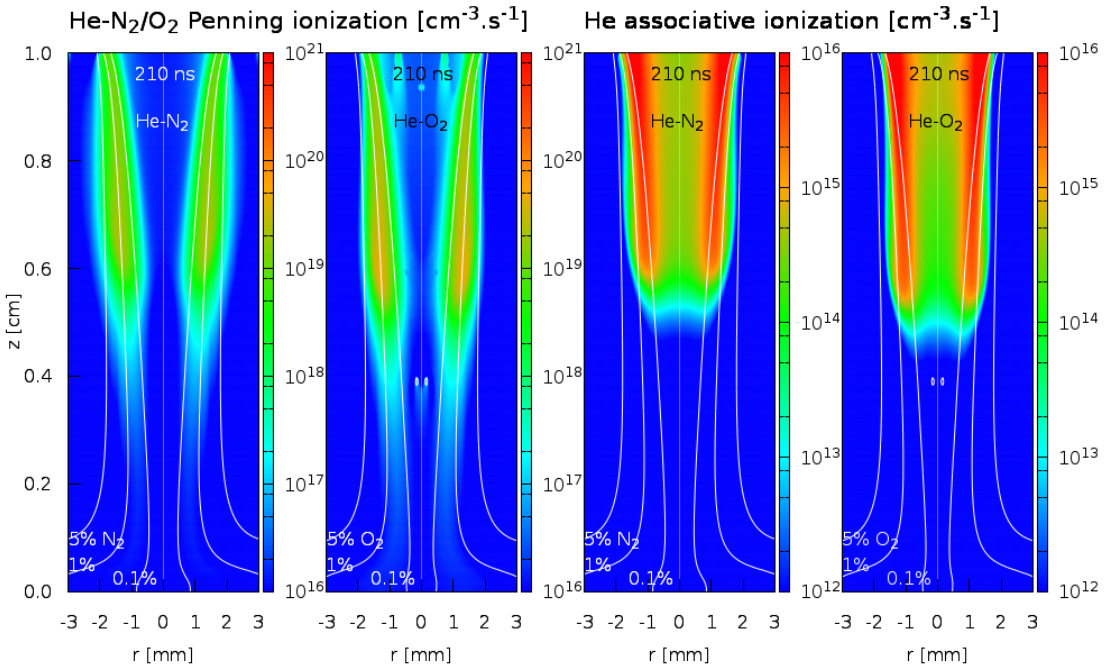

Figure III.36: Cross sectional views of the Penning ionization (on the left) and associative ionization (on the right) source terms, during propagation in the plume, with $L = 2.5$ cm and $d = 1.0$ cm, 2 slm flow of He into N_2 and O_2 atmospheres and $V_P = +6$ kV.

the figures. Therefore, the small difference in propagation of the discharge front (at $t = 210$ ns we see that the maximum of the e-He direction ionization source term is more advanced in He-O_2 than in He-N_2) is due to phenomena in the plume. In fact, we see that the main ionization processes present slightly higher values in the plasma plume of the He-O_2 mixture than in He-N_2. Yet, the shape formed by the plasma in the plume is very similar in the two cases, both with radial confinement along the propagation. Then, if we compare each source term, we see that the main ionization processes are electron-impact direct ionization and Penning ionization. These have been represented all in the same scale, between 10^{16} and 10^{21} cm^{-3}. The other ionization processes have a role in the plasma channel (mostly stepwise ionization of He) but are clearly less important in the discharge front and do not seem to contribute to the production of electrons ahead of the discharge head. Therefore, we can conclude that the production of seed electrons and the definition of the path of propagation is determined together by the electron-impact and Penning ionization reactions. In fact, even though the maximum of the e-He direct ionization source term is located in the region between 0.1 and 1% N_2/O_2, where the electric field and electron density are higher, ahead of the discharge it appears to have a centered structure, therefore higher where there is more He density. On the other hand, if we follow the ionization source terms ahead of the front, we see that ionization both through Penning and through e-N_2/O_2 reactions are not centered and tend to follow the 1% N_2/O_2 contour. The path of propagation is the result of the combination of these contributions. Later in section III.6.6, the importance of Penning ionization for the discharge structure will be further investigated.
Finally, in Fig. III.37, where the electron loss terms are compared, we can notice the main difference between He-N_2 and He-O_2 mixtures. This consists in the attachment, that presents values two orders of magnitude higher than electron-ion recombination. Even though attach-

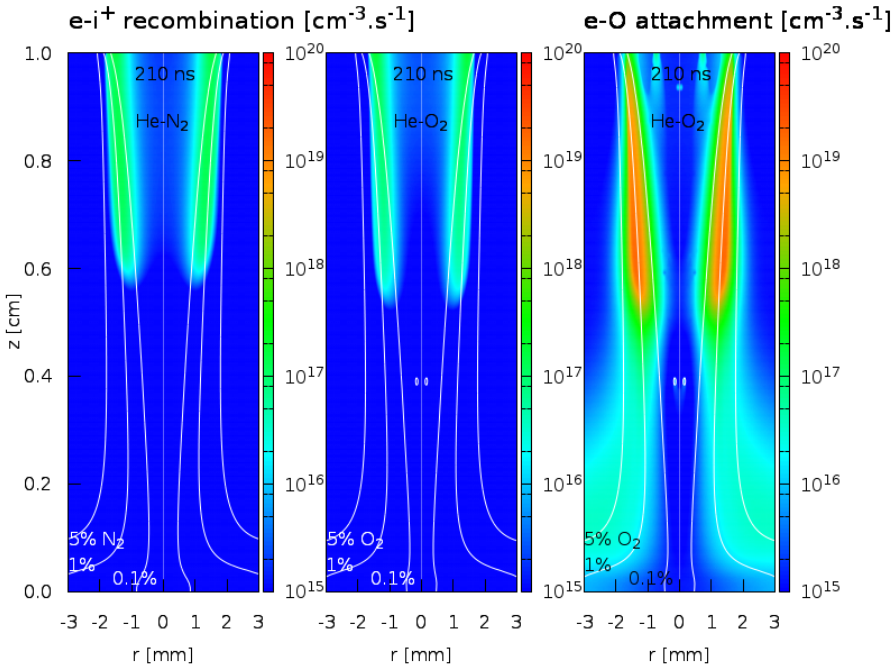

Figure III.37: Cross sectional views of the recombination (on the left) and attachment (on the right) loss terms, during propagation in the plume, with $L = 2.5$ cm and $d = 1.0$ cm, 2 slm flow of He into N_2 and O_2 atmospheres and $V_P = +6$ kV.

ment is visibly lower than the ionization source terms in the discharge front and in the plasma channel, it has a strong effect ahead of the discharge front, decreasing the availability of electrons in the regions with O_2 density higher than 1%, as suggested in the experimental study in *Xian et al.* [2014a]. For example, at $z = 0.2$ cm and $r = 2$ mm, where the relative density of O_2 is 5.56%, the electron density decreases by one order of magnitude in 200 ns, before the arrival of the discharge front. In longer timescales (either the interpulse ms timescale or the μs timescale for longer pulses), the attachment in the He-O_2 mixture leads to the shaping of the pre-discharge electron density according to the O_2 concentration. That is not the case in the He-N_2 mixture and is a factor that distinguishes the two mixtures and allows to consider O_2 as being closer to air as shielding gas, as will be shown later in appendix F.

III.6.6 Role of each property of the gas mixing in the plasma plume on discharge dynamics

In section II.4.3 we've seen that coupling the flow calculations with the plasma model requires:

- Removing the air tube between the dielectric tube and the target and consider that region as plasma;
- Consider each local mixture, i.e. the local densities of He and N_2 or O_2, in the electron-impact reaction rates, that are calculated from the EEDF (see Fig. II.3);
- Consider each local mixture in the chemistry source terms;
- Consider each local mixture in the photoionization source term (eq. (II.44));

- Consider each local mixture in the electron mobility and diffusion coefficients.

Here, to understand the effect of each of these procedures, we analyze some discharge results where some of these effects are isolated, i.e. where the coupling between plasma and flow is incomplete and therefore results can correspond to non-physical hypothesis. We take the case of a tube with $r_{in} = 1.25$ mm, $r_{out} = 2$ mm and 3 cm length (tip of powered point electrode of 1 mm radius at $z = 3.0$ cm), 5 mm tube-target distance, $V_P = +6$ kV, flow of 0.5 slm of He with 10 ppm of N_2 into a N_2 atmosphere and $n_{init} = 10^9$ cm^{-3}. In Figure III.38 the spatial distribution of the total ionization source term S_i is shown always at $t = 170$ ns in four different cases:

- First, there is no gas mixing, i.e. the plasma is always composed of He with 10 ppm of N_2. An air tube of $\epsilon_r = 1$ is present with $r_{in} = 1.25$ mm between the dielectric tube ($x = 0.5$ cm) and the target ($x = 0$). Charges impacting the air surface are conserved as surface charges, as it happens in the dielectric tube, i.e. charge conservation is guaranteed although the position of charges is limited by the tube. Moreover, the condition of electron flux from the tube towards the plasma exclusively due to secondary emission is kept.

- In the second case the air tube is removed, and therefore a gas of He with 10 ppm of N_2 occupies the whole region between the tube and the target.

- In the third case the flow of 0.5 slm is taken into account, with complete coupling between the plasma model and the flow calculation.

- In the fourth representation, while keeping the same coupling, Penning ionization has been removed, which allows to evaluate its impact on the discharge dynamics in the plasma plume.

Firstly, we should take note that inside the dielectric tube, until $t = 160$ ns, the discharge dynamics is the same in every case, with a tubular structure, and thus it only differs when the discharge front reaches the end of the tube of $\epsilon_r = 4$. Then, we see that with an air tube, the discharge propagates towards the target with the usual shape of a positive discharge propagating in a tube. Even though the change of the surrounding ϵ_r (from 4 inside the tube towards 1 in air) provokes a change of discharge structure, making it less tubular, the kind of radial confinement induced by gas mixing is not verified. Then, in the second case of Figure III.38, without the air tube, the discharge expands both radially and axially after reaching the end of the tube and, in the current case with close grounded target, propagates towards the target with centered maximum of S_e, as did the discharge without tube described in section III.2.3. The radial expansion in a He atmosphere has been verified also in *Breden et al.* [2012]. Finally, considering the actual distribution of gas-mixture induced by the flow of 0.5 slm, the plasma plume takes the shape studied in the previous sections, that cannot be described neither with the air tube nor with the homogeneous gas-mixture. In the fourth representation of Figure III.38 we confirm that in the current conditions Penning ionization does not play a crucial role in the radial confinement of the discharge and in the definition of its path of propagation, as reported by *Naidis* [2011b].
In Figure III.39 the spatial distribution of S_i again at $t = 170$ ns is compared between four

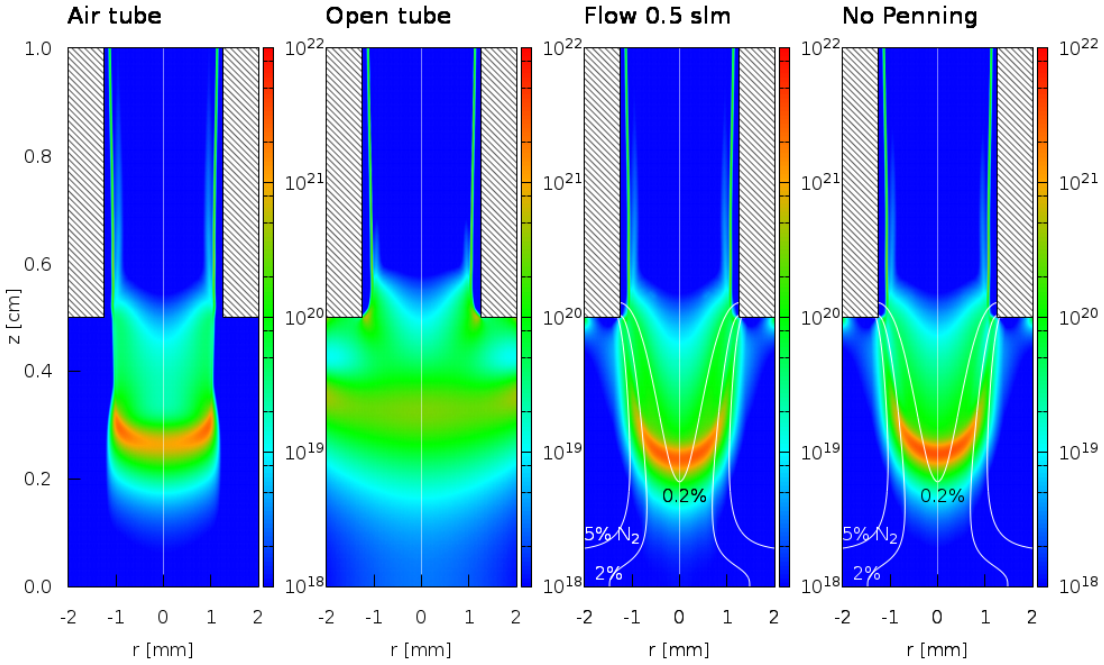

Figure III.38: Cross sectional views of the total ionization source term, for several mixing conditions, at $t = 170$ ns, with $L = 3.0$ cm, $d = 5$ mm, 0.5 slm of He flowing into N_2 atmosphere and $V_P = +6$ kV.

distinguished cases. The case from the previous figure with full plasma-flow coupling is maintained. Then, we also study the effect of partial plasma-flow coupling. In the second figure from the left, denoted "coupling only chem", is presented the situation where the coupling is performed exclusively on the chemistry source terms, i.e. neglecting the coupling in electron transport parameters and in photoionization, leaving them as for He with 10 ppm N_2. Then, the coupling is performed exclusively on the densities in the chemistry source terms (third figure, denoted "coupling only den") and on the electron-impact rate coefficients in the chemistry source terms (last figure, called "coupling only k").
Figure III.39 shows that taking into account local gas-mixtures exclusively in the determination of the electron-impact rate coefficients (figure "coupling only k") already leads to very strong differences in discharge dynamics in the plasma plume with respect to the case with homogeneous gas-mixture (figure "open tube"). In fact, with fixed densities (He with 10 ppm N_2) and mixture-dependent rate coefficients, as these coefficients are generally inversely proportional to N_2 density for concentrations higher than 0.1% (Fig. II.3), so are the chemistry source terms. Consequently, the discharge front tends to propagate where the N_2 density is the lowest (until 1%), which leads to its radial confinement in the plasma plume. If we take the reverse course, of keeping the electron-impact rate coefficients fixed for He with 10 ppm of N_2, and consider the variation in densities in the chemistry source terms (figure "coupling only den"), the result is reversed. As the electron-nitrogen rate coefficients are very high with low N_2 concentrations, that situation leads to very high source terms in the regions with more N_2 and then the discharge does not propagate in the He channel. Instead, the region with higher N_2 concentration ionizes when only a small electric field is present, before the arrival of the discharge front at the end of the tube, and then the discharge front joins the ionized region. Hence, the consideration of the mixture in the rate coefficients is crucial

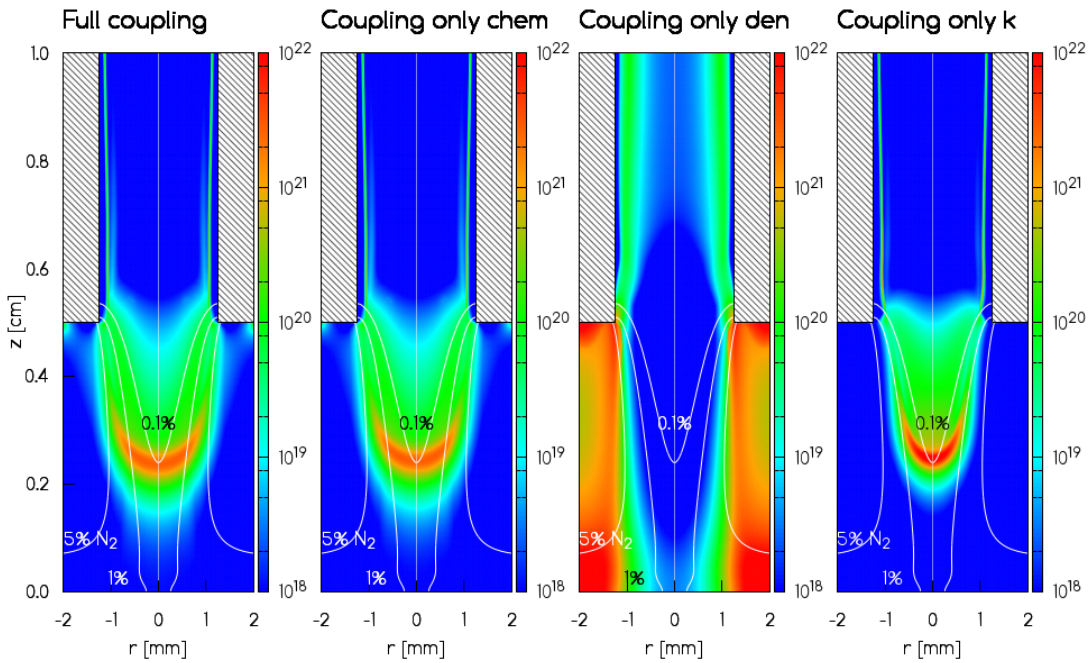

Figure III.39: Cross sectional views of the total ionization source term, for several conditions of plasma-flow coupling, at $t = 170$ ns, with $L = 3.0$ cm, $d = 5$ mm, 0.5 slm of He flowing into N_2 atmosphere and $V_P = +6$ kV.

to describe the plasma plume. However, when considering the local gas-mixture in the whole chemistry source term (figure "coupling only chem"), the two effects balance and the radial confinement takes place while being less extreme than in the case "coupling only k". Finally, it is important to conclude from Figure III.39 that the discharge dynamics with coupling in the chemistry source terms and with full coupling are very similar. Therefore, in the current conditions, the main effect of the plasma-flow coupling on the discharge dynamics consists on the changes it induces in chemistry, and not in the photoionization source term and electron transport parameters. This has been confirmed through other calculations isolating the effect of the coupling in photoionization and electron transport that have revealed a negligible influence when compared to that of chemistry.

One last note can be taken from the analysis of Figures III.38 and III.39, concerning the geometry conditions to induce the radial confinement of the discharge in the plasma plume. In fact, although the tube radius, the flow rate and the tube-target distance are different than in the previous sections (for instance than in Figure III.30), the same general discharge characteristics are present. In both cases there is a tubular front at the end of the tube with $V_P = +6$ kV. Then, even though the gas-mixtures along which the discharge front propagates in the plume are not exactly the same with the two geometries (N_2 concentration in the propagation region in the case with 0.5 slm is generally higher), the radial confinement of the ionization front in the plume is similar. This is due to the combination of the different parameters (geometry, flow, applied voltage) that define discharge structure, and is not explained by the N_2 distribution alone. We can conclude that for each of the studied parameters, the others can be adapted to find convenient radial confinement and production of species.

III.6.7 Conclusions

In this section, the discharge dynamics in the plasma plume has been studied in detail. This study has aimed to provide a basis to understand the results of next chapters where a plume is present, but also to improve our knowledge on the role of the gas mixing in the plasma plume on discharge dynamics. The main conclusions arising from this investigation can be listed as follows:

- The He-N_2 or He-O_2 radial gas mixing confines both the ionization front and the plasma channel. In the studied cases, the path taken by the discharge front is variable but usually follows the gas-mixtures with N_2 or O_2 relative densities between 0.1% and 5%.
- With positive polarity the ionization front tends to center in the plasma plume more easily and form a spherical head, while with negative polarity the plasma channel in the plume acquires a sword-like shape.
- The path of propagation, the shape of the plasma plume and thus the distribution of species production are not determined solely by the values of gas-mixture but also by the electric field distribution resulting from the combination of all the parameters.
- The identification of the propagation mechanisms in the plume, and particularly the evaluation of the role of photoionization, is highly dependent on preionization.
- In our standard conditions, the most important propagation mechanisms are electron-impact direct ionization of both He and N_2/O_2 and Penning ionization.
- Penning ionization is not essential for the definition of the discharge structure.
- When coupling the distribution of gas-mixture with the plasma model, the most important aspect to describe the radial confinement of the discharge is the consideration of the variable mixture in the chemistry source terms.
- To account for mixture is crucial both due to the densities in the chemistry source terms, where the mixture leads the discharge to expand radially, and to the electron-impact rate coefficients, where the mixture leads the discharge to confine radially. The electron-impact ionization source terms and the path of discharge propagation are then determined by the balance between the two features.

III.7 Conclusions

In this chapter, the dynamics of ignition and propagation of He plasma jets has been characterized. The discharge dynamics inside tubes and in the plasma plume has been assessed, before the discharge interacts with a grounded metallic target. The following conclusions have been taken:

(i) The mechanical confinement induced by the introduction of a tube with $\epsilon_r = 1$ significantly increases the transfer of electric potential in the plasma channel, which leads to an increase of electric field on the discharge front, charged species densities and velocity of propagation. With positive polarity, the increase of potential is achieved through the increase of ρ, while with negative polarity it is due to the deposition of σ.

(ii) Point-plane discharges without tube in a 99% He - 1% N_2 environment have very similar discharge structures with positive and negative polarities of applied voltage. With tube, the discharge dynamics and structure inside the tube have been found to be significantly different with different polarities, in agreement with experimental results: more homogeneous in the negative case and more filamentary with positive polarity.

(iii) The tubular structure of the discharge propagating inside the tube is similar in all electrode configurations where the powered electrode is placed inside the tube.

(iv) The velocity of discharge propagation and the discharge radius inside the tube tend to be proportional to the value of applied voltage at each moment.

(v) No significant differences in discharge dynamics and structure inside the tube have been obtained with different He-N_2 and He-O_2 mixtures (10 ppm until 1% N_2 or O_2) as buffer gas.

(vi) Considering plasma jet configurations, the path of propagation of the discharge front and the shape of the plasma plume are not determined uniquely by the values of gas-mixture, but are rather a consequence of all the discharge conditions: geometry, flow rate and applied voltage. The results reported in the literature concerning the different structure of positive and negative discharges in the plasma plume have been confirmed.

(vii) The path of propagation of positive discharges is defined by the production of seed electrons ahead of the discharge front and the identification of the mechanisms for that production is highly dependent on preionization.

(viii) In our standard conditions, with high preionization, the most important propagation mechanisms are electron-impact direct ionization of both He and N_2/O_2 and Penning ionization, even though this last process is not crucial for the discharge structure.

(ix) In our conditions the most important aspect in the plasma-flow coupling is the consideration of the variable mixture in the chemistry source terms. To account for gas mixing in the densities in the chemistry source terms leads the discharge to expand radially, and in the electron-impact rate coefficients leads the discharge to confine radially. Therefore, the electron-impact ionization source terms and the path of propagation are determined by the balance between these two features.

Chapter IV

Study of a plasma jet interacting with a grounded metallic target: comparison with experiments

Contents

IV.1 Introduction 112

IV.2 Studied conditions to comply with experiments 113

IV.3 Dynamics of discharge propagation inside a dielectric tube closed by a grounded metallic target 115

IV.4 Influence of the discharge dynamics on the electric field outside the dielectric tube: comparison with experiments 122

IV.5 Rebound front as ionization wave of partial neutralization of the plasma channel 125

IV.6 Derivation of discharge properties from the electric field outside the dielectric tube: how simulations can complement experiments 128

IV.7 Dynamics of first ionization and rebound fronts in plasma jet configurations and influence on the production of reactive species 133

IV.8 Conclusions 138

IV.1 Introduction

We have seen in section I.4 that currently many efforts are done to carry out detailed characterization of plasma jets and that different groups are working on several diagnostics to measure the electric field in plasma jets. Then, in section I.3 we have reported on the state of the art about jet interaction with different kinds of targets. In this chapter, we characterize the evolutions of electric field in time and space in plasma jets, in the particular case of interaction with a grounded metallic target.
In *Darny* [2016]; *Darny et al.* [2017b], a detailed experimental study has been carried out to measure the helium metastable density and electric field components, both spatially and temporally resolved, for a plasma jet interacting with a grounded metallic target. The time-resolved electric field components have been measured with an electro-optic probe in the vicinity of the dielectric tube [*Robert et al.*, 2015]. The experimental set-up used in *Darny et al.* [2017b] and the resulting temporal profiles of the axial and radial electric field components measured at a given axial position in the vicinity of the tube are shown in Figure IV.1. The pulse of applied voltage has 2.2 μs rise-time, -18 kV amplitude and then approximately 2 μs fall-time. Figure IV.1 shows results obtained for the case of free jet and with a metallic grounded target at 1 cm from the end of the tube.

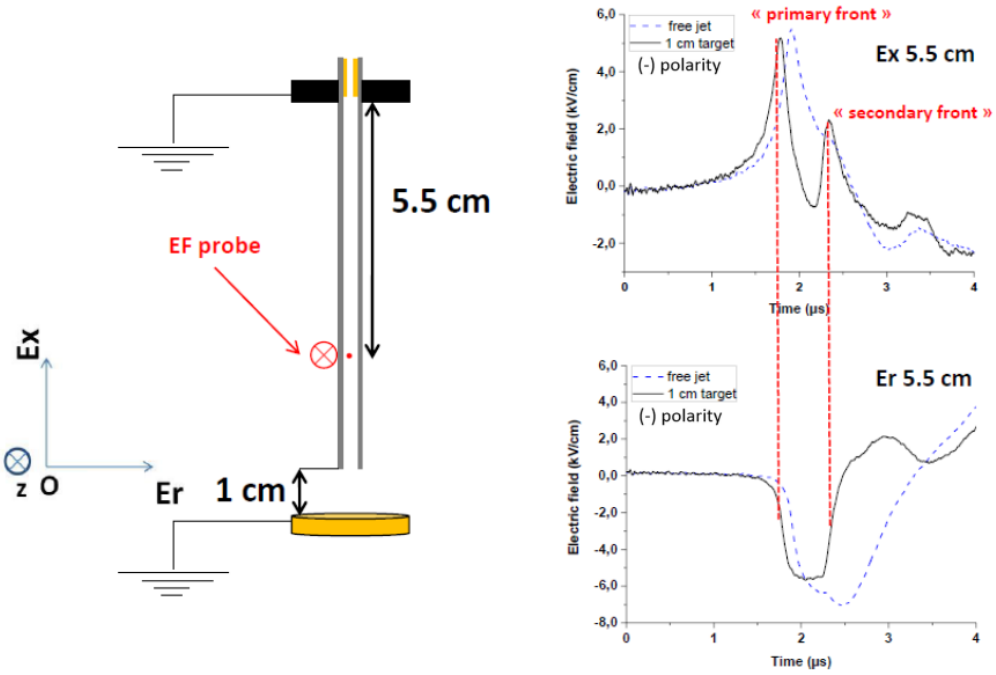

Figure IV.1: Experimental set-up from *Darny et al.* [2017b] and corresponding results of $E_z(t)$ and $E_r(t)$ measured with a probe at $r = 6$ mm in the middle of the tube.

For both positive and negative polarities, with a plasma jet impinging a grounded metallic target, it has been shown in *Darny et al.* [2017b] that the axial component of the electric field outside the tube presents a first peak corresponding to the first ionization wave propagating from the high voltage electrode towards the metallic target. After the impact of the first ionization wave on the grounded metallic target, a second peak is observed, corresponding to a second ionization front propagating more rapidly from the target to the high voltage electrode. The radial component of the electric field outside the tube is observed to increase

(in absolute value) when the first peak of the axial component of electric field is reached, and to decrease (in absolute value) when the second peak of axial electric field is reached, as shown in Figure IV.1. Then, smaller peaks of the axial component of the electric field are observed in *Darny et al.* [2017b], attributed to several reflections of ionization waves. In *Darny et al.* [2017b], the rebounds of ionization waves observed are attributed to the impedance mismatching between the conductive ionized channel, the high voltage electrode and the grounded metallic plane. Indeed, after the impact of the first ionization wave on the grounded metallic target, an ionized channel is formed between the two metallic electrodes. This channel acts as a transient transmission line between the electrodes. The high voltage applied on the inner electrode is transiently and partially transferred to the metallic target through the conductive ionized channel, with a voltage drop due to the channel impedance. The impedance mismatching between the ionized channel impedance and the very low metallic target impedance leads to a reflection phenomenon, with a secondary ionization front starting from the metallic target towards the inner electrode. Then, successive but damped reflections propagate in the ionized channel between both metallic electrodes, as long as the ionized channel persists.
In this chapter, we study the evolutions of electric field in He plasma jets interacting with a grounded metallic target for positive and negative polarities of applied voltage. One of the goals of this work is to better understand the electric field measurements carried out in the GREMI laboratory in Université d'Orléans with an electro-optic probe outside the dielectric tube (part of it published in *Darny* [2016]; *Darny et al.* [2017b]). Part of the work presented in this chapter has been published in *Viegas et al.* [2018a]. In section IV.2, the geometry and discharge conditions studied in this chapter are presented, taking the experimental conditions into account. First, in section IV.3, we discuss the discharge dynamics inside a dielectric tube filled with a He-N_2 gas mixture, which is closed by a grounded metallic target. This simplified geometry is chosen to study the time evolutions of the electric field at several points inside the dielectric tube and then, outside the dielectric tube in section IV.4, with no influence of the end of the tube nor the gas mixing downstream the tube exit. Then, in section IV.5 the propagation of the second ionization front is explained through a scheme supported by simulation results. In section IV.6, using the same configuration, we evaluate in which conditions the discharge properties inside the tube, and in particular the charge densities in the plasma, can be retrieved from electric field measurements outside the tube. Finally, in section IV.7, a plasma jet configuration is used, with 5 mm distance between the end of the tube and the target, where the buffer gas mixes with the environment gas. Using this geometry, the influence of the first ionization and rebound fronts on the production of reactive species in the plasma plume close to the grounded target is discussed in both He-N_2 and He-O_2 mixtures.

IV.2 Studied conditions to comply with experiments

The discharge set-ups used in this chapter are shown in Figure IV.2. A dielectric quartz tube with a relative permittivity of $\epsilon_r = 4$ and with an internal radius $r_{in} = 2$ mm and an outer radius $r_{out} = 3$ mm is used as in *Darny et al.* [2017b]. The length of the tube is of 3.0 cm in sections IV.3 and IV.6, between $z = 0$ and $z = 3.0$ cm. Then, in section IV.4,

we also consider a 5 cm length tube, set between $z = -2.0$ cm and $z = 3.0$ cm. Finally, in section IV.7, we consider a plasma jet configuration with a 2.5 cm length tube and 0.5 cm tube-target distance. As in the experiments [*Darny et al.*, 2017b] the powered electrode is set inside the tube, here a point electrode composed of a cylinder with 4 mm length and 1 mm radius and a spherical tip of 1 mm radius is set inside the tube. It has been verified in section III.3 that with different powered electrodes inside the tube the resulting discharge structure is similar. The axial position of the tip of the point is fixed at $z = 2.5$ cm. A point holder, a metallic disc with a 0.3 cm radius, is set at $z = 3.0$ cm. A grounded metallic target is set at $z = 0$ ($z = -2.0$ cm with the 5 cm tube). As shown in Figure IV.2, the discharge set-ups are placed inside a grounded cylinder with a radius of 10 cm. The discharge is powered by a voltage that rises linearly between 0 and V_P, then is constant with a plateau value V_P, and then decreases back to 0. The rise-time is 50 ns and the voltage can be either positive or negative, with plateau values of $V_P = +6$ kV or $V_P =$ -6 kV. The plateau lasts until $t = 300$ ns ($t = 1000$ ns with the 5 cm tube). Then, the applied voltage decreases linearly during 50 ns and is zero from $t = 350$ ns until the end of the calculation at $t = 600$ ns.

In experiments [*Darny et al.*, 2017b], the helium flow (2 slm) is high enough to have a discharge that clearly impacts the target. In this chapter we consider two different conditions of gas mixture. These are slightly different than those used in *Viegas et al.* [2018a]. In sections IV.3 to IV.6, a volume filled with a static gas 99.9% He - 0.1% N_2 is considered, filling the domain between the powered electrode and the grounded target and radially from $r = 0$ to r_{in}, similarly to *Viegas et al.* [2018a] where 99% He - 1% N_2 is used. In *Viegas et al.* [2018a], to study the influence of the electric field evolutions on species production in jet configuration, a 2.5 cm tube is used with 0.5 cm tube-target distance. In the tube-target gap, Helium-air mixing is neglected. The mixture is considered uniform until $r = r_{in}$ and a dielectric with $\epsilon_r = 1$ is considered for $r > r_{in}$. Here, unlike in *Viegas et al.* [2018a], in section IV.7 we consider a flow of 2 slm of either 99.9% He - 0.1% N_2 or 99.9% He - 0.1% O_2 flowing downstream into a N_2 or O_2 environment, respectively. The spatial distribution of N_2 in the He-N_2 mixture is presented in Figure IV.2. There are also added the contour curves of 0.5% and 5% N_2 in the He-N_2 mixture, to put forward the mixture region studied in this chapter. As shown in section II.4.3, the spatial distribution of N_2 in a He-N_2 mixture is very similar to that of O_2 in a He-O_2 mixture, particularly considering a high flow of 2 slm and a short tube-target distance of 0.5 cm. Therefore, the spatial distribution of O_2 in the He-O_2 mixture is omitted from Figure IV.2. The kinetic schemes used to describe the He-N_2 and He-O_2 plasmas at atmospheric pressure are the ones presented in section II.4.2. As repetitive voltage pulses are used in experiments [*Bourdon et al.*, 2016; *Darny et al.*, 2017b] ($f = 1$ kHz), we take into account a uniform initial preionization density $n_{init} = 10^9$ cm^{-3} of electrons and positive ions (N_2^+ or O_2^+) in the gas-mixture in the tube.

A cartesian mesh is used with an axial size of 10 μm. Radially, the mesh size is 10 μm between $r = 0$ and r_{out} and then is expanded using two geometric progressions until reaching the boundary of the computational domain (20 cells between $r = 0.3$ cm and $r = 0.4$ cm and then 50 cells until $r = 10$ cm). This refinement requires, for the smallest domain considered in this chapter, a mesh of $n_z \times n_r = 3000 \times 370 = 1.1$ million points. The average computational time required for a simulation run to obtain the results presented in this chapter is of one day with 32 MPI processes on the multicore cluster "Hopper".

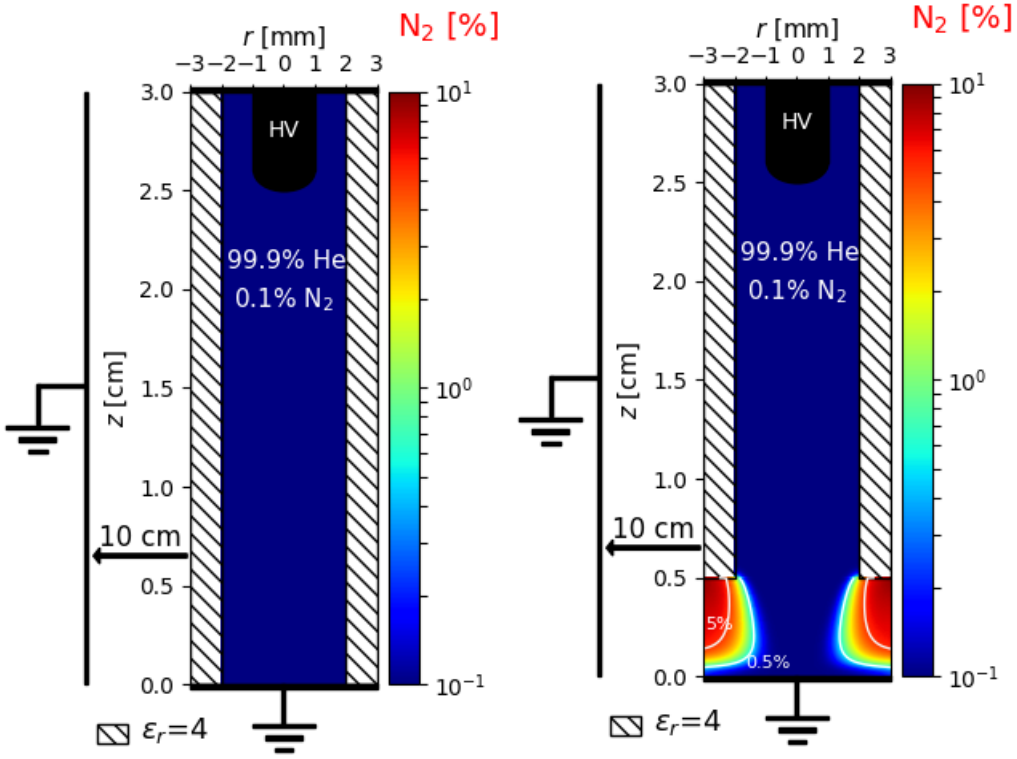

Figure IV.2: Side view schematics of the discharge set-ups used in this chapter. On the left, the set-up used in sections IV.3, IV.4 and IV.6: the tube is closed by the target and there is no gas mixing. On the right, the set-up used in section IV.7: the He buffer gas and the N_2 environment gas mix at the end of the tube. The colour plot and the white curves show the N_2 spatial distribution in the He-N_2 mixture.

IV.3 Dynamics of discharge propagation inside a dielectric tube closed by a grounded metallic target

In this section, simulation results are presented on the dynamics of the discharge in a 3 cm long dielectric tube touching the grounded target at $z = 0.0$ cm. This simplified geometry is chosen to study the time evolutions of electric field at several points with no influence of the end of the tube nor the gas mixing downstream the tube exit.

Figures IV.3 and IV.4 show the time sequence of the distributions of absolute values of electric field E_t in the discharge, for applied voltages of $V_P = +6$ kV and $V_P = -6$ kV, respectively. In each figure, the two cross sectional views on the left show the distribution of absolute values of electric field at the beginning of discharge propagation close to the tip of the point electrode and then when the ionization front crosses the position $z = 1.0$ cm, and the two cross sectional views on the right show the distribution of E_t when the ionization front hits the grounded target and then a few nanoseconds later.

During the discharge propagation, Figures IV.3 and IV.4 show that the maximum of electric field in the ionization front is higher with positive polarity of applied voltage than with negative polarity ($\sim$ 25 vs 10 kV/cm). To better compare the discharge structures for both polarities, Figures IV.5 and IV.6 show the time sequence of the distributions of the electron-

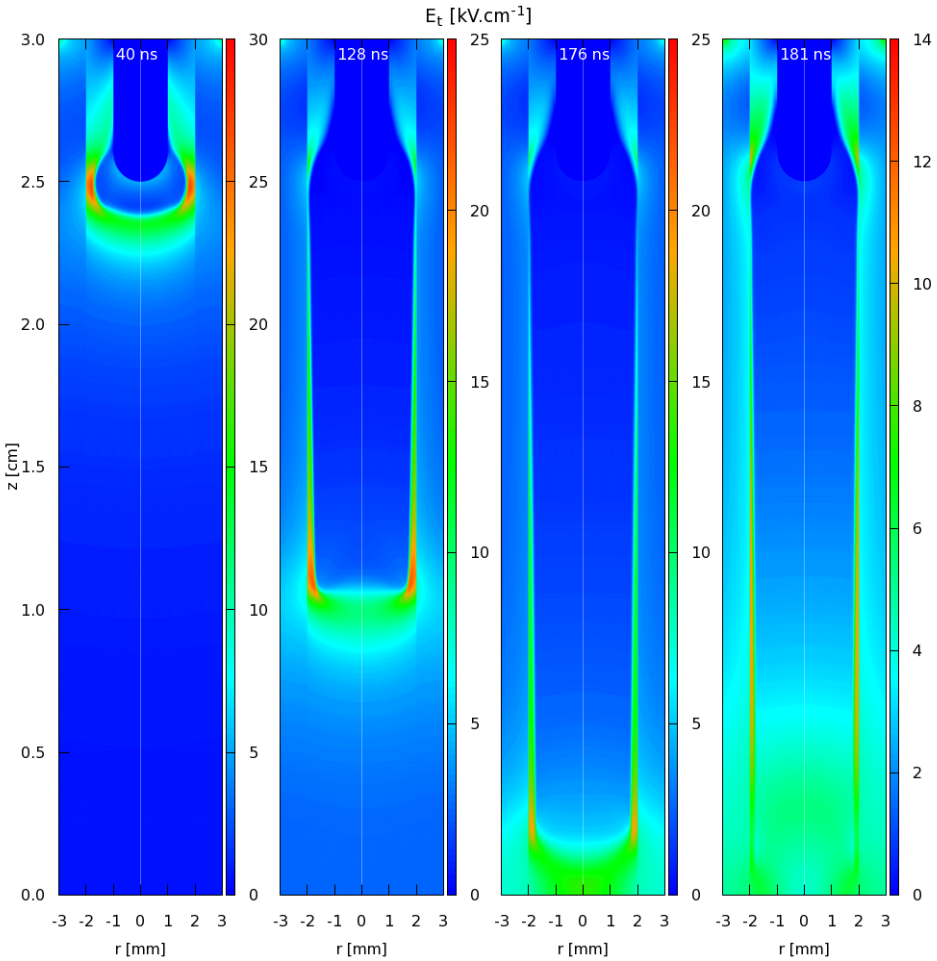

Figure IV.3: Cross sectional views of the magnitude of the electric field at t = 40, 128, 176 and 181 ns, for a 3 cm long tube closed by a grounded target for V_P = +6 kV.

impact ionization source term S_e in the discharge, for applied voltages of V_P = +6 kV and V_P = −6 kV, respectively. At t = 128 ns (for V_P = +6 kV) and t = 138 ns (for V_P = −6 kV), Figures IV.3 to IV.6 show that the maximum of electric field during propagation with positive polarity is close to the tube, while the front of propagation with negative polarity is more radially homogeneous inside the tube. These effects of the polarity on the structure of discharges propagating in dielectric tubes have been already observed and discussed in section III.2. After the impact on the grounded target, Figures IV.3 and IV.4 show that the magnitude of the electric field in the discharge decreases, as a conductive channel is now formed between the metallic point electrode and the metallic grounded target. For both polarities, Figures IV.5 and IV.6 show the propagation of a second front from the grounded target towards the powered electrode (for 176 ≤ t ≤ 257 ns for V_P = +6 kV, and for 206 ≤ t ≤ 307 ns for V_P = -6 kV). In the following, this second front, also observed experimentally in plasma jets impacting a grounded metallic target [*Darny*, 2016; *Darny et al.*, 2017b], is called "rebound front". In experiments [*Darny*, 2016; *Darny et al.*, 2017b; *Gerling et al.*, 2012] several reflections are observed as long as the ionized channel is persisting. In this work, we focus on the first rebound front.

To compare the dynamics of discharges for positive and negative polarities, Figure IV.7 shows the axial position of the maximum axial component of electric field on the symmetry axis

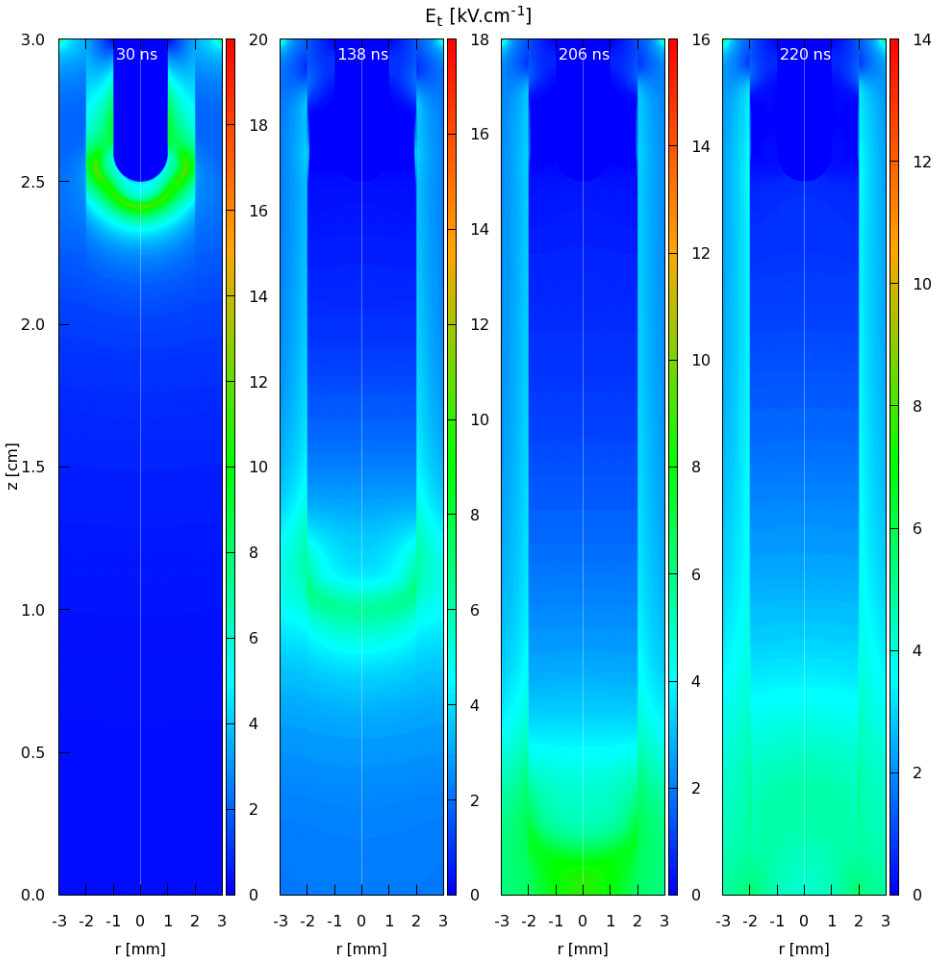

Figure IV.4: Cross sectional views of the magnitude of the electric field at t = 30, 138, 206 and 220 ns, for a 3 cm long tube closed by a grounded target for V_P = -6 kV.

$|E_z|(r = 0)$ inside the tube for the same conditions as in Figures IV.3 to IV.6. These results are obtained post-treating output files with a temporal resolution of 1 ns. Figure IV.7 shows that the ignition of the ionization front at the point electrode occurs slightly earlier ($t = 27$ ns) for a negative applied voltage than for a positive one ($t = 29$ ns). However, the propagation of the ionization front is slightly faster in positive polarity than in negative polarity as often reported in plasma jet experiments [*Darny et al.*, 2017b; *Jiang et al.*, 2009; *Xiong et al.*, 2010; *Naidis*, 2011a]. For the positive polarity, the propagation velocity between the point and the target is on average $\sim 2.0 \times 10^7$ cm/s (20 cm/μs) with an increase near the target up to 6.7×10^7 cm/s (67 cm/μs). For the negative polarity, the velocity of propagation between the point and the target is lower, on average $\sim 1.7 \times 10^7$ cm/s (17 cm/μs) with an increase near the target up to 8.1×10^7 cm/s (81 cm/μs). Then, the ionization front touches the grounded target at $t = 176$ ns in positive polarity and only at $t = 206$ ns in negative polarity. After the impact on the grounded metallic target, Figure IV.7 shows that for both polarities a maximum of electric field can be also detected and this maximum propagates from the grounded target towards the powered electrode. This corresponds to the propagation of the rebound front. As shown on Figures IV.3 and IV.4, during the rebound front propagation, the electric field values are lower than in the first ionization front, and due to the electric field redistribution, the electric field at the point electrode becomes of

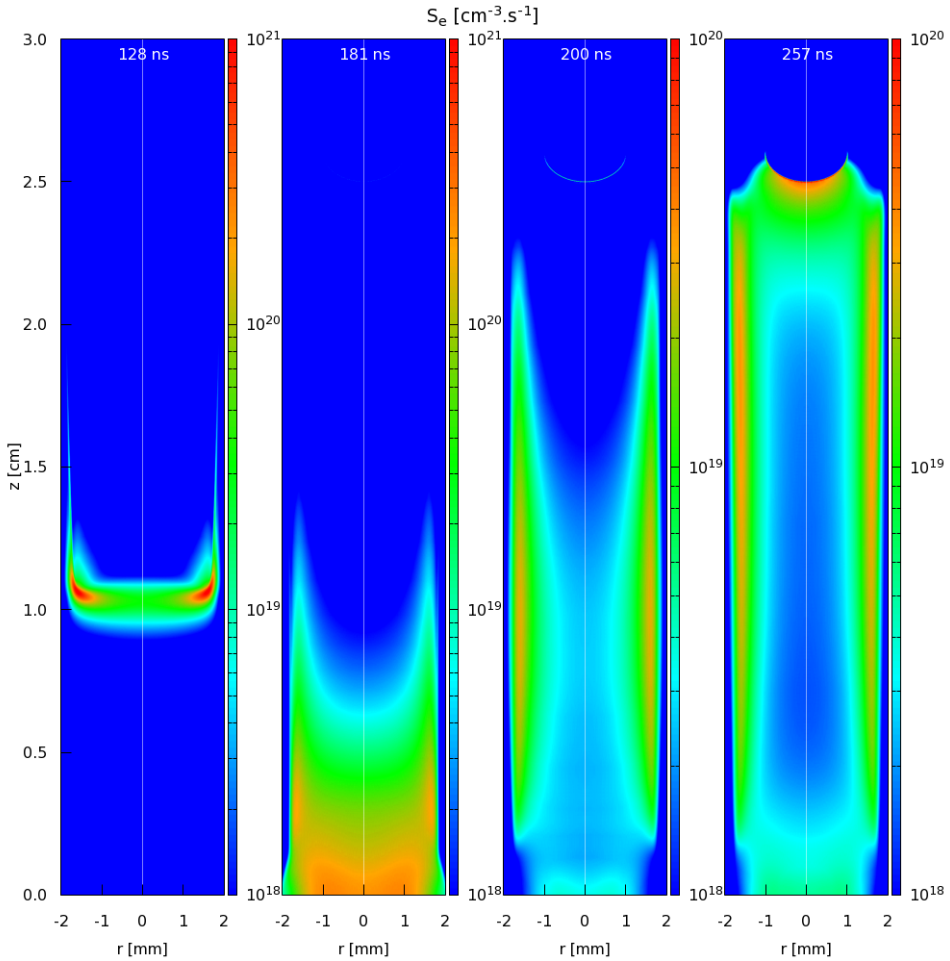

Figure IV.5: Cross sectional views of the electron-impact ionization source term at $t = 128$, 181, 200 and 257 ns, for a 3 cm long tube closed by a grounded target for $V_P = +6$ kV.

the same order as the maximum electric field in the rebound front (as shown also for S_e in Figures IV.5 and IV.6). Then, in Figure IV.7, after the impact on the grounded metallic target, filled circles correspond to positions found for the maximum of $|E_z|$ in the whole domain until the maximum is detected again at the point electrode, and crosses correspond to positions of the maximum of $|E_z|$ found by specifying the direction of propagation of the rebound front from the target towards the point electrode. Figure IV.7 clearly shows that the propagation velocity of this rebound front is higher than the one of the first ionization front for both polarities. For the positive polarity, the propagation velocity of the rebound is on average $\sim 3.1 \times 10^7$ cm/s (31 cm/μs), i.e. about 1.5 times the one of the first ionization front. For negative polarity, it is on average $\sim 2.5 \times 10^7$ cm/s (25 cm/μs), also around 1.5 times as fast as the first ionization front propagation velocity. It is interesting to note that similar velocity increases between the first ionization front and the rebound front have been observed experimentally in *Darny* [2016]; *Darny et al.* [2017b]. The rebound front touches the high voltage point electrode at $t = 257$ ns in positive polarity and at $t = 307$ ns in negative polarity.

Figure IV.8 presents the temporal evolution of E_z on the symmetry axis ($r = 0.0$ cm), for the same conditions as Figures IV.3 to IV.7, and at different axial positions: $z = 0.25$, 1.0 and 1.75 cm between the grounded target located at $z = 0.0$ cm and the powered point electrode

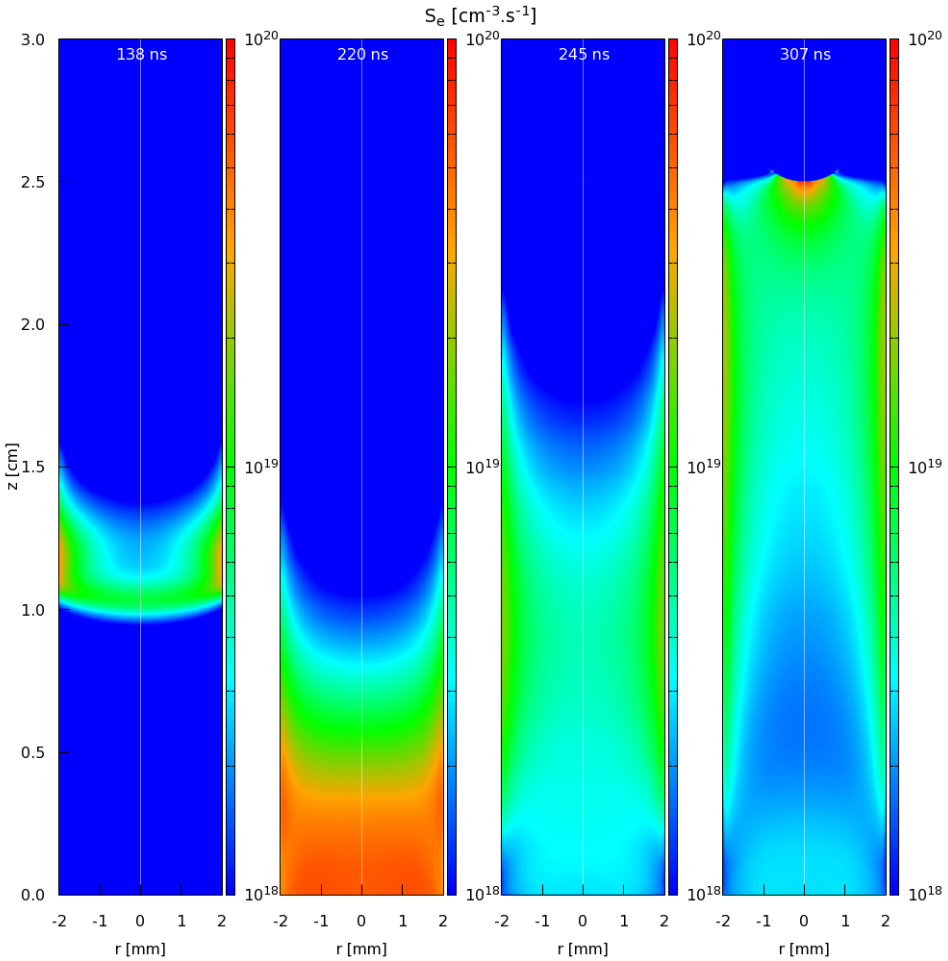

Figure IV.6: Cross sectional views of the electron-impact ionization source term at t = 138, 220, 245 and 307 ns, for a 3 cm long tube closed by a grounded target for V_P = -6 kV.

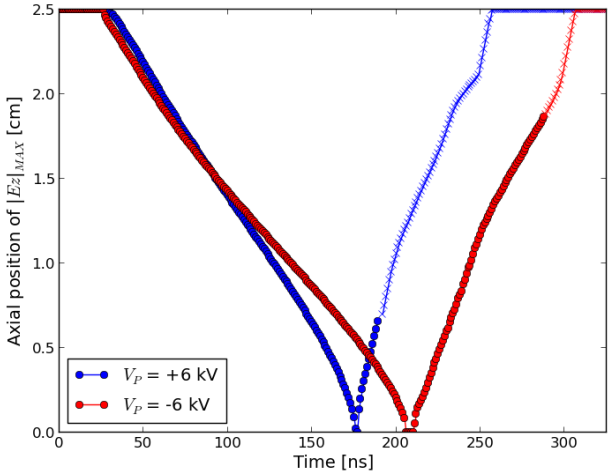

Figure IV.7: Temporal profiles with ns resolution of the axial position of the maximum of $|E_z|$ on the symmetry axis ($r = 0$), for the same conditions as in Figures IV.3-IV.6. After the impact on the grounded metallic target ($z = 0$), filled circles correspond to the positions found for $|E_z|_{MAX}$ in the whole domain, until the maximum is detected again at the point electrode, and crosses correspond to positions of $|E_z|_{MAX}$ found by specifying the direction of propagation of the rebound front from the target towards the point electrode.

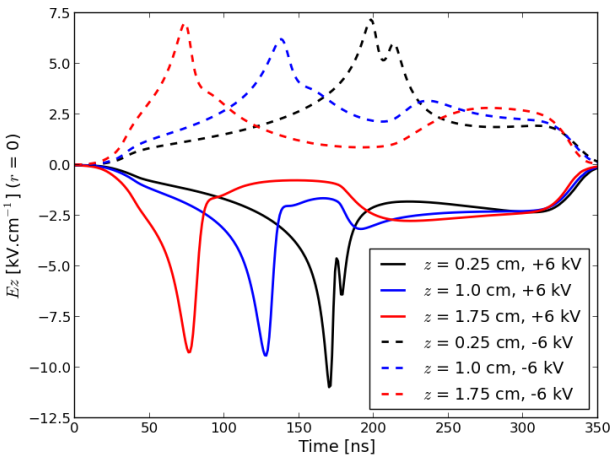

Figure IV.8: Temporal profiles of E_z at $r = 0$ and at $z = 0.25$, 1.0 and 1.75 cm, for the same conditions as in Figures IV.3-IV.6. Solid lines: $V_P = +6$ kV. Dashed lines: $V_P =$ -6 kV.

at $z = 2.5$ cm. In Figure IV.8 we notice that for all axial positions and for both polarities, there are two peaks of $|E_z|$ during the temporal evolution shown up to $t = 350$ ns, when the voltage applied to the powered electrode is back to zero. The first peak appears earlier for axial positions closer to the powered point electrode and corresponds to the first ionization front. Between $z = 1.0$ and 1.75 cm, the discharge propagation is stable and the peak of $|E_z|$ on the symmetry axis is of $\sim$ 7.5 kV/cm for negative polarity and $\sim$ 10 kV/cm for positive polarity. Close to the grounded target, at $z = 0.25$ cm, the absolute values of the first peak of electric field increase, leading to the acceleration of the discharge front observed on Figure IV.7. After this first peak of $|E_z|$, a second peak of electric field is observed related to the rebound propagation from the target towards the point electrode, as it appears earlier for positions closer to the target. Close to the target, at $z = 0.25$ cm, the second peak of $|E_z|$ has a magnitude of $\sim$ 7 kV/cm for $V_P = +6$ kV and of $\sim$ 6 kV/cm for $V_P =$ -6 kV and $|E_z|$ decreases rapidly after the peak. At $z = 1.0$ and 1.75 cm, the second peak has a magnitude of $\sim$ 3 kV/cm for both polarities with a slow decrease after the peak. It is interesting to notice that the times at which the second peak is registered are very close for all studied axial positions, confirming that the propagation of the return wave is much faster than the first ionization front as observed on Figure IV.7. Finally, between $t = 300$ ns and $t = 350$ ns, as the applied voltage evolves from V_P to zero, it is visible that all the fields assessed in Figure IV.8 decrease in absolute value until ~ 0. In fact, at $t = 350$ ns the plama is connecting two electrodes (point and target) at the same applied voltage, which is zero. In such conditions, the impedance in the plasma is no longer required to connect the two voltages and the potential drop in the plasma, along with E_z, decrease to zero.
As the discharge is confined in a dielectric tube, it is interesting to study the time evolution of surface charges on the tube wall during the propagation of the first ionization and the rebound fronts. Figure IV.9 shows the profiles of the net surface charge density σ deposited on the inner dielectric wall ($r = 0.2$ cm) at several moments in time for $V_P = +6$ kV (on the left) and $V_P =$ -6 kV (on the right).

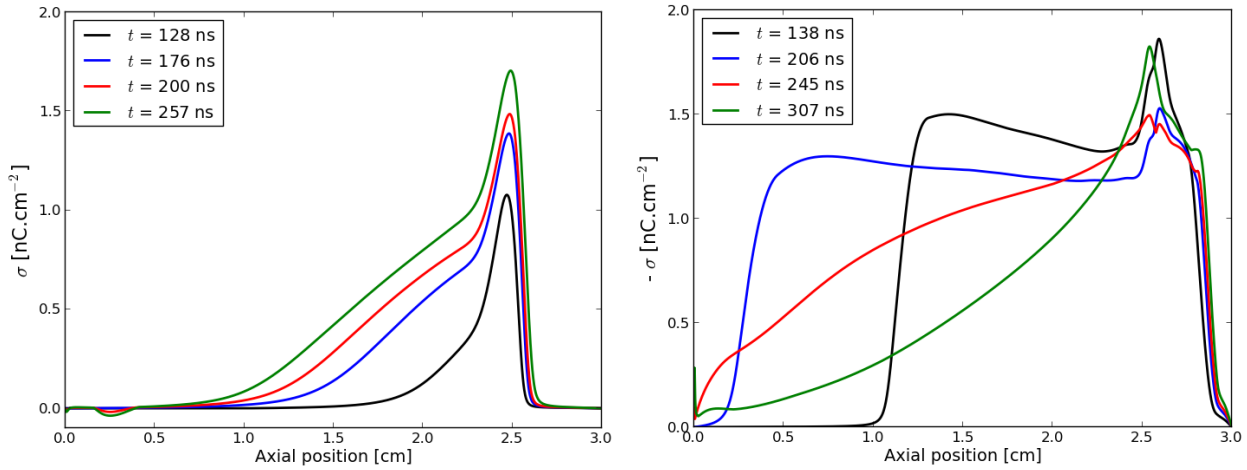

Figure IV.9: Axial profiles of σ deposited on the tube wall. On the left, $\sigma(z)$ at t = 128, 176, 200 and 257 ns, for the same conditions as in Figure IV.3 with V_P = +6 kV. On the right, $\sigma(z)$ at t = 138, 206, 245 and 307 ns, for the conditions of Figure IV.4 with V_P = -6 kV.

Figure IV.9 shows that in both cases the surface charge distribution is not uniform along the inner tube surface and that the surface charge distribution evolves during the discharge dynamics. Due to the radial expansion of the discharge after its ignition at the point electrode, we note that a peak of surface charges is observed on the dielectric tube surface around the axial position of the point electrode (z = 2.5 cm), with positive surface charges for V_P = +6 kV and negative ones for V_P = -6 kV, as described in section III.2. For the positive polarity discharge, as the first ionization front propagates towards the target for 29 $\leq t \leq$ 176 ns, Figure IV.9 shows that positive charges are slowly deposited on the inner tube surface behind the ionization front. For the negative polarity discharge, during the first ionization front propagation for 27 $\leq t \leq$ 206 ns, Figure IV.9 shows that the dynamics of negative surface charging behind the ionization front is much faster. Negative surface charge densities of the order of $\sim$ -1.2 nC/cm^2 are observed behind the first ionization front. This different dynamics of surface charging between positive and negative discharges is due to the higher mobility of electrons in comparison to ions ($\mu_e \sim 100 \times \mu_i$, for $E/N >$ 1 Td in He) and to the formation of the radial positive sheath described in section III.2 and has been already observed in other simulation studies of dielectric barrier discharges as in *Pechereau and Bourdon* [2014]. For V_P = +6 kV, after the impact on the metallic target and during the propagation of the rebound front (176 $\leq t \leq$ 257 ns), Figure IV.9 shows that the surface charge distribution evolves slowly due to the electric field redistribution. For V_P = -6 kV, Figure IV.9 shows that during the propagation of the rebound for 206 $\leq t \leq$ 307 ns, the surface charge density evolves more rapidly than in positive polarity. We notice that the amount (in absolute value) of negative charges deposited on the inner tube surface decreases due to the electric field redistribution. It is interesting to notice that at the time of the impact of the rebound front on the high voltage point electrode (t = 257 ns for V_P = +6 kV, and t = 307 ns for V_P = -6 kV) the axial profile of the surface charge density deposited on the inner tube surface is very close (in absolute value) between the positive and negative discharges.

IV.4 Influence of the discharge dynamics on the electric field outside the dielectric tube: comparison with experiments

To compare with time evolutions of the electric field components measured on the side of the dielectric tube with an electro-optic probe in *Darny et al.* [2017b], in this section we study the time evolutions of the electric field components at $r = 0.6$ cm (i.e. 0.3 cm from the tube outer wall). Furthermore, the radial profiles of electric field outside the tube are assessed in this section to study its relationship with the discharge dynamics inside the tube.

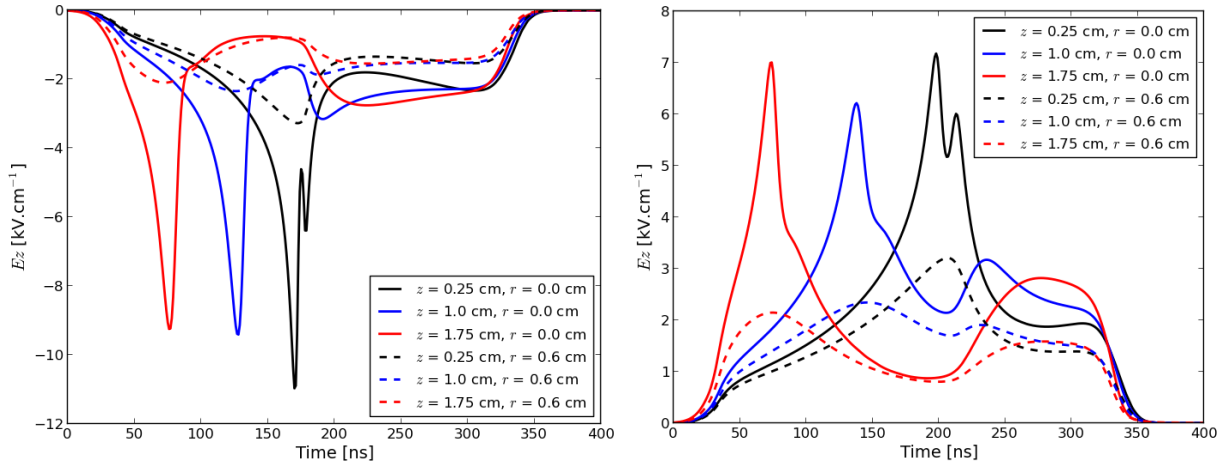

Figure IV.10: Temporal profiles of the axial component of electric field E_z on the symmetry axis at $r = 0$ (solid lines) and outside the tube at $r = 0.6$ cm (dashed lines), at $z = 0.25$, 1.0 and 1.75 cm, for $V_P = +6$ kV (on the left) and -6 kV (on the right).

Figure IV.10 shows the time evolutions of the axial component of electric field (E_z) on the symmetry axis ($r = 0.0$ cm, solid lines) and outside the tube at $r = 0.6$ cm (dashed lines) for $V_P = +6$ kV (on the left) and -6 kV (on the right) and the same conditions as in Figure IV.8. For both polarities, outside the tube, Figure IV.10 shows peaks of $|E_z|$, corresponding to the propagation of the first ionization and the rebound fronts. It is interesting to notice that the peaks of the first ionization front occur slightly earlier (1-5 ns) on the symmetry axis than at $r = 0.6$ cm. Close to the target, at $z = 0.25$ cm, outside the tube at $r = 0.6$ cm, as the first ionization and rebound fronts are close in time, Figure IV.10 shows only one peak of $|E_z|$ for both the first ionization and the rebound fronts. As expected, the peak values of $|E_z|$ for both fronts and both polarities are smaller outside of the tube at $r = 0.6$ cm than on the symmetry axis. For the first ionization front, the decrease is of about a factor 3 and of only ~ 2 for the rebound front.

Figure IV.11 shows the time evolutions of both axial and radial components of electric field for the same conditions as in Figure IV.10 but only outside the tube radially, at $r = 0.6$ cm, and at only one axial position $z = 1.0$ cm. It is interesting to notice that the peak of $|E_z|$ is reached while $|E_r|$ is still rising at the same position, as observed experimentally in *Darny et al.* [2017b] and in Figure IV.1. For instance, for $V_P = -6$ kV, $|E_z|$ is maximum around $t = 150$ ns, while $|E_r|$ still rises until approximately $t = 200$ ns. The temporal profiles of E_r for both polarities of applied voltage are presented in Figure IV.12 (on top) at the

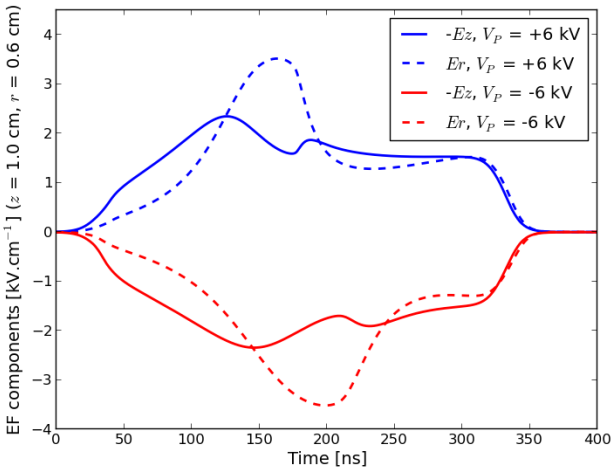

Figure IV.11: Temporal profiles of E_z (solid lines) and E_r (dashed lines) outside the tube at r = 0.6 cm and at z = 1.0 cm, for V_P = +6 kV (blue lines) and V_P = -6 kV (red lines).

axial positions z = 0.25 cm (on the left) and z = 1.75 cm (on the right). Additionally, that figure presents $E_z(t)$ (on bottom) for positive polarity at the same positions and the time evolution of each contribution to the electric fields, as described in section II.3.3: Laplacian potential, potential due to net volume charge and potential due to surface charges. Figures IV.10 and IV.11 show that as the first front passes a studied axial position, at that position, $|E_z|$ decreases rapidly, even at r = 0.6 cm. However, by comparing Figures IV.11 and IV.12, we notice that the time evolution of E_r depends on the studied axial position. In particular, at z = 1.0 cm, we notice that $|E_r|$ first tends to form a plateau and then decreases rapidly around t = 190 ns for V_P = +6 kV and around t = 220 ns for V_P = -6 kV. Figure IV.11 shows that the sharp decrease of $|E_r|$ corresponds to the second peak of $|E_z|$ and therefore to the propagation of the rebound front. These results are in agreement with the time evolutions of electric field measured in *Darny et al.* [2017b] and shown in Figure IV.1. This dynamics is also observed for z = 1.75 cm in Figure IV.12 with a smoother decrease of $|E_r|$ during the rebound propagation. For z = 0.25 cm, close to the target, as the time between the first ionization front and the rebound front is small, the time evolution of $|E_r|$ only shows a peak.

Through the different charge contributions to E_r represented in Figure IV.12, we see that the temporal evolution of E_r between the first and rebound ionization fronts is determined mostly by ρ for V_P = +6 kV and by σ for V_P = -6 kV. Moreover, it is interesting to notice that after the propagation of the two fronts, the values of $|E_r|$ depend on the studied axial position. For z = 0.25 cm, $|E_r|$ decreases almost to zero, but $|E_r|$ after the rebound increases as z increases (i.e. for axial positions closer to the point electrode). This is due to the surface charges remaining after the propagation of the two fronts, on the inner dielectric tube surface, that are higher close to the powered electrode than close to the target, as illustrated in Figure IV.9. We see in Figure IV.12 that at z = 1.75 cm, for V_P = +6 kV, even though the evolution of E_r until the rebound is determined by the net volume charge density, after the rebound it is mostly the presence of the surface charges close to the powered electrode that sets the remaining E_r at $\sim$ 3 kV.cm^{-1}. $E_z(t)$ for V_P = +6 kV is also mostly determined by ρ but the surface charges remaining close to the powered electrode provide an important field directed downstream after the discharge impact on the target. It is interesting to notice that E_z due

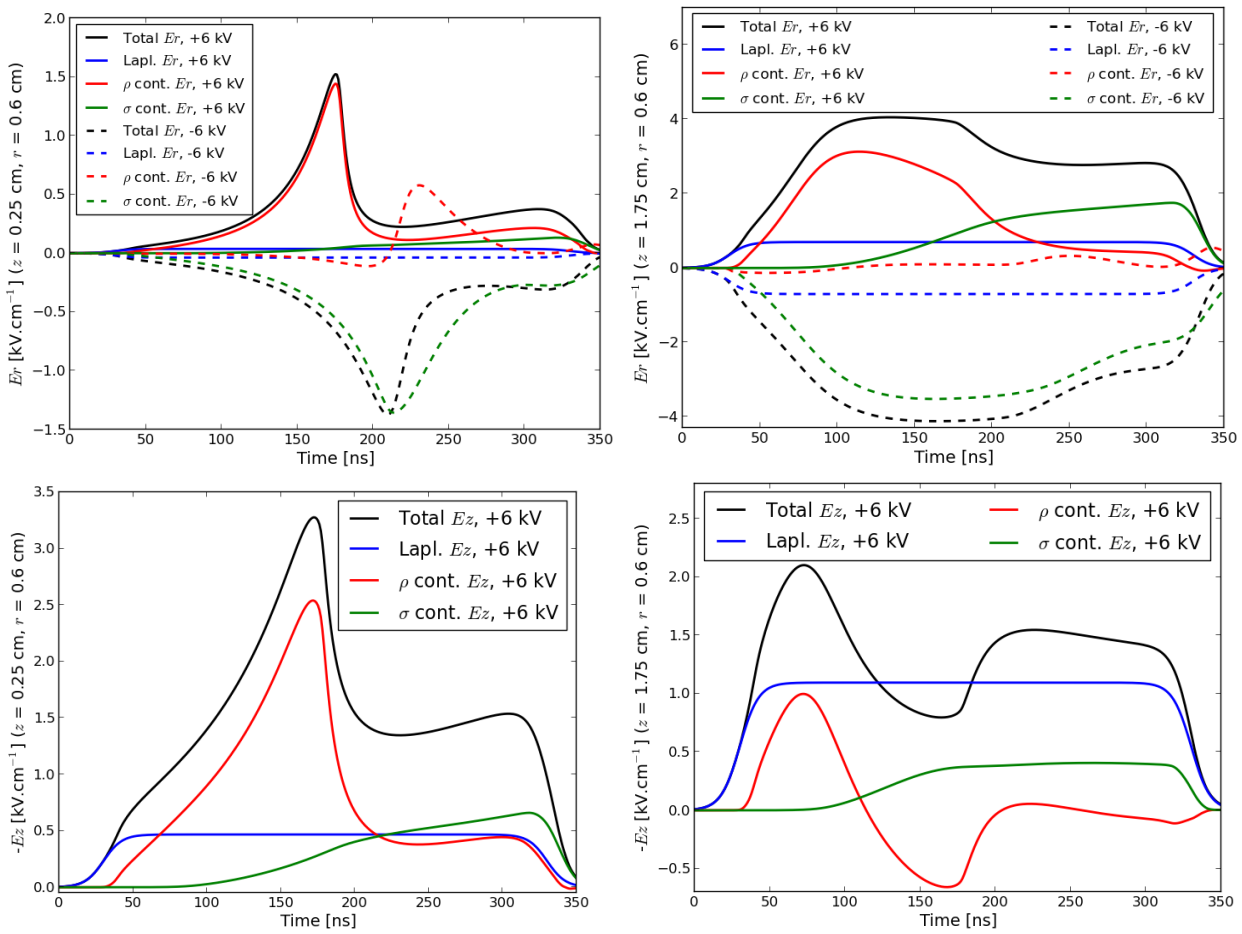

Figure IV.12: Temporal profiles of E_r (on top) and E_z (on bottom) at $r = 0.6$ cm, at $z = 0.25$ cm (on the left) and $z = 1.75$ cm (on the right) and its three contributions: Laplacian, from ρ and from σ. Results obtained for $V_P = +6$ kV (solid lines) and -6 kV (dashed lines).

to ρ at $z = 1.75$ cm is negative after the passage of the first ionization front because the positive discharge head is located at lower z positions, and then becomes close to zero with the rebound. Furthermore, it is also interesting to notice that at $z = 0.25$ cm, for $V_P =$ -6 kV, the rebound leads to a decrease of $|E_r|$ despite the increase of the σ contribution to $|E_r|$, because of the opposite polarity contribution of ρ generated by the rebound. Finally, Figures IV.11 and IV.12 show that from $t = 350$ ns, when the applied voltage is zero, both components of electric field are zero outside the tube.

In order to confirm that the fast decrease of $|E_r|$ at a given point outside the dielectric tube observed in Figures IV.11 and IV.12 and in experiments [*Darny et al.*, 2017b] is due to the propagation of the rebound front, we compare in Figure IV.13 the temporal evolution of E_r outside the tube at $r = 0.6$ *cm* for tubes with different lengths (tube with 3 cm length i.e. target at $z = 0.0$ cm and tube with 5 cm length i.e. target at $z =$ -2.0 cm) for a given axial position $z = 1.0$ cm for $V_P = +6$ kV (blue lines) and $V_P =$ -6 kV (red lines).

Figure IV.13 shows that for both polarities and both tube lengths, $|E_r|$ increases as the first ionization front propagates in the tube. With a longer dielectric tube, the increase of $|E_r|$ lasts longer. Indeed, as the interelectrode gap distance is increased for the same applied voltage, the propagation velocity of the discharge in the 5 cm tube is slightly lower than in

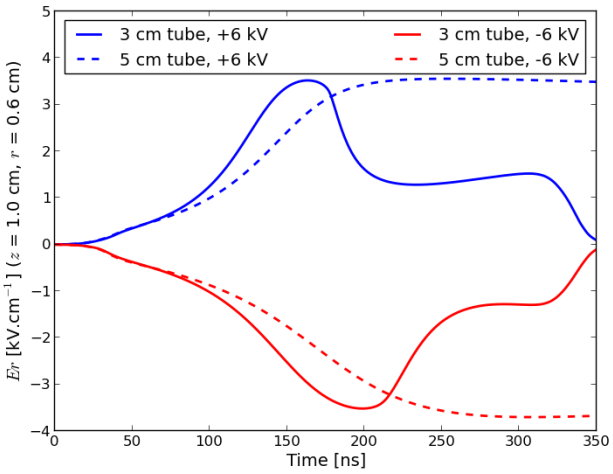

Figure IV.13: Comparison of the time evolution of E_r at r = 0.6 cm and z = 1.0 cm, for a 3 cm long tube closed by a grounded target (solid lines) and a 5 cm long tube closed by a grounded target (dashed lines) for V_P = +6 kV (blue lines) and V_P = -6 kV (red lines).

the 3 cm tube, as described in section III.3. For a 5 cm tube, we have checked that the first ionization front impacts the grounded plane at t = 424 ns for V_P = +6 kV and t = 538 ns for V_P = -6 kV. These values have to be compared to t = 176 ns and 206 ns for a 3 cm tube, respectively. Figure IV.13 shows the time evolution of E_r at z = 1.0 cm up to t = 350 ns, and therefore after the rebound propagation in the 3 cm tube, but before the impact of the first ionization front for the 5 cm tube. After the passage of the first ionization front at z = 1 cm in the 5 cm tube, for both polarities, Figure IV.13 shows that $|E_r|$ is kept constant or decreases slowly up to t = 350 ns. No steep decrease of $|E_r|$ is observed when no rebound front propagates. This confirms that the steep decrease of $|E_r|$ with the 3 cm tube is due to the rebound front propagation.

IV.5 Rebound front as ionization wave of partial neutralization of the plasma channel

To summarize the dynamics of the rebound discharge and of the electric field evolution outside the tube, a scheme is presented in Figure IV.14, aimed at describing the case with positive polarity of applied voltage. With negative polarity, the dynamics is the same, but the signs are reversed. To demonstrate the dynamics in the scheme, in Figure IV.15 we follow the axial profiles of electric potential on the axis of propagation (r = 0) for V_P = +6 kV (on top) and V_P = -6 kV (on bottom) at the instant of impact of the first ionization front with the target (t = 176 ns for V_P = +6 kV and t = 206 ns for V_P = -6 kV) and some nanoseconds later, when the peak of the rebound front is crossing z = 1.0 cm (t = 200 ns for V_P = +6 kV and t = 245 ns for V_P = -6 kV). The potential distribution is divided into its three contributions: Laplacian, from ρ and from σ. The representation in the scheme in Figure IV.14 is symbolic and not completely accurate. It symbolizes the movement of charges and the direction of E_z inside and outside the tube and of E_r outside the tube.
The propagation of the first ionization front leaves behind a channel of positive (for V_P = +6 kV) or negative (for V_P = -6 kV) ρ and σ. The electric potential applied to the powered

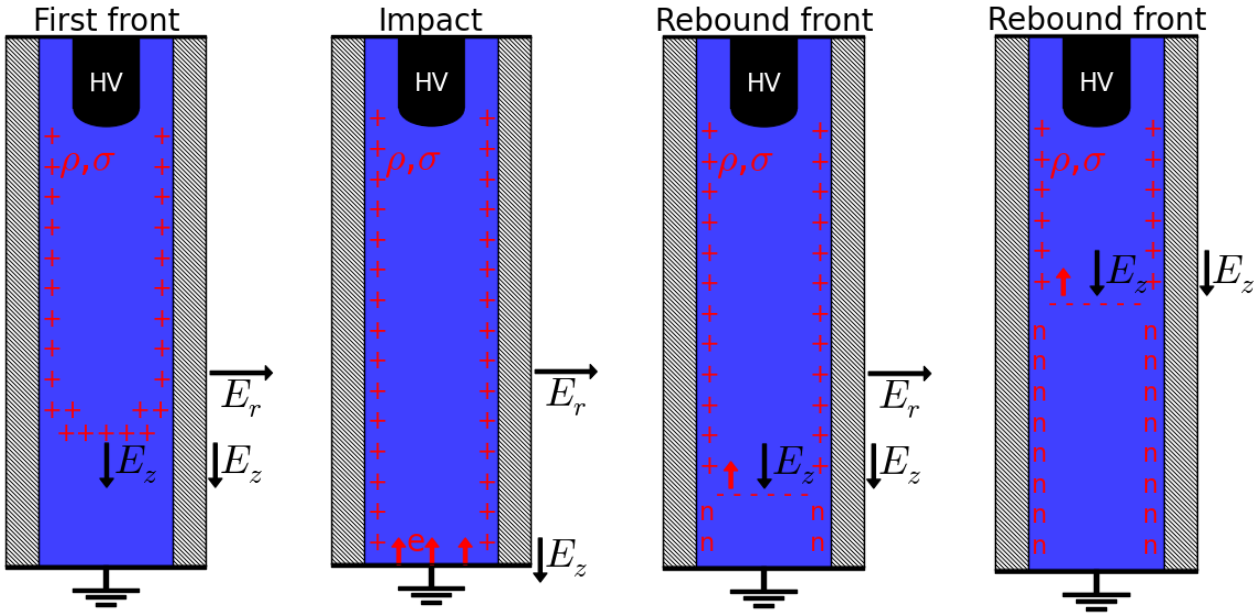

Figure IV.14: Side view schematics of the temporal sequence representing the dynamics of the rebound discharge and of the electric field evolution described in this chapter, aimed at describing the case with positive polarity of applied voltage. Charges and charge movement are represented in red. 'n' stands for charge neutrality. Axial and radial components of electric field are represented in black.

electrode (Laplacian, blue curve in Fig. IV.15) is partially transferred through that channel to the ionization front. In the positive case the potential is transferred mostly through ρ (red curve) and with negative polarity mostly through σ (green curve).
With the impact on the target, the discharge head is partially neutralized. In the positive case, this neutralization occurs through the emission of electrons from the metallic plate. In negative polarity, it takes place through electron recombination. However, the neutralization of the discharge head does not fully neutralize the plasma channel immediately.
The potential drop remains between the plasma channel and the grounded target and therefore the maximum of E_z remains near the target, where the origin of the new ionization front, called rebound front, takes place. This time, as the ionization starts at the grounded target, the new propagating net charge density has the opposite sign and the front is directed towards the plasma channel and the powered electrode. There is, therefore, a reversion of polarity at the target.
Unlike the first ionization front, the rebound front propagates in an already ionized channel. While the first front carries the electric potential from the powered electrode towards the target, the rebound fronts redistributes that potential. It can be seen in Figure IV.15, at t = 200 ns for V_P = +6 kV and at t = 245 ns for V_P = -6 kV, that the electric potential (black curves) tends to an almost linear axial distribution, by effect of the rebound. The channel is therefore partially neutralized, as suggested in *Raizer* [1991]. Here is shown that the neutralization is obtained by the propagation of net volume charge density of opposite polarity and the deposition of surface charges of opposite sign by the rebound discharge front. The redistribution of electric potential is stronger close to the target, where the axial slope of electric potential is higher at the beginning of the rebound propagation, which justifies the

higher peak of rebound electric field close to the target assessed in Figure IV.8. Moreover, Figure IV.15 shows that in the case of positive applied voltage, the redistribution of potential between $t = 176$ ns and $t = 200$ ns is performed by the propagation of negative charge that partially cancels the positive ρ in the plasma channel. On the contrary, in the case of negative applied voltage, Figure IV.15 shows that the potential redistribution between $t = 206$ ns and $t = 245$ ns is accomplished by both the production of positive ρ and by partially canceling the negative σ through positive ion deposition.

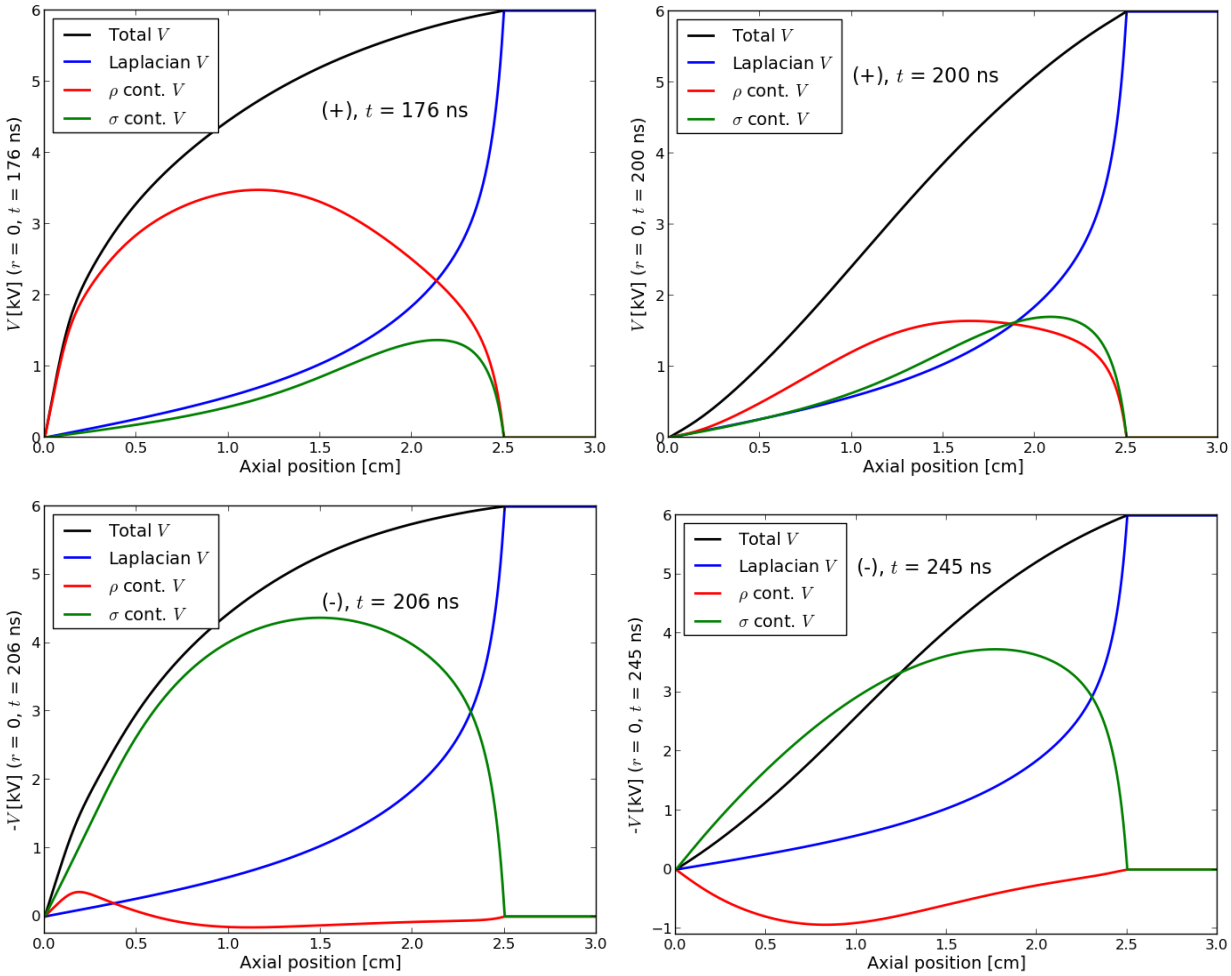

Figure IV.15: Axial profiles of the electric potential V on the symmetry axis ($r = 0$) before and after the rebound and its three contributions: Laplacian, from ρ and from σ. On top, $V(z)$ for the same conditions as in Figure IV.3 with $V_P = +6$ kV. On the bottom, $V(z)$ for the same conditions as in Figure IV.4 with $V_P =$ -6 kV.

IV.6 Derivation of discharge properties from the electric field outside the dielectric tube: how simulations can complement experiments

As measurements with probes are only possible outside the dielectric tube [*Darny et al.*, 2017b] and optical measurements obtain the peak values of electric field on the discharge front inside the tube [*Sretenovic et al.*, 2017], it is interesting to study with simulations the time evolutions of the axial and radial components of electric field inside and outside the tube, in order to complement the information retrieved experimentally. Figure IV.16 presents the radial distribution between r = 0.0 cm and r = 0.6 cm at a given axial position z = 1.0 cm and at several instants in time of E_z (on top) and E_r (on bottom) with V_P = +6 kV (on the left) and V_P = -6 kV (on the right) for a 3 cm dielectric tube. Vertical dashed lines show the separation between the plasma region, the dielectric quartz tube and air outside of the tube (modeled as a dielectric).

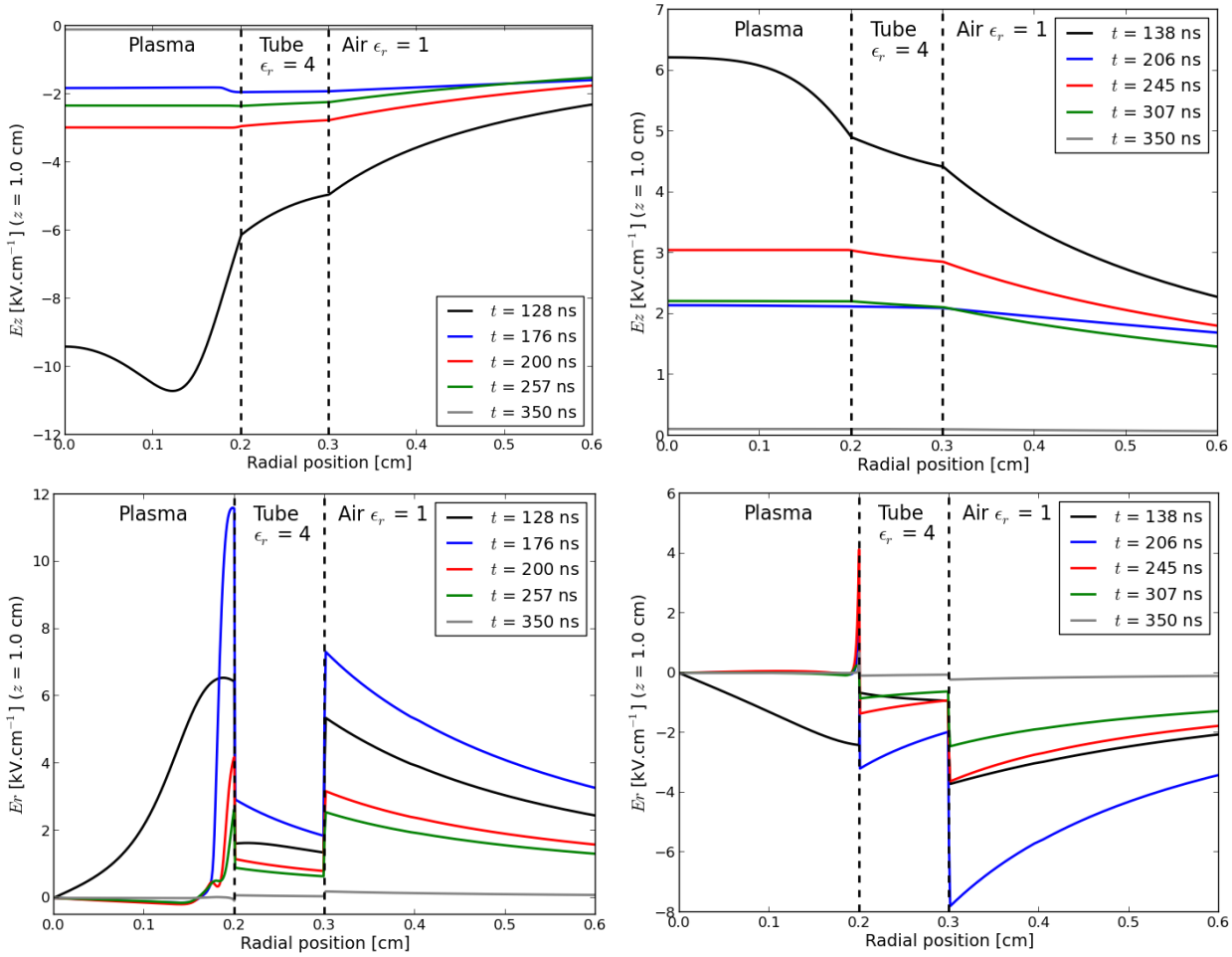

Figure IV.16: Radial profiles of the electric field components at z = 1 cm and several times. On top, $E_z(r)$ for V_P = +6 kV on the left and for V_P = -6 kV on the right. On the bottom, $E_r(r)$ for V_P = +6 kV on the left and for V_P = -6 kV on the right.

It is interesting to notice that the radial evolutions of both electric field components with both polarities strongly depend on time. In agreement with Gauss's law, jumps of $|E_r|$

are observed at the dielectric tube interfaces with the gas in the tube and air outside the tube. These jumps are due to the permittivity difference between the dielectric tube and the surrounding gases. Furthermore, surface charges deposited on the inner dielectric surface, also contribute to the jumps of $|E_r|$ at the interface between the gas in the tube and the dielectric tube. For instance, at the interface between the tube and the inside gas, at r_{in} = 0.2 cm, Gauss's law can be written as: $(\epsilon_0 \epsilon_r E_{r\rightarrow r^+}) - (\epsilon_0 E_{r^-\rightarrow r}) = \sigma$.
The first ionization front passes the position z = 1.0 cm (t = 128 ns for V_P = +6 kV and t = 138 ns for V_P = -6 kV) with a net charge density in the ionization front of corresponding polarity. In the case of negative polarity, the value of E_z is maximum on the symmetry axis and decreases as r increases, while with positive polarity the maximum of $|E_z|$ is closer to the tube. It is interesting to notice that $|E_z|$ at $r = 0$ with positive polarity, of approximately 9.5 kV.cm^{-1}, is in the range of values reported in *Sretenovic et al.* [2017] for maximum electric field measured by Stark polarization spectroscopy on the axis of symmetry during positive discharge propagation inside a tube. Figure IV.16 shows that $|E_r|$ in the plasma region is maximum close to the inner dielectric tube surface for both polarities. In the dielectric tube (0.2 cm $< r <$ 0.3 cm), $|E_r|$ is smaller than in the plasma for both polarities, but due to the change of permittivity, $|E_r|$ at the dielectric tube interface with air is maximum and decreases as r increases. Then, as the discharge impacts the metallic target (t = 176 ns for V_P = +6 kV and t = 206 ns for V_P = -6 kV), we notice that $|E_z|$ has significantly decreased at z = 1.0 cm, and is almost constant along r, whereas $|E_r|$ is equal to zero in the plasma channel except close to the inner dielectric charged surface. As a consequence of the charging of the tube, a high value of $|E_r|$ is obtained at the dielectric tube/air interface. During the rebound front propagation ($176 < t < 257$ ns for V_P = +6 kV and $206 < t < 307$ ns for V_P = -6 kV), a slow and smooth evolution of $E_z = f(r)$ is observed. It increases in absolute value at the passage of the rebound front (t = 200 ns for V_P = +6 kV and t = 245 ns for V_P = -6 kV) and decreases afterwards. Conversely, the radial profile of E_r is more complex due to the change of permittivity and the surface charges on the inner dielectric surface. With positive polarity, E_r decreases during the rebound front propagation both inside and outside the tube, as the positive volume net charge density cancels. On the other hand, with negative polarity, during the rebound front propagation, E_r is positive between the plasma and the tube inner surface, where the negative surface charge is partially canceled by positive charge deposition, and negative on the outside, where $|E_r|$ decreases in time. Finally, after the decrease of the applied voltage, at t = 350 ns, all the electric field components are down to zero, inside as outside the tube.
From these results, it is interesting to discuss how measurements of electric field outside the tube as in *Darny et al.* [2017b] can be used to derive information on the electric field inside the plasma. Based on the results shown in Figure IV.16, it appears clearly that the amplitude of the time evolutions of both components of the electric field decreases rapidly outside the tube, as r increases. Then, to follow the nanosecond timescale variations of the electric field, measurements outside the tube have to be done only at a few mm from the tube outer surface. The electric field outside the tube can also be related to the charges in the plasma. In Figure IV.17 are presented the radial profiles of E_r exclusively outside the tube, between r = 0.3 cm and r = 4.5 cm, at the same axial position as in Figure IV.16 (z = 1.0 cm) and at the times of impact of the first ionization front on the grounded target, t = 176 ns for V_P =

+6 kV, and t = 206 ns for V_P = -6 kV. These are the times when the charge distribution is the most uniform in the tube. Along with $E_r(r)$ are presented the contributions from the applied voltage (Laplacian), from ρ and from σ, for both polarities (positive on the left and negative on the right). In each curve, symbols signal the radial position of the center of the mesh cells.

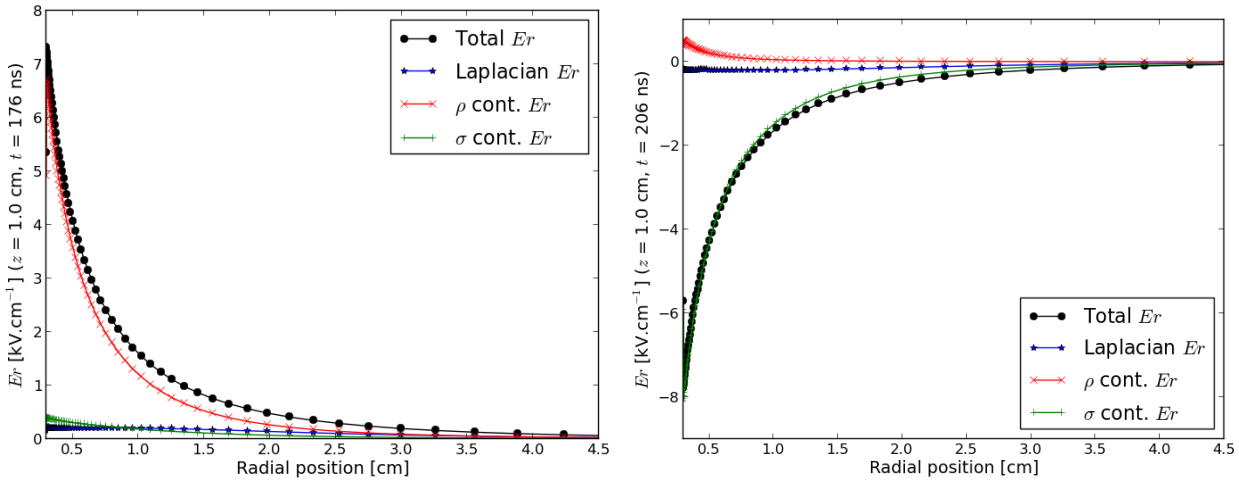

Figure IV.17: Radial profiles of the radial component of electric field E_r and of its three contributions: Laplacian, from ρ and from σ; at z = 1.0 cm. On the left, for V_P = +6 kV at t = 176 ns. On the right, for V_P = -6 kV at t = 206 ns.

Firstly, Figure IV.17 shows that all the electric field contributions decrease to very low values as r increases. Then, we can notice that in both cases the Laplacian contribution to $E_r(r)$ is negligible, unlike the ρ and σ contributions. Therefore, we can say that far from the electrodes the electric field is generally due to both surface charges and volume charges. However, the influence of each contribution is clearly dependent on the polarity of the applied voltage. Figure IV.17 shows that for V_P = +6 kV, the radial profile of E_r outside the tube is mostly determined by the volume charge density ρ, while for V_P = -6 kV, the radial profile of E_r outside the tube is mostly determined by the surface charge density σ. Then, the actual ρ and σ values in the simulation can be evaluated. Figure IV.18 shows the axial profiles of σ (on the left) and ρ averaged radially through the tube cross section (on the right), along with the axial averages σ_{av} and ρ_{av}, for both V_P = +6 kV and V_P = -6 kV.
Figure IV.18 shows that in any situation are σ or ρ homogeneous in space. Moreover, σ_{av} is negative for V_P = -6 kV and positive for V_P = +6 kV, but has much higher magnitude for the negative polarity case. Concerning ρ_{avr}, it is positive all along the channel of the positive discharge and has a peak at the discharge front. On the other hand, ρ_{avr} for negative polarity is only negative in the discharge front, being positive in some regions of the plasma channel. As a result, ρ_{av} is slightly positive in negative polarity, while it is clearly positive in positive polarity. These results explain why the radial electric field outside the tube is mostly related to σ in negative polarity and to ρ in positive polarity.
Following the same reasoning, recent experiments conducted by Xavier Damany in GREMI have been carried out to assess the charge densities inside a dielectric tube where a plasma jet propagates, in similar configuration as that in *Darny et al.* [2017b] and in Figure IV.1. The procedure to investigate those charges consists firstly in the measurement of the radial

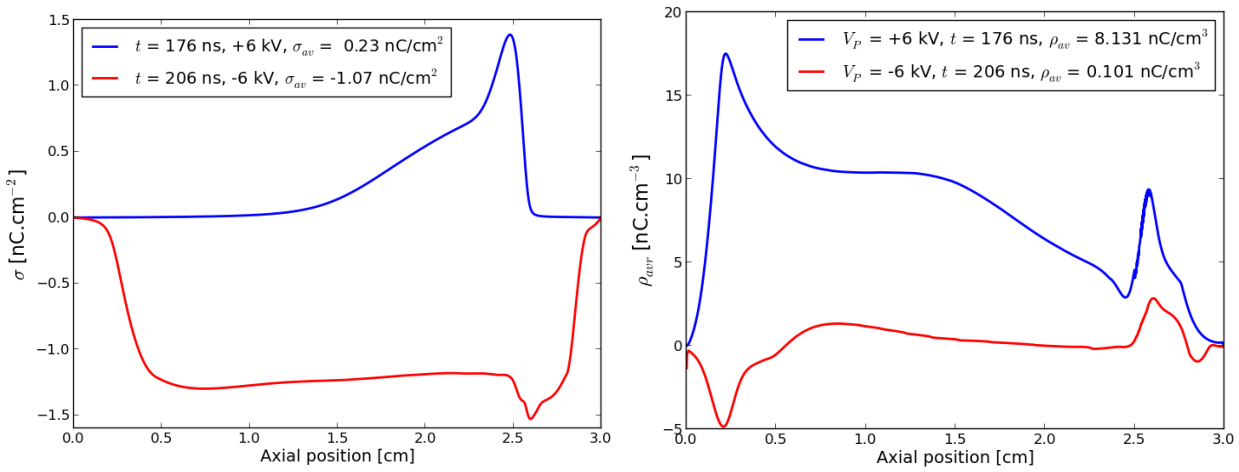

Figure IV.18: Axial profiles of the surface (on the left) and volume (on the right) net charge densities, along with their averages through the tube length, with V_P = +6 kV (blue lines) and V_P = -6 kV (red lines). On the right, $\rho_{avr}(z)$ is ρ averaged radially through the tube cross section and ρ_{av} is the average of ρ both radially and axially.

profile of the radial component of electric field $E_r(r)$ outside the tube at a given time and axial position. Then, Gauss's law in an isolated system on the outside of a cylinder of radius R and length $L \gg R$ with Q charges uniformly distributed, gives:

$$E_r(r) = \frac{Q}{\epsilon_0 2\pi L r} \tag{IV.1}$$

This law can be rewritten if we consider the particular cases of Q consisting exclusively on an uniform distribution of surface charge density σ or exclusively on an uniform distribution of volume charge density ρ:

$$E_r(r) = \frac{\sigma R}{\epsilon_0 r} \tag{IV.2}$$

$$E_r(r) = \frac{\rho R^2}{2\epsilon_0 r} \tag{IV.3}$$

In such conditions, the values of σ or ρ can be retrieved from the measurements of $E_r(r)$. Using the model, we can evaluate the validity of the hypothesis of using equations IV.2 and IV.3 to retrieve charge densities. Figure IV.19 presents the radial profiles of $E_r(r)$ in the same conditions of Figures IV.17 and IV.18 on the outside of the tube between r = 0.3 cm and r = 10 cm, with crosses in the radial position of the center of the mesh cells. The figure also shows the result of the fits of the radial profiles to equations IV.2 and IV.3, where $R = r_{in}$ = 0.2 cm, for both V_P = +6 kV and V_P = -6 kV. The results of the fits shown in Figure IV.19 ($E_r(r) = 2108.9/r$ for positive polarity and $E_r(r) = -2232.3/r$ for negative polarity) are very close to the ones obtained experimentally ($E_r(r) = 2059/r$ for positive polarity and $E_r(r) = -1795/r$ for negative polarity) at the GREMI laboratory, despite the different geometry and applied voltage, described in section IV.2. These different conditions are not relevant because in both cases the axial position is taken in the middle of the tube, far from the electrode influence, and the time is taken when the charges are more uniformly distributed and equations IV.2 and IV.3 can be considered.

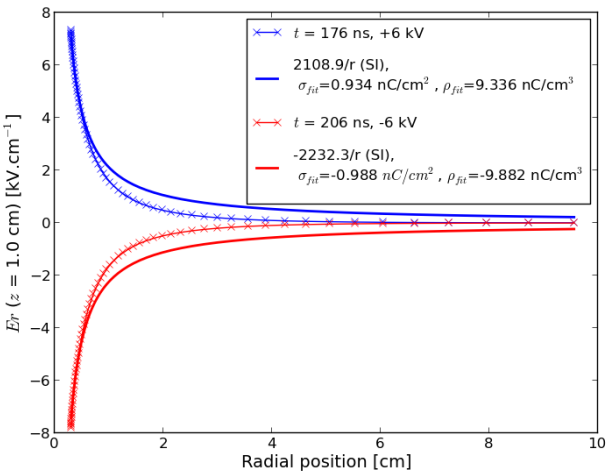

Figure IV.19: Radial profiles of E_r at $z = 1$ cm with the radial mesh spatial resolution (lines with crosses). For both $V_P = +6$ kV at $t = 176$ ns (blue lines) and $V_P =$ -6 kV at $t = 206$ ns (red lines) is included the fit (full lines) to the function $E_r(r) = a/r$ and σ_{fit} and ρ_{fit} calculated according to equations IV.2 and IV.3.

The radial profiles for the two polarities are almost symmetric, and the fits show that if the hypothesis of equation IV.2 is valid in the situations under study, the uniform σ has a value of 0.934 nC.cm^{-2} for positive polarity and -0.988 nC.cm^{-2} for negative polarity. Likewise, the fits show that if the hypothesis of equation IV.3 is valid in the situations under study, the uniform ρ has a value of 9.336 nC.cm^{-3} for positive polarity and -9.882 nC.cm^{-3} for negative polarity. We have seen in the study of Figure IV.17 that far from the electrodes the radial profile of E_r outside the tube is mostly determined by the net volume charge density ρ, while for $V_P =$ -6 kV, $E_r(r)$ is mostly determined by σ. Therefore, it is interesting to compare the result of the fit to equation IV.3 for $V_P = +6$ kV with the actual ρ values in the simulation at $t = 176$ ns from Figure IV.18. Likewise, the result of the fit to equation IV.2 for $V_P =$ -6 kV can be compared with the actual σ values in the simulation at $t = 206$ ns from Figure IV.18. Table IV.1 compares these values. We notice that σ_{av} for $V_P = +6$ kV is very different from σ_{fit} assuming equation IV.2, just like ρ_{av} for $V_P =$ -6 kV is very different, even in signal, from ρ_{fit} assuming equation IV.3. Finally, ρ_{av} for $V_P = +6$ kV presents a difference of only around 15% with respect to ρ_{fit} assuming equation IV.3, and σ_{av} for $V_P =$ -6 kV presents a difference of only around 8% with respect to σ_{fit} assuming equation IV.2. We conclude that the average charge densities σ_{av} and ρ_{av} can be obtained from experimental measurements of $E_r(r)$ through fits to equations IV.2 and IV.3 in particular conditions when it is known which type of charges determines the electric field distribution outside the tube.

V_P [kV]	ρ_{av} [nC.cm^{-3}]	ρ_{fit}	$(\rho_{av} - \rho_{fit})/\rho_{av}$	σ_{av} [nC.cm^{-2}]	σ_{fit}	$(\sigma_{av} - \sigma_{fit})/\sigma_{av}$
+6	8.13	9.33	14.8%	0.23	0.93	-
-6	0.10	-9.88	-	-1.07	-0.99	7.5%

Table IV.1: Comparison of ρ/σ_{av} obtained from the simulation results with ρ/σ_{fit} obtained from fitting $E_r(r)$ outside the tube, for $V_P = +6$ kV and $V_P =$ -6 kV.

IV.7 Dynamics of first ionization and rebound fronts in plasma jet configurations and influence on the production of reactive species

In this section, we study the discharge dynamics in typical plasma jet conditions with a gap between the tube and the target, as shown on the right side of Figure IV.2.We should notice that the results are obtained with a 2 slm flow of 99.9% He- 0.1% N_2 or O_2 through the tube into a N_2 or O_2 atmosphere. Therefore, gas mixing is considered at the end of the tube. As in *Viegas et al.* [2018a] the same study has been performed without gas mixing, with uniform 99% He - 1% N_2/O_2, the results presented here will be commented with respect to those published in *Viegas et al.* [2018a] and presented in appendix E.

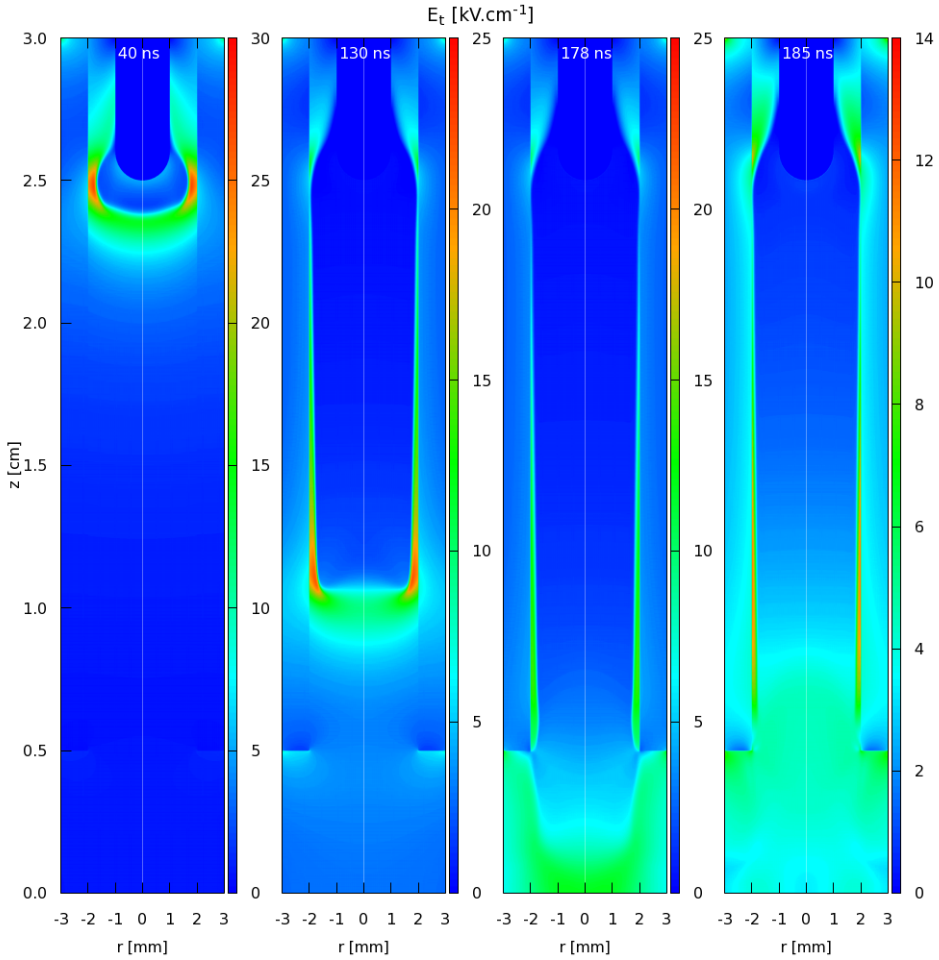

Figure IV.20: Cross sectional views of the magnitude of the electric field at $t = 40$, 130, 178 and 185 ns, for a 2.5 cm long tube and a 0.5 cm tube-target distance, for $V_P = +6$ kV.

Figures IV.20 and IV.21 show the time sequence of the distributions of absolute values of electric field E_t, for $V_P = +6$ kV and $V_P =$ -6 kV, respectively, and a 2.5 cm length tube with 0.5 cm target-tube distance (i.e. target at $z = 0$ and end of tube at $z = 0.5$ cm) and with 2 slm of 99.9% He - 0.1% N_2 flowing into a N_2 atmosphere at the end of the tube. As in Figures IV.3 and IV.4, Figures IV.20 and IV.21 show the distribution of absolute values of electric field at the beginning of discharge propagation close to the tip of the point electrode;

during the first ionization front propagation between the point and the target, when the front is crossing the position z = 1.0 cm; at a moment when the front of propagation hits the grounded target; and then a few nanoseconds later.

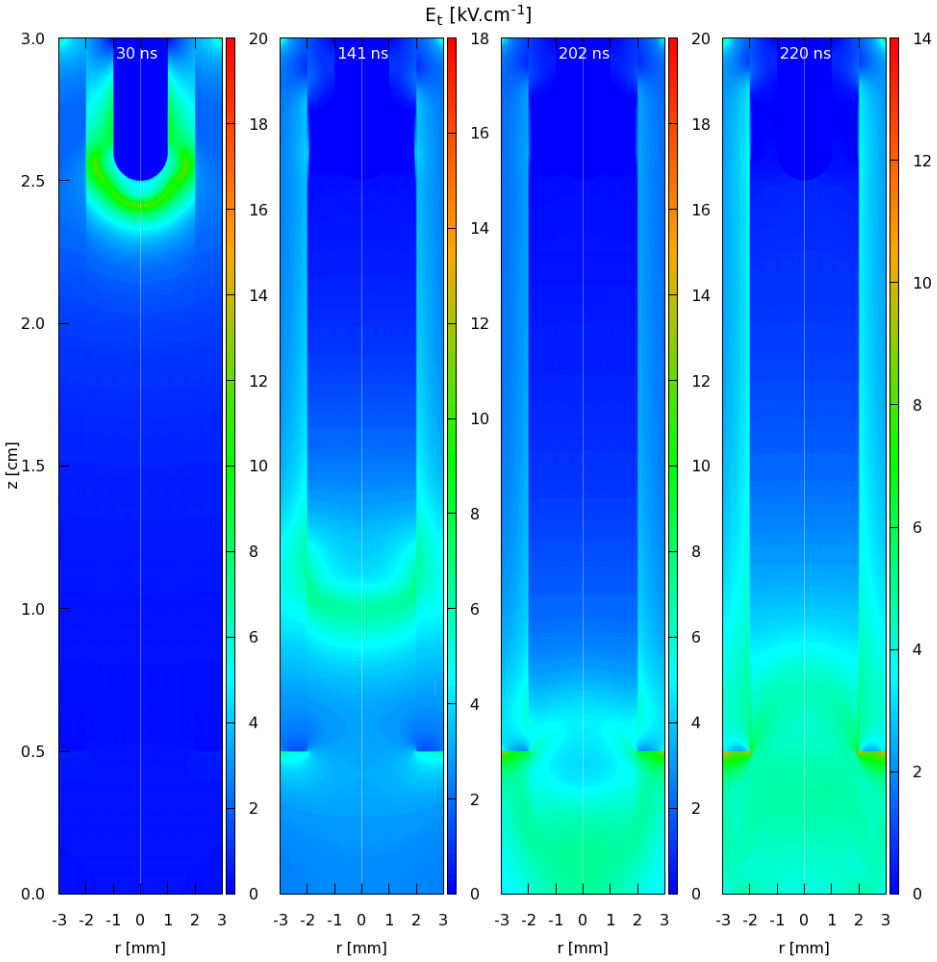

Figure IV.21: Cross sectional views of the magnitude of the electric field at t = 30, 141, 202 and 220 ns, for a 2.5 cm long tube and a 0.5 cm tube-target distance, for V_P = -6 kV.

For both positive and negative polarities, the discharge ignition and the propagation of the first ionization front inside the dielectric tube are similar in the cases with a 2.5 cm length tube with 0.5 cm target-tube distance and a 3 cm tube. With a 2.5 cm long tube and a 0.5 cm tube-target distance, the discharge hits the grounded target at t = 178 ns (176 ns for a 3 cm tube) for V_P = +6 kV and at t = 202 ns (206 ns for a 3 cm tube) for V_P = -6 kV. After the impact on the grounded metallic target, Figures IV.20 and IV.21 show that the electric field is significantly reduced, and then a second front propagates from the grounded target towards the powered electrode, as already observed for a 3 cm tube. For a 2.5 cm length tube with 0.5 cm tube-target distance, we note that the end of the tube at z = 0.5 cm induces a local increase of the electric field which is more significant for V_P = -6 kV than for V_P = +6 kV. This increase is due to the change of permittivity at the end of the tube, and to the higher amount (in absolute value) of surface charge density deposited on the inner dielectric tube surface in negative than in positive polarity, as already observed in Figure IV.9. With respect to the results presented in *Viegas et al.* [2018a] (Figure E.1) where the 0.5 cm tube-target gap is described with a uniform gas-mixture and an air dielectric tube at

$r > r_{in}$, the electric field characteristics identified are the same, but the shape of the plasma plume is slightly different, since some radial confinement is imposed by the gas mixing, as discussed in section III.6.

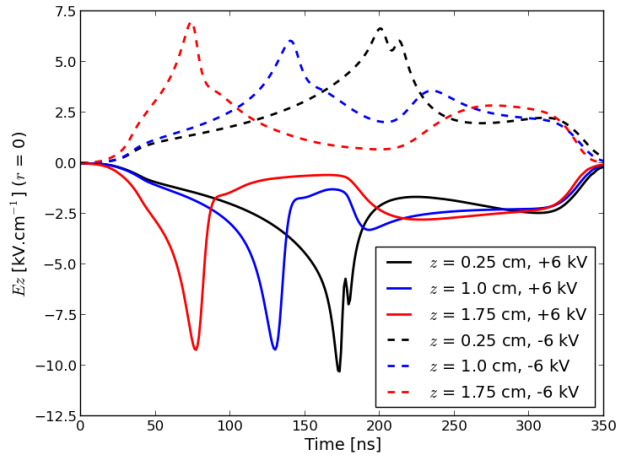

Figure IV.22: Temporal profiles of the axial component of electric field E_z on the symmetry axis ($r = 0$) and at $z = 0.25$, 1.0 and 1.75 cm, for the same conditions as in Figures IV.20 and IV.21. Solid lines: V_P = +6 kV. Dashed lines: V_P = -6 kV.

Figure IV.22 shows the temporal profile of E_z on the axis of symmetry ($r = 0.0$ cm) and at different axial positions: $z = 0.25$ cm (i.e. between the end of the tube and the grounded target) and $z = 1.0$ and 1.75 cm (i.e. between the end of the tube and the high voltage point electrode), for the same conditions as in Figures IV.20 and IV.21. The dynamics observed for both polarities are very close to those obtained for a 3 cm tube on Figure IV.8 with two peaks of electric field, one for the first ionization front and a second for the rebound front. This shows that with a dielectric tube not touching the grounded target, as in plasma jet configurations, the rebound front can also be observed. The main difference is observed at z = 0.25 cm (i.e. outside the tube) with lower peak values of $|E_z|$ for the first ionization front for a 2.5 cm long tube with 0.5 cm tube-target distance than for a 3 cm tube. The same feature has been observed in *Viegas et al.* [2018a] (Figure E.2) without gas mixing at the end of the tube. Therefore, in the current conditions of strong flow (2 slm) and short tube-target gap (0.5 cm), this decrease of the peak of $|E_z|$ is due to the lower radial confinement and more diffusive shape after the end of the tube.
Then, we study the influence of the first ionization and rebound fronts on the production of reactive species close to the target. First, Figure IV.23 shows the temporal evolutions of the density of electrons, for V_P = +6 kV (on the left) and V_P = -6 kV (on the right). These profiles are represented for two different buffer gas-mixtures (99.9% He - 0.1% N_2 and 99.9% He - 0.1% O_2) for the same geometry as in Figures IV.20 and IV.21 (i.e. with a 2.5 cm long tube and a 0.5 cm tube-target distance). Figure IV.23 presents the time evolutions of the densities on the axis of symmetry ($r = 0.0$ cm) for two axial positions $z = 0.25$ cm (i.e. between the end of the tube and the grounded target) and $z = 1.0$ cm (i.e. between the end of the tube and the high voltage point electrode). With the kinetic schemes used in this work (section II.4.2), electrons are firstly created through electron impact direct ionization collisions, dependent on the electric field magnitude in the ionization fronts, and then in the plasma channel through Penning ionization reactions of N_2 or O_2 through He* collision.

Then, electrons are mostly lost by recombination reactions that do not play a dominant role in the 275 ns timescale analysed in Figure IV.23 and by attachment reactions in the case of the He-O_2 mixture, also not relevant in the mentioned timescale with the current O_2 relative density that is lower than 0.5% (see Figure IV.2).

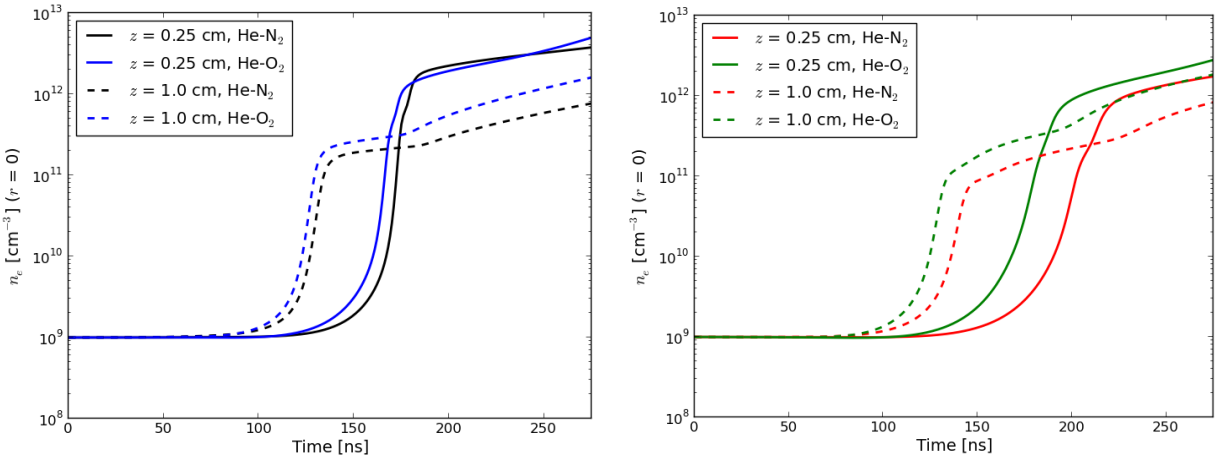

Figure IV.23: Temporal profiles of the density of electrons on the axis of symmetry ($r = 0$) at $z = 0.25$ cm and $z = 1.0$ cm, for a 2.5 cm long tube with 0.5 cm target-tube distance for He-N_2 and He-O_2 mixtures and $V_P = +6$ kV (on the left) and -6 kV (on the right).

For both polarities, Figure IV.23 shows that the time evolutions of the electron density in these He-N_2 and He-O_2 mixtures are rather close, with almost the same values. We note that the propagation of the first ionization front is slightly faster in He-O_2 mixtures than in He-N_2 mixtures as the electron density starts increasing slightly earlier in He-O_2 mixtures than in He-N_2 mixtures. For $V_P = +6$ kV, we notice that the electron density first increases at $z = 1$ cm, due to the propagation of the first ionization front. Then, the density slowly increases in the plasma channel and a faster increase is observed when the rebound front propagates. At $z = 0.25$ cm, close to the target, the first ionization and rebound fronts are very close in time, and then, only one clear increase of electron density is observed, followed by a slow increase in the plasma channel. Nevertheless due to the effect of these two fronts, the electron density at a given time after the rebound propagation is about five times higher at $z = 0.25$ cm than at $z = 1.0$ cm. For V_P = -6 kV, Figure IV.23 also shows two fast increases on the time evolution of the electron density at $z = 1.0$ cm and only one at $z = 0.25$ cm. It is interesting to point out that the electron densities at $z = 0.25$ cm in negative polarity are about twice as low as the ones obtained in positive polarity.
Finally, to study the influence of the first ionization and rebound fronts on the production of reactive species close to the target, Figure IV.24 shows the temporal evolutions of the density of metastable He*, composed by the densities of both metastable states He(2^3S) and He(2^1S), with $V_P = +6$ kV (on the left) and V_P = -6 kV (on the right). These profiles are represented for the same conditions and positions as in Figure IV.23. With the kinetic schemes used in this work (section II.4.2), He* is primarily created through electron-He excitation collisions, dependent on the electric field magnitude, and is mostly destroyed through the Penning ionizations of N_2 or O_2. Although He* is not a long life-time reactive species directly interesting for applications, its high internal energy (19.82 eV for He(2^3S) and 20.62 eV for He(2^1S)) is a reservoir of energy which facilitates either ionizing collisions

or the transfer of energy to other more reactive nitrogen or oxygen species. Furthermore, its density has been measured experimentally in *Darny et al.* [2017b].

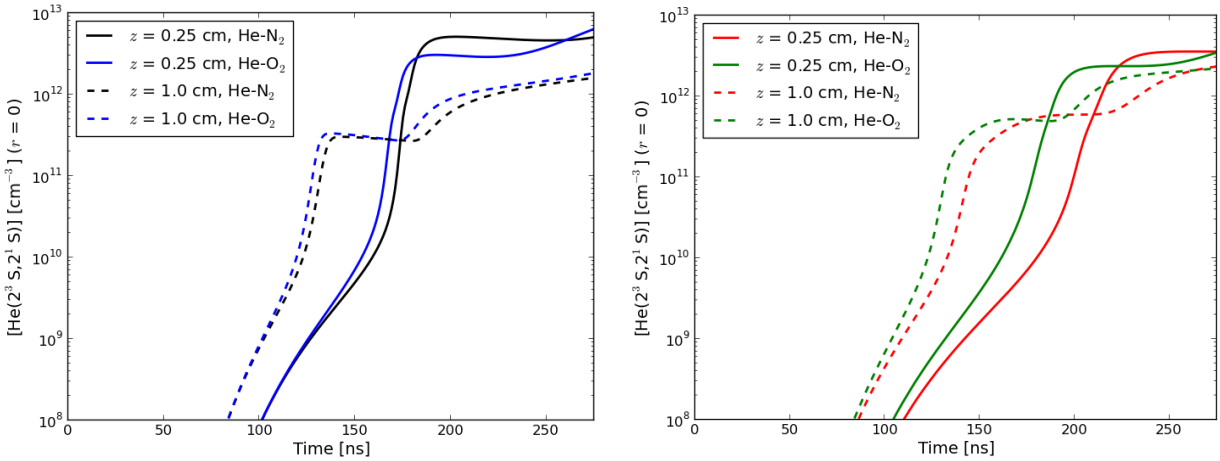

Figure IV.24: Temporal profiles of the density of metastable He(2^3S,2^1S) on the axis of symmetry ($r = 0$) at $z = 0.25$ cm and $z = 1.0$ cm, for He-N_2 and He-O_2 mixtures and V_P = +6 kV (on the left) and -6 kV (on the right).

As observed earlier for the electron density, Figure IV.24 shows that the time evolutions of the density of He* in these He-N_2 and He-O_2 mixtures are rather close, with almost the same peak values. We notice the same dynamics of the density of He* at $z = 1.0$ cm as we did for the electron density, with a first increase due to the propagation of the first ionization front and then a second increase observed when the rebound front propagates. It is important to underline that the maximum electric field in the rebound front is much lower than the one of the first ionization front. However, as the rebound front propagates in an ionized channel, the electron density is high enough to allow an efficient production of He* by the rebound front, which explains the second fast increase of He* observed at $z = 1.0$ cm, more clear than for the electron density. At $z = 0.25$ cm, close to the target, the first ionization and rebound fronts are very close in time, and then, only one peak of He* is observed, as in experiments [*Darny et al.*, 2017b]. The effect of these two fronts, along with the difference in electron density, leads to a first peak of He* density at $z = 0.25$ cm about one order of magnitude higher than the one at $z = 1.0$ cm. These results are in qualitative agreement with experiments [*Darny et al.*, 2017b], as is the order of magnitude of the He* densities, and allow to conclude that the propagation of the rebound front has a strong effect on species production close to the metallic target. Similarly to the electron density, the peak densities of He* at $z = 0.25$ cm in negative polarity are about two times lower than those obtained in positive polarity. The same tendencies reported here have been observed in *Viegas et al.* [2018a] (Figure E.3) without gas mixing. Yet, as the fixed gas-mixture in *Viegas et al.* [2018a] contains 1% of N_2 or O_2, Penning ionization reactions have higher rates and thus the loss of He* occurs faster.

IV.8 Conclusions

In this chapter we have used the 2D fluid simulations to analyze the electric field evolutions, its origins and consequences, in the case of a Helium discharge with N_2 and O_2 admixtures, propagating in a dielectric tube between a point electrode and a grounded metallic target for positive and negative applied voltages. The main results of the studies presented in this chapter can be summarized as follows:
(i) First, for both polarities of the applied voltage and for various lengths of the dielectric tube, we have shown that a first ionization front propagates from the point electrode towards the grounded metallic target. Then, in the conductive channel formed between both metallic electrodes, a rebound front propagates from the target to the point electrode. The propagation velocity of the rebound front is about 1.5 times higher than the propagation velocity of the first ionization front. These results are in good agreement with experiments in plasma jets impacting grounded metallic targets [*Darny et al.*, 2017b].
(ii) Second, we have shown that the rebound front propagates as a neutralization wave with reverse polarity with respect to the first ionization front. As the first discharge impacts the target, a new ionization front, called rebound front, starts at the grounded target and propagates in an already ionized channel towards the powered electrode. The new charge separation and propagating net charge density have the opposite sign.
(iii) Third, for both polarities of the applied voltage and for various lengths of the dielectric tube, the magnitude of the electric field in the rebound front is much smaller than in the first ionization front. The study of the time evolutions of E_z and E_r outside the dielectric tube has put forward that the propagation of the first and rebound fronts correspond to peaks of $|E_z|$. At a given axial position, during the first ionization front propagation, we have shown that the peak of $|E_z|$ is reached while $|E_r|$ is still rising, as observed in experiments. We have also shown that the fast decrease of $|E_r|$ observed in the experiments corresponds to the second peak of $|E_z|$ and then to the propagation of the rebound front.
(iv) Fourth, we have studied in simulations how both E_z and E_r vary in time inside and outside the tube. These results clearly show the interest to use plasma jet experiments and simulations in a complementary way to derive from electric field measurements outside the tube, the electric field in locations where it is difficult to carry out measurements. Then, we have pointed out that $E_r(r)$ outside the tube is mostly related to ρ inside the tube in the case of positive polarity of applied voltage, and to σ inside the tube in the case of negative polarity of applied voltage.
(vi) Finally, we have shown that the density of both electrons and metastable He* in 99.9% He - 0.1% N_2 and 99.9% He - 0.1% O_2 discharges in plasma jet configuration with gas mixing at the end of the tube are very close. We have observed that at an axial position far from the target, the densities show two increases, corresponding to the first and rebound front propagations. Close to the target, the first ionization and rebound fronts are very close in time, and then, only one peak of density is observed. Due to the combined effect of these two fronts, the densities close to the target are higher than close to the point electrode. Similar results are obtained for both voltage polarities, but we have observed that the peak density of metastable He* close to the target is about two times lower in negative polarity than in positive polarity, reflecting approximately the same difference for electron density.

Chapter V

Discharge interaction with targets of different electrical character

Contents

V.1 Introduction 140

V.2 Modeling of the discharge interaction with different targets . . . 141

V.2.1 Experimental diagnostics 141

V.2.2 Simulation conditions 142

V.2.3 Model used for a metallic target at floating potential 144

V.3 Influence of the permittivity of the dielectric target on the discharge dynamics 145

V.3.1 Model used for a dielectric target 145

V.3.2 Influence of the permittivity of the dielectric target on the discharge dynamics 149

V.4 Influence of the electrical character of the target on the discharge dynamics 152

V.4.1 Propagation dynamics for different targets 152

V.4.2 Post-impact dynamics for different targets 154

V.4.3 End of pulse dynamics for different targets 157

V.5 Conclusions 161

V.1 Introduction

To proceed with the characterization of plasma jets, it is interesting to analyze the interaction of the discharge with different kinds of targets. The state of the art on that subject has been exposed in section I.3. In chapter IV the electric field evolutions have been characterized in detail in the case with a grounded metallic target and in chapter VI the electric field distributions in a jet impinging on a dielectric target of floating potential will be examined and compared with experimental results. In this chapter, we evaluate how the discharge propagation is affected by the presence of metallic or dielectric targets and the procedure to model the discharge interaction with each kind of target. Besides analyzing the cases with grounded metallic target and floating dielectric target, an intermediate case with a metallic target at floating potential is studied.

In *Norberg et al.* [2015a] it has been studied numerically the impact of He jets on dielectric and metallic grounded surfaces with a -15 kV voltage pulse. The approach of the ionization waves has been described, followed by the spreading on the target surface in the case of dielectric targets of different permittivities, along with the resulting electric field distribution inside the target. Furthermore, the differences between the different targets have been reported, along with their impact on species production in the plasma plume. With low values of ϵ_r the target has lower capacitance and a shorter RC time constant for charging the surface, which quickly leads to the depletion of the axial component of electric field and the rise of the radial component that sustains the propagation of the discharge on the surface. With high values of ϵ_r and with metallic targets, the charging of the surface is slower or inexistent, there is no radial component of electric field and no discharge propagation on the surface. Instead, higher voltage drop remains in the gap, which promotes the rebound front propagation (called restrike of the ionization wave in *Norberg et al.* [2015a]) and the formation of a conductive channel until the target surface.

In this chapter, we assess the discharge dynamics in positive polarity with different targets and we investigate the dependence of the rebound front and of the electric field reversal at the falling edge of the pulse of applied voltage on the electrical character of the target. In section V.2, we present the conditions used in the model to describe the interaction of the discharge with different targets. In particular, the conditions to assess a metallic target with floating potential are described. Then, in section V.3 a test of several hypothesis of numerical parameters to describe the interaction with dielectric targets is presented. In the same section, the influence of the dielectric permittivity of the target is shown, by comparing the discharge dynamics with targets with ϵ_r 4 and 40. Then, in section V.4, results are presented to describe how the electrical character of the target influences the discharge dynamics. Three different targets are examined: a grounded metallic target, as the one studied in chapter IV; the floating dielectric target studied in detail in chapter VI; and a metallic target at floating potential, to evaluate the influence of the metallic/dielectric character of the target and of the floating/grounded character of the target separately. The discharge dynamics is divided in three timescales: discharge propagation, post-impact dynamics and end-of-pulse dynamics. The presence or absence of the rebound front and of the end-of-pulse electric field reversal with each target is shown and explained with a more microscopic approach than that of previous works.

V.2 Modeling of the discharge interaction with different targets

In this chapter, even though results are not directly compared with experiments, we take steps to describe the experimental conditions of Elmar Slikboer, Ana Sobota and Olivier Guaitella at Laboratoire de Physique des Plasmas, École Polytechnique, for which detailed comparison will be performed in chapter VI.

V.2.1 Experimental diagnostics

Firstly, we briefly describe the experimental set-up used to examine the plasma-target interaction and the discharge dynamics observed experimentally. The propagation of a non-thermal atmospheric pressure plasma jet towards targets at floating potential has been monitored experimentally.

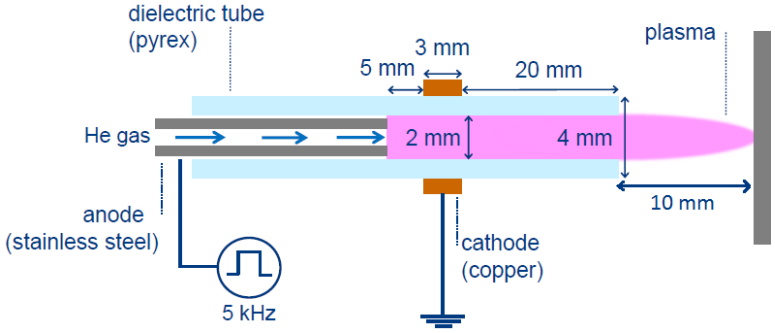

Figure V.1: Jet design used in the experiments to study the plasma jet propagation and interaction with a floating target.

The jet design used in this experiment is shown in Figure V.1, is essentially the same as used in *Hofmans* [2017]; *Klarenaar et al.* [2018] and is described more comprehensively in *Sobota et al.* [2013]. The plasma jet operates in coaxial configuration where 1 slm (standard liter per minute) helium flows first through an inner stainless steel tube into the pyrex capillary (inner radius 1.25 mm and outer 2.0 mm) before it mixes with air. The inner tube operates as a powered electrode driven by a 1 μs pulse of V_P plateau applied voltage at a 5 kHz repetition rate with a rise-time of 50 ns. The ionization wave travels from the edge of the inner tube towards the grounded ring, which is 5 mm downstream around the pyrex capillary. After charging the dielectric tube between the powered and grounded electrodes, the ionization wave travels further downstream, creating a plasma plume appearing outside the tube. The discharge then interacts with the target placed perpendicularly to its propagation. This is visualized by capturing the light emission from the plasma as the ionization wave travels towards the 0.5 mm thick target and spreads over its surface, as seen in Figure V.2 with a dielectric glass target ($\epsilon_r \sim 4$), for different time delays t_d relative to the rise of the voltage pulse, using 25 ns exposure frames.
The gap between the end of the capillary and the glass target is 10 mm. When the front of the ionization wave reaches the target (approximately at $t_d = 400$ ns), it starts propagating radially on the surface. At the surface, the radial spreading corresponds firstly to a disk of

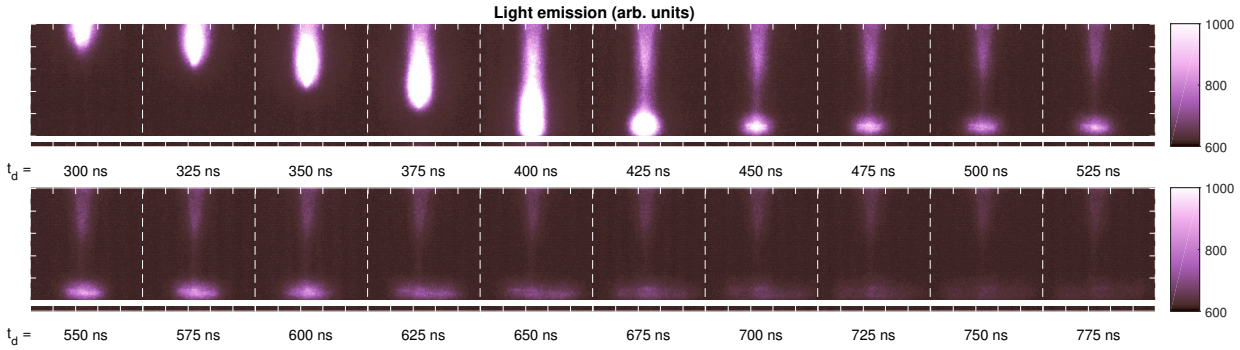

Figure V.2: Imaging of light emission showing the discharge propagation between the end of the capillary tube (on top) and the target (bottom white layer), visualizing the impact on the target surface, at several time delays t_d relative to the rise of the voltage pulse. Results from Elmar Slikboer.

increasing diameter. At 625 ns, when the disk already has more than 2 mm of diameter, the spreading splits into several streamer branches, reproducible in number for a given voltage and gas flow. This has been confirmed with top-view imaging, complementary to the side-view imaging shown in Figure V.2. At the same time, light emissions start to diminish.

V.2.2 Simulation conditions

The model set-up for the simulations presented in this chapter is shown in Figure V.3. As in the experiments, a dielectric pyrex tube with relative permittivity of $\epsilon_r = 4$, length 2.5 cm (between $z = 1.0$ cm and $z = 3.5$ cm), internal radius $r_{in} = 1.25$ mm and outer radius $r_{out} = 2.0$ mm is used. At $z = 0$, at 1 cm from the tube, the target is placed perpendicularly to the tube. In the case of the grounded metallic target, it is placed as a grounded plane. The floating dielectric and metallic targets are defined as cylinders of 2 cm radius and 0.5 mm thickness, set between $z =$ -0.5 mm and $z = 0$, as in the experiments. A grounded plane is set 10 cm behind them and therefore they are at a floating potential. Therefore, the inter-electrode distance is 3 cm with the grounded metal and 13 cm with the floating targets, which affects the Laplacian electric field in the domain. In section V.4 three targets are used: a grounded metal, a floating metal and a floating dielectric target with $\epsilon_r = 4$. The grounded metal is modeled the same way as in chapter IV. The conditions to describe the floating metallic target are described in the next section. The dielectric target is described the same way as the dielectric tube. At the surface of both dielectrics, secondary emission of electrons by ion bombardment ($\gamma = 0.1$ for all ions) is taken into account. Surface charge density σ on the surface of the dielectrics is obtained by time integrating charged particle fluxes through electric drift between the surface and the plasma. On the metal target surfaces, electrons can be emitted following a Neumann boundary condition for their fluxes through electric drift, and not through secondary emission by ion bombardment. There is no σ on the metal surfaces, since charges are considered to be conducted immediately once transported to the metal, unlike on the dielectric surfaces where they remain immobile.
Moreover, a ring electrode of inner radius 0.4 mm and outer radius 1.25 mm is set inside the tube between $z = 3.0$ cm and $z = 3.5$ cm. This electrode is powered by a pulsed voltage

that rises linearly in t_{rise} = 50 ns between 0 and V_P, as in the experiments, then is constant during the pulse duration t_P = 750 ns and then decreases back to 0 also in t_{rise}, reaching it at t = 850 ns. V_P is +4 kV in section V.4. The calculation lasts until t = 2000 ns, after the end of the pulses. Figure V.3 also shows that the discharge set-up is placed inside a grounded cylinder with a radius of 10 cm. Between the dielectric target and the grounded plane, as well as between the dielectric tube and the grounded cylinder, the space is considered as a dielectric of air permittivity ϵ_r = 1.

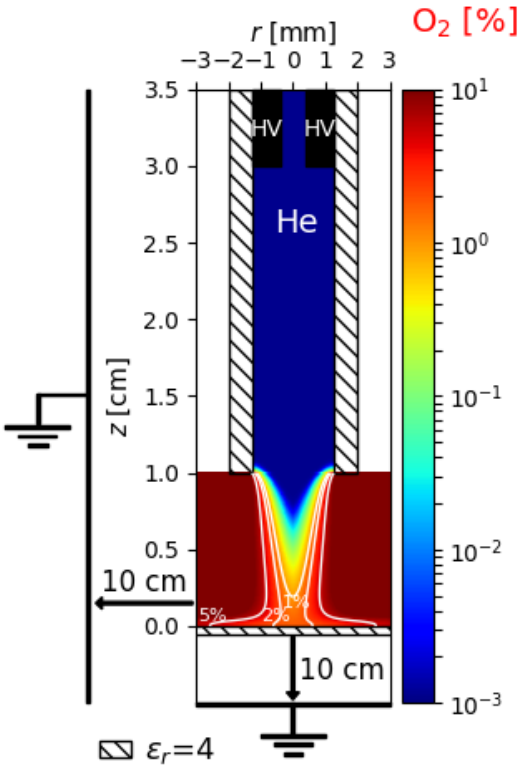

Figure V.3: Side view schematics of the discharge set-up used in the simulations in this chapter. The colour plot and the white curves show the O_2 spatial distribution in the He-O_2 mixture (percentage over a total of 2.45 × 10^{19} cm^{-3} gas density).

To model the experimental conditions, in which He flows at 1 slm through the tube into air, the plasma model has been coupled with flow calculations as described in section II.4.3. As a first approximation, the model considers a flow of 1 slm of He with 10 ppm of O_2 impurities flowing downstream into an O_2 environment. The spatial distribution of O_2 in the He-O_2 mixture obtained from the flow calculation is presented in Figure V.3. There are also added the contour curves of 1, 2 and 5% O_2 in the He-O_2 mixture, to point out the mixture region studied in this chapter. The reaction scheme used for the He-O_2 mixture is the one described in section II.4.2. As repetitive voltage pulses are used in the experiments (f = 5 kHz), we take into account a uniform initial preionization density n_{init} = 10^9 cm^{-3} of electrons and O_2^+ positive ions. However, no initial surface charges are considered on the dielectric surfaces, which will be shown in section V.4.3 to be a reasonable assumption, due to the almost zero surface charge densities calculated after the end of the pulse of applied voltage.
The mesh size is 10 μm axially between z = -0.05 cm and z = 3.5 cm and radially between r = 0 and r = 3.0 mm. Then, both behind the target (except with grounded metallic target)

and for $r > 3.0$ mm, the mesh size is expanded using a geometric progression until reaching the boundaries of the computational domain at $r = 10$ cm (20 cells between $r = 3$ mm and $r = 4$ mm and 50 more cells until $r = 10$ cm) and $z =$ -10 cm (50 cells between $z =$ -0.05 cm and $z =$ -10 cm). This refinement requires a mesh of $n_z \times n_r = 3600 \times 370 = 1.332$ million points. The average computational time required for a simulation run to obtain the results presented in this chapter was of three days with 32 MPI processes on the multi-core cluster "Hopper".

V.2.3 Model used for a metallic target at floating potential

In this section we present our current understanding of the characteristics of a metallic target at floating potential and thus of the conditions to model its interaction with the discharge. The characteristics are listed as follows:

- Even though the electric potential is floating, the metal plate has to be isopotential and the electric field in its boundaries has to be perpendicular to the metal surface. In order to guarantee that the variations of potential inside the target are minimized, a very high permittivity $\epsilon_r = 1000$ is attributed to the material. In section V.4 we show that there are no visible spatial variations of electric potential inside the floating metallic target.

- Unlike the case with the grounded metal, with a floating metal the material can charge and uncharge with the interaction with the plasma. However, unlike the case with the dielectric surface, where the charges remain immobile, with the metal we consider that charges can be conducted instantaneously inside the material. Then, for the floating metal we integrate the fluxes of inwards- and outwards-directed charged particles k in all the radial positions r_j in time, to obtain the total net charge in the material Q and we distribute this charge instantaneously and homogeneously in the target as net volume charge density ρ_M:

$$Q = \int_t \sum_k \sum_j q_k n_{k,j} v_{k,j} \pi \Delta r_j^2 dt; \qquad \rho_M(i,j) = Q \times \frac{\pi \Delta r_j^2 \Delta z_i}{\pi R^2 L} \tag{V.1}$$

  Using this formulation, the potential of the target when interacting with the plasma is defined by the potential conducted from the powered electrode through the plasma and by the charge exchange between the target and the plasma.

- As the metallic target has much larger radial dimensions than the plasma (2 cm vs 2 mm), we consider that it has an infinite number of free conducting charges that can be emitted by the action of the electric field when interacting with the plasma. Therefore, we consider the same condition as for the grounded metallic target, where electrons are emitted following a Neumann boundary condition for their fluxes through electric drift.

V.3 Influence of the permittivity of the dielectric target on the discharge dynamics

In this section, first we describe the conditions to describe positive discharge interaction with a dielectric target, and then we compare two targets with the same electrical character, dielectrics at floating potential, but with different dielectric permittivity: low permittivity with $\epsilon_r = 4$ and high permittivity with $\epsilon_r = 40$.

V.3.1 Model used for a dielectric target

The modeling of the plasma plume and of its interaction with a dielectric target presents a few challenges. In particular, in appendix F some figures are shown to illustrate the depletion of seed charges that may occur close to the dielectric target during the first ionization front propagation in the tube and in the plume. The cases shown in appendix F show conditions in which this depleted zone impacts the first ionization front as it gets closer to the dielectric target. In fact, the propagation of the discharge front towards the target and its interaction with the surface are very sensitive to several simulation parameters. In this section, to describe the discharge interaction with a dielectric target, its sensitivity to these parameters and the choice of parameters for the next sections, we show results of simulations with the conditions explained in section V.2, with $V_P = +4$ kV, keeping the model with the local electric field approximation and using four sets of parameters:

- Standard conditions: Minimum electron density 10^4 cm^{-3} (it has been checked that it has no influence in the cases presented here, since n_e doesn't decrease from 10^4 cm^{-3}); Photoionization coefficient 10; Secondary electron emission by ion impact on the dielectric target surface with $\gamma = 0.1$.

- Minimum electron density 10^8 cm^{-3} (when n_e is lower than 10^8 cm^{-3}, electrons are created to fulfill that condition, and O_2^+ is also produced to fulfill quasineutrality); Photoionization coefficient 10; Secondary electron emission by ion impact on the dielectric target surface with $\gamma = 0.1$.

- Photoionization coefficient 1000; Minimum electron density 10^4 cm^{-3}; Secondary electron emission by ion impact on the dielectric target surface with $\gamma = 0.1$.

- Electron emission from the dielectric target surface towards the plasma following a Neumann boundary condition for the electron flux; Minimum electron density 10^4 cm^{-3}; Photoionization coefficient 10.

Firstly, Figure V.4 presents the spatial distribution of the electron density at the moment the discharge front reaches the end of the tube at $z = 1.0$ cm, for each case listed above. In every condition the discharge ignites close to the powered electrode at $z = 3.0$ cm and $t = 50$ ns and then propagates until the end of the tube with a velocity around 5 cm.μs^{-1}. In the standard case, the discharge structure inside the tube presents an average radius around 0.75 mm, within which the electron density has values between 0.5 and 2.5 $\times$ 10^{12} cm^{-3}, and slowly deposits positive surface charges on the tube wall, reaching maximum values of

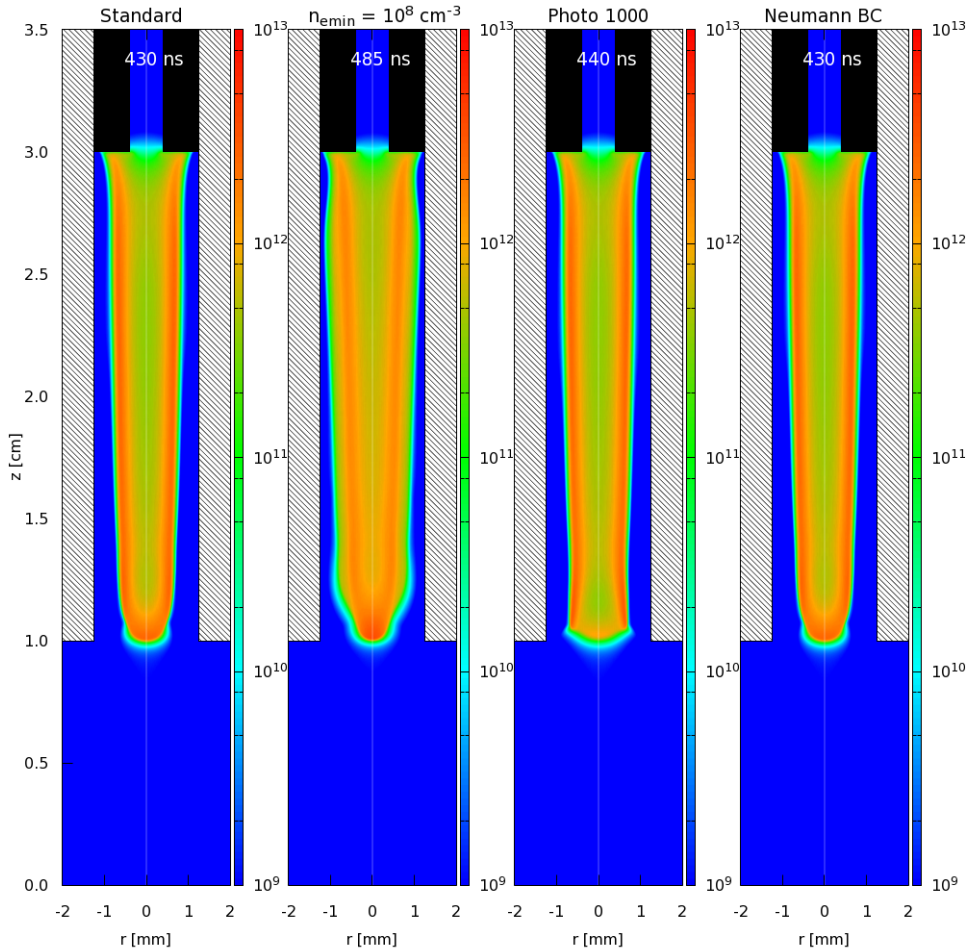

Figure V.4: Cross sectional views of n_e, in cm^{-3}, with $V_P = +4$ kV, at the time when the discharge reaches the end of the tube at $z = 1.0$ cm. From left to right: Standard conditions; Condition with $n_{emin} = 10^8$ cm^{-3}; Condition with photoionization coefficient 1000; Condition with Neumann boundary condition for the electron flux.

0.7 nC.cm^{-2} in the present case. The maximum n_e shown here agrees with those measured through Thomson scattering in Helium jets in positive polarity at the exit of capillary tubes in *Hübner et al.* [2014]; *Klarenaar et al.* [2018], close to 10^{12} cm^{-3}, while n_e at $r = 0$ is in the range of values estimated in *Sretenovic et al.* [2017] from electric field measurements inside the tube, between 10^{11} and 10^{12} cm^{-3}. The maximum value of the axial component of electric field on the discharge front inside the tube is always close to 15 kV.cm^{-1} and its radial position moves from r = 0.75 mm to r = 0 as the discharge front gets farther from the powered electrode, being already positioned on the axis of symmetry when reaching the end of the tube. In the remaining conditions, the characteristics of the discharge in the tube are similar. It is visible that the imposition of minimum electron density at 10^8 cm^{-3} already has an effect inside the tube, decreasing the width of the radial sheath between the plasma bulk and the tube wall and decreasing the velocity of propagation. The increase of the photoionization coefficient has a negligible impact in a medium with only 10 ppm O_2, but an influence is visible when the front approaches the end of the tube, due to an increase of electron production in front of the discharge propagation in the region where He and O_2 start mixing. Finally, the Neumann boundary condition for the electron flux on the plasma-target

interface has no effect on the discharge propagation as far as 1 cm from the target.

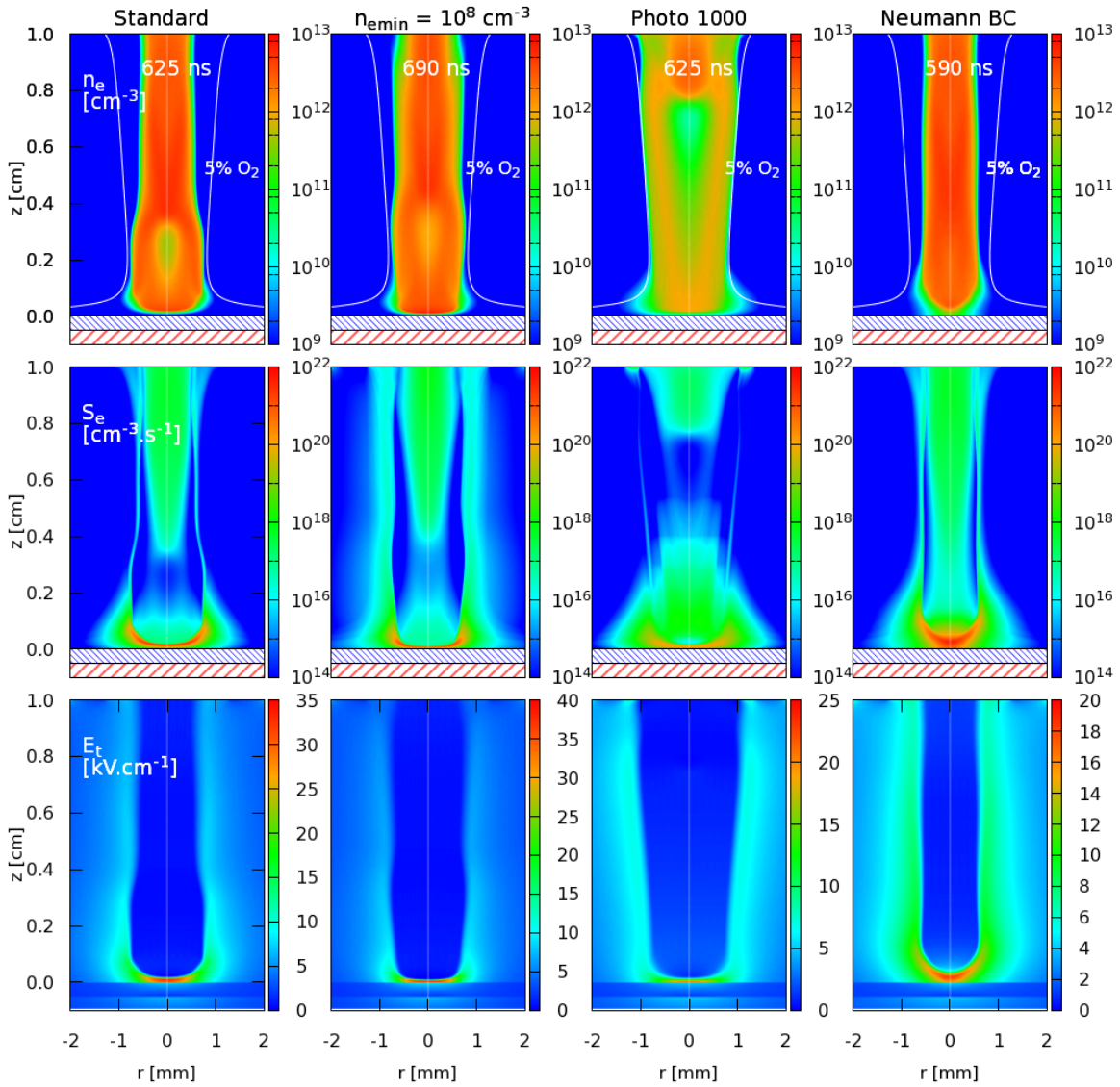

Figure V.5: Cross sectional views of n_e, S_e and E_t (from top to bottom), with $V_P = +4$ kV, at the time when the discharge reaches the dielectric target at $z = 0$. From left to right: Standard conditions; Condition with $n_{emin} = 10^8$ cm^{-3}; Condition with photoionization coefficient 1000; Condition with Neumann boundary condition for the electron flux;

Then, in Figure V.5 are represented the distributions of electron density n_e, the ionization source term by electron impact S_e and the magnitude of electric field E_t, for the same conditions as in Figure V.4. These are shown only in the plasma plume between $z = 1.0$ cm and $z = 0$ and at a time of impact of the discharge front on the dielectric target. There is also presented the contour curve of 5% O_2 in the He-O_2 mixture, to clearly show the mixture region where the discharge dynamics takes place in each case. In every case the discharge is centered at the end of the tube where there is only 10 ppm of O_2, and approaches the mixture of 5% O_2 in the plasma plume. We can conclude that in every case the discharge front crosses several He-O_2 mixtures between the tube and the target. Then, it is visible that the discharge structure is different in each of the four cases. Therefore, even though the

impact of the discharge on the target is centered (takes place at $r = 0$) in every case, we see that the trajectory of the discharge front is different.
In the case with standard conditions, the propagation is centered from the end of the tube until $z = 0.4$ cm. During the propagation, there is a decrease of the electron density in the regions of higher O_2 density, due to fast attachment reactions (see section III.6.5). Simultaneously, the electric drift of electrons from the gas close to the dielectric target towards the positive discharge causes a depletion of electrons close (some mm) to the dielectric surface, decreasing the electron density from the initial $n_{e0} = 10^9$ cm^{-3} to as low as 10^5 cm^{-3}. This depletion leads to a decrease of the ionization source term ahead of the discharge front, which is the quantity that defines the path of propagation (see section III.6.5). Thus, the discharge front deviates from its axial path and propagates partially outwards until the gas-mixture and the electron production around the front are more favorable to propagate axially and towards the center. Therefore, the electron depletion leads the discharge propagation to uncenter between $z = 0.4$ cm and $z = 0.1$ cm, before centering again close to the target, when the axial component of electric field is reinforced due to the dielectric permittivity ϵ_r. By imposing a minimum electron density of 10^8 cm^{-3}, the depletion of electrons is lower, and so is the uncentering of the discharge propagation, but in absolute it is maintained, being visible the lower n_e between $z = 0.4$ cm and $z = 0.1$ cm at $r = 0$ than at higher radial positions.
The artificial increase of the photoionization leads to a very different structure. Indeed, the discharge front gets further from the axis as soon as it exits the tube, not because of electron depletion, but due to the much easier electron production through photoionization in the regions of higher O_2 density, up to 5% O_2. In this case, photoionization becomes a main propagation mechanism in the plasma plume, contrarily to what has been described in section III.6.5 with photoionization coefficient 10. Even though the photoionization increases with O_2, the absorption length of photons decreases with O_2, and therefore the radial expansion of the discharge is limited. In these conditions the front tends to $r = 0$ during the propagation in the plume and reaches the target with a centered structure. Finally, using the Neumann boundary condition for the electron flux, the electron depletion is completely avoided by the continuous flux of electrons, and the propagation is centered during the whole trajectory of the discharge front.
For each of the studied conditions, as the discharge structure and the impact on the target are different, charge deposition on the target is affected and thus the choice of simulation conditions is important for the proceeding studies of interaction between plasma and dielectric target. The artificial increase of photoionization and the inclusion of the Neumann boundary condition for the electron flux have been useful to evaluate the effect of the electron depletion on the discharge dynamics, but we consider them to be less physical conditions. In this chapter, the standard conditions are used, as we take them to be the closest to physical reality.

V.3.2 Influence of the permittivity of the dielectric target on the discharge dynamics

In this section we compare two targets with the same electrical character, dielectrics at floating potential, but different dielectric permittivity: low permittivity with $\epsilon_r = 4$ and high permittivity with $\epsilon_r = 40$. These calculations have been performed using the model exposed in section II.4.5, to be able to describe the discharge interaction with the target of high permittivity. The tube is slightly shorter than in the rest of the chapter, with the powered electrode at $z = 2.0$ cm and $V_P = +6$ kV, with the same pulse of applied voltage. In Figure V.6 the distribution of E_t is represented for these two cases at several times: During propagation in the plume; at the time of impact on the target; at the beginning of the radial spreading on the target, 20 ns after the impact; when the discharge front spreading radially reaches $r = 2$ mm.

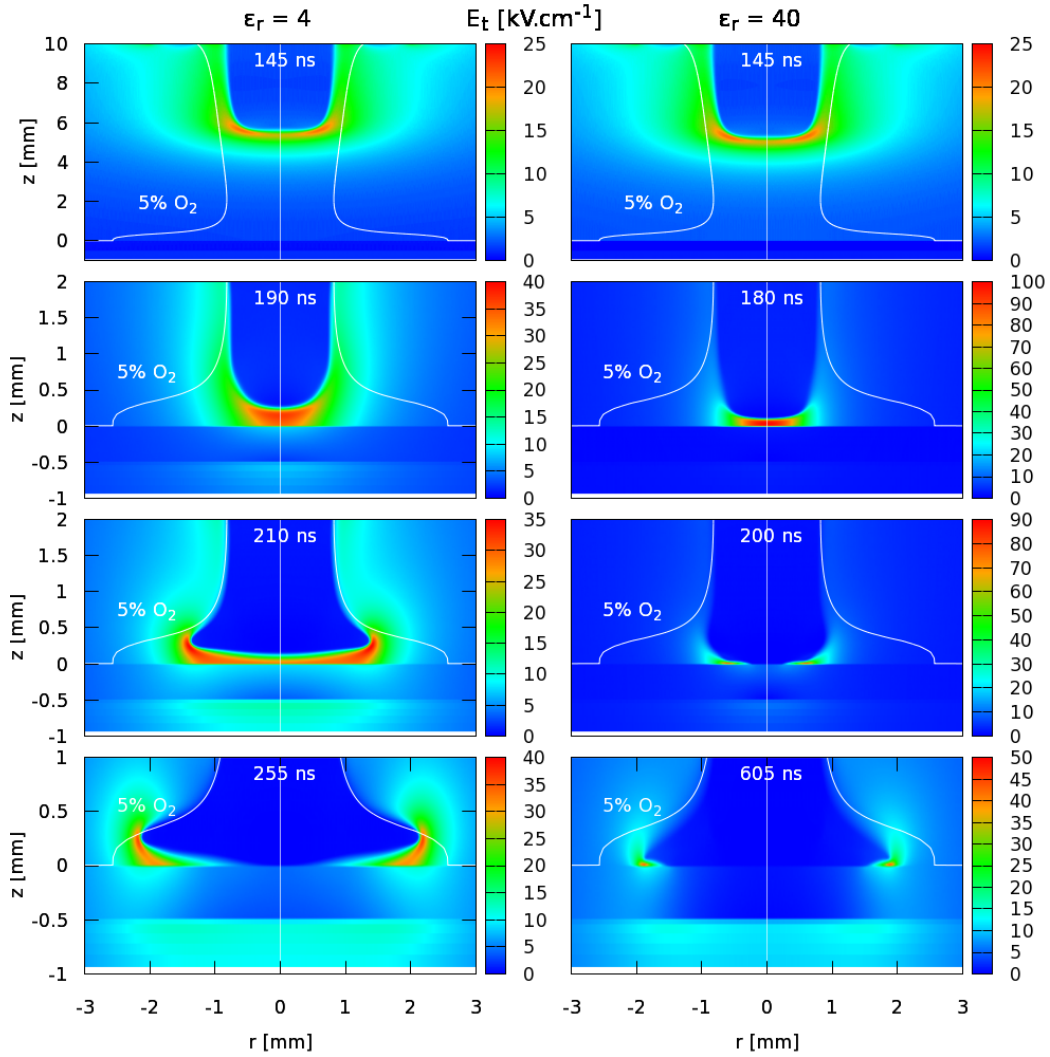

Figure V.6: Cross sectional views of E_t close to the target, at several times, for the cases with floating dielectric targets of $\epsilon_r = 4$ and $\epsilon_r = 40$ and with $V_P = +6$ kV.

Figure V.6 shows that the discharge propagation until the middle of the plume is the same with dielectric targets of different permittivity. Then, we see that the propagation between $z = 5$ mm and $z = 0$ takes 45 ns with $\epsilon_r = 4$ and only 35 ns with $\epsilon_r = 40$, even though

the electron boundary conditions are the same. This shows that the difference in velocity is induced by the stronger axial electric field on the discharge front when it is approaching the target of higher permittivity. Twenty ns after the impact, we notice that the discharge propagates radially on the target surface in both cases. However, with $\epsilon_r = 4$ we notice that the discharge front (i.e. the maximum of the radial component of electric field) has a variable axial position but remains at ~ 260 μm from the surface while with $\epsilon_r = 40$ it stands at ~ 50 μm. Moreover, in the first case a positive sheath remains at the center between the plasma and the surface, which means that the target keeps charging at that position, while with $\epsilon_r = 40$ the strong axial electric field has lead to a faster deposition at $r = 0$ and the sheath has already vanished at that position. Finally, it is visible that the radial spreading is faster with lower ϵ_r, in agreement with *Pechereau et al.* [2012]; *Norberg et al.* [2015a]; *Wang et al.* [2016a]. With $\epsilon_r = 4$, the discharge takes 65 ns to propagate 2 mm (average velocity 3.08 cm/μs), while with $\epsilon_r = 40$ this time increases to 425 ns (average velocity 0.47 cm/μs, almost 6 times slower). In fact, with higher ϵ_r, as the electric potential is more homogeneous inside the target, the radial electric field on its surface is lower and then the radial propagation is slower. To verify this hypothesis, the maximum values of $|E_z|$ and E_r during the radial spreading on the target are represented as function of time in Figure V.7 (on the left). These are found on the discharge front every 5 ns. In the case of $|E_z|$, its maximum is located on the interface between the dielectric and the positive discharge head, while the maximum of E_r is located above the surface. On the right side of Figure V.7 is represented the temporal profile of the charging of the dielectric, both locally through σ at $r = 0$, and globally through the total charge deposited on the surface Q, obtained by integrating σ (eq. II.25).

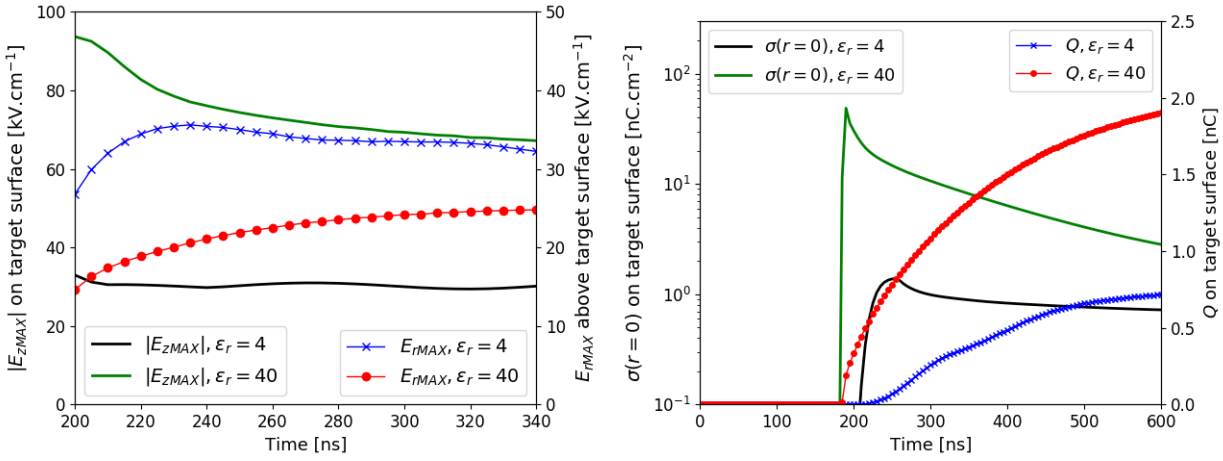

Figure V.7: Temporal profiles of $|E_z|_{MAX}$ and E_{rMAX} during the radial propagation on the target surface (on the left) and $\sigma(r = 0)$ and Q (on the right), for two floating dielectric targets with $\epsilon_r = 4$ and $\epsilon_r = 40$, with $V_P = +6$ kV. Values obtained every 5 ns.

Figure V.7 shows that indeed $|E_z|_{MAX}$ is more than two times higher with $\epsilon_r = 40$ than with $\epsilon_r = 4$, which leads to a faster local charging of the surface. Moreover, with $\epsilon_r = 40$ E_{rMAX} has values between 15 and 25 kV.cm^{-1}, while with $\epsilon_r = 4$ these stand between 25 and 35 kV.cm^{-1}, which explains the faster radial spreading on the target surface. On the right-hand side figure, we notice that σ on the axis attains much higher values with $\epsilon_r = 40$ than with $\epsilon_r = 4$ (~ 50 nC.cm^{-2} vs 1.4 nC.cm^{-2}). Furthermore, σ reaches its temporal maximum with $\epsilon_r = 40$ in only 10 ns, while with $\epsilon_r = 4$ it takes 65 ns to reach the maximum. However, even

though the discharge spreads faster on the surface with lower permittivity, the global charge on the target surface Q also rises faster with higher ϵ_r. Lower surface charge deposition and higher E_{rMAX} for lower ϵ_r has also been reported in *Wang et al.* [2016a]. Then, in Figure V.8 we evaluate how the change of permittivity can affect the electric field rebound and the profiles of electric potential studied in chapter IV. $E_z(t)$ is represented on the left, at $r = 0$ and $z = 0.25$ cm, and $V(z)$ is represented on the right, before the impact on the target at $t = 175$ ns and 10 ns after the impact on the target for each case. In fact, the electric field rebound is visible in Figure V.8 for $\epsilon_r = 40$, but is more subtle than the ones studied with the metallic targets in chapter IV and also shown in the next section in Figure V.11.

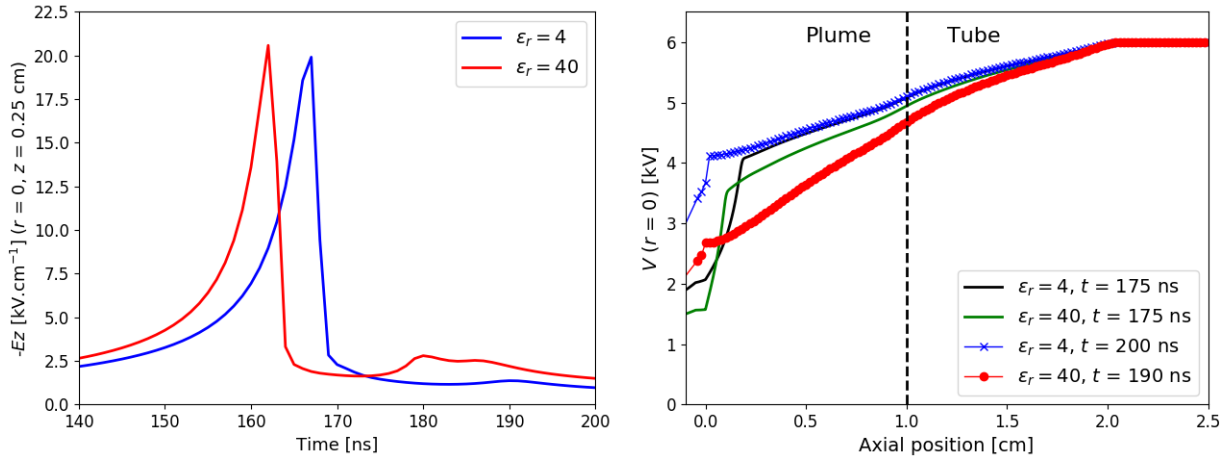

Figure V.8: Temporal profiles of E_z (on the left) and axial profiles of V (on the right), for two floating dielectric targets with $\epsilon_r = 4$ and $\epsilon_r = 40$, with $V_P = +6$ kV.

In fact, the right side of Figure V.8 shows that even before the discharge impact on the target, at the same time $t = 175$ ns, the electric potential is already higher with $\epsilon_r = 4$ than with $\epsilon_r = 40$ on the target and in the plasma plume. On the one hand, the Laplacian potential on the target is higher with lower ϵ_r. On the other hand, as mentioned earlier, higher ϵ_r provides lower E_r close to the target. Then, with lower ϵ_r, E_r is also higher in the plasma plume and more ρ is produced on the radial edges of the plasma channel, as reported in *Norberg et al.* [2015a], conducting more potential from the powered electrode. As the discharges impact the target, even though the local and global charging of the dielectrics are higher and faster with higher ϵ_r, the targets have a big volume that is not charged. As with higher ϵ_r the potential is more homogeneous inside this volume, the potential of the target at $z = 0$ and $r = 0$ increases slower with higher ϵ_r. Finally, as the target potential increases slower with higher ϵ_r, a subtle electric field rebound can propagate in the axial direction. This result confirms that the existence or absence of the rebound front is defined by the electric potential on the target shortly after the impact, which decreases with ϵ_r. This is in agreement with the results reported in *Norberg et al.* [2015a], where the rebound is related to the "RC time constant for charging the surface".

V.4 Influence of the electrical character of the target on the discharge dynamics

In this section, a comparison is carried out between the properties of the discharge dynamics with positive polarity in the case where the target is a grounded metal, as in the cases studied in chapter IV, in the case where the target is a floating dielectric, as in chapter VI, and in a third case where the target is a metal at floating potential. The conditions are as described in section V.2. The study of the floating metallic target allows to evaluate if the differences between the cases with floating dielectric and grounded metallic targets are due to the inter-electrode distance, the charging of the target or the conductivity of the target.

V.4.1 Propagation dynamics for different targets

Figure V.9 shows the spatial distribution of the magnitude of the electric field E_t at different times for each case of different target. E_t is presented in the plasma plume, as well as inside the target and slightly below, until z = -1 mm. There is also presented the contour curve of 5% O_2 in the He-O_2 mixture, to clearly show the mixture region where the discharge dynamics takes place. For each case, four time instants have been chosen to present the discharge dynamics in the plume: when the discharge front is crossing the gap between the tube and the target, approximately in the middle at $z = 5$ mm; the instant of impact of the discharge front on the target surface at $z = 0$; some ns later when is visible the redistribution of electric field after the impact; at the time immediately before the end of the pulse of applied voltage, at $t = 800$ ns.
In every case studied in Figure V.9 the discharge propagates between the end of the tube and the target with an approximately centered front. When the front propagates in the middle of the gap, it presents a clear maximum of electric field on the axis of symmetry with positive polarity of applied voltage. We notice that the discharge front reaches the middle of the gap at the same time ($t = 510$ ns) with floating dielectric and metallic targets, which shows that the difference of the target permittivity (4 vs 1000) does not change the discharge dynamics in the tube and in the first 5 mm of the plasma plume during the propagation towards the target. However, when the metallic target is grounded, Figure V.9 shows that the discharge front reaches the same position faster ($t = 430$ ns), which is attributed to the lower inter-electrode distance, that accelerates the discharge dynamics in the tube and in the plume. Then, the propagation from the middle of the gap until the target takes approximately the double of time with the floating dielectric target (115 ns) than with the floating metallic target (60 ns) and the grounded target (51 ns). In fact, it is noticeable that the difference in the electrical character of the floating dielectric and metallic targets (permittivity and electron emission) justifies a different dynamics of propagation in the last 5 mm before the impact on the target, mostly due to the lack of electrons and the positive sheath formed between the discharge and the target.
Figure V.10 presents the axial velocities of propagation of the ionization waves as they travel from the powered electrode towards the target, for the three different targets, as well as the maximum of E_z on the axis during the propagation. In agreement with what has been shown in Figure V.9 and reported in *Ji et al.* [2018], the velocity is always higher with the grounded

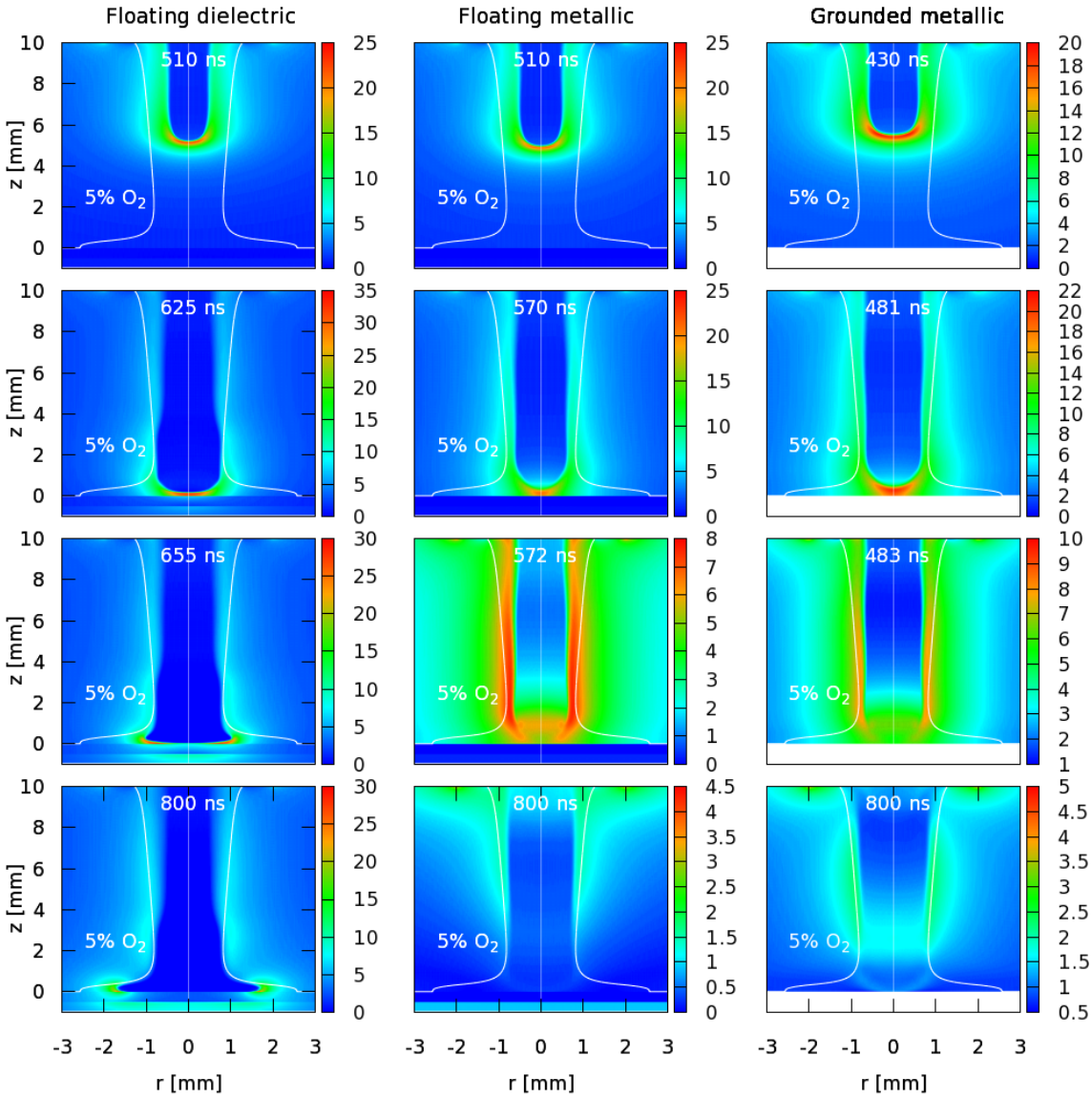

Figure V.9: Cross sectional views of the magnitude of the electric field E_t in kV.cm^{-1}, at several times with floating dielectric target (on the left), floating metallic target (on the center) and grounded metallic target (on the right), for $V_P = +4$ kV.

metallic target than with the targets at floating potential. Moreover, the propagation with both floating targets presents approximately the same velocity of propagation and E_{zMAX} until the middle of the plasma plume. Then, in the last 5 mm of propagation, the front velocities increase as the discharges approach the metallic targets, due to the proximity to either the ground or the surface of $\epsilon_r = 1000$. Conversely, with the dielectric target of $\epsilon_r = 4$, the velocity of the ionization front and E_{zMAX} only increase in the last 1 mm of propagation. We should point out that in the case with positive polarity and dielectric target, the velocity and maximum electric field decrease in the last 5 mm of propagation due to the electron depletion explained in the previous section. Moreover, with the dielectric target, we also notice the strong increase of the peak electric field as the discharge front reaches the target surface, represented also in Figure V.9 for $t = 625$ ns. This increase is higher than with the metallic targets because a positive sheath with a strong potential drop is generated as

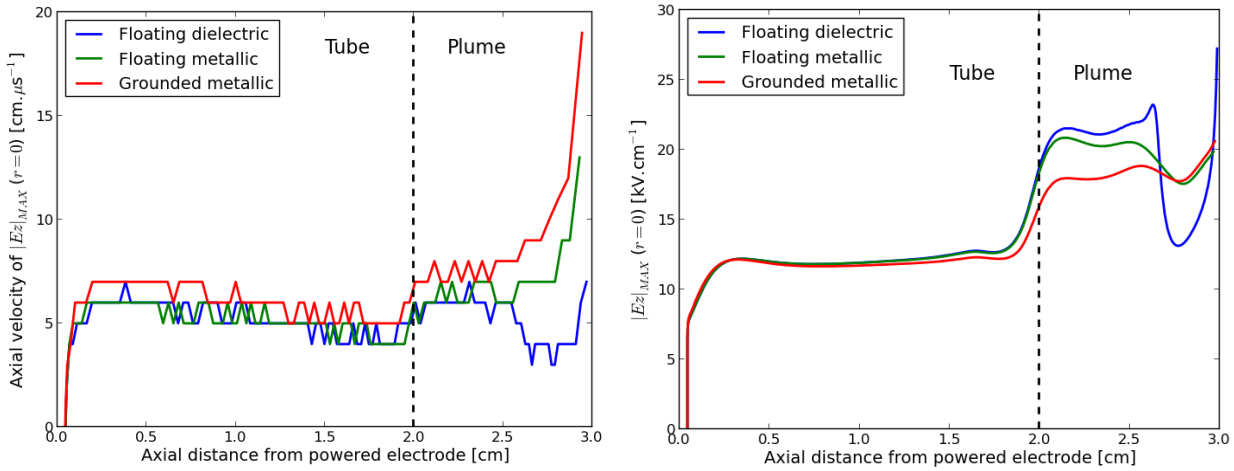

Figure V.10: Axial velocity of propagation of $|E_z|_{MAX}$ (on the left) and $|E_z|_{MAX}$ (on the right) at $r = 0$ between the powered electrode and the target, with 5 ns temporal resolution, for floating dielectric, floating metallic and grounded metallic targets, with $V_P = +4$ kV.

the discharge propagates through the depletion zone and approaches the dielectric surface. Sharp increases of the peak electric field of a He jet propagation when reaching a water target have been reported in *Kovacevic et al.* [2018]. Furthermore, we can take note that the peak electric field in the plume is generally lower with grounded metallic target than with the floating targets, contrarily to the numerical results in *Norberg et al.* [2015a] in negative polarity and in *Ji et al.* [2018] for a positive case. To understand why, we should notice that the discharge structure is different in each of these works. In our case, it is visible in Figure V.9 that the discharge front is broader with grounded metallic target than with the floating targets, and then the discharge is faster even with lower peak electric field. Finally, we notice that in all the cases the maximum of $|E_z|$ increases in the plume, as the discharge radial confinement is reinforced by the He-O_2 mixture, as described in section III.6. An increase of the maximum of electric field (close to $r = 0$) at the exit of the tube has been measured experimentally in He jets with different positive applied voltages, both in free jet conditions and with different targets [*Hofmans*, 2017; *Sobota et al.*, 2016; *Sretenovic et al.*, 2014a, 2017]. In addition, similar values of peak electric field have been measured along the propagation inside the dielectric tube in similar jet conditions and positive polarity of applied voltage in *Hofmans* [2017].

V.4.2 Post-impact dynamics for different targets

After the impact of the discharge on the target, Figure V.9 shows that the electric field penetrates inside and below the dielectric target and spreads on its surface, as charges are deposited on the surface, until the end of the pulse at $t = 800$ ns, as it is known to happen in streamer interaction with dielectric surfaces [*Pechereau et al.*, 2012; *Pechereau and Bourdon*, 2014]. It is also noticeable that the electric field remains in the plasma plume, surrounding the plasma channel, but is almost zero in the quasineutral channel. As far as the metallic targets are concerned, no penetration of the electric field inside the targets is visible, even at floating potential, due to the very high dielectric permittivity. However, with metallic target at floating potential, it is visible that at $t = 800$ ns the target is sufficiently charged

and at sufficiently high potential to originate an electric field behind it. With both metallic targets, the plasma interacting with the target remains close to the axis of symmetry, in agreement with what is reported in *Sakiyama et al.* [2008], and the electric field propagates back in direction of the tube and the powered electrode, as in the cases studied in chapter IV. These results are in agreement with *Norberg et al.* [2015a]; *Yue et al.* [2018]; *Klarenaar et al.* [2018], where is reported that the interaction with metallic targets promotes the rebound front propagation. Furthermore, it is visible in Figure V.9 that between the impact of the discharge front on the metallic targets and the end of the pulse at $t = 800$ ns the electric field surrounding the plasma plume decreases in magnitude to about half its value, which is not the case with the dielectric target. The higher remaining volume charge densities in the plasma plume and associated electric field with dielectric target is a feature that has also been reported in *Norberg et al.* [2015a]. That is the case because after the impact on a metallic target the electric field rebound partially uncharges the plasma channel, as described in chapter IV. In order to investigate the electric field rebound with the different targets, the temporal profiles of E_z at $r = 0$ and E_r at $r = 0.6$ cm until the end of the pulse at $t = 800$ ns are presented for each target in Figure V.11. Two axial positions are assessed: $z = 0.25$ cm, in the plume close to the targets, and $z = 1.0$ cm, at the position of the end of the tube.

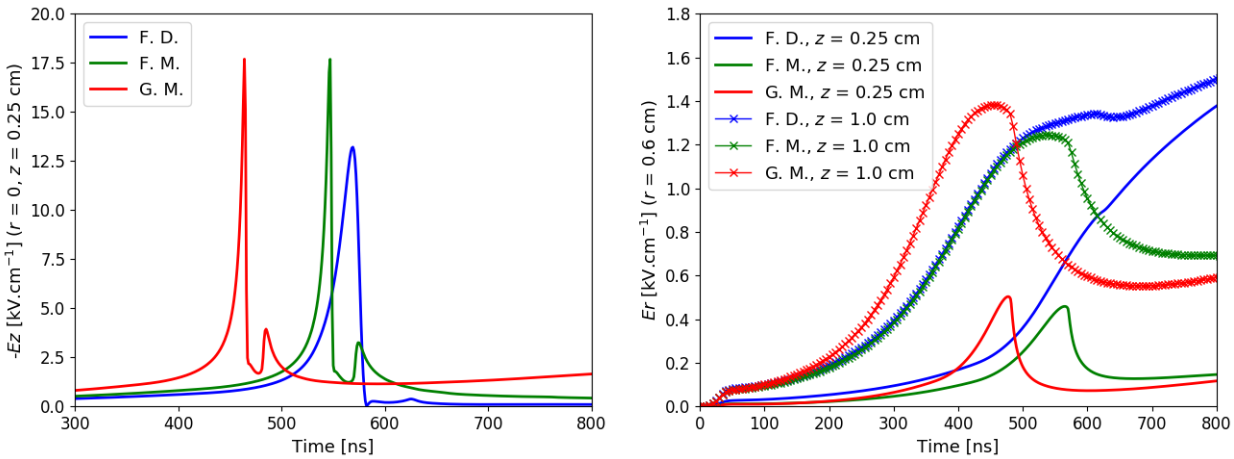

Figure V.11: Temporal profiles of E_z at $r = 0$ and $z = 0.25$ cm (on the left) and of E_r at $r = 0.6$ cm and $z = 0.25$ and 1.0 cm (on the right), for floating dielectric (F.D.), floating metallic (F.D.) and grounded metallic (G.M.) targets, with $V_P = +4$ kV.

In Figure V.11 we find that at $z = 0.25$ cm, with metallic targets, $E_z(t)$ presents two peaks and $E_r(t)$ presents only one small peak, which is the signature of the electric field rebound close to the target, studied already in chapter IV. Conversely, with dielectric target, in the absence of rebound, $|E_z|(t)$ decreases to practically zero and $E_r(t)$ continues rising after the arrival of the discharge front, due to the charges cumulating firstly in the plasma plume and then close to the target surface and deposited on the surface, as the discharge spreads radially. Further from the target, at $z = 1.0$ cm, Figure V.11 shows that with metallic targets $E_r(t)$ follows again the same profile as studied in Figure IV.11, characteristic of the electric field rebound, and $|E_r|$ decreases to about half its peak value due to the partial uncharging of the plasma. This means that the rebound propagation is not limited to the region close to the target, but continues through the plume and into the tube. On the other hand, with the

dielectric target, $E_r(t)$ keeps increasing due to the remaining charges in the tube and in the plume and also the increasing charges close to the target and on its surface. Even though the electric field evolutions look very similar with the two metallic targets, we should notice that after the rebound, $E_r(t)$ remains higher with the floating metal than with the grounded metal, which reveals that the plasma channel remains more charged in the first case. Then, in Figure V.12, to complete the investigation on the effect of the electrical character of the target on the post-impact discharge dynamics, we compare the axial profiles at $r = 0$ of the electric potential in each case at different times. For each case has been picked a time of propagation in the plume, the time of impact of the first discharge front on the target as in Figure V.9, the time of end of the pulse, $t = 800$ ns, and one instant in between.

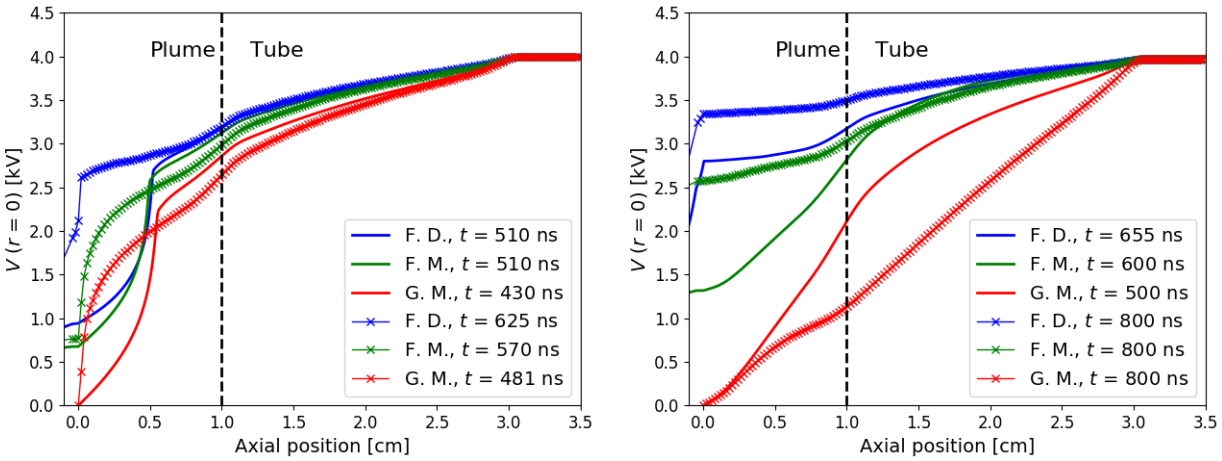

Figure V.12: Axial profiles of electric potential at $r = 0$, at several times, for floating dielectric, floating metallic and grounded metallic targets and with $V_P = +4$ kV.

It is visible in Figure V.12 that for every case the potential is maximum at the position of the powered electrode, and then decreases until the target at $z = 0$ and beyond the target (the target is placed between z = -0.05 cm and $z = 0$; in the figure, $V(z)$ is represented until z = -0.1 cm). Then, the representation of $V(z)$ during the discharge propagation in the plume shows that the target and its permittivity affect the distribution of potential already before the discharge interaction with the target. Until reaching the target, the biggest slope of the potential is in any case located between the ionization front and the target. Then, as studied in Figure IV.15, with grounded metallic target, the potential is obliged to decrease to zero at $z = 0$. In this case, as the discharge front hits the target, the discharge head is neutralized by the positive ion recombination and the electron emission. Then, unable to penetrate into the target, the electric field bounces back towards the powered electrode and the electric potential is redistributed, as studied in chapter IV and visible in Figure V.12. With a metallic target at floating potential, the positive charge in the discharge head is also partially neutralized. In fact, the net charge in the head is conserved as we are considering charge conservation in the charge exchanges between the plasma and the target. However, as the metal is conductive, its surface does not charge locally and charges are distributed over a large volume. Even though total charge is conserved, the distribution of net charge is severely affected by the interaction with the floating metal. Thus, as the discharge front reaches the target, a part of its potential is transferred to the target but the transfer of potential is much lower than with the dielectric target that charges locally. Then, in the case with floating

metal, as the slope of potential is still highest between the target and the plasma channel, the electric field rebound follows.
If we look at longer timescales, we see that between $t = 600$ ns and $t = 800$ ns, the interaction between the plasma and the target slowly but significantly charges the target and raises its electric potential. Contrarily to the case with grounded metallic target, the linear distribution of $V(z)$ does not connect 4 kV to zero, but to a floating potential (at $t = 800$ ns, around 2.5 kV). While with the grounded target between $t = 500$ ns and $t = 800$ ns, subtle rebounds still exist due the slope of electric potential and continue to partially neutralize the plasma, with the floating metal, between $t = 600$ ns and $t = 800$ ns, the slope of $V(z)$ is reduced, the neutralization is stopped and instead the target is charged. The result in long timescales is a plasma channel more charged, with higher potential and with less potential drop in the case with the floating metal than with the grounded target. Therefore, E_z inside the plasma is lower and E_r on the outside of the plasma is higher with the floating metal, as verified in Figure V.11. Finally, with the dielectric target ($\epsilon_r = 4$) at floating potential, the potential transfer from the plasma at the discharge impact is much higher and faster than with the metallic target (at time of impact, ~ 2.5 kV). This transfer is increased by the charge separation in volume close to the target and by the surface charge deposition. Then, the slope of potential between the target and the plasma channel is no longer high enough for a second electric field front to propagate. The region close to the target and the target surface are charged and the electric potential increases at the surface (~ 3.4 kV) and in the whole plasma channel until the end of the pulse. During this process, after the discharge locally charges the target, the highest slope of electric field remains on the discharge front but on the radial direction, and gives origin to the radial spreading visible in Figure V.9. These results are in agreement with those presented in *Norberg et al.* [2015a], showing that the rebound front does not takes place with floating dielectric targets because they charge fast. However, for the floating metal, after it is charged, no ionization wave propagates on its surface, as it happens with the dielectric targets. That is the case because with the floating metal the net charge density (either as ρ or σ) is no longer localized on the discharge front, which ceases to exist when the discharge impacts the target. Moreover, as metallic targets are isopotential, the radial field close to the target is very low and cannot sustain an ionization wave on the target surface.

V.4.3 End of pulse dynamics for different targets

As the value of applied voltage starts decreasing at $t = 800$ ns and goes down to zero in 50 ns, it is interesting to analyze how charges and electric fields keep evolving in the plasma. First, to understand the macroscopic effect of the end of the pulse, we study in Figure V.13 how the profiles of $V(z)$ presented in Figure V.12 keep evolving when the applied voltage decreases. Four instants in time are presented for each target, two during the decrease of applied voltage, and two in longer timescales after the decrease.
Figure V.13 shows that the electric potential along the plasma does not decrease uniformly with the applied voltage. In fact, as the applied voltage starts decreasing, the potential in the plasma can be higher than the potential in the electrode, already during the voltage decrease at $t = 825$ ns. Particularly, close to the powered electrode, a significant slope of potential

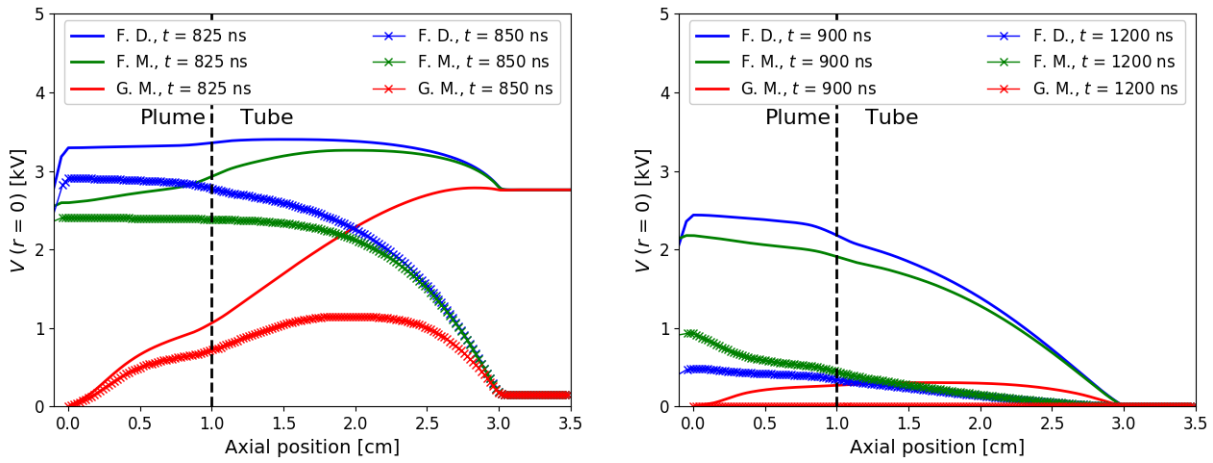

Figure V.13: Axial profiles of electric potential at $r = 0$, at several times, for floating dielectric, floating metallic and grounded metallic targets and with $V_P = +4$ kV.

is visible at $t = 850$ ns. Thus, we can conclude that if the applied voltage decreases faster than in 50 ns, as the potential in the plasma would have less time to decrease, the slope of potential close to the electrode would be higher. In fact, in *Kim et al.* [2018], numerical results show that sharper pulse terminations induce stronger field reversals. Moreover, we should notice that at $t = 850$ ns, in the two cases with floating targets, the plasma is connecting a grounded electrode at $z = 3.0$ cm, to a charged target at $z = 0$, while with the grounded metallic target, the channel is now connecting two grounded electrodes. Therefore, we expect the redistribution of potential at the end of the pulse to be different between these cases. In fact, in all the cases the redistribution is slow, taking approximately 700 ns for the potential in all the channel to cancel, but with the grounded target only the potential in the plasma decreases to zero. Instead, with the floating targets also the target itself uncharges after the end of the pulse and the total decrease of potential in the plume close to the target is visibly higher than with the grounded target. To evaluate if the redistribution of potential at the end of the pulse gives rise to an axial propagation of an electric field front, in Figure V.14 is represented the temporal evolution of $E_z(r = 0)$ after the rebound propagation, from $t = 700$ ns, at two axial positions: $z = 0.25$ cm, in the plume, close to the target (on the left), and $z = 2.5$ cm, in the tube, close to the powered electrode (on the right).
In fact, Figure V.14 shows an inversion of E_z for all targets close to the source electrode and also close to the floating targets. However, while close to the source the inverted electric field presents a peak, close to the targets its evolution is very diffuse. This redistribution of electric field is even more subtle than the one of the rebound studied in chapter IV and we do not consider it as a front or a wave of propagation. Yet, the low electric fields presented here can justify the faint discharge detected in *Yue et al.* [2018].The radial component of electric field outside the tube is expected to evolve in time in the same way as the electric potential in the plasma, since E_r is a measure of the slope between the plasma potential and the ground at $r = 10$ cm. Then, to understand the dynamics of charges that leads to the redistribution of potential, we evaluate in Figure V.15 the temporal evolution of E_r after $t = 700$ ns, along with its charge contributions (Laplacian, from σ and from ρ) at $r = 0.6$ cm and at the same axial positions as in Figure V.14. These quantities are represented exclusively in the case with floating dielectric target. We should notice that close to the target, the σ

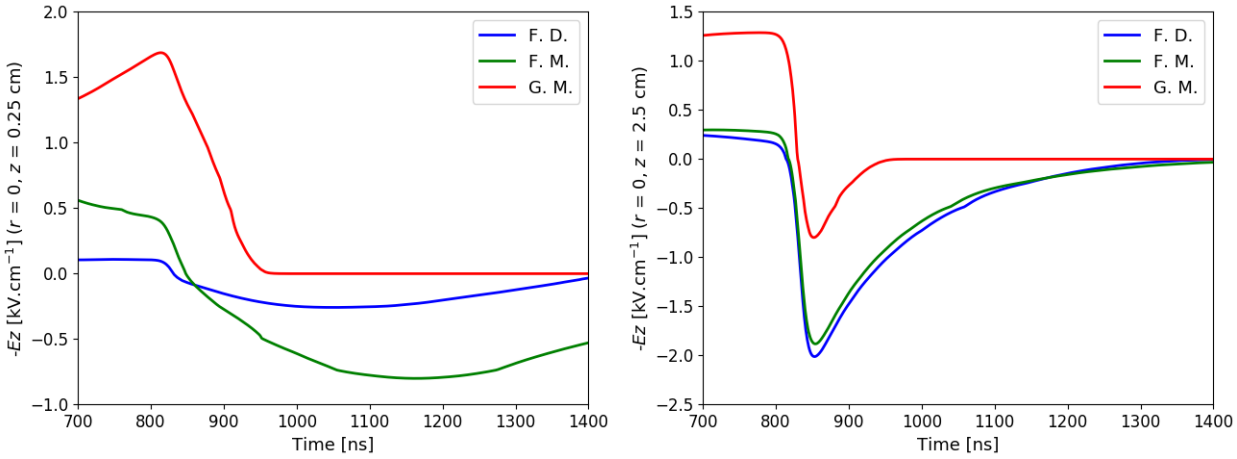

Figure V.14: Temporal profiles of E_z at $r = 0$ and at $z = 0.25$ cm (on the left) and $z = 2.5$ cm (on the right), for the three different targets, with $V_P = +4$ kV.

contribution to E_r is mostly due to σ in the target, while close to the source, it is σ in the tube that contributes the most.

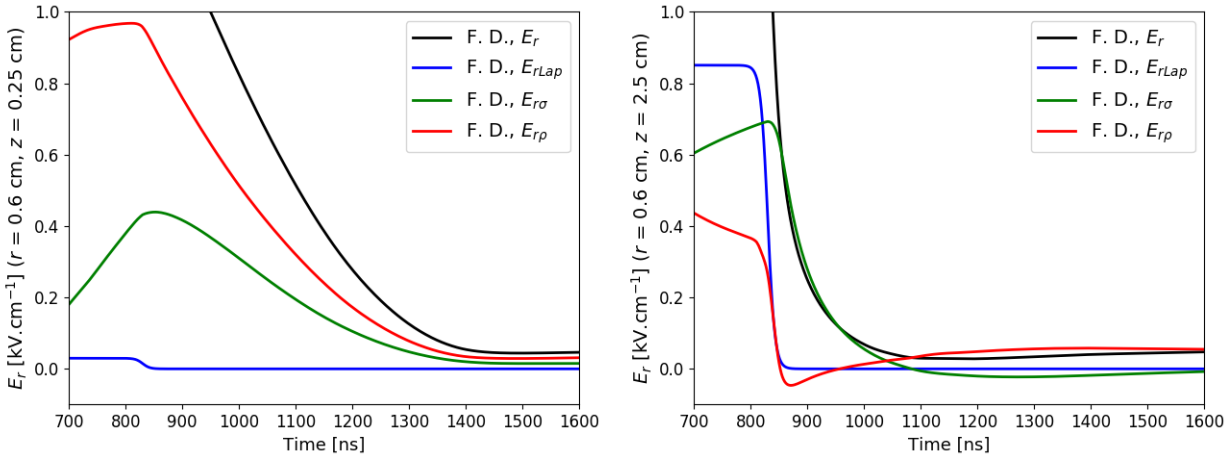

Figure V.15: Temporal profiles of E_r and its contributions at $r = 0.6$ cm and at $z = 0.25$ cm (on the left) and $z = 2.5$ cm (on the right), for floating dielectric target, with $V_P = +4$ kV.

Figure V.15 shows that the timescale of charge dynamics significantly differs with the axial position. While close to the source the evolutions mostly takes place until $t = 1100$ ns, close to the target they require more time, until $t = 1400$ ns. Close to the source, as soon as the Laplacian potential decreases and the slope of potential is created, the tube is uncharged through deposition of negative charges, mostly electrons. Simultaneously, ρ is neutralized through charge transport and even reaches negative values. Close to the target, the decrease of the applied voltage does not play a role on charge dynamics so fast. As the plasma potential slowly decreases, a small electric field is generated in the opposite direction to that of the first discharge, that slowly separates charges with the opposite signal and slowly deposits negative charges on the target, bringing both the channel and the target to charge neutrality. Therefore, the redistribution of the end of the pulse can clearly be considered as a neutralization phenomenon as suggested in *Yue et al.* [2018]. While the rebound front in the conditions studied in chapter IV is an ionization wave that partially neutralizes the plasma

to form a linear axial distribution of potential, the end-of-pulse redistribution observed here almost completely neutralizes the plasma to bring its electric potential to zero. In order to assess whether or not this redistribution is an ionization phenomenon like the rebound discharge, we represent in Figure V.16 the electron-impact ionization source term at four times at the end of the pulse in the whole tube, with floating dielectric target.

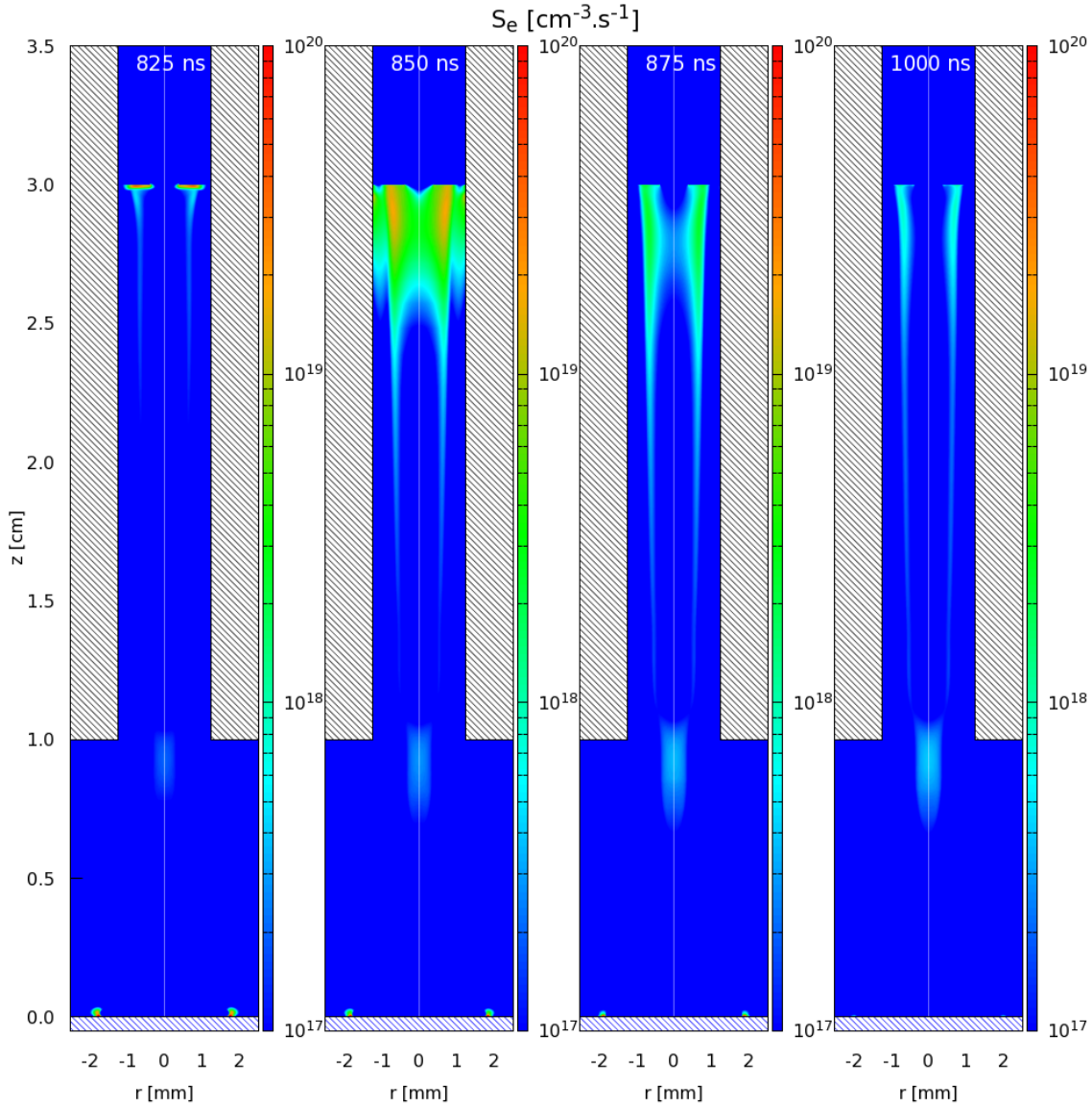

Figure V.16: Cross sectional views of the electron-impact ionization source term S_e, at the end of the pulse of V_{APP}, at several times with floating dielectric target and $V_P = +4$ kV.

In fact, Figure V.16 shows that while there is an ionization phenomenon close to the source, mostly visible at $t = 850$ ns, it does not propagate in the tube and in the plume. To compare the results in Figure V.16 with those for the rebound front, we should notice that S_e represented in Figure IV.5 and IV.6 for the rebound is clearly visible in the range $10^{18}-10^{20}$ cm^{-3}.s^{-1}, while here the visible S_e in the plasma has values mostly between 10^{17} and 10^{19} cm^{-3}.s^{-1}, and is therefore very low. We can also notice in Figure V.16 that S_e remains close to the surface of the target after $t = 800$ ns. However, this is the discharge front propagating radially on the surface due to dense positive net volume charge density and E_r. Therefore, it

is not representative of the uncharging of the target, but is rather a remaining of the positive discharge. Then, the positive discharge front vanishes and is no longer visible at $t = 1000$ ns. In conclusion, in the case studied here, the redistribution at the end of the pulse is not an ionization wave traveling back in the tube but only a redistribution of charges to neutralize the plasma, as suggested in *Norberg et al.* [2015a]. While the applied voltage is zero and the plasma is not completely neutralized, as an electric field subsists in the plasma and in the plasma-target interface, it transports charges and can be high enough to justify reactions that provide light emission.

V.5 Conclusions

In this chapter the interaction between a plasma jet and different targets has been simulated and the influence of the electrical character of the target on the discharge dynamics has been investigated. We have used positive polarity of applied voltage and three targets of fundamentally different electrical character: floating dielectric, floating metallic and grounded metallic. For floating dielectric targets, we have tested the cases with targets of low ($\epsilon_r = 4$) and high ($\epsilon_r = 40$) permittivity. The main conclusions to retain from the studies presented in this chapter can be summarized as follows:

(i) First, the challenges of modeling the interaction between a thin and centered positive plasma plume and a dielectric target have been presented. It has been shown how to avoid the uncentering of discharge propagation and its origins in electron depletion. Using the hypothesis that seems most physical to us, the discharge front uncenters during the propagation but it impacts the target with a centered structure, as in the experiments, and the plasma-surface sheath can be described.

(ii) Second, the propagation of the discharge towards different targets has been described. The inter-electrode gap significantly affects the discharge velocity during the whole propagation. For the same inter-electrode gap, the permittivity of the target only affects the discharge velocity in the last 5 mm of propagation in the plume. The electric field in the front of propagation is lower with grounded metallic target but the propagation is faster due to the broader front. Furthermore, the electron depletion in the case with dielectric target severely affects the velocity and electric field in the discharge front in the last 5 mm of propagation.

(iii) Third, the post-impact dynamics has also been compared with different targets. It has been confirmed that lower capacitance (lower ϵ_r) of the target promotes a faster radial spreading on the target and that higher capacitance (higher ϵ_r) slows the discharge radial spreading and promotes the electric field rebound in the plasma channel, propagating in the axial direction. As lower ϵ_r promotes higher E_r close to the target, it leads not only to the radial spreading but also to increased ρ production in the radial edge of the plasma plume and higher potential in the plasma channel. It has been demonstrated that the presence and intensity of the rebound are directly related to the electric potential on the target surface after the impact and thus to the drop of potential in the plasma channel and between the plasma and the target.

(iv) Fourth, the dynamics of charges and electric fields has also been analyzed at the end of the pulse of applied voltage. When the applied voltage falls, a redistribution of electric

potential in the channel is imposed. While the applied voltage is zero and the plasma is not completely neutralized, an electric field of reverse direction subsists in the plasma and in the plasma-target interface. This electric field is higher when the plasma is connecting a grounded source electrode to a charged target than when it is connecting two grounded electrodes. Moreover, it is higher close to the source electrode. Unlike the rebound, in the cases under study this redistribution of potential consists in a redistribution of surface and volume charges that neutralizes the plasma completely without ionization or propagation as a wave or front. We should notice that neutralization refers to net charge and not to absolute charged species densities.

(v) Finally, the simulation conditions to model a metallic target at floating potential have been proposed. These conditions allow to consider an isopotential volume whose electric potential varies through charge exchange with the plasma. Moreover, the target is large enough to consider that free electrons can be continuously emitted, as with a metallic target connected to the ground. As the impedance of this target is very low and the electric potential increases very slowly after the discharge impact, in the timescales of the impact on the target and of the rebound front, the behavior of the discharge interacting with this target is the same as interacting with a grounded metallic target. Then, the electric potential on the target significantly increases in some hundreds ns. In these timescales the axial electric field in the channel tends to decrease, along with the partial neutralization of the channel, and the result is a plasma channel that conducts most of the potential from the source to the target, as it happens with dielectric targets. Thus, the redistribution of potential at the fall of the applied voltage pulse takes place between a grounded source and a highly charged target, as it happens when using dielectric targets.

Chapter VI

Electric field characterization of He plasma jets interacting with a floating dielectric target: comparison with experiments

Contents

VI.1 Introduction 164

VI.2 Previous studies of electric field in plasma-target interaction . . 165

VI.3 Electric field distribution in plasma-dielectric target interaction 169

VI.3.1 Studied conditions to comply with experiments 169

VI.3.2 Electric field distribution in plasma-dielectric target interaction and comparison with experiments 171

VI.3.3 Analysis of the electric field inside the target 177

VI.4 Conclusions 181

VI.1 Introduction

In this chapter we examine the spatio-temporal evolutions of electric field inside targets of dielectric character where a plasma jet impinges, which are of paramount importance for applications. The state of the art on electric field characterization of jets and on plasma-target interaction has been exposed in sections I.4 and I.3, respectively, and in chapter V the discharge interaction with targets of different electrical character has been described. In this chapter the highlight is put on comparing and complementing experimental measurements of electric field inside and close to dielectric targets.

In *Sobota et al.* [2016]; *Sretenovic et al.* [2017], the maximum electric field in a discharge front driven by a sinusoidal voltage has been measured through Stark polarization spectroscopy of the He lines in the plasma plume in free jet conditions and maximum values around 18 kV.cm^{-1} have been reported for different gas flow conditions. Then, in *Hofmans* [2017] the maximum electric field at the discharge front of a pulsed He jet has been measured using the same technique but the jet impinges on different targets and different tube-target distances have been used. Close to the targets, values as high as 20 kV.cm^{-1} have been obtained.

Other experimental studies have focused on the examination of electric fields inside dielectric targets exposed to discharge impact. These are investigated with Mueller polarimetry using electro-optic crystals, since their refractive index changes linearly with the induced electric field. The measured change in refractive index is used to visualize the electric field to which the crystals are exposed to. As the electric field values are solely due to charge deposition on the surface, an estimation of the surface charge densities can be made when a homogeneous field approximation is applicable or a homogeneously charged disk is considered [*Slikboer et al.*, 2017]. The examination of electric field or surface charge density using electro-optic targets has been applied by *Kawasaki et al.* [1991]; *Zhu et al.* [1995] to study the propagation of streamers on dielectrics and used with plasma jets by *Sobota et al.* [2013]; *Wild et al.* [2014]; *Slikboer et al.* [2016, 2017]. Recent developments show the possibility to simultaneously measure and decouple all electric field components (axial and radial) inside the electro-optic crystal [*Slikboer et al.*, 2018b]. The simultaneous detection of the axial and radial components of the electric field is an important tool to also investigate the dynamics of the discharge propagation on the surface. Still, it is unknown how the measured field, which is averaged throughout the thickness of the crystal, relates to the electric field values on the plasma-surface interface and in the plasma plume. For instance, in *Slikboer et al.* [2016] the maximum electric field values measured inside the target have values between 3 and 5 kV.cm^{-1}, lower than those measured in the plasma plume. Furthermore, as the discharge is filamentary and transient, the homogeneous field approximation is not applicable and the relationship between the measured field and the surface charges is not obvious.

To understand in detail the dynamics of the plasma-surface interaction, both surface and volume net charge densities in proximity of the target have to be investigated. Charges and electric field influence each other and determine the discharge dynamics to a great extent. However, the measurement of charges in volume in these filamentary transient discharges is difficult. Then, we can use experiments and simulations in a complementary way to derive electric field and charge values in locations where it is difficult to carry out experiments. In *Viegas et al.* [2018b] a first effort has been performed in that sense.

VI.2 Previous studies of electric field in plasma-target interaction

In *Viegas et al.* [2018b], the plasma–target interaction has been examined experimentally by using an electro-optic crystal ($Bi_{12}SiO_{20}$ with $\epsilon_r = 56$) as a dielectric target, to visualize the electric field inside the target under exposure of the plasma. The jet design is the same as in Fig. V.1, with a positive applied voltage pulse of 1 μs width, V_P plateau, 5 kHz repetition rate and a rise-time of 50 ns. The general discharge dynamics is the same as described in section V.2. Then, to evaluate the electric field inside the target, Mueller polarimetry is applied to examine the target under the jet exposure. The refractive index of electro-optic crystals changes linearly with the applied electric field, according to the Pockels effect. Experimentally, it has been verified that this electric field is exclusively induced by surface charges on the target surface. The imaging Mueller polarimeter used in this work is more comprehensively discussed in *Slikboer et al.* [2018a, b]; *Slikboer* [2018]. The resulting separate electric field components are shown in Figure VI.1 for $V_P = 4$ kV for different time delays t_d relative to the rise of the voltage pulse. Exposure times of 100 ns are used. The axial E_z field is shown to be positive during the pulse, i.e. directed downwards, resulting from positive charge deposition on the front side of the crystal.

The electric field inside the electro-optic crystal, shown in Figure VI.1, indicates the impact on the BSO ($\epsilon_r = 56$) surface at $t_d = 400$ ns, as happened with glass (Figure V.2). All electric fields shown in Figure VI.1 are induced by surface charge density σ. A continuous charging of the surface is observed with a radial spreading following the ionization front from the moment of impact at $t_d = 0.4$ μs until the end of the pulse at $t_d = 1.0$ μs. In the center of the impact region, constant fields, indicating stable surface charge densities, are observed for several hundreds ns until the pulse ends. Then, the electric field components diminish starting from the center of the impact region and it takes approximately 0.4 μs for the surface charges to be removed to a great extent. The observed maximum value of E_z is 5 kV.cm^{-1}, measured in the center of the impact point. This value is higher than the radial component of 3 kV.cm^{-1}. A homogeneous spreading is observed within the first 300 ns after impact. Afterwards, patterns from radial surface streamers are observed, enlarging the total area of the plasma–surface interaction. Charges deposited by the surface streamers are the last to be removed.

Then, in *Slikboer* [2018] (chapter 5) the same procedure has been performed for different maxima of applied voltage: 3, 4, 5 and 6 kV, using the same shape of pulse. In Figure VI.2 are presented the experimentally obtained temporal evolutions of the radial position of the discharge front when spreading on a glass target surface (obtained through imaging of light emission) and of the axial component of electric field measured at $r = 0$ in the BSO crystal. An additional curve is presented in that figure, with 6 kV applied voltage and 1.5 slm He flow, which does not present qualitatively different results with respect to the case with 1 slm flow. We should take into account that even though the time of impact is approximately the same on glass and BSO targets, the radial spreading is about two times slower on BSO than on glass, due to the higher ϵ_r, as shown in section V.3.2.

Figure VI.2 shows that the time of impact of the discharge on the target is shorter for higher applied voltages, due to the higher velocity of propagation. Moreover, the radial spreading

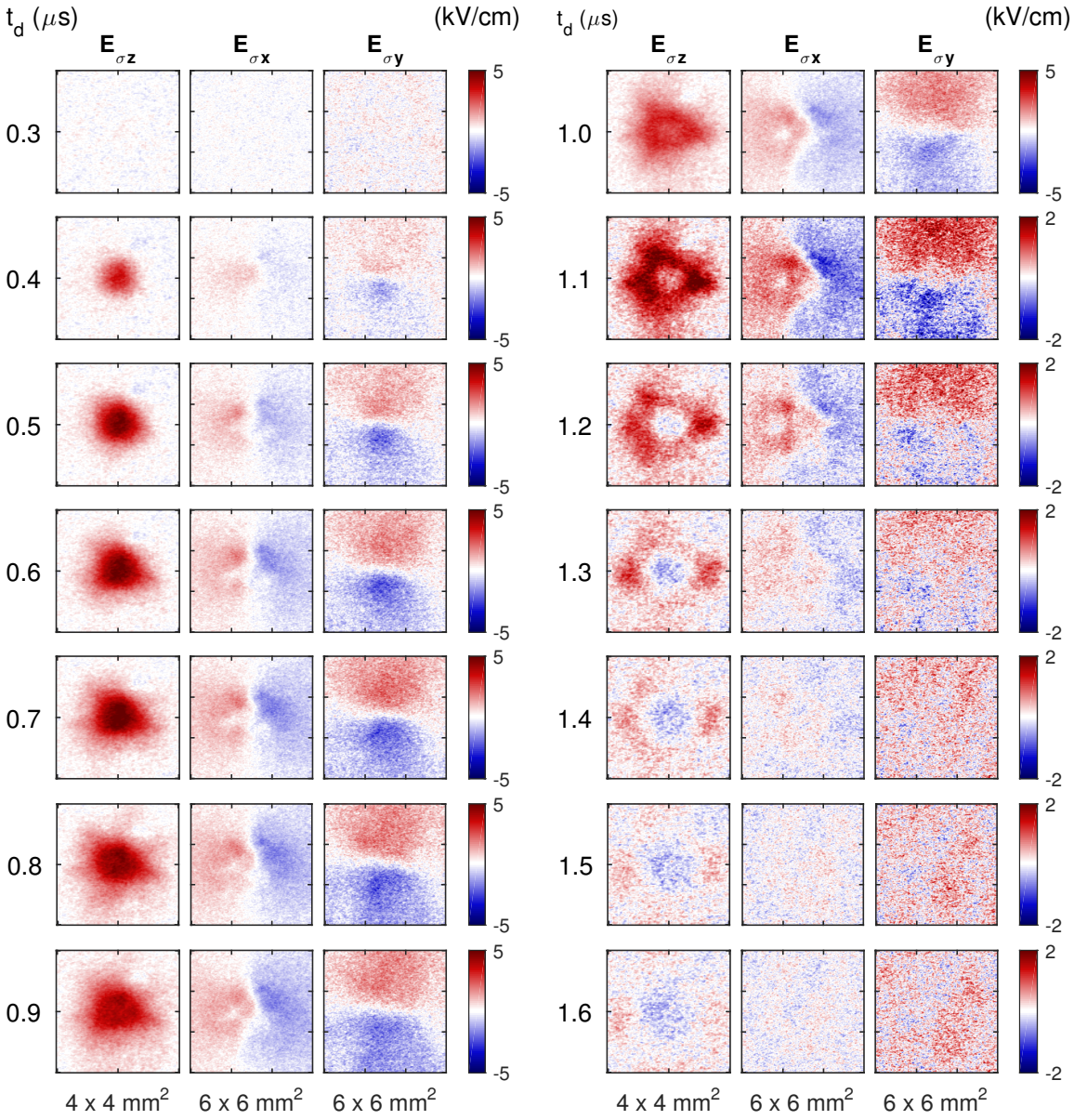

Figure VI.1: The obtained electric field patterns (axial E_z and radial E_x and E_y) inside the electro-optic target (top-view), due to σ deposited by the ionization wave, for $V_P = +4$ kV. The pulse ends at $t_d = 1$ μs. Afterwards, a different color scale is used. Figure from *Viegas et al.* [2018b].

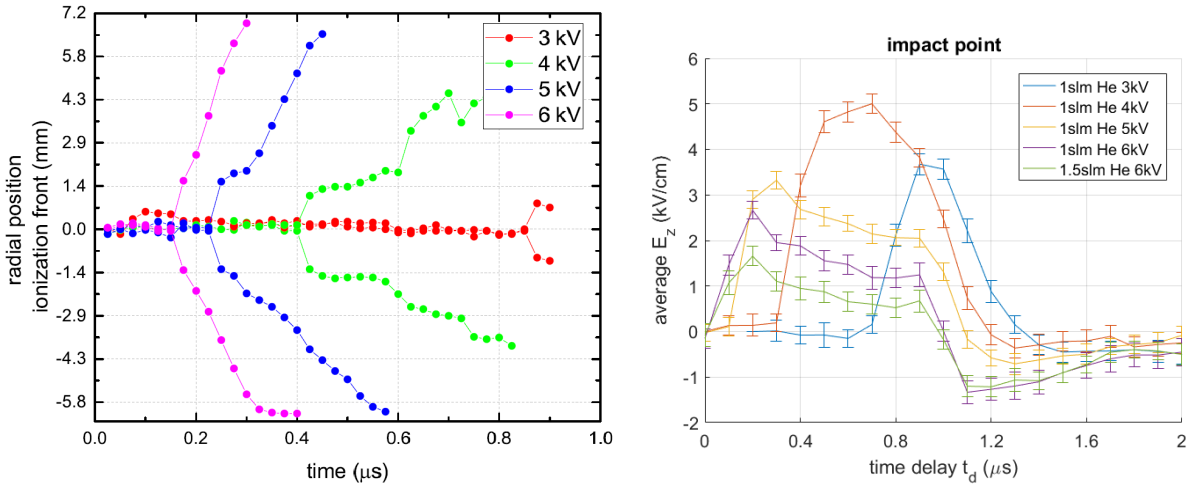

Figure VI.2: Experimentally measured temporal evolutions: In the figure on the left, the radial position of the ionization front when impacting on the target, with 25 ns resolution. In the figure on the right, $E_z(t)$ inside the dielectric target, with 100 ns resolution. Figures from *Slikboer* [2018].

on the target is also faster with higher applied voltage. Then, in the figure on the right, it is visible that, counter-intuitively, the maximum of the measured electric field is lower for higher applied voltages ($\sim$ 5 kV.cm^{-1} for V_P = 4 kV and $\sim$ 3 kV.cm^{-1} for V_P = 5 kV). Furthermore, the figure allows to evaluate the shape of the temporal profiles of the measured E_z at $r = 0$. The maximum is reached soon after the discharge impact, then the value slowly decreases until the end of the pulse, when negative charges are deposited and negative values of E_z are obtained.

Several questions arise from the electric field measurements. The values of electric field measured are an average throughout the optical path that the light has traveled and are exclusively due to surface charges. As such, the value of electric field on the target surface is expected to be higher. Moreover, the measured electric field experienced by the target is lower than the ones in the plasma plume reported in several works, of around 20 kV.cm^{-1}. To understand how these fields relate to each other, in *Viegas et al.* [2018b] the model described in section V.2 has been used for a phenomenological evaluation of the electric field distribution with $V_P = 4$ kV. The electrode configuration (without grounded ring around the tube), pulse duration (800 ns instead of 1000 ns) and dielectric target permittivity ($\epsilon_r = 4$ instead of 56) are not exactly the same in simulations and experiments, and then the work in *Viegas et al.* [2018b] is not a quantitative comparison between experiments and simulations. Although the conditions are not the same, in both experiments and simulations a centered discharge front impacts a dielectric surface and spreads on it, keeping the same timescales of discharge propagation as in the experiments. The model has been used to better understand the role of the averaging over the dielectric thickness in the experiments and the importance of the electric field induced by surface charges in comparison with the total electric field in the dielectric target. Figure VI.3 shows the temporal evolution with ns resolution of the axial components of electric field E_z at $r = 0$ in the plasma plume and averaged inside the target ($\epsilon_r = 4$) through its 0.5 mm thickness. The temporal profile of the averaged field in the target is presented as total value and separated into the volume charge and surface charge

contributions $E_{z\rho}$ and $E_{z\sigma}$.

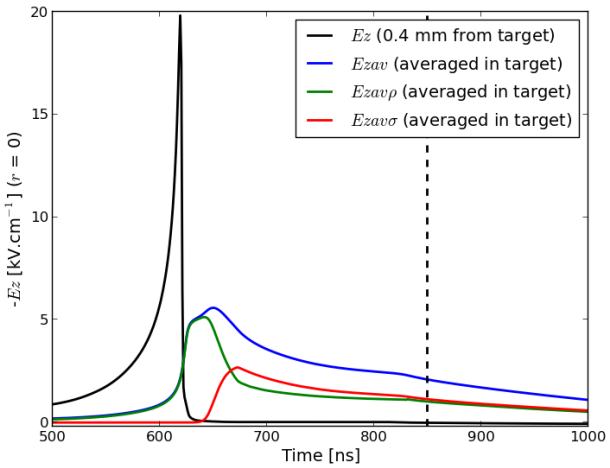

Figure VI.3: Temporal profiles of the axial component of electric field E_z at $r = 0.0$ mm in the plasma plume at $z = 0.4$ mm (black line) and inside the dielectric target, averaged through its thickness: E_{zav} (blue), $E_{zav\rho}$ (green) and $E_{zav\sigma}$ (red). The dashed black line signals $t = 850$ ns, when the applied voltage becomes zero. Figure from *Viegas et al.* [2018b].

The black curve in Figure VI.3 represents the temporal profile of E_z close to the target surface, at 0.4 mm distance. We notice that E_z at this position increases as the volume charges in the discharge front approach the target, and attains a maximum of around 20 kV.cm^{-1}. After the passage of ρ at this spatial position, the electric field at that position cancels almost instantly. The peak value of E_z in the plume is comparable to the one measured in *Sobota et al.* [2016]. Inside the target, the electric field values are lower, both before and during the plasma-surface interaction. The maximum of the averaged E_z inside the dielectric target is about 4 times lower than the value at 0.4 mm from the target. It has the same order of magnitude as the field measured experimentally with the electro-optic dielectric crystal, presented in Figure VI.1. These simulation results have confirmed the experimental finding that the electric field experienced by the target is lower than generally reported for discharge front propagation. The field inside the dielectric target of $\epsilon_r = 4$ is due to both a contribution of ρ and σ. By separating E_z inside the target into $E_{z\rho}$ and $E_{z\sigma}$, we can distinguish the different influences on the electric field to which the target is exposed to. In fact, during the plasma-surface interaction, two effects sequentially determine the electric field inside the target: firstly, a relatively high electric field is observed due to the proximity of the ionization front and high volume charge density ρ; afterwards, in longer timescales, lower electric fields are induced due to the contribution of both leftover volume charges close to the target and surface charges deposited on its surface. The work in *Viegas et al.* [2018b] has shown the interest to use, in a complementary way, space and time-resolved measurements and simulations of electric field components to better understand plasma-surface interactions. In appendix G we study the effect of the magnitude of the applied voltage on the electric field distribution in positive plasma-dielectric target interaction, using the same model as in *Viegas et al.* [2018b]. The simulation results are compared with the experimental ones for different applied voltages and are used to explain the differences observed between them.
Then, in this chapter, in section VI.3, we use the model in conditions very close to the experiments (same geometry, pulse width and target permittivity) to perform a quantitative

comparison. The influence of volume and surface charges on the spatio-temporal evolution of electric fields is investigated numerically in these conditions, following the electric field associated to each type of charge. This electric field characterization is not only focused on surface and volume charge contributions, but also on the spatial and temporal distributions of the axial and radial components of electric field in the plasma plume and inside the target. The results are compared to the experimental measurements by Elmar Slikboer, of the time-resolved electric field patterns using Mueller polarimetry. Lastly, a special interest is taken in the conversion between the measurements inside the target and the values of field and charges on its surface.

VI.3 Electric field distribution in plasma-dielectric target interaction

VI.3.1 Studied conditions to comply with experiments

The model set-up for the simulations presented in this section is shown in Figure VI.4 and corresponds to the experimental set-up presented in Fig. V.1. As in the experiments, a dielectric pyrex tube with relative permittivity of $\epsilon_r = 4$, length 3.3 cm (between $z = 1.0$ cm and $z = 4.3$ cm), internal radius $r_{in} = 1.25$ mm and outer radius $r_{out} = 2.0$ mm is used. Also, a dielectric BSO target with $\epsilon_r = 56$ is placed perpendicularly to the tube at 1 cm from the end of the tube. The target is defined as a cylinder of 2 cm radius and 0.5 mm thickness, set between z = -0.5 mm and $z = 0$. It is at a floating potential as in the experiments, and in the simulations a grounded plane is set 10 cm behind it.
A ring electrode of inner radius 0.4 mm and outer radius 1.25 mm is set inside the tube between $z = 4.3$ cm and $z = 3.8$ cm and a grounded ring is set around the tube, at 5 mm distance from the powered electrode, with 0.5 mm width and 3 mm length (between $z =$ 3.3 cm and $z = 3.0$ cm). In order to accurately describe the plasma interaction with the grounded ring around the tube and with the high-permittivity target, the model exposed in section II.4.5 has been used, considering the transport of electron energy and the local mean energy approximation. A positive pulsed voltage is applied to the powered electrode, that rises linearly in 50 ns between 0 and +5.5 kV, then is constant during the pulse duration until $t = 1000$ ns and then decreases back to 0 at $t = 1050$ ns, as in the experiments. The magnitude of the applied voltage is different than in the experimental results exposed in Fig. VI.1 with 4 kV. The value 5.5 kV has been chosen in order to obtain a time of impact of the discharge front on the dielectric target close to that of experiments, close to 400 ns after the beginning of the pulse rise. The calculation lasts until $t = 2000$ ns, after the end of the pulse. Figure VI.4 also shows that the discharge set-up is placed inside a grounded cylinder with a radius of 10 cm. Between the dielectric target and the grounded plane, as well as between the dielectric tube and the grounded cylinder, the space is considered as a dielectric of air permittivity $\epsilon_r = 1$. On the last boundary of the domain (i.e. at $z = 4.3$ cm), the axial gradient of electric potential is set to zero. At the surface of both the tube and the dielectric target, secondary emission of electrons by ion bombardment ($\gamma = 0.1$ for all ions) is taken into account. Surface charge density σ on the surface of the dielectrics is obtained by time integrating charged particle fluxes through electric drift to the surface (see section II.3.2).

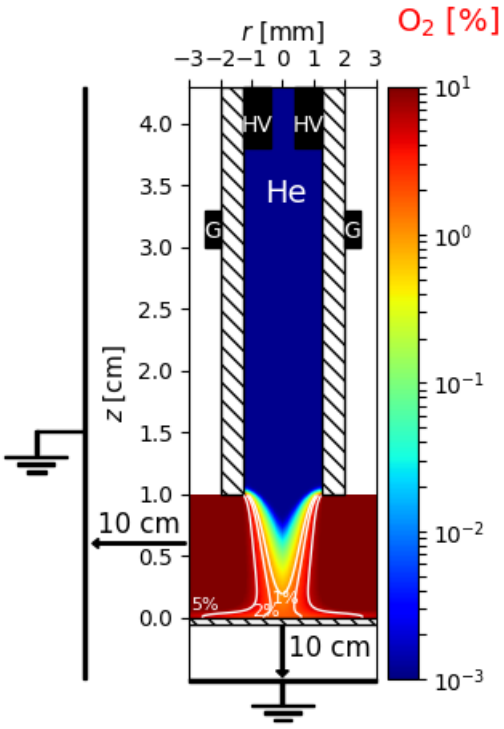

Figure VI.4: Side view schematics of the discharge set-up used in the simulations in this section. The colour plot and the white curves show the O_2 spatial distribution in the He-O_2 mixture (percentage over a total of 2.45×10^{19} cm^{-3} gas density).

These charges then remain immobile on the surface of the dielectrics.

To model the experimental conditions, in which Helium flows at 1 slm through the tube into air, the plasma model has been coupled with flow calculations as described in section II.4.3. As a first approximation, the model considers a flow of 1 slm of He with 10 ppm of O_2 impurities flowing downstream into an O_2 environment. The spatial distribution of O_2 in the He-O_2 mixture at atmospheric pressure and at $T_g = 300$ K (total gas density $N = 2.45 \times 10^{19}$ cm^{-3}) obtained from the flow calculation is presented in Figure VI.4. There are also added the contour curves of 1, 2 and 5% O_2 in the He-O_2 mixture, to point out the mixture region studied in this work. The reaction scheme used for the He-O_2 mixture is the one described in section II.4.2. As repetitive voltage pulses are used in the previously described experiments ($f = 5$ kHz), we take into account a uniform initial preionization density $n_{init} = 10^9$ cm^{-3} of electrons and O_2^+ positive ions. However, no initial surface charges are considered on the dielectric surfaces.

The mesh size is 10 μm in the plasma and in the dielectric, i.e. axially between z = -0.05 cm and z = 4.3 cm and radially between $r = 0$ and $r = 3.0$ mm. Then, both behind the target (except with grounded metallic target) and for $r > 3.0$ mm, the mesh size is expanded using a geometric progression until reaching the boundaries of the computational domain at r = 10 cm (20 cells between $r = 3$ mm and $r = 4$ mm and 50 more cells until $r = 10$ cm) and z = -10 cm (50 cells between z = -0.05 cm and z = -10 cm). This refinement requires a mesh of $n_z \times n_r = 4400 \times 370 = 1.628$ million points. The computational time required for the simulation run to obtain the results presented in this section was of five days with 64 MPI

processes on the multi-core cluster "Hopper".

VI.3.2 Electric field distribution in plasma-dielectric target interaction and comparison with experiments

For the conditions described in section VI.3.1, the discharge ignites close to the powered electrode at $z = 3.8$ cm and $t = 40$ ns and then propagates until the end of the tube at $z =$ 1.0 cm and $t = 250$ ns, with a velocity around 13 cm.μs^{-1} and an average radius 0.75 mm. This dynamics of propagation presents a good agreement with the experiments where the discharge leaves the capillary shortly before $t_d = 300$ ns (Fig. V.2). The maximum value of the axial component of electric field on the discharge front inside the tube is always close to 15 kV.cm^{-1} and its radial position moves from the tube wall to r = 0 as the discharge front gets farther from the grounded electrode, being already positioned on the axis of symmetry when reaching the end of the tube. As the discharge front has a centered profile of electric field at the end of the tube, it continues propagation in the plasma plume with a centered structure. The centered profile of the discharge in the plasma plume is common to simulations and experiments. The discharge structure is the same as in the tube, with approximately 0.75 mm radius, until the impact on the target, at $t = 358$ ns. The discharge dynamics at that time is shown in Figure VI.5, where the spatial distributions of the electric field magnitude E_t, electron density n_e and electron-impact ionization source term S_e are presented. The result for the time of impact is close to experiments, where it takes place between 375 and 400 ns.

The structure of the discharge in the plasma plume shown in Figure VI.5 presents a good agreement with that obtained in the experiments through light emission (Fig. V.2). After the discharge impact on the target, the plasma spreads radially on the dielectric surface with an average velocity ~ 0.2 cm.μs^{-1} and the front reaches a radial position of approximately 1.5 mm at 1000 ns when the applied voltage starts decreasing and the spreading significantly slows down. Then, Figure VI.6 shows the spatial distribution of the volume charge density ρ and of the axial E_z and radial E_r electric field components at several instants between the impact and $t = 2000$ ns, focused in the region between 0.4 mm above the target surface and 0.4 mm axially inside the target. The radial profiles of surface charge density σ on the target surface are represented for the same instants in time in Figure VI.7.

In Figure VI.6 we first notice the discharge arrival on the target at $t = 358$ ns. A downwards-directed axial component E_z is created between the positive space-charge ρ and the grounded plane at $z =$ -10 cm and therefore gives rise to a flux of positive charged species towards the target of $\epsilon_r = 56$. In Figure VI.7 it is shown that there is a centered charge deposition during 10 ns due to the mentioned E_z, arising σ from approximately zero at $t = 358$ ns to $\sim$ 90 nC.cm^{-2} on the axis of symmetry at $t = 368$ ns. Indeed, the surface charge deposition is much higher than in *Viegas et al.* [2018b] where the maximum of σ is lower than 4 nC.cm^{-2}, mostly because of the different ϵ_r of the target: 4 in that work and 56 here. We have checked that the positive species deposited are dominantly oxygen ions, which suggests that in a He-air mixture they would be mainly nitrogen and oxygen ions, as has been reported in *Breden and Raja* [2014]; *Ning et al.* [2018]. It is also shown in Figure VI.6 that E_z and E_r inside the target at $t = 368$ ns have much lower intensity than in the plasma. As the discharge

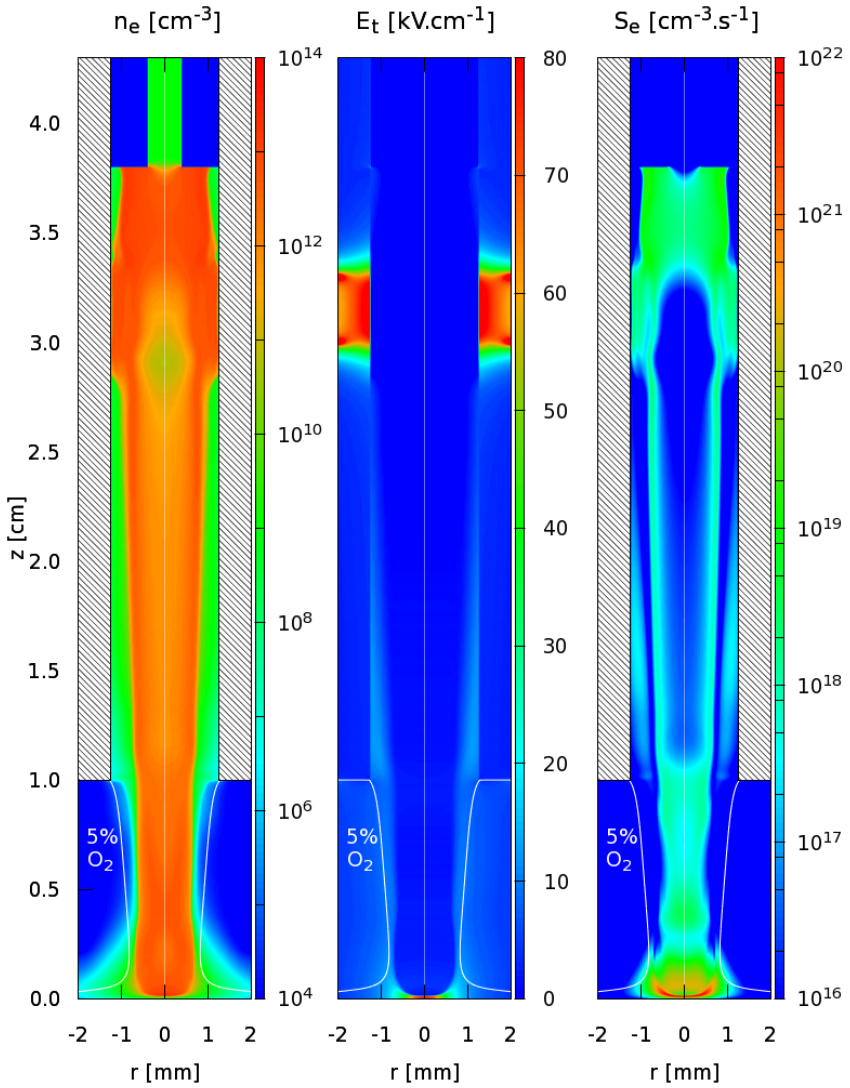

Figure VI.5: Cross sectional views of the electron density n_e (left), the electric field magnitude E_t (center) and the electron-impact ionization source term S_e (right) at the moment of discharge impact on the dielectric target, at $t = 358$ ns.

is mechanically hampered from propagating downwards, this E_r leads the positive discharge front to spread radially, at about 50 μm from the target surface. Figure VI.6 also shows that at $t = 368$ ns the volume charge density ρ and E_z in the plasma plume are no longer centered, even though σ has its peak at $r = 0$. Then, between $t = 368$ ns and $t = 1000$ ns, we notice that E_z and the peak of σ follow the discharge spreading. At the center, σ decreases. The decrease of σ in this region is justified by an electric field reversal (explained later in the text) and therefore a deposition of negative charges that cancel part of the positive surface charges. The negative charges deposited through electric drift are dominantly electrons, that have a plasma mobility at least 50 times higher than negative ions (see section II.3.4). The decrease of σ at the center is very fast at first (between $t = 368$ ns and $t = 700$ ns) and then slows down (until $t = 1000$ ns). The maximum of ρ and of the downwards-directed E_z significantly decrease during the radial spreading between $t = 368$ ns and $t = 1000$ ns, and so does the rate of positive σ deposition on the discharge front.
From the analysis of Figure VI.6 it is visible that the values of the electric field components

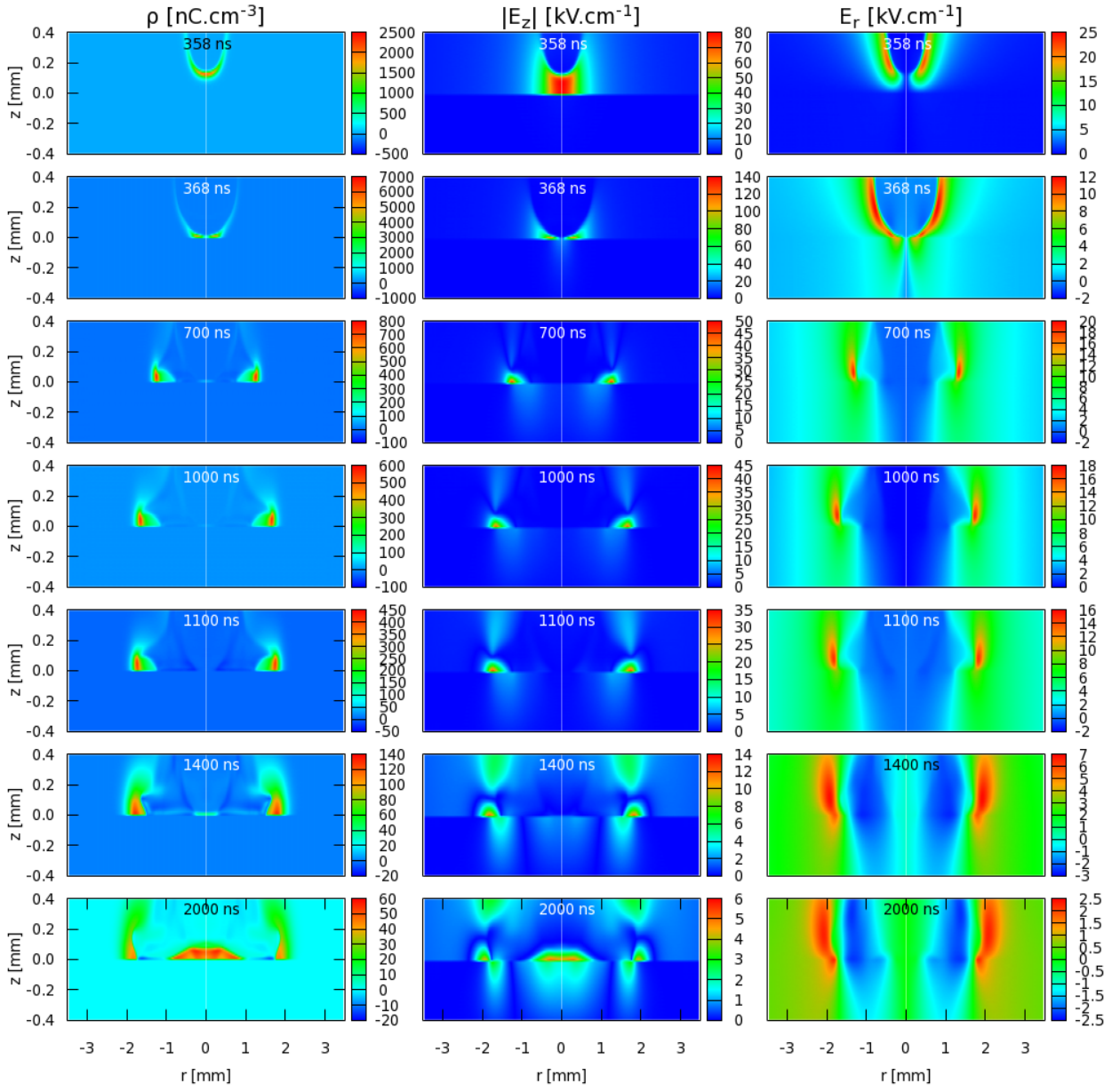

Figure VI.6: Cross sectional views of the volume charge density (left) and of the magnitude of the axial (center) and radial (right) components of electric field during plasma-dielectric interaction at t = 358, 368, 700, 1000, 1100, 1400 and 2000 ns.

are very different in the plasma and inside the target. Moreover, the spatial distributions of E_z and E_r present each significant differences inside the target, not only radially but also axially, being higher close to the surface and lower farther from the surface. Then, at t = 1000 ns, the pulse of applied voltage starts decreasing and therefore the electric potential on the discharge front, connected to the powered electrode, decreases with it, which leads to a visible fast decrease of electric field and of ρ. However, we can notice that between t = 1000 ns and the posterior moments there are still E_z and E_r present inside the target, as well as there is still a slow radial spreading, due to the remaining values of ρ and E_r. Concerning σ, Figure VI.7 shows that after the end of the voltage pulse it decreases to zero and then to negative values, which implies that in this phase E_z on the surface creates a flux

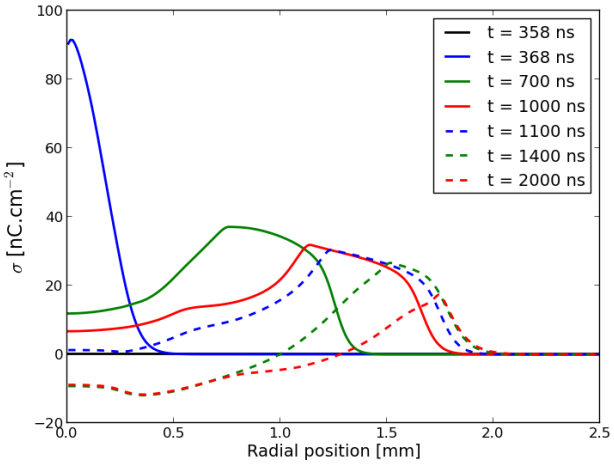

Figure VI.7: Radial profiles of the surface charge density deposited on the dielectric target surface at $t = 358$, 368, 700, 1000, 1100, 1400 and 2000 ns. Solid lines represent times during the pulse, while dashed lines refer to times after the pulse has ended.

of deposition of negative charges. The negative charge deposition starts from the center and spreads radially with time. This result agrees with the experimental result of electric field due to σ in Fig. VI.1 where the same evolution is observed after the fall of the pulse.
In order to obtain more detail into the dynamics between each type of charge and the electric field components, the separate contributions to the electric field calculation of ρ in volume exclusively and of σ on the target surface exclusively are assessed. These contributions are obtained as described in section II.3.3. It has also been verified that the geometrical Laplacian contribution of electric field due to the applied voltage in the region of the dielectric target has a maximum value of $\sim$0.3 kV.cm^{-1}, which is negligible when compared to the other contributions during the plasma-dielectric interaction under study. Figure VI.8 presents the axial and radial components of electric field separately due to ρ and σ, at the same moments and in the same region as Figure VI.6.
As the discharge arrives at the target surface at $t = 358$ ns, Figure VI.8 shows that the electric field is firstly exclusively due to ρ, since no σ is present on the surface. Then, at $t = 368$ ns, as ρ is not centered, the fields created by it ($E_{z\rho}$ and $E_{r\rho}$) follow the same radial structure. However, we notice that E_z created by σ, $E_{z\sigma}$, has its peak at r = 0, corresponding to the radial profile of σ present in Figure VI.7 at $t = 368$ ns. It is also noticeable that $E_{z\sigma}$ presents an almost symmetrical distribution in the region close to $r = 0$, directed downwards inside the target and upwards in the plasma region. The jump of E_z at the dielectric target interface with the plasma and the quasi-symmetrical distribution of $E_{z\sigma}$ are due to the permittivity difference between the dielectric and the plasma and to the surface charges deposited on the dielectric surface, in agreement with Gauss's law: $(\epsilon_0 E_{z\to z^+}) - (\epsilon_0 \epsilon_r E_{z^-\to z}) = \sigma$. This distribution implies that E_z in the plasma in this region is the sum of opposite contributions. On the one hand, ρ creates E_z downwards, and on the other hand, σ originates an upwards E_z. In the discharge front, $E_{z\rho}$ is higher in absolute value than $E_{z\sigma}$. In fact, as positive charges deposit at the center of the target surface between $t = 358$ ns and $t = 368$ ns, the maximum of ρ spreads radially, ρ decreases at $r = 0$ and σ increases at the center. This dynamics of charges leads to E_z decreasing in value and then reversing direction at $z = 0$,

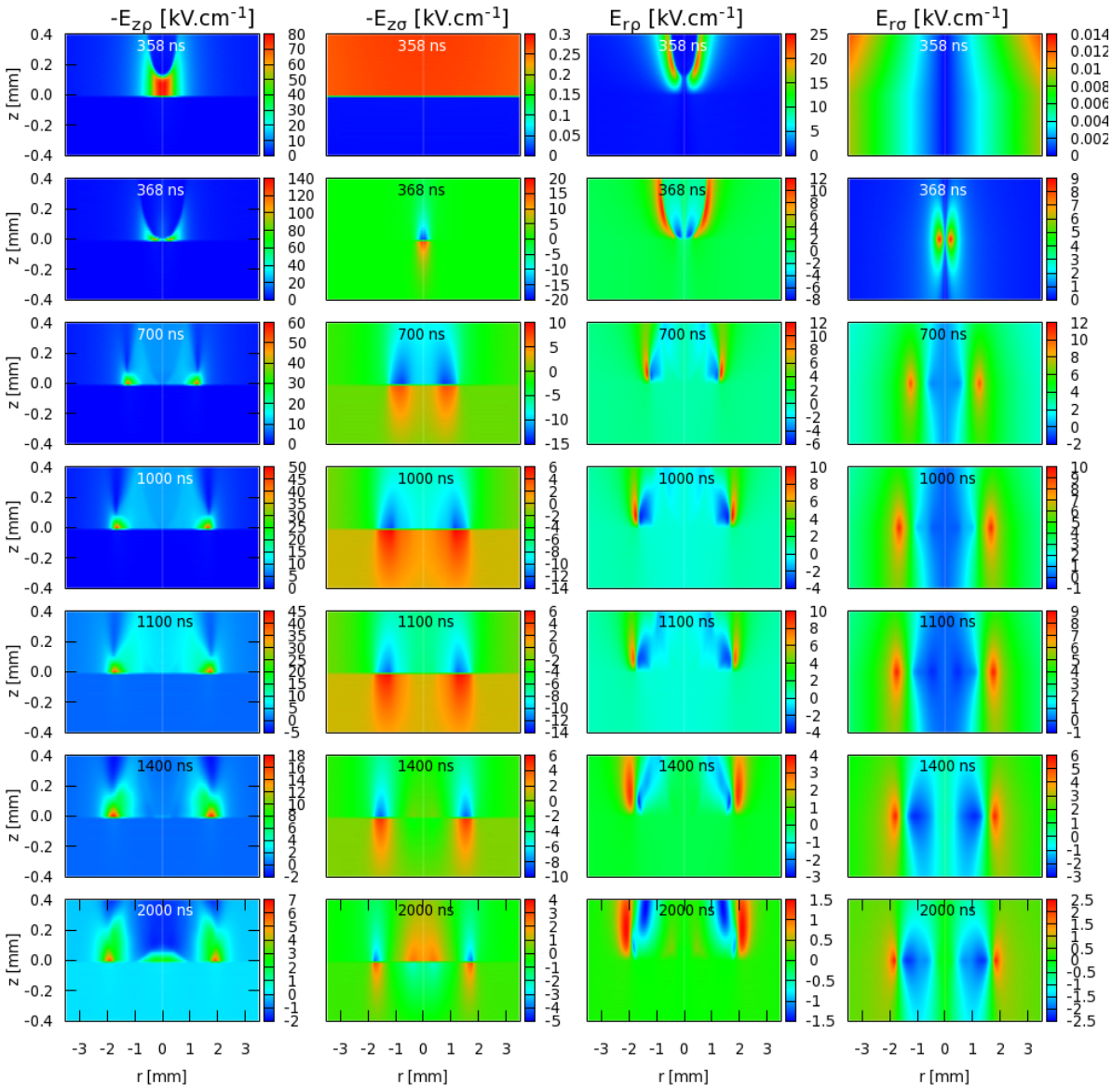

Figure VI.8: Cross sectional views of the ρ and σ contributions to E_z and E_r during plasma-dielectric interaction at t = 358, 368, 700, 1000, 1100, 1400 and 2000 ns.

leading to negative charge deposition, which explains the decrease of σ at the center between $t = 368$ ns and $t = 1000$ ns. Then, with the decrease of positive σ, the upwards $E_{z\sigma}$ decreases and thus E_z tends to cancel on the surface at $r = 0$ as result of a quasi-equilibrium between the two contributions to E_z. The electric field reversal after surface charge deposition on a dielectric target and the consequent opposite-polarity deposition have been reported in other works for negative discharge, such as *Soloviev and Krivtsov* [2009]; *Pechereau and Bourdon* [2014]. The same kind of evolution of E_z takes place along the radial spreading on the target surface, behind the passage of the maximum of ρ. During the radial spreading of the discharge, between $t = 368$ ns and $t = 1000$ ns, we see that both electric field components, close to the surface and inside the target, are higher on the edge of the deposition region and result from both ρ and σ contributions. This coincides with the ρ and σ distributions in Figures VI.6 and VI.7.

After $t = 1000$ ns, as the applied voltage decreases to zero, ρ decreases and so do the electric field components originated by ρ. In particular, we notice that $E_{z\rho}$ that pushes positive charges towards the surface decreases. Then, at the positions where positive σ is present, the upwards $E_{z\sigma}$ leads to the formation of a slightly negative ρ layer (down to -50 nC.cm^{-3} at $t = 1100$ ns) and to negative charge deposition. The presence of the negative ρ layer, that generates a small upwards-directed E_z, justifies that negative charge deposition can exceed the cancellation of positive surface charges and thus a negative σ can remain on the target, as observed at $t = 1400$ ns. This effect starts at $r = 0$ and extends radially to the regions where ρ and σ are higher at the end of the pulse. Then, the negative ρ layer dissipates, the negative σ generates a downwards-directed E_z and a positive ρ layer (up to 60 nC.cm^{-3} at $t = 2000$ ns) forms close to the surface. In these simulation results, the downwards-directed E_z (generated by both the negative σ and the positive ρ) at those positions is not strong enough for a fast positive ion deposition. Therefore, the negative charges remain on the target surface between $t = 1400$ ns and $t = 2000$ ns. In that time interval, at $r = 0$, σ decreases in absolute value only around 0.5 nC.cm^{-2}.

As a result of the described dynamics, we obtain the electric field components inside the BSO target, that can be compared with the experimental results. The fields to compare with experimental results are exclusively due to σ and are an average through the axial thickness of the target, i.e. between the first and last cells inside the target. In Figure VI.9 are presented the temporal profiles of the electric field components obtained in simulations ($V_P = 5.5$ kV) and experiments ($V_P = 4$ and 5 kV). We evaluate $E_{zav\sigma}$ at $r = 0$ and at $r = 0.5$ mm, and $E_{rav\sigma}$ at this latter position. The experimental points have been retrieved at a position along the axis y, where the measured E_x is zero and thus $E_r = E_y$ (see Fig. VI.1).

Figure VI.9 shows a good agreement between numerical and experimental results. Concerning the axial component of electric field, the same maximum values are obtained in simulations with $V_P = 5.5$ kV and in experiments with $V_P = 4$ kV, for which cases the time of impact is also the same: ~ 5 kV.cm^{-1} at $r = 0$ and ~ 3.5 kV.cm^{-1} at $r = 0.5$ mm. Then, the decrease of $E_{zav\sigma}$ in time takes a different shape in experiments and simulations, but the values remain in the same range. Indeed, both the rise and the fall of $E_{zav\sigma}$ are faster in the simulations than in the experiments during the pulse of applied voltage. The inversion of signal of $E_{zav\sigma}$ and $E_{rav\sigma}$ at the end of the pulse is a result of the dynamics of surface charge deposition described above, and is also common to simulations and experiments, but the field becomes more negative in the simulation results. Finally, the peak of $E_{rav\sigma}$ at $r = 0.5$ mm is clearly different in simulations and experiments, but its magnitude between $t = 600$ ns and $t = 1100$ ns is in the same range.

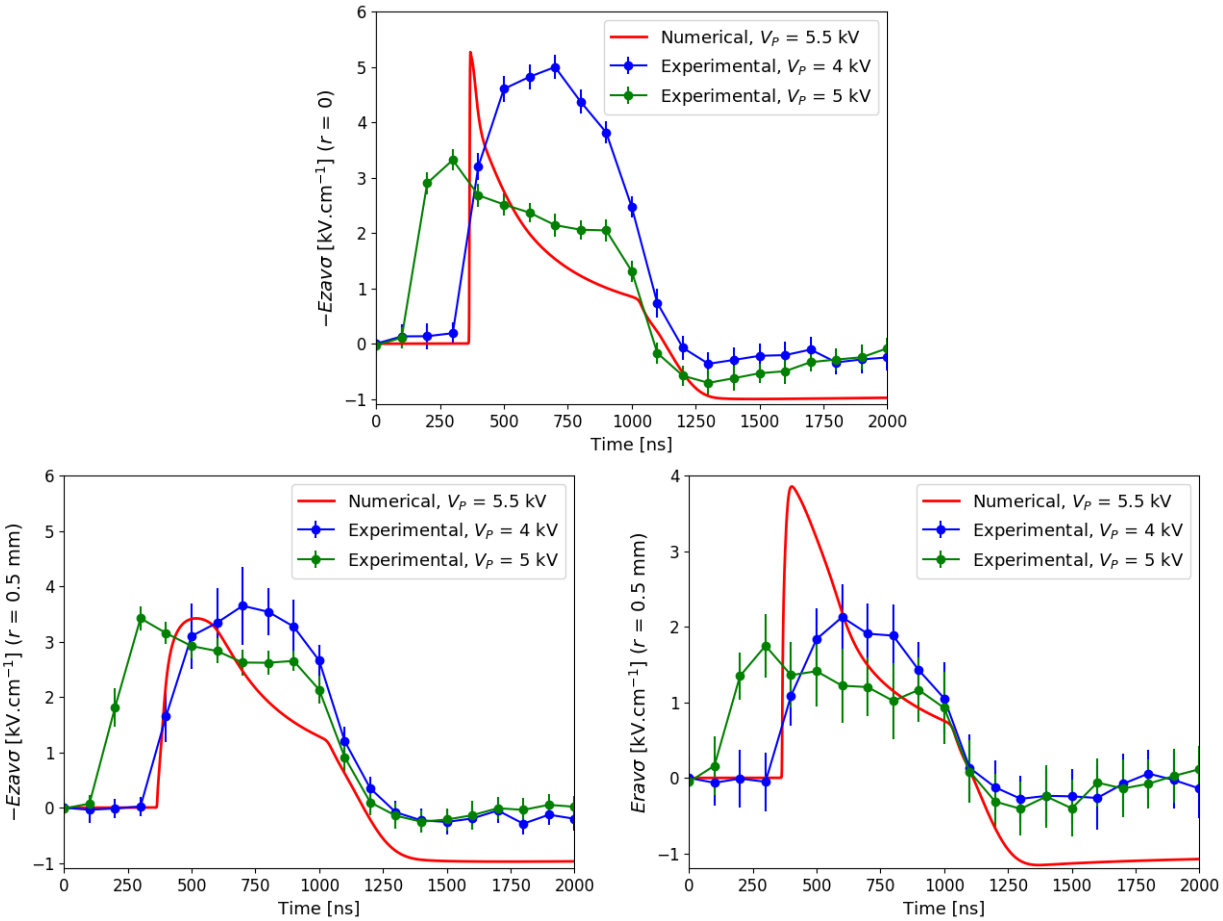

Figure VI.9: Temporal profiles of the σ contribution to the electric field components, averaged inside the target: numerical ($V_P = +5.5$ kV) and experimental ($V_P = +4$ kV and $V_P = +5$ kV) results. On top: $E_{zav\sigma}$, at $r = 0$. On bottom: $E_{zav\sigma}$ (on the left) and $E_{rav\sigma}$ (on the right), at $r = 0.5$ mm. Experimental data points by Elmar Slikboer with 100 ns resolution. Numerical data with 1 ns resolution.

VI.3.3 Analysis of the electric field inside the target

Using the numerical results presented in Figures VI.6 - VI.8, it is possible to provide further explanation on the electric field values due to σ averaged inside the target. It is interesting to relate the averaged values with those on the target surface to assess the effect of the axial averaging inside the target. Moreover, it is useful to relate the total electric field inside the target with that exclusively due to σ to understand how the measured electric field values represent the field the target is exposed to. Figure VI.10 (on the left) shows how $E_{zav\sigma}$ (red curve) relates to the total E_z averaged inside the target (blue curve) and to the σ contribution $E_{z\sigma}$ inside the target, on its surface (green curve), in the simulation results. The same results are shown in Figure VI.11 for E_r instead of E_z. The radial profiles of E_z and E_r are presented at $t = 1000$ ns, before the decrease of the applied voltage. Additionally, on the right side of each of those figures are presented the calculated ratios between the σ contribution to each electric field component averaged inside the target and: the total averaged electric field component (dashed blue curves); the σ contribution to the electric field component on its surface (dashed green curves).

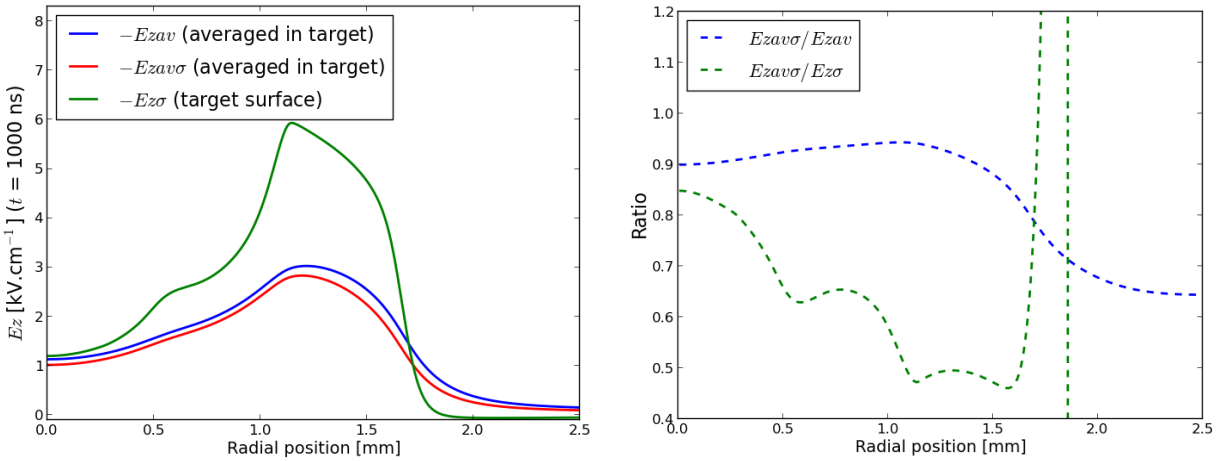

Figure VI.10: Radial profiles at the end of the pulse at $t = 1000$ ns. In the figure on the left, E_z inside the target, averaged through its thickness: total E_{zav} (blue) and $E_{zav\sigma}$ (red); and on the target surface at $z = 0$: $E_{z\sigma}$ (green). In the figure on the right, the ratios between $E_{zav\sigma}$ and E_{zav} (dashed blue) and between $E_{zav\sigma}$ and $E_{z\sigma}$ at $z = 0$ (dashed green).

The discharge front is at approximately $r = 1.6$ mm. The peaks of the total $E_{z\sigma}$ and $E_{r\sigma}$ on the surface are of ~ 6 kV.cm^{-1} and 9 kV.cm^{-1} respectively. The difference between the profiles of electric field due to σ on the surface (green curves) and averaged inside the 0.5 mm thick target (red curves) is clearly visible. It proves that the measured fields are inhomogeneous inside the target. This has been pointed out already in *Slikboer et al.* [2017], along with the fact that surface charge densities cannot be estimated from the measured $E_{zav\sigma}$ without any compensation. There, a procedure has been proposed to estimate the value of the axial electric field on the surface, due to σ, from the measured average value. The value of $E_{z\sigma}$ on the surface can then be used to estimate the surface charge density. If no compensation is taken into account, an error on the estimation of the density values on the surface is introduced. The compensation procedure in *Slikboer et al.* [2017] assumes a uniformly charged disk on the target surface and converts $E_{z\sigma}$ averaged in the target into its value on the surface through a ratio depending on the size of the charged disk and the thickness of the target. With the model, considering the full distribution of σ, we show that the uniformity of that distribution is also important to evaluate the compensation procedure. In fact, we see in Figure VI.10 that the ratio between $E_{z\sigma}$ averaged in the target and on the surface (dashed green) is more stable in the region behind the discharge spreading, where it takes values between 0.6 and 0.9, than in the region of the discharge front where σ is going through fast variations. Concerning E_r, we notice in Figure VI.11 that the ratio between $E_{rav\sigma}$ and $E_{r\sigma}$ at the surface (dashed green) is never stable. While $E_{r\sigma}$ at the surface decreases rapidly to zero behind the discharge front, that is not the case of $E_{r\sigma}$ averaged through the target thickness.

Then, we can compare how $E_{zav\sigma}$ and $E_{rav\sigma}$ relate to the total fields experienced on average by the target. Surprisingly, these are remarkably close, with ratios (dashed blue) near 0.9 in the region where the discharge has propagated, including in the region of the discharge front, where ρ has high magnitudes. This result implies that the obtained fields due to σ averaged inside the target are very (i.e. up to 90%) representative of the total electric field the target is exposed to, on average. We should notice that this is not the case in *Viegas et al.* [2018b]

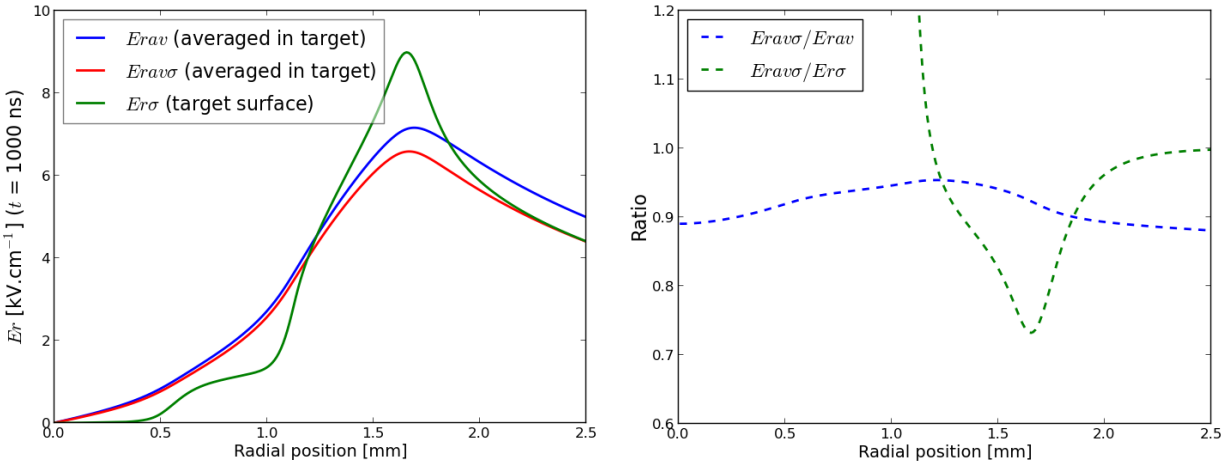

Figure VI.11: Radial profiles at the end of the pulse at $t = 1000$ ns. In the figure on the left, E_r inside the target, averaged through its thickness: total E_{rav} (blue) and $E_{rav\sigma}$ (red); and on the target surface at $z = 0$: $E_{r\sigma}$ (green). In the figure on the right, the ratios between $E_{rav\sigma}$ and E_{rav} (dashed blue) and between $E_{rav\sigma}$ and $E_{r\sigma}$ at $z = 0$ (dashed green).

where a target with $\epsilon_r = 4$ is used and E_{zav} is about the double of $E_{zav\sigma}$. The difference is due to both the value of ϵ_r that strongly impacts the electric field variations on the surface through Gauss's law mentioned above and to the much higher σ values reported here (90 nC.cm^{-2} instead of 4 nC.cm^{-2}). In order to deepen the understanding on the electric field distributions leading to these differences between the components and charge contributions on the target surface and averaged inside the target, Figure VI.12 presents the axial profiles at the same instant $t = 1000$ ns of E_z at $r = 0$ (on the left, black curve), where it is ~ 0 at the target surface, and of both E_z (on the left) and E_r (on the right) and their charge contributions at $r = 1.5$ mm, behind the discharge front.

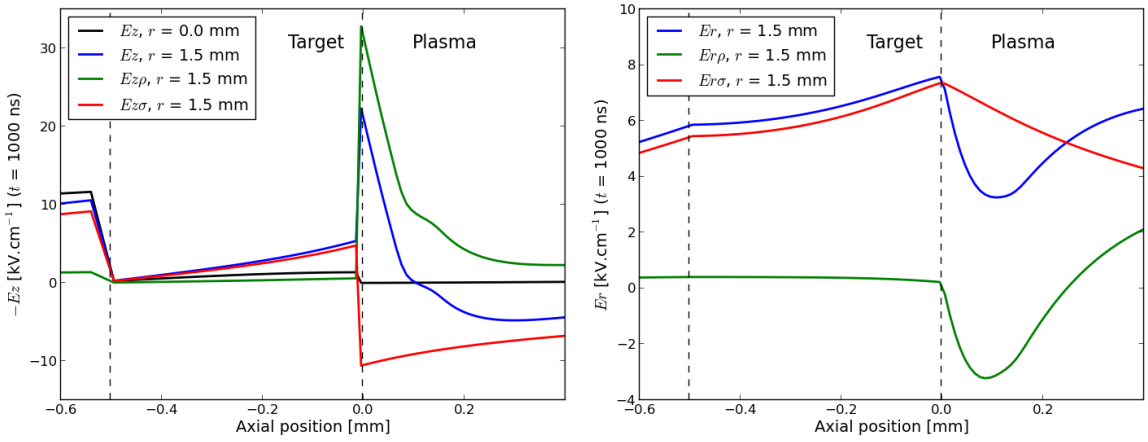

Figure VI.12: Axial profiles at the end of the pulse at $t = 1000$ ns. In the figure on the left, E_z at $r = 0.0$ mm and $r = 0.15$ mm. Also, the ρ and σ contributions to E_z at $r = 1.5$ mm. In the figure on the right, the same for E_r instead of E_z.

At the surface and in the plasma region close to the surface, at $r = 0$, some hundreds of ns after the passage of the discharge front, the total value of E_z is approximately zero, since the downwards ρ and upwards σ contributions are in quasi-equilibrium there, as already observed in Figure VI.8. Nevertheless, inside the target, as the positive ρ and σ both generate

E_z directed downwards, the total E_z is also directed downwards, with very low variation across the target thickness at $r = 0$. Then, by studying the axial profiles of E_z and its charge contributions at a position only a few ns behind the passage of the discharge front, as in Figure VI.12 for $r = 1.5$ mm and $t = 1000$ ns, we can see the situation leading to the equilibrium at $r = 0$. In the plasma region, due to the radial spreading and the charge deposition, the downwards directed $E_{z\rho}$ is decreasing and the upwards directed $E_{z\sigma}$ is increasing with time, leading the total E_z to zero in the plasma region and then at the surface, where it is still positive in this situation. Inside the target, all the contributions to E_z are directed downwards and are decreasing through the target thickness. Moreover, as ρ is located in the plasma, the electric field it originates is severely depleted inside the dielectric with $\epsilon_r = 56$, according to the Gauss law. That is why $E_{z\rho}$ is so low inside the target, even at a position where the magnitudes of ρ and $E_{z\rho}$ in the plasma are very high. On the other hand, as σ is located in the boundary between the plasma and the dielectric, its electric field contribution is less depleted in the plasma-dielectric transition, still according to Gauss law $((\epsilon_0 E_{z\to z^+})-(\epsilon_0\epsilon_r E_{z^-\to z}) = \sigma)$. This, along with the very high σ values, justifies that inside the target $E_z \simeq E_{z\sigma}$. These profiles explain the differences between E_z at the surface in the plasma region, E_z at the surface inside the dielectric, $E_{z\sigma}$ at the surface and $E_{z\sigma}$ averaged inside the target. Then, Figure VI.12 also shows that at $t = 1000$ ns and $r = 1.5$ mm, $E_{r\sigma}$ in the plasma region is directed outwards because most of the σ is deposited at lower radial positions. Conversely, $E_{r\rho}$ is directed inwards because the discharge front, and therefore the strongest and closest ρ contribution, has already crossed this position and is located close to $r = 1.6$ mm. The resulting E_r in the plasma region is clearly influenced by both contributions. However, inside the target of $\epsilon_r = 56$, at the same radial position, the depletion of $E_{r\rho}$ and the strong σ lead it to have positive values and $E_r \simeq E_{r\sigma}$.

Finally, we find interesting to propose a first estimation for the conversion procedure between $E_{zav\sigma}$ and $E_{z\sigma}$ at the surface (already evaluated in Fig. VI.10) and from there to obtain values of charges deposited on the surface. Even though the model does not require such a procedure since σ is self-consistently calculated, an accurate estimation of this conversion procedure would allow to understand exactly how to use measured values of $E_{zav\sigma}$ to determine the charges on the surface. In Figure VI.13, on the left side, is presented the temporal evolution at $r = 0$ of $E_{z\sigma}$ on the surface, $E_{zav\sigma}$, σ and the total charge deposited on the target surface Q. The left side of Figure VI.13 shows that, apart from the intervals when the temporal derivatives are strongest (discharge impact on target and fall of voltage pulse), the temporal evolutions of $E_{z\sigma}$ at $z = 0$ and $E_{zav\sigma}$ are comparable, and so are those of $E_{zav\sigma}$ and $\sigma(r = 0)$. On the contrary, the temporal evolution of Q is significantly different. Then, on the right side of the same figure, the ratios between $E_{zav\sigma}$ and $E_{z\sigma}$ at $z = 0$ and between $E_{z\sigma}$ at $z = 0$ and σ are presented, also as function of t and at $r = 0$.

As in *Slikboer et al.* [2017], the ratio $E_{zav\sigma}/E_{z\sigma}$ increases during the radial spreading of the discharge. However, despite the ratios not being constant, putting aside the intervals of strong temporal derivatives, we can determine them from Figure VI.13 with a reasonable accuracy: The first ratio $E_{zav\sigma}/E_{z\sigma}$ as 0.68 ± 0.03 during the pulse and 0.56 ± 0.03 after the end of the pulse and the second ratio $E_{z\sigma}/\sigma$ as 0.19 ± 0.02 kV.nC^{-1}.cm. Then, from a

measurement of $E_{zav\sigma}$ at $r = 0$ during the pulse, we can estimate:

$$E_{z\sigma}(z = 0, r = 0) = (1.47 \pm 0.07) \times E_{zav\sigma}(r = 0) \quad \text{(VI.1)}$$

$$\sigma(r = 0)[\text{nC.cm}^{-2}] = (5.26 \pm 0.55) \times E_{z\sigma}(z = 0, r = 0)[\text{kV.cm}^{-1}] \quad \text{(VI.2)}$$

$$\sigma(r = 0)[\text{nC.cm}^{-2}] = (7.74 \pm 0.88) \times E_{zav\sigma}(r = 0)[\text{kV.cm}^{-1}] \quad \text{(VI.3)}$$

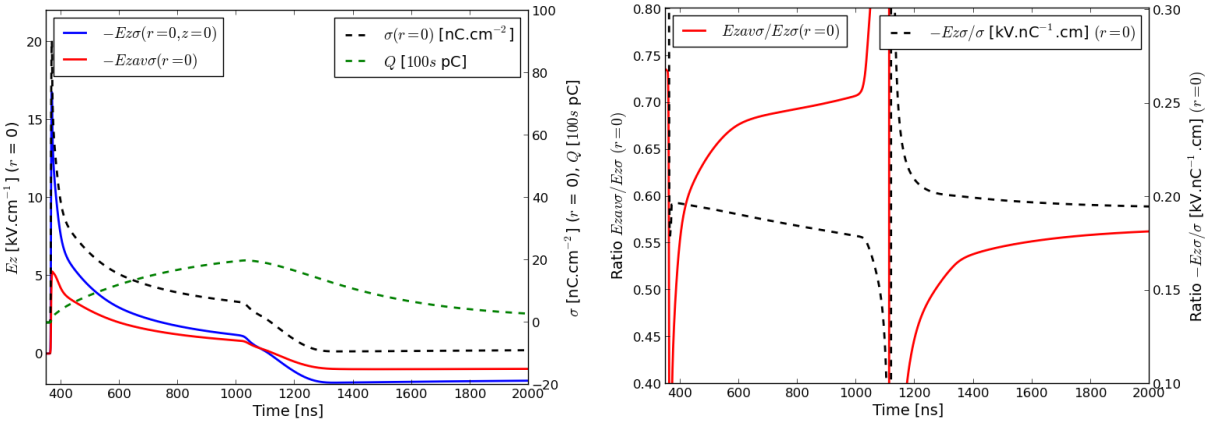

Figure VI.13: Temporal profiles at $r = 0$. In the figure on the left, $E_{z\sigma}(z = 0)$, $E_{zav\sigma}$, σ and Q. In the figure on the right, the ratios $E_{zav\sigma}/E_{z\sigma}$ and $E_{z\sigma}/\sigma$.

VI.4 Conclusions

In this chapter we have investigated the plasma-target interaction occurring between a pulsed Helium plasma jet and a BSO dielectric target with $\epsilon_r = 56$. The experimental results by Elmar Slikboer have been exposed, as well as our previous studies confirming that the electric field experienced by the target is lower than generally reported for discharge front propagation. Then, the electric field distribution in the plasma-target interaction has been studied in detail with the model, using conditions as close as possible to experiments. The focus has been put on the evolution of volume charge density ρ and surface charge density σ and of their electric field contributions, direct comparison of electric field in the target with experiments, and the procedure to obtain σ from the measured electric field. The main conclusions retrieved from the research presented in this chapter are the following:

(i) First, a good agreement is obtained between simulations and experiments. The radial and temporal evolutions of $E_{zav\sigma}$ inside the target present the same shape, during the pulse and after the pulse. The same maximum values of $E_{zav\sigma}$ of 5 kV.cm^{-1} are obtained in simulations with $V_P = 5.5$ kV and in experiments with $V_P = 4$ kV, for which cases the time of impact is also the same. The inversion of sign of $E_{zav\sigma}$ at the end of the pulse, corresponding to negative surface charge deposition, is obtained in both simulations and experiments.

(ii) Second, the electric field in the plasma due to ρ is severely depleted by the change of permittivity and thus is much higher in magnitude than inside the target. As a result, the electric field components experienced inside the target, both E_z and E_r, are almost exclusively ($\sim 90\%$) originated by the high densities (up to 90 nC.cm^{-2}) of charge deposited on

the target surface σ and therefore the measured electric field components are representative of the total electric field the target is exposed to.
(iii) Third, the magnitudes of the electric field components decrease inside the target and thus the values on the surface are tendentiously higher than the values averaged through the target thickness. The ratio between the two values is different for E_z and E_r and is temporally and spatially inhomogeneous. For these simulation results, during the pulse, at $r = 0$ and in the intervals without strong temporal derivatives, we have proposed a conversion procedure.
(iv) Fourth, the temporal evolution of $E_{zav\sigma}(r)$ is representative of the temporal evolution of $\sigma(r)$, but not of the total charge deposited Q. Then, for the same conditions as before, we have proposed a computation to estimate $\sigma(r = 0)$ from $E_{zav\sigma}(r = 0)$.
(v) Finally, the numerical investigation of the spatial and temporal distributions of the separate ρ and σ contributions to the electric field has allowed to complement the information obtained experimentally to better understand plasma-target interactions that are crucial for many plasma applications.

Chapter VII

Conclusions and prospects for future research

VII.1 Contributions of this thesis

This PhD thesis has contributed to deepen the understanding on fundamental questions of plasma jet dynamics and interaction with targets. In particular, numerical simulations have been used to characterize the temporal and spatial evolutions of electric field in pulsed plasma jets and complement the information obtained from electric field measurements from the last years.

The two-dimensional axisymmetric fluid model for Helium plasma jets at LPP has been developed to describe He jets flowing in N_2 and O_2 atmospheres and interacting with targets. In order to study He discharges with O_2 admixtures, a new reaction scheme has been implemented in the model. Moreover, to describe the plasma in the tube-target gap, the spatial inhomogeneity of the gas mixtures is now taken into account by coupling the static solution of flow calculations to the transient discharge model. Then, in order to describe the interaction between positive discharges and targets of high permittivity, the electron energy equation has been discussed and implemented in the model, along with the local mean electron energy approximation, that replaces the local electric field approximation.

Using that two-dimensional model, the role of the tube in He discharge propagation and structure has been studied. It has been shown that the mechanical confinement induced to a He discharge by the introduction of a tube with $\epsilon_r = 1$ significantly increases the transfer of electric potential in the plasma channel, which leads to an increase of electric field on the discharge front, charged species densities and velocity of propagation. We have demonstrated that with positive polarity the increase of potential is achieved through the increase of net volume charge density ρ, while with negative polarity it is due to the deposition of net surface charge density σ. Furthermore, while point-to-plane discharges without tube in a 99% He - 1% N_2 environment have very similar dynamics and structures with positive and negative polarities of applied voltage, these significantly change with the introduction of the tube. With tube, the negative discharges are more homogeneous and the positive ones more filamentary. It has been demonstrated through the simulation of different boundary conditions that the source of those differences is mostly the different type of interaction between positive and

negative streamers with dielectric surfaces, in this case the dielectric tube. With positive polarity, the presence of the surface blocks the movement of electrons towards the positive front, creating a positive radial sheath between the plasma bulk and the tube inner wall.

Considering plasma jet configurations where the discharge propagates between a tube and a target in a spatially inhomogeneous gas mixture, the mechanisms defining the path of propagation of the discharge front have been investigated. The path of propagation of the discharge front and the shape of the plasma plume are not determined uniquely by the values of gas-mixture, but are rather a consequence of all the discharge conditions: geometry, flow rate and applied voltage. The path of propagation of positive discharges is defined by the production of seed electrons ahead of the discharge front and the identification of the mechanisms for that production is highly dependent on preionization. In our standard conditions, with high preionization to simulate residual charges from previous discharges, of the order of 10^9 cm^{-3}, it has been demonstrated through the analysis of the different ionization source terms that the most important propagation mechanisms are electron-impact direct ionization of both He and N_2/O_2 and Penning ionization, even though this last process is not crucial for the determination of the discharge structure. The most important aspect in the plasma-flow coupling in regions with He and small admixtures of N_2 or O_2 is the consideration of the variable mixture in the chemistry source terms. This has been proved by coupling the different properties where the distribution of species densities impacts the plasma separately. To account for gas mixing in the densities in the chemistry source terms leads the discharge to expand radially, and in the electron-impact rate coefficients leads the discharge to confine radially. Therefore, the electron-impact ionization source terms and the path of propagation are determined by the balance between these two features.

The discharge dynamics in He jets impacting a grounded metallic target has been analyzed with both positive and negative polarities of applied voltage. We have shown that a first ionization front propagates from the powered electrode towards the grounded metallic target and then, in the conductive channel formed between both metallic electrodes, a rebound front propagates from the target to the powered electrode, with the same characteristics as those reported from experimental results. It has been demonstrated that the rebound front propagates as a neutralization wave with reverse polarity with respect to the first ionization front. As the first discharge impacts the target, the flux of electrons from the grounded metallic plate towards the plasma in positive polarity or from the plasma towards the target in negative polarity partially neutralize the discharge head. However, the neutralization of the discharge head does not fully neutralize the plasma channel immediately. A new ionization front, called rebound front, starts at the grounded target, the new charge separation and propagating net charge density have the opposite sign and the front is directed towards the plasma channel and the powered electrode. Unlike the first ionization front, the rebound front propagates in an already ionized channel. The channel is partially neutralized by the propagation of the rebound. For positive polarity, the redistribution of potential is accomplished mostly by the partial cancellation of the positive ρ in the plasma channel, while for negative polarity the potential neutralization is performed through the creation of positive ρ and by partially canceling the negative σ on the tube wall through positive ion deposition.

This result on the character of the potential redistribution is obtained by calculating the contributions of volume and surface charges to the distributions of electric potential and field and gives complementary information to the experimental findings on the rebound front. It has also been shown that close to the grounded target, the density of reactive species may be significantly increased due to the synergy between the first and rebound ionization fronts.

Still considering He jets with a grounded metallic target, we have investigated how electric field measurements outside the tube can be related to discharge properties. The study of the temporal variations of E_z and E_r inside and outside the tube shows the interest to use plasma jet experiments and simulations in a complementary way to derive from electric field measurements outside the tube, the electric field in locations where it is difficult to carry out measurements. Then, we have pointed out that under certain conditions when it is known the uniformity of charges and the predominance of one type of charges, experiments can relate measurements of $E_r(r)$ outside the tube to the Gauss's law hypothesis to estimate the average net charge densities inside the tube (ρ in positive polarity and σ in negative polarity).

The interaction between positive He jets and different targets has been simulated to investigate the influence of the electrical character of the target on the discharge dynamics. It has been confirmed that lower capacitance (lower ϵ_r) of the target promotes a faster radial spreading on the target and that higher capacitance (higher ϵ_r) slows the discharge radial spreading and promotes the electric field rebound in the plasma channel, propagating in the axial direction. We have shown that the presence and intensity of the rebound are directly related to the electric potential on the target surface after discharge impact and thus to the drop of potential in the plasma channel and between the plasma and the target. Moreover, the simulation conditions to model a metallic target at floating potential have been proposed and the character of the discharge interaction with metallic targets at floating potential has been examined. As the impedance of this target is very low and the electric potential increases very slowly after the discharge impact, in the timescales of the impact on the target and of the rebound front, the behavior of the discharge interacting with this target is the same as interacting with a grounded metallic target. Then, the electric potential on the target significantly increases in some hundreds ns. In these timescales the axial electric field in the channel tends to decrease, along with the partial neutralization of the channel, and the result is a plasma channel that conducts most of the potential from the source to the target, as it happens with dielectric targets.

Then, with positive polarity and different targets, the dynamics of charges and electric fields has also been analyzed at the end of a pulse of applied voltage. When the applied voltage falls, a redistribution of electric potential in the channel is imposed, which is sometimes called in the literature 'back discharge'. While the applied voltage is zero and the plasma is not completely neutralized, an electric field of reverse direction subsists in the plasma and in the plasma-target interface. This electric field is higher when the plasma is connecting a grounded source electrode to a charged target than when it is connecting two grounded electrodes. Moreover, it is higher close to the source electrode. It has been shown that, unlike the rebound, in the cases under study this redistribution of potential at the end of the

pulse consists in a redistribution of surface and volume charges that neutralizes the plasma completely without ionization or propagation as a wave or front.

Finally, we have investigated the plasma-target interaction occurring between a positive pulsed Helium plasma jet and a BSO dielectric target with $\epsilon_r = 56$ and we have directly compared results with experiments. The focus has been put on the evolution of volume charge density ρ and surface charge density σ and of their electric field contributions, direct comparison of electric field due to σ averaged inside the target ($E_{zav\sigma}$) with experiments, and the procedure to obtain σ from the measured electric field. A good agreement has been obtained between simulations and experiments. The radial and temporal evolutions of $E_{zav\sigma}$ inside the target present the same shape, during the pulse and after the pulse. The same maximum values of $E_{zav\sigma}$ of 5 kV.cm^{-1} have been obtained in simulations with $V_P = 5.5$ kV and in experiments with $V_P = 4$ kV, for which cases the time of impact is also the same. The inversion of sign of $E_{zav\sigma}$ at the end of the pulse, corresponding to negative surface charge deposition, has been obtained in both simulations and experiments. It has been shown that the high electric field in the plasma due to ρ (dozens or hundreds kV.cm^{-1}), associated to discharge propagation and to the radial spreading on the target surface, is severely depleted by the change of permittivity. Thus, it is much lower in magnitude inside the target. As a result, the electric field components experienced inside the target, both E_z and E_r, are almost exclusively ($\sim 90\%$) originated by the high values (up to 90 nC.cm^{-2}) of σ on the target surface and therefore the measured electric field components are representative of the total electric field the target is exposed to. The numerical investigation of the spatial and temporal distributions of the separate ρ and σ contributions to the electric field has allowed to complement the information obtained experimentally to better understand plasma-target interactions that are crucial for many plasma applications.

VII.2 Prospects for future research

In the near future, using a two-dimensional fluid model for He jets as the one used and developed in this thesis, more progresses in the understanding of plasma jets and their interaction with targets can be carried out. As experimental techniques reach increasingly detailed temporal and spatial distributions of plasma characteristics in streamer-like discharges and He jets, increasingly quantitative comparison between numerical and experimental results must be pursued. In our opinion, future research on the following five topics would be of great interest:

Plasma-flow coupling

In order to advance to conditions closer to experiments, air atmosphere should be considered in the tube-target gap where the He gas flows. This requires the implementation of Helium-air chemistry. Then, a comparison could be performed with the He jet flowing to different atmospheres: air, N_2 and O_2. Other steps to improve the description of the plasma plume and plasma-surface interactions include taking into account heating from some reactions, which allows to study the effect of gas temperature on plasma kinetics, as well as diffusion of

neutral species and reactions of species in the plasma with surfaces. Another way to improve convergence with experiments is to confront the spatial distribution of He and air species in the tube-target gap with experimental measurements. As the plasma jet may have an effect on the flow channeling, the actual distribution of species in the presence of plasma in experiments may be different than the one calculated without plasma, as used in the simulations in this thesis. In that case, that distribution can be corrected to address the experimental conditions.

Plasma jet arrays

Arrays of plasma jets propagating parallel to each other in air are considered as a practical way to increase the area being treated in surface modification and biomedical applications. The physics of such discharges is studied in both simulations and experiments [*Babaeva and Kushner*, 2014; *Robert et al.*, 2015]. Individual plasma jets in an array tend to interact with each other, which can lead to different discharge structures, both in volume and interacting with surfaces. Depending on the conditions, the jets can merge or split. This behavior is determined by the mixing of each individual He flow with air and between He flows, the electric attraction or repulsion between discharges due to the net charge in the plasma and the interaction between photoionization issuing from each discharge and its neighbor discharges. Thus, the arrays of jets present physical interactions that are different than those studied in this thesis and whose implications are not yet fully understood. It would be interesting to investigate such a system through numerical modeling to distinguish the physical mechanisms responsible for the discharge behavior in different conditions and to assess its implications in plasma-target interactions. It should be noticed that such a study requires a three-dimensional description of discharge dynamics or a two-dimensional description without axial symmetry.

Multipulse discharge simulations

We have registered in section I.5 the interest in the community to research long timescale effects in plasma jets, as well as the memory effects between pulses of applied voltage that define the initial conditions in repetitive conditions. In order to study the physics of multiple pulses in plasma jets, the model needs to simulate ms timescales. We have also noticed in section II.4.4 that with 10 μm mesh size, 1.295 million cells, 8 ps average time-step, 13 species (He-N_2), 32 MPI processes on "Hopper" and without the energy equation, the calculation time per iteration is around 2 s. Hence, if we consider the same conditions, to calculate 1 ms would require 125 million iterations and almost 8 years of calculation (250 million s or 2894 days). In this thesis, no more developments to the model are implemented, but in this section we discuss strategies to simulate long timescales.

In reality, keeping the same model, after the discharge propagation and after the fall of the applied voltage, the maximum E/N or ϵ_m are significantly lower than during the discharge propagation and thus the time-step increases (see Figs. II.2 and II.14). Moreover, the time-step coefficients A_c and A_d in eq. II.28 can be increased after the voltage fall keeping calculation stability. Using these factors, trials have been carried out to simulate multiple pulses keeping calculation stability. In the most successful trial, the conditions were as follows:

Chapter VII. Conclusions and prospects

A simplified plane-to-plane electrode geometry with tube and without plasma plume, with $n_z \times n_r = 1200 \times 270 = 324$ thousand cells and 10 μm mesh size, in a fixed 99.9% He - 0.1 N_2 mixture (13 species), with +4 kV pulsed applied voltage with 50 ns rise-time, 100 ns plateau, 50 ns fall-time and 100 μs period of pulse repetition (corresponding to $f = 10$ kHz). The coefficient of the lowest time-step A_d has been varied linearly from 0.125 at the start of the pulse until 0.5 after 250 ns from the start of the pulse. As a result, the calculation of a full repetition (100 μs, pulse + post-pulse) has taken 5 days (around 4 hours for pulse and the rest for post-pulse) with 32 MPI processes on "Hopper" with a post-pulse average time-step $0.5 \times \Delta t_{de} = 500$ ps, which correponds to a maximum electric field in a 10 μm cell of around 0.1 kV.cm^{-1}. As we want to simulate more complex conditions, longer pulses, longer repetition periods and higher number of periods, the reported calculation time is not satisfying. The following strategies can be followed to decrease the calculation time between pulses:

1. As we have seen in section II.4.4, one way to decrease the calculation time is to have access to more cores and run calculations with more MPI processes.

2. Another strategy consists on increasing the time-step, while verifying code stability and accuracy.

3. We have also noticed in section II.4.4 that the calculation time is significantly dependent on the number of species in the model and the number of interpolations to run, and thus it can be decreased through reaction scheme reduction.

4. Another direction that can be taken is to search for better performance of the ODE solver for chemistry and of the interpolation algorithms.

Here we discuss only strategies 2. and 3. In fact, one way to release the limit of timescale consists on implicit or semi-implicit time-stepping. Implicit calculations can be harder to implement and more expensive in calculation time than explicit ones, but allow the time-step to increase. In our model, as the time-step is defined by diffusion, if diffusion is calculated implicitly and the minimum time-step becomes $0.5 \times \Delta t_c$, in the limit of low E/N or ϵ_m the time-step can be up to ten times higher than the curent one (see Fig. II.14). Alternatively, if both drift and diffusion are calculated implicitly, the time-step can be defined *a priori*, as long as stability and accuracy are verified. Moreover, depending on conditions, it should be evaluated in which time intervals it is interesting to keep the calculation of Poisson's equation and electric drift. These are required to follow the movement of charges and eventually to evaluate the effect of electric wind on multipulse timescales but can be discarded if the electric field is negligible, which can contribute to decrease the calculation time. Apart from Poisson and drift, the simulation in the time between pulses requires the calculation of chemistry, transport through flow advection and through diffusion of all species, reactions with walls and eventually heating effects.

Reduction of chemistry

Another known resource to improve the performance of numerical simulations is the reduction of the dimension of kinetics . There are several techniques to proceed with kinetic reduction,

depending on the aim. In *Liu et al.* [2010] a sensitivity study has selected the main species in a He-O_2 global model as those whose density after reaching steady-state is at least 5% of the total density of charged species. On the other hand, a reaction scheme for He-O_2 has been reduced with a zero-dimensional model in *Turner* [2016] by the application of the Morris method [*Morris*, 1991] or Elementary Effects Method (EEM) that identifies the parameters that most strongly influence the model predictions. Recently, the same method has been used in *Obrusník et al.* [2018] on a full N_2/O_2 plasma kinetics model to find a minimal set of processes that are influential for the dependence of the intensity ratio of selected bands on the reduced electric field strength. The EEM is capable of identifying inputs to which a numerical model is insensitive. Working in collaboration with Petr Bílek, Adam Obrusník and Zdenek Bonaventura from Masary University, we intend to use the EEM to reduce the number of species and reactions in our He jet model.

Not only are we interested in using reduced kinetic schemes, we also aim at describing the plasma plume more accurately with He and air, instead of N_2 or O_2. Therefore, we aim at using the EEM on a He-air scheme. We have chosen the reaction scheme in *Murakami et al.* [2013a, b, 2014] with 65 species and 1360 reactions. In *Murakami et al.* [2013a] that scheme has been used to describe in zero dimensions radio-frequency-driven atmospheric pressure He plasmas with 5000 ppm admixture of oxygen and up to 500 ppm of humid air, and validated against experiments in plasma jets. The same model has been used in *Murakami et al.* [2013b] with 500 ppm O_2 admixture and relative humidity from 0 to 100%. Finally, in *Murakami et al.* [2014] the same model has been used also to describe a few miliseconds of post-discharge with validation against plasma jet experiments. These ranges of gas-mixture are close to those of interest to describe the plasma plume with the 2D model. Moreover, the validation of this scheme for post-discharge conditions is a clear advantage, since we want to describe plasma chemistry in the time between pulses.

Then, we have used the zero-D model described in section II.4.2 with this reaction scheme. We have chosen a fixed gas-mixture 99.5% He - 0.5% air. Conditions of repetitive pulses have been taken, with $f = 1$ kHz. The model is dependent on T_e and not E/N and we have provided the temporal profile of T_e on the left side of Fig. VII.1, representative of ionization wave propagation and equal at each pulse. Initial and minimum densities of electrons and N_2^+ as natural preionization have been set at 10^4 cm^{-3}.

As we want a reduced scheme to describe multiple jet pulses, our aim with the zero-D model is to attain repeatability and to preserve repeatability after the scheme reduction. We can see on the right side of Figure VII.1 that repeatability is obtained after the third pulse and maximum electron density corresponds to typical He jet values. Then, a choice of observables for the EEM is required, i.e of the quantities with respect to which the sensitivity with each reaction and species is assessed. As our aim is not to describe detailed reactivity of some particular species but to be able to reproduce discharge dynamics, we focus on electron density and its repeatability. We have chosen to take as observables the integral of $log_{10}(n_e)$ during the 4^{th} pulse and the exact time at which the maximum of n_e is obtained. Then, to guarantee repeatability, a third observable has been chosen: the difference between $log_{10}(n_e)$ during the 5^{th} and 4^{th} pulses.

As a result, the EEM will provide us with the list of species and reactions which the observables are insensitive to. This method guarantees that discarding the selected species

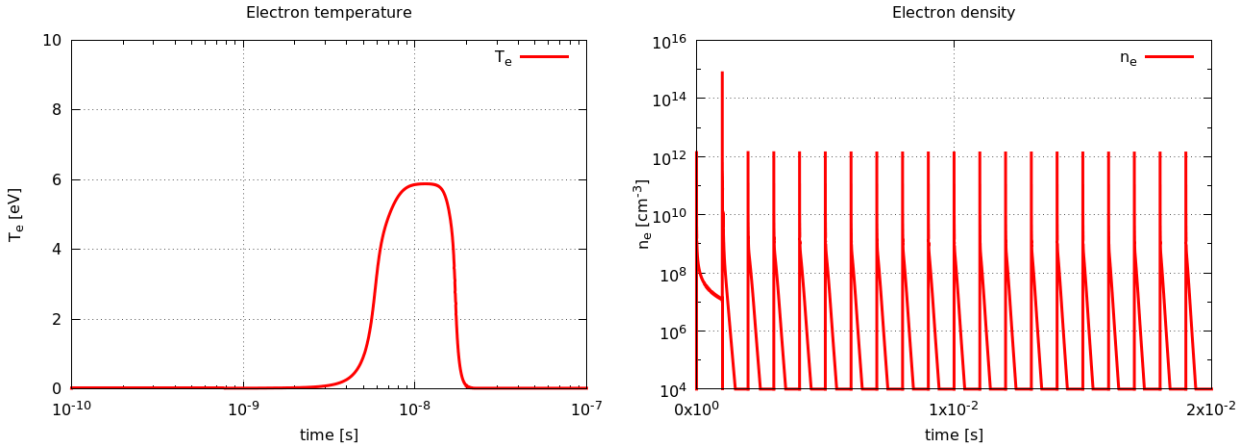

Figure VII.1: On the left, temporal profile of T_e during each pulse. On the right, temporal profile of n_e during the whole 20 pulses using the full scheme in *Murakami et al.* [2014].

and reactions does not influence the general discharge dynamics and the aimed repeatability. Then, the resulting kinetic scheme can be implemented in the 2D discharge model to simulate multiple jet pulses in different configurations. For each configuration, with that reduced scheme, we can study with the 2D model when is repeatability attained and with which initial conditions of species densities in volume and of charges on surfaces, along with other long term effects.

Discharge interaction with targets

Following the studies of chapter VI, for He jet interaction with dielectric targets, it would be interesting to investigate how the dynamics between charges and electric fields during the pulse and at the end of the pulse changes in case a negative discharge propagates and interacts with the target. Moreover, those results could be compared with experimental results of electric field inside electro-optic targets. As in the simulations presented in this thesis, with positive polarity, surface charges remain on the target surface 1 μs after the end of the pulse with a target of permittivity 56 and not 4, it would be interesting to study in which conditions that is the case and how long the charges remain.
More generally, concerning the interaction of plasma jets with different targets, it would be interesting to also consider targets with limited conductivity, such as liquids, that are used in applications. In such targets, deposited charges are transported inside the target volume but this process is not instantaneous as inside metals. Hence, we can expect a different discharge-target interaction than the ones studied in this thesis.

Appendix A

Key results from *Bourdon et al.* [2016]

This appendix is meant to help following the introduction in section I.2.3, where the results from *Bourdon et al.* [2016] are cited.

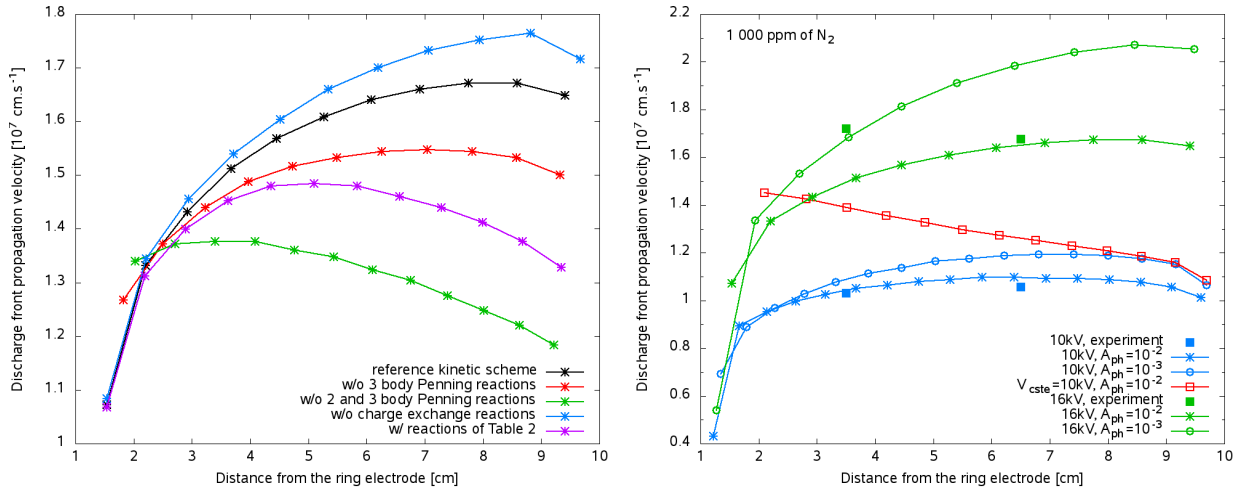

Figure A.1: On the left, for an admixture of 1000 ppm of N_2 and an applied voltage of 16 kV, influence of the reactions considered in the kinetic scheme on the propagation velocity of the ionization front. Simulations have been carried out with a preionization level $n_{init} = 10^4$ cm^{-3} and for a photo-ionization coefficient $A_{ph} = 10^{-2}$ or $\xi = 10$.
On the right, for the same mixture, comparison of the experimental and numerical ionization front propagation velocities for applied voltages of 10 and 16 kV and constant 10 kV. Simulations have been carried out with a preionization level $n_{init} = 10^4$ cm^{-3} and for two values of the photoionization coefficient $A_{ph} = 10 \times X_{N_2} = 10^{-2}$ and $A_{ph} = X_{N_2} = 10^{-3}$.

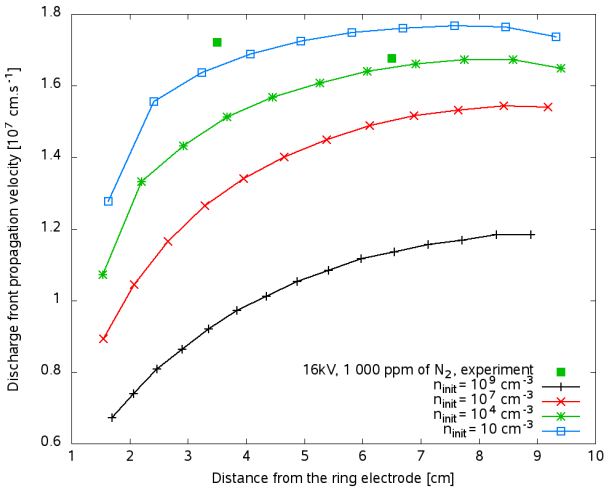

Applied voltage (kV)	10	16
$\tau_{\text{igni}}^{\text{exp}}$ (ns)	1690	1240
$\tau_{\text{igni}}^{\text{sim}}$ (ns) for n_{init} =		
10 cm^{-3}	1500	1150
10^4 cm^{-3}	1400	1050
10^7 cm^{-3}	1100	900
10^9 cm^{-3}	1050	750

Figure A.2: On the left, for an admixture of 1000 ppm of N_2, comparison of the experimental and numerical ionization front propagation velocities for an applied voltage of 16 kV. Simulations are carried out for different preionization levels n_{init} and a photo-ionization coefficient $A_{ph} = 10^{-2}$.
On the right, for 1000 ppm of N_2, influence of the preionization level n_{init} on the discharge ignition time in the simulations τ_{igni}^{sim}, and comparison with the measured ignition time τ_{igni}^{exp}.

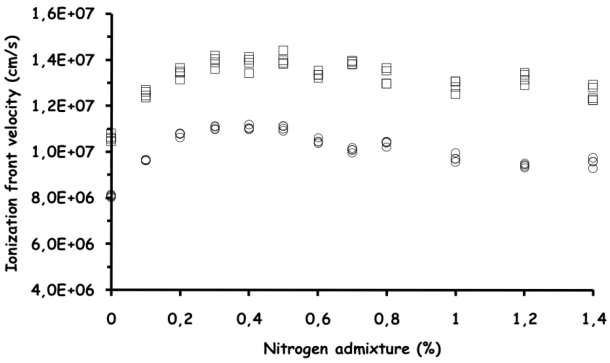

ppm of N_2	'0'	10	100	1000	5000	10 000
$\tau_{\text{igni}}^{\text{exp}}$ (ns)	1340	—	—	1240	1200	1340
$\tau_{\text{igni}}^{\text{sim}}$ (ns)	—	1150	1100	1050	1000	1050

Figure A.3: On the left, experimental average ionization front velocity inside the tube for different He-N_2 mixtures.
On the right, influence of the amount of N_2 admixture on the measured τ_{igni}^{exp} and computed τ_{igni}^{sim} ignition times of the discharge for an applied voltage of 16 kV with $n_{init} = 10^4$ cm^{-3}.

Appendix B

Influence of electrode geometry on the Laplacian distribution of electric field

In this appendix, the Laplacian distributions (i.e. without the presence of volume or surface net charge) of electric potential and electric field obtained with the different electrode configurations presented in section III.3 are studied. In every case, the voltage applied to the powered electrode is +4 kV. In Figure B.1 are represented the axial profiles of potential (on the left) and of E_z (on the right) at $r = 0$ for cases 1 to 4 (see section III.3). In Figure B.2 are shown the same quantities but at $r = 1.5$ mm. Finally, in Figure B.3 are represented the radial profiles of electric potential (on the left) and of E_r (on the right) at $z = 1.45$ cm, at 5 mm from the powered electrodes.

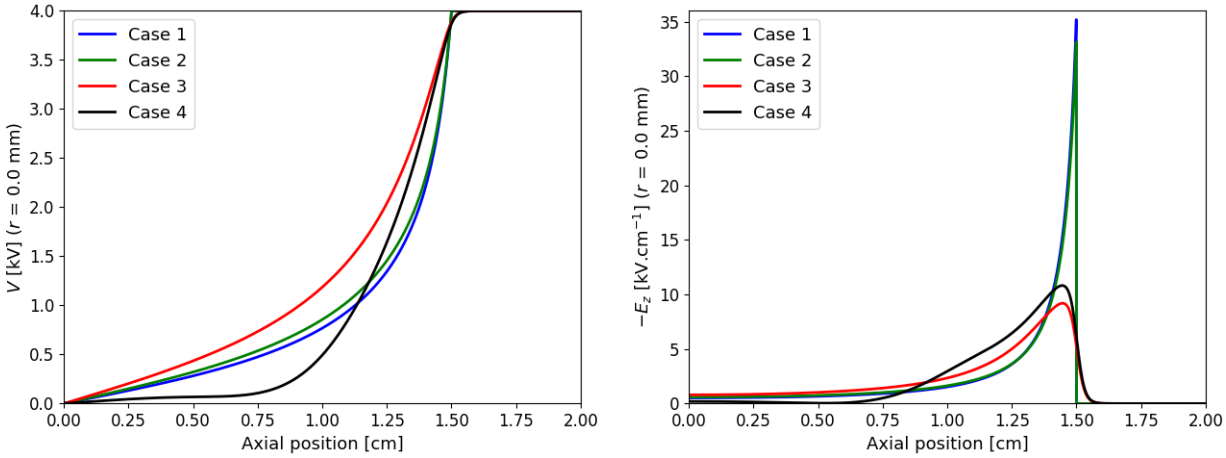

Figure B.1: Axial profiles of Laplacian V and E_z at $r = 0$ with applied voltage +4 kV, with the different electrode configurations presented in section III.3. On the left, $V(z)$. On the right, -$E_z(z)$.

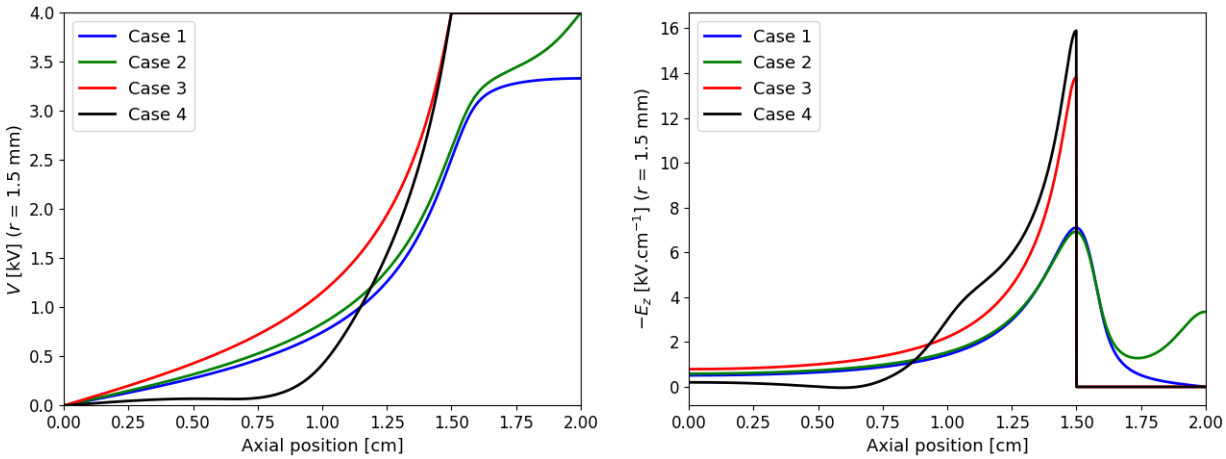

Figure B.2: Axial profiles of Laplacian V and E_z at $r = 1.5$ mm with applied voltage +4 kV, with the different electrode configurations presented in section III.3. On the left, $V(z)$. On the right, -$E_z(z)$.

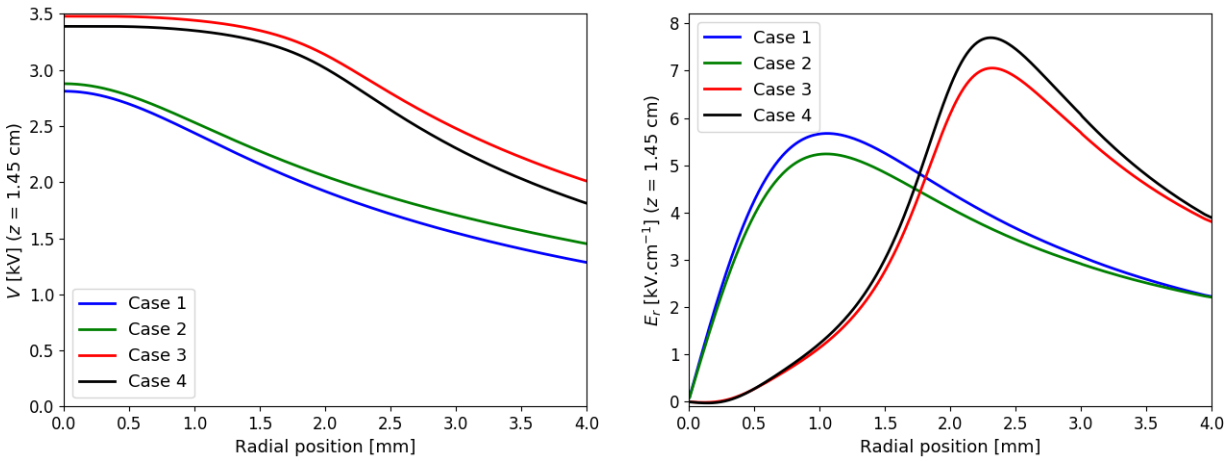

Figure B.3: Radial profiles of Laplacian V and E_r at $z = 1.45$ cm with applied voltage +4 kV, with the different electrode configurations presented in section III.3. On the left, $V(r)$. On the right, $E_r(r)$.

Appendix C

Solution of a chemistry problem with coupled rate coefficient calculation against an exact stationary solution

This appendix is a contribution to the *Round Robin* discussion in the low-temperature plasma community ("A proposal for a test of plasma chemistry solvers against an exact stationary solution"). As written in the proposal, we have considered a chemistry model with three states - a ground state, an excited state and an ionized state. We assume quasi-neutrality, and denote the density of species in each of these states by N_0, N_1 and N_2. The following initial conditions have been used:

$$N = 10^{25}\mathrm{m}^{-3} \tag{C.1}$$

$$N_1 = 10^{16}\mathrm{m}^{-3} \tag{C.2}$$

$$N_2 = 10^{16}\mathrm{m}^{-3} \tag{C.3}$$

$$N_0 = N - N_1 - N_2 \tag{C.4}$$

We assume electronic excitation (k_1), de-excitation (k_1'), ionization (k_2) and recombination ($k_r = k_2'/N_2$), occurring at rate coefficients given in the proposal and represented in Figure C.1 (on the left). The analytical solution of this system for a stationary state, given in the proposal, is represented in Figure C.1 (on the right) for values of electronic temperature T_e between 0.5 and 10 eV with 0.5 eV steps. Then, to compare with the stationary analytical solutions of rate coefficients and species densities, first, we have computed the rate coefficients from an electron Boltzmann equation solver. Then, we have tested the chemistry solver by calculating the numerical solution with analytical rate constants. Finally, we have computed the numerical solution using the calculated rate coefficients.

Computation of rate constants from a Boltzmann equation solver

We have taken the tables of cross sections provided in the proposal: one set of "effective" cross sections and two sets of inelastic cross sections. Then, the rate coefficients have been calculated considering a Boltzmann EEDF with given electron mean energy. The rate coefficients have been calculated with Bolsig+ (version 03/2016 for Windows) [*Hagelaar and*

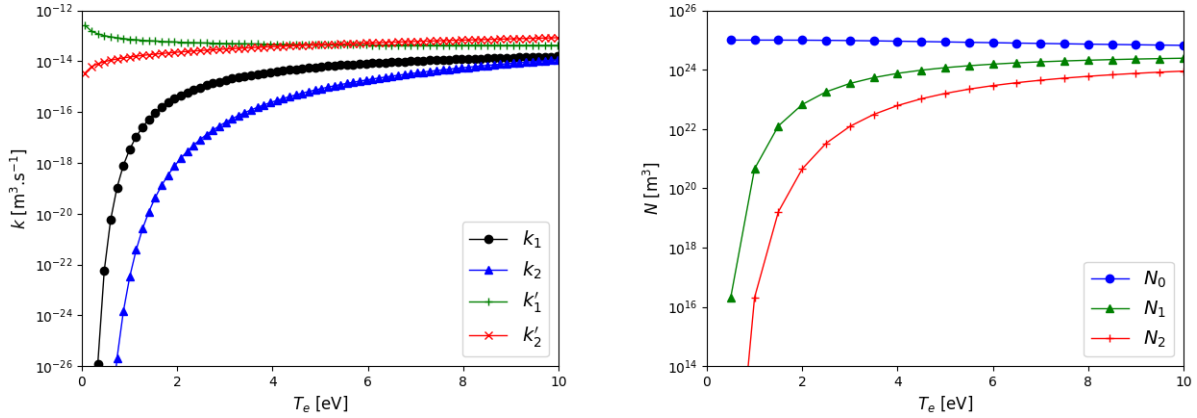

Figure C.1: Analytical rate coefficients (on the left) and solution (on the right) given in the proposal.

Pitchford, 2005]. With Bolsig+, no extrapolation of cross sections has been considered. The energy grid used has 1000 intervals. Precision has been set to 10^{-11}, convergence to 10^{-9} and maximum number of iterations to 1000. 100 calculations have been performed for electron mean energies between 0.1 and 20 eV, equally distanced in energy space (0.201 eV steps). In Figure C.2, the relative difference between the obtained coefficients and the analytical solutions is shown. The relative difference is of the order of 10^{-4}, except for low T_e where it reaches high values.

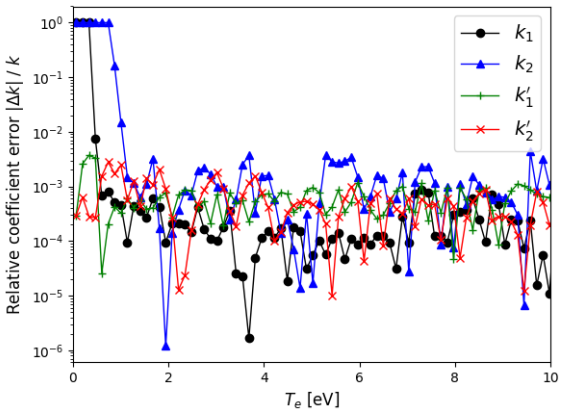

Figure C.2: Relative errors of the rate coefficients calculated considering a Boltzmann EEDF, using Bolsig+ with the conditions explained in the text.

Solution with analytical rate coefficients

Numerically, the solution to the chemistry problem is reached by time integration. The time integration is performed by the RADAU5 solver [*Hairer and Wanner*, 1996]. RADAU5 provides a numerical solution of a stiff system of first order ordinary differential equations, using an implicit Runge-Kutta method of order 5 with step size control and continuous output. Two calculations have been performed. In both, the time-step rises as a geometric progression with a scale factor 1.5, starting at 10^{-13} s.

Calculation 1:
The convergence condition to consider a stationary state is specified as:

$$max(|Ni(t) - Ni(t - \Delta t)|/Ni(t - \Delta t), i = 0, 1, 2) < 10^{-13} \tag{C.5}$$

The relative and absolute error tolerances of the solver were set as 10^{-14}. Figure C.3 shows that using the analytical rate coefficients and these numerical parameters with the RADAU5 solver provides density results very close to the analytical densities in Figure C.1. The relative difference between the analytically and numerically obtained densities is of the order of magnitude of the convergence criterion. The physical time taken for calculation 1 to converge for each T_e is also reported in Figure C.3.

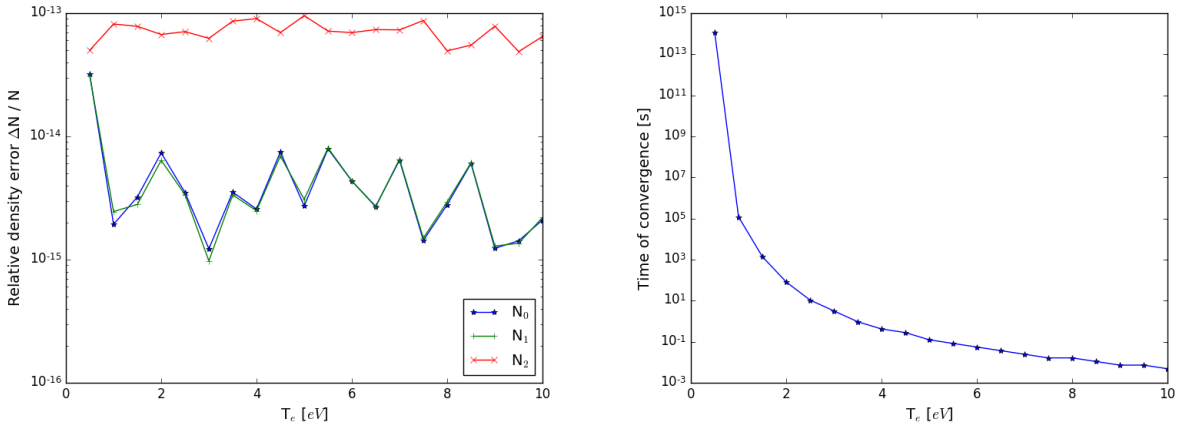

Figure C.3: Relative errors of the solution considering exact rate coefficients of calculation 1 (on the left) and time of convergence (on the right).

Calculation 2:
The convergence condition to consider a stationary state is specified as:

$$max(|Ni(t) - Ni(t - \Delta t)|/Ni(t - \Delta t), i = 0, 1, 2) < 10^{-11} \tag{C.6}$$

The relative and absolute error tolerances of the solver were set as 10^{-12}. Figure C.4 shows that using the analytical rate coefficients and these numerical parameters with the RADAU5 solver provides density results very close to the analytical densities in Figure C.1. The relative difference between the analytically and numerically obtained densities is of the order of magnitude of the convergence criterion. The physical time taken for calculation 2 to converge for each T_e is also reported in Figure C.3. The relative difference with respect to the analytical solution is higher than for calculation 1 but is still very low, and the time of convergence is over one order of magnitude lower than in calculation 1.

Solution with rate coefficients from EBE solver calculations

The calculated rate coefficients are tabulated in the Bolsig+ output format as function of $T_e = 2/3\epsilon$. Then, for each value of T_e used in the chemistry solver (from 0.5 to 10 eV with 0.5

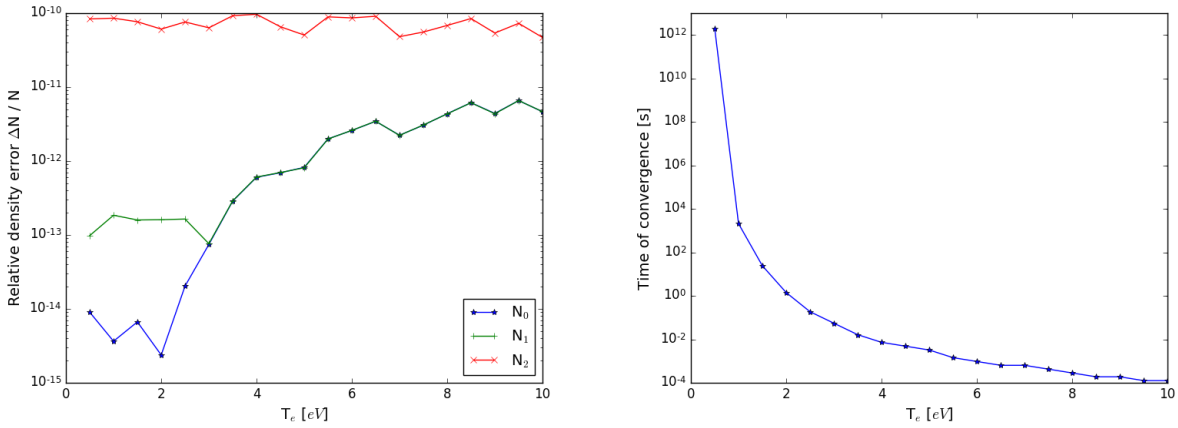

Figure C.4: Relative errors of the solution considering exact rate coefficients of calculation 2 (on the left) and time of convergence (on the right).

eV steps), the rate coefficients are automatically calculated by linear interpolation between the tabulated values. The results of the relative difference between the densities obtained using the rate coefficients and the numerical conditions of "Calculation 1" and the analytical results (Figure C.1) are shown in Figure C.5.

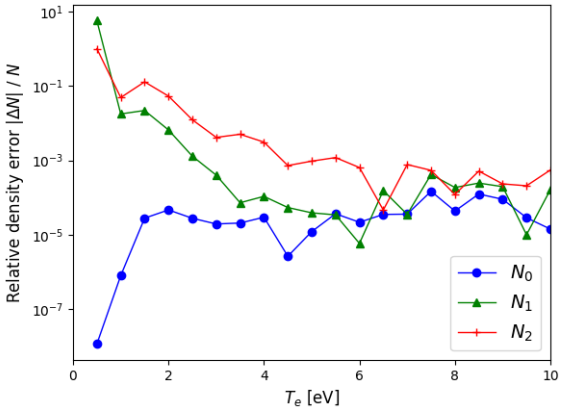

Figure C.5: Relative errors of the solution considering calculated rate coefficients.

These differences have higher order of magnitude than the ones using analytical rate coefficients. In fact, the order of magnitude of the relative errors of densities in Figure C.5 is similar to the one of the relative errors of rate coefficients in Figure C.2. The results presented in Figure C.5 are the same using the numerical conditions of "Calculation 1" or of "Calculation 2". This study has allowed us to put forward the causes of the error of the calculated densities under the studied conditions. This error is mostly associated to the calculation of the rate coefficients, rather than the error induced by the chemistry solver and its convergence and tolerance criteria.

Appendix D

He-O_2 reaction scheme for atmospheric pressure plasmas from *Liu et al.* [2010]

No	Reaction[a)]	Rate coefficient[b)]
1	$e + He \rightarrow e + He$	$f(T_e)$
2	$e + O_2 \rightarrow e + O_2$	$f(T_e)$
3	$e + He \rightarrow He^+ + 2e$	$f(T_e)$
4	$e + He^* \rightarrow He^+ + 2e$	$f(T_e)$
5	$e + He_2^* \rightarrow He_2^+ + 2e$	$9.75 \times 10^{-10} T_e^{0.71} \exp(-3.4/T_e)$
6	$e + O \rightarrow O^+ + 2e$	$f(T_e)$
7	$e + O(^1D) \rightarrow O^+ + 2e$	$f(T_e)$
8	$e + O(^1S) \rightarrow O^+ + 2e$	$f(T_e)$
9	$e + O^- \rightarrow O + 2e$	$f(T_e)$
10	$e + O_2 \rightarrow O_2^+ + 2e$	$f(T_e)$
11	$e + O_2 \rightarrow O^+ + O + 2e$	$f(T_e)$
12	$e + O_2(a) \rightarrow O_2^+ + 2e$	$f(T_e)$
13	$e + O_2(a) \rightarrow O^+ + O + 2e$	$f(T_e)$
14	$e + O_2(b) \rightarrow O_2^+ + 2e$	$f(T_e)$
15	$e + O_2(b) \rightarrow O + O^+ + 2e$	$f(T_e)$
16	$e + O_2(v) \rightarrow O_2^+ + 2e$	$f(T_e)$
17	$e + O_2(v) \rightarrow O^+ + O + 2e$	$f(T_e)$
18	$e + He \rightarrow e + He^*$	$f(T_e)$
19	$e + He^* \rightarrow e + He$	$f(T_e)$
20	$e + He_2^* \rightarrow e + 2He$	3.8×10^{-9}
21	$e + O \rightarrow O(^1D) + e$	$f(T_e)$
22	$e + O(^1D) \rightarrow O + e$	$f(T_e)$
23	$e + O \rightarrow O(^1S) + e$	$f(T_e)$
24	$e + O(^1S) \rightarrow O + e$	$f(T_e)$
25	$e + O_2 \rightarrow 2O + e$	$f(T_e)$
26	$e + O_2 \rightarrow O(^1D) + O + e$	$f(T_e)$
27	$e + O_2 \rightarrow O(^1S) + O + e$	$f(T_e)$
28	$e + O_2 \rightarrow O_2(b) + e$	$f(T_e)$
29	$e + O_2 \rightarrow O_2(a) + e$	$f(T_e)$
30	$e + O_2 \rightarrow O_2(v) + e$	$f(T_e)$
31	$e + O_2(a) \rightarrow O_2(b) + e$	$f(T_e)$
32	$e + O_2(a) \rightarrow O(^1D) + O + e$	$f(T_e)$
33	$e + O_2(a) \rightarrow O(^1S) + O + e$	$f(T_e)$
34	$e + O_2(a) \rightarrow 2O + e$	$f(T_e)$
35	$e + O_2(a) \rightarrow O_2 + e$	$f(T_e)$
36	$e + O_2(b) \rightarrow O(^1D) + O + e$	$f(T_e)$
37	$e + O_2(b) \rightarrow O(^1S) + O + e$	$f(T_e)$
38	$e + O_2(b) \rightarrow 2O + e$	$f(T_e)$
39	$e + O_2(b) \rightarrow O_2 + e$	$f(T_e)$
40	$e + O_2(v) \rightarrow O_2(a^1\Delta_g) + e$	$f(T_e)$
41	$e + O_2(v) \rightarrow O_2\left(b^1\sum_g^+\right) + e$	$f(T_e)$

No	Reaction[a)]	Rate coefficient[b)]
42	$e + O_2(v) \rightarrow 2O + e$	$f(T_e)$
43	$e + O_2(v) \rightarrow O(^1D) + O + e$	$f(T_e)$
44	$e + O_2(v) \rightarrow O(^1S) + O + e$	$f(T_e)$
45	$e + O_2(v) \rightarrow O_2 + e$	$f(T_e)$
46	$e + O \rightarrow O^-$	$f(T_e)$
47	$e + O_2 \rightarrow O + O^-$	$f(T_e)$
48	$e + O_2(a) \rightarrow O + O^-$	$f(T_e)$
49	$e + O_2(b) \rightarrow O + O^-$	$f(T_e)$
50	$e + O_2(v) \rightarrow O^- + O$	$f(T_e)$
51	$e + O_3 \rightarrow O + O_2^-$	$f(T_e)$
52	$e + O_3 \rightarrow O^- + O_2$	$f(T_e)$
53	$e + He^+ \rightarrow He^*$	$6.76 \times 10^{-13} T_e^{-0.5}$
54	$e + He_2^+ \rightarrow He^* + He$	$7.12 \times 10^{-15} (T_e/T_g)^{-1.5}$
55	$e + O^+ \rightarrow O(^1D)$	$5.3 \times 10^{-13} T_e^{-0.5}$
56	$e + O_2^+ \rightarrow O + O$	$1.2 \times 10^{-8} T_e^{-0.7}$
57	$e + O_2^+ \rightarrow O + O(^1D)$	$8.88 \times 10^{-9} T_e^{-0.7}$
58	$e + O_2^+ \rightarrow 2O(^1D)$	$6.87 \times 10^{-9} T_e^{-0.7}$
59	$e + O_4^+ \rightarrow 2O_2$	$2.25 \times 10^{-7} T_e^{-0.5}$
60	$2e + He^+ \rightarrow He^* + e$	$7.8 \times 10^{-38} (T_e/T_g)^{-4.4}$
61	$2e + He_2^+ \rightarrow He^* + He + e$	2.8×10^{-20}
62	$2e + He_2^+ \rightarrow He_2^* + e$	1.2×10^{-21}
63	$2e + O^+ \rightarrow O + e$	$5.12 \times 10^{-27} T_e^{-4.5}$
64	$2e + O_2^+ \rightarrow O_2 + e$	$7.18 \times 10^{-27} T_e^{-4.5}$
65	$2e + O_4^+ \rightarrow 2O_2 + e$	$7.18 \times 10^{-27} T_e^{-4.5}$
66	$e + He^+ + He \rightarrow He^* + He$	$7.4 \times 10^{-35} (T_e/T_g)^{-2}$
67	$e + He_2^+ + He \rightarrow He^* + 2He$	3.5×10^{-27}
68	$e + He_2^+ + He \rightarrow He_2^* + He$	1.5×10^{-27}
69	$e + O^+ + O_2 \rightarrow O + O_2$	$2.49 \times 10^{-29} T_e^{-1.5}$
70	$e + O^+ + He \rightarrow O + He$	$6.45 \times 10^{-31} T_e^{-2.5}$
71	$e + O_2^+ + O_2 \rightarrow 2O_2$	$2.49 \times 10^{-29} T_e^{-1.5}$
72	$e + O + O_2 \rightarrow O^- + O_2$	1.0×10^{-31}
73	$e + O + He \rightarrow O^- + He$	1.0×10^{-31}
74	$e + O_2 + O_2 \rightarrow O_2^- + O_2$	$2.26 \times 10^{-30} (T_g/300)^{-0.5}$
75	$e + O_2 + He \rightarrow O_2^- + He$	1×10^{-31}
76	$e + O_3 + O_2 \rightarrow O_3^- + O_2$	1.0×10^{-31}
77	$e + O_3 + He \rightarrow O_3^- + He$	1.0×10^{-31}
78	$He^+ + O^- \rightarrow O + He$	$2 \times 10^{-7} (T_g/300)^{-1}$
79	$He^+ + O^- + M \rightarrow O + He + M$	$2 \times 10^{-25} (T_g/300)^{-2.5}$
80	$He^+ + O_2^- \rightarrow O_2 + He$	$2 \times 10^{-7} (T_g/300)^{-1}$

No	Reaction[a)]	Rate coefficient[b)]
81	$He^+ + O_3^- \rightarrow O_3 + He$	$2 \times 10^{-7} (T_g/300)^{-1}$
82	$He^+ + O_4^- + M \rightarrow He + 2O_2 + M$	$2 \times 10^{-25} (T_g/300)^{-2.5}$
83	$He_2^+ + O^- \rightarrow O + 2He$	1×10^{-7}
84	$He_2^+ + O^- + M \rightarrow O + 2He + M$	$2 \times 10^{-25} (T_g/300)^{-2.5}$
85	$He_2^+ + O_2^- \rightarrow O_2 + 2He$	1×10^{-7}
86	$He_2^+ + O_2^- + M \rightarrow O_2 + 2He + M$	$2 \times 10^{-25} (T_g/300)^{-2.5}$
87	$He_2^+ + O_3^- \rightarrow O_3 + 2He$	1×10^{-7}
88	$He_2^+ + O_3^- + M \rightarrow O_3 + 2He + M$	$2 \times 10^{-25} (T_g/300)^{-2.5}$
89	$He_2^+ + O_4^- + M \rightarrow 2He + 2O_2 + M$	$2 \times 10^{-25} (T_g/300)^{-2.5}$
90	$O^+ + O^- \rightarrow 2O$	$2 \times 10^{-7} (T_g/300)^{-1}$
91	$O^+ + O^- \rightarrow O + O(^1D)$	$4.9 \times 10^{-10} (T_g/300)^{-0.5}$
92	$O^+ + O^- + M \rightarrow 2O + M$	$2 \times 10^{-25} (T_g/300)^{-2.5}$
93	$O^+ + O_2^- \rightarrow O_2 + O$	$2.7 \times 10^{-7} (T_g/300)^{-0.5}$
94	$O^+ + O_2^- + M \rightarrow O_2 + O + M$	$2 \times 10^{-25} (T_g/300)^{-2.5}$
95	$O^+ + O_3^- \rightarrow O_3 + O$	$2 \times 10^{-7} (T_g/300)^{-1}$
96	$O^+ + O_3^- + M \rightarrow O_3 + O + M$	$2 \times 10^{-25} (T_g/300)^{-2.5}$
97	$O^+ + O_4^- + M \rightarrow O + 2O_2 + M$	$2 \times 10^{-25} (T_g/300)^{-2.5}$
98	$O_2^+ + O^- \rightarrow O_2 + O$	$2 \times 10^{-7} (T_g/300)^{-0.5}$
99	$O_2^+ + O^- + M \rightarrow O_2 + O + M$	$2 \times 10^{-25} (T_g/300)^{-2.5}$
100	$O_2^+ + O_2^- \rightarrow 2O_2$	$2.0 \times 10^{-7} (T_g/300)^{-0.5}$
101	$O_2^+ + O_2^- \rightarrow O_2 + 2O$	$1.01 \times 10^{-7} (T_g/300)^{-0.5}$
102	$O_2^+ + O_2^- + M \rightarrow 2O_2 + M$	$2 \times 10^{-25} (T_g/300)^{-2.5}$
103	$O_2^+ + O_3^- \rightarrow O_3 + 2O$	1×10^{-7}
104	$O_2^+ + O_3^- \rightarrow O_3 + O_2$	$2 \times 10^{-7} (T_g/300)^{-1}$
105	$O_2^+ + O_3^- + M \rightarrow O_3 + O_2 + M$	$2 \times 10^{-25} (T_g/300)^{-2.5}$
106	$O_2^+ + O_4^- + M \rightarrow 3O_2 + M$	$2 \times 10^{-25} (T_g/300)^{-2.5}$
107	$O_4^+ + O^- \rightarrow 2O_2 + O$	1×10^{-7}
108	$O_4^+ + O_2^- \rightarrow 3O_2$	1×10^{-7}
109	$O_4^+ + O_3^- \rightarrow 3O_2 + O$	1×10^{-7}
110	$O_4^+ + O^- + M \rightarrow 2O_2 + O + M$	$2 \times 10^{-25} (T_g/300)^{-2.5}$
111	$O_4^+ + O_2^- + M \rightarrow 3O_2 + M$	$2 \times 10^{-25} (T_g/300)^{-2.5}$
112	$O_4^+ + O_3^- + M \rightarrow 2O_2 + O_3 + M$	$2 \times 10^{-25} (T_g/300)^{-2.5}$
113	$O_4^+ + O_4^- + M \rightarrow 4O_2 + M$	$2 \times 10^{-25} (T_g/300)^{-2.5}$
114	$O^- + He \rightarrow He + O + e$	$2.5 \times 10^{-18} (T_g/300)^{0.6}$
115	$O^- + He^* \rightarrow O + He + e$	3×10^{-10}

No	Reaction[a)]	Rate coefficient[b)]
116	$O^- + He_2^* \rightarrow O + 2He + e$	3×10^{-10}
117	$O^- + O \rightarrow O_2 + e$	$2.0 \times 10^{-10}(T_g/300)^{0.5}$
118	$O^- + O(^1D) \rightarrow 2O + e$	1×10^{-10}
119	$O^- + O(^1S) \rightarrow 2O + e$	1×10^{-10}
120	$O^- + O_2(b) \rightarrow O_2 + O + e$	$6.9 \times 10^{-10}(T_g/300)^{0.5}$
121	$O^- + O_2(a) \rightarrow O_3 + e$	$3 \times 10^{-10}(T_g/300)^{0.5}$
122	$O^- + O_2 \rightarrow O_3 + e$	$5 \times 10^{-15}(T_g/300)^{0.5}$
123	$O^- + O_3 \rightarrow 2O_2 + e$	$3.01 \times 10^{-10}(T_g/300)^{0.5}$
124	$O_2^- + He \rightarrow He + O_2 + e$	$3.9 \times 10^{-10}\exp(-7400/T_g)$
125	$O_2^- + He^* \rightarrow O_2 + He + e$	3×10^{-10}
126	$O_2^- + He_2^* \rightarrow O_2 + 2He + e$	3×10^{-10}
127	$O_2^- + O \rightarrow O_3 + e$	$1.5 \times 10^{-10}(T_g/300)^{0.5}$
128	$O_2^- + O(^1D) \rightarrow O + O_2 + e$	1×10^{-10}
129	$O_2^- + O(^1S) \rightarrow O + O_2 + e$	1×10^{-10}
130	$O_2^- + O_2 \rightarrow 2O_2 + e$	$2.7 \times 10^{-10}\exp(-5590/T_g)$
131	$O_2^- + O_2(b) \rightarrow 2O_2 + e$	3.6×10^{-10}
132	$O_2^- + O_2(a) \rightarrow 2O_2 + e$	$2.0 \times 10^{-10}(T_g/300)^{0.5}$
133	$O_3^- + He^* \rightarrow O + O_2 + He + e$	3×10^{-10}
134	$O_3^- + He_2^* \rightarrow O + O_2 + 2He + e$	3×10^{-10}
135	$O_3^- + O \rightarrow 2O_2 + e$	1×10^{-11}
136	$O_3^- + O(^1S) \rightarrow O + O_3 + e$	1×10^{-10}
137	$O_4^- + He^* \rightarrow 2O_2 + He + e$	1×10^{-10}
138	$O_4^- + He_2^* \rightarrow 2O_2 + 2He + e$	1×10^{-10}
139	$O_4^- + O(^1D) \rightarrow O + 2O_2 + e$	1×10^{-10}
140	$O_4^- + O(^1S) \rightarrow O + 2O_2 + e$	1×10^{-10}
141	$O_4^- + O_2\left(b^1\sum_g^+\right) \rightarrow 3O_2 + e$	1×10^{-10}
142	$He^+ + 2He \rightarrow He_2^+ + He$	$1.4 \times 10^{-31}(T_g/300)^{-0.6}$
143	$He^+ + O \rightarrow O^+ + He$	$5 \times 10^{-11}(T_g/300)^{0.5}$
144	$He^+ + O(^1D) \rightarrow O^+ + He$	$5 \times 10^{-11}(T_g/300)^{0.5}$
145	$He^+ + O(^1S) \rightarrow O^+ + He$	$5 \times 10^{-11}(T_g/300)^{0.5}$
146	$He^+ + O_2 \rightarrow O^+ + O + He$	$1.07 \times 10^{-9}(T_g/300)^{0.5}$
147	$He^+ + O_2 \rightarrow O_2^+ + He$	$3.3 \times 10^{-11}(T_g/300)^{0.5}$
148	$He^+ + O_2(a) \rightarrow O^+ + O + He$	$1.07 \times 10^{-9}(T_g/300)^{0.5}$
149	$He^+ + O_2(a) \rightarrow O_2^+ + He$	$3.3 \times 10^{-11}(T_g/300)^{0.5}$
150	$He^+ + O_3 \rightarrow O^+ + O_2 + He$	$1.07 \times 10^{-9}(T_g/300)^{0.5}$
151	$He_2^+ + O \rightarrow O^+ + 2He$	$1 \times 10^{-9}(T_g/300)^{0.5}$

No	Reaction[a)]	Rate coefficient[b)]
152	$He_2^+ + O(^1D) \rightarrow O^+ + 2He$	$1 \times 10^{-9}(T_g/300)^{0.5}$
153	$He_2^+ + O(^1S) \rightarrow O^+ + 2He$	$1 \times 10^{-9}(T_g/300)^{0.5}$
154	$He_2^+ + O_2 \rightarrow O_2^+ + 2He$	$1 \times 10^{-9}(T_g/300)^{0.5}$
155	$He_2^+ + O_2(b) \rightarrow O_2^+ + 2He$	$1 \times 10^{-9}(T_g/300)^{0.5}$
156	$He_2^+ + O_2(a) \rightarrow O_2^+ + 2He$	$1 \times 10^{-9}(T_g/300)^{0.5}$
157	$He_2^+ + O_3 \rightarrow O^+ + O_2 + 2He$	$1 \times 10^{-9}(T_g/300)^{0.5}$
158	$O^+ + O + M \rightarrow O_2^+ + M$	$1 \times 10^{-29}(T_g/300)^{0.5}$
159	$O^+ + O_2 \rightarrow O_2^+ + O$	$2.0 \times 10^{-11}(T_g/300)^{-0.5}$
160	$O^+ + O_3 \rightarrow O_2^+ + O_2$	1×10^{-10}
161	$O^- + O_2(a) \rightarrow O_2^- + O$	$1.1 \times 10^{-11}(T_g/300)^{-0.5}$
162	$O^- + O_3 \rightarrow O_2^- + O_2$	$1.02 \times 10^{-11}(T_g/300)^{0.5}$
163	$O^- + O_3 \rightarrow O_3^- + O$	$1.99 \times 10^{-10}(T_g/300)^{0.5}$
164	$O^- + O_2 + M \rightarrow O_3^- + M$	$1.1 \times 10^{-30}(T_g/300)^{-1}$
165	$O_2^+ + He^* \rightarrow O^+ + O + He$	1×10^{-10}
166	$O_2^+ + He_2^* \rightarrow O^+ + O + 2He$	1×10^{-10}
167	$O_2^+ + O(^1D) \rightarrow O_2(a) + O^+$	$1 \times 10^{-12}(T_g/300)^{-0.5}$
168	$O_2^+ + 2O_2 \rightarrow O_4^+ + O_2$	$2.4 \times 10^{-30}(T_g/300)^{-3.2}$
169	$O_2^+ + O_2 + He \rightarrow O_4^+ + He$	$5.8 \times 10^{-31}(T_g/300)^{-3.1}$
170	$O_2^- + O \rightarrow O^- + O_2$	$1.5 \times 10^{-10}(T_g/300)^{0.5}$
171	$O_2^- + O_3 \rightarrow O_3^- + O_2$	$6 \times 10^{-10}(T_g/300)^{0.5}$
172	$O_2^- + O(^1S) \rightarrow O^- + 2O$	1×10^{-10}
173	$O_2^- + O_2 + M \rightarrow O_4^- + M$	$3.5 \times 10^{-31}(T_g/300)^{-1}$
174	$O_3^- + O \rightarrow O_2^- + O_2$	$2.5 \times 10^{-10}(T_g/300)^{0.5}$
175	$O_3^- + O(^1D) \rightarrow O^- + O + O_2$	1×10^{-10}
176	$O_3^- + O(^1S) \rightarrow O^- + O + O_2$	1×10^{-10}
177	$O_3^- + O(^1S) \rightarrow O_2^- + 2O$	1×10^{-10}
178	$O_3^- + O_2\left(b^1\sum_g^+\right) \rightarrow O^- + 2O_2$	1×10^{-10}
179	$O_4^+ + He^* \rightarrow O^+ + O + O_2 + He$	1×10^{-10}
180	$O_4^+ + He_2^* \rightarrow O^+ + O + O_2 + 2He$	1×10^{-10}
181	$O_4^+ + O \rightarrow O_2^+ + O_3$	3×10^{-10}
182	$O_4^+ + O(^1D) \rightarrow O_2^+ + O_3$	3×10^{-10}
183	$O_4^+ + O(^1S) \rightarrow O_2^+ + O_3$	3×10^{-10}
184	$O_4^+ + O_2 \rightarrow O_2^+ + 2O_2$	$3.3 \times 10^{-6}\left(\frac{T_g}{300}\right)^{-4} \exp\left(-\frac{5030}{T_g}\right)$
185	$O_4^+ + O_2(a) \rightarrow O_2^+ + 2O_2$	1×10^{-10}
186	$O_4^+ + O_2(b) \rightarrow O_2^+ + 2O_2$	1×10^{-10}

No	Reaction[a)]	Rate coefficient[b)]
187	$O_4^+ + He \rightarrow O_2^+ + O_2 + He$	3×10^{-17}
188	$O_4^- + M \rightarrow O_2^- + O_2 + M$	$1 \times 10^{-10}\exp(-1044/T_g)$
189	$O_4^- + O \rightarrow O_3^- + O_2$	4×10^{-10}
190	$O_4^- + O \rightarrow O^- + 2O_2$	3×10^{-10}
191	$O_4^- + O(^1D) \rightarrow O_2^- + O_2 + O$	1×10^{-10}
192	$O_4^- + O(^1S) \rightarrow O^- + 2O_2$	1×10^{-10}
193	$O_4^- + O_2(a^1\Delta_g) \rightarrow O_2^- + 2O_2$	1×10^{-10}
194	$O_4^- + O_2\left(b^1\sum_g^+\right) \rightarrow O_2^- + 2O_2$	1×10^{-10}
195	$O_4^- + O_3 \rightarrow O_3^- + 2O_2$	3×10^{-10}
196	$2He^* \rightarrow He_2^+ + e$	$2.03 \times 10^{-9}(T_g/300)^{0.5}$
197	$2He^* \rightarrow He^+ + He + e$	$8.7 \times 10^{-10}(T_g/300)^{0.5}$
198	$He^* + He_2^* \rightarrow He^+ + 2He + e$	$5 \times 10^{-10}(T_g/300)^{0.5}$
199	$He^* + He_2^* \rightarrow He_2^+ + He + e$	$2 \times 10^{-9}(T_g/300)^{0.5}$
200	$2He_2^* \rightarrow He^+ + 3He + e$	$3 \times 10^{-10}(T_g/300)^{0.5}$
201	$2He_2^* \rightarrow He_2^+ + 2He + e$	$1.2 \times 10^{-9}(T_g/300)^{0.5}$
202	$He^* + O \rightarrow O^+ + He + e$	$3.96 \times 10^{-10}(T_g/300)^{0.17}$
203	$He^* + O(^1D) \rightarrow O^+ + He + e$	$3.96 \times 10^{-10}(T_g/300)^{0.17}$
204	$He^* + O(^1S) \rightarrow O^+ + He + e$	$3.96 \times 10^{-10}(T_g/300)^{0.17}$
205	$He^* + O_2 \rightarrow O_2^+ + He + e$	$2.54 \times 10^{-10}(T_g/300)^{0.5}$
206	$He^* + O_2(b) \rightarrow O_2^+ + He + e$	$2.54 \times 10^{-10}(T_g/300)^{0.5}$
207	$He^* + O_3 \rightarrow O_2^+ + O + He + e$	$2.54 \times 10^{-10}(T_g/300)^{0.5}$
208	$He_2^* + O \rightarrow O^+ + 2He + e$	$1 \times 10^{-10}(T_g/300)^{0.5}$
209	$He_2^* + O(^1D) \rightarrow O^+ + 2He + e$	$1 \times 10^{-10}(T_g/300)^{0.5}$
210	$He_2^* + O(^1S) \rightarrow O^+ + 2He + e$	$1 \times 10^{-10}(T_g/300)^{0.5}$
211	$He_2^* + O_2 \rightarrow O_2^+ + 2He + e$	$1 \times 10^{-10}(T_g/300)^{0.5}$
212	$He_2^* + O_3 \rightarrow O_2^+ + O + 2He + e$	$1 \times 10^{-10}(T_g/300)^{0.5}$
213	$He_2^* + M \rightarrow 2He + M$	1.5×10^{-15}
214	$O(^1D) + O \rightarrow 2O$	8×10^{-12}
215	$O(^1D) + O_2 \rightarrow O + O_2$	$4.8 \times 10^{-12}\exp(67/T_g)$
216	$O(^1D) + O_2 \rightarrow O + O_2(a)$	$1.6 \times 10^{-12}\exp(67/T_g)$
217	$O(^1D) + O_2 \rightarrow O + O_2(b)$	$2.56 \times 10^{-11}\exp(67/T_g)$
218	$O(^1D) + O_3 \rightarrow 2O_2$	1.2×10^{-10}
219	$O(^1D) + O_3 \rightarrow 2O + O_2$	1.2×10^{-10}
220	$O(^1D) + He \rightarrow O + He$	1.0×10^{-13}
221	$O(^1S) + O \rightarrow O(^1D) + O$	$1.67 \times 10^{-11}\exp(-300/T_g)$
222	$O(^1S) + O \rightarrow 2O$	$3.33 \times 10^{-11}\exp(-300/T_g)$

No	Reaction[a)]	Rate coefficient[b)]
223	$O(^1S) + O_2 \rightarrow O + O_2$	$1.6 \times 10^{-12}\exp(-850/T_g)$
224	$O(^1S) + O_2 \rightarrow O(^1D) + O_2$	$3.2 \times 10^{-12}\exp(-850/T_g)$
225	$O(^1S) + O_2(a) \rightarrow O + O_2$	1.1×10^{-10}
226	$O(^1S) + O_2(a) \rightarrow 3O$	3.2×10^{-11}
227	$O(^1S) + O_2(a) \rightarrow O(^1D) + O_2(b)$	2.9×10^{-11}
228	$O(^1S) + O_3 \rightarrow 2O_2$	4.63×10^{-10}
229	$O_2(a) + O \rightarrow O_2 + O$	7.0×10^{-16}
230	$O_2(a) + O_2 \rightarrow 2O_2$	$2.2 \times 10^{-18}(T_g/300)^{0.8}$
231	$O_2(a) + O_2 \rightarrow O + O_3$	$2.95 \times 10^{-21}(T_g/300)^{0.5}$
232	$2O_2(a) \rightarrow 2O_2$	$9 \times 10^{-17}\exp(-560/T_g)$
233	$2O_2(a) \rightarrow O_2(b) + O_2$	$9 \times 10^{-17}\exp(-560/T_g)$
234	$O_2(a) + O_3 \rightarrow 2O_2 + O$	$5.2 \times 10^{-11}\exp(-2840/T_g)$
235	$O_2(a) + He \rightarrow O_2 + He$	$8 \times 10^{-21}(T_g/300)^{0.5}$
236	$O_2(b) + O \rightarrow O_2 + O$	$8.0 \times 10^{-15}(T_g/300)^{0.5}$
237	$O_2(b) + O \rightarrow O_2(a) + O$	$7.2 \times 10^{-14}(T_g/300)^{0.5}$
238	$O_2(b) + O_2 \rightarrow 2O_2$	$4.0 \times 10^{-18}(T_g/300)^{0.5}$
239	$O_2(b) + O_2 \rightarrow O_2(a) + O_2$	$3.6 \times 10^{-17}(T_g/300)^{0.5}$
240	$2O_2(b) \rightarrow O_2(a) + O_2$	$3.6 \times 10^{-17}(T_g/300)^{0.5}$
241	$O_2(b) + O_3 \rightarrow 2O_2 + O$	$7.33 \times 10^{-12}(T_g/300)^{0.5}$
242	$O_2(b) + O_3 \rightarrow O_2(a) + O_3$	$7.33 \times 10^{-12}(T_g/300)^{0.5}$
243	$O_2(b) + O_3 \rightarrow O_2 + O_3$	$7.33 \times 10^{-12}(T_g/300)^{0.5}$
244	$O_2(b) + He \rightarrow O_2(a) + He$	$1 \times 10^{-17}(T_g/300)^{0.5}$
245	$O_2(v) + O \rightarrow O_2 + O$	$1 \times 10^{-14}(T_g/300)^{0.5}$
246	$O_2(v) + M \rightarrow O_2 + M$	$1 \times 10^{-14}(T_g/300)^{0.5}$
247	$O_3 + O \rightarrow 2O_2$	$8 \times 10^{-12}\exp(-2060/T_g)$
248	$O_3 + M \rightarrow O_2 + O + M$	$1.56 \times 10^{-9}\exp(-11490/T_g)$
249	$He^* + 2He \rightarrow He_2^* + He$	2×10^{-34}
250	$3O \rightarrow O + O_2$	$9.21 \times 10^{-34}(T_g/300)^{-0.63}$
251	$3O \rightarrow O + O_2(a)$	$6.93 \times 10^{-35}(T_g/300)^{-0.63}$
252	$2O + O_2 \rightarrow 2O_2$	$2.56 \times 10^{-34}(T_g/300)^{-0.63}$
253	$2O + O_2 \rightarrow O_2 + O_2(a)$	$1.93 \times 10^{-35}(T_g/300)^{-0.63}$
254	$2O + O_2 \rightarrow O_3 + O$	$3.4 \times 10^{-34}\exp(345/T_g)$
255	$2O + O_2(a) \rightarrow O_2 + O_2(a)$	7.4×10^{-33}
256	$2O + He \rightarrow He + O_2$	$1.3 \times 10^{-32}\left(\frac{T_g}{300}\right)^{-1}\exp\left(-\frac{170}{T_g}\right)$
257	$2O + He \rightarrow O_2(a) + He$	9.88×10^{-35}

No	Reaction[a)]	Rate coefficient[b)]
258	$O + 2O_2 \rightarrow O_3 + O_2$	$6 \times 10^{-34}(T_g/300)^{-2.8}$
259	$O + O_2 + He \rightarrow O_3 + He$	$1.1 \times 10^{-34}\exp(510/T_g)$
260	$O + O_3 + O_2 \rightarrow 2O_3$	$1.5 \times 10^{-34}\exp(710/T_g)$
261	$O + O_2(a) + O_2 \rightarrow 2O_2 + O$	1×10^{-32}
262	$O + O_2(a) + He \rightarrow O_2 + O + He$	1×10^{-32}
263	$2O_2(a) + O_2 \rightarrow 2O_3$	1×10^{-31}
264	$O(^1D) \rightarrow O + h\upsilon$	$5.0 \times 10^{-3} s^{-1}$
265	$O(^1S) \rightarrow O(^1D) + h\upsilon$	$1.34 s^{-1}$
266	$O_2(a) \rightarrow O_2 + h\upsilon$	$2.7 \times 10^{-4} s^{-1}$
267	$O_2(b) \rightarrow O_2 + h\upsilon$	$8.3 \times 10^{-2} s^{-1}$

Figure D.1: Table of He-O_2 reactions from *Liu et al.* [2010]. He* represents He(2^3S) and He(2^1S); He_2* represents $He_2(a^3\Sigma_u^+)$; O_2(a) represents O2($a^1\Delta_g$); O_2(b) represents $O_2(b^1\Sigma_g^+)$; $O_2(v)$ represents the vibrational excited states $O_2(v = 1 - 4)$. M represents the background gases He and O_2. Rate coefficients have units $cm^3.s^{-1}$ for two-body reactions, $cm^6.s^{-1}$ for three-body reactions and s^{-1} for radiative transitions; T_e has units eV; T_g has units K. $f(T_e)$ indicates that the rate coefficient is obtained using the electron-impact cross sections.

Appendix E

Key results from *Viegas et al.* [2018a]

This appendix is meant to help following the studies in section IV.7, where the results are compared with those from *Viegas et al.* [2018a].

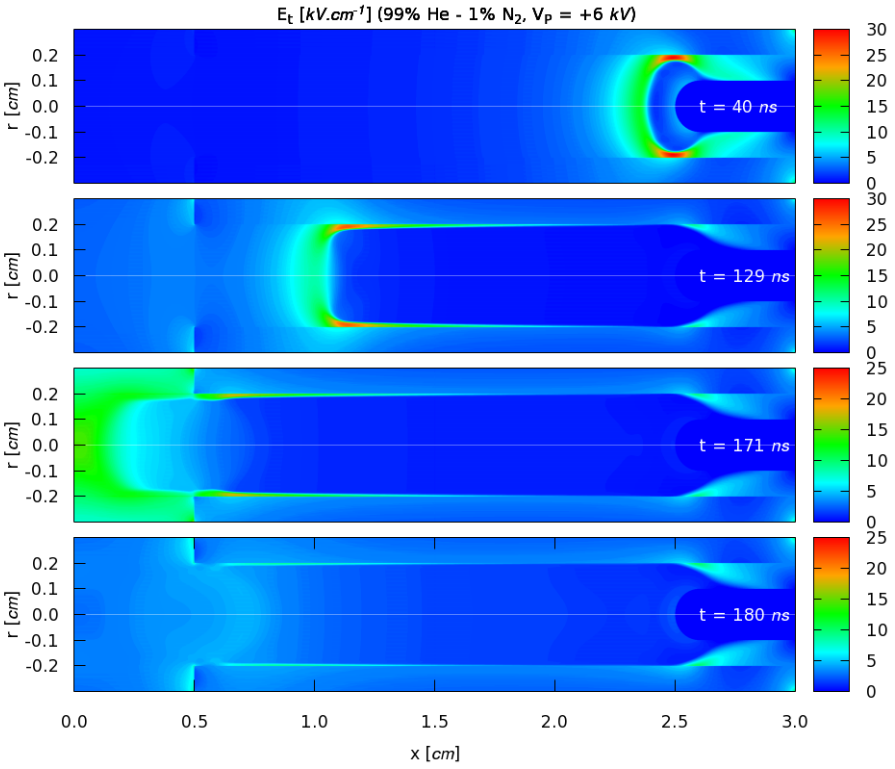

Figure E.1: Cross sectional views of the magnitude of the electric field at t = 40, 129, 171 and 180 ns, for a 2.5 cm long tube with 0.5 cm target-tube distance (i.e. x_{target} = 0.0 cm and x_{tube} = 0.5 cm) for a 99% He - 1% N_2 mixture and V_P = +6 kV.

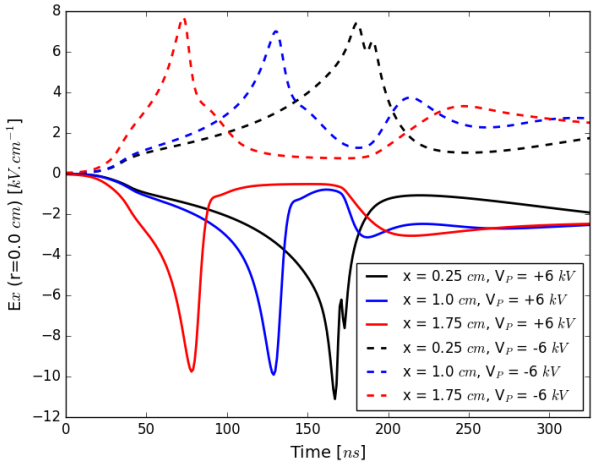

Figure E.2: Temporal profiles of the axial component of electric field E_x on the symmetry axis (r = 0.0 cm) and at x = 0.25, 1.0 and 1.75 cm, for the same conditions as in Figure E.1. Solid lines : V_P = +6 kV. Dashed lines: V_P = -6 kV.

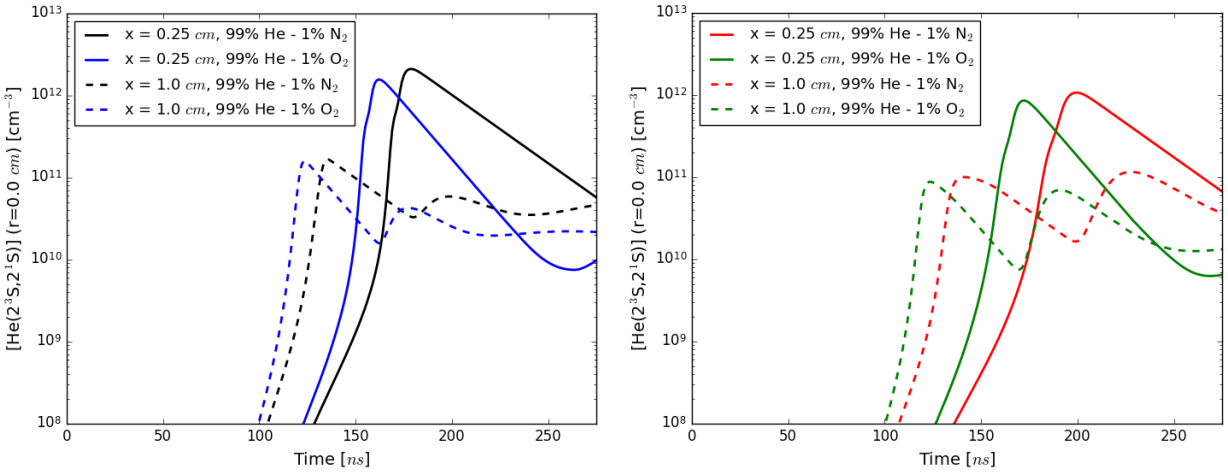

Figure E.3: Temporal profiles of the density of metastable He(2^3S,2^1S) on the axis of symmetry (r = 0.0 cm) at x = 0.25 cm and x = 1.0 cm, for a 2.5 cm long tube with 0.5 cm target-tube distance (i.e. x_{target} = 0.0 cm and x_{tube} = 0.5 cm) for He-N_2 and He-O_2 mixtures and V_P = +6 kV (on the left) and -6 kV (on the right).

Appendix F

Positive discharge interaction with dielectric targets with He-N_2 and He-O_2 mixtures

In this appendix, the electron depletion when positive discharges approach a dielectric target is depicted. The electron depletion consists in the movement of electrons close to the target towards the discharge, i.e., towards higher axial positions, through electric drift. As electrons are only emitted from the dielectric surface through ion impact, a decrease of electron density takes place close to the target. Moreover, the differences in the structure of the plasma plume by using He-N_2 and He-O_2 mixtures obtained are shown from simulation results. In Figure F.1 are represented the spatial distributions of electron density at an instant shortly before discharge impact on the dielectric target placed at $x = -0.5$ cm with both He-N_2 and He-O_2 mixtures.

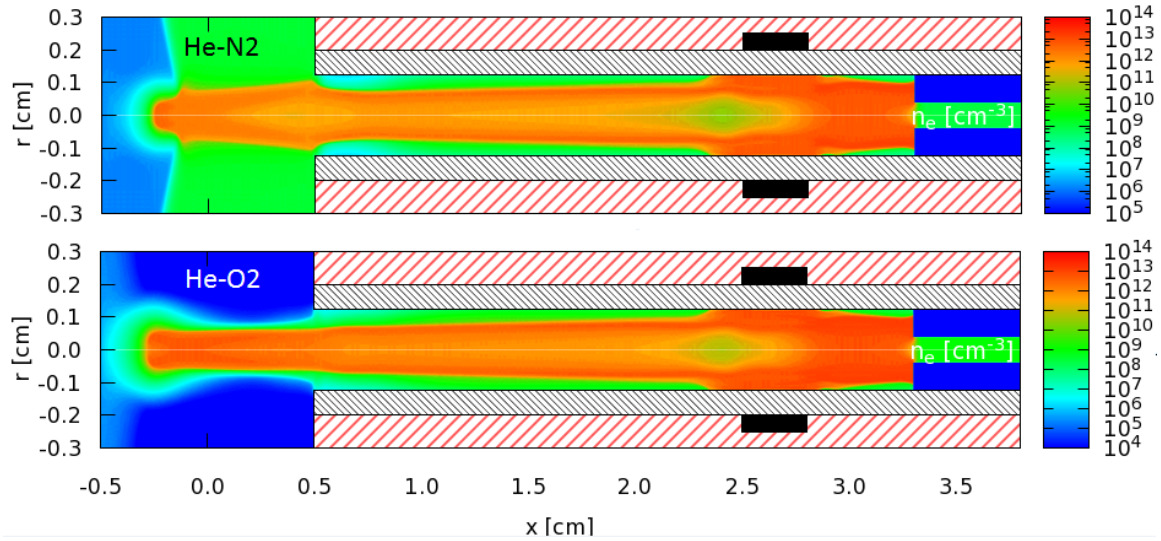

Figure F.1: Spatial distributions of n_e. On top, He with 10 ppm N_2 flows at 1 slm into a N_2 atmosphere, represented at $t = 370$ ns. On the bottom, He with 10 ppm O_2 flows at 1 slm into an O_2 atmosphere, represented at $t = 340$ ns. The applied voltage is $V_P = +5.5$ kV and ϵ_r of the target at $x = -0.5$ cm is 56. The model described in section II.4.5 is used, taking into account the LMEA.

With He-O_2, there is also the effect of electron attachment described earlier in section III.6.5,

that depletes electron density also radially, where O_2 density is higher. With He-O_2, the discharge front propagates with a centered structure between the end of the tube and the target. However, the depletion associated to the dielectric surface and the decrease of n_e due to attachment, together, cause the discharge front to unfocus from the axis at $x = -0.1$ cm due to the higher availability of seed electrons farther from the axis. Then, the discharge front recenters at $x = -0.4$ cm when the conditions are more favorable to the reinforcement of the axial component of electric field at $r = 0$.
With He-N_2, the lack of attachment in the plasma plume causes the discharge front to expand radially when leaving the tube. Thus, it does not propagate with a centered structure when leaving the tube, which is why the use of He-O_2 mixtures allows for a better description of the plasma plume obtained experimentally and presented in Fig. V.2 than the use of He-N_2, which confirms the importance of considering a gas with attachment to reproduce air as environment gas. Then, the effect of the electron depletion from the target surface is also felt in these simulations with He-N_2, where the lack of electrons leads the radius of the discharge front to suddenly decrease.

Appendix G

Effect of the magnitude of the applied voltage on the electric field distribution in positive plasma-dielectric target interaction

The experiments in *Slikboer* [2018] have assessed several values of magnitude of positive applied voltage: 3, 4, 5 and 6 kV. In all the cases the same shape of pulse has been used with approximately 50 ns rise-time and decrease between 1000 and 1050 ns. Here, we study with simulations several cases of positive applied voltage: $V_P = 3.5$ kV, with decrease of pulse between 1000 and 1050 ns; $V_P = 4$ kV, with decrease between 800 and 850 ns; $V_P = 5$ kV, with decrease between 450 and 500 ns; $V_P = 6$ kV, with decrease between 260 and 310 ns. In the experiments, the higher the applied voltage, the earlier the discharge branching on the dielectric surface, described earlier in section VI.2. With the axisymmetric model, the 3D discharge branching is not described and the applied voltage is decreased earlier to describe the discharge dynamics as it starts propagating on the dielectric surface. The simulation conditions are the same as in *Viegas et al.* [2018b], with $\epsilon_r = 4$, and have been described in section V.2, and in this appendix include the condition of minimum electron density of 10^8 cm^{-3} (see section V.3.1). The dynamics between the different types of charges and electric fields during plasma-dielectric target interaction has been studied in detail in *Viegas et al.* [2018b]. In this appendix, the goal is to understand how the variation of the applied voltage can affect the distribution of electric field in the plasma and inside the dielectric target.

G.1 Dynamics of discharge propagation

Firstly, to provide a two-dimensional description of the discharge propagation in the plume, the impact on the dielectric target and the spreading on its surface, Figure G.1 shows the spatial distribution of the magnitude of electric field E_t with different applied voltages. For each voltage, E_t is represented at a time during propagation in the tube-target gap, at a moment of impact on the target surface and, after the discharge spreads on the dielectric target, at a moment when the applied voltage has decreased back to zero.
We can notice in Figure G.1 that the time of impact decreases with the magnitude of applied voltage, and thus the velocity of propagation increases, as it is also the case in the experiments

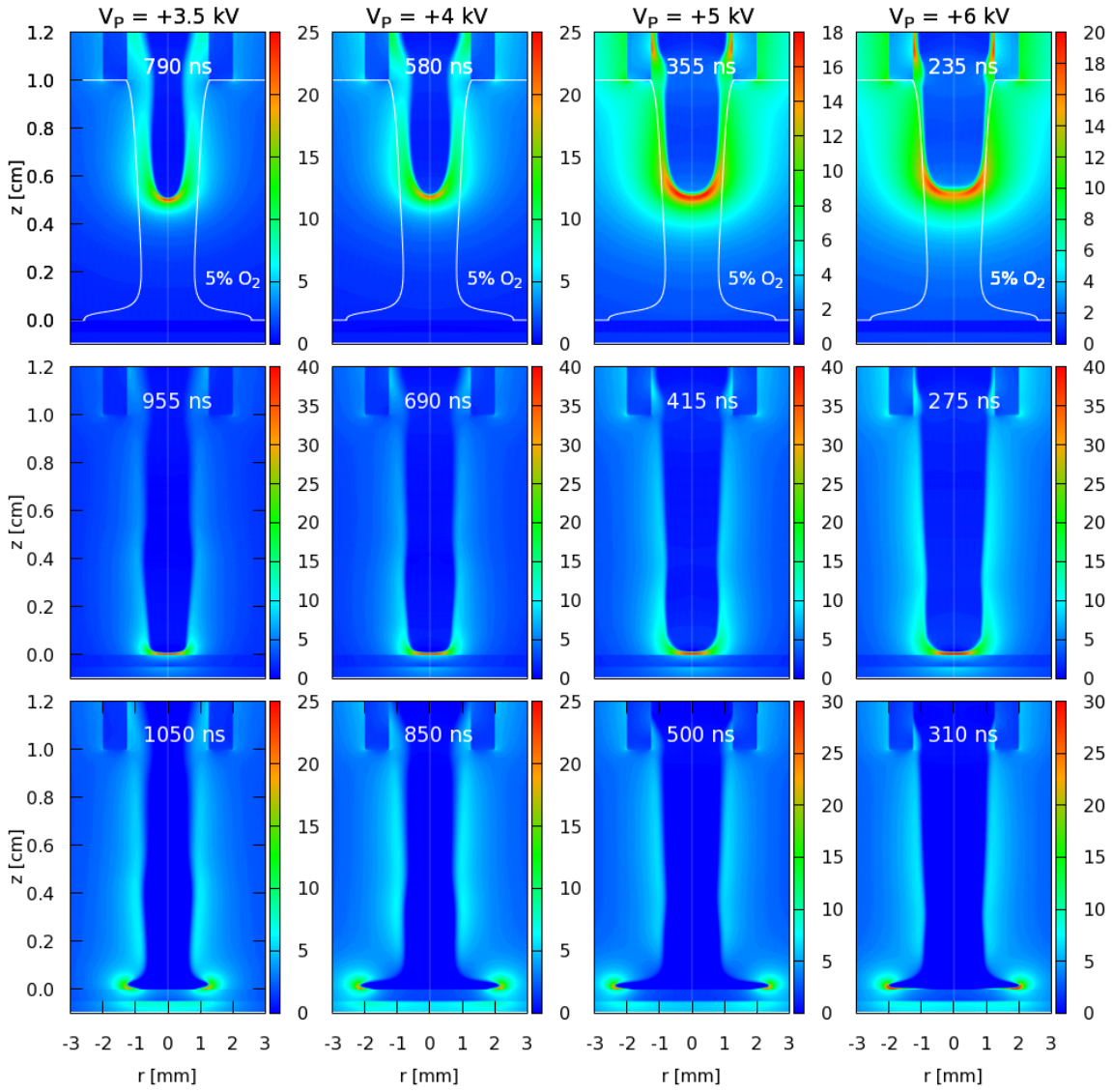

Figure G.1: Cross sectional views of E_t of the discharge in the plasma plume and spreading on the target surface. For $V_P = +3.5$ kV, at $t = 790$, 955 and 1050 ns. For $V_P = +4$ kV, at $t = 580$, 690 and 850 ns. For $V_P = +5$ kV, at $t = 355$, 415 and 500 ns. For $V_P = +6$ kV, at $t = 235$, 275 and 310 ns.

(Fig. VI.2). Given the different electrode configurations in simulations and experiments (Figs. V.3 and V.1), the discharge dynamics of propagation is not comparable quantitatively. However, a qualitative agreement between the numerical and experimental velocity results is obtained. The axial velocity generally decreases during the propagation inside the tube, and then increases when the discharge propagates in the plasma plume and approaches the dielectric target. Then, it is visible in Figure G.1 that the maximum values of E_t during propagation in the plume and when impacting the target vary very little with the value of applied voltage. On the other hand, the radial structure of the discharge is dependent on the applied voltage, with larger radius for higher applied voltage, both inside the tube and in the plasma plume. For the lowest applied voltages $V_P = 3.5$ and 4 kV, while propagating in the tube-target gap, the maximum of electric field is very localized on the axis of symmetry, while

for $V_P = 5$ and 6 kV the electric field on the head of the ionization wave forms a broader front. These results are in agreement with *Babaeva and Naidis* [1996], where a positive streamer has been simulated in two dimensions and it has been reported that the electric field in the streamer head and in the plasma channel and the electron number density do not change appreciably with the value of applied voltage, while the streamer dimensions and velocity do. In *Naidis* [2012] the simulation of a helium jet has also concluded that the increase of the applied voltage leads to the increase of the streamer velocity and radius in the plasma plume. Despite the differences, Figure G.1 shows that the impact on the dielectric target is centered for all the values of applied voltage. Then, it is visible that the radial spreading on the dielectric surface is faster for higher applied voltages, due to tendentiously higher values of volume net charge and radial electric field, which also agrees with the experimental results (Fig. VI.2). For instance, we can notice that for $V_P = 5$ kV the radial spreading between the impact and the end of the pulse is higher (in 85 ns) than for $V_P = 4$ kV (in 160 ns).
These results show that a similar maximum of E_z can correspond to different velocities of propagation because the discharge dynamics is not unidimensional and the velocity is not exclusively determined by the axial component of electric field at $r = 0$. In Figure G.2 are represented the radial profiles of E_z until $r = 1.25$ mm (the tube inner radius) during the propagation, for the four cases of different V_P. In the figure on the left, these are represented during the propagation inside the tube at $z = 1.5$ cm, 0.5 cm from the end of the tube. On the right side, $E_z(r)$ is shown in the plasma plume very close to the target, at $z = 0.1$ mm. For each case, $E_z(r)$ is represented at the instant when $|E_z|$ at any radial position is maximum, that is, at the passage of the ionization front. Additionally, the figure includes for each situation the calculated value of flux of electric field through the circular surface with center on the axis of symmetry and radius 1.25 mm, at each of the axial positions and times represented. This flux is defined as:

$$\Gamma = \int_0^{1.25} |E_z(r)| 2\pi r dr \tag{G.1}$$

This value of flux is used here to hypothesize about its relation with the axial velocity of propagation of the discharge inside the tube and in the discharge front.
On the left side of Figure G.2 we notice that during the propagation inside the tube the maximum of $|E_z|$ is not always centered, but has a close value for every case: at $z = 1.5$ cm between 14 kV.cm^{-1} and 16 kV.cm^{-1}. Then, on the right side of the same figure, we observe that the maximum of $|E_z|$ close to the target, at $z = 0.1$ mm, is always located at $r = 0$, but also presents close values between each case of V_P: between 32 kV.cm^{-1} and 36 kV.cm^{-1}. In both results the radial profile of E_z is broader for higher V_P. Inside the tube, the broader radial profile includes a non-centered maximum of $|E_z|$. At $z = 0.1$ mm, it consists in a slower radial decrease of $|E_z|$. As a result, the flux of electric field Γ, that quantifies the radial broadening of E_z, increases with V_P both inside the tube and close to the target, as does the velocity of propagation. In section III.2 we had observed that the velocity of propagation inside tubes is higher for a more centered discharge front and lower for the more tubular cases. Here, we can add that the discharge propagation is faster for broader rather than thinner discharge fronts.

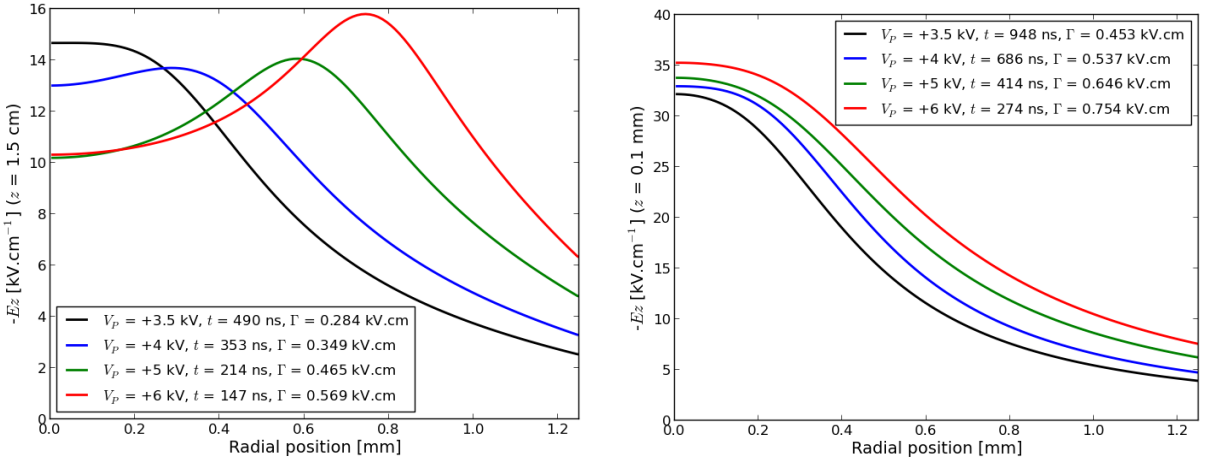

Figure G.2: Radial profiles of E_z for $V_P = +3.5$, 4, 5 and 6 kV, at the time of maximum $|E_z|$, along with the flux of electric field through the surface of radius 1.25 mm, at each axial position. In the figure on the left, inside the tube, at $z = 1.5$ cm. In the figure on the right, in the plasma plume, very close to the target surface, at $z = 0.1$ mm.

G.2 Electric field inside the target

The result of the different plasma-target interactions on the surface charge deposition can be observed in Figure G.3. $\sigma(r)$ is represented at a moment a few ns after the discharge impact, when the peak of the deposited charge is centered, and at the instant when this peak is maximum. The value of the total charge deposited on the target Q is added in the figure for each case, obtained by integrating σ through the surface of the target.

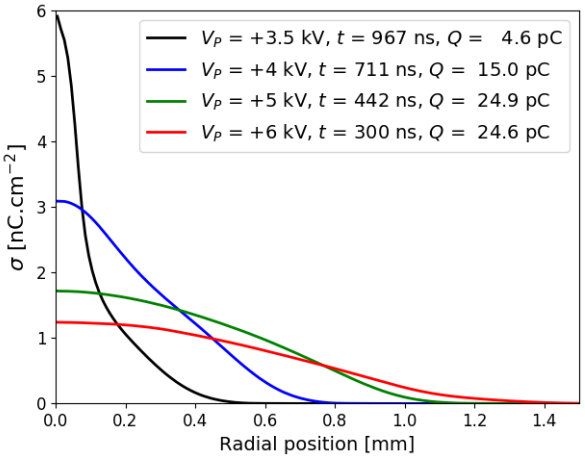

Figure G.3: Radial profiles of σ and total charge deposited Q, for several applied voltages, at a moment when the deposited charge is centered and σ is maximum at $r = 0$.

The charge deposition is more centered for lower applied voltages. Before the maximum of σ starts moving radially and $\sigma(r = 0)$ decreases (described in section VI.3), the value of $\sigma(r = 0)$ is higher for lower V_P, whereas the total charge deposited Q increases with V_P, which is representative of the different radial structure of the discharge front at the time of impact. We should notice that with $V_P = 6$ kV, the applied voltage is already decreasing at $t = 300$ ns, which slows down the discharge propagation and the positive charge deposition,

and justifies obtaining approximately the same Q at the represented instant with $V_P = 5$ and 6 kV. Indeed, the total charge deposited tends to be lower for lower applied voltages, but as there is less radial spreading, the surface charge is more concentrated close to the center, with higher values of σ. Considering the differences of discharge dynamics and interaction with the target with the different applied voltages, it is interesting to characterize in detail the electric field in the plasma plume and in the target. We have seen that E_z in the plasma plume has approximately the same maximum in every case. However, in the experimental results of electric field inside the BSO target ($\epsilon_r = 56$) at the point of impact (Fig. VI.2), E_z rises tendentiously to higher values for lower applied voltages, even though broader radial distributions are obtained for higher voltages [*Slikboer*, 2018]. In order to provide explanation to the experimental results, Figure G.4 shows the temporal evolution at $r = 0$ of the axially-averaged axial component of electric field E_z for the several cases of applied voltage inside the target with $\epsilon_r = 4$. On the left, the total E_z is represented, and on the right the contribution of surface charge only $E_{z\sigma}$ is distinguished.

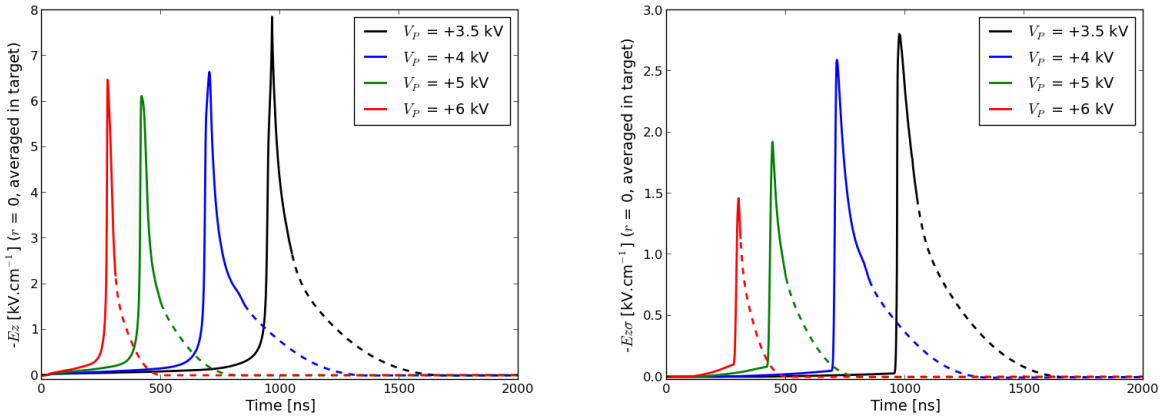

Figure G.4: Temporal evolutions of E_z at $r = 0$ averaged through the thickness of the dielectric target ($\epsilon_r = 4$) of 0.5 mm, with different applied voltages, with 1 ns resolution. In the figure on the left, the total $E_z(t)$. In the figure on the right, the surface charge contribution $E_{z\sigma}(t)$. Dashed lines are used when the applied voltage becomes zero.

Firstly, we notice that both $E_z(r = 0)$ and $E_{z\sigma}(r = 0)$ rise quickly at the discharge arrival on the target, and then slowly decrease during the discharge spreading and at the end of the pulse. The upward directed electric fields measured in the experiments after the end of the pulse are not present in these simulation results with $\epsilon_r = 4$, where $E_z(r = 0)$ and $E_{z\sigma}(r = 0)$ averaged through the target thickness decrease only to zero. Secondly, we should take note that the peak values of $E_z(r = 0)$ and $E_{z\sigma}(r = 0)$ inside the target are not obtained at the same time, which reveals the different dynamics of ρ and σ, as noticed in *Viegas et al.* [2018b]. For example, with $V_P = +3.5$ kV, $E_z(r = 0)$ has its peak at $t = 966$ ns, 11 ns after the discharge impact on the target, while the peak of $E_{z\sigma}(r = 0)$ is reached at $t = 975$ ns, when more σ has been deposited close to $r = 0$. Finally, and most importantly, we evaluate the relations of E_z and $E_{z\sigma}$ between the different values of applied voltage. E_z inside the target at $r = 0$ has approximately the same peak for every case, as does $E_z(r = 0)$ in the plasma plume in Figure G.2. However, the values of the peaks of the surface charge contribution to $E_z(r = 0)$ increase with decreasing V_P. This result agrees qualitatively with

the experimental result presented in Figure VI.2. The difference between $E_z(r = 0)$ and $E_{z\sigma}(r = 0)$ implies that the contribution of net volume charge to the axial component of electric field averaged inside the target $E_{z\rho}(r = 0)$ is higher for higher magnitude of applied voltage. The higher volume net charge with higher V_P is consistent with the result of faster propagation, faster spreading and higher discharge radius with increasing V_P, as presented in Figure G.1. Then, the higher $E_{z\sigma}(r = 0)$ with decreasing V_P is justified by the more centered surface charge deposition, described in Figure G.3. The higher $\sigma(r = 0)$ is not due to a stronger downward directed electric field at $r = 0$ at the moment of impact generated by the discharge front, since this is approximately the same (Figure G.2), but to the thinner radial profile and the slower radial spreading. Table G.1 summarizes the relationship between the maximum electric fields at $r = 0$ in the plume (at 0.1 mm from the target), inside the target, inside the target exclusively due to σ (corresponds to experiments) and the maximum σ at $r = 0$ for each case of applied voltage.

V_P [kV]	E_{zMAX} [kV.cm^{-1}] ($r = 0$, $z = 0.1$ mm)	E_{zMAX} [kV.cm^{-1}] ($r = 0$, avg. target)	$E\sigma_{zMAX}$ [kV.cm^{-1}] ($r = 0$, avg. target)	σ_{MAX} [nC.cm^{-2}] ($r = 0$)
3.5	32.2	7.9	2.8	6.0
4.0	33.0	6.6	2.6	3.1
5.0	33.8	6.1	1.9	1.7
6.0	35.3	6.5	1.5	1.3

Table G.1: Relationship between maximum $E_z(r = 0)$ in the plume, inside the target, inside the target exclusively due to σ and the maximum $\sigma(r = 0)$ for each case of applied voltage.

G.3 Conclusions

Using the simulation results to study the effect of the magnitude of the applied voltage on the electric field distribution in positive plasma-dielectric interaction with a target with $\epsilon_r = 4$, we have reached the following conclusions:

- The maximum of electric field at the discharge front during the discharge propagation is approximately the same for every applied voltage.
- However, the discharge is faster with higher applied voltage because the axial electric field at its front has a broader radial profile.
- Even though the maximum E_z is the same for every V_P and the total charge deposited per time increases with V_P, the maximum of σ at the center is inversely proportional to V_P.
- This tendency is explained by a higher local charge deposition at $r = 0$ when the discharge front is thinner and the radial spreading on the target surface is slower.
- Higher local charge deposition for lower V_P explains the higher electric field values measured in the experiments, at $r = 0$ and exclusively due to σ, for lower V_P.

Bibliography

Allen, N. L., and P. N. Mikropoulos (1999), Streamer propagation along insulating surfaces, *IEEE Transactions on Dielectrics and Electrical Insulation*, *6*(3), 357–362.

Alves, L. L., A. Bogaerts, V. Guerra, and M. M. Turner (2018), Foundations of modelling of nonequilibrium low-temperature plasmas, *Plasma Sources Sci. Technol.*, *27*(023002).

Arjunan, K. P., A. Obrusník, B. T. Jones, L. Zajickova, and S. Ptasinka (2016), Effect of additive oxygen on the reactive species profile and microbicidal property of a helium atmospheric pressure plasma jet, *Plasma Process. Polym.*, *13*, 1089–1105.

Babaeva, N. Y., and M. J. Kushner (2014), Interaction of multiple atmospheric-pressure micro-plasma jets in small arrays: He/O_2 into humid air, *Plasma Sources Sci. Technol.*, *23*(015007).

Babaeva, N. Y., and G. Naidis (1996), Two-dimensional modelling of positive streamer dynamics in non-uniform electric fields in air, *J. Phys. D: Appl. Phys.*, *29*(2423).

Babaeva, N. Y., and G. Naidis (1997), Dynamics of positive and negative streamers in air in weak uniform electric fields, *IEEE Trans. Plasma Sci.*, *25*(2).

Babaeva, N. Y., A. N. Bhoj, and M. J. Kushner (2006), Streamer dynamics in gases containing dust particles, *Plasma Sources Sci. Technol.*, *15*, 591–602.

Barwe, B., A. Stein, O. E. Cibulka, I. Pelant, J. Ghanbaja, T. Belmonte, and J. Benedikt (2015), Generation of silicon nanostructures by atmospheric microplasma jet: The role of hydrogen admixture, *Plasma Process. Polym.*, *12*, 132–140.

Bazelyan, E., and Y. P. Raizer (1998), *Spark discharge*, CRC Press.

Begum, A., M. Laroussi, and M. R. Pervez (2013), Atmospheric pressure he-air plasma jet: Breakdown process and propagation phenomenon, *AIP Advances*, *3*(062117).

Bílek, P., A. Obrusník, T. Hoder, M. Simek, and Z. Bonaventura (2018), Electric field determination in air plasmas from intensity ratio of nitrogen spectral bands: II. Reduction of the uncertainty and state-of-the-art model, *Plasma Sources Sci. Technol.*, *27*(085012).

Boeuf, J.-P., L. L. Yang, and L. C. Pitchford (2013), Dynamics of a guided streamer ('plasma bullet') in a helium jet in air at atmospheric pressure, *J. Phys. D: Appl. Phys.*, *46*(015201).

Bibliography

Bogaczyk, M., R. Wild, L. Stollenwerk, and H.-E. Wagner (2012), Surface charge accumulation and discharge development in diffuse and filamentary barrier discharges operating in He, N_2 and mixtures, *J. Phys. D: Appl. Phys.*, *45*(465202).

Bohm, P., M. Kettlitz, R. Brandenburg, H. Hoft, and U. Czrnetzki (2016), Determination of the electric field strength of filamentary dbds by cars-based four-wave mixing, *Plasma Sources Sci. Technol.*, *25*(054002).

Bonaventura, Z., A. Bourdon, S. Celestin, and V. P. Pasko (2011), Electric field determination in streamer discharges in air at atmospheric pressure, *Plasma Sources Sci. Technol.*, *20*(035012).

Bornholdt, S., M. Wolter, and H. Kersten (2010), Characterization of an atmospheric pressure plasma jet for surface modification and thin film deposition, *Eur. Phys. J. Appl. Phys.*, *60*, 653–660.

Boselli, M., V. Colombo, E. Ghedini, M. Gherardi, R. Laurita, A. Liguori, P. Sanibondi, and A. Stancampiano (2014), Schlieren high-speed imaging of a nanosecond pulsed atmospheric pressure non-equilibrium plasma jet, *Plasma Chem. Plasma Process.*, *34*, 853–869.

Bourdon, A., V. P. Pasko, N. Liu, S. Célestin, P. Ségur, and E. Marode (2007), Efficient models for photoionization produced by non-thermal gas discharges in air based on radiative transfer and the helmholtz equations, *Plasma Sources Sci. Technol.*, *16*, 656–678.

Bourdon, A., T. Darny, F. Pechereau, J. Pouvesle, P. Viegas, S. Iséni, and E. Robert (2016), Numerical and experimental study of the dynamics of a μs helium plasma gun discharge with various amounts of N_2 admixture, *Plasma Sources Sci. Technol.*, *25*(035002).

Breden, D., and L. L. Raja (2014), Computational study of the interaction of cold atmospheric helium plasma jets with surfaces, *Plasma Sources Sci. Technol.*, *23*(065020).

Breden, D., K. Miki, and L. L. Raja (2011), Computational study of cold atmospheric nanosecond pulsed helium plasma jet in air, *Appl. Phys. Lett.*, *99*(111501).

Breden, D., K. Miki, and L. L. Raja (2012), Self-consistent two-dimensional modeling of cold atmospheric-pressure plasma jets/bullets, *Plasma Sources Sci. Technol.*, *21*(034011).

Bruggeman, P. J., F-Iza, and R. Brandenburg (2017), Foundations of atmospheric pressure non-equilibrium plasmas, *Plasma Sources Sci. Technol.*, *26*(123002).

Celestin, S. (2008), Study of the dynamics of streamers in air at atmospheric pressure, Ph.D. thesis, École Centrale Paris, France.

Celestin, S., and V. Pasko (2010), Effects of spatial non-uniformity of streamer discharges on spectroscopic diagnostics of peak electric fields in transient luminous events, *Geophys. Res. Lett.*, *37*(L07804).

Celestin, S., Z. Bonaventura, O. Guaitella, A. Rousseau, and A. Bourdon (2009a), Influence of surface charges on the structure of a dielectric barrier discharge in air at atmospheric pressure: experiment and modeling, *Eur. Phys. J. Appl. Phys.*, *47*(22810).

Celestin, S., Z. Bonaventura, B. Zeghondy, A. Bourdon, and P. Ségur (2009b), The use of the ghost fluid method for poisson's equation to simulate streamer propagation in point-to-plane and point-to-point geometries, *J. Phys. D: Appl. Phys.*, *42*(065203).

Chen, Z., D. Liu, C. Chen, D. Xu, Z. Liu, W. Xia, M. Rong, and M. G. Kong (2018), Analysis of the production mechanism of H_2O_2 in water treated by helium DC plasma jets, *J. Phys. D: Appl. Phys.*, *51*(325201).

Cheng, H., X. Lu, and D. Liu (2015), The effect of tube diameter on an atmospheric-pressure micro-plasma jet, *Plasma Process. Polym.*, *12*, 1343–1347.

Collet, G., E. Robert, A. Lenoir, M. Vandamme, T. Darny, S. Dozias, C. Kieda, and J. M. Pouvesle (2014), Plasma jet-induced tissue oxygenation: potentialities for new therapeutic strategies, *Plasma Sources Sci. Technol.*, *23*(012005).

COMSOL (2017), CFD module user's guide, version 5.3, www.comsol.com/cfd-module.

Courant, R., K. Friedrichs, and H. Lewy (1928), On the partial differential equations of mathematical physics, *Mathematische Annalen (German)*, *100*, 32–74.

Cussler, E. L. (2009), *Diffusion: Mass Transfer in Fluid Systems*, Cambridge: Cambridge University Press.

Darny, T. (2016), Étude de la production des espèces réactives de l'oxygène et de l'azote par décharge plasma gun à pression atmosphérique pour des applications biomédicales, Ph.D. thesis, University of Orléans, France.

Darny, T., E. Robert, S. Dozias, and J.-M. Pouvesle (2014), Modulation of ionization front propagation velocity in a μs plasma gun helium discharge with nitrogen admixture, *20^{th} International Conference on Gas Discharges and their Applications (GD)*.

Darny, T., C. Douat, V. Puech, J.-M. Pouvesle, S. Dozias, and E. Robert (2016), Conductive target influence on helium metastable production in a μs plasma gun discharge, *6^{th} International Conference on Plasma Medicine*.

Darny, T., J.-M. Pouvesle, J. Fontane, L. Joly, S. Dozias, and E. Robert (2017a), Plasma action on helium flow in cold atmospheric pressure plasma jet experiments, *Plasma Sources Sci. Technol.*, *26*, 105,001.

Darny, T., J.-M. Pouvesle, V. Puech, C. Douat, S. Dozias, and E. Robert (2017b), Analysis of conductive target influence in plasma jet experiments through helium metastable and electric field measurements, *Plasma Sources Sci. Technol.*, *26*(4), 045,008.

Deloche, R., P. Monchicourt, M. Cheret, and F. Lambert (1976), High-pressure helium afterglow at room temperature, *Phys. Rev. A*, *13*(3).

Eichwald, O., O. Ducasse, N. Merbahi, M. Yousfi, and D. Dubois (2006), Effect of order fluid models on flue gas streamer dynamics, *J. Phys. D: Appl. Phys.*, *39*, 99–107.

Eichwald, O., O. Ducasse, D. Dubois, A. Abahazem, N. Merbahi, M. Benhenni, and M. Yousfi (2008), Experimental analysis and modelling of positive streamer in air: towards an estimation of O and N radical production, *J. Phys. D: Appl. Phys.*, *41*(23), 234,002.

Ellis, H. W., R. Y. Pai, E. W. McDaniel, E. A. Mason, and L. A. Viehland (1976), Transport properties of gaseous ions over a wide energy range, *At. Data Nucl. Data Tables*, *17*(177).

Ferziger, J., and M. Peric (2002), *Computational Methods for Fluid Dynamics*, Springer-Verlag.

Fridman, A., and G. Friedman (2013), *Plasma Medecine*, Wiley.

Fridman, G., G. Friedman, A. Gutsol, A. B. Shekhter, V. N. Vasilets, and A. Fridman (2008), Applied plasmas medicine, *Plasma Process. Polym.*, *5*, 503–533.

Fruchtman, A. (2017), Neutral gas depletion in low temperature plasma, *J. Phys. D: Appl. Phys.*, *50*(473002).

Gaens, W. V., S. Iseni, A. Schmidt-Bleker, K.-D. Weltmann, S. Reuter, and A. Bogaerts (2015), Numerical analysis of the effect of nitrogen and oxygen admixtures on the chemistry of an argon plasma jet operating at atmospheric pressure, *New J. Phys.*, *17*(033003).

Gallimberti, I., J. K. Hepworth, and R. C. Klewe (1974), Spectroscopic investigation of impulse corona discharges, *J. Phys. D: Appl. Phys.*, *7*, 880–899.

Georghiou, G. E., A. P. Papadakis, R. Morrow, and A. C. Metaxas (2005), Numerical modelling of atmospheric pressure gas discharges leading to plasma production, *J. Phys. D: Appl. Phys.*, *38*, R303–R328.

Gerling, T., A. Nastuta, R. Bussiahn, E. Kindel, and K. Weltmann (2012), Back and forth directed plasma bullets in a helium atmospheric pressure needle-to-plane discharge with oxygen admixtures, *Plasma Sources Sci. Technol.*, *21*(3), 034,012.

Goldberg, B. M., P. S. Bohm, U. Czarnetzki, I. V. Adamovich, and W. R. Lempert (2015), Electric field vector measurements in a surface ionization wave discharge, *Plasma Sources Sci. Technol.*, *24*(055017).

Golubovskii, Y. B., V. A. Maiorov, J. Behnke, and J. F. Behnke (2003), Modelling of the homogeneous barrier discharge in helium at atmospheric pressure, *J. Phys. D: Appl. Phys.*, *36*, 39–49.

Graves, D. B. (2015), Low temperature plasma biomedicine: A tutorial review, *Phys. Plasmas*, *21*.

Grubert, G. K., M. M. Becker, and D. Loffhagen (2009), Why the local-mean-energy approximation should be used in hydrodynamic plasma descriptions instead of the local-field approximation, *Phys. Rev. E*, *80*(036405).

Guaitella, O., and A. Sobota (2015), The impingement of a kHz helium atmospheric pressure plasma jet on a dielectric surface, *J. Phys. D: Appl. Phys.*, *48*(255202).

Hagelaar, G. J. M., and L. C. Pitchford (2005), Solving the Boltzmann equation to obtain electron transport coefficients and rate coefficients for fluid models, *Plasma Sources Sci. Technol.*, *14*(722).

Hairer, E., and G. Wanner (1996), *Solving ordinary differential equations II: Stiff and differential algebraic problems*, Springer-Verlag.

Hasan, M. I., and J. W. Bradley (2016), Reassessment of the body forces in a He atmospheric-pressure plasma jet: a modelling study, *J. Phys. D: Appl. Phys.*, *49*(055203).

Hasted, J. B. (1964), *Physics of Atomic Collisions*, London: Butterworths.

Hübner, S., J. S. Sousa, V. Puech, G. M. W. Kroesen, and N. Sadeghi (2014), Electron properties in an atmospheric helium plasma jet determined by thomson scattering, *J. Phys. D: Appl. Phys.*, *47*(432001).

Hoder, T., M. Simek, Z. Bonaventura, V. Prukner, and F. J. Gordillo-Vázquez (2016), Radially and temporally resolved electric field of positive streamers in air and modelling of the induced plasma chemistry, *Plasma Sources Sci. Technol.*, *25*(045021).

Hofmann, S., K. van Gils, S. van der Linden, S. Iseni, and P. Bruggeman (2014), Time and spatial resolved optical and electrical characteristics of continuous and time modulated rf plasmas in contact with conductive and dielectric substrates, *Eur. Phys. J. D.*, *68*(56).

Hofmans, M. (2017), Spectroscopic measurement of the electric field of a helium plasma jet, Master's thesis, Eindhoven University of Technology, Netherlands.

Hu, J. T., J. G. Wang, X. Y. Liu, D. W. Liu, X. P. Lu, J. J. Shi, and K. Ostrikov (2013), Effect of a floating electrode on a plasma jet, *Phys. Plasmas*, *20*(083516).

HYPRE (2007), HYPRE: a library of high performance preconditioners, https://computation.llnl.gov/projects/hypre-scalable-linear-solvers-multigrid-methods.

IST (2014), IST-Lisbon database, www.lxcat.net, retrieved on March 2014.

IST (2018), IST-Lisbon database, www.lxcat.net, retrieved on January 2018.

Ito, Y., Y. Fukui, K. Urabe, O. Sakai, and K. Tachibana (2010), Effect of series capacitance and accumulated charge on a substrate in a deposition process with an atmospheric-pressure plasma jet, *Japan J. Appl. Phys.*, *49*(066201).

Ivkovic, S. S., G. B. Sretenovic, B. M. Obradovic, N. Cvetanovic, and M. M. Kuraica (2014), On the use of the intensity ratio of he lines for electric field measurements in atmospheric pressure dielectric barrier discharge, *J. Phys. D: Appl. Phys.*, *47*(055204).

Jánský, J., and A. Bourdon (2011a), Simulation of helium discharge ignition and dynamics in thin tubes at atmospheric pressure, *Apl. Phys. Lett.*, *99*(161504).

Jánský, J., and A. Bourdon (2011b), Surface charge deposition inside a capillary glass tube by an atmospheric pressure discharge in air, *Eur. Phys. J. Appl. Phys.*, *55*(13810).

Jánský, J., and A. Bourdon (2014), Simulation of two counter-propagating helium discharges at atmospheric pressure, *Plasma Sources Sci. Technol.*, *23*(025001).

Jánský, J., F. Tholin, Z. Bonaventura, and A. Bourdon (2010), Simulation of the discharge propagation in a capillary tube in air at atmospheric pressure, *J. Phys. D: Appl. Phys.*, *43*(395201).

Jánský, J., P. LeDelliou, F. Tholin, P. Tardiveau, A. Bourdon, and S. Pasquiers (2011), Experimental and numerical study of the propagation of a discharge in a capillary tube in air at atmospheric pressure, *J. Phys. D: Appl. Phys.*, *44*(335201).

Jánský, J., Q. T. Algwari, D. O'Connell, and A. Bourdon (2012), Experimental–modeling study of an atmospheric-pressure helium discharge propagating in a thin dielectric tube, *IEEE Trans. Plasma Sci.*, *40*(11).

Ji, L., W. Yan, Y. Xia, and D. Liu (2018), The effect of target materials on the propagation of atmospheric-pressure plasma jets, *J. Appl. Phys.*, *123*(183302).

Jiang, C., M. Chen, and M. Gundersen (2009), Polarity-induced asymmetric effects of nanosecond pulsed plasma jets, *J. Phys. D: Appl. Phys.*, *42*(232002).

Jogi, I., R. Talviste, J. Raud, K. Piip, and P. Paris (2014), The influence of the tube diameter on the properties of an atmospheric pressure he micro-plasma jet, *J. Phys. D: Appl. Phys.*, *47*(415202).

Kang, W. S., H.-S. Kim, and S. H. Hong (2010), Gas temperature effect on discharge-mode characteristics of atmospheric-pressure dielectric barrier discharge in a helium-oxygen mixture, *IEEE Trans. Plasma Sci.*, *38*(8).

Kawakami, R., S. Okuda, T. Miyazaki, and N. Ikuta (1995), Variations of reduced mobilities in gases under 12-4 potentials, *Journal of the Physical Society of Japan*, *65*(1270).

Kawasaki, T., Y. Arai, and T. Takada (1991), Two-dimensional measurement of electrical surface charge distribution on insulating materials by electrooptic pockels effect, *Japanese Journal of Applied Physics, Part 1: Regular Papers and Short Notes and Review Papers*, *30*(6), 1262–1265.

Kim, H. Y., M. Golkowski, C. Golkowski, P. Stoltz, M. B. Cohen, and M. Walker (2018), PIC simulations of post-pulse field reversal and secondary ionization in nanosecond argon discharges, *Plasma Sources Sci. Technol.*, *27*(055011).

Kim, S. J., T. H. Chung, S. H. Bae, and S. H. Leem (2010), Induction of apoptosis in human breast cancer cells by a pulsed atmospheric pressure plasma jet, *Appl. Phys. Lett.*, *97*(023702).

Klarenaar, B., O. Guaitella, R. Engeln, and A. Sobota (2018), How dielectric, metallic and liquid targets influence the evolution of electron properties in a pulsed he jet measured by Thomson and Raman scattering, *Plasma Sources Sci. Technol.*, *27*(085004).

Komuro, A., R. Ono, and T. Oda (2012), Numerical simulation for production of o and n radicals in an atmospheric-pressure streamer discharge, *J. Phys. D: Appl. Phys.*, *45*(26), 265,201.

Komuro, A., R. Ono, and T. Oda (2013), Effects of pulse voltage rise rate on velocity, diameter and radical production of an atmospheric-pressure streamer discharge, *Plasma Sources Sci. Technol.*, *22*(4), 045,002.

Komuro, A., K. Takahashi, and A. Ando (2015), Numerical simulation for the production of chemically active species in primary and secondary streamers in atmospheric-pressure dry air, *J. Phys. D: Appl. Phys.*, *48*(21), 215,203.

Kong, M. G., G. Kroesen, G. Morfill, T. Nosenko, T. Shimizu, J. van Dijk, and J. L. Zimmermann (2009), Plasma medicine: an introductory review, *New Journal of Physics*, *11*, 115,012.

Kossyi, I. A., A. Y. Kostinsky, A. A. Matveyev, and V. P. Silakov (1992), Kinetic scheme of the non-equilibrium discharge in nitrogen-oxygen mixtures, *Plasma Sources Sci. Technol.*, *1*, 207–220.

Kovacevic, V. V., G. B. Sretenovic, E. Slikboer, O. Guaitella, A. Sobota, and M. M. Kuraica (2018), The effect of liquid target on a nonthermal plasma jet–imaging, electric fields, visualization of gas flow and optical emission spectroscopy, *J. Phys. D: Appl. Phys.*, *51*(065202).

Kozlov, K. V., H. E. Wagner, R. Brandenburg, and P. Michel (2001), Spatio-temporally resolved spectroscopic diagnostics of the barrier discharge in air at atmospheric pressure, *J. Phys. D: Appl. Phys.*, *34*, 3164–3176.

Kulikovsky, A. A. (1997), Positive streamer between parallel plate electrodes in atmospheric pressure air, *J. Phys. D: Appl. Phys.*, *30*(441).

Kulikovsky, A. A. (1998a), Positive streamer in a weak field in air: A moving avalanche-to-streamer transition, *Phys. Rev. E*, *57*(6), 7066–7074.

Kulikovsky, A. A. (1998b), Analytical model of positive streamer in weak field in air: application to plasma chemical calculations, *IEEE Trans. Plasma Sci.*, *26*, 1339–1346.

Kuraica, M. M., and N. Konjevic (1997), Electric field measurement in the cathode fall region of a glow discharge in helium, *Appl. Phys. Lett.*, *70*(1521).

Laimer, J., and H. Stori (2007), Recent advances in the research on non-equilibrium atmospheric pressure plasma jets, *Plasma Process. Polym.*, *4*(3), 266–274.

Laroussi, M. (2015), Low-temperature plasma jet for biomedical applications: A review, *IEEE Trans. Plasma Sci.*, *43*, 703–12.

Laroussi, M., and T. Akan (2007), Arc-free atmospheric pressure cold plasma jets: A review, *Plasma Process. Polym.*, *4*(9), 777–788.

Lazarou, C., D. Koukounis, A. S. Chiper, C. Costin, I. Topala, and G. E. Georghiou (2015), Numerical modeling of the effect of the level of nitrogen impurities in a helium parallel plate dielectric barrier discharge, *Plasma Sources Sci. Technol.*, *24*(035012).

Lazarou, C., T. Belmonte, A. S. Chiper, and G. E. Georghiou (2016), Numerical modeling of the effect of dry air traces in a helium parallel plate dielectric barrier discharge, *Plasma Sources Sci. Technol.*, *25*(055023).

Levko, D., and L. L. Raja (2017), Fluid versus global model approach for the modeling of active species production by streamer discharge, *Plasma Sources Sci. Technol.*, *26*(035003).

Li, J. (2008), Upstream nonoscillatory advection schemes, *Monthly Weather Review*, *136*(12), 4709–4729.

Lietz, A. M., E. Johnsen, and M. J. Kushner (2017), Plasma-induced flow instabilities in atmospheric pressure plasma jets, *Appl. Phys. Lett.*, *111*(114101).

Liu, D. X., M. Z. Rong, X. H. Wang, F. Iza, M. G. Kong, and P. Bruggeman (2010), Main species and physicochemical processes in cold atmospheric-pressure He + O_2 plasmas, *Plasma Process. Polym.*, *7*(846).

Liu, N., S. Célestin, A. Bourdon, V. P. Pasko, P. Ségur, and E. Marode (2007), Application of photoionization models based on radiative transfer and the helmholtz equations to studies of streamers in weak electric fields, *Appl. Phys. Lett.*, *91*(211501).

Liu, X. Y., X. K. Pei, X. P. Lu, and D. W. Liu (2014), Numerical and experimental study on a pulsed-dc plasma jet, *Plasma Sources Sci. Technol.*, *23*(035007).

Liu, Z., D. Liu, D. Xu, H. Cai, W. Xia, B. Wang, Q. Li, and M. G. Kong (2017), Two modes of interfacial pattern formation by atmospheric pressure helium plasma jet-ito interactions under positive and negative polarity, *J. Phys. D: Appl. Phys.*, *50*(195203).

Loeb, L. B. (1965), *Electrical Coronas*, Univ. of California Press, Berkeley.

Loeb, L. B., and J. M. Meek (1940a), The mechanism of spark discharge in air at atmospheric pressure i, *J. Appl. Phys.*, *11*, 438–447.

Loeb, L. B., and J. M. Meek (1940b), The mechanism of spark discharge in air at atmospheric pressure ii, *J. Appl. Phys.*, *11*, 459–474.

Lu, X., and M. Laroussi (2006), Dynamics of an atmospheric pressure plasma plume generated by submicrosecond voltage pulses, *J. Appl. Phys.*, *100*(063302).

Lu, X., and K. Ostrikov (2018), Guided ionization waves: The physics of repeatability, *Appl. Phys. Rev.*, *5*(031102).

Lu, X., M. Laroussi, and V. Puech (2012), On atmospheric-pressure non-equilibrium plasma jets and plasma bullets, *Plas Sources Sci. Technol.*, *21*(034005).

Lu, X., G. V. Naidis, M. Laroussi, and K. Ostrikov (2014), Guided ionization waves: Theory and experiments, *Physics Reports*, *540*, 123–166.

Lu, Y., S. Wu, W. Cheng, and X. Lu (2017), Electric field measurements in an atmospheric-pressure microplasma jet using stark polarization emission spectroscopy of helium atom, *Eur. Phys. J. Special Topics*, *226*, 2979–2989.

Luque, A., V. Ratushnaya, and U. Ebert (2008), Positive and negative streamers in ambient air: modelling evolution and velocities, *J. Phys. D: Appl. Phys.*, *41*(234005).

Marode, E. (1975), The mechanism of spark breakdown in air at atmospheric pressure between a positive point and plane. ii. theoretical: Computer simulation of the streamer track, *J. Appl. Phys.*, *46*(5), 2016–2020.

Meek, J. M. (1940), A theory of spark discharge, *Phys. Rev.*, *57*(8), 722–728.

Mericam-Bourdet, N., M. Laroussi, A. Begum, and E. Karakas (2009), Experimental investigations of plasma bullets, *J. Phys. D: Appl. Phys.*, *42*(055207).

Metelmann, H.-R., T. V. Thi, T. D. Hoang, N. B. L. Thi, T. T. P. Thi, M. L. L. Tran, T. D. Van, T. T. H. Nguyen, T. L. Nguyen, D. Q. Le, T. K. X. Le, T. von Woedtke, R. Bussiahn, K.-D. Weltmann, R. Khalili, and F. Podmelle (2013), Scar formation of laser skin lesions after cold atmospheric pressure plasma (cap) treatment: A clinical long term observation, *Clin. Plasma Med.*, *1*, 30–35.

Mirpour, S., H. Ghomi, S. Piroozmand, M. Nikkah, S. H. Tavassoli, and S. Z. Azad (2014), The selective characterization of nonthermal atmospheric pressure plasma jet on treatment of human breast cancer and normal cells, *IEEE Trans. Plasma Sci.*, *42*, 315–22.

Morris, M. D. (1991), Factorial sampling plans for preliminary computational experiments, *Technometrics*, *33*(2).

Murakami, T., K. Niemi, T. Gans, D. O'Connell, and W. G. Graham (2013a), Chemical kinetics and reactive species in atmospheric pressure helium–oxygen plasmas with humid-air impurities, *Plasma Sources Sci. Technol.*, *22*(015003).

Murakami, T., K. Niemi, T. Gans, D. O'Connell, and W. G. Graham (2013b), Interacting kinetics of neutral and ionic species in an atmospheric-pressure helium-oxygen plasma with humid air impurities, *Plasma Sources Sci. Technol.*, *22*(045010).

Murakami, T., K. Niemi, T. Gans, D. O'Connell, and W. G. Graham (2014), Afterglow chemistry of atmospheric-pressure helium-oxygen plasmas with humid air impurity, *Plasma Sources Sci. Technol.*, *23*(025005).

Mussard, M. (2015), Physics of the propagation of atmospheric pressure discharges in dielectric tubes (plasma jets) and their interaction with surfaces for biomedical application, Ph.D. thesis, École Polytechnique, France.

Mussard, M. D. V. S., E. Foucher, and A. Rousseau (2015), Charge and energy transferred from a plasma jet to liquid and dielectric surfaces, *J. Phys. D: Appl. Phys.*, *48*(424003).

Naidis, G. (1997), Effects of nonlocality on the dynamics of streamers in positive corona discharges, *Tech. Phys. Lett.*, *23*(6).

Naidis, G. (2009), Positive and negative streamers in air: Velocity-diameter relation, *Physical Review E*, *79*(057401).

Naidis, G. (2010), Modelling of streamer propagation in atmospheric-pressure helium plasma jets, *J. Phys. D: Appl. Phys.*, *43*(402001).

Naidis, G. (2011a), Simulation of streamers propagating along helium jets in ambient air: Polarity-induced effects, *Appl. Phys. Lett.*, *98*(14), 141,501.

Naidis, G. (2012), Modeling of helium plasma jets emerged into ambient air: Influence of applied voltage, jet radius, and helium flow velocity on plasma jet characteristics, *J. Appl. Phys.*, *112*(103304).

Naidis, G. V. (2011b), Modelling of plasma bullet propagation along a helium jet in ambient air, *J. Phys. D: Appl. Phys.*, *44*(215203).

Naidis, G. V. (2015), On the ring-shaped structure of helium plasma jets, *IEEE Trans. Plasma Sci.*, *43*(3), 733–736.

Niemi, K., J. Waskoenig, N. Sadeghi, T. Gans, and D. O'Connell (2011), The role of helium metastable states in radio-frequency driven helium-oxygen atmospheric pressure plasma jets: measurement and numerical simulation, *Plasma Sources Sci. Technol.*, *20*(055005).

Ning, W., D. Dai, Y. Zhang, Y. Han, and L. Li (2018), Effects of trace of nitrogen on the helium atmospheric pressure plasma jet interacting with a dielectric substrate, *J. Phys. D: Appl. Phys.*, *51*(125204).

Norberg, S. A., E. Johnsen, and M. J. Kushner (2015a), Helium atmospheric pressure plasma jets touching dielectric and metal surfaces, *J. Appl. Phys.*, *118*(013301).

Norberg, S. A., E. Johnsen, and M. J. Kushner (2015b), Formation of reactive oxygen and nitrogen species by repetitive negatively pulsed helium atmospheric pressure plasma jets propagating into humid air, *Plasma Sources Sci. Technol.*, *24*(035026).

Obradovic, B. M., S. S. Ivkovic, and M. M. Kuraica (2008), Spectroscopic measurement of electric field in dielectric barrier discharge in helium, *Appl. Phys. Lett.*, *92*(191501).

Obrusník, A., P. Bílek, T. Hoder, M. Simek, and Z. Bonaventura (2018), Electric field determination in air plasmas from intensity ratio of nitrogen spectral bands: I. Sensitivity analysis and uncertainty quantification of dominant processes, *Plasma Sources Sci. Technol.*, *27*(085013).

Odrobina, I., and M. Cernak (1995), Numerical simulation of streamer-cathode interaction, *J. Appl. Phys.*, *78*(6).

Oh, J.-S., O. T. Olabanji, C. Hale, R. Mariani, K. Kontis, and J. W. Bradley (2011), Imaging gas and plasma interactions in the surface-chemical modification of polymers using micro-plasma jets, *J. Phys. D: Appl. Phys.*, *44*(155206).

Olszewski, P., E. Wagenaars, K. McKay, J. Bradley, and J. Walsh (2014), Measurement and control of the streamer head electric field in an atmospheric-pressure dielectric barrier plasma jet, *Plasma Sources Sci. Technol.*, *23*(1), 015,010.

Ono, R. (2016), Optical diagnostics of reactive species in atmospheric-pressure nonthermal plasma, *J. Phys. D: Appl. Phys.*, *49*(8), 083,001.

Pancheshnyi, S., S. Sobakin, S. Starikovskaia, and A. Starikovskii (2000), Discharge dynamics and the production of active particles in a cathode-directed streamer, *Plasma Phys. Rep.*, *26*, 1054–1065.

Pancheshnyi, S., S. Biagi, M. Bordage, G. Hagelaar, W. Morgan, A. Phelps, and L. Pitchford (2012), The LXCat project: Electron scattering cross sections and swarm parameters for low temperature plasma modeling, *Chemical Physics*, *398*, 148.

Papadopoulos, P. K., P. Vafeas, P. Svarnas, K. Gazeli, P. M. Hatzikonstantinou, A. Gkelios, and F. Clément (2014), Interpretation of the gas flow field modification induced by guided streamer ('plasma bullet') propagation, *J. Phys. D: Appl. Phys.*, *47*(425203).

Park, S., U. Cvelbar, W. Choe, and S. Y. Moon (2018), The creation of electric wind due to the electrohydrodynamic force, *Nature Comm.*, *9*(371).

Pechereau, F. (2013), Numerical simulation of the interaction of a plasma discharge at atmospheric pressure with dielectric surfaces, Ph.D. thesis, École Centrale Paris, France.

Pechereau, F., and A. Bourdon (2014), Influence of the polarity of the applied voltage on the reignition of a discharge below a dielectric layer in air at atmospheric pressure, *J. Phys. D: Appl. Phys.*, *47*(445206).

Pechereau, F., J. Jánský, and A. Bourdon (2012), Simulation of the reignition of a discharge behind a dielectric layer in air at atmospheric pressure, *Plasma Sources Sci. Technol.*, *21*(055011).

Pouvesle, J., A. Bouchoule, and J. Stevefelt (1982), Modeling of the charge transfer afterglow excited by intense electrical discharges in high pressure helium nitrogen mixtures, *J. Chem. Phys.*, *77*(817).

Qaisrani, M. H., Y. Xian, C. Li, X. Pei, M. Ghasemi, and X. Lu (2016), Study on dynamics of the influence exerted by plasma on gas flow field in non-thermal atmospheric pressure plasma jet, *Phys. Plasmas*, *23*(063523).

Raizer, Y. P. (1991), *Gas Discharge Physics*, Springer-Verlag.

Razavizadeh, S., H. Ghomi, and A. Sobota (2018), Atmospheric pressure plasma jet in controlled atmosphere: electric fields and propagation dynamics, *Plasma Sources Sci. Technol.*, *27*(075016).

Reuter, S., T. von Woedtke, and K.-D. Weltmann (2018), The kinpen - a review on physics and chemistry of the atmospheric pressure plasma jet and its applications, *J. Phys. D: Appl. Phys.*, *51*(233001).

Robert, E., E. Barbosa, S. Dozias, M. Vandamme, C. Cachoncinlle, R. Viladrosa, and J.-M. Pouvesle (2009), Experimental study of a compact nanosecond plasma gun, *Plasma Process. Polym.*, *6*, 795–802.

Robert, E., V. Sarron, D. Riès, M. Vandamme, and J.-M. Pouvesle (2012), Characterization of pulsed atmospheric-pressure plasma streams (PAPS) generated by a plasma gun, *Plasma Sources Sci. Technol.*, *21*(034017).

Robert, E., M. Vandamme, L. Brullé, S. Lerondel, A. L. Pape, V. Sarron, D. Riès, T. Darny, S. Dozias, G. Collet, C. Kieda, and J. M. Pouvesle (2013), Perspectives of endoscopic plasma applications, *Clin. Plasma Med.*, *1*, 8–16.

Robert, E., V. Sarron, T. Darny, D. Riès, S. Dozias, J. Fontane, L. Joly, and J.-M. Pouvesle (2014), Rare gas flow structuration in plasma jet experiments, *Plasma Sources Sci. Technol.*, *23*(012003).

Robert, E., T. Darny, S. Dozias, S. Iseni, and J. M. Pouvesle (2015), New insights on the propagation of pulsed atmospheric plasma streams: From single jet to multi jet arrays, *Phys. Plasmas*, *22*(122007).

Sakiyama, Y., and D. B. Graves (2007), Nonthermal atmospheric rf plasma in one-dimensional spherical coordinates: Asymmetric sheath structure and the discharge mechanism, *J. Appl. Phys.*, *101*(073306).

Sakiyama, Y., D. B. Graves, and E. Stoffels (2008), Influence of electrical properties of treated surface on rf-excited plasma needle at atmospheric pressure, *J. Phys. D: Appl. Phys.*, *41*(095204).

Sakiyama, Y., D. B. Graves, J. Jarrige, and M. Laroussi (2010), Finite element analysis of ring-shaped emission profile in plasma bullet, *Appl. Phys. Lett.*, *96*(041501).

Sands, B. L., B. N. Ganguly, and K. Tachibana (2008), A streamer-like atmospheric pressure plasma jet, *Appl. Phys. Lett.*, *92*(151503).

Sarron, V. (2013), Étude et optimisation d'une décharge "Plasma Gun" à pression atmosphérique, pour des applications biomédicales, Ph.D. thesis, University of Orléans, France.

Scharfetter, D., and H. Gummel (1969), Large-signal analysis of a silicon read diode oscillator, *IEEE Trans. Plasma Sci.*, *16*(1).

Schmidt-Bleker, A., S. A. Norberg, J. Winter, E. Johnsen, S. Reuter, K. D. Weltmann, and M. J. Kushner (2015), Propagation mechanisms of guided streamers in plasma jets: the influence of electronegativity of the surrounding gas, *Plasma Sources Sci. Technol.*, *24*(035022).

Schutze, A., J. Y. Jeong, S. E. Babayan, J. Park, G. S. Selwyn, and R. F. Hicks (1998), The atmospheric-pressure plasma jet: a review and comparison to other plasma sources, *IEEE Trans. Plasma Sci.*, *26*(6), 1685–1694.

Shao, X.-J., Z.-S. Chang, H.-B. Mu, W.-L. Liao, and G.-J. Zhang (2013), Experimental and numerical investigation on the interaction between Ar flow channel and Ar plasma jet at atmospheric pressure, *IEEE Trans. Plasma Sci.*, *41*(4), 899–906.

Shashurin, A., M. N. Shneider, A. Dogariu, R. B. Miles, and M. Keidar (2009), Temporal behavior of cold atmospheric plasma jet, *Appl. Phys. Lett.*, *94*(231504).

Shashurin, A., M. N. Shneider, and M. Keidar (2012), Measurements of streamer head potential and conductivity of streamer column in cold nonequilibrium atmospheric plasmas, *Plasma Sources Sci. Technol.*, *21*(034006).

Sigmond, R. (1984), The residual streamer channel: Return strokes and secondary streamers, *J. Appl. Phys.*, *56*(5), 1355–1370.

Simeni, M. S., B. M. Goldberg, C. Zhang, K. Frederickson, W. R. Lempert, and I. V. Adamovich (2017), Electric field measurements in a nanosecond pulse discharge in atmospheric air, *J. Phys. D: Appl. Phys.*, *50*(184002).

Simeni, M. S., E. Baratte, C. Zhang, K. Frederickson, and I. V. Adamovich (2018), Electric field measurements in nanosecond pulse discharges in air over liquid water surface, *Plasma Sources Sci. Technol.*, *27*(015011).

Slikboer, E. (2018), Investigation of Plasma Surface Interactions using Mueller Polarimetry, Ph.D. thesis, École Polytechnique, France and Eindhoven University of Technology, Netherlands.

Slikboer, E., O. Guaitella, and A. Sobota (2016), Time-resolved electric field measurements during and after the initialization of a khz plasma jet—from streamers to guided streamers, *Plasma Sources Sci. Technol.*, *25*(03LT04).

Slikboer, E., E. Garcia-Caurel, O. Guaitella, and A. Sobota (2017), Charge transfer to a dielectric target by guided ionization waves using electric field measurements, *Plasma Sources Sci. Technol.*, *26*(035002).

Slikboer, E., A. Sobota, O. Guaitella, and E. Garcia-Caurel (2018a), Electric field and temperature in a target induced by a plasma jet imaged using Mueller polarimetry, *J. Phys. D: Appl. Phys.*, *51*(025204).

Slikboer, E., A. Sobota, O. Guaitella, and E. Garcia-Caurel (2018b), Imaging axial and radial electric field components in dielectric targets under plasma exposure, *J. Phys. D: Appl. Phys.*, *51*(115203).

Sobota, A., A. Lebouvier, N. J. Kramer, E. M. van Veldhuizen, W. W. Stoffels, F. Manders, and M. Haverlag (2009), Speed of streamers in argon over a flat surface of a dielectric, *J. Phys. D: Appl. Phys.*, *42*(1), 015,211.

Sobota, A., O. Guaitella, and E. Garcia-Caurel (2013), Experimentally obtained values of electric field of an atmospheric pressure plasma jet impinging on a dielectric surface, *J. Phys. D: Appl. Phys.*, *46*(37), 372,001.

Sobota, A., O. Guaitella, G. Sretenovic, I. Krstic, V. Kovacevic, A. Obrusník, Y. Nguyen, L. Zajickova, B. Obradovic, and M. Kuraica (2016), Electric field measurements in a kHz-driven He jet - the influence of the gas flow speed, *Plasma Sources Sci. Technol.*, *25*(065026).

Soloviev, V. R., and V. M. Krivtsov (2009), Surface barrier discharge modelling for aerodynamic applications, *J. Phys. D: Appl. Phys.*, *42*(125208).

Sretenovic, G. B., I. B. Krstic, V. V. Kovacevic, B. M. Obradovic, and M. M. Kuraica (2011), Spectroscopic measurement of electric field in atmospheric-pressure plasma jet operating in bullet mode, *Appl. Phys. Lett.*, *99*(161502).

Sretenovic, G. B., I. B. Krstic, V. V. Kovacevic, B. M. Obradovic, and M. M. Kuraica (2014a), Spatio-temporally resolved electric field measurements in helium plasma jet, *J. Phys. D: Appl. Phys.*, *47*(102001).

Sretenovic, G. B., I. B. Krstic, V. V. Kovacevic, B. M. Obradovic, and M. M. Kuraica (2014b), The isolated head model of the plasma bullet/streamer propagation: electric field-velocity relation, *J. Phys. D: Appl. Phys.*, *47*(355201).

Sretenovic, G. B., O. Guaitella, A. Sobota, I. B. Krstic, V. V. Kovacevic, B. M. Obradovic, and M. M. Kuraica (2017), Electric field measurement in the dielectric tube of helium atmospheric pressure plasma jet, *J. Appl. Phys.*, *121*(123304).

Stafford, D. S., and M. J. Kushner (2004), $O_2(^1\delta)$ production in He/O_2 mixtures in flowing low pressure plasmas, *J. Appl. Phys.*, *96*(5).

Starikovskaia, S. M., K. Allegraud, O. Guaitella, and A. Rousseau (2010), On electric field measurements in surface dielectric barrier discharge, *J. Phys. D: Appl. Phys.*, *43*(124007).

Stollenwerk, L., J. G. Laven, and H.-G. Purwins (2007), Spatially resolved surface-charge measurement in a planar dielectric-barrier discharge system, *Physical Review Letters*, *98*(255001).

Synek, P., A. Obrusník, S. Hubner, S. Nijdam, and L. Zajickova (2015), On the interplay of gas dynamics and the electromagnetic field in an atmospheric Ar/H_2 microwave plasma torch, *Plasma Sources Sci. Technol.*, *24*(025030).

Talviste, R. (2016), Atmospheric-pressure He plasmajet: effect of dielectric tube diameter, Ph.D. thesis, University of Tartu, Estonia.

Talviste, R., I. Jogi, J. Raud, and P. Paris (2016), The effect of dielectric tube diameter on the propagation velocity of ionization waves in a he atmospheric-pressure micro-plasma jet, *J. Phys. D: Appl. Phys.*, *49*(195201).

Teschke, M., J. Kedzierski, E. G. Finantu-Dinu, D. Korzec, and J. Engemann (2005), High-speed photographs of a dielectric barrier atmospheric pressure plasma jet, *IEEE Trans. Plasma Sci.*, *33*, 310–311.

Tholin, F. (2012), Numerical simulation of nanosecond repetitively pulsed discharges in air at atmospheric pressure: Application to plasma-assisted combustion, Ph.D. thesis, École Centrale Paris, France.

Tholin, F., and A. Bourdon (2013), Simulation of the hydrodynamic expansion following a nanosecond pulsed spark discharge in air at atmospheric pressure, *J. Phys. D: Appl. Phys.*, *46*(365205).

Topala, I., and M. Nagatsu (2015), Capillary plasma jet: A low volume plasma source for life science applications, *Appl. Phys. Lett.*, *106*(054105).

Tschiersch, R., M. Bogaczyk, and H. E. Wagner (2014), Systematic investigation of the barrier discharge operation in helium, nitrogen, and mixtures: Discharge development, formation and decay of surface charges, *J. Phys. D: Appl. Phys.*, *47*(36).

Tschiersch, R., S. Nemschokmichal, M. Bogaczyk, and J. Meichsner (2017), Surface charge measurements on different dielectrics in diffuse and filamentary barrier discharges, *J. Phys. D: Appl. Phys.*, *50*(105207).

Turner, M. M. (2015), Uncertainty and error in complex plasma chemistry models, *Plasma Sources Sci. Technol.*, *24*(035027).

Turner, M. M. (2016), Uncertainty and sensitivity analysis in complex plasma chemistry models, *Plasma Sources Sci. Technol.*, *25*(015003).

Urabe, K., T. Morita, K. Tachibana, and B. N. Ganguly (2010), Investigation of discharge mechanisms in helium plasma jet at atmospheric pressure by laser spectroscopic measurements, *J. Phys. D: Appl. Phys.*, *43*(095201).

van der Schans, M., P. Bohm, J. Teunissen, S. Nijdam, W. Ijzerman, and U. Czarnetzki (2017), Electric field measurements on plasma bullets in n 2 using four-wave mixing, *Plasma Sources Sci. Technol.*, *26*(115006).

van Doremaele, E. R. W., V. S. S. K. Kondeti, and P. J. Bruggeman (2018), Effect of plasma on gas flow and air concentration in the effluent of a pulsed cold atmospheric pressure helium plasma jet, *Plasma Sources Sci. Technol.*, *27*, 095,006.

van Gessel, B., R. Brandenburg, and P. Bruggeman (2013), Electron properties and air mixing in radio frequency driven argon plasma jets at atmospheric pressure, *Appl. Phys. Lett.*, *103*(064103).

Viegas, P. (2015), Ionization in atmospheric-pressure helium plasma jets, Master's thesis, Instituto Superior Técnico, Universidade de Lisboa.

Viegas, P., F. Pechereau, and A. Bourdon (2018a), Numerical study on the time evolutions of the electric field in helium plasma jets with positive and negative polarities, *Plasma Sources Sci. Technol.*, *27*(025007).

Viegas, P., E. Slikboer, A. Obrusník, Z. Bonaventura, A. Sobota, E. Garcia-Caurel, O. Guaitella, and A. Bourdon (2018b), Investigation of a plasma–target interaction through electric field characterization examining surface and volume charge contributions: modeling and experiment, *Plasma Sources Sci. Technol.*, *27*(094003).

von Keudell, A., and V. S. von den Gathen (2017), Foundations of low-temperature plasma physics - an introduction, *Plasma Sources Sci. Technol.*, *26*(113001).

Vorác, J., A. Obrusník, V. Procházka, P. Dvorak, and M. Talába (2014), Spatially resolved measurement of hydroxyl radical (OH) concentration in an argon RF plasma jet by planar laser-induced fluorescence, *Plasma Sources Sci. Technol.*, *23*(025011).

Wang, L., Y. Zheng, and S. Jia (2016a), Numerical study of the interaction of a helium atmospheric pressure plasma jet with a dielectric material, *Phys. Plasmas*, *23*(103504).

Wang, Q., D. J. Economou, and V. M. Donnelly (2006), Simulation of a direct current microplasma discharge in helium at atmospheric pressure, *J. Appl. Phys.*, *100*(023301).

Wang, R., K. Zhang, Y. Shen, C. Zhang, W. Zhu, and T. Shao (2016b), Effect of pulse polarity on the temporal and spatial emission of an atmospheric pressure helium plasma jet, *Plasma Sources Sci. Technol.*, *25*(015020).

Waskoenig, J., K. Niemi, N. Knake, L. M. Graham, S. Reuter, V. S. von der Gathen, and T. Gans (2010), Atomic oxygen formation in a radio-frequency driven micro-atmospheric pressure plasma jet, *Plasma Sources Sci. Technol.*, *19*(045018).

Weltmann, K.-D., and T. von Woedtke (2017), Plasma medicine - current state of research and medical application, *Plasma Phys. Control. Fusion*, *59*(014031).

Wild, R., T. Gerling, R. Bussiahn, K.-D. Weltmann, and L. Stollenwerk (2014), Phase-resolved measurement of electric charge deposited by an atmospheric pressure plasma jet on a dielectric surface, *J. Phys. D: Appl. Phys.*, *47*(042001).

Winter, J., R. Brandenburg, and K.-D. Weltmann (2015a), Atmospheric pressure plasma jets: an overview of devices and new directions, *Plasma Sources Sci. Technol.*, *24*(064001).

Winter, J., J. S. Sousa, N. Sadeghi, A. Schmidt-Bleker, S. Reuter, and V. Puech (2015b), The spatio-temporal distribution of $He(2^3S_1)$ metastable atoms in a Mhz-driven helium plasma jet is influenced by the oxygen/nitrogen ratio of the surrounding atmosphere, *Plasma Sources Sci. Technol.*, *24*(025015).

Wu, S., and X. Lu (2014), The role of residual charges in the repeatability of the dynamics of atmospheric pressure room temperature plasma plume, *Phys. Plasmas*, *21*(123509).

Wu, S., Q. J. Huang, Z. Wang, and X. P. Lu (2011), The effect of nitrogen diffusion from surrounding air on plasma bullet behavior, *IEEE Trans. Plasma Sci.*, *39*(11), 2286–2287.

Wu, S., X. Lu, Y. Yue, X. Dong, and X. Pei (2016), Effects of the tube diameter on the propagation of helium plasma plume via electric field measurement, *Phys. Plasmas*, *23*(103506).

Xian, Y., P. Zhang, X. Pei, and X. Lu (2014a), Study on plasma jets generated with different working gases and propagating in different surrounding gases, *IEEE Trans. Plasma Sci.*, *42*, 2448–2449.

Xian, Y. B., Y. F. Yue, D. W. Liu, Y. Yang, X. P. Lu, and Y. Pan (2014b), On the mechanism of ring-shape structure of plasma bullet, *Plasma Process. Polym.*, *11*(2), 1169–1174.

Xiong, Z., and M. Kushner (2012), Atmospheric pressure ionization waves propagating through a flexible high aspect ratio capillary channel and impinging upon a target, *Plasma Sources Sci. Technol.*, *21*(034001).

Xiong, Z., X. Lu, Y. Xian, Z. Jiang, and Y. Pan (2010), On the velocity variation in atmospheric pressure plasma plumes driven by positive and negative pulses, *J. Appl. Phys.*, *108*(103303).

Yan, W., F. Liu, C. Sang, and D. Wang (2014), Two-dimensional modeling of the cathode sheath formation during the streamer-cathode interaction, *Phys. Plasmas*, *21*(013504).

Yang, Y., Y. Zhang, Z. Liao, X. Pei, and S. Wu (2018), OH radicals distribution and discharge dynamics of an atmospheric pressure plasma jet above water surface, *IEEE Trans. Rad. Plasma Med. Sci.*, *2*, 223–228.

Yonemori, S., and R. Ono (2015), Effect of discharge polarity on the propagation of atmospheric-pressure helium plasma jets and the densities of OH, NO, and O radicals, *Bointerphases*, *10*(029514-2).

Yue, Y., X. Pei, D. Gidon, F. Wu, S. Wu, and X. Lu (2018), Investigation of plasma dynamics and spatially varying O and OH concentrations in atmospheric pressure plasma jets impinging on glass, water and metal substrates, *Plasma Sources Sci. Technol.*, *27*(064001).

Zhang, Q., J. Zhuang, T. von Woedtke, J. F. Kolb, J. Zhang, J. Fang, and K.-D. Weltmann (2014), Synergistic antibacterial effects of treatments with low temperature plasma jet and pulsed electric fields, *Appl. Phys. Lett.*, *105*(104103).

Zhang, S., A. Sobota, E. M. van Veldhuizen, and P. J. Bruggeman (2015), Gas flow characteristics of a time modulated appj: the effect of gas heating on flow dynamics, *J. Phys. D: Appl. Phys.*, *48*(015203).

Zhu, Y. (2018), Numerical study of nanosecond capillary and surface dielectric barrier discharges: Kinetics, transport and fluid responses, Ph.D. thesis, École Polytechnique, France.

Zhu, Y., T. Takada, and D. Tu (1995), An optical measurement technique for studying residual surface charge distribution, *J. Phys. D: Appl. Phys.*, *28*, 1468–1477.

université PARIS-SACLAY | ÉCOLE DOCTORALE Ondes et Matière (EDOM)

Titre : Étude numérique du champ électrique dans les jets de plasma d'Hélium à pression atmosphérique et comparaisons avec des expériences

Mots clés : Jet de plasma, Champ électrique, Hélium, Simulation numérique

Résumé : Dans cette thèse de doctorat, des simulations numériques basées sur un modèle fluide 2D sont utilisées pour caractériser des jets de plasma d'Hélium pulsés. Le modèle pour les jets de plasma d'Hélium est développé pour décrire des jets qui s'écoulent dans des atmosphères de N_2 et O_2 et interagissent avec des cibles. La dynamique de la décharge dans les jets d'Hélium impactant une cible métallique à la masse est analysée pour des polarités positive et négative de la tension appliquée. Les évolutions temporelles et spatiales de champ électrique associées au premier front d'ionisation et au front de rebond sont en bon accord qualitatif avec des mesures récentes de champ électrique. Puis, l'interaction plasma-cible entre une décharge positive et une cible diélectrique en BSO est examinée en détail et les résultats sont directement comparés aux expériences. Un bon accord est obtenu entre les simulations et les expériences sur les évolutions temporelles et spatiales de champ électrique. Des valeurs maximales de champ électrique dans la cible de 5 $kV.cm^{-1}$ ont été obtenues expérimentalement et numériquement. Le champ électrique dans le plasma de l'ordre de quelques dizaines de $kV.cm^{-1}$ est fortement diminué par le changement de permittivité de la cible. Le champ électrique dans la cible est presque exclusivement dû aux fortes valeurs de charges de surface déposées sur la surface de la cible. Finalement, l'influence des évolutions de champ électrique sur la production d'espèces actives près des cibles est évaluée. On démontre qu'avec des cibles métalliques la synergie entre le premier front et le front de rebond augmente la production d'espèces près de la cible.

Title: Electric field characterization of atmospheric pressure Helium plasma jets through numerical simulations and comparisons with experiments

Keywords: Plasma jet, Electric field, Helium, Numerical simulation

Abstract: In this PhD thesis numerical simulations based on a 2D fluid model are used to characterize pulsed Helium plasma jets. The model for He plasma jets is developed to describe He jets flowing in N_2 and O_2 atmospheres and interacting with targets. The discharge dynamics in He jets impacting a grounded metallic target is analyzed with both positive and negative polarities of applied voltage. The temporal and spatial evolutions of electric field associated to the first and rebound ionization fronts are in good qualitative agreement with recent electric field measurements. Then, the plasma-target interaction occurring between a positive discharge and a BSO dielectric target is investigated in detail and results are directly compared with experiments. A good agreement is obtained between simulations and experiments concerning the temporal and spatial profiles of electric field. Maximum values of electric field inside the target of 5 $kV.cm^{-1}$ are found. The high electric field in the plasma of the order of dozens of $kV.cm^{-1}$ is severely depleted by the change of permittivity. As a result, the electric field experienced inside the target is almost exclusively originated by the high values of surface charge deposited on the target surface. Finally, the influence of the electric field evolutions on the production of chemically active species close to the targets is evaluated. It is shown that with metallic targets the synergy between the first and rebound fronts increases species production close to the target.

Université Paris-Saclay
Espace Technologique / Immeuble Discovery
Route de l'Orme aux Merisiers RD 128 / 91190 Saint-Aubin, France